UNIVERSITY OF SOUTHAMPTON

EVALUATION OF AN AIRBORNE OPTICAL REMOTE SENSING SYSTEM AND OPERATIONAL PRE-PROCESSING METHODS

Kyu-Young Choi

A thesis submitted for the degree of

Doctor of Philosophy

Faculty of Engineering, Science, and Mathematics

School of Geography

September 2003

UNIVERSITY OF SOUTHAMPTON

ABSTRACT

FACULTY OF ENGINEERING, SCIENCE, AND MATHEMATICS
SCHOOL OF GEOGRAPHY

Doctor of Philosophy

EVALUATION OF AN AIRBORNE OPTICAL REMOTE SENSING SYSTEM AND OPERATIONAL PRE-PROCESSING METHODS

by Kyu-young Choi

For remote sensing (RS) to be a truly useful technique in environmental science, the remotely sensed data need to be of known quality and reliability. The various steps known collectively as 'pre-processing' are vitally important as error and uncertainty at this stage has the potential to cause large errors in the final data product. Two important aspects of pre-processing were investigated in this research. First, the radiometric conversion by which acquired signals are converted into physically meaningful values, and which allows the comparison of datasets from different sensors or from different dates with the same sensor was studied. Second, the process by which the influence of the atmosphere is removed from the remotely sensed signal was investigated, focusing upon practical methods to correct data collected by CASI-2, an imaging spectrometer produced by Itres Research.

The radiometric (and other) characteristics of any sensor system are normally obtained by laboratory calibration. Several experiments were conducted to investigate and enhance knowledge of the performance of the CASI-2. The results suggested that wavelength calibration could reveal systematic optical distortion due to the 'optical smile' effect, and that the uncertainty of the wavelength calibration could be reduced if this was taken into account. Another possible source of error in the sensor calibration was identified and traced to a spatially non-uniform radiance standard, improvement of which could greatly reduce systematic error across the image. In addition to investigation of the conventional sensor calibration, several studies were conducted to acquire new information. For example, the spectral response function of the CASI-2 was determined independently of the manufacturer for the first time, using an innovative iterative procedure.

In addition to the research conducted on assessing the laboratory calibration procedure of the CASI, and investigating its performance, a series of laboratory investigations were undertaken to characterise the CASI Incident Light Sensor (ILS). Generally, the performance of the ILS, such as its angular response and radiometric linearity were acceptable for the purpose for which it was designed. However, signals in the short wavelength region seemed to suffer from relatively low signal-to-noise ratio.

In the interest of operational aspects of airborne multispectral RS, the contribution of atmospheric variation to remotely sensed data was reviewed, focusing, in particular, upon numerical models developed to characterise the sky radiance distribution. Atmospheric effects on remotely sensed data were reviewed and the effects of atmospheric variability studied in terms of how this influences the remotely sensed signal. Temporal variations in atmospheric clarity (and by extension, spatial variations typical of RS image data), were shown to cause errors which also affected multispectral ratio-based analysis. Two novel practical methods of atmospheric correction were developed following a series of practical experiments and theoretical studies.

Finally, two novel practical methods of correcting remotely sensed data for the effect of the atmosphere were presented. The first was an image-based method which can be used to achieve a qualitative improvement in image quality, a reduction in scene noise where this is due to shadowing, and an improvement in the accuracy of multispectral ratios. The second described an innovative way to use the data on downwelling irradiance measured by a roof-mounted sensor to correct for irradiance radiation affecting RS data. The method also has the potential to provide data on the sky irradiance distribution at the time of sensing.

When it is dark enough, you can see the stars.

- Charles A. Beard -

Acknowledgements

Conducting a PhD research is a very lonely journey with moments of joy of findings and deepness of confusions. This thesis is the result achieved during my travel in the long tunnel whereby I have been accompanied and supported by many people. I would like to take this opportunity to express my gratitude individually, all those who have assisted me in one way or the other with my PhD research.

My first thanks should go for my supervisor, Professor Ted Milton. Without his endless supporting and encouragement, this output would never exist. As well as academic advice, I owe him in the guidance, with patience, of me on the right track when some difficult moments. I am thankful also for other academic staffs in the department, i.e. Professor Peter Atkinson, Professor Giles Foody, Professor Paul Curran, Professor Dave Martin, Dr Fulong Wu, and Dr Jurgen Essletzbichler. They all have inspired and encouraged me with many forms of support.

It was great honour to accompany my colleagues and friends. Sally Kelday dedicated a lot of working hours and kindly went through my very first draft of this thesis. Karen Anderson and Michael Riedmann were great company in the UK Natural Environment Research Council Equipment Pool for Field Spectroscopy, and at the same time, shared ideas and advices on each other's interests. Dr Elizabeth Rollin gave me an insight of field spectroscopy and was always a joy of learning her inspiration and experience. Mr. Bill Damon made the impossible to the possible with his skilful hands. There are so many others who could not individually mention on this little paper. Some are finishing writing-up and some had left the department already, but I want to thank all of them who knows me for my achieve today.

For the thesis, the UK Natural Environment Research Council Equipment Pool for Field Spectroscopy supported this thesis through advice from Dr Elizabeth Rollin and by the loan of a field spectroradiometer. I gratefully acknowledged the provision of CASI and aircraft attitude data from Kyle Brown in the UK Environmental Agency. Jennifer Youngberg, University of Waterloo, Canada, kindly provided an original source code of the sky radiance distribution model. Tyme Witterbrood shared information about CASI-2 airborne hyperspectral sensor. Working with Fabrizio Tadina, David Davis, and other crews in The UK Natural Environment Research Council Airborne Remote Sensing Facility allows my own experiments with their instruments. When I stuck in developing my idea, many questions in the thesis were helped and inspired by members of Korean Students in Southampton University (KSSU) with various different subjects. Especially, I thank Dr. Ju-Han Lee and Ju-Neoung Jang in Opto-Electronics Research Centre (ORC), University of Southampton, UK, for many invaluable discussions about optic systems and fibre optic cables. Ju-Neoung Jang also helped me to setup and use his optical spectrum analyser.

I am very grateful for my wife, Kyo-Sook, for her love and patience during the PhD period. One of the great experiences that we lived through in this period was the birth of our son Junho, who provided an additional and joyful dimension to our life. Encouragements from by brother Kyu-Hong and parents cannot be forgotten. Their love and support were invaluable in both happy and struggle moments.

My gratitude would definitely be incompleted if I would forget to thank the cause of this whole achievement, using Aristotle's words, The Prime Mover. My deepest and sincere gratitude for inspiring and guiding this humble being.

Table of Contents

List of Figures

List of Tables

Glossary

a	Slope in linear regression line
A	Corrected absolute value [DN]
α	Azimuthal angle at the maximum slope angle [$degree$]
α_N	Absolute slope direction of ILS with respect to the North
α_{sam}	Spectral angle mapper
$a0,a1,a2,a3$	Parameters of assignable value that allow the sky radiance model to respond to the atmospheric radiation conditions
ACR	Absolute correction ratio
A_{dn}	DN for each DC record at a given IT
$ARVI$	Atmospheric resistant vegetation index
b	Intercept in linear regression line
β	Angle of slope due to the motion of aircraft [$degree$]
c	Column index
c_j	The ILS centroid value
c_s	Start number of the ILS region
D	Least square regression coefficients
D_{along}	Alongtrack pizel size on ground
DC	Dark current
$dcgr$	Dark current generation rate [DNs^{-1}]
D_{cross}	Crosstrack pixel size on ground [m]
DDV	Dense dark vegetation
D_{IFOV}	Alongtrack ground IFOV [$degree$]
DN	Digital number [DN]
$DPVE$	Dark point virtual endmember
$DS_{r,c}$	Dark current signal
ε	Residual error
E_o	Solar radiance at the top of the atmosphere
$E^{\bullet}$	Incident irradiance under shadow
E°	Incident irradiance under sunlit

Ed	Diffuse irradiance
e_{dark}	Sample electrons from DC
EFL	Effective Focal Length [*mm*]
EO	Electronic offset
Es	Solar radiance at ground
Es_{diff}	Diffuse solar radiance at the Earth's surface
Es_{dir}	Direct solar radiance at the Earth's surface
$etotal$	Total electrons sampled
FOV	Field of view [*degree*]
FSS_c	Frame shift smear for each pixel column
FTT	Frame transfer time [*msec*]
$FWHM$	Full-width half maximum [*nm*]
$g0,g1,g2,g3$	G-numbers
G	System gain [*electron* DN^{-1}]
G_d	Diffuse irradiance on a horizontal plane
$G_{d,i}$	Diffuse irradiance on an inclined surface
$Gf_{d,j}$	Flexible diffuse irradiance
G_h	Global solar irradiance on horizontal plane
$Gh_{d,j}$	Heliocentric diffuse irradiance
$Gi_{d,j}$	Isotropic diffuse irradiance
H	Sensor altitude [*m*]
ICU	Instrument control unit
$IFOV_{along}$	Alongtrack IFOV [*degree*]
$ILS_{i,j}$	ILS values [*DN*]
it	Integration time [*msec*]
Λ	Spectrum line wavelength dataset
$L^{\bullet}$	Reflected radiance under shadow
L°	Reflected radiance under sunlit
λ	Wavelength [*nm*]
$\lambda(r)$	Wavelength as a function of the CCD row [*nm*]
$<\lambda>$	Centre wavelength [*nm*]
L_{CCD}	Fixed CCD pixel size
$Lmin_{r,c}$	Minimum radiometric coefficients

Lp	Atmospheric path radiance [$\mu Wcm^{-2}sr^{-1}nm^{-1}$] (or [$mWm^{-2}sr^{-1}nm^{-1}$])
Ls	Radiance measured by a sensor [$\mu Wcm^{-2}sr^{-1}nm^{-1}$] (or [$mWm^{-2}sr^{-1}nm^{-1}$])
Lt	Radiance of ground target [$\mu Wcm^{-2}sr^{-1}nm^{-1}$] (or [$mWm^{-2}sr^{-1}nm^{-1}$])
LTC	Light transfer curve
μ	Cosine of the zenith angle of either incoming or reflected direction
MNF	Minimum noise fraction
N	$E^{\bullet}_n / E^{O}_n$
ne	Number of electrons
nfl	Noise floor
NPL	National Physical Laboratory, UK
$OCVI$	Offset corrected vegetation index
ϕ	Azimuth angle [*degree*]
Ψ	Angular distance in radian [*degree*]
ϕ_s	Solar azimuth angle in a slope plane [*degree*]
PCA	Principal component analysis
$Pc_{r,c}$	Corrected data value for pixel [*DN*]
$P_{r,c}$	32-bit summed raw data value [*DN*]
Q_0	Quantisation error
R	$E^{\bullet}_r / E^{O}_r$
$\Re$	Direct-to-diffuse ratio, *(1-N)/(1-R)*
ρ	Reflectance inside a hollow sphere
ρt	Reflectance of ground target
$<r>$	Weighted mean position of the CCD rows
rad	Radiance
rs,re	Start, end row number, respectively
$RSC_{r,c}$	Radiometric sensitivity coefficients for row r and column c
σ	Bandwidth, or standard deviation
σ_0	Instrument-induced signal variance
σ_{PT}	Photo/thermal-induced signal variance
σ_T	Total signal variance
s	Spherical albedo
S	Aircraft speed [*knot*]

S_0	Instrument-induced sample variance
s	Dark signal
S^2_T	Total variation
SHU	Sensor head unit
S_k	Polynomial coefficient (S-coefficient)
SL_c	Scattered light for row r at a given column c
SNR_{max}	Maximum Signal-to-Noise Ratio
SP_T	Photo/thermal-induced sample variance
SRF	Spectral response function
S_T	Total sample variance
t	Time [*minute*]
T	Transmittance
$T(\theta)$	Normalised total transmittance at incoming…
τ	Optical thickness
θ	Angular distance from the zenith in radians [*degree*]
θ_p	Pitch angle [*degree*]
θ_r	Roll angle [*degree*]
θ_s, ϕ_s	Solar position [*degree*]
θ_{sun}	Solar zenith angle in a horizontal plane [*degree*]
θ_y	Yaw angle [*degree*]
Ti	Atmospheric incident transmittance
U	The product of an arbitrary column-diagonal matrix
U	Corrected uniformity value for pixel
V'	Transpose of a matrix W of diagonal columns
W	The singular value array
X	Independent variable
$<x>$	Sample mean
Y	Dependent variable

Chapter 1

Introduction

1.1. Remote Sensing for Environmental Science

The goal of environmental remote sensing (RS) is to derive information about an object, area or phenomenon on the Earth's surface using data acquired with no direct contact (Campbell, 1995; Lillesand and Kiefer, 1994; Danson *et al.*, 1995; Mather, 1999). RS provides affordable quantitative data covering large area which conventional *in situ* measurements cannot achieve. The contribution of remote sensing to long-term global scale data collection has been highlighted by international level cooperation ever two decades, such as the World Climate Research Program and the NASA (National Aeronautics and Space Administration) Earth Science Enterprise (ESE) (NASA, 2000).

The volume of RS data continues to increase due to the increased number of newly developed RS instruments and better quality of data. There are more than 80 high spatial resolution spaceborne and airborne RS systems, for environmental research and other purposes, operating now and planned (Nieke *et al.*, 1997). most commonly optical sensors at altitudes of less than 800 *km*. As well as the quantity of RS data, rapid development of the sensing technology and the information management has contributed the capability to make remotely sensed measurements with finer spatial, spectral, temporal and angular resolution.

There have been dramatic developments in electronic engineering technologies, yet such developments are still underway in order to make RS sensors with more spectral bands as a complete tool for environmental science. This presents the user with several challenges. Firstly, the volume of data by hyperspectral sensors produced per unit area is much larger than that from conventional multispectral sensors. For example, for the same spatial dimensionality a full

spectral dataset from the Compact Airborne Spectrograph Imager (CASI) sensor (288 bands) is 24 times larger than that from the Airborne Thematic Mapper (ATM) sensor (12 bands). Some factors that should be addressed to help with such large datasets are sensor design in terms of higher rate signal acquisition, telecommunication technology that allows transmitting or restoring large amount of data more efficiently and data handling technology for use with hyperspectral remote sensing data. Secondly, new methods should be developed to retrieve information from higher spectral data that is not possible from the traditional multispectral data. Since the conventional multispectral remotely sensed data have only a handful of spectral bands with wider range of wavelengths, the recognition or comparison with the reference spectra is relatively simple and the algorithm is easily applied to the entire image. However, the uncertainty will increase in hyperspectral data because spectra of the objects on the ground are more sensitive to geometric changes, such as bidirectional effect of either incident or reflected radiance, in narrower wavelengths and because subtle difference in continuum spectrum is likely to occur in most wavelengths due to, for instance, non-uniformity of atmospheric conditions or other nonlinear factors. Of these, acquiring and handling large volume of data is continuously required for higher technical advances in computing and electronic engineering.

1.2. Environmental variables of interest

All the exciting advances in RS as described in the previous section, however, have little value without confronting the use of RS data in order to obtain new and valuable information on our understanding of nature (Danson *et al.*, 1995). The information obtained by RS methods, i.e. state variable, does not necessarily have a direct relation to the environmental variable of interest that is to be observed using RS instruments (Curran *et al.*, 1998). Curran *et al.* (1998) suggested that remotely sensed radiation (or the signal) is, due to the nature of the RS method, a mixture of several *state* variables that are the preliminary set of variables that contribute to the detected change in radiance.

The successful application of RS for these environmental variables of interest is attained by clearly understanding the nature of the problem at hand and the appropriate use of available RS resources with respect to spectral, spatial and temporal attributes of the objects of interest (Lillesand and Kiefer, 1994). These three aspects should be addressed with care: the data must be at an appropriate spatial scale, the temporal sampling interval must match the environmental event of interest, and the observed changes in the electromagnetic radiation (EMR) must represent the geophysical and biophysical processes of interest. Usually it is difficult to accomplish all three dimensions at the same time, and hence researchers should decide between what 'can' and 'cannot' be achieved for their particular problem in the environmental applications of remote sensing (Curran *et al.*, 1998).

Depending on the relationship between those factors, environmental variables of interest that are recorded by RS systems, may be split into two groups (Jensen, 1996). First, those variables which are to be closely (or directly) correlated with the remotely sensed data without additional information. For instance, leaf area index (LAI, as state variable) is closely related to the biophysical variables, i.e. vegetation biomass. Another example of RS in geophysics shows that thermal infrared RS data is directly associated with the apparent temperature of a rock outcrop. The second class of variables, known as *hybrid* variables or *inference* variables were defined by Danson *et al.* (1995), and involve more difficult and complicated processing. The example in this case is to establish a model of vegetation, or crop, stress by using more than one biophysical variable, such as chlorophyll absorption, temperature and moisture content. Multi-temporal change detection is also a part of the hybrid product, as

biophysical variables in remotely sensed data are compared with those from others in the same area. The temporal application of the RS data has been increasingly recognised by many research groups.

The number of variables that can be directly obtained from remotely sensed data is unfortunately very small in comparison to those obtained indirectly. Thus, most effort is still being put into the development of the second method that potentially yields a large quantity of environmental information and expands applications of the remotely sensed data. Danson *et al.* (1995) outlined that there are three ways to extract environmental variables of interest for the *hybrid* variables: empirical, semi-empirical and theoretical approaches. The appropriate method from these groups is determined as a function of the background knowledge involved, i.e. statistics, mathematics and physics, and is at the core of digital image processing methods in RS as a method of enhancing information from the data (Jensen, 1996).

1.3. From data to information

The spectral responses of the environmental attributes discussed previously are often closely related to biophysical variables. For example, in studies of vegetation using data acquired by optical RS instruments, such as chlorophyll, leaf structure, or cells, it is of primary importance, whereas for the texture of the canopies, for instance, spectral data would be either of little use or too complex. Multispectral remote sensing data allow three ways to assess such information, i.e. spatial domain, spectral space, and feature space (Curran *et al.*, 1998). Subtle differences in 'greenness' of true colour, for example, could help in distinguishing types of vegetation, while NIR images provide the distinction between deciduous and coniferous trees that an ordinary RGB composite image of visible bands would be difficult to interpret with the human eye. Spectral assessment contains fundamental spectral information - within a specific range of wavelengths available in the instrument - of the Earth's surface. Since radiant energy reflected from vegetation canopy is often much greater in the NIR than in visible spectrum, the magnitude of the NIR 'plateau' in vegetation spectrum is used to determine differences between vegetation classes. In most multi- or hyper-spectral RS studies, multi-band processing in feature space is increasingly popular, because it has advantages for both spatial and spectral applications, with not much more complexity. In order to maintain its simplicity, it is commonly assumed that the spectral characteristics due to spectral mixing are linear, i.e. more than one ground target within a single pixel in the image can be represented by the simple addition of individual target spectra.

Spectral endmember analysis in feature space is a technique that is commonly applied to multi- or hyper-spectral data, but, as Adams *et al.* (1989) point out, it also has a role to play in global land cover mapping using data from conventional multispectral sensors with relatively few spectral bands, such as Landsat Thematic Mapper or NOAA (National Oceanic and Atmospheric Administration) AVHRR (Advanced Very High Resolution Radiometer). The reason for this is that, although the intrinsic dimensionality of TM and other optical sensors may be low for vegetated scenes (typically band 2 or 3 of Landsat TM), this is sufficient to capture the important features present, such as the proportion of green vegetation within a pixel. Further information is often neither required nor desirable for many global scale applications due to the volume of data involved.

Generic endmembers for agricultural scenes in optical wavelengths have been known for decades, and were described as the 'point of maximum greenness', the 'point of all shadow', the 'nonesuch or yellowstuff point' and the 'plane of soils' by early researchers such as Kauth and Thomas (1976) and Richardson and Wiegand (1977). Later work has added to our understanding of the plane of soils (e.g. Huete, 1988) and the point of maximum greenness (e.g. Tucker, 1977), but there has been relatively little investigation of the shadow endmember and even less on the yellowstuff endmember. The importance of shadow in controlling the reflectance of an incomplete vegetation canopy was demonstrated very clearly in a field experiment conducted by Ranson and Daughtry (1987) and shadow is an important parameter in many vegetation canopy models.

All applications of spectral unmixing presuppose a model of the scene being imaged (Milton, 1999). Furthermore, spectral unmixing is most meaningful when applied to a data set calibrated to physical units and for which the reference endmembers are known and characterised, both in physical terms and in their spectral properties.

1.4. Sources of uncertainty

As digital data, rather than *pictorial*, are widely preferable in today's RS systems (Lillesand and Kiefer, 1994), the remotely sensed data acquired by most RS sensors are no more than (spectral and spatial) records of counts or volts transformed into digital numbers (DN) within a sensor-specific range of digitisation quantisation. Therefore, the electrical response of the EMR emitted or reflected from the ground objects should be converted into physical units, i.e. radiance (for example, $[mWm^{-2}sr^{-1}]$), prior to image analysis to retrieve environmental variables of interest (Hildum *et al.*, 2001). They should be traceable to internationally recognised standards, such as SI units (Pollock *et al.*, 2003). This is particularly important when the data, once converted into a physical unit, are used as parameters in physical models for environmental studies.

This operation of retrieving environmental variables from state variables received by RS sensors, consists of 'pre-processing' and 'information extraction analysis'. While the latter is relatively deterministic depending upon the applications of RS data, the former is to discriminate true signal changes caused by objects of interest from noise sources in remotely sensed data and is a preliminary processing to the subsequent main analysis. While definition of pre-processing is relatively vague since there is no 'standard' list of the processing stages it is often the crucial factor in determining the successive failure of subsequent information-extraction and analysis. Three factors are the most common sources of deficiency in operational RS: the sensor itself (e.g. such as electronic and mechanical errors or flaws); the nature of the interaction between emitted radiation with the object on the ground and atmospheric constituents between the sensor and the target; and the sensor position relative to the radiance source (Danson, *et al.*, 1995).

The understandings of uncertainties of the sensor performance are obtained by calibration. Nonetheless, the signal recorded by a sensor detector still contains deficiencies resulting from the interaction of the EMR energy and objects other than the target of interest. The interferences occur because of constituents in the atmosphere or materials adjacent to the target that are sensitive to the visible and near-infrared (NIR) wavelength of the spectrum used in most optical RS systems.

As the result of such flaws or deficiencies, the accuracy of subsequent analysis and interpretation can be degraded (Meyer *et al.*, 1993). Since, unlike *in situ* measurements (as opposed to remote measurement), the data measured at a distance are not often directly related to the environmental variable of interest (Strangeways, 2000). To understand the processes (between the measured RS data and the inherent surface spectral signature) is therefore vital especially when the intention of using the remotely sensed data is to provide measurements to parameterise climate and ecological models at a more detailed spatial scale (Pinty and Verstraete, 1991).

In addition to providing a sensor calibration for conversion of each detector output to meaningful values, it is also necessary to characterise each individual sensor system, as different sets of data from the same type of sensor are always expected to show different properties in spectral, radiometric or spatial dimensions. As well as an understanding of the limitations of the sensor (determined during calibration), sensor characteristics are important to understand subtle variations in the spectral properties of the components being imaged

The signal detected by the remote sensing systems varies due to the following parameters: the geometry of Sun-target-sensor, the targets, the atmosphere and the sensor characteristics. In general, they may need additional field or laboratory data, thus imposing large costs and efforts, in order to identify true spectral properties on the ground and to interpret them as biophysical variables for the environmental applications with high accuracy.

The solar spectrum in visible and NIR wavelengths interacts with the various paths of the radiation travelling within the geometry of Sun-target-sensor. Due to the nature of the optical sensing and instrument design, signals detected by remote sensing systems are not directly associated with the inherent characteristics of objects in the natural environment. The link between the radiance measured by remote sensors and the environmental variables sought is still a centre of attention in the most remote sensing literature, even with the great achievements in environmental remote sensing during the decades.

The effects of atmospheric constituents (gaseous and particulate components in the atmosphere) on EMR are primarily in the form of scattering and absorption. Their contributions among the total radiation interaction vary in time and space with different spectral properties across the spectrum, resulting in adding and diminishing of the true ground-leaving radiance. In

a remotely sensed scene image, atmospheric effects are evident as, for example, blurring (e.g. due to abundance of aerosol particles), lowered signal (e.g. due to spectral absorption from atmospheric gases or reduced illumination from even higher density of aerosols, such as clouds), or non-uniform pixel values across the scene (e.g. due to anisotropic radiance distribution as a result of different viewing angles). More complicated effects can arise due to non-Lambertian target, or varying atmospheric path radiance caused by viewing or illuminating the target at different angles.

1.5. Pre-processing of remote sensing data

The correction of the aforementioned radiant interactions in remotely sensed data is named *pre-processing* (Campbell, 1996; Mather, 1999) or *image rectification and restoration* (Lillesand and Kiefer, 1994; Jensen, 1996). It is usually carried out prior to any retrieval or analysis of information from raw remotely sensed data (Teillet, 1986). Ironically, it is hard to define the exact meaning of pre-processing, mainly because there are several independent (in some ways quite dependent) tasks involved under the heading of 'pre-processing' (Mather, 1999). This is because the exact definition and significance of pre-processing varies entirely depending upon the nature of the problem to be analysed. There is still an ongoing debate regarding how much the original data are modified after pre-processing operations and what type of processing should be involved.

Pre-processing of remotely sensed data consists of geometric and radiometric corrections. As mentioned earlier, one of the advantages of remote sensing is the spatial scale it covers as an Earth observation tool, and for this reason remotely sensed data are often incorporated with map data, for instance, in geographical information systems or in land use data superimposed on a corresponding map. Geometric correction of remotely sensed data is essential in the case of image transformation to a map projection, change detection, or multi-sensor comparison. Remotely sensed data, though, cannot be used with maps without geometric correction. There are various sources of geometric distortions in the data (Table 1-1) (Bannari *et al.*, 1995; Jensen, 1996). Geometric correction is implemented as two steps, i.e. rectification of systematic and random distortions. The disadvantage of this correction is that the altered pixel values after re-sampling may have to be compensated with the modification in some analysis results.

The radiometric correction consists of sensor calibration and atmospheric correction, this is one of the key areas in remote sensing. Sensor calibration is an operation converting digital brightness values in remotely sensed data into accurate physical units, such as radiance or reflectance, in addition to verification of systematic and random errors of the sensor system itself. The precise calibration of remote sensing instruments is critical for those working in multi-sensor analysis, performing change detection, or running physical models (Milton *et al.*, 1995).

Nevertheless the information extraction problem often still remains even after sensor calibration. Radiation used for remote sensing must pass through the Earth's atmosphere, this may substantially influence the quality of images and data required from the sensors (Campbell, 1996). The signal received by the sensor, especially in the optical spectrum, is not only a record of the ground-leaving radiance that is to be used at that point, but also some proportion of reflected radiance that is attenuated by both atmospheric absorption and scattering between the radiance reflected target and the sensor. The physical property of radiance interaction through the atmosphere is extremely complex and highly dynamic (Mather, 1999). As applications of remote sensing demand more accurate products, these problems are being increasingly recognised. For example, overcast skies and cloud shadows on the ground in the United Kingdom (see Darch and Barber, 1983), frequently hamper multispectral data collection from both airborne and satellite remote sensing.

Type of error	Source of error	Description
Systematic	Scan skew	Caused by the forward motion of the platform during the time required for each mirror sweep. The ground swath is not normal to the ground track but is slightly skewed, producing cross-scan geometric distortion.
	Mirror-scan velocity	The mirror scanning rate is usually not constant across a given scan, producing along-scan geometric distortions.
	Panoramic distortions	The ground area imaged is proportional to the tangent of the scan angle rather than to the angle itself. Because data are sampled at regular intervals, this produces along-scan distortion.
	Platform velocity	If the speed of the platform changes, the ground track covered by successive mirror scans changes, producing along-track scale distortion.
	Earth rotation	Earth rotation as the sensor scans the terrain. This results in a shift of the ground swath being scanned, causing along-scan distortion.
	Perspective	For some applications it is desirable to have the MSS images represent the projection of points on Earth on plane tangent to Earth with all projection lines normal to the plane. This introduces along-track distortion.
Random	Altitude	If the sensor platform departs from its normal altitude or the terrain increase in elevation, this produces changes in scale.
	Attitude	One sensor system axis is usually maintained normal to Earth's surface and the other parallel to the platform's direction of travel. If the sensor departs from the altitude, geometric distortion results.

Table 1-1. List of geometric error sources in remote sensing scanning system (reproduced from Jensen, 1996). Some sources of error may only be applicable to specific type of sensor.

Atmospheric correction is an important research topic and as yet there is not a single solution or standard method. The methods for atmospheric correction are approached at the stage of sensor design in order to allow for atmospheric absorption and/or scattering properties. MERIS (MEdium Resolution Imaging Spectrometer) installed in ENVISAT-1 (ENVIronment SATellite) has, for example, several water absorption wavelength regions in one or more spectral bands, as well as an additional probe to measure solar irradiance at-top-of atmosphere at sensor platform level. Some other approaches have been developed in order to help minimise atmospheric effects from remotely sensed data, i.e. using image analysis (Railyan and Korobov, 1993), using radar sensor (Bouman and Hoekman, 1993; Moran *et al.*, 1997b), and crop growth/yield modelling or radiative transfer (RT) models (Maas, 1988; Moran *et al.*, 1995; Bouman, 1992). Cloud screening was discussed by Moran *et al.* (1998), and they concluded that the most successful methods are generally based on the combined analysis of both VIS and thermal IR data in order to obtain an image at a given time of year or a time series of high-quality images, as introduced by Derrien *et al.* (1993), Gutman *et al.* (1994), and Marshall *et al.* (1994).

The method of radiometric correction, including atmospheric correction, depends on the nature of the problem; the type of remote sensing data available (e.g. spatial and spectral resolution), accessibility of the ancillary data (e.g. *in situ* atmospheric information) and the requirement of accuracy of the biophysical information that is to be extracted as a by-product of remote sensing data (Jensen, 1996). Because of these, atmospheric correction in pre-processing data often tends to be limited or left to the user. Many remote sensing data providers currently produce some pre-processing products and distribute them to end-users. Table 1-2 shows that similar data standards are available from the pre-processing products throughout illustrated environmental agencies and organisations, and hence the end-user can choose a level of pre-processed product depending on the nature of problem that is to be investigated. Most pre-processing data products implement NASA's reference classification, while there may be some modifications depending on the sensor, platform types and available resources. Level 3 products for CASI-2 data are not currently available from NERC (Natural Environment Research Council) ARSF (Airborne Remote Sensing Facility) in which standard data product levels are based on NASA's definitions and will soon be offered using a radiative transfer model (Personal communication, NERC ARSF). It is interesting to note that in contrast to the other pre-processing techniques, i.e. radiometric and geometric products, atmospheric correction is not always available as a standard data product from all data providers.

Platform/Sensor	NASA reference		Landsat 7 (ETM+)		ENVISAT-1 (MERIS)		Dornier 228-101 (CASI-2)	
Data provider	**NASA**		**USGS**		**ESA**		**NERC ARSF**	
Raw data	Level 0	Reconstructed, unprocessed instrument/payload data at full resolution; any and all communications artifacts (e.g., synchronization frames, communications headers, duplicate data removed).	Level 0Rp	No radiometric or geometric correction applied. Scan lines are reversed and nominally aligned. Image data is provided in 8-bit (DN) values	Level 0	Time ordered instrument source	Level 0	Raw "sensor format" data at original resolution
Radiometric correction	Level 1A	Reconstructed, unprocessed instrument data at full resolution, time-referenced, and annotated with ancillary information, including radiometric and geometric calibration coefficients and georeferencing parameters (e.g., platform ephemeris computed and appended but not applied to the Level 0 data).	Level 1R	Including radiometric correction, but no geometric correction. Scan lines are reversed and nominally aligned. Image data is provided in 16-bit (radiance) values.			Level 1A	Level 0 data reformatted to image files with ancillary files appended
	Level 1B	Level 1A data that have been processed to sensor units (not all instruments will have a Level 1B equivalent).					Level 1B	Level 1a data to which radiometric calibration algorithms have been applied, to produce radiance or irradiance, and to which location and navigational information has been appended.
Atmospheric correction	Level 2	Derived geophysical variables at the same resolution and location as the Level 1 source data.					Level 2	Geophysical or environmental parameters derived from Level 1a or 1b data, may include atmospheric correction.
Geometric correction	Level 3	Derived geophysical variables mapped on uniform space-time grid scales, usually with some completeness and consistency.	Level 1G	Including both radiometric and geometric correction. Pixel value rescaled 8-bit (DN) values. The scene will be rotated, aligned, and georeferenced to a user-defined map projection. Geometric accuracy of the systematically corrected product should be within 250 meters (1 sigma) for low-relief areas at sea level.	Level 1B	Geolocated and calibrated TOA Radiance (angles and auxiliary data appended)	Level 3A/3B	Level 1b or 2 data mapped to a geographic co-ordinate system using on-board attitude and positional information only. 3B: 3A plus additional ground control points.
Biophysical information product	Level 4	Model output or results from analyses of lower level data (e.g., variables derived from multiple measures).			Level 2	Geolocated ocean, atm., land, geophysical param. + norm. water leaving rad (reflectance)	Level 4	Multi-temporal/multi-sensor gridded data products.

Table 1-2. Data products from four different remote sensing data provider and their own definitions (King and Greenstone, 1999; USGS, 2002; ESA, 1998, NERC ARSF, 2002).

1.6. Outline of the thesis

The work in this thesis (Figure 1-1) is directed at operational preparatory processing (i.e. pre-processing) to the main image analysis, in order to recover the true scene-leaving spectral radiance from the apparent signals acquired by a RS instrument. The main aim is to evaluate 'operational' pre-processing and its contribution to the applications of airborne multispectral RS sensors in terms of the accuracy and precision of the remotely sensed data. The relationship between the signal detected by the RS instruments and environmental variables are only achieved if the data represent physically meaningful values of the object of interest. Any discrepancies can be avoided, or at least minimised, once a good knowledge of the capabilities and limitations of the currently available optical RS systems is gained. This will be achieved by two approaches: sensor calibration that provides consistent quantitative measurement in physical units, and minimisation of the atmospheric effect that often limits the suitability of spaceborne and airborne RS as a true year-round tool (operational windows are determined by, for instance, the amount of cloud in mid-latitude regions).

Airborne RS is a viable means of testing new sensor technologies and providing the opportunity for the RS community to become familiar with state-of-the-art instruments, which may be planned for future satellite missions. Moreover, airborne sensors have shown a unique ability in the RS community to collect multispectral (or even hyperspectral) data whenever time constraints do not allow the use of spaceborne scanners, for example, to monitor oil spills, and events such as floods or forest fires (Mather, 1999). For nearly two decades, a number of RS sensors (or imaging spectroscopy) with high spectral/spatial resolution for airborne platform have been developed by many commercial and research organisations, and have played a significant role in various Earth resources and environmental mapping and monitoring tasks. In **Chapter 2**, the above aspects of airborne RS, regarding operational issues in environmental studies with comparison of those in spaceborne sensing will be reviewed. The contents include the characteristics of the RS systems with the aid of describing various types of currently operating airborne RS sensors.

For the RS system, the main focus in this thesis is the Itres instruments Compact Airborne Spectrographic Imager (CASI-2). The CASI-2 is a programmable imaging spectrometer designed to operate from light aircraft or helicopters. It is one of the most well-

known airborne multi- and hyper-spectral RS sensors and has the ability to measure down-welling spectral irradiance at the same level as the scene spectral radiance sensor. The CASI-2 is currently one of the most popular operating airborne RS systems in the UK. While the flexibility of airborne platform in terms of flight position (such as altitude and attitude of aircraft) and its speed determines the variable spatial and spectral resolutions of the scene image, the major sensor specifications are often established due to signal detection type decided during the sensor's designing stage. The detailed system characteristics of the CASI-2 are discussed in **Chapter 3**, where the sensor specifications, such as system architecture, laboratory calibration, operational performance, signal-to-noise ratio (SNR) and operational stability, are considered in addition to the manufacturer provided specifications.

The manufacturer's calibration procedure of the CASI-2 has been designed with some degree of compromise in terms of financial and time restrictions, resulting in limitations in several (spectral and radiometric) aspects of the sensor system. A summary of the full laboratory calibration procedure of CASI-2 routinely performed by myself on behalf of the UK Natural Environment Research Council (NERC) is presented in **Appendix A. Chapter 4** is dedicated to additional information about the CASI-2 determined from my own investigations independently from Itres Research Ltd.

One of the unique abilities of CASI-2 is simultaneous recording of incident solar irradiance with the scene image using a cosine receptor mounted on top of the aircraft, called the Incident Light Sensor (ILS). It is optional equipment provided by the CASI-2's manufacturer, which supposedly offers a route for the correction of at-sensor radiance to at-sensor reflectance and ideally toward at-ground reflectance. Unfortunately, there is not enough information available about the ILS either from the manufacturer or laboratory calibration to achieve this aim. A more thorough investigation of ILS was carried out and is presented in **Chapter 5**.

In **Chapter 6**, as well as background information about atmospheric effects on RS image data, the conventional approaches for minimising such interferences are briefly introduced in the second part of the thesis. The following three categories of atmospheric correction are identified,

1) Retrieval of atmospheric influence from the scene image itself,

2) Direct measurement on atmospheric condition at the time of sensing, and
3) Analytical approaches based upon radiative transfer (RT) theory.

In many RS applications, radiation transfer approaches are often used in conjunction with the others. Since most of the analytical methods were originally developed for atmospheric research purposes, their accuracy and precision are supposedly better than the other methods. However, operational application of the RT model-based methods is limited by their complexity in terms of their user interface and computational burden and the requirements of the generalised extra information, e.g. visibility at the time of the data acquisition (Vermote *et al.*, 1997). On the other hand, scene-based and direct measurement methods are relatively simple to apply with fewer variables and, in some cases, yield sufficient accuracy for removal of deficiencies caused by the effect of the atmosphere in the remotely sensed images. The effect of temporal changes of atmosphere in spectral feature space is tested in **Chapter 7** to investigate short-term temporal changes in the atmosphere as these place a fundamental limit on every method of atmospheric correction. Also, an improved definition of the shadow endmember which is present in virtually all natural scenes is tested on the basis of a series of field experiments and an empirical model is developed for the extension of the concept.

The third part of the thesis introduces practical atmospheric standardisation methods based on these approaches with the aid of the results from the first section. For the scene-based method, the precise selection of spectral endmember from the scene is acquired by highly accurate spectral and radiometric calibration of the RS instrument (Winter, 2001). Also when enhancing the usability of an ancillary measurement for the atmospheric correction, characterisation of the additional instrument and its synchronisation with the scene imaging sensor should also be verified (Kiedron and Michalsky, 2003). These requirements will be achieved using two approaches: scene based and additional direct measurement based methods. Thus, the subsequent chapters are divided into two parts:

1) The development of an operational image standardisation method that corrects spatially and temporally non-uniform illumination across the scene affected by atmospheric and geometric effects (**Chapter 8**), and
2) The establishment of sensor performance using data collected with the ancillary instrument (**Chapter 9**).

Finally, **Chapter 10** presents the conclusions from this study.

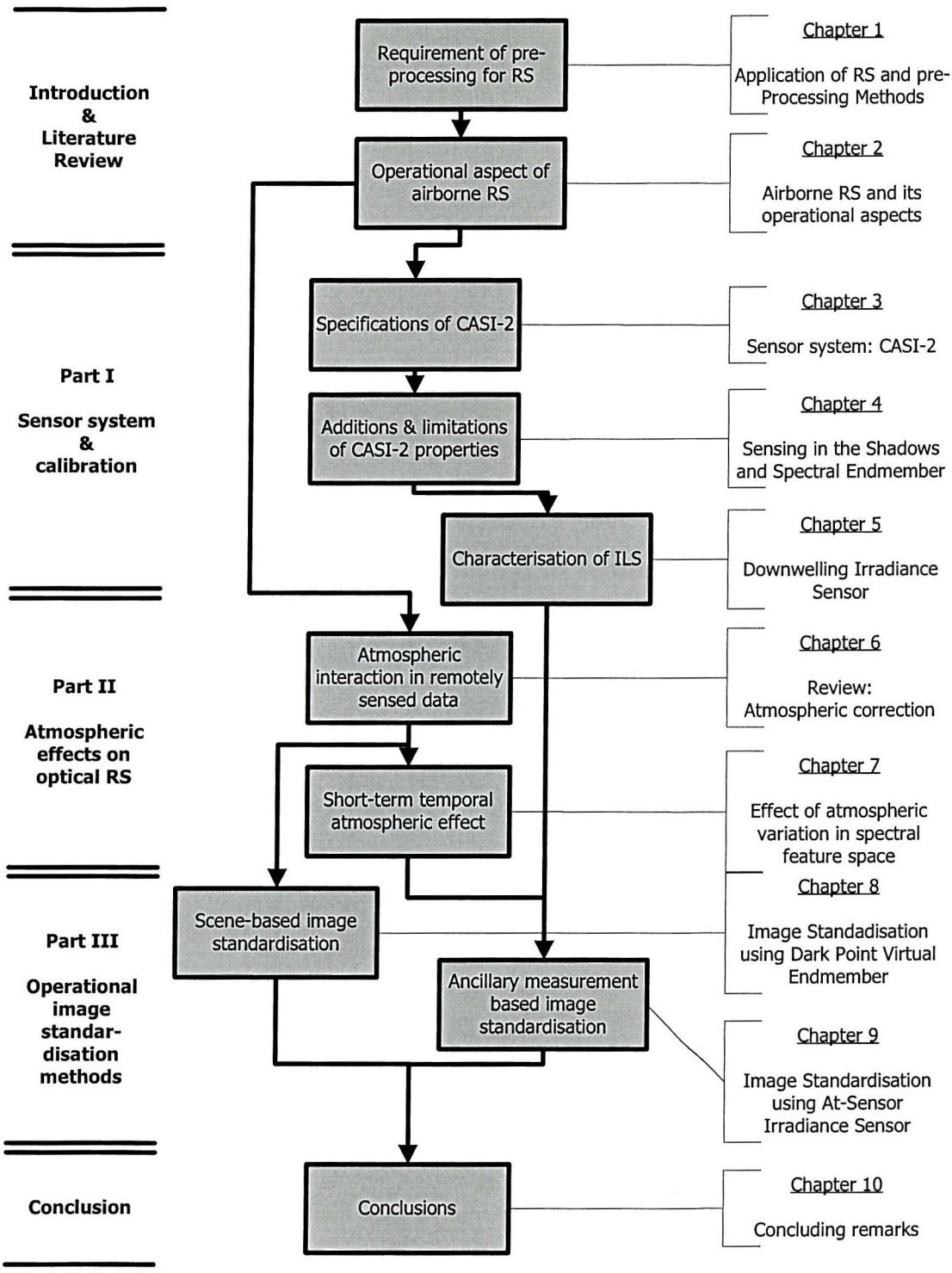

Figure 1-1. A flow chart of the structure of this thesis.

Chapter 2

Airborne multispectral remote sensing as an operational tool

2.1. Operational aspects of remote sensing

Many issues in environmental monitoring require the end-user to trade-off the variety of demands in spectral, spatial, and temporal dimensions of the Earth. Various remote sensing systems currently operating have their own capabilities and strengths in specific areas (Figure 2-1).

2.1.1. Spaceborne remote sensing

Remote sensing from satellite platforms provides a great opportunity for repeatable temporal sampling by orbiting around the Earth. This is an important benefit especially for long-term (e.g. seasonal or annual) data collection for environmental monitoring. The spacecraft orbit determines the number of imaging opportunities for any given site, through both the imaging repeat frequency and the degree of overlap between adjacent satellite swaths. Commonly used satellite sensors revisit the same area on the Earth's surface at intervals ranging from hours to days and provide data with spatial resolutions from over one kilometre (NOAA AVHRR) to one-metre panchromatic images (IKONOS-1). Remote sensing from satellite platforms has provided a special role in the investigation of dynamic phenomena at the level of the biome or continent, i.e. global scale (Justice and Townshend, 1994; Defries and Townshend, 1994), and its data acquisition contributes to studies of climate, biogeochemical and biophysical parameters, and ecosystem (Townshend *et al.*, 1994).

According to the many international global observing programs described in Section 1.1, remote sensing systems from satellites provide huge data sets and information to produce new knowledge of the Earth system. Unfortunately, there are few cases of truly operational, repeated applications using satellite sensor data (Legg, 1988, 1991). Cloud cover is the major constraint for operational applications of spaceborne multispectral remote sensing data in the optical region (Gastellu-Etchegorry, 1988). Whether for operational reasons or because of the nature of the phenomena being investigated, clouds and cloud shadows are a frequent problem, particularly in temperate latitudes and even in tropical regions. Some applications such as hydrocarbon or mineral exploration may require only one remotely sensed data set no matter what the season is. Most vegetation-related applications, however, require several scenes at very specific times in the phenological cycle (Legg, 1991; Phinn and Stow, 1996, Emery *et al.*, 1998).

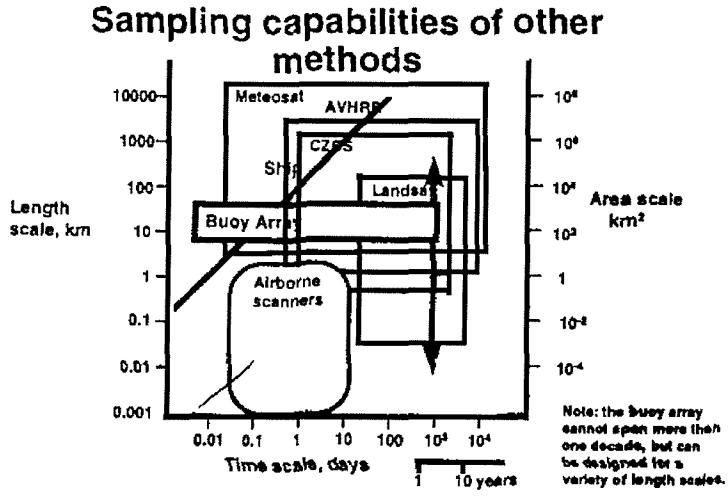

Figure 2-1. A plot comparing sensor coverage of area versus repeat time. Airborne sensors compensate the area where satellite sensors cannot cover (Adapted from a lecture note by I.S. Robinson).

In North Wales, UK, Darch and Barber (1983) carried out multitemporal monitoring of geobotanical variations in a copper bog, using four Landsat-2 images and a set of multispectral aerial photos. Bimonthly ground sampling was also conducted and showed that the multitemporal geobotanical variation may vary because of acquiring images from inappropriate times of the year. The authors resulted that the maximum plant-copper concentration occurred in April and May for which three out of four Landsat-2 images were available. Copper cycles from *in situ* field measurements, however, indicated that the concentration of copper in a plant increased toward flowering (Chebaevskaya, 1960) from November, for instance, in the case of

Armeria maritima. This copper bog monitoring, unfortunately, was not able to determine the successive year-round results from satellite imagery, because the number of images available was limited due to cloud-contamination over 10% of the study area and no data were available of cloud-free winter scenes.

The potential and application of multitemporal remote sensing are also reviewed by Moran *et al.* (1998), for providing spatial and temporal information for Precision Crop Management (PCM). Based on the information requirements of PCM, several parameters are identified in which remote sensing could provide information that is currently lacking or inadequate. Some of these parameters, such as crop phenology and crop growth, need multitemporal spectral measurements for time-specific crop management. Such seasonally variable characteristics are one of most common approaches in remote sensing

The two examples described above indicate how important seasonal monitoring is in using remote sensing, particularly for the detection of geobotanical variations, at times of year when weather conditions disturb the image.

A few researchers have reviewed the impact of cloud cover on multitemporal images in the UK (Cushnie, 1988; Legg, 1991). Landsat 4 (band 4) and Landsat 1, 2, and 3 (Band 7) were used to determine a point-sampling approach to score cloud-free images over 69 reference sites in Britain (Legg, 1991). There were a total of 4302 cloud-free views recorded over the reference sites out of approximately 11,000 images dating from 1975 to 1988, and around 80% of all acquired remotely sensed images over entire UK were insufficient for environmental monitoring without appropriate pre-processing. SPOT-1 HRV images, both panchromatic and multispectral, acquired from mid-1986 to mid-1987, reveal similar results; only about 30% of the total images had less than 25% cloud coverage (Cushnie, 1988). Multitemporal coverage at four time-windows for crop monitoring was even poorer; and soil survey during winter was barely possible (Legg, 1991). With current spacecraft sensors, crude land-cover mapping for automatic classification or some operational coastal environment monitoring might be feasible. They conclude that remote sensing applications requiring frequent imagery within specific time intervals are impractical in the UK (Cushnie, 1988; Legg, 1991).

2.1.2. Airborne remote sensing

Remote sensing operated by aircraft is another way of obtaining remotely sensed data. Not only is it an alternative remote sensing method, but also airborne remote sensing systems provide a unique opportunity to overcome problems from satellite platform systems. Figure 2-1 shows the sampling range of a number of remote sensing systems with an assumption of cloud-free conditions. Airborne remote sensors are filling the gap that other spaceborne sensors cannot cover in terms of temporal and spatial domain.

Considerable flexibility and timeliness, in particular, are a valuable aid to effective research of environmental systems in terms of spatial, spectral, and temporal resolution (Barnsley and Curran, 1990). Several authors, e.g. Barnsley and Curran (1990), Anger (1999) and van der Meer *et al.* (2001) have discussed the benefits (and disadvantages) of airborne remote sensing (see also Table 2-1).

- Airborne RS has always had better spectral resolution and signal-to-noise ratio than satellite RS. This is basically due to both longer exposure times, to much slower platform speed of airborne systems, and to finer spatial resolution and less atmospheric interference of reflected radiance due to relatively low sensor altitudes.

- Airborne remote sensing may actually expand rather than contract with the advent of the next-generation remote sensing due to the nature of its temporal sampling flexibility. It is possible to collect simultaneous radiometric data with ground-based measurements (Barnsley and Curran, 1990).

- One of the most important roles of satellite remote sensing, i.e. multitemporal sampling, is in reality restricted by atmospheric effects. This limitation may be compensated for using airborne sensors in terms of either highly variable environmental properties (i.e. tidal cycles) or its demanding critical date (i.e. growth phases of crops).

- With the help of data storage and processing technology, airborne sensors enable larger than mesoscale environmental monitoring (Barnsley and Curran, 1990; Pentreath, 1999). Al-Hargan (1997) surveyed over 400km of Qatar's coastlines in the Gulf, using an airborne Multi-detector Electro-optical Imaging Scanner (MEIS). The flight lines

covered the whole coastline of the Qatar peninsula, and investigated the vulnerability to oil contamination in coastal areas with 2*m* spatial resolution. Achal *et al.* (1999) flew the Compact Airborne Spectrographic Imager (CASI) from Buenos Aires to Calgary, Canada through more than 6 countries. The flight collected hyperspectral data of various ground types in weather ranging from clear skies to thick haze to moderate rain.

- Airborne remote sensing systems are capable of providing cost effective and speedy data, and can be easily upgraded using the rapid changes in their state-of-art design from a number of vendors. Even if a new satellite is launched to its orbit, its technology is already several years old because it takes about 10 years to develop satellite instrument, e.g. limited waveband range of SPOT HRV (Fuller and Parsell, 1990), and JERS-1 (Fuyo-1) sensor defect in SWIR bands (Nishidai, 1993). Repair of the sensor is difficult and impractical, although not impossible. As technology advances, the sensor development is becoming shorter. The Compact High Resolution Imaging Spectrometer (CHRIS), a new imaging spectrometer, was launched in October 2001 on board a novel space platform called PROBA (Project for On Board Autonomy). With a coalition of academic and commercial sectors, this whole project was developed very quickly for a major space project of this kind, from concept to delivery of the instrument took just two years (Cutter *et al.*, 1999).

- Programmable sensors were not available on spaceborne remote sensing systems until MERIS was launched in 2000, but it has been operational in airborne sensors since 1988 when the CASI sensor was developed.

- Spontaneous operation is possible for airborne remote sensing, such as an oil spill in the ocean or a forest fire. Sharma *et al.* (1996) depicted and assessed the flood maps of both 1988 and 1993 in Punjab, India. IRS-1A and ERS-SAR were used for the maps. The maps were superimposed to extract flood prone areas, and suggested the main reasons for each flood. They failed, however, to map detailed contouring, and recommended the use of small format aerial photos, i.e. using a multispectral sensor.

- Aircraft can fly under clouds or smoke, the sampling altitude of the platform is flexible. When extensive cloud cover obscures the Earth's surface, often during floods, the use of satellite multispectral images can easily miss the event, although there are some

lingering traces which one can detect up to several days later, e.g. wet soil in a flooded area. Airborne multispectral images enable the recovery of detailed land cover information under cloudy conditions.

Collaboration of airborne with satellite sensing systems produces synergistic output for global study. BOREAS (Boreal Ecosystem Atmosphere Study) in 1994 was set up to identify the exchange of radiative energy, heat, water, carbon cycling, and trace gases between the lower atmosphere and the boreal forest covering 17% of the world's land surface area. Over 350 airborne remote sensing missions were flown in this project. Their contributions to long-term environmental study are as promising as those of spaceborne remote sensing.

The biggest limitation of airborne remote sensing, however, is the limited area coverage, but this does not mean airborne remote sensing can only be used for local studies. Airborne sensed data shows more flexibility in special cases, such as in covering regions of interest (ROI) in 'linear' study areas rather than those of rectangular imagery obtained from most satellite images, e.g. coastlines (Gould and Arnone, 1997), river corridors, pipelines (Jadkowski *et al.*, 1994).

Category	**Airborne**	**Spaceborne**
Development cost	Variable	$10-$10000m
Launch cost	$10k-$100k	$10-$10000m
Cost per image	$10-$2000	$0-$4k
Infrastructure needed	Aircraft/airfield	Ground stations
Mission duration	Hours	Years
Flying height	0.2-10km	100-40000km
Flight path	Flexible	Fixed to orbital path
Ground speed	Variable	Fixed (6-7km/s or higher)
Ground Resolution	0.1-100m	1-1000m
Coverage	Local to regional	Regional to global
Calibration	Needed at least every season	Normally linear sensor degradation
Geometry	GPS/INS data	Earth curvature
Data transport	Anything	X-band downlink
Main advantages	Flexible and versatile	Regular revisits and global coverage

Table 2-1. Comparison of airborne and spaceborne remote sensing system (modified from van der Meer *et al.*, 2001).

The research reported in this thesis relates to studies undertaken with two of the major civilian airborne remote sensing organizations in the UK: the Natural Environment Research

Council (NERC) and the Environment Agency (EA). Both are actively operating a number of airborne sensors mainly in the UK, as well as an occasional campaign abroad. Figure 2-2 shows NERC flight missions during a flight season (normally from March to October every year) for the last three years, categorised by atmospheric conditions at the time of imaging. The number of flight missions has increased as well as the total number of images. The proportion of different atmospheric conditions of each flight mission, and its resulting image quality, are relatively uniform throughout the period, bearing in mind that flight cancellations due to poor weather were not taken into account.

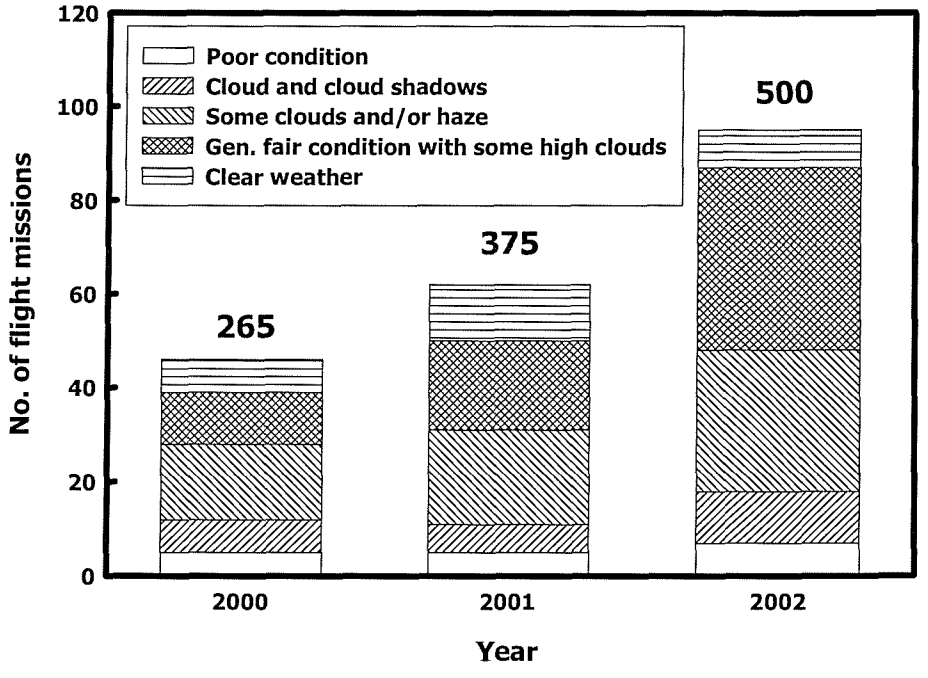

Figure 2-2. Yearly variation of atmospheric conditions of airborne remote sensing data from NERC ARSF. Numbers on top of each bar represent the total number of images throughout a year. Data were provided by NERC ARSF, 2003.

The proportion of airborne RS images with acceptable quality out of total number of images throughout a year is greater than that of satellite data, as described earlier. However, more than half of the airborne data still requires some degree of processing for atmospheric correction even for very simple applications in remote sensing.

The most significant constraints on the operational aspects of optical remote sensing are atmospheric conditions at the time of imaging. The spatial distribution of aerosol density, for

example, is highly variable and changes rapidly over relatively short periods, resulting in variable illumination at ground level. Many remote sensing systems are designed to avoid such variations, but in reality this limitation is often still problematic in operational remote sensing.

2.2. Multispectral remote sensing systems in airborne platforms

With the characteristics of optical airborne remote sensing as described in the previous section, remote sensing from airborne platforms plays an important role in many applications in environmental science and monitoring – either on its own or in association with satellite remote sensing. Airborne multispectral remote sensing systems can operate successfully in adverse conditions and under cloud when data acquisitions from satellites are limited. For example, airborne platform systems are more flexible for monitoring episodic events, such as forest fires, volcanic events, flooding, or oil spills (Tucker *et al.*, 1991; Robinove *et al.*, 1981; Stow *et al.*, 1993). Moreover, due to their low altitude operation and flexibility, airborne RS is also applied to acquire data at multiple altitudes over the same ground targets in order to establish atmospheric effects at the time of the image acquisition (Steven and Rollin, 1986). The comparison between airborne and satellite remote sensing data, in particular, provides a snap shot of vertical atmospheric conditions as long as aircraft flies over the ground target simultaneously with satellite overpass. Holm *et al.* (1989) compared nearly simultaneous low altitude airborne radiometer data with an aerial video system and Landsat TM data. They showed clearly that the surface reflectance values from both platforms are very different even under clear atmospheric conditions and succeeded in verifying their atmospheric correction algorithm using datasets from the two different platforms.

This section will review the main multi- and hyper-spectral remote sensing systems operated on airborne platforms by characterisation of the airborne sensors. In the following sections, classifications of the airborne data are based on the main objectives of the instrument and types of spatial and spectral information, such as shown by Nieke *et al.* (1997).

2.2.1. Airborne simulators

In terms of development and application of the airborne imaging spectrometer, there are two distinctive aspects that are not possible on orbital platforms. First, maintenance of the sensor system is easy and its upgrade to the state-of-art electro-optical engineering technologies

is prompt, since the airborne remote sensing system is based on the ground. Second, due to much slower platform speed than the satellite, the airborne sensor has greater exposure time for a detector, with the result that the signal reaching the sensor becomes sufficient for finer spatial resolution, higher spectral resolution, and greater signal-to-noise ratio performance. Airborne remote sensing systems currently operating worldwide have taken advantage of these attributes.

Flexible maintenance and operation of airborne remote sensing system allow researchers and developers to have the opportunity to become familiar and experiment with new instruments. In particular, airborne simulators for orbital remote sensing instruments are increasingly used to support future and planned spaceborne imaging spectrometer missions (van der Meer *et al.*, 2001).

The main objective of an airborne simulator is to develop and validate algorithms for the sensor design, calibration, and post-processing methods for its data product. For example, during the Airborne PRISM Experiment (APEX), which was developed by the European Space Agency (ESA) to support the future Land Surface Processes and Interactions Mission (LSPIM), a software simulator named Software Environment for the Simulation of Optical Remote sensing systems (SENSOR) was developed to investigate the interactions between elements of the remote sensing system with physical, mathematical or algorithmic models (Boerner *et al.*, 1999). These efforts helped to develop and launch a hyperspectral spaceborne imaging spectrometer (Compact High-Resolution Imaging Spectrometer; CHRIS-PROBA) within 2 years (Cutter *et al.*, 1999). More often, the sensor specification can be physically modified throughout a number of tests even after their results are applied to the development of a spaceborne sensor. For more than 10 years, a total of 24 field experiment campaigns have been conducted with the MODIS Airborne Simulator (MAS) since 1991, and more than half of the experiments were related to support upgrading and validating the Moderate Resolution Imaging Spectrometer (MODIS) on NASA's Terra mission (King *et al.*, 1996; NASA, 2003).

Although they are the prototype of the orbital system, even after their spaceborne versions are launched, most airborne simulators are often still used as independent instruments for scientific studies or as a temporary replacement when atmospheric conditions prevent the useful collection of satellite data (King *et al.*, 1996).

The sensor specifications are however not always identical to their spaceborne versions because of the financial constraints and/or the nature of differences between airborne and spaceborne platforms. Instead, some instruments are modifications of available airborne sensors, for example,

- Calibrated Airborne Multispectral Scanner (CAMS) from the Daedalus multispectral scanning systems as a simulator of Landsat Thematic Mapper, or of the cut-down version of its planned speceborne sensor
- Airborne Multi-angle Imaging SpectroRadiometer (AirMISR) instrument that only has a single camera in a pivoting gimbal mount unlike nine individual cameras in the Earth Observing System (EOS-AM1, now known as TERRA platform) MISR (Diner *et al.*, 1998)
- The airborne Polarization and Directionality of the Earth's Reflectances (POLDER) instrument that contains nine slots in a interference filter in comparison to sixteen slots including an opaque filter to estimate the CCD detector dark current in the POLDER aboard the Japanese Advanced Earth Observing Satellite (ADEOS) platform (Deschamps *et al.*, 1994; Leblanc *et al.*, 1999).

Some independent developments of airborne multispectral sensors tend to have the same (or similar) spectral bandset as in the spaceborne multispectral sensor. For example, the VNIR spectral bands (6 out of 12) of the (Enhanced) Airborne Thematic Mapper (ATM), developed by Daedalus Enterprise Inc.) have been matched to those of Landsat TM. In addition, mid- and thermal-infrared images are also recorded with a single detector with three individual dewars (NERC ARSF, 2003).

2.2.2. Hyperspectral sensors

The relatively slow speed of airborne platform allows more radiant energy to be exposed onto a detector in the instrument (~60 ms^{-1} of aircraft speed compared to ~6000 ms^{-1} for satellite), and its ability to fly in variable altitudes within the Earth's atmosphere provide finer and flexible spatial resolutions and wider swath angle (Anger, 1999). Consequently, for engineering perspectives of sensor design, airborne systems would have greater chances of providing radiometric and finer spectral resolution with some degree of compensation in other

dimensions. High spectral resolution, *imaging spectrometry*, that is to acquire images in hundreds of relatively narrow spectral bands, is assumed to give more precise information about the Earth surface, for applications such as mineralogy (Goetz, 1991), and hence reveal Earth resources in greater detail (Vane and Goetz, 1993). The word "hyperspectral" recently entered the remote sensing literature and is used to distinguish sensors with many tens or hundreds of bands from the more traditional multispectral sensors of which Landsat MSS and TM are probably the best known examples.

The first scanning imaging spectrometer, known as the Scanning Imaging Spectroradiometer (SIS), was developed by NASA's Johnson Space Center in the early 1970s. While the first imaging device was developed by Canada's Department of Fisheries and Oceans in early 80s (the Programmable Line Imager, PMI) and was soon followed by the Airborne Imaging Spectrometer (AIS), and its successor AIS-2. These were originally built to test newly developed infrared detector arrays and to demonstrate them as a proof-of-concept engineering test bed (Goetz *et al.*, 1985). Following the success of the AIS, non-experimental imaging spectrometers started to operate from 1987, namely the Airborne Visible/Infrared Imaging Spectrometer (AVIRIS). AVIRIS routinely provided well-calibrated hyperspectral data and allowed the science community to get familiar with hyperspectral data in preparation for the future spaceborne instruments, (Vane *et al.*, 1993). Until now, AVIRIS has been one of the most active airborne hyperspectral sensors that covers the electromagnetic spectrum from 400 to 2500 *nm* with 224 continuous spectral bands at <10 *nm* intervals. In Europe, most government organised research bodies operate imaging spectrometers in co-operation with private companies. The Reflective Optics System Imaging Spectrometer (ROSIS, since 1992, 430-850 *nm*) in the German Space Agency (DLR) was jointly developed by Dornier Satellite Systems (DSS, former MBB), GKSS Research Centre (Institute of Hydrophysics) and the DLR (Institute of Optoelectronics), and was also operated as an airborne simulator for the preparation of MERIS (Medium Resolution Imaging Spectrometer) on ESA's ENVISAT as well as MODIS. The DLR also jointly funded with the European Union to support the Digital Airborne Imaging Spectrometer (DAIS-7915, since 1995) from the Geophysical Environmental Research Company (GER) with wider spectral range than the ROSIS (400-1230 *nm*) (Lehmann *et al.*, 1995).

Since the first the civilian airborne spectrometer* was launched in 1981, developments in airborne imaging spectrometry have accelerated when many commercial companies started to become involved in sensor development in the late 1980s. The variety of airborne sensing systems currently available has various spectral and spatial capabilities, depending upon their major applications. New types of sensors are still under development both in the commercial sectors and in research communities.

Due to the nature of the commercial world, private companies tend to be prompt in responding in terms of adopting new technology. The NASA's AVIRIS was proposed in 1983 and took about 4 years to operation. Since two-dimensional detector array (CCD) technology was too immature at AVIRIS' design stage to be used for imaging spectrometry, especially for the short wavelengths, NASA decided to use linear array technology. In 1989, two years after the AVIRIS had been in operation, a Canadian company, Itres Research Ltd developed the Compact Airborne Spectrographic Imager (CASI) and brought it to the market. This hyperspectral sensor had 288 continuous spectral bands and used a two-dimensional CCD array that allowed almost a snapshot of cross track spatial imaging and better signal-to-noise ratio. The number of imaging spectrometers using a CCD array like CASI is increasing as it is one of the fastest growing areas in the imaging industry today (Hopkinson *et al.*, 2000). A similar type of imaging spectrometer would be the Airborne Imaging Spectrometer (AISA) developed by Specim based in Finland (Spectral Imaging Ltd, 2003), while other non-pushbroom type sensors, include the Hyperspectral Mapper (HyMap) developed by the Australia based Integrated Spectronics and operated by HyVista (Cocks *et al.*, 1998).

Despite the advantages of hyperspectral remote sensing revealed through over 20 years of airborne imaging spectrometers, most spaceborne systems still provide limited spectral information of terrestrial objects due to a relatively small number (4 to 12 bands) of broad bandwidths, e.g. Landsat TM or SPOT. While hyperspectral imaging spectrometry is still dominated by airborne platforms in the RS community, NASA initiated the development of the High Resolution Imaging Spectrometer (HIRIS) with 192 bands over wavelength range of 400-2500 *nm* in the early Earth Observing System (EOS) as an attempt to improve the spectral resolution of the spaceborne sensing system (Goetz and Herring, 1989). However, after the Challenger accident, this plan was postponed until a new future hyperspectral sensor is in orbit, and instead NASA decided to keep AVIRIS as a long-term facility (Vane *et al.*, 1993). The plan

* It was developed by Geophysical Environmental Research Company (GER) and used one-dimensional profile spectrometer acquiring 576 channels over 400-3500 *nm* spectral region.

to develop spaceborne hyperspectral sensors carried on afterwards through the Hyperspectral Imager (HSI), within NASA's small satellite program, but unfortunately the platform failed to operate after one month in 1988. After these incidents, space agencies tended to focus on the medium spectral resolution sensors, i.e. either selecting a few more spectral bands with medium size bandwidths between 10 and 100 *nm* or narrower bandwidths on specific features within the broader visible and NIR wavelength region. The Advanced Spaceborne Thermal Emission and Reflectance Radiometer (ASTER, launched in 1999) is a collaboration of scientific and industry organizations between NASA and Japan's 'Ministry of Economy, Trade and Industry (METI)' formerly known as Ministry of International Trade and Industry (MITI), as well as from France and Australia. The sensor has the highest spatial resolution (~15 m for VNIR and ~30 m for SWIR) of all instruments on the TERRA platform, and three separate instrument subsystems are effective in different spectral regions (VNIR, SWIR, and thermal). With a broad spectral range, the ASTER only has 14 bands: 4 bands in VNIR (including one backward looking), 6 bands in SWIR, and 5 bands in thermal infrared (TIR) region. On the same TERRA platform, the MODIS is operating mainly for global change research with rapid revisiting intervals (once in two days). With the wavelength range from 400 to 1440 *nm*, only two bands are imaged at spatial resolution of 250 *m* at nadir, whereas five bands have 500 *m* resolution and the remaining 29 bands (out of 36 bands) have 1 *km* spatial resolution.

However, with the experience and rapidly advancing technology from airborne imaging spectrometers over two decades, true hyperspectral data from a spaceborne platform is coming closer to the remote sensing community. The NASA's New Millennium Program (NMP) established in 1995 aimed to achieve technical advances mainly in a new generation of future space science and Earth science missions, including the development of hyperspectral remote sensing sensors. As one of its products, the Earth Observing –1 satellite (EO-1) was launched in 2000 and successfully completed its one-year sensor performance validation program (NASA, 2003). One of the advantages of the platform is that it passes exactly the same point of orbit within a minute of the Landsat TM satellite, so that sensors in both platforms are collecting data of the same ground areas. The EO-1 satellite carries the Hyperion instrument that transmits high quality hyperspectral data based on its heritage from the HIS. The Hyperion provides 220 spectral bands with continuous 10 *nm* intervals between 430 and 2400 *nm*. Due to the limitation of the data transmission capacity, each image has spatial dimensions of only 7.7 *km* of cross track by 42 *km* of along-track with 30 *m* pixel resolution, i.e. approximately 256 by 1400 pixels per image (~400 *Megabytes*). The operation of the Hyperion could be limited because it collects

the data on the basis of user-requested missions in order to extend its operation period and to lessen the burden of data transmission from the satellite to the ground receiving station. To date, the typical signal-to-noise ratio of a pixel spectrum in the Hyperion is around 60 (Cramer and Speciale, 2002), which is comparably smaller than that from conventional spaceborne sensors (up to 500). Another spaceborne imaging spectrometer under development, the Naval EarthMap Observer (NEMO) currently put on hold, has a target signal-to-noise ratio greater than 200 over the entire spectral range (it is typically greater than 250 for ocean scenes).

2.2.3. Multi-purpose and experimental sensors

Airborne remote sensing has the advantage of testing new types of instruments as well as to those for the future spaceborne instruments as described in previous sections. The Itres Research Ltd, manufacturer of CASI, developed a new SWIR sensor called the Shortwave Infrared Spectrographic Imager (SASI, range of 900-2500 *nm*) in 2002. During its development stage, a prototype of the SASI was available only for a short period and intensively tested in 17 sites of the UK and Belgium with various operating settings acquiring over 120 *Gigabytes* of data. Simultaneously with the flights, field spectroscopy instruments were deployed in order to calibrate and validate the SASI. NERC ARSF's aircraft had been rearranged to fit SASI and its navigation/attitude equipment.

There are examples of not only a single instrument test but also comparison between multiple instruments. For example, integration of the imaging spectrometer with a scanning Light Detection and Ranging (LIDAR) provides a powerful synergy for airborne remote sensing. Spectral information of ground objects and three-dimensional topographic information, as a new dimensionality, helps applications such as in vegetated areas where canopy height above the surface is important, in monitoring flood events, or in land topography and geomorphology. It is essential for such combinations that both systems should have highly accurate geometric correction systems, as well as positional (GPS) and aircraft attitude information from conventional airborne imaging systems. This type of synergistic system integration helps to improve the accuracy of both image and DEM products. The UK Environment Agency is one of organisations who are successful in application of the combined system (CASI and the Optech's Airborne Laser Terrain Mappers (ALTM) LIDAR).

2.3. Summary

Over the last two decades, the potential of RS techniques has been proved as the only affordable method of obtaining quantitative information in various areas of global environmental science. Initially, research was mainly focused on testing RS methods and collecting large quantities of data, but we are now beginning to develop methods to extract information from RS data and use them to help us understand our environment (NASA, 2000). Thus, the effective application and management of information from remotely sensed data is ever more important as huge amounts of data are produced by the increasing numbers of RS instruments with rapidly developing sensing technology.

Unfortunately, not all data are useable, since every RS system has its own limitations in terms of spectral, spatial, and temporal dimensions, hampering what would otherwise be an operational tool for environmental monitoring. For example, despite repeatable temporal sampling and spatial coverage, optical multispectral sensors in spaceborne platform are often hampered by atmospheric conditions, e.g. cloud in mid-latitude regions, which means that data acquisition at a specific time is not always guaranteed.

Airborne RS sensors improve this problem, as they fly underneath cloud which spaceborne sensors cannot see through. Also, airborne multispectral RS plays a unique role in environmental sciences, in parallel with spaceborne systems. This low altitude platform usually provides better spectral resolution and signal-to-noise ratio with temporal sampling flexibility. The spontaneous operation of airborne sensors makes data collecting for highly variable environments (e.g. tidal cycles and crop phenology) or episodic events (e.g. oil spills or forest fires) possible with relatively less constraint by atmospheric conditions.

The flexible maintenance and operation of airborne remote sensing systems allow airborne RS to be used as several types of test platforms. First, one of the strong airborne programmes is the use of airborne simulators for future orbital RS instruments, in order to develop and validate algorithms of the prototype sensor systems (i.e. instrumental design, calibration, and post-processing methods). Second, the development of RS sensors with new technology is tested and operated easily and quickly by airborne platforms. Hyperspectral sensing was operational more than a decade earlier in aircraft than in orbital platform. Lastly,

the flexibility of the instrument installation permits a variety of combinations of multiple sensors, such as hyperspectral sensor with thermal infrared sensors, or with LIDAR.

Even if a state-of-the-art airborne sensor acquires remotely sensed data at low altitude, and hence avoids much effect of the atmosphere (e.g. cirrus clouds), some level of pre-processing is necessary in most cases (Figure 2-2). The link between the physically meaningful information and the raw form of RS data requires us to move beyond RS as just a tool for obtaining 'pretty' pictures of the Earth's surface in time and space. Remotely sensed data acquired by most RS sensors is potentially a highly accurate record of the spectral and/or spatial records of electromagnetic radiation (EMR) emitted or reflected from an environmental variable of interest without direct contact (Mather, 1994).

Part I.

Evaluation of an airborne imaging spectrometer: the Itres Instrument CASI

The following three chapters describe a series of experiments performed by the author to investigate the performance of the Itres instruments CASI-2 sensor.

These were made possible because since 2002 the author has been responsible for performing the regular laboratory calibrations of the NERC CASI, and also because in 2002 the author was contracted to develop a software system to enhance the CASI-2 owned by the Environment Agency. The software package developed from this contract is described by Choi and Milton (2001 and 2002), but some associated laboratory investigations are described in Chapter 5.

It should be stressed that the material in chapters 4 and 5 especially develops significantly upon the routine calibration of the CASI-2 system, a summary of which is presented in Appendix A.

Chapter 3

Description of CASI system

3.1. Operation of CASI-2 in the UK

The NERC CASI-2 is mounted on a Dornier DO-228 aircraft leased from Deutsches Zentrum für Luft- und Raumfahrt e.V. (DLR), and operated by the NERC Airborne Remote Sensing Facility (ARSF) based in Oxford, UK. Data processing, archiving, and production line is operated by the NERC Remote Sensing Application Development Unit (RSADU), Monks Wood, UK.

Figure 3-1. Dornier Do228-101 D-CALM operated by NERC ARSF (NERC ARSF, January 2003).

The CASI image data from NERC ARSF are provided in level 1B format (Table 1-2) supplied on CD-ROMs in Hierarchical Data Format (HDF) (Figure 3-2). The HDF data contain information from various ancillary devices for recording the attitude and position of the aircraft (i.e. sensors) and basic meteorological and atmospheric parameters during the mission, as well as radiometrically corrected band sequential (BSQ) image file or other proprietary file formats.

The aircraft navigation data are obtained from four GPS antennae installed on top of the aircraft. The JAVAD AT-4 GPS operating of 20Hz synchronises the positional information of the aircraft with the scan line acquisition time from both CASI and Daedalus 1268 (ATM) sensors. The data integration system (IDS), AZ-16, originally developed for upgrading Daedalus scanning systems, combines the imagery from the scanners with the navigation and attitude data in order to provide remote sensing data mapped to a geographic coordinate system without the use of ground control points defined as Level 3A in NASA HDF product standard.

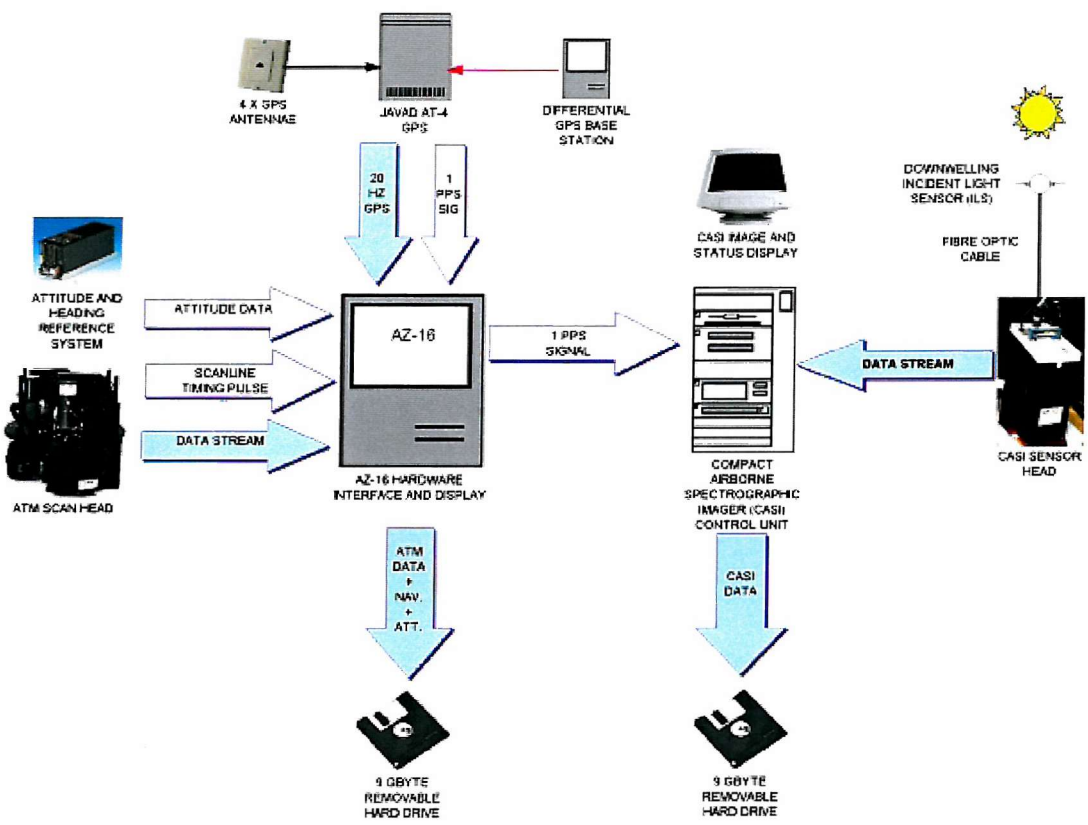

Figure 3-2. Schematic diagram of data integration system using in NERC ARSF (NERC ARSF, January 2003).

Software called AZGCORR, developed for the IDS, enables the user to extract the geometric correction information, which is subsequently applied to the data to create a Level 3A image. The geometrically corrected images are used to evaluate the pre-processing methods for atmospheric corrections throughout this thesis.

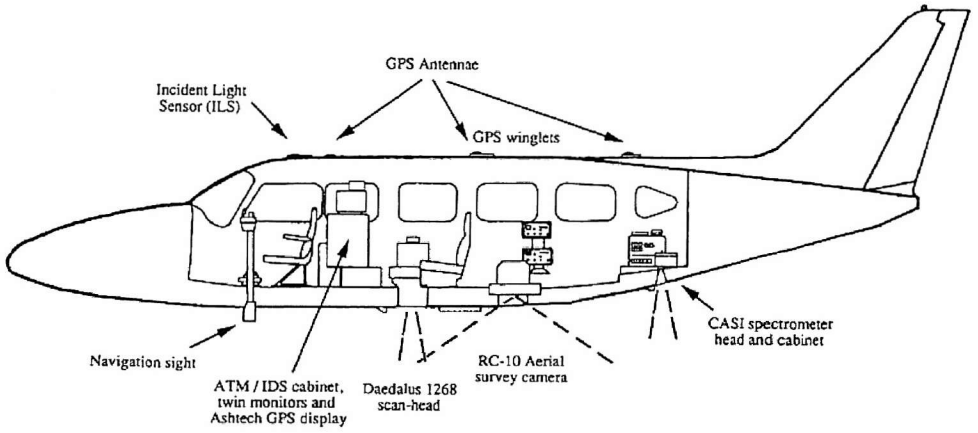

Figure 3-3. Illustration of the ILS installation and the position of the CASI on the aircraft. The diagram also shows the other instruments simultaneously operating with the CASI. It is from an old layout used by NERC ARSF before 2000, and proportion and scale may have been changed (Wilson, 1995).

The CASI-2 owned by the UK Environment Agency operates on a leased Cessna 404, twin piston-engine aircraft, based at Coventry airport, UK. For the flight navigation, a Novatell Millennium GPS system is currently used, while aircraft attitudes are recorded by an inertial navigation system synchronised with both CASI-2 and Optech 2033 LiDAR sensor.

Figure 3-4. Piper Navajo Chieftain G-WIND operated by the Environment Agency, UK. The photo was taken at Southampton Airport in 2001.

The National Centre for Environmental Data and Surveillance (NCEDS) in Bath, UK, performs data processing and archiving. The CASI-2 sensor in the EA aircraft is maintained and calibrated only once a year by the manufacturer. The uncertainty of radiometric performance of the sensor is, therefore, presumably relatively greater than that of NERC system, which is calibrated 2~3 times a year. Specifications of the CASI-2 systems owned by both organisations

are basically identical, except for the angle of field-of-view (FOV) of the foreoptic lens, 54.4° for the NERC and 37.8° for the EA. With the same cross-track pixel number, the EA system is expected to have finer spatial resolution but narrower ground coverage at the same flight altitude.

3.2. The Compact Airborne Spectrographic Imager (CASI-2): Overview

The Compact Airborne Spectrographic Imager (CASI) is a programmable multi- and hyper-spectral imaging spectrometer designed to operate from light aircraft or helicopters. The original CASI, as the first programmable pushbroom imaging spectrograph using two-dimensional CCD (Charge Cooled Device), was introduced by Itres Research Ltd. in 1989 (Figure 3-5). In addition to the continual improvements from its original specifications, a major upgrade of the sensor system was put on the market in 1998, namely CASI-2, effectively as 'second generation CASI'. The new CASI has been developed with lighter and smaller body and more controllable features, while the most operational specifications remained the same. Next generation of CASI, known as CASI-3, was announced in late 2002 with bigger CCD arrays, i.e. better spectral and spatial resolutions.

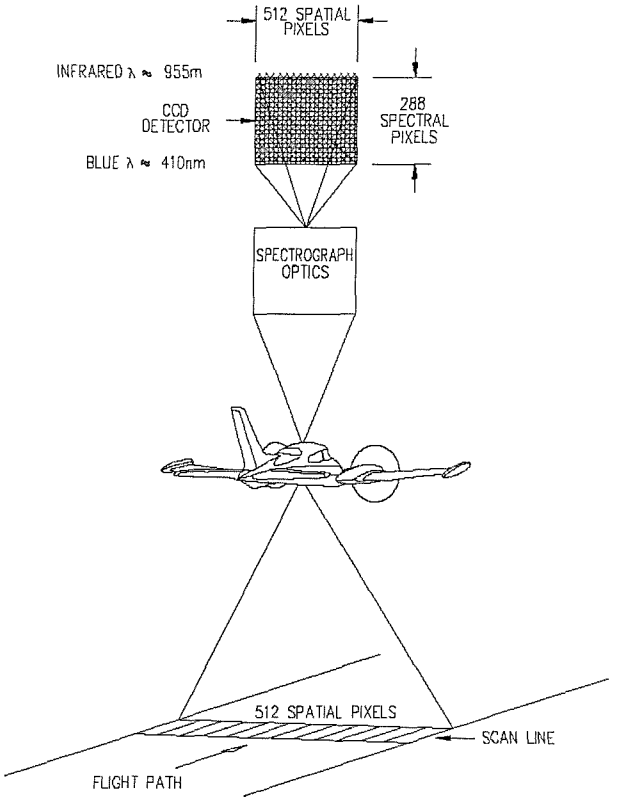

Figure 3-5. Principles of data acquisition in CASI-2 (Itres Research Ltd., 2001).

The CASI is successfully operated by more than a dozen of private and government organisations in more than nine countries, e.g. Canada, the United States, Germany, France, Spain, England, Japan, Italy, and Australia. In the UK, CASI is one of the most favoured airborne optical remote sensing systems and there are currently two CASI systems operated by government organisations, for environmental monitoring and environmental science research communities.

There are several characteristics of the CASI system that are distinctive in terms of their applications and instruments design, as follows,

1) Programmable pushbroom imaging spectrometer: The user defines the spectral bandset of the CASI within certain limitations. Such flexibility was not available on spaceborne remote sensing systems until the MERIS instrument was launched in 2000.

2) Controllable exposure time for the detector: It allows CASI image acquisition under various sky conditions, while maintaining high signal-to-noise ratio values. The sensor is normally more sensitive than aerial photography.

3) Simultaneous downwelling solar irradiance at sensor level: The CASI has an optional piece of equipment called the Incident Light Sensor (ILS). It is mounted on top of the aircraft and operates with the CASI, which provides the potential to convert the radiance pixel values into at-sensor reflectance values.

The following sections are an introduction to hardware specifications of the CASI systems, and the application and operation of the CASI currently using in the UK are reviewed. As the sensor performance is directly related to the detection method and the data storage speed for an acceptable signal-to-noise ratio, the imaging mechanism of the CASI is compared with the other currently operating sensors.

The CASI consists of three main components, the sensor display unit, the Instrument Control Unit (ICU), and the Sensor Head Unit (SHU) (Figure 3-6). Each component is connected with cables and is installed separately depending upon the aircraft layout.

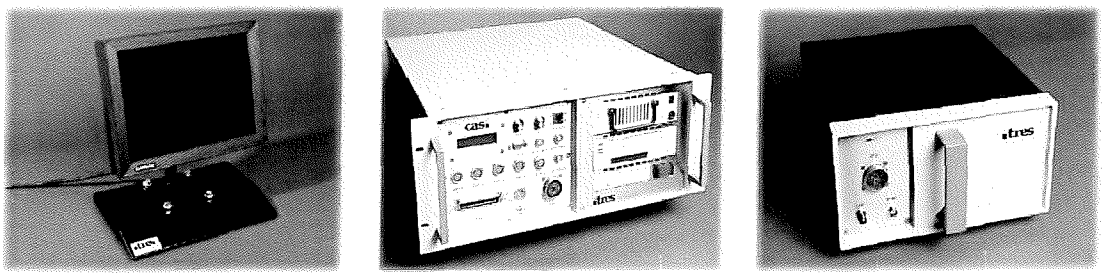

(a) (b) (c)

Figure 3-6. Components of the CASI-2 system. Sensor display unit (a), Instrument Control Unit (b), Sensor Head Unit (c) (From http://www.itres.com).

3.2.1. The Instrument Control Unit

The ICU contains the main processor and data storage devices. It deals with acquisition, processing, storage of data either in a removable hard disk drive (HDD) or in a digital tape drive, and transferring data from the SHU including the optional instruments such as navigation/position instruments or ILS (Figure 3-7). This component is basically a personal computer (166 *MHz* of processor speed) that controls all the other units with an input commands via a keyboard. The current status of the instrument is monitored and displayed via a display unit, as well as information on data acquisition or storage and modification of its configuration parameters.

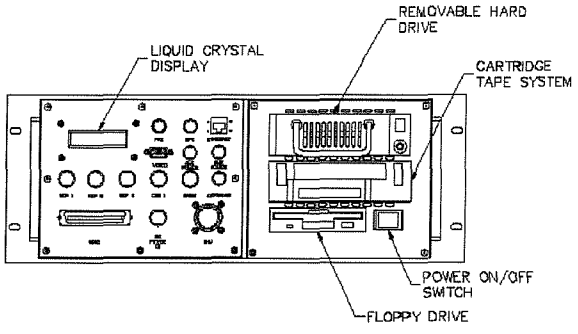

Figure 3-7. A schematic diagram of the ICU. Due to the aircraft installation issue, all functional connectors and buttons are to be found in the front panel of the ICU (Itres Research Ltd., 2001).

3.2.2. The Sensor Head Unit

The SHU has all necessary '*sensing*' parts. It mainly consists of a cooling system, an optical system, and a CCD detector. The mechanism of this component is similar to an ordinary camera. All optical components, i.e. entrance slit, lenses, mirrors, and reflection diffraction grating, are completely sealed in a vacuum chamber with a two-dimensional silicon charge coupled device (CCD) array detector. In the optical system, the cooling device maintains a temperature of 275 K (±5 ℃) with a constant humidity in order to avoid condensation in the chamber and to reduce/stabilise its own noise from dark current.

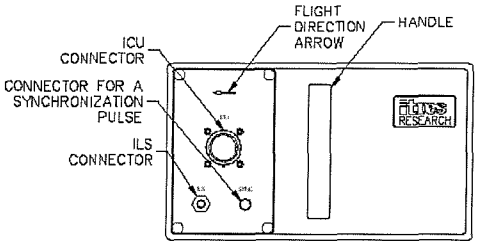

Figure 3-8. Top view of the SHU (Itres Research Ltd., 2001).

When light enters the CASI's SHU, it should pass the optical system before reaching and being detected by the CCD detector (Figure 3-8). An 'objective lens' focuses light onto the plane of a slit (~15μm). Only small portion of light passes the slit with the desired instantaneous field of view, since a single cross-track scan needs 1×512 pixels. A collimator lens parallelises the light in order to project onto a diffraction grating which disperses the light into a spectrum. Finally, a 'camera lens' refocuses the guided light onto a CCD array. Figure 3-9 shows the simplified light path within the optical system, but actually it uses a total of 17 lenses.

It has been suggested that loss of signal at short wavelengths is expected mainly due to the anti-reflective coating on the lenses. For example, at 440 *nm* transmission of light reached onto the CCD array is approximately 73 %, while by 425 *nm* it suddenly decreases to about 40 % according to the equation below.

$$T = (1-\rho)^n \qquad [3.1]$$

where, T Transmittance

ρ Intrinsic reflectance of a lens coating (between 0 and 1)
n Number of coated surfaces, i.e. 34 for CASI since each lens has two sides of coating (17×2)

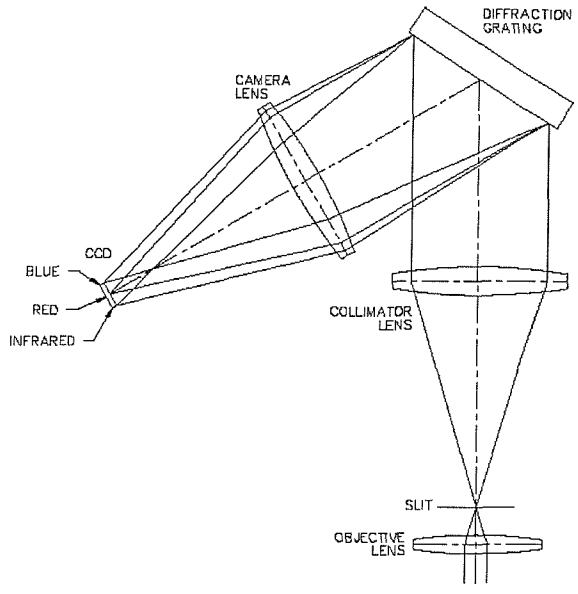

Figure 3-9. A simplified schematic diagram of the optical system in the CASI. Scales are not to scale (Itres Research Ltd., 2001).

The amount of light is controlled by an aperture setting. There are in total 7 aperture modes (including '*closed*' aperture). In CASI-2 this is controlled by software in the ICU, whereas it was manually control in the previous version of CASI. Aperture in the CASI system is altered by changing '*diameter*' of the opening through which light first enters the system. During the CASI operation, a higher aperture setting means that more light is entering the SHU. In general, aperture 3 is used under mid-latitude sky conditions.

The silicon CCD array has a pixel size of 578 (rows) and 612 (columns), and each pixel is 15 μm wide and 22.5 μm high. The physical dimension of the CCD is therefore 0.92×1.3 *cm*. In effect, 288×612 of the CCD array is used for image data, whereas 270 pixels in the bottom of the CCD array is mainly for data storage. However, only a part of the imaging area is reserved for the image data (Figure 3-10). 17 columns in both left and right sides in the CCD are kept for 'house-keeping purposes'. The rest of the area (288×578) is capable of accepting light, although only 512 of its columns and 288 of its rows are truly effective for the scene image. Rows of the imaging scene area (288) record spectral information at a given wavelength, whereas its 512 of columns are associated with spatial information. The remaining 66 columns are sensitive to

light but not used for the scene. Signals from this area is called 'auxiliary image data', and most of them are illuminated by signal from an optional ILS that will be described in the next subsection.

Aperture setting	*f*-stop
0	Closed
1	*f*/11
2	*f*/8
3	*f*/5.6
4	*f*/4
5	*f*/2.8[†]
6	*f*/2.8

Table 3-1. Aperture settings of the CASI available and its *f*-stop values.

The other dimension of the array detector in the CASI-2 measures spectral information in 288 rows at a given wavelength. The system has a "pushbroom" configuration, i.e. the full swath width is imaged instantaneously in a large number of spectral wavebands covering the visible and NIR regions of the spectrum between 430 and 900 *nm*. The wavelength corresponding to the position of pixels increases with decreasing row number, for example, the first row (row = 0) is active at 955 *nm* according to Figure 3-10. In general, the range of wavelengths effective to the CASI-2 is 545 *nm* ranging from 400 to 1000 *nm*, and its exact range is determined by manufacturer's routine calibration.

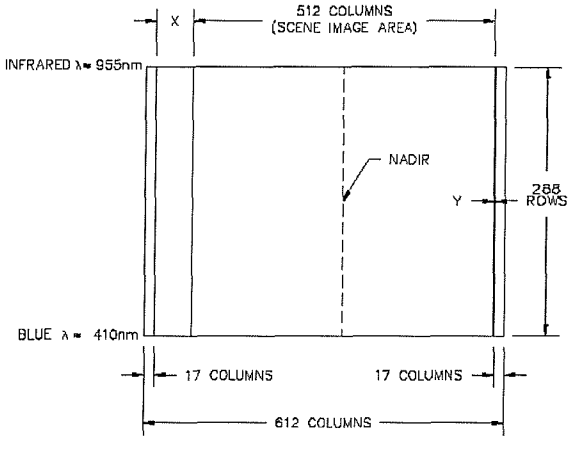

Figure 3-10. Schematic diagram of the CCD array used in CASI-2. This is only a part of the entire CCD pixels which are sensitive to light (Itres Research Ltd., 2001).

[†] The *f*-stops for the last 2 aperture settings are identical despite their aperture diameters actually being different. They are called 'limiting aperture' of the system, but the last aperture setting 6 is generally not used (Itres, 1998).

3.2.3. The Incident Light Sensor

The CASI-2 is one of the few airborne imaging spectrometers that have the ability to measure downwelling spectral irradiance at the sensor during operation as well as the scene spectral radiance. The incident light sensor (ILS) is an optional device in the CASI-2, and is designed as a cosine-corrected receptor designed to measure downwelling irradiance coincidentally with the CASI-2 (Figure 3-11). It is a simple device with no electric parts for the incident solar irradiance measurements, and its characteristics are established on the basis of the CASI-2 system. As the ILS is intended to measure the downwelling irradiance at the aircraft during data collection, it is typically mounted on the outside of the aircraft.

The sensor head has a diffused glass with a diameter of around 2*cm* fitted in the metal housing, and is connected to a 6 to 8 *m* of fibre optic cable. The other end of the cable has a FC/PC connector that is widely used in fire optic industry, plugging into the CASI-2 SHU (see Figure 3-8) and inside the SHU it is extended to the spectrograph slit in the optical system.

The irradiance received by the ILS travels through the fibre optic cable and is imaged in the hidden section of the CCD array (column from around 30 to 40, normally in the CCD column of 'X' as shown in Figure 3-10). The signal recorded in spectral bands is identical to those from the scene viewed by the CASI-2. In other words, number of spectral bands of the ILS will be the same as that of the scene data.

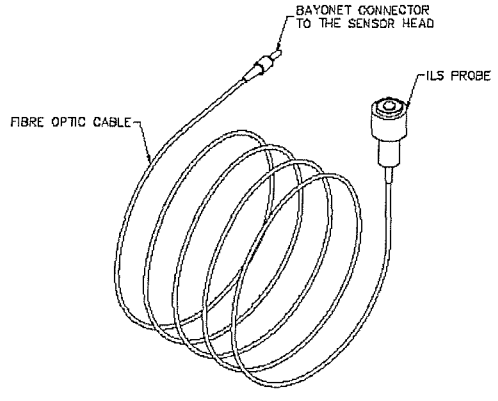

Figure 3-11. Components of the ILS (Itres Research Ltd., 2001).

3.3. Operation Modes

One of the important advantages of using an array detector in an imaging spectrometer is that users are able to select spectrum bands or sum them for specific bandwidths according to the nature of interests. The CASI-2 is one of the remote sensing instruments that allows user-defined spectral band selection in addition to the spatial parameters.

Such ability is required not only to give user flexibilities of data acquisition, but also to trade off between high spatial resolution, a maximal swath width and high spectral resolution due to technical limitations on the data recording rate (e.g. write speed of either tape drive or removable hard drive).

Operating Modes	
Spatial and Enhanced spectral	512 spatial pixels (across-track) ≤19 programmable spectral bands
Hyperspectral	≤511 programmable adjacent spatial pixels ≤288 spectral bands over the full spectral range
Full Frame	512 spatial pixels (across-track) 288 spectral bands

Table 3-2. Operational modes available in CASI-2 system

The following sections present available operating modes for the CASI-2 data acquisition (Table 3-2) and their constraints. This will provide information on understanding the CASI-2 image and planning the future missions.

3.3.1. Considerations of operation modes

Once a region of interest (ROI) is decided, three aspects are mainly considered in terms of the CASI-2 operation to obtain the most suitable CASI-2 data. First, a single pixel resolution determines details of ground features and size of area covered by an image. Second, radiometric sensitivity is controlled by aperture and integration time (IT) prior to the image acquisition. Third, the number of spectral bands and their bandwidth should be defined depending on the variables of interest on the ground.

Ground spatial resolution of a single pixel is divided into along track and cross track distance. This is directly related to the number of pixels in the image (particularly cross track scan) as well as the size of area covered. Due to the nature of CASI's scanning method, sizes of along track and cross track pixel may differ. They can be however coordinated to be the same when optimising the control factors.

The spatial resolution is a function of an angle of FOV from the object lens (Table 3-7) and the aircraft altitude during the CASI operation. While the FOV of 54.4° has EFL of 7.47 *mm* (11.22 *mm* for 37.8° FOV; see also equation [3.6]), cross track spatial resolution is,

$$D_{cross} = \frac{L_{CCD}}{EFL} \cdot H \qquad [3.2]$$

where, D_{cross} Cross track pixel size on ground [*m*]
L_{CCD} Fixed CCD pixel size (0.015 *mm*) [*mm*]
H Sensor altitude [*m*]
EFL Effective focal length [*mm*]

For along track pixel resolution, on the other hand, IT plays significant role in addition to the aircraft altitude that was the only factor controlled during the image acquisition, i.e. the along track resolution is the sum of the ground IFOV (GIFOV) and the product of flight speed and IT (Equation [3.3]). The GIFOV is the distance on the ground corresponding to the along track FOV, as follows,

$$D_{IFOV} = H \cdot \tan(IFOV_{along}) \qquad [3.4]$$

where, D_{IFOV} Along track ground IFOV (GIFOV) [*m*]
$IFOV_{along}$ Along track IFOV [degree]

And the along track pixel resolution is computed by equation using the additional term from Equation [3.4].

$$D_{along} = (S \cdot IT) + D_{IFOV} \qquad [3.5]$$

where, D_{along} Along track pixel size on ground [*m*]
S Aircraft speed (1 *knot* $\approx$ 0.5144 ms^{-1}) [ms^{-1}]
IT Integration time [*ms*]

Operator(s) of CASI-2 suggest checking the above equations in order to estimate IT, flight altitude, and its speed, mainly for 'square' pixel resolution. Since flight altitude is a factor in both cross track and along track resolution, it is more to do with overall spatial resolution, whereas IT and flight speed are mainly for along track direction. For example, with variable flight altitudes, cross track and along track resolutions are closely matched with IT of 25 *ms* and flight speed of 250 *knot* (Figure 3-12), and they can be closer either (or both) with faster IT or slower flight speed. Nonetheless, the differences between both pixel sizes remain same with the different flight altitude.

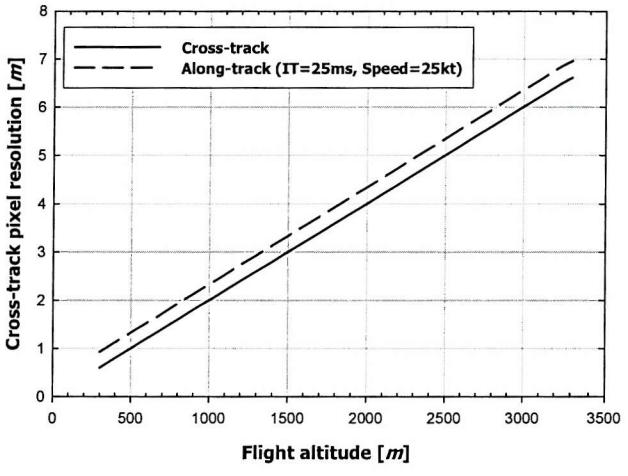

Figure 3-12. Example of cross track and along track pixel resolutions with flight altitude of the NERC ARSF CASI-2 (Itres Research Ltd., 2001).

Although the whole effort so far is mainly for 'square' pixel resolution, some variables from the spatial pixel resolution are also related to establishing the sensitivity of light detected by CASI-2, which leads to the radiometric resolution (see Section 3.4.2). In particular, IT plays important role of the radiometric resolution of CASI-2, since it controls a period of time during which the sensor opens the electronic gates and receives photons in the detector. Under a bright sunny sky, enough light will be detected even near the lower limit of IT, but in contrast, longer time will be needed for acquiring an appropriate signal under poor illumination conditions such as an overcast sky.

The aperture controls the amount of light entering the CASI-2 optical system with one closed and five open aperture settings (Table 3-1). These settings allow management of the

amount of light exposed to the imaging detector. Under normal conditions of sky illumination in the UK, for example, an aperture setting 3 (or 4 for patches of clouds) is used with typical IT of ~50 *ms*.

Spectral band selection is often limited by the processing speed of the CASI-2 hardware. Although the array detector in SHU has 288 spectral channels per spatial pixel, the full capacity has to be traded off against the number of spatial pixels. CASI-2 currently offers four operational modes to help user prioritising between spatial and spectral resolution: Full frame mode, Spatial mode, Original spectral mode, and Enhanced spectral mode. The following sections are description of these options.

There may be several other aspects to be considered for the most appropriate CASI-2 image acquisition, such as orientation of flight path and time (for optimised illumination condition), length of individual flight line (in terms of storage capacity), and so on.

3.3.2. Spatial mode

Spatial mode of CASI-2 allows full spatial resolution, 512 cross track pixels. In contrast, the number of spectral bands is reduced with a capability of up to 19 bands. Each bandwidth and its centre wavelength are to be programmable by user input of upper and lower wavelengths, as long as there is no overlap between neighbouring spectral bands (Figure 3-13.).

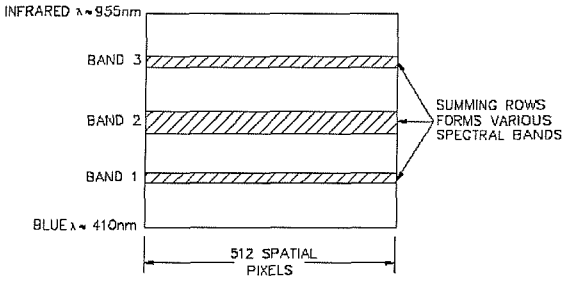

Figure 3-13. Band selection of CASI-2's spatial mode (Itres Research Ltd., 2001).

The narrowest band is possible at the estimated average spectral interval (~1.9 *nm*) by selecting a single row of the CCD array. Wider bandwidth can also be chosen and obtained by summation of adjacent rows in onboard memory before recording. Depending on the number of

spectral bands and their bandwidths, the minimal IT varies between 5 *ms* (1 band) and 30 *ms* (19 band). The lower minimal IT provides more flexibility for finer along track spatial resolution for a given flight speed (Equation [3.5]).

3.3.3. Original spectral mode

The original spectral mode is to collect full spectral information (288 bands) for given spatial resolution. As compensation due to the limited data transfer rate in the system, only partial spatial pixels are selected by number of 'Look directions'. Up to 39 columns of look directions are given by the user with an appropriate spacing (4,8, and 12) (Figure 3-14), i.e. there are gaps between each spatial pixel to increase area covered. The position of whole look directions can be changed by specifying the 'Centre Look Column' within 512 spatial pixels. With one look direction, the minimal IT will be 77 *ms*, while 162 *ms* for 39 look directions. The original spectral mode requires greater value of minimal IT than that in spatial mode by a factor of around 6. This suggests that care is needed to plan a flight mission in terms of spatial resolution (especially for along track pixel resolution).

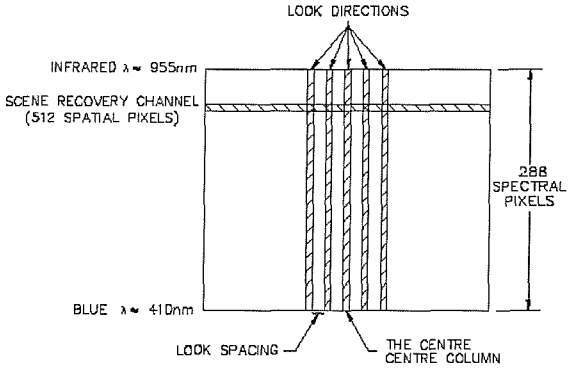

Figure 3-14. Band selection and SRC channel in CASI-2's original spectral mode (Itres Research Ltd., 2001).

Due to the small number of spatial pixels, a full scene image with 512 columns is simultaneously collected using just a single row (Figure 3-14) in order to find correct spatial pixel positions of look directions and to provide ground features around the look directions. This is called 'Scene Recovery Channel (SRC)', which is a monochromatic scene image. The spectral band of SRC is freely chosen within 288 rows.

3.3.4. Enhanced spectral mode

In Spatial Mode, there is full ability in the spatial domain (512 columns) but a restricted maximum number of spectral bands up to 19. In contrast, all 288 spectral bands are used in Original Spectral Mode with a limited selection of spatial pixels up to a maximum of 39 discontinuous columns. The constraints of both spatial and spectral modes as described above are flexibly traded off in Enhanced Spectral Mode. While summation of spectral rows in a given interval (for example, every 2 or 3 rows) reduces the total number of spectral bands, users will obtain continuous spatial columns even if the number of spatial pixels decreases (Figure 3-15). RSC is not recorded in this mode, because there is no gap between spatial pixels (i.e. continuous CCD columns).

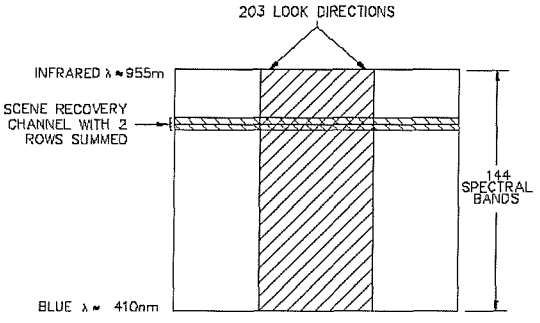

Figure 3-15. Band and spatial pixel selection of Enhanced spectral mode operation (Itres Research Ltd., 2001).

There are 14 configurations available in Enhanced Spectral Mode giving a set of optimal compensation between spatial and spectral dimension of the CASI-2 array detector. A list of the options is shown in Table 3-3. The full swath width of scene image is acquired with the maximum number of spectral bands, i.e. 48 bands, and a complete bandset available to the CASI-2 is offered with 101 spatial columns. Decreasing the number of spectral bands increases the maximum swath width, i.e. 6 to 36 bands at 511 spatial pixels.

Spatial resolution [pixels]	Spectral resolution [bands]	Number of rows summed [rows]	Approx. bandwidth [*nm*]
511	6	48	91.1
511	8	36	68.4
511	9	32	60.9
511	12	24	45.7
511	16	18	34.4
511	18	16	30.6
511	24	12	23.0
511	32	9	17.3
511	36	8	15.4
511	48	6	11.7
405	72	4	7.9
303	96	3	6.0
203	144	2	4.1
101	288	1	2.2

Table 3-3. List of available configurations in enhanced spectral mode (Itres Research Ltd., 2001). The approximate bandwidths are estimated by an assumption of the average FWHM of ~2.2 *nm* (Itres Research Ltd., 2001).

3.3.5. Full-frame mode

Full frame mode records entire signals available from the CCD array (Figure 3-16). Its operation during the ordinary flight condition is impractical due to significantly slower IT than any other operational modes (approximately 2 seconds for a single frame). Instead, this mode is mainly used for ground-based studies with stationary targets or instrument calibration.

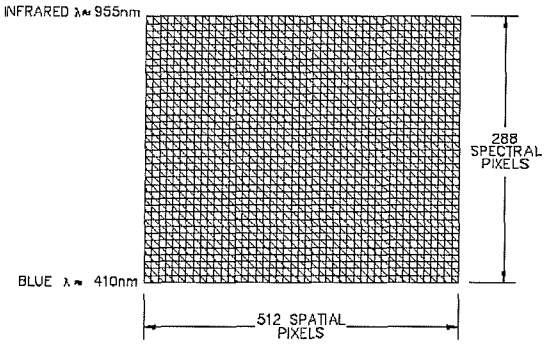

Figure 3-16. Operation of Full frame mode (Itres Research Ltd., 2001).

3.4. System Specification

CASI-2 has a typical system specification. Although every system is unique, the system specifications of CASI-2 are typical for a pushbroom sensor in that it has a two-dimensional array. The performance specifications for CASI-2 are outlined in detail in Table 3-4. In this section, items that characterise the CASI system are described, while their methods for establishing and maintaining the system are presented in the sensor calibration section later in this chapter.

Performance	
Instrument Type	Pushbroom Imaging Spectrograph
Instantaneous Field of View	Up to 37.8° across-track (mode-dependent) 0.077° along-track Other field of view options are available
Max. No. of Spatial Pixels	512 (across-track)
Max. No. of Spectral Bands	288 per spatial pixel (~1.9nm intervals)
Spectral Range	545 nm (anywhere between 400 and 1000nm)
Aperture	1 closed setting and 5 open settings from f/2.8 to f/11.0 (all under automated control)
Dynamic Range	4096:1 (12 bits)
Noise Floor	~1 DN (Digital Number)
Signal-to-Noise Ratio	~480:1 (peak)
Maximum Scan Rate	333 scan lines/second
Absolute Accuracy of Measured Radiance	± 2% (470 ~ 800 *nm*) ± 5% (430 ~ 870 *nm*)

Table 3-4. Performance specifications of CASI-2 with a standard FOV object lens described in CASI-2 Users Manual. This information represents the EA instrument and those for NERC are slightly different (see also page 39).

Specifications of the sensor systems are often determined by types of imaging scanning mechanism (spatial information) (Jensen, 1996). Scene data are built up by successive cross-track scanning and the along-track direction of the airborne platform. In terms of the optical sensor design, there are two types of cross-track scanning methods, i.e. a mechanical scan (using rotating or oscillating mirrors) and a simultaneous line scan using a slit. Conventionally, the latter is known as 'pushbroom' imaging spectrograph, whereas the former the 'whiskbroom' type. Because of the differences in mechanical and electrical scanning methods, pushbroom type sensors, such as CASI, normally have the advantage of higher instantaneous data rate over the whiskbroom sensor. This yields a better signal-to-noise ratio (SNR) with smaller instantaneous

field-of-view (IFOV), whereas greater angular coverage and higher spatial resolution are advantages for the whiskbroom sensor (Winter, 2001).

The characteristics of the sensor system are also influenced by its detection method (spectral information). There are basically two different ways of acquiring spectral information in an optical sensor: using discrete detectors (e.g. AVIRIS) or a line or area array (e.g. CASI). The discrete detector type which uses a single detector in each spectral band is normally used in the whiskbroom sensor, which scans from side to side to build up one cross-track line (Vane *et al.*, 1993). One of the advantages of the discrete detector type is that the radiometric performance is uniform across the image data and the sensor calibration is relatively easier. On the other hand, a two-dimensional array detector imaging spectrometer is more complex in terms of the system design and its maintenance since different detectors are used for spatial and spectral pixel values. Care is needed to monitor the variations of the sensor characteristics regularly, so as to keep a high standard of radiometric and spectral accuracy (Hildum *et al.*, 2001). Failure to do so could result in problems such as in spectral mixing/unmixing or spatial pattern analysis, though the problem may not be noticeable from visual inspection (Winter, 2001).

The CASI system is characterised mainly by two related specifications, i.e. signal and imaging. The signal related properties of CASI are about electrical behaviour of the signal received by each CCD pixel and the variation of illumination passing through the optical system. For the CCD signal in the imaging spectrometer, there are parameters that indicate the system performance, these are dynamic digital range, electronic offset (EO), dark current (DC), frame shift smear (FSS) rate, linearity, and pattern noise. Three factors produce optical distortions or unwanted signal onto the detector: optical smile (OS), keystoning, and scattered light (SL). The imaging related specifications are to specify the minimum and maximum limits of scene parameters, such as spatial, spectral, and radiometric properties. Some of them are not determined routinely during the CASI calibration since they are provided from the CASI's manufacturer, although all parameters play an important role in the sensor characteristics and monitoring its performance.

3.4.1. Signal related specifications

A description of the system parameters about signal is listed in Table 3-5 (array detector related) and Table 3-6 (optical system related).

Parameters			Description
Signal	Electrical	Dark current (DC)	The magnitude of the DC is a function of the CCD temperature and the integration time (IT). The temperature induced DC behaves exponentially, whereas the relationship between DC and IT is linear. While the CASI SHU encloses a cooling system for the optical chamber, the CCD temperature is maintained uniformly to 275 K during operation and thereby it is assumed that there is no portion of DC generated by the temperature variation. It is important to check DN with IT every routine CASI calibration, since it is directly related to the accurate radiometric conversion of the raw CASI DN, i.e. IT changes all the time during its operation depending upon the illumination condition.
		Electronic offset (EO)	The purpose of EO is to prevent the negative DN values when a noise component is included. A single photon observed by the silicon substrate in the CCD makes an electron-hole pair. The photon detection processing is a collection of free electrons that do not recombine with the lattice while an electronic gate opens (integration time, IT). The collected free electrons first of all should be amplified to an appropriate level of electrical signal or voltage values. EO is the smallest level where the amplifier starts recognising a 'signal' and transferring it to the following analogue-to-digital (A/D) conversion in the video digitiser of the CASI's ICU. Typical range for CASI is between 50 and 90 *DN*.
		System gain	In relation to EO, system gain represents the linear relationship (slope of the linear line) between the electrical signal output from the CCD pixels and the range of signal required at A/D input. In other words, it is a number of photoelectrons with respect to the unit DN. Typical range of the system gain for CASI is between 60 and 70 *electrons/DN*.

Dynamic range	The signal, amplified through the photoelectrons/signal relationship using EO and system gain, is transformed into a certain discrete integer numbers in an A/D/ converter. The range of these values is directly related to the radiometric resolution of the instrument. This is a pre-determined value that indicates the sensitivity of the detector. Currently, CASI-2 uses 12-bit (2^{12}, 0-4095).
Frame shift smear (FSS)	As long as the instrument is not fitted with a mechanical shutter, the detection of photon in each CCD pixel is a successive processing throughout every CCD pixel, which is controlled by electrical trigger. This is known as 'smear', and the time taken to complete scanning an entire detector array is called the 'frame shift smear (FSS)'. FSS is particularly important for most imaging systems, since it causes a time delay between adjacent pixels until it completes a single frame of scan. Although it is much faster than the cross-track scanning using mechanically rotating mirrors in whiskbroom sensors, FSS should be taken into account in two-dimensional detector array imaging spectrometers. In CASI, the time taken to complete scanning in light sensitive CCD pixels (288×612) is 1.8 *ms*. Since it is around 3% of normal IT (~50 *ms*) for image acquisition, FSS plays an important role especially low signal in the blue part of the spectrum (Babey and Soffer, 1992).
Linearity	To see if the sensor response is a linear function of the received illumination. It was reported that the overall linearity of the CCD array is less than 1% (Haron *et al.*, 1992). Although it is not measured during the manufacturer's calibration procedure, linearity of the CCD is generally assumed.
Pattern noise	This is mainly due either to the mechanical interference (such as in the alignment of the CCD array or whole system) or due to non-linearity in DC (generally induced by a noisy detector). It is expressed as a combination of both non-uniformity in pixel EO and nonlinear responsivity. Pattern noise generated by the CCD array itself (from 'electronic' sources) is often ignored since in many cases of imaging spectrometer EO is uniform and fixed during the sensor operation. On the other hand, pattern noise due to the mechanical alignment is more important for imaging spectrometers because of the harsh condition during operation, such as vibrations and shock usually encountered by aircraft between take-off and landing. This pattern effects may occur randomly or consistently depending upon the source of the error.

Table 3-5. A list of system parameters (electrical) derived by an array detector of CASI-2 (Itres Research Ltd., 2001).

Parameters			Description
Signal	Optical	Optical smile	A systematic (but small) spectral line curvature across the spatial dimension is called optical smile. The reason for this is due to the differences between the centre and the edge of the swath. These wavelength discrepancies in CASI-2 are known to be less than about 0.5nm, i.e. less than a fifth of a pixel, according the manufacturer's specification for wavelengths below 700nm. The optical smile is derived purely by the optical system, i.e. lenses and slit, in the SHU. As the optical distortion from the lens itself is minimised when the CASI is designed, misalignment between the slit (or lenses) and the array detector is more the likely cause and should be checked routinely. A simple comparison method is used for CASI, and was around 0.11 *nm* for the NERC owned CASI-2 in February 2003.
		Keystoning	Keystoning is also one of the optical distortions, and it is caused by different optical path lengths, or magnification, within the optical system. For example, the distance between the centre of a detector array and the objective lens may be longer than that to the edge of the detector array. This means that the scene could become large and the same is possibly projected onto adjacent detectors. This characteristic is considered in the system design stage, and no routine check is carried out during the manufacturer's calibration procedure.
		Scattered light (SL)	There are various sources of secondary scattering of light inside the optical system of the SHU, i.e. the inner structure of the detector array or inhomogeneous anodised black coating of the interior of the optical system. As SL may randomly vary depending on the amount of light or state of the optical system, it is simultaneously measured with the scene data in reserved detector columns. CASI uses the first 80 columns of the array detector that is designed to prevent any direct scene information. The variation of SL in CASI dominates in the spectral dimension of the detector array, rather than the spatial. When image is produced (in radiance unit), SL for each row (wavelength) is estimated by the mean of 11 columns of the corresponding regions centred on column 50 for NERC CASI, subtracted by the DC and the FSS.

Table 3-6. A list of system parameters (optical) derived by an optical system of CASI-2 (Itres Research Ltd., 2001).

3.4.2. Image related specifications

3.4.2.1. Spatial properties

Spatial properties of the imaging related parameters of CASI are related to the size of the scene image. While all CASI-2 systems have the same pixel size of array detector, their FOVs vary. Depending on the users' needs, the CASI-2's manufacturer (Itres Research Ltd) provides a range of objective lenses with several focal lengths (Table 3-7). It should be noted that along track FOV proportionally increases with the cross track FOV. The NERC ARSF has a 54.4° cross track FOV (1.8 *mrad* per pixel FOV), while EA has a 37.8° of FOV (1.3 *mrad* per pixel FOV) as a standard specification from Itres. Since the NERC ARSF operates CASI-2 with ATM (whiskbroom multispectral sensor with 90.0° of FOV and 938 cross track pixels), similar ground coverage and pixel size from both sensors was preferable. With the wider FOV (81.2°; 2.8 *mrad*, ~0.16° per pixel FOV) - closer to that of ATM (2.5 *mrad*, ~0.14° per pixel FOV) -, pixel resolution became too coarse while the number of cross track pixels remained the same (512 pixels) and there were sometimes difficulties in the calibration procedure.

Objective Lens Focal Length (*mm*)	**Effective Focal Length [*mm* or Pixels]**	**IFOV (across-track) [Degrees]**	**IFOV (along-track) [Degrees]**
4.80	4.48 *mm* ≅ 298.68 pixels	81.2°	0.1918°
8.00*	7.47 *mm* ≅ 498.12 pixels	54.4°	0.1151°
12.00+	11.20 *mm* ≅ 747.71 pixels	37.8°	0.0767°
17.00	15.8 *mm* ≅ 1058.18 pixels	27.2°	0.0542°
23.00	21.5 *mm* ≅ 1429.95 pixels	20.3°	0.0400°
35.00	32.7 *mm* ≅ 2179.22 pixels	13.4°	0.0263°
70.00	65.3 *mm* ≅ 4373.43 pixels	6.7°	0.0132°

Table 3-7. Available lenses for CASI-2 from Itres Research Ltd. Lens marked with * represents the NERC ARSF's CASI-2, whereas + for EA.

The effective focal length is used to estimate the ground pixel size (see Section 3.3.1). The figures in the Table 3-7 are calculated using the following equation.

$$EFL = \frac{N \cdot L_{CCD}}{2 \cdot \tan\left(\frac{FOV}{2}\right)} \qquad [3.6]$$

where, EFL Effective focal length [*mm*]

FOV	Field of view [degree]
L_{CCD}	Fixed CCD pixel size (0.015 *mm*) [*mm*]
N	Number of spatial pixels (512)

The optical axis, i.e. cross track pixel position of the CASI's nadir view, is not exactly in the centre of the imaging area (column 338 from Itres). Independent measurements from the Rutherford Appleton Laboratory (RAL), UK, showed that the centre of the image is column 333.88.

3.4.2.2. Spectral properties

As well as cross track spatial scanning, an array detector of the CASI-2 allows up to 288 spectral pixels per spatial pixel, as light coming through an optical system of the sensor is dispersed by a grating and is projected onto it. According to the generalised specifications of the CASI-2 (Table 3-4), 545 *nm* of the spectral range is laid out anywhere between 400 and 1000 *nm*, and varies in each individual system. For example, the NERC ARSF's CASI-2 has at least 545 *nm* of spectral range between 403 and 948 *nm*.

The average wavelength interval between neighbouring bands is estimated as typically ~1.9 *nm* (545 *nm* / 288 rows). In other words, the peak response wavelength of a single pixel of the array detector is generally apart from its adjacent detector element by this 1.9 *nm* (Table 3-4). However, this is only the approximate wavelength separation between adjacent spectral bands of the array detector, and is considered as the 'Minimum spectral sampling interval' (Itres Research Ltd, 2001).

The accurate spectral sampling interval for each spectral band can be found by using a monochromator or a tuneable laser point source. Also, by using these calibration instruments, the sensor point spread function (PSF) for the spatial domain and the bandpass response function (spectral response function, SRF) for the spectral domain can be obtained. This information is not provided by the manufacturer of the CASI-2 or by the routine calibration procedure, due to not being considered as a high priority in the research community the large cost using such high precision calibration instruments. Another reason is that most applications of the CASI-2, and most other systems, do not require these spatial/spectral response characteristics of a single pixel in the array detector. They are, however, necessary in the integration of different types of spectroradiometric instruments, such as the comparison of field

spectroscopy data with the CASI imagery. In addition, routine check of PSF and SRF is important as a minute misalignment between the CCD array and the optical system will result very different result for the image applications (Hildum *et al.*, 2001; Winter, 2001).

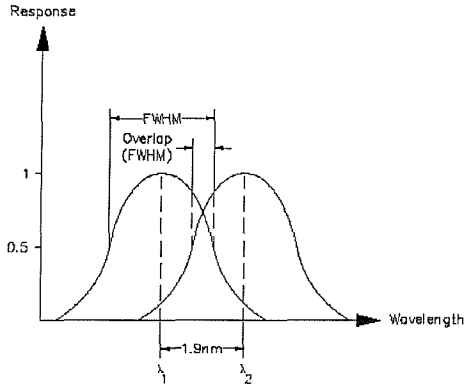

Figure 3-17. Schematic diagram of wavelength interval between neighbouring bands (Itres Research Ltd., 2001).

The possible bandpass may be achievable using numerical models to match the response functions of the array detector with a known reference source (see Section 4.4). There must be an assumed filter function that represents SRF (and possibly also PSF), e.g. Gaussian function. This study referred forward to Chapter 4, showed that despite its limited spectral range due to an insufficient number of reference sources, the SRF of the CASI-2 tends to change with wavelengths and there might be more overlap in the spectral ranges of neighbouring detector elements for some wavelength region (Figure 3-7).

It has been reported that the spectral resolution of the CASI-2 is a function of individual bands, and the manufacturer suggested that the minimum spectral interval was measured to be around ~2.2 *nm* at 650 *nm* (Itres Research Ltd, 2001). The spectral resolution is measured by the half maximum value (full width half maximum, FWHM) of the appropriate spectral response curve. For CASI-2 system, a Gaussian function is used to represent the spectral response (This will be discussed in Section 4.4). The fact that the minimum bandwidth ~2.2 *nm* is greater than the estimated average spectral interval (~1.9 *nm*) indicates that minimum overlap between neighbouring spectral bands is 0.3 *nm* (~14 %)[‡] and that the sampling spectrum has no gaps between wavelength intervals. An over-sampled spectrum, on the other hand, will be an

‡ $100 \cdot (2.2 - 1.9) / 2.2 \cong 14[\%]$

ineffective wavelength interval when the FWHM overlap is greater than 50 %. With the estimated average spectral interval, FWHM value of greater than 3.8 *nm* is considered as spectral oversampling.

3.4.2.3. Radiometric properties

The radiometric resolution of the CASI-2 determines its ability to distinguish features on the ground with different in radiance or initially DN values. CASI-2 has a predetermined dynamic range of pixel values from the quantisation process (Table 3-5.). This continuum, 0-4095 represents discrete levels of the total range generated by the sensor's electrical signal. The spectral radiance, as an output pixel value, is a function of IT and the radiance sensitivity coefficient (RSC) created from the manufacturer's routine calibration (see Appendix A). Each level of pixel value (unit DN) represents a certain range of radiance variation, called the minimum radiometric resolution, with the following relationship.

$$L_{r,c}^{\min} = \frac{1}{RSC_{r,c} \cdot IT} \qquad [3.7]$$

Where, $L_{r,c}^{min}$ Minimum radiometric coefficient $[\mu Wcm^{-2}sr^{-1}nm^{-1}]$
$RSC_{r,c}$ RSC for row r and column c $[DN(\mu Wcm^{-2}sr^{-1}nm^{-1})^{-1}ms^{-1}]$
IT Integration time $[ms]$

Equation [3.7] shows that the minimum radiometric resolution can be reduced by increasing IT value. At the same time the total range of radiance variation decreases ($L_{r,c}^{min}$ ×4096), this means that the image could be saturated in the upper limit of DN values.

3.5. Laboratory Calibration of CASI-2 System

Laboratory calibration of CASI-2 is a fundamental process in the provision of high quality data to the end-user for the independent instrument characteristics (Winter, 2001). Regular laboratory calibration also provides a rigorous way of monitoring system performance over time and is in particular important for CASI-2 system as a delicate electro-optic instrument operating under harsh conditions, e.g. high frequency vibration from the aircraft's engine (Hildum, 2001).

As well as undergoing an annual maintanence procedure by the manufacturers, the CASI-2 instrument operated by NERC ARSF is routinely calibrated (at least 2-3 times a year). This is undertaken in the laboratory of the NERC Equipment Pool for Field Spectroscopy (EPFS) at the University of Southampton, UK, in a dedicated laboratory. The scheduled calibrations are for pre- and post-season of a year-round basis operation of the CASI-2. The additional calibration is normally performed mid-season or after upgrades or modifications by the manufacturer. In order to check overall system performance before and after the laboratory calibrations, in-flight calibration of the CASI has been proposed and is being developed for the absolute radiometric calibration as a possible replacement of a mid-season laboratory calibration (Rollin *et al.*, 2002)

The laboratory calibration procedure of the CASI-2 system follows the method developed by the manufacturer, Itres Research Ltd., and relies upon a radiometric standard traceable to the UK National Physical Laboratory (NPL) (Appendix A.2). The CASI-2 calibration mainly consists of four main parts: pre-calibration check, wavelength calibration, radiometric calibration, and irradiance calibration for the ILS.

1) ***Pre-calibration***: A series of checks performed to determine spectrometer characteristics. There are in total twelve categories as shown in Table 3-8.

2) ***Wavelength calibration***: Test of spectral response for corresponding CCD rows. Using the low-pressure gas lamps with precisely defined spectral emission peaks provides the average row position of these peaks (see Appendix A.3).

3) ***Radiometric calibration*:** Generating the radiant sensitivity coefficients (RSC) which is used for converting raw DN of the detector array in CASI-2 to the absolute radiometric unit for every aperture setting as a function of IT.

4) ***ILS calibration*:** The ILS probe is a simple cosine receptor that does not have any electrical parts, and the light guided via a fibre optic cable is projected onto column 36 (for NERC CASI-2) of the CCD array. The calibration of ILS is an irradiance correction with uncalibrated light source, and the CASI-2's SHU that is radiometrically corrected in 3) is used as a measurement standard.

The aim of the pre-calibration is to find out the mechanical and internal stability and uniformity of the instrument, i.e. the chamber temperature and humidity for stable operation of the CCD array, the alignment and contamination checks of the optical system (including spectral alignment test for the wavelength calibration), and other system variable checks. The instrument-induced systematic noise from the pre-calibration, i.e. dark current, electronic offset, frame shift smear, and scattered light, are important pieces of information prior to the retrieval of accurate radiometric calibration results. More details of pre-calibration are shown in the calibration manual (ITRES Research Ltd., 1995a).

For the radiometric calibration of CASI-2, as a detector array type of sensor, radiometric characteristics of each CCD pixel should be established. Thus, it is important to make sure that every discrete detector is illuminated from the radiance source (i.e. integrating sphere). The uniformity calibration aims to obtain relative pixel-to-pixel response variations due to irregularity of the CCD elements or non-uniformity of optical sub-systems for the CCD array. Hence, the objective lens of the CASI-2 SHU has to be as close as possible to the exit port of the integrating sphere, to ensure that a highly uniform source of light arrives at the CCD array without any alteration. Since the effective area of the integrating sphere is smaller than the FOV angle of the objective lens in NERC's SHU (54.4°), the two spatial halves of the imaging part of the CCD array in the centre of the slit axis, i.e. left (columns between 82 and 335) and right sides (columns between 336 and 512), are acquired separately for the uniformity test and later merged as if both were collected under the same light. The uniformity datasets however contain invalid values which are not suitable for the absolute radiometric calibration due to secondary reflection from the close proximity of the objective lens to the exit port of the integrating sphere (see Appendix 4.1). The absolute radiometric response of CASI-2 is obtained during the

absolute spectral radiance calibration, where only the central region of the CCD array is illuminated, as there is a defined distance between CASI-2 and the integrating sphere to eliminate the reflection effect.

Test	Type	Purpose	System specification
Verifying the parameter file	Parameters	The contents of two parameter files (camvga.prm and casi.ini) are checked and compared each other.	Various predetermined parameters
Focus check	Hardware condition	The SHU views arbitrary objects with infinitive distance. Check if the CASI-2 records a sharp picture.	
Temperature Humidity	Parameters	The temperature of the TED (Thermo-electric device) is guaranteed to be a very stable temperature of 275 *K*. Therefore, humidity inside the vacuum chamber of optical system should be less than 25 *%*.	TED CCD Temp. Ambient Hum. Chamber Hum
Voltage level	Parameters	There are various voltage levels that indicate the sensor status. All should be within limits specified by Itres Research Ltd.	Analogue supply voltages
Clean objective lens	Hardware condition	Visual inspection of objective lens to determine if any dust or scratches are present.	
Vignetting test	Hardware condition	Check whether the signal level is uniform in cross-track pixels in spatial image. This is about the degradation of pixel values due to either the entrance slit misalignment or its blockages.	
Slit contamination	Hardware condition	In addition to the Vignetting test, the slit contamination check tests for any persistent pixel values across the spatial profile of the CASI image due to dust or particles in the entrance slit.	
Mechanical stability	Hardware condition	Test for any loose parts in the SHU by shaking it on all axes. Listen for any strange noises and compare pixel values before and after trembling.	
ILS centroid determination	Signal	To determine the maximum ILS response column between the CCD columns.	ILS column
DC generation rate	Signal	To find out the dark current generation rate.	DC EO
Light transfer curve (LTC)	Signal	To quantify several CCD specification parameters, such as system gain, noise floor, electronic offset, and the maximum signal-to-noise-ratio (SNR).	Sys. Gain Noise Floor SNR DN Offset Saturation
Spectral alignment	Signal	This verifies the alignment of the optical system in the SHU, for example, the CCD, grating, lenses, and slit.	Opt. Smile

Table 3-8. The tests conducted during the pre-calibration of the CASI-2.

The radiometric calibration procedure of ILS is performed with a different light source, since it uses a different part of CCD array with different physical unit in comparison to the imaging part of calibration. The measurement uses the 1,000 *kW* Kaiser videolamp as an irradiance source, and the CASI-2 performs as a reference calibrator for the ILS calibration procedure. The reason for using a videolamp is that it is bright enough to activate the ILS CCD region and to simulate solar irradiance in spite of its relative instability compared to the integrating sphere. Prior to this, the RSC matrix of the CASI-2 is obtained and updated for accurate radiometric values. Two steps are required, the ILS probe response and the source irradiance measurements, and the data from these are compared, i.e. spectral response of the ILS region in the CCD array and the radiance values of the illumination source collected from the CASI-2. The relationship between them is defined and used in the radiometric calibration of the CASI-2, except that the π steradians have to be taken into account for the ILS assumed as a cosine receptor and that calibrated reflectance of the Spectralon™ reference reflectance panel is multiplied to the irradiance of the illumination source (see Appendix A.6).

Comprehensive description of laboratory calibration of CASI-2 performed in NERC EPFS is attached at the end of this thesis (Appendix A). This includes not only a calibration procedure, but also background information of the processing theory.

3.6. Summary

The CASI (Compact Airborne Spectrographic Imager) manufactured by Itres Research Ltd, is an airborne pushbroom type imaging spectrometer firstly introduced in late 1980s. It was the first commercial hyperspectral imager with programmable user-defined bandsets using a two-dimensional array detector. To date, continuous upgrades with technological advances have made it possible to put the third generation of CASI (known as CASI-3) on the market. As a result of its operational flexibility, CASI is currently operating in nearly ten countries, and governmental organisations in the UK own two CASI-2 systems for environmental science and monitoring.

A scene image from CASI-2 is built up by continuous scans of a single instance of cross-track image recording over a two dimensional CCD array, while the aircraft is flying forward. For each scan, ground leaving radiation enters the SHU of CASI-2. A portion of a single line of the scene image is filtered by the entrance slit, and the collimated light is dispersed to a certain range of wavelengths by a diffraction grating before it is projected onto the CCD array. Consequently, one dimension of the CCD array measures spatial information in 512 columns of detector elements, whereas another dimension is used for the spectral data (288 rows) for each corresponding spatial position. The amount of radiation that reaches the detector elements is controlled by IT (integration time) and aperture setting, depending upon the atmospheric condition (clear or overcast) or type of ground objects in the majority of the scene, such as desert or snow (relatively large surface with a high albedo), or deep seawater (dark object).

One of the distinctive specifications of CASI-2 is the ILS (Incident Light Sensor). This simple device is a cosine-corrected receptor designed to measure downwelling irradiance simultaneously with the scene scanning of CASI-2. The ILS probe is mounted on top of the aircraft and potentially offers the possibility of acquiring at-aircraft reflectance from at-sensor radiance of the scene image. The probe is connected by a fibre optic cable which guides the received light to the CASI-2 SHU and is eventually attached onto the spectrograph slit in the optical sub-system. The irradiance received by the ILS is therefore imaged in the hidden section of the CCD array (from around column 30 to 40), and recorded in spectral bands identical to those from the scene viewed by the CASI-2.

The CASI-2 is an electro-optical device and the specifications of its operation can be characterised by two categories: signal related and image related. The signal related specifications are related to the properties of electrical signal, mainly generated by the CCD array and by the optical system of the SHU, such as distortions or misalignment of optical components. Some parameters are already recognised by the manufacturer and are determined as a part of instrumental specification (e.g. FSS, Frame shift smear), while the others are subject to change over time hence routine re-calibration is necessary. On the other hand, most parameters of image related specifications that are associated with spatial, spectral, and radiometric dimensions of the CASI-2 image, are either vendor specified or generalised for all models of CASI-2.

The sensor specifications described above only provide broad information about the instrument, as it is presumed that all CASI-2 systems are identical. In reality, however, each individual CASI-2 is unique in terms of its performance and its precision and accuracy varies over time. Accounting for this is the main objective of sensor calibration. There are various types of imaging sensor calibration, e.g. laboratory (for CASI, Babey and Soffer, 1992; for HyMap, Cocks *et al.*, 1998), in-flight (for HYDICE, Basebow *et al.*, 1995; for POLDER, Hagolle, *et al.* 1999), and ground-based (Slater, 1984). Among those, laboratory calibration offers the most accurate results due to the controlled environment, although there are arguments of possible uncertainties of calibration performance between the laboratory and the in-flight operation, i.e. transport and installation (Hildum, 2001; Secker *et al.*, 2001). The importance of routine calibration is emphasised in this chapter because of the sensor maintenance for the high quality product from the sensor due to harsh condition during its operation (Hildum *et al.*, 2001). The demands of high accuracy from sensor calibration increase over time as sensor technology is progressing rapidly and users demand higher quality data.

One of the important tasks in the sensor calibration is to characterise the sensor response to internationally recognised physical units (Système International, SI). The CASI-2 laboratory calibration consists of four parts: pre-calibration, wavelength calibration, radiometric calibration, and ILS calibration. For the CASI-2 operated by NERC ARSF, a total of four laboratory calibrations are performed each year (three times in NERC EPFS and once by Itres Research Ltd) to ensure a high quality end-product.

Chapter 4

Limitations of radiometric and spectral performance of the CASI-2

4.1. Introduction

The routine laboratory calibration of CASI-2 maintains the performance of the sensor system (in terms of radiometric, spectral and spatial aspects) and validates the absolute radiometric response of each CCD detector which might have changed due to the nature of harsh conditions during operation. The design and structure of the calibration procedure vary depending on factors, such as, the sensor type, the available resources, and time and cost. For example, the wavelength calibration of NERC CASI-2 does not include the test of spectral band width (or spectral response function, SRF), whereas the bandpass shapes of each spectral band in HyMap are derived using a monochromator (or tuneable laser) with a wavelength accuracy of 0.2 *nm* (Cocks *et al.*, 1998). The characteristics of SRF, as well as PSF (point spread function) for the spatial dimension of the CCD arrays of the CASI-2 may contribute to the total cost of the calibration system and be considered as relatively less important by the manufacturer. Also, merging two halves of uniformity radiometric measurements of the NERC's CASI-2 due to the small exit port of the integrating sphere related to the FOV of the object lens, could result in greater uncertainty than if a larger integrating sphere were used, such as 40×50 *cm* rectangular output of the 1.65 *m* diameter integrating sphere used for the laboratory calibration of DAIS-7915 (79-channel Digital Airborne Imaging Spectrometer) (Lehmann *et al.*, 1995).

The following sections will address limitations and uncertainties of the CASI-2's laboratory calibration method and their probable impact. The main interests are the sensitivity of the wavelength calibration and its susceptibility to error in normal use. In addition, a numerical approach to derive the CASI-2's SRF from accurate spectral widths of emission peaks of low-

pressure gas lamps which are employed for the conventional routine laboratory calibration of the CASI-2 is described.

4.2. Spectral anisotropy across full spatial width

The wavelength calibration is considered as one of the most important aspects in characterising imaging spectroradiometers, since it is directly associated with detection and recognition of spectral signature from measured spectrum. During the wavelength calibration, the spectral characteristics of CASI-2 are determined by the position of the detector element that determines a specific wavelength in the spectral dimension of the CCD array and its uniformity (or variation) across the entire spatial column (Appendix A.4).

Several spectral emission peaks with the approved wavelengths are employed from low-pressure gas lamps as wavelength standards. For the conventional wavelength calibration of CASI-2, spectral responses of row detector elements are recorded only in the centre of spatial pixels (column 335). The neighbouring spectral pixel values at an emission peak are used to locate the sub-pixel position of the peak. The repeated processing for given reference emission lines is plotted against wavelength, and their least square regression curve is used for the wavelength conversion. It has been experienced that the accuracy of wavelength calibration is very sensitive depending upon the ranges of CCD rows sampled.

The spectral alignment problem is basically an intrinsic property of the CASI-2's optical system (Section 3.4.1). The temporal variation of the spectral alignment is tested during the laboratory calibration by averaging sub-pixel values of both ends of pixels in columns (spatial domain) at around 656 *nm*. This may be suitable for detecting the rotating motion of the detector array along the optical axis, e.g. wavelength changes for the specific detector element, but not for the change detection when entire CCD array is shifted perpendicular with respect to the optical axis, e.g. the spectral alignment changes. The spectral smile feature is determined at the designing stage of the sensor system, although the manufacturer tries to minimise it. Therefore, it is a consistent problem and the main purpose of spectral alignment procedure for the CASI-2 is to monitor whether this feature is changing either randomly or systematically over time.

In this section, the procedure of wavelength calibration is reviewed mainly focusing on the problems highlighted above and extended with respect to its susceptibility in data acquisition and processing.

4.2.1. Spectral data acquisition in full-frame mode

As the main objective of this experiment was to investigate the spectral properties from the wavelength calibration in spatial dimension of the array detector, the data acquisition was designed to collect spectral responses over the entire imaging part of the CCD array. Thus, sub-pixel positions of spectrum lines were obtained with full pixel resolution across the imaging swath.

Spectral Tube	Frame summed	No. of recordings	Notes
Hydrogen	4	22	Valid number of summed frame from 1 to 16.
Oxygen	4	18	Valid number of summed frame from 1 to 16.
Helium	4	18	Valid number of summed frame from 1 to 16.
Mercury	4	40	Valid number of summed frame from 18 to 34. (Earlier recordings were for the lamp warm-up.)

Table 4-1. Description of raw full-frame mode data collected to investigate wavelength uncertainty.

The full-frame spectral calibration data were recorded during the last day of a routine laboratory calibration of CASI-2 in NERC EPFS, University of Southampton (Ref. No. NERC26; 4 July 2002). The instrument setup was identical to the normal wavelength calibration, i.e. the CASI SHU was mounted on the lab jack with the slit horizontal and the opal glass diffuser attached in front of the objective lens (f/5.6) in order to disperse the narrow light from spectrum tubes and to uniformly illuminate whole range of the CCD array against four wavelength standards (Hydrogen, Oxygen, Helium, and Mercury). Because the power of the low-pressure gas lamps is generally weak, the CASI integration time was set at 10,000 *ms* for each frame with a fixed aperture setting at 3. More than 16 summed frames were collected from each gas lamp, each of which was the sum of four 12-bit frames in the instrument's on-chip memory (Table 4-1).

The DN values in spectral regions other than spectral emission mainly consist of dark current, that is electrons generated by thermal excitation of the CCD's silicon substrate. To consider dark current is important in this particular application, since illumination from the spectral tubes is generally small and some low emission peaks needed to be distinguished from adjacent dark signals. Moreover, the integration time setting in this experiment was much longer than ordinary operations of image acquisition, and as a consequence SNR is expected to be

lower. Ideally, before and after the measurements, dark data would be collected with the same instrument settings but with the aperture closed. The direct measurement of dark dataset in full-frame mode was unavailable during the CASI operation, and therefore dark current signals are generated from the dark current generation rate.

The magnitude of the dark current signal is a function of the CCD temperature and the integration time (*IT*). As the CCD temperature is constant (275*K*) during operation, the dark noise is only linearly proportional to the *IT*. There are in total five full-frame dark current datasets available for radiant sensitivity coefficient (RSC) from the CASI calibration. The relation between the detector signal (DN values in a CCD pixel) and the *IT* is supposed to be linearly correlated and if least square regression coefficients, *d*, are computed by equation [4.1].

$$d = (A_{dn}^{T} \cdot A_{dn})^{-1} \cdot A_{dn}^{T} \cdot it \qquad [4.1]$$

where

	A_{dn}	$A_{i,j}=dn_i^j$
	it	Integration set for each DC record ($it=A_{dn} \cdot g$) [$msec$]
	i	Index of the dark data set (0…4)
	j	Index of the first order regression (0…1)

A typical plot of dark values with a fitted line is shown in Figure 4-1. The intercept of the regression line fitted to the measurements with the DN axis represents the electronic offset (EO), while the slope represents the dark current generation rate. The vertical axis represents the DN values after one integration period (per frame). Since dark data from CASI calibration contains four summed frames with 32 recordings, each pixel value in the file needs to be divided by 128 (4×32). The dark value for the full-frame spectral data becomes $c_0 + c_1 \times 10000$, where the *IT* for the data acquisition is 10 seconds. Then, the estimated dark value is to be multiplied by 64 (4×16), in order to be compatible with the spectrum line images. The dark current generation is applied on a pixel-by-pixel basis.

Sixteen summed frames were summed for each spectral tube, the resulting summation of 64 frames in total reduces defects that might occur during a series of recordings. Figure 4-2 shows an example output after the summation. Bright horizontal lines represent spectral peaks across the detector's spatial pixels. The maximum values in spectral emission peaks appear around 20,000 *DN*, whereas most pixels are as small as zero after dark signal subtraction. The subtraction of dark current signal from the dataset is important because it discriminates the actual signal of spectral tubes from instrument-dependent white noise (see the plot in the right,

Figure 4-2), as the original wavelength calibration procedure also compensates for the signal offset due to dark current.

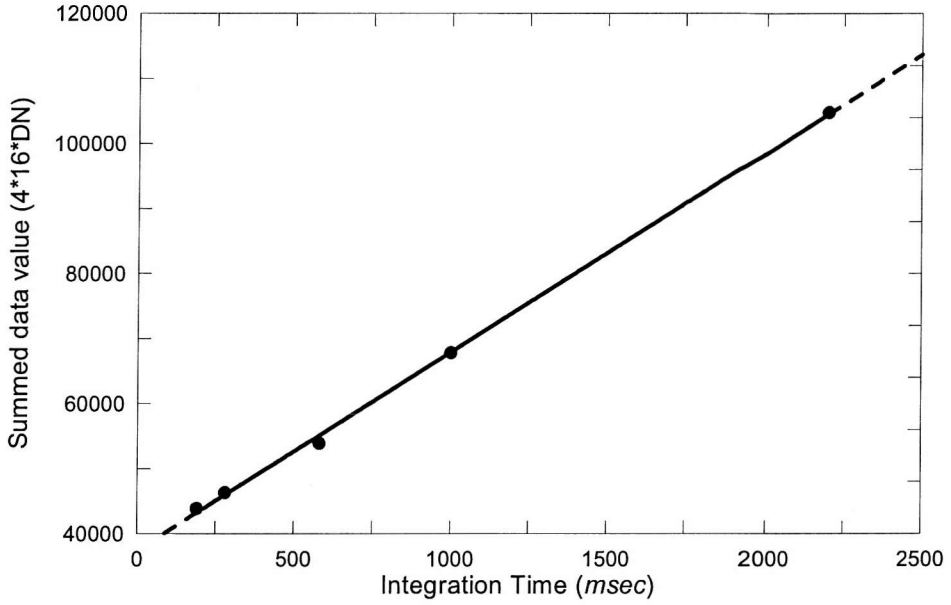

Figure 4-1. Dark current estimation.

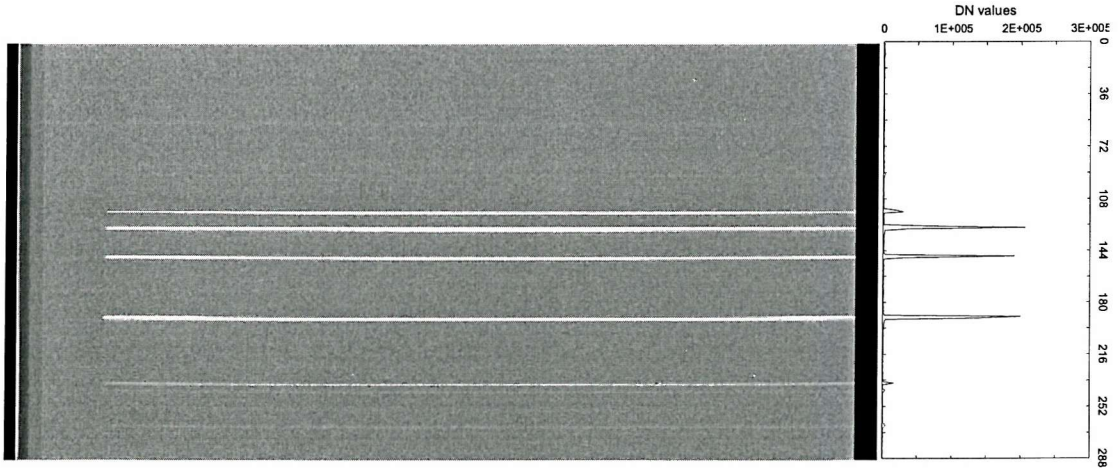

Figure 4-2. NERC CASI-2's full-scale frame measured against Helium lamp (612×288 pixels). Top-left pixel position is (0,0). A transect plot in the right is sampled in CCD row of 335 (y-axis represents row numbers of CCD array).

4.2.2. Sub-pixel position of the spectrum line

To find the relation between row number of the CCD and wavelength for the calculation of the spectral resolution is fairly straightforward. However, care must still be taken into account for this. Due to the sampling nature of an array detector, the spectral signals are discrete, rather than the continuous analogue function (Figure 4-3). These discrete records are compared with the accurate pixel position of the emission peak only by using interpolation. Some approaches have been described and tested by several authors (Scopatz *et al.*, 1989; Sullivan and Quimby, 1990; Hopkinson *et al.*, 2000):

1) FWHM on linearly interpolated data points (with a cubic spline fit)
2) Quadratic fit to more than three pixel values surrounding the maximum point
3) Median method: a fractional pixel position that divides the DC-corrected area
4) Centre of gravity method (used for the CASI-2 calibration)

Among these, there is evidence that the centre of gravity method has advantages over the others in terms of its efficiency and ease of use, although Hopkinson *et al.* (2000) showed that the error range of centre of gravity method is slightly greater than the FWHM method. The laboratory calibration of CASI-2 employs the centre of gravity method for the sub-pixel determination as used in the ILS centroid calculation (equation [4.2], see also Appendix A.3.3), which is a proportion of the sum of the dark current corrected DN values weighted CCD row numbers.

$$\langle r \rangle = \frac{\sum_{r=rs}^{re} r \cdot DN_r}{\sum_{r=rs}^{re} DN_r} \qquad [4.2]$$

where

$\langle r \rangle$	Weighted mean position of the CCD rows [*pixel*]
r	Row number index [*pixel*]
DN_r	DN value of the CCD row r [*DN*]
rs,re	Start, end row number, respectively [*pixel*]

There are several points to be considered when applying the centre of gravity method.

1) Due to the nature of the weighted mean calculation, the result from this method is sensitive to the number of data points and the sampling position. For optimal results, at least five detector elements are required.
2) Like most of the above methods, except those fitting to the centre of the peak position, DN values without DC correction may alter the method's output.
3) Failure of 'defect' pixel discrimination results the wrong centre wavelength. Although there is a way to avoid 'dead' pixels (Berlot and Locascio, 1991), recognition of low pixel responsivity could be more difficult.

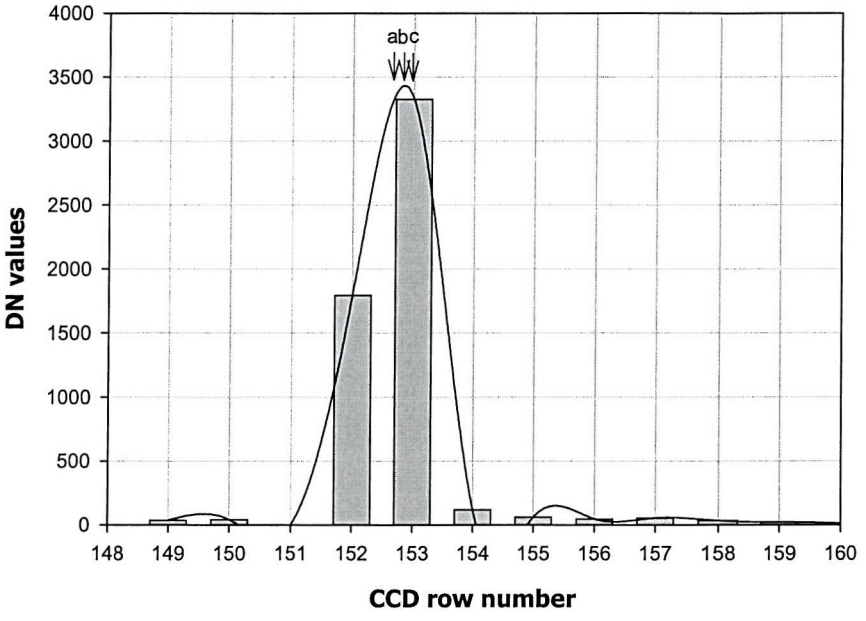

Figure 4-3. Histogram of pixel values recorded by Hydrogen spectrum tube at centre CCD column (335) during the CASI-2 calibration (February 2003). The solid curve is from a cubic spline fit over the data. See text for description of annotations with arrows.

To minimise these weaknesses, it is necessary to employ the same sampling range in the same position as for routine calibration with a particular instrument. In Figure 4-3, the central wavelength from centre of gravity method was used. The results for rows 149 to 158 (152.76; *a* in Figure 4-3) is different from results for 150 to 159 (152.81; *c* in Figure 4-3), assuming that the peak of cubic spline fit curve (*b*) is a correct value. The differences may be small (~0.05 *nm*),

but more than a single emission line for a complete wavelength calibration of a spectrometer can result in serious uncertainty.

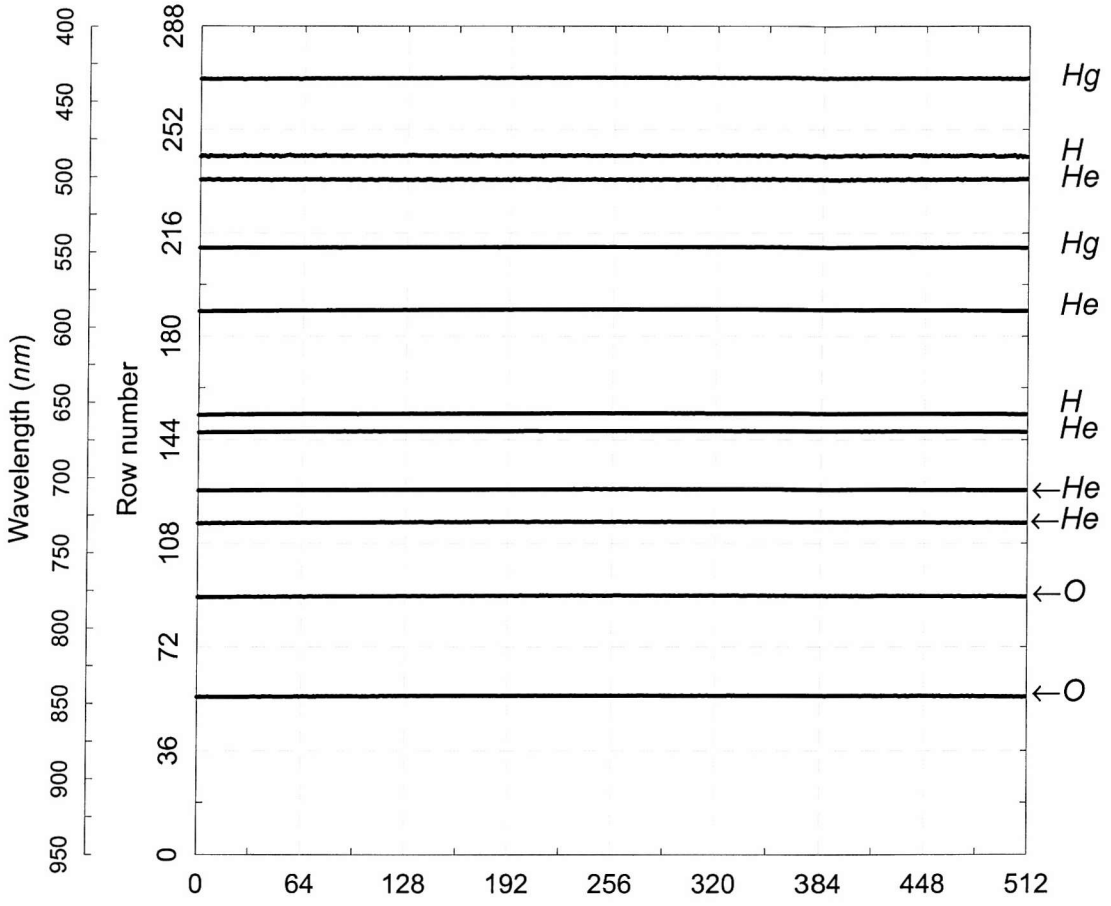

Figure 4-4. Spectrum lines across the CCD columns. Types of gas tubes are placed next to each line. The wavelength axis is only roughly scaled.

Using the conventional method, the row response values around the emission peaks are recorded only for a column near to the CASI's optical axis (column 335). The sub-pixel positions over the entire range of spatial columns show that there are not abrupt changes or obvious optical smile features within the spatial range (Figure 4-4). The average variation of sub-pixel changes for all emission lines is ~0.6 pixels from the sub-pixel position in the centre of image, i.e. the mean wavelength difference of ~1.14 *nm* (0.6×1.9 *nm*) with the same number of rows between the centre of image and that at the edge. It is assumed by the fact that the shifts of sub-pixel position across the spatial pixels are equal in the entire spectral range (~1.9 *nm* over 288 rows, as shown in Section 3.4.2.2 in page 60).

The following paragraphs examine if these assumptions are true, thus help to determine whether the variation of the sub-pixel position can, to the same extent, be ignored.

This variation across the range of columns is actually greater than the expected errors from the sub-pixel computation method, and suggests that systematic optical smiling feature occurred in the CASI-2 system. Figure 4-5 shows individual sub-pixel plots for each emission line that are used for the wavelength calibration of the NERC CASI-2. The *y*-axes in the plots represent the differences between mean sub-pixel value and those in each column, and therefore the range of variation can be compared to each other. The noise levels (i.e. high frequency fluctuations) in the plots may be related to the magnitude of emitted energy and distinctiveness of the emission peak with comparison to the adjacent signals. Equally, however, one should note that magnitude of smiling effect tends to be smaller as it moves toward both ends of CCD due to the nature of optic system (plot *a* and *k* in Figure 4-5).

Apart from these relatively noisy plots, the gradients of the sub-pixel curves and the min/max values change with the CCD rows. The maximum differences in the sub-pixel position across the image tend to be shown in between the centre of the image and ones in both ends of the image. Among the reference spectral positions, these bell-shape curves are the least significant in the centre of the detector array (centre of the spectral pixels), for example, with 0.4 pixels, i.e. the wavelength difference of ~0.76 *nm* (0.4×1.9 *nm*), at ~144 rows out of 288 pixels; plot *g* in Figure 4-5), and tend to increase gradually up to ~0.8 pixels (~1.52 *nm* of the maximum wavelength offset) toward both ends of the spectral pixels. Consequently, the wavelength values in the same number of rows in the CCD array are different due to the optical smiling feature and their differences vary depending on the spectral position. Thus, the mean wavelength interval, ~1.9 *nm*, should change as a function of wavelength.

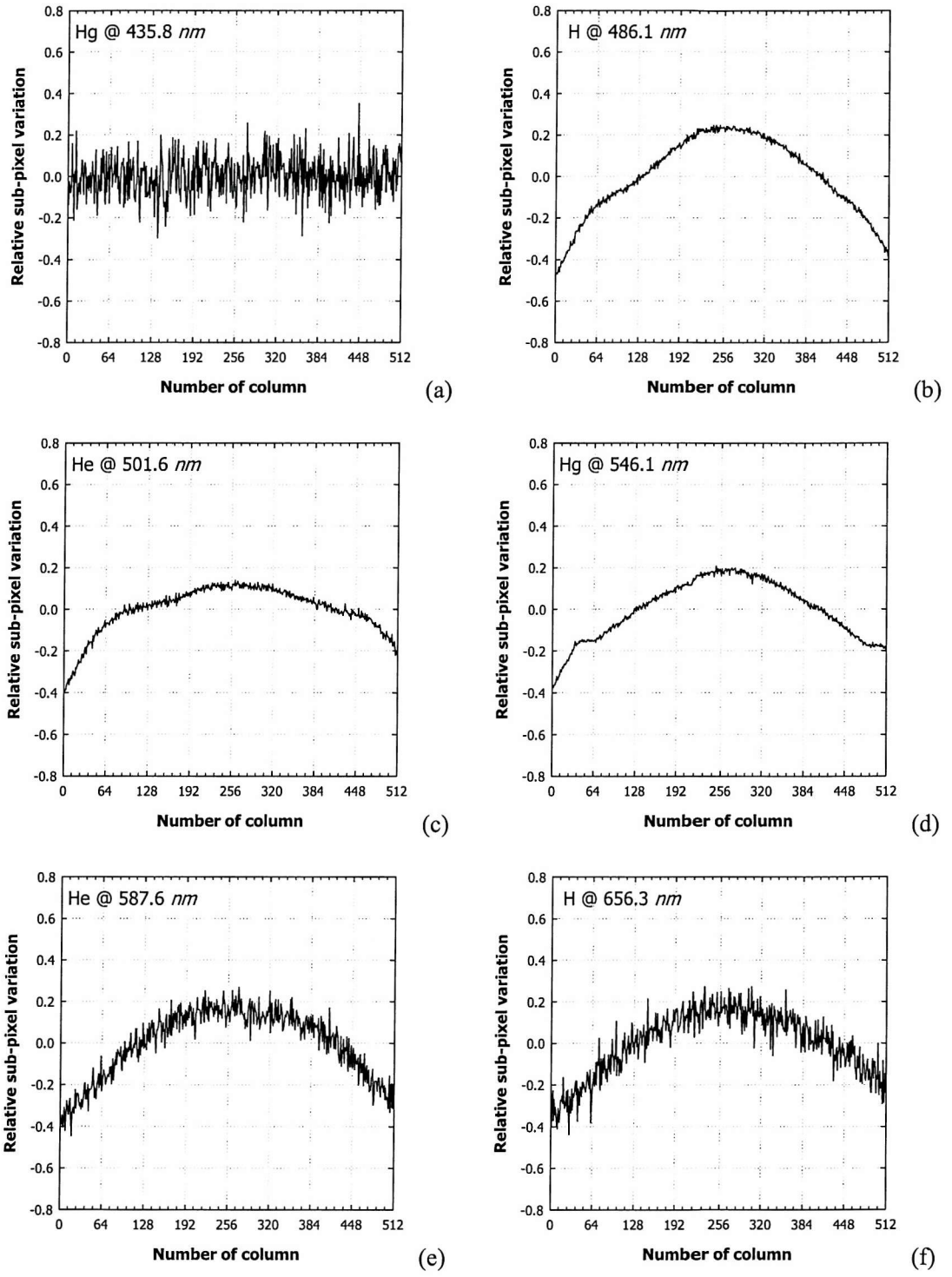

Figure 4-5. A closer look of sub-pixel positions in a full imaging swath pixels of individualised plots (*a* ~ *k*) from Figure 4-4. The measurements were obtained during the NERC CASI-2 calibration in July 2002 (ref. NERC26). In the top left corner of each plot, the type of low-pressure gas lamp and wavelength of the corresponding emission peaks are presented.

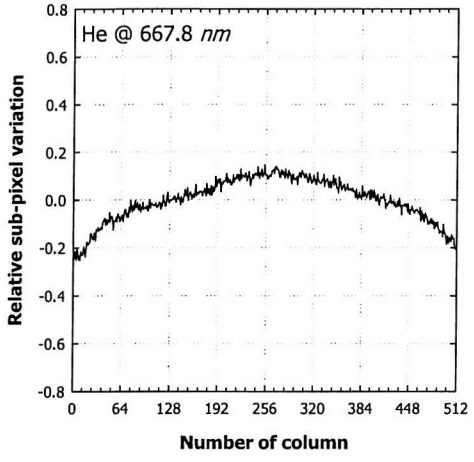

(g)

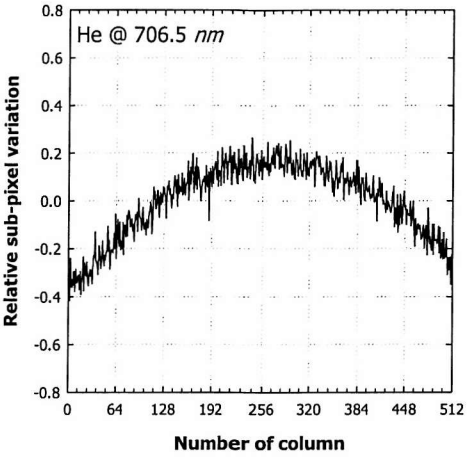

(h)

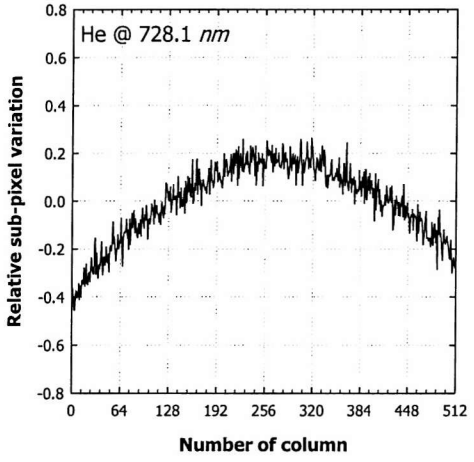

(i)

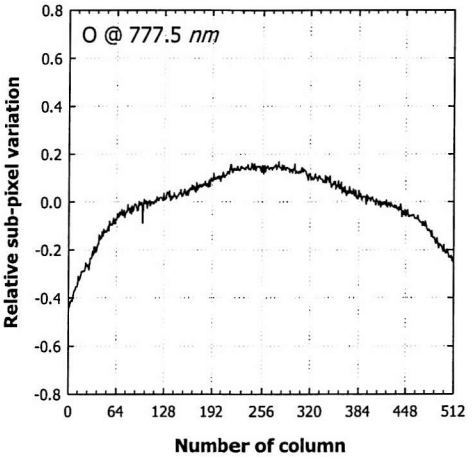

(j)

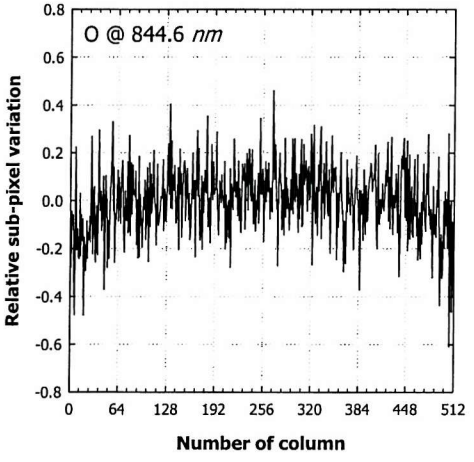

(k)

Continued.

The results from this experiment shows that the real spectral alignment is less accurate than the limit stated by the manufacturer, and that there are obvious smile features across the spatial pixels even if the value from the data processing of the routine laboratory CASI-2 calibration is within the limit (e.g. sub-pixel difference of –0.038 pixels across the image observed during NERC26). According to the Equation [A.15] in Appendix A, sub-pixel positions in columns 135 and 535 are averaged for the spectral alignment, but due to the spatially symmetrical smiling feature the currently used formula does not seem to represent the complete overview of spectral characteristics over the entire CCD array. Instead, it would only give an idea of temporal alignment changes between the optical system and the array detector of CASI-2.

4.2.3. Spatial variation of wavelength calibration

The optical smiling feature shown in the previous section amplifies spectral nonlinear changes. This will directly affect the wavelength calibration results, and consequently wavelength values will be different across the image. From the spatial variation of sub-pixel positions, spatial properties of wavelength calibration results are examined by following the wavelength calibration process currently conducted for the NERC CASI-2 system.

The conventional wavelength calibration method for CASI-2 is to compare sub-pixel positions (at the centre of image) of given emission peaks from four low-pressure gas lamps with a corresponding true wavelength. The average sub-pixel positions of the emission peaks are spread evenly across the entire spectral range of the CCD rows. Due to constant space between the CCD pixels and reliable angular dispersion of the diffraction grating, the relationship between wavelength and CCD row is assumed to be linear. A possible source for a non-linear relationship between the sub-pixel positions and the true wavelength is the alignment error in the sensor optic systems, i.e. any irregularities in the position of the grating grooves or lens placement, and they should also be taken into account. Thus, the wavelength calibration method of CASI-2 employs a third-order polynomial fit to allow for both the main linear characteristics of the row-to-wavelength function and potential non-linearity in the sensor system (Equation [A.16] in Appendix A). Itres Research Ltd, manufacturer of CASI-2, claims that the accuracy of the wavelength calibration method using the sub-pixel values from only the centre of gravity method is 0.1 *nm*, and that the result can be applied across the whole image

with the assumptions that spectral response across the image is uniform and that optical smiling effect, as a systematic error, is ignored.

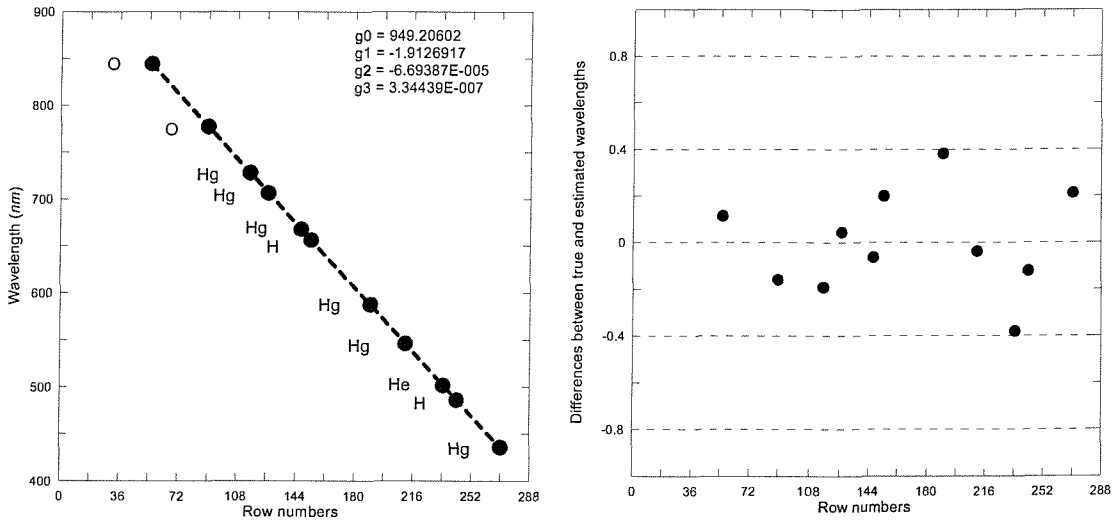

(a) (b)

Figure 4-6. Centre wavelengths of 11 emission peaks from 4 gas spectrum tubes across 512 spatial pixels. An example of G-number calculation in the centre of CASI-2 image (column number of 256) (a) and differences in *nm* between measured and fitted wavelengths for the 11 data pairs (b).

Polynomial coefficients	NERC26	Full-frame calibration data		
		Centre	Left	Right
g0	949.106	949.526 (949.507)	949.478 (-0.01 %)	949.032 (-0.05 %)
g1	-1.907	-1.920 (-1.926)	-1.940 (1.06 %)	-1.923 (-0.13 %)
g2	$-1.025 \cdot 10^{-4}$	$-1.484 \cdot 10^{-5}$ ($2.605 \cdot 10^{-5}$)	$1.211 \cdot 10^{-4}$ (112.31 %)	$-6.905 \cdot 10^{-6}$ (-114.88 %)
g3	$4.701 \cdot 10^{-7}$	$2.260 \cdot 10^{-7}$ ($1.504 \cdot 10^{-7}$)	$-2.223 \cdot 10^{-8}$ (1116.53 %)	$2.398 \cdot 10^{-7}$ (5.74 %)

Table 4-2. Comparison of polynomial coefficients from NERC CASI-2 calibration and current dataset. The 'centre' of the full-frame data are sampled by mean of 8 columns in the in column number 335, and the 'left and 'right' are average sub-pixel values of 8 columns in both edge of the image, i.e. 1-8 for the 'left' and 504-512 for the 'right'. Numbers in parentheses in the 'centre' column of the full-frame data represent mean values across spatial pixels, whereas those in 'left' and 'right' are percentage difference from the G-numbers in the centre of the image.

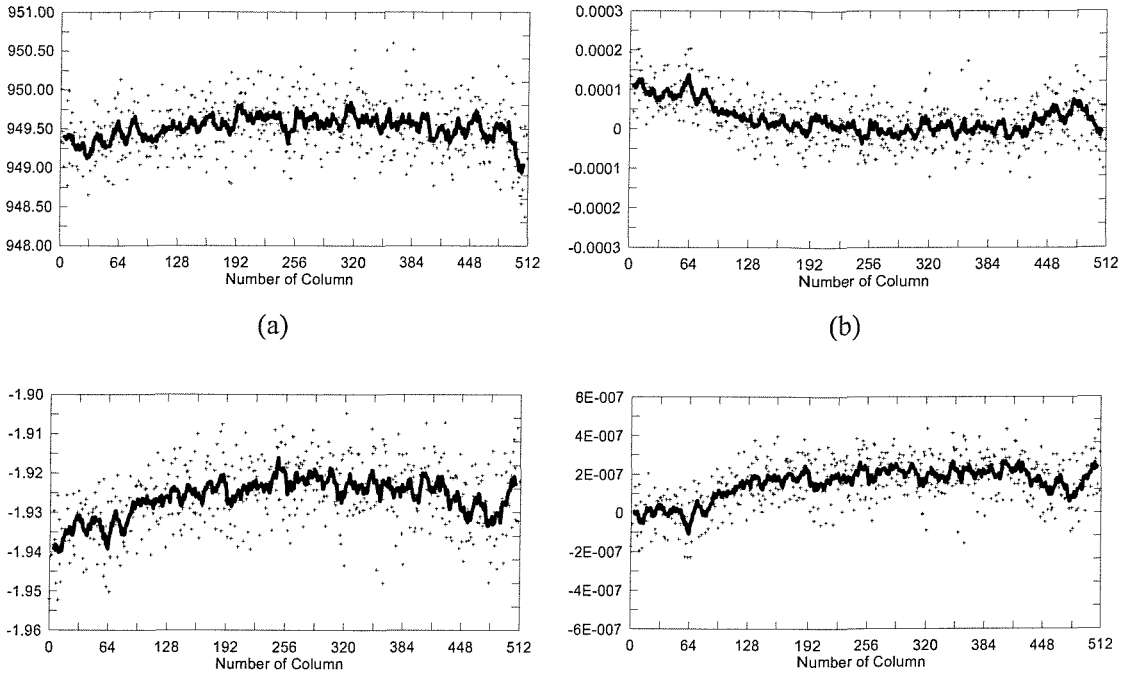

Figure 4-7. Coefficients of third-order polynomial curve fitted to the wavelength across 512 spatial pixels. Solid lines in the first (a), second (b), third (c), and forth (d) coefficients are averaged over every 9 columns of raw coefficients (dotted).

Figure 4-6 shows an example of wavelength calibration result of CASI-2 from the measurements used in the previous section, i.e. selecting the centre column of the CCD array (the same position as that chosen for the NERC CASI-2 calibration). The polynomial curve fit of the group of sub-pixel values against the true wavelengths matches closely within ±0.4 pixels of the residual error in the polynomial fit (plot *b* in Figure 4-6). A set of coefficients of the third-order polynomial regression, called G-numbers, are computed using the full-frame wavelength calibration dataset and compared with that from NERC CASI-2 calibration (NERC26) (Table 4-2). The values are similar but not identical. Different G-numbers between the routine wavelength calibration and the full-frame spectral dataset indicate that the accuracy of the wavelength calibration is susceptible to error and that there is a degree of uncertainty even if the calibration was to be repeated in a very sort time period, e.g. two hours. A possible explanation is that this is due to low responses of noisy emission lines, resulting in an apparent wavelength shift in the row position, although more than a single measurement might possibly minimize the effect to some extent.

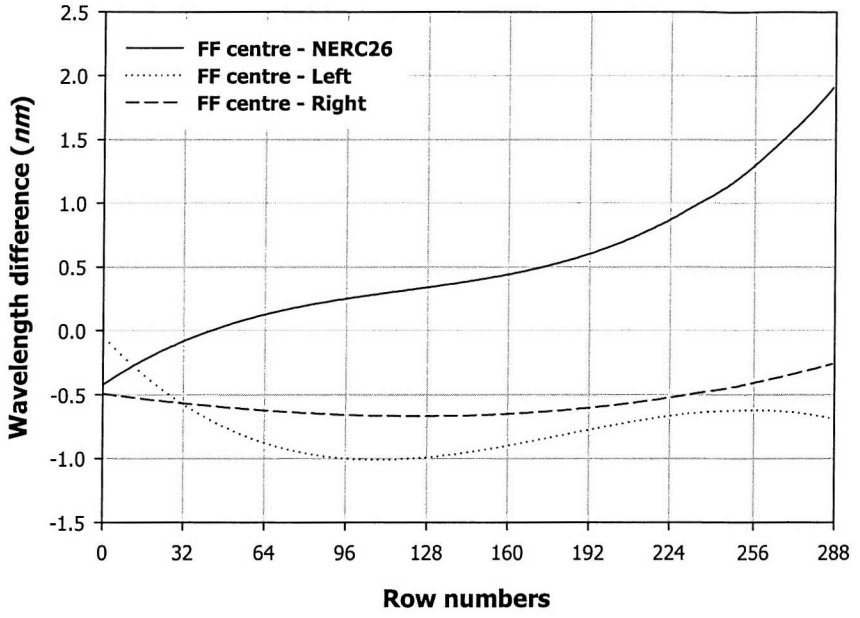

Figure 4-8. Differences of wavelengths generated by G-numbers shown in Table 4-2. The solid line represents the differences between NERC26 and the centre column of the full-frame (FF) measurements, whereas the others are the differentiation depending upon the spatial positions in the image.

The variations of polynomial coefficients along with the CASI's spatial dimension tend to be parabolic in shape from the centre of optical axis, as expected due to the smile features for the row-to-wavelength functions (Figure 4-7). Small differences in the first coefficients from two wavelength calibrations, which tend to have the greatest impact on whole range of wavelengths, suggest the optical smile effect is not great. In addition to the systematic optical distortions across the spatial dimension, the scattered spatial variations of all coefficients suggest that noisy sub-pixel positions, due to low signal at some emission peaks, may contribute the accuracy of the wavelength calibration results in CASI-2 system.

The spatially non-uniform G-numbers, as shown in Figure 4-7, result in different wavelengths depending on the spatial pixel position of the image. The continuous functional relationship between wavelength and CCD row are expressed by using a third order least square polynomial fitted to a series of data.

$$\lambda(r) = g_0 + g_1 \cdot r + g_2 \cdot r^2 + g_3 \cdot r^3 = \sum_{l=0}^{3} g_l \cdot r^l \qquad [4.3]$$

Where $\lambda(r)$ Wavelength as a function of the CCD row [*nm*]
g_l G-numbers ($l = 0...3$)
r Number of row from 0 to 287

Figure 4-8 shows the wavelength differences from groups of G-numbers in Table 4-2. Even with the dataset obtained in virtually the same conditions, the wavelengths between NERC26 and full-frame measurements have a maximum difference of around 1.8 *nm* in the short wavelength region, which is nearly an average wavelength interval between pixels (i.e. 1.9 *nm*). The curvilinear shape of G-number distribution across the image due to the optical smiling feature results in inconsistent wavelength values across the image. Although maximum differences are not greater than those presented in the previous section, they are generally around ~0.5 *nm* and up to ~1.0 *nm* less than that estimated in the centre of the image. This error could be worse if we take into account spatial fluctuations of sub-pixel values as shown in Figure 4-7.

The magnitude of uncertainty – up to 0.8 *nm* according to the manufacturer's specification (0.3*nm* for optical distortion error plus 0.5*nm* of wavelength ambiguity; maximum uncertainty per pixel of 36%) – means that the swath pixels of CASI-2 images have irregular wavelengths. However, this experiment has shown that the spectral uncertainty is, in fact, greater than that suggested by the manufacturer (with a magnitude of up to 0.1 *nm*) in the spatial domain of the image. This is not currently detectable during routine CASI-2 laboratory calibrations, but should be carefully checked in the future.

4.3. Case study: Sensitivity problem with wavelength calibration

As an extension of the previous section, the consequences of using wrong wavelength calibration are addressed here by considering an incident reported in April 2003.

The routine laboratory calibration of CASI-2 is always performed before the image acquisition. In other words, when the CASI-2 data are obtained, some parameters which have already been stored in the CASI-2 system are used to calibrate the data during generation of the HDF datafiles for the end-users. Spectral bands in the CASI-2, in spatial mode, are determined by a pre-programmed set of wavelengths, and because the wavelength value in a certain row number is not fixed, the number of rows or the position of the CCD array is assigned depending on the range of wavelengths generated by G-numbers.

In July 2002, the NERC owned CASI-2 SHU (ref. 2007) had to be repaired by Itres Research Ltd, and a temporary replacement was supplied for the second half of the flight season. The temporary SHU (ref. 2001) was calibrated by the manufacturer and was flown by NERC ARSF as soon as it arrived in the UK. At the end of the season, the SHU (ref. 2001) was brought into the NERC EPFS for post-flight calibration (ref. NERC27) and then sent back to the manufacturer. As a result, the CASI-2 images acquired during the period were acquired with the configuration from the manufacturer's calibration results.

NERC ARSF had a contract with VITO group in Belgium to obtain CASI-2 images over Belgian coastal area in October 2002. The replaced SHU (ref. 2001) was used for the data acquisition. The user reported problems with reflectance spectra after an RT model, ATCOR which is based on Modtran, had been applied for atmospheric corrections on the CASI-2 images. The reflectance spectra were extremely noisy. Figure 4-9 shows large peaks in the reflectance values. These peaks occur mainly in the wavelength range from 650 to 850 nm, as well as in the short wavelength region, and are inconsistent with ground reference spectra.

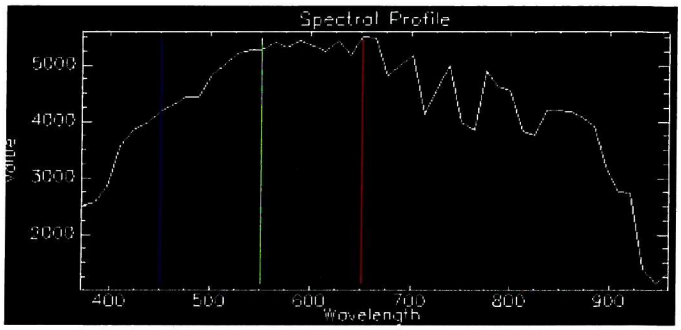

(a)

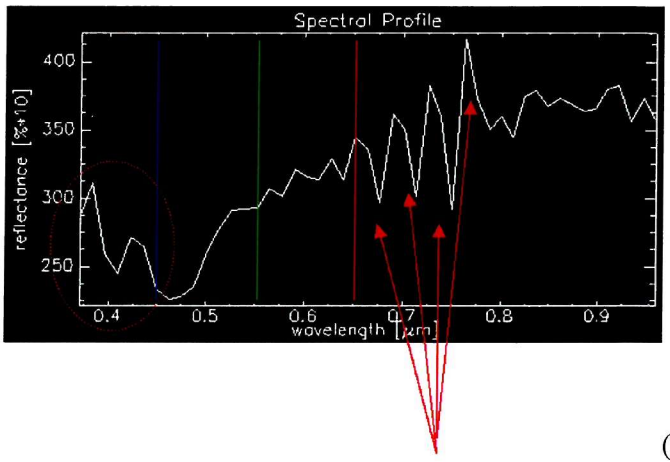

(b)

Figure 4-9. Spectrum of a pixel in the pixel position of (200,200) in Figure 4.10. Radiance spectrum (a) and reflectance spectrum (b) after atmospheric correction algorithm.

The possible causes of the problem were tested as follows,

1) Raw CASI image: No apparent spatial inconsistency was found.
2) RSC files: Comparison of RSC files, before and after the image acquisition, shows neither spectral nor spatial abnormality were found. Pixel spectra after the radiance correction was not considered to be associated with the problem reported.
3) G numbers (Wavelengths): Pixel spectra with wavelengths calibrated before and after the image acquisition showed that water absorption features were well matched with the wavelength calibration from NERC27.

4.3.1. Raw CASI-2 image

Visual inspection of the raw CASI-2 image was the initial test to check whether there might have had been defects on the CCD array or failure of the optical systems in the SHU, both of which could cause spatial inconsistencies from pixel to pixel in the image. Moreover, if textures in the raw image are different from those in the radiometrically corrected (using RSC coefficients) image, it would indicate that there are problems in the RSC coefficients generated during the laboratory calibration (NERC27).

The pixel values in the raw image were subset and converted into radiance unit by running the manufacturer provided utility software, RADCOR. Figure 4-10 compares raw and radiance image. They show that there is no spatial inconsistency on raw image, since their spatial patterns are almost identical. In other words, the faulty spectra shown in Figure 4-9a would exist in entire image.

(a) (b)

Figure 4-10. Comparison of spatial variations of raw CASI image (a) and radiometric corrected image (b). Both images are composition of band 28 (R), 30(G) and 33 (B), that are corresponding to 714, 738 and 775 *nm* respectively.

4.3.2. Differences of RSC between Itres and NERC27

The comparisons of RSC coefficients before and after the image acquisition often give an idea whether the RSC file from NERC27 is contaminated in certain spectral dimension of the CCD array and conflicts with Itres' calibration results. For a comparison of the quality of the RSC values from NERC's calibration (NERC27), Itres provided the RSC file that was created just before the NERC loan.

Both RSC coefficients are illustrated in Figure 4-11, these show that there is generally less than 15 % difference between two RSC files. This figure seems marginally slightly greater than that from previous experience. Possible explanations of the differences could be the different radiometric standard used for each RSC file and the different sets of wavelength values. Nonetheless, since no obvious differences of the plot patterns are observed, it is concluded that there is no fault in the RSC coefficients.

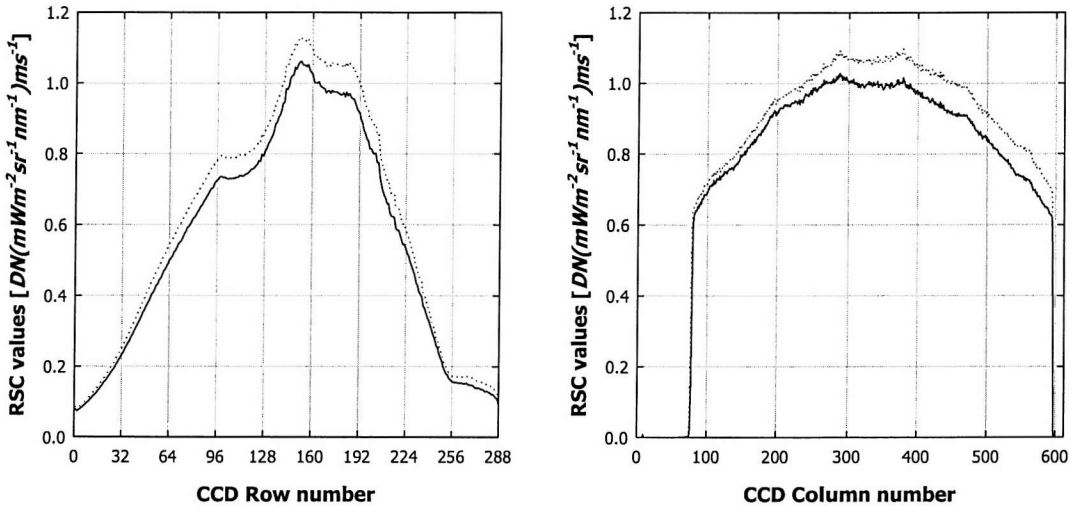

Figure 4-11. Transactions of RSC coefficients (aperture 3) generated by Itres (before the NERC loan; solid line) and by NERC27 (after the image acquisition; dotted line). The plots are selected at column 335 for (a) and row 144 for (b).

4.3.3. Wavelength test between Itres and N27

Visual inspection of the CASI-2 images and the comparison of the RSC coefficients generated before and after image acquisition suggests that the apparent defects are not due to detector elements or radiometric calibration results. The only other variable that was applied during the image acquisition with the different parameter values was the wavelength calibration file. This was initially discarded, or its significance was not fully realised, because the first coefficient of G-numbers, *g0*, was the most important to determine the wavelength variations according to the polynomial equation while the rest (*g1-g3*) decreased so that their contributions were exponentially diminished on the polynomial curve.

G numbers	Itres (Before image acquisition)	NERC27 (After image acquisition)
g0	961.217	960.451 (-0.08 %)
g1	-1.98098	-1.96659 (-0.73 %)
g2	$-2.65194 \cdot 10^{-4}$	$1.92341 \cdot 10^{-4}$ (237.88 %)
g3	$-2.15304 \cdot 10^{-7}$	$-9.51033 \cdot 10^{-8}$ (-126.39 %)

Table 4-3. G numbers before and after the image acquisition. The figures in parentheses represent percentage differences of G-numbers derived by Itres (before image acquisition) from those by laboratory calibration in NERC EPFS (ref. NERC27) (after).

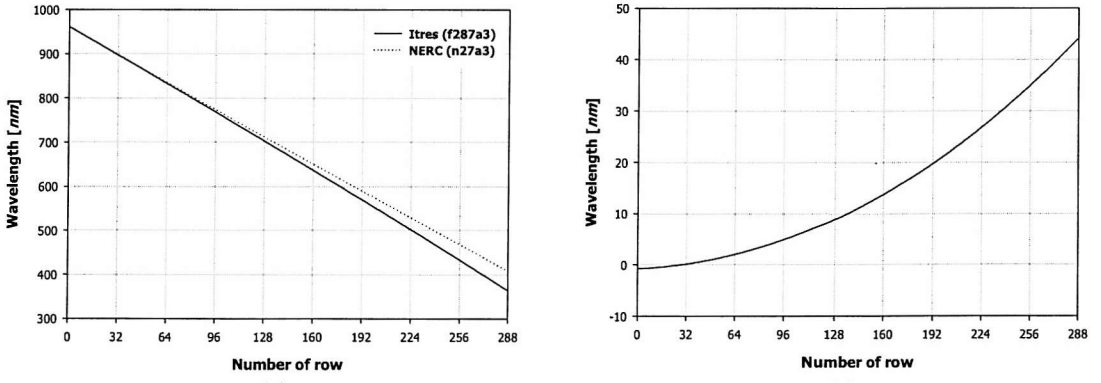

(a) (b)

Figure 4-12. Wavelength calculated by G numbers (a), before (black) and after (dotted) the image acquisition. The wavelength difference for each CCD pixel increases as row number increases.

Table 4-3 shows G-numbers used before and after the CASI-2 operation. The difference of less than 0.8 *nm* is observed at *g0*, which would have been acceptable in the light of previous experience. The normalised differences between two sets of G-numbers suggest that the

differences of the rest of G-numbers (*g1-g3*) are also considered usual if compared it with Table 4-2.

However, such small differences of G-numbers can result in dramatic changes of wavelengths. Figure 4-12 is wavelengths plotted against the CCD rows from G-numbers inverted from Equation [4.3]. The two wavelength curves (before and after the image acquisition) gradually diverge with increasing row numbers (i.e. toward the shorter wavelengths), and the maximum differences are around 44 *nm* at row number 288, which is more than a twenty CCD pixel offset (~1.9 *nm* as the mean wavelength interval between detector elements). Such differences could result in completely different spectra.

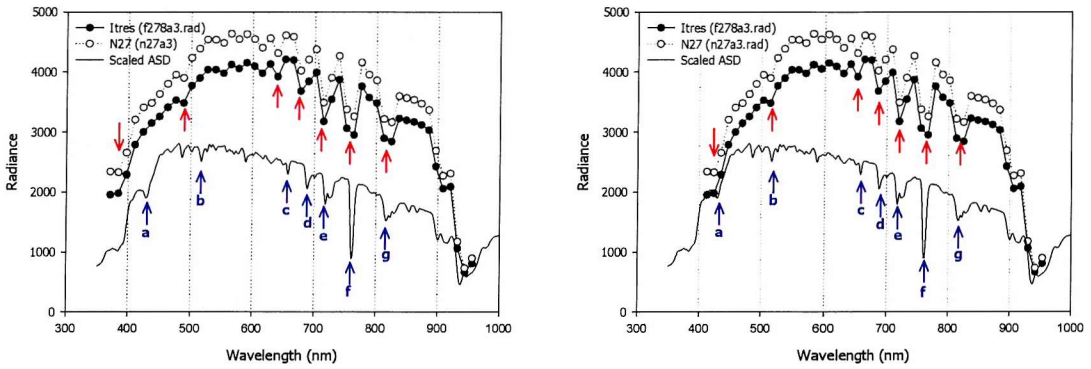

Figure 4-13. Comparison of solar spectrum (EPFS owned ASD Field SpecPro) and pixel spectra of radiance corrected images using RSC files, before and after the image acquisition. Wavelengths in (a) are from Itres' G numbers, whereas in (b) from NERC27. Pixel spectra were extracted from a pixel position of (201, 200) in subset images shown in Figure 4-10. The solar spectrum was scaled in order to compare with image spectra.

Figure 4-13 shows pixel spectra versus two sets of wavelengths, as well as a solar spectrum obtained from ASD Field SpecPro owned by NERC EPFS. The main differences between the two plots are in short wavelengths. The CASI pixel spectra tend to be stretched towards shorter wavelengths with Itres' wavelengths than these with NERC27 wavelengths. More importantly, the CASI spectra in both plots represent water absorption bands (*e-g*), which match relatively well with field spectroscopy data. However, more differences are apparent at shorter wavelengths. While NERC27 wavelengths tend to keep water absorption features (*a-d*) in short wavelength, Itres' wavelengths soon fail to match the ASD spectrum. Also, magnitudes of the spectral offset (red and blue arrows) increase with shorter wavelengths.

It is therefore concluded that the CASI image reported to have a problem with the pixel spectra would be more accurate using the wavelengths measured during the NERC27 calibration. Such differences in wavelength are feasible after the long distance journey of SHU, since Itres performed its calibration by the manufacturer before the SHU dispatch for NERC ARSF.

4.4. Spectral response function of the CASI-2

In addition to the uncertainty in wavelength calibration (Section 4.2), spectral response (or bandpass) function (SRF) of the CASI-2 detector elements is also an important characteristic, as a spectrometric imaging instrument. Such information is especially important for applications of CASI-2 image in, for example, spectral feature analysis or integration of the image with other spectroradiometer instruments, such as water absorption features (Carrere and Conel, 1993) or sensitivity of spectral band width on vegetation indices (Teillet *et al.*, 1997).

The current procedure of routine CASI-2 calibration does not include SRF for each detector element, since the laboratory calibration is optimised in terms of the financial and temporal limitations. Normally, as with the determination of the sensor's spatial point spread function (PSF) the spectrally variable band response function is measured using a tuneable laser point source or a monochromator. For example, the spectral calibration procedure of the HyMap airborne hyperspectral sensor uses a monochromator (Oriel MS257) scanning wavelengths with a 0.2 *nm* accuracy against the sensor recording the signal levels at each wavelength (Cocks *et al.*, 1998). Instead of direct measurement of SRF, the spectral resolution of CASI-2 is assumed to be approximately a Gaussian curve and its minimum bandwidth which is defined by FWHM value, is presumed to be approximately 2.2 *nm* at 650 *nm* for all CASI-2 systems. As seen in the previous sections, predetermined system parameters, particularly in the spectral domain, should be dealt with carefully.

In this section, the estimation of CASI-2 SRF is developed by using iterative numerical models with minimal laboratory measurements. The method basically uses spectral emission peaks from the same low pressure gas lamps that were employed for the wavelength calibration. With an assumption that SRF follows the Gaussian function, the FWHM of each emission lines are considered as the spectral width standard to determine the SRF around the specific wavelength. Although the method is still under development, the results show that, with the same assumptions, the CASI-2 SRF could possibly be estimated by using a numerical method. Further development of the model may increase the accuracy to which this is achieved.

4.4.1. The emission peaks in fine spectral resolution data

The bandwidths of the spectral emission peaks are determined by combinations of various physical factors, such as the purity of gas, pressure in the bulb, voltage level as an energy source, etc. Moreover, the gas lamps are originally supplied to measure spectral emission peaks, but not their width, i.e. the quality of the lamps is not the best available. For these reasons, spectral bandwidths are difficult to obtain either theoretically or from the manufacturer.

On the 14th September 2002, bandwidths with precise and very fine spectral resolution of emission peaks were measured using an optical spectrum analyser (OSA) (Figure 4-14). The OSA (AQ-6315B), owned by Opto-Electronics Research Centre (ORC), University of Southampton, UK, is manufactured by Ando Electric Corporation Ltd[§] and is capable of measuring a wavelength range between 350 and 1750*nm* with a spectral resolution of 0.05*nm* at 1550*nm*, depending upon the wavelength span.

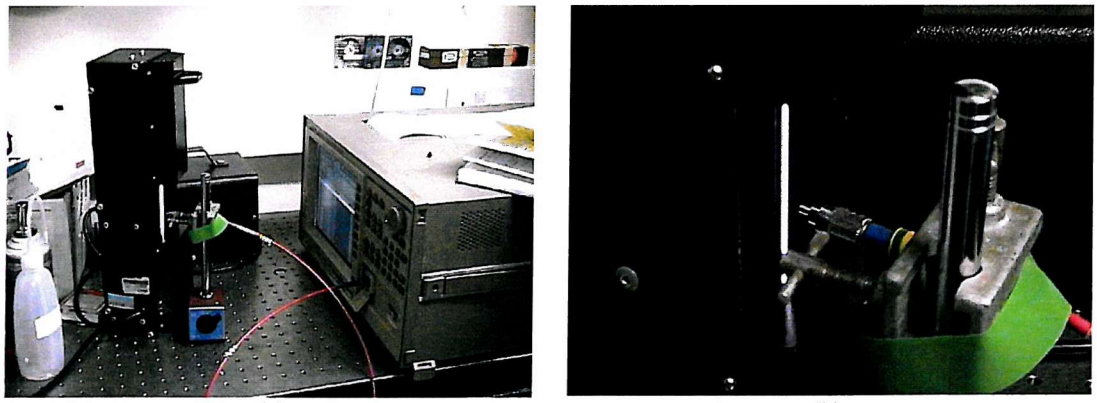

(a) (b)

Figure 4-14. Instrument setting of OSA with spectrum tubes (a). An optical fibre was attached in the optical input connector of OSA, and the other end of the cable was positioned closely to the lamp (b).

Although a fibre optic cable connector in the front panel of the OSA allows direct input signal as the lamp is placed in close proximity, such as unstable setting causes too much noise from adjacent objects or the LCD screen next to the connector and the scattered emission decreases the total signal detected by the OSA, especially for low emission signal (e.g. Figure 4-15*b*). Instead, an optical fibre was used to minimise the source of such errors. It was attached

[§] http://www.ando.com

to an optical input connector in the OSA, and the other end was mounted close to the lamp. Figure 4-15 shows a typical example of data collected. The signal is as small as 1/40, where it is nearly equivalent to white noise. It is interesting to note that the bandwidth of the emission peaks tend to increase without the optical fibre.

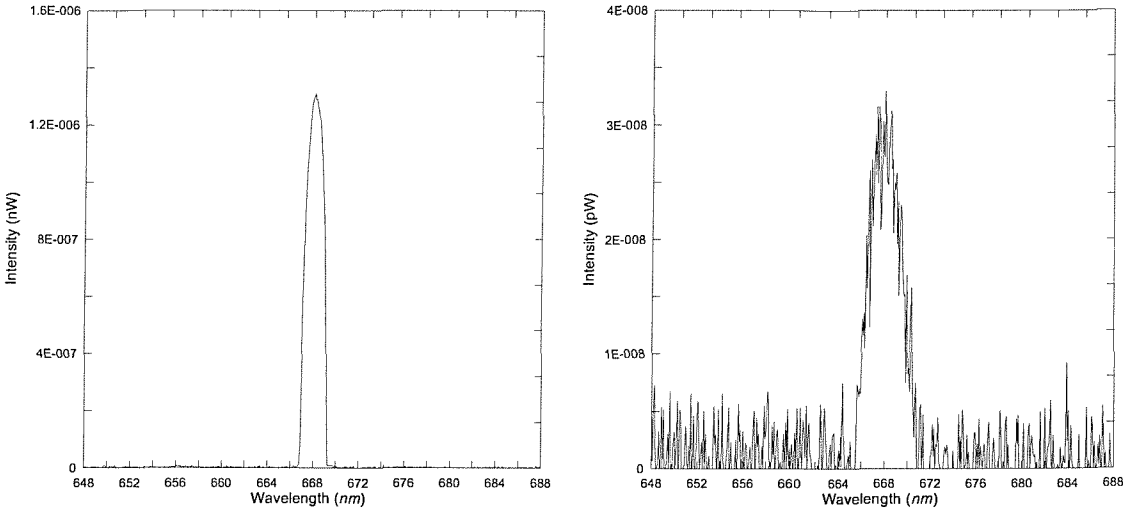

Figure 4-15. Differences with (a) or without (b) using an optical fibre for the same spectrum. These plots are from Helium tube at 648-688*nm* regions.

Gas tube	Wavelength (nm)	Filename	Notes	Data quality
Hydrogen	656.3	W0001.txt	Spectral resolution of 0.1nm	Poor
	486.1	W0002.txt	Spectral resolution of 1.0nm	Poor
Helium	728.1	W0003.txt	Spectral resolution of 1.0nm	Poor
	706.5	W0004.txt	Spectral resolution of 1.0nm	Poor
	667.8	W0005.txt	Spectral resolution of 1.0nm	Poor
	587.6	W0006.txt	Spectral resolution of 1.0nm	Poor
	501.6	W0007.txt	Spectral resolution of 1.0nm	Poor
Using an optical fibre				
Helium	501.6	W0008.txt	Spectral resolution of 1.0nm	Good
	728.1	W0009.txt	Spectral resolution of 1.0nm	Good
	667.8	W0010.txt	Spectral resolution of 1.0nm	Good
	706.5	W0011.txt	Spectral resolution of 1.0nm	Good
Mercury	546.1	W0012.txt	Spectral resolution of 1.0nm	Good
	435.8	W0013.txt	Spectral resolution of 1.0nm	Good
Krypton	753-897	W0014.txt	Low energy; Spectral resolution of 1.0nm	Good
	753-897	W0015.txt	High energy; Spectral resolution of 1.0nm	Good

Table 4-4. List of spectral emission measurements with OSA.

The experiment design was originally intended to acquire the same emission peaks from the same types of low pressure gas lamps as used for the CASI-2 wavelength calibration. Unfortunately, only two out of four lamps were available for use with the optical fibre. The oxygen lamp was unavailable due to poor illumination condition and the Hydrogen lamp was out of order during the time of the measurements. Table 4-4 shows a list of emission lines measured with OSA, nearly half of the initial measurements were rejected due to low signal. All emission lines available for CASI-2 were assessed individually in order to increase spectral resolutions down to 0.1 *nm* with a range of around ±20*nm* in the centre of emission peak.

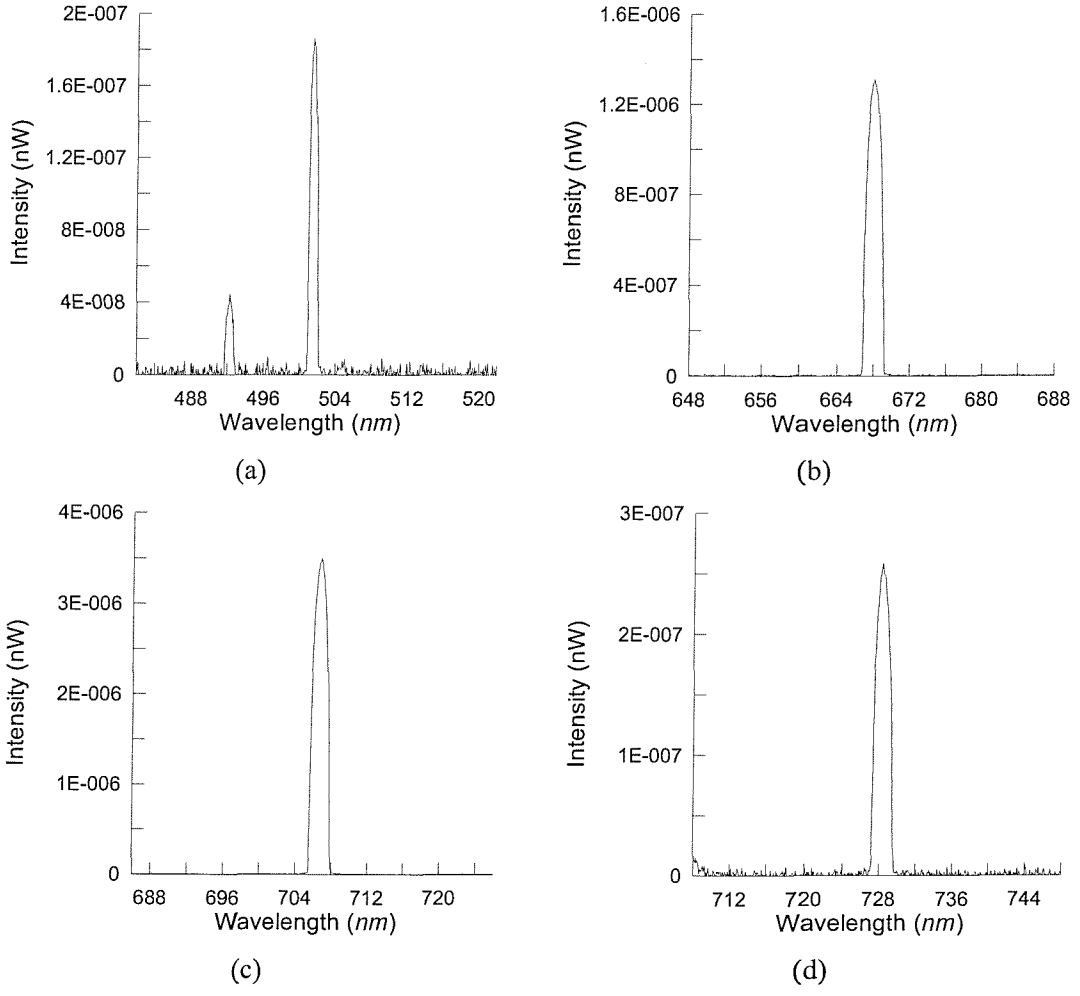

Continued.

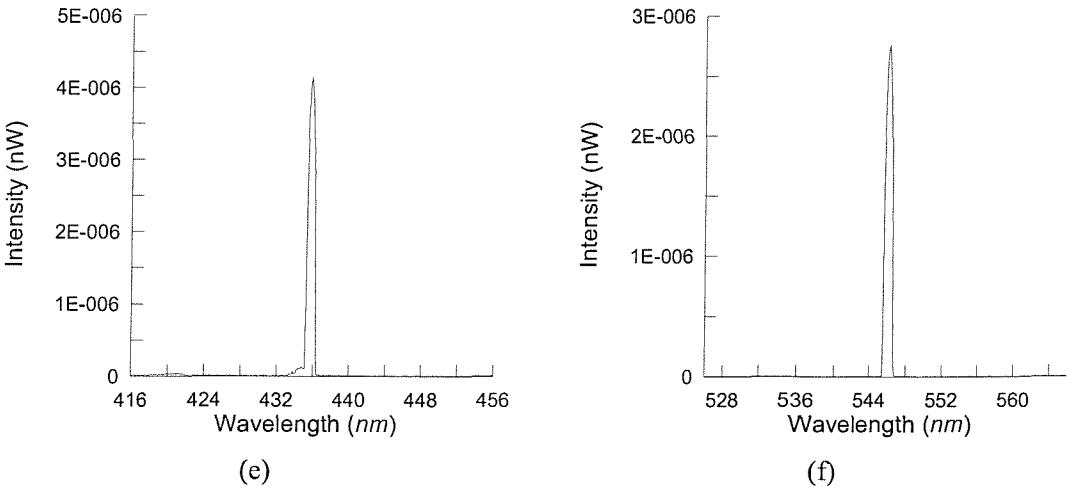

Figure 4-16. Spectral peaks for the dataset used in this study. Centre wavelength of 501.6*nm* (*a*), 667.8 *nm* (*b*), 701.6 *nm* (*c*), and 728.1 *nm* (*d*) for Helium tube, and 435.8 *nm* (*e*) and 546.1 *nm* (*f*) for Mercury tube. The widths of emission peaks vary as well as their intensity levels. However, they do not exceed more than ~3 *nm*.

Figure 4-16 shows the emission peaks measured by the OSA. All spectral response curves were symmetrical and their FWHM varied depending on the energy levels and types of gas in the lamp, while the emission peaks were exactly placed on the known true wavelength. Signals around each peak were very small, and some noisy signals were observed in low emission peak regions (plots *a* and *d* in Figure 4-16).

4.4.2. Estimation of SRF of CASI-2

The estimation of CASI-2 SRF is based on an iterative process by sequentially giving the wavelength range of spectral response in a group of detector elements of CASI-2, until their relative values are close enough to the measured spectrum of the emission line (Figure 4-17). In other words, a numerical model aims to simulate the observed spectral responses from the wavelength standards. Several assumptions are made, as follows,

1) The high spectral resolution emission peaks obtained in the previous section, as reference spectra, can be best approximated by Gaussian functions, as well as the spectral response of each detector element in CASI-2.
2) Each array detector in CASI-2 has a wavelength range of spectral response greater than the spectral resolution of the reference data.

3) The wavelength value of each detector element is accurate although some degree of error is recognised from the routine wavelength calibration procedure (< 0.3 *nm*, Appendix A.4) and from the possible uncertainty of spatial variations (< ~1.0 *nm*, Section 4.2).

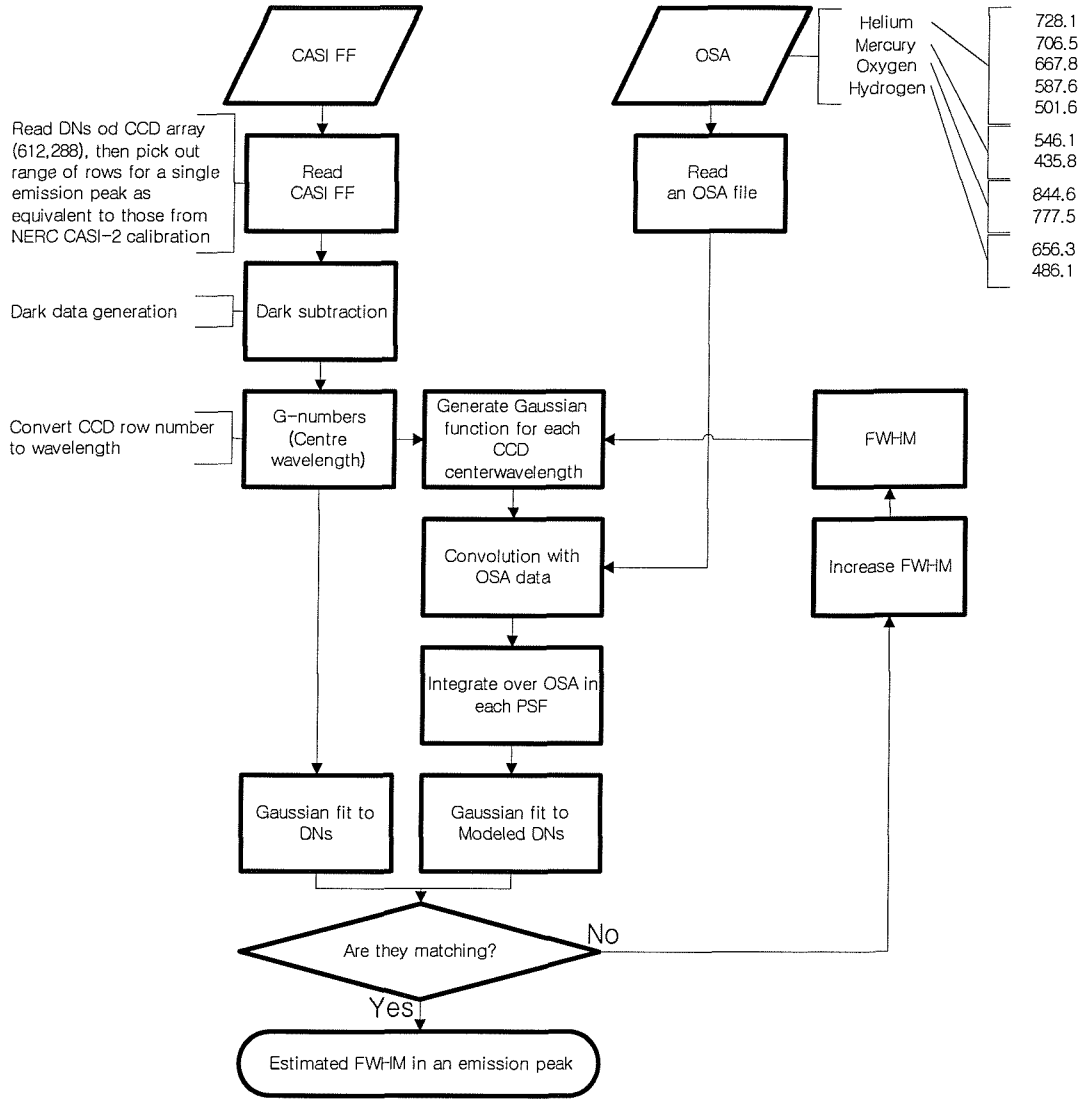

Figure 4-17. Illustration of SRF model processing. This routine was repeated for PSFs from entire emission line wavelengths.

Precise representation of SRF of every detector element is very difficult and is not practical since there are too many factors to determine its characteristics. Despite these, there are general rules that approximately specify the SRF: rectangular if a grating is plane, Gaussian if a grating is curved, trapezoidal if a pixel response is rectangular with curved grating, and

triangular if the entrance slit and the detector width is the same size (Hopkinson *et al.*, 2000). In reality, the edge of the function is often rounded due to the effect of diffraction, scattered radiation in the optical system, and non-rectangular detector response. Thus, a Gaussian function is widely accepted for many array detector instruments and is reasonably constant across the detector array within the same optical system (personal communication with Nigel Fox, UK NPL).

The Gaussian function, $f(\lambda_i, \sigma)$, can be represented by the centre wavelength and the bandwidth (σ) as a function of FWHM (Equation [4.5]). The peak of the Gaussian function is assumed to be the centre wavelength of the spectral dimension of the CASI's CCD.

$$\sigma = \frac{FWHM}{2 \cdot \sqrt{2 \cdot \ln 2}} \qquad [4.4]$$

$$f(\lambda_i, \sigma) = \exp^{-\frac{(\lambda_i - \langle\lambda\rangle)^2}{2 \cdot \sigma^2}} \qquad [4.5]$$

where

$f(\lambda_i, \sigma)$	Gaussian function
λ_i	Wavelength [*nm*]
$<\lambda>$	Centre wavelength [*nm*]
σ	Bandwidth, or standard deviation

All emission peaks measured by the OSA were matched relatively well by Gaussian functions, and expressed by two variables, i.e. a true emission peak position as a centre wavelength, and a FWHM corresponding to the width of the emission spectrum. This could make further processing easier, but alternatively, cubic spline fit on the measured spectrum may also be used if one ignores fluctuating behaviour at both ends of the spectrum (as shown in Figure 4-3).

The range of wavelengths is specified surrounding each emission line, normally ±20 *nm* as long as there are no other spectral peaks nearby (except one spectral peak of Helium at 501.6 *nm*, Figure 4-16*a*). Within the wavelength region the pixel values in the detectors, which are predetermined by the routine wavelength calibration, of the CASI-2 CCD array are normalised, as well as the normalisation of the reference spectral peaks from the OSA. As pointed out in the previous sections, it was important to eliminate dark current signal from the measured spectra in order to recognise true spectral responses of emission peaks. Hence, the relative spectral

responses of the emission peaks from both measurements were obtained and compared. Figure 4-18*a* is an example plot of these. From Gaussian functions fitted to the normalised pixel values of CASI-2, the emission curve has wider FWHM than the reference spectrum. This is shown for all emission lines available. It suggests that the FWHMs of detector elements are wider than those of the reference spectra. If FWHM of the CASI-2 CCD array is similar to the sampling resolution of the OSA, i.e. 0.1 *nm*, the spectral signals from CASI-2 should be the same as those of the reference data. A slight wavelength offset in the emission peak in the plot indicates that, as expected, the wavelength determination from the CASI-2 calibration (that is estimated wavelength from polynomial regression) is slightly erroneous, despite still being acceptable according to the manufacturer's specification.

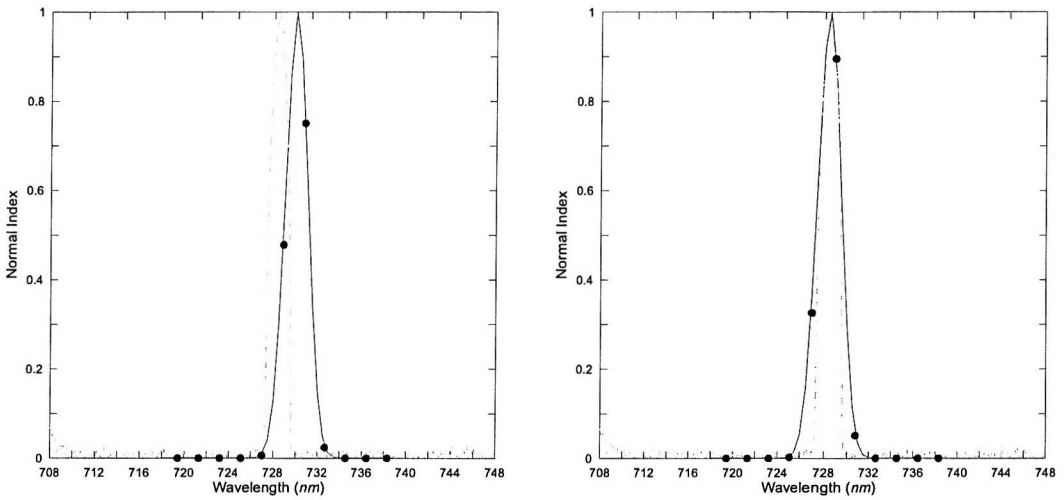

Figure 4-18. The comparison of normalised CASI DNs (a) and model output (b). Dashed lines represent one of the emission peaks from Helium (Centre wavelength of 728.1*nm*) as a reference. The FWHM of Gaussian fit is approximately 4.14 *nm*. Solid lines are Gaussian fit curves over data values (dots).

This disagreement between the two plots, shown in Figure 4-18*a*, in terms of FWHM is a key input parameter of the model. If a CASI-2 detector element has a true FWHM value greater than 0.1 *nm* (minimum spectral resolution of the OSA) at the spectral emission peak, the Gaussian fit of the spectral data points of the CASI-2 supposedly have wider width than the spectral curve of the reference emission. The entire reference spectral values within the region are scaled with the Gaussian curve and they will contribute to the total signal received by the CASI-2 detector, i.e. calculation of the area where the data value is greater than zero. To simplify the processing, FWHM of all CASI-2 detector elements within the wavelength span around an emission peak is assumed to be uniform although this may not be true according to

the information provided by Itres Research Ltd, which will be discussed in the later this section. The initial FWHM starts at 0.1 *nm* and increases every 0.01 *nm*. This iteration interval yields the model accuracy for FWHM of around 0.02 *nm* if all assumptions are correct (Equation [4.4]). With a given FWHM, all CASI-2 detector elements in the spectral region carry out the integration processing, and apply a Gaussian fit to the data points. The resulting data points are scaled between zero and one in order to compare the FWHM with that from the observed CASI-2 spectral responses.

The Gaussian fit on model output shows quite similar distributions to the observed CASI-2 spectral responses (Figure 4-18*b*). The spectral offset (around 2 *nm*) of the centre wavelength from the CASI-2 data is corrected after the model run, but the more important result is the FWHM of Gaussian fit over the estimated data points. Table 4-5 lists the model results from the available spectral emission lines. The specification of CASI-2 system states that its minimum spectral resolution, i.e. FWHM, is around 2.2 *nm* at 650 *nm*. My result shows a similar figure, 2.71 *nm* at 667.8 *nm* and demonstrates variable FWHM over the wavelength range.

Gas lamp	Centre wavelength of (Emission line [*nm*])	Bandwidth, σ	FWHM [*nm*]
Helium	501.6	1.51	3.56
	667.8	1.15	2.71
	706.5	2.23	5.25
	728.1	1.76	4.14
Mercury	435.8	3.64	8.57
	546.1	1.70	4.00

Table 4-5. The model results for FWHM values derived by available emission lines.

Due to no previous record of the measurement of NERC CASI-2 SRF from either a tuneable laser or a monochromator, comparison of the model results is not possible. However, there is unpublished CASI-2 SRF from Itres Research Ltd (personal communication with NERC ARSF in 1999). The manufacturer provided generally applicable SRF of CASI-2, as a fifth order polynomial fit, as a function of wavelengths ([4.6]). The method used for estimating the PSF coefficients from the manufacturer is not known and it does not apply to every CASI system. Nevertheless, it gives an indication that the PSFs in the CASI's spectral dimension vary with wavelength.

$$FWHM(\lambda) = \sum_{i=0}^{5} a_i \cdot \lambda^i \qquad [4.6]$$

Where λ Wavelength [*nm*]

a_i Polynomial coefficients

$a_0 = -2.309\times10^{2}$

$a_1 = 1.3342$

$a_2 = -3.1068\times10^{-3}$

$a_3 = 3.0701\times10^{-6}$

$a_4 = -1.0579\times10^{-9}$

$a_5 = -3.0166\times10^{-14}$

The model output is generally within the range of the manufacturer provided values, except a FWHM in the lowest wavelength (486.1 *nm* from Mercury). Without this, a polynomial fit would have shown acceptable FWHMs for each spectral detector elements (Figure 4-19). An exceptionally large value in shortest wavelength requires more investigations. This may be because the low energy emitted resulted in a high SNR, and/or because of instrument-induced systematic noise other than dark current, i.e. frame shift smear and scattered light estimation, both of which affect significantly in the spectral CCD dimension, especially for low signal spectra in the blue part of the spectrum (Babey and Soffer, 1992).

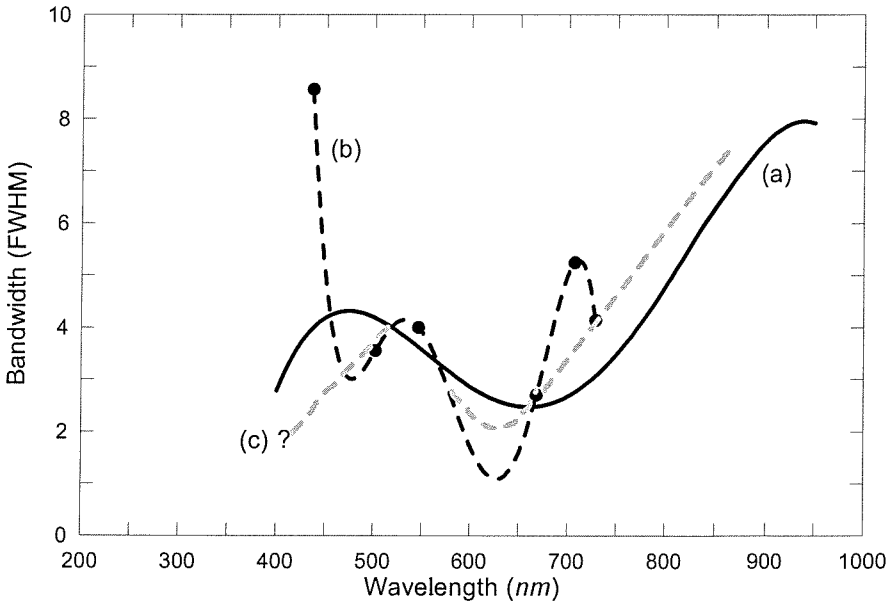

Figure 4-19. Estimated CASI's spectral bandwidths. Data in a solid line (a) are provided by S. Achal at Itres Research Ltd. The model output for NERC CASI is shown in (b) superimposed regression lines. Possible spectral bandwidth of the NERC CASI-2 with the model developed in this chapter is thought to be (c) due to extraordinary estimated value in 486.1 *nm* region.

4.5. Non-uniformity problem on radiometric calibration

The uniformity test of CASI-2 with a wide FOV (54.4°) is achieved by illuminating the two halves of the CCD columns separately. This is one of the most delicate parts of the calibration data acquisition for determining radiometric accuracy across the image, as merging them is always difficult even if care is taken not to disturb the instrument alignment and its distance during the series of measurements. The tolerance of this discrepancy is however neither clearly described, nor properly tested.

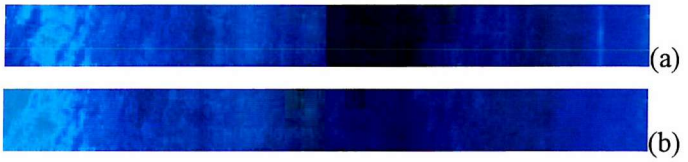

Figure 4-20. Non-uniformity image (*a*) is generated by using old radiometric correction coefficients (NERC22, February 2000) with an image subset from NERC's flight (March 2003) that was meant to test the new calibration result obtained in February 2003, while the same image is used with more recent RSC coefficients acquired just before the data acquisition (NERC29, February 2003) (*b*). Therefore, although pixel values from the old RSC are pseudo-radiometric units (*a*), different spatial variations are observed. Both images are the colour composite of R (651.9 *nm*, Band 5), G (552.2 *nm*, Band 3), and B (450.0 *nm*, Band 1) and apply image contrast of +35% from their original.

This spatial uniformity is a unique problem in a detector array imaging instrument (Winter, 2001). Non-uniform calibration data are often directly responsible not only for incorrect pixel values but also for spatially inconsistent image over supposedly spatially uniform objects on the ground once raw DN is converted into radiometric units. For example, a NERC CASI-2 image was obtained over coastal water for the calibration result test where radiometric pixel values are supposed to be relatively uniform (Figure 4-20). Two RSC coefficients were applied to the raw CASI-2 image: one from NERC22 (February 2000) and another from NERC29 (March 2003). The earlier calibration, NERC22, produced the first two-halves-merging RSC coefficients since a wider FOV had only recently been employed. In other words, experience of the data acquisition technique for two halves of uniformity data was limited, so that spatial non-uniformity due to non-matching uniformity data was possible. The RSC coefficients from NERC22 results in a distinctive step in the centre of the image (Figure 4-20a), as a result of spatially non-uniform RSC coefficients. More apparent radiomatric non-uniformity across the image is illustrated by normalised differences of spatial pixels in the

image with the old RSC coefficients against new image (Figure 4-21). The left half of the image has negative values from the centre of the image, whereas there is a positive relationship in the right side of the image. This example implies that inaccurate uniformity measurement could increase uncertainties of pixel values across the image.

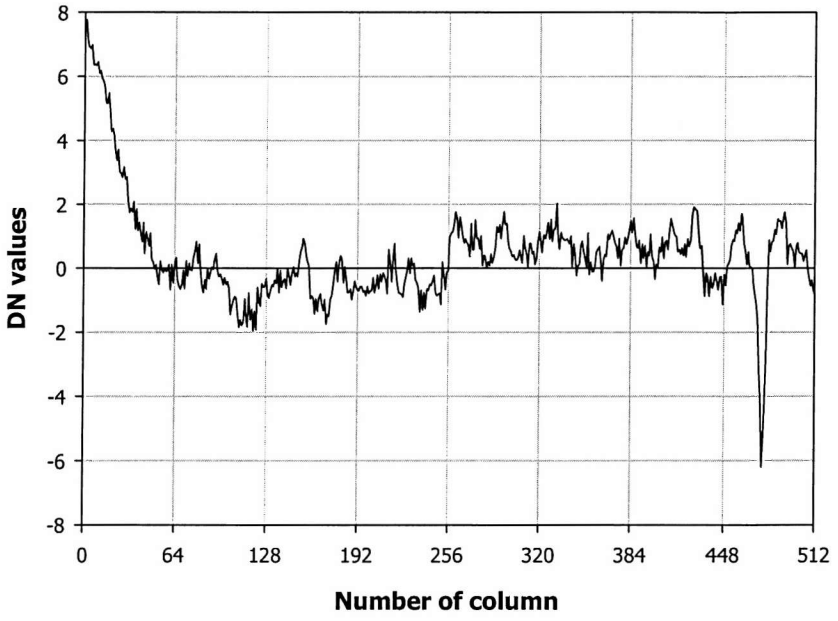

Figure 4-21. Normalised difference plot is illustrated in the cross-track pixels in the original images described in Figure 4-20. The plot is relative percentage differences of between image with old RSC coefficients and those new.

4.5.1. Merging two uniformity datasets

The uniformity problem in RSC is mainly induced by laboratory calibration, rather than instrumental error. During 2002, three CASI-2 calibrations were performed within a month because of the SHU repair. Due to the mechanical problem in the optical system of the SHU (sensor reference number of 2007), the calibration results from NERC28 were discarded, and NERC28a was conducted as a simplified post-repair test calibration after the manufacturer's repair. After some minor adjustment of the SHU carried out in NERC EPFS, a full calibration procedure was performed and its results were accepted for the CASI-2 data acquired during the first half of the flight season in 2003. Within the relatively short period, even when there was no

actual operation on the aircraft, the calibration results are expected to represent the repeatability of the calibration procedure. Although the RSCs from two earlier calibrations (NERC28 and NERC28a) are radiometrically invalid, the comparison between these results gives feasible relative spatial uniformities from different calibration data.

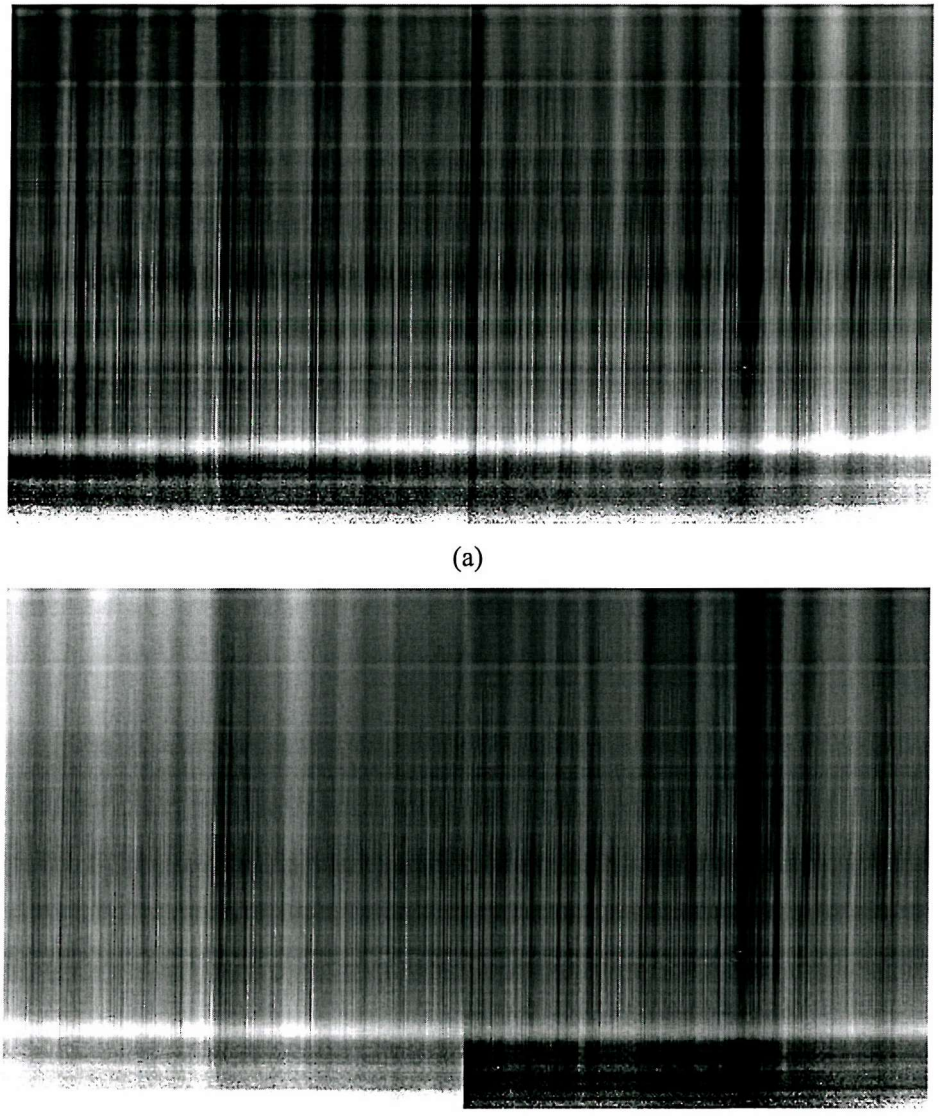

(a)

(b)

Figure 4-22. Percentage difference of RSC coefficients in Aperture 3, subset of (81:493, 1:288) from entire imaging part of CCD array. They are before (ref. NERC28) and after (ref. NERC28a) the repair in the Itres Research Ltd (a), and between the two calibration measurements (ref. NERC28a and NERC29) after the in-house repair in NERC EPFS (b). Top-left pixel represents (81, 0) in CCD array, and grey scales in the images are not the same.

Comparison between pairs of RSCs is depicted in Figure 4-22. Vertical stripes in the compared RSC image in Figure 4-22*a* suggests that an optical alignment, such as focal length, in the SHU were changed between two calibrations, perhaps as a result of the repair and physical shocks from overseas shipment. On the contrary, horizontal discrepancies mainly arise from wavelength change due to different spectral alignments, which has already been discussed in the previous section (Section 4.3). One of the important factors to notice is the relatively dark vertical line in the centre of the RSC image, this is caused by the problem of merging uniformity data. This effect is however rather difficult to recognise because the post-repair alignment change is dominant in this case.

A more distinctive uniformity problem was observed between NERC28a and NERC29. There were only a couple of days between the measurement intervals and virtually no spectral, spatial or radiometric property changes in spite of the minor in-house repair. The overall variation between the datasets was supposedly minor compared with those for the comparison from the earlier dataset. However, a side-to-side differential in the blue range of the CCD was clearly shown in addition to the slight aliasing effect which was also seen in the previous comparison (Figure 4-22*b*). The bright region corresponds to positive values, i.e. greater pixel values than the older RSC, whereas dark represents reduced RSC values. Despite this non-uniform RSC problem, the radiometric performances of both RSCs were accepted independently by the error analysis. The reason for this is that the evaluation method suggested by the manufacturer does not consider the non-uniformity problem since it tests only the centre column of the image.

The apparent step of RSCs in the centre of the imaging part of the CCD array suggests that it is not a detector induced problem but that it is most likely introduced in the process of merging two sides of uniformity data. The uniformity data for both sides of the image are overlapped in the centre region of the CCD columns, and they are supposed to be equal since the illumination source, i.e. integrating sphere, is highly uniform across its exit port (Figure 4-23). CASI-2 calibration processing software cuts both uniformity data at column 335 and joins them as if the detector elements were illuminated under the spatially uniform light source. Figure 4-23 shows that for two different calibrations the spectral responses on both uniformity data are matched well over the wavelength range. In reality, however, they are not exactly the same, and this causes the spatially non-uniform RSC values. The sources of error could be associated with changes of the alignment axis between the SHU and the light source when

switching illumination positions for left and right uniformity data or spatial uncertainty of the light source.

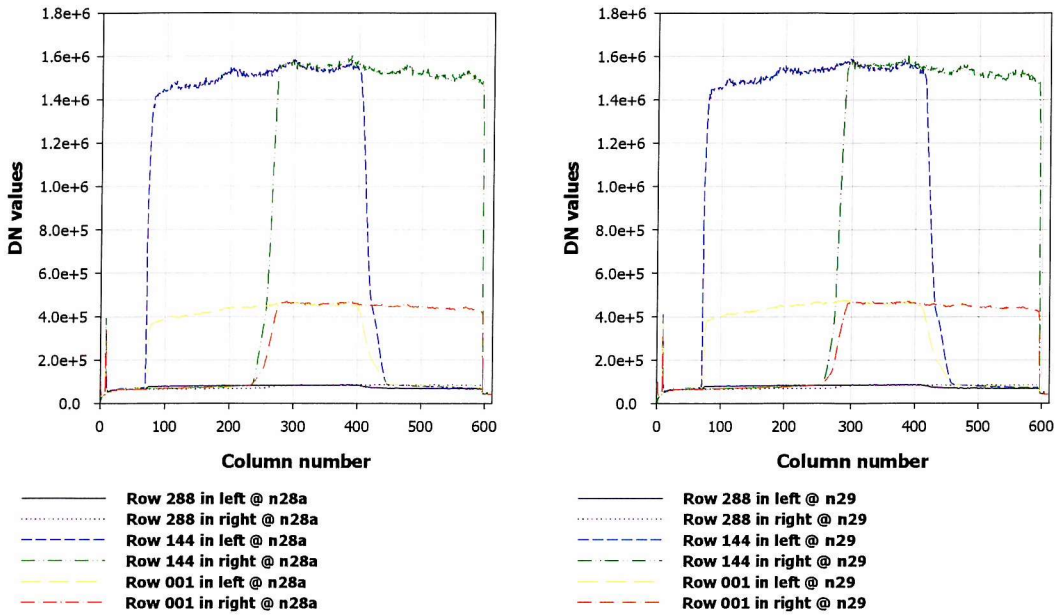

(a) (b)

Figure 4-23. Typical uniformity data of left and right sides from NERC28a (*a*) and NERC29 (*b*). For left side of the image, the illumination source is centred in column 185, while column 485 is used for the right side. Three spectral positions are selected: short wavelength (row 288), middle (row 144), and NIR (row 1).

Closer investigation in the commonly illuminated columns for both uniformity datasets implies that spatially non-uniform illumination may contribute to the disagreement of the uniformity dataset. Figure 4-24 is the relative difference of the left uniformity data to the right side, i.e. positive value represents greater response (DN values) in the left side, and vice versa. There is spectral dependence. However, for the entire spectral region, the spatial response in the left uniformity data tends to be decreased as it moves toward the edge of illumination source (i.e. increasing column number), whereas in the right side data its relative response is getting stronger toward the centre of the light. Spatial variation of the relative response may be due to changes of instrument alignment. More importantly, the fact that the same trend appears in both calibration sessions indicates that this problem is mainly systematic, such as non-uniform illumination.

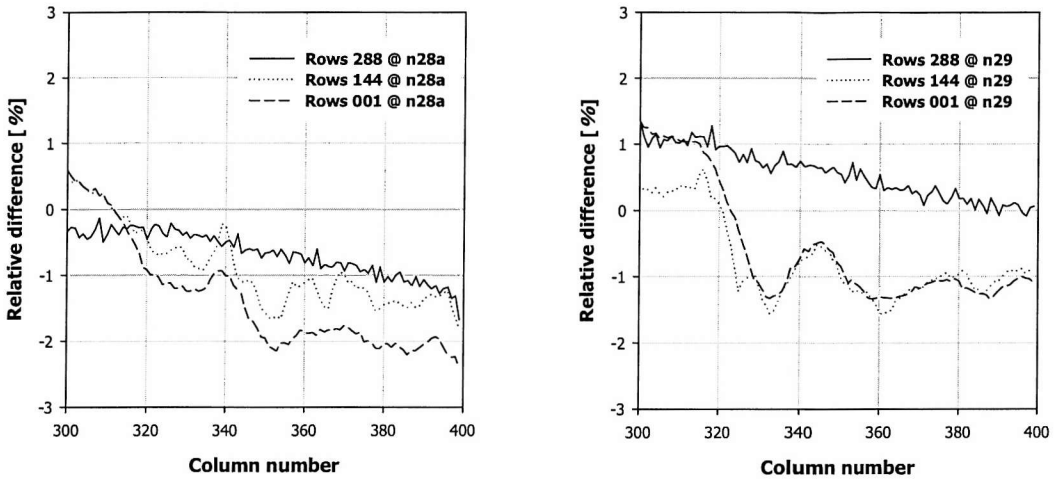

(a) (b)

Figure 4-24. Relative percentage difference ratio of the left uniformity data to the right from NERC28a (*a*) and NERC29 (*b*). Column range is limited to the centre of the image between 300 and 400 where left and right uniformity data are overlapped.

4.5.2. Spatial non-uniformity due to integrating sphere

The Hoffman integrating sphere is used for the CASI-2 calibration. The spatial uniformity of illumination from the sphere is reported by the manufacturer to be within 0.1 % across the diameter of the sphere exit port, but it is not tested for a specific sphere. The routine radiometric calibration performed by the UK NPL after every 100 hour of usage is only certified within diameter of around 5 mm in the centre of the exit port, they do not measure its spatial characteristics. However previous experiences of the sphere suggest that variation of the sphere illumination would be around 0.4 % across its diameter.

A spectroradiometer, the ASD FieldSpec Pro, was used to test the spatial uniformity of illumination. The data were measured by placing the fibre optic probe of ASD close to the exit port of the sphere (1000 fL [**] with 3.195 A) in total thirteen evenly separated positions across the diameter. The fibre optic cable itself and surrounding objects, such as the probe mounting, were

[**] Footlambert (fL) is a unit of photometric brightness ($cd\pi^{-1}ft^{-2}$, where cd is candela (luminous flux per steradian)). Since luminous flux can be expressed by radiant flux (lm = 1/683 W), $fL \cong 5\times10^{-3}\ Wm^{-2}sr^{-1}$ between 380 and 760 nm.

covered by non-reflective dark cloth to prevent any secondary scattering. To reduce uncertainty, the dark current spectrum of ASD was also removed from the acquired data.

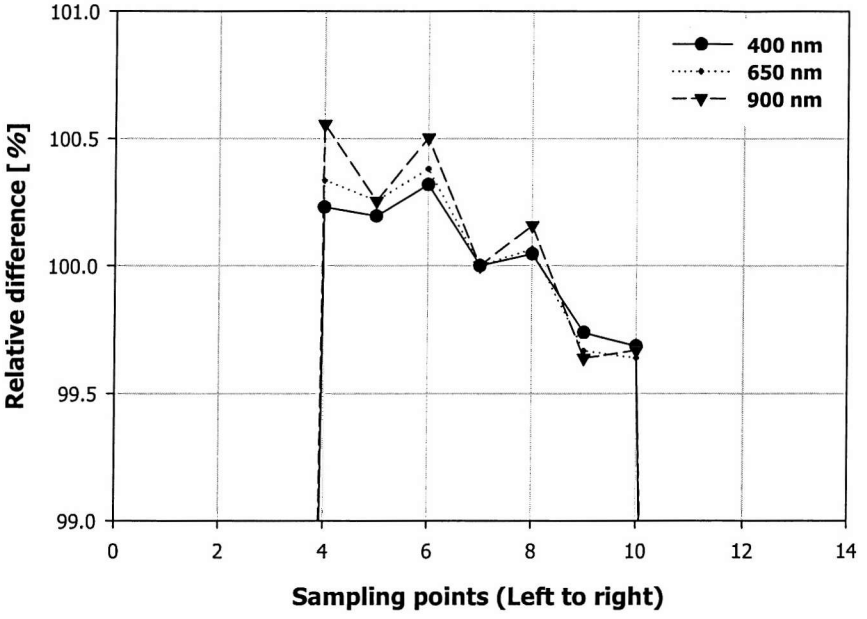

Figure 4-25. Spatial uniformity of the Hoffman integrating sphere against ASD Field Spec Pro. The plot values are relative percentage difference with respect to the value in the centre of the sampling points.

The relative illumination differences across the horizontal diameter of the exit port are shown in Figure 4-25. For three spectral regions, spatial variation of the sphere is clearly observed: greater to the left side of the sphere, and less to the right in comparison to its centre. The overall difference is around ~1.0 % (i.e. ±5 %), which is greater than the manufacturer's sphere specification. The spectral dependence of this spatial variation shown in Figure 4-25, i.e. the variability increases with wavelength, is also similarly replicated in Figure 4-24. Since the difference in two sided uniformity data is around ~±2.0 %, the CASI-2 non-uniformity problem could be reduced by ~50 % with a homogeneous illumination source.

The spatially non-uniform sphere results in a step in the centre of the merged uniformity data. In the left side uniformity data at columns near 335, relatively less illumination (left of the sphere exit port) is entered. On the other hand, relatively greater intensity than it should be is projected in the uniformity data for the right side (right of the sphere exit port). Hence, the

inverse relationship between output radiance and RSC value produces smaller radiance values in the right side from the centre of the image than its true radiance value, and the opposite on the left side.

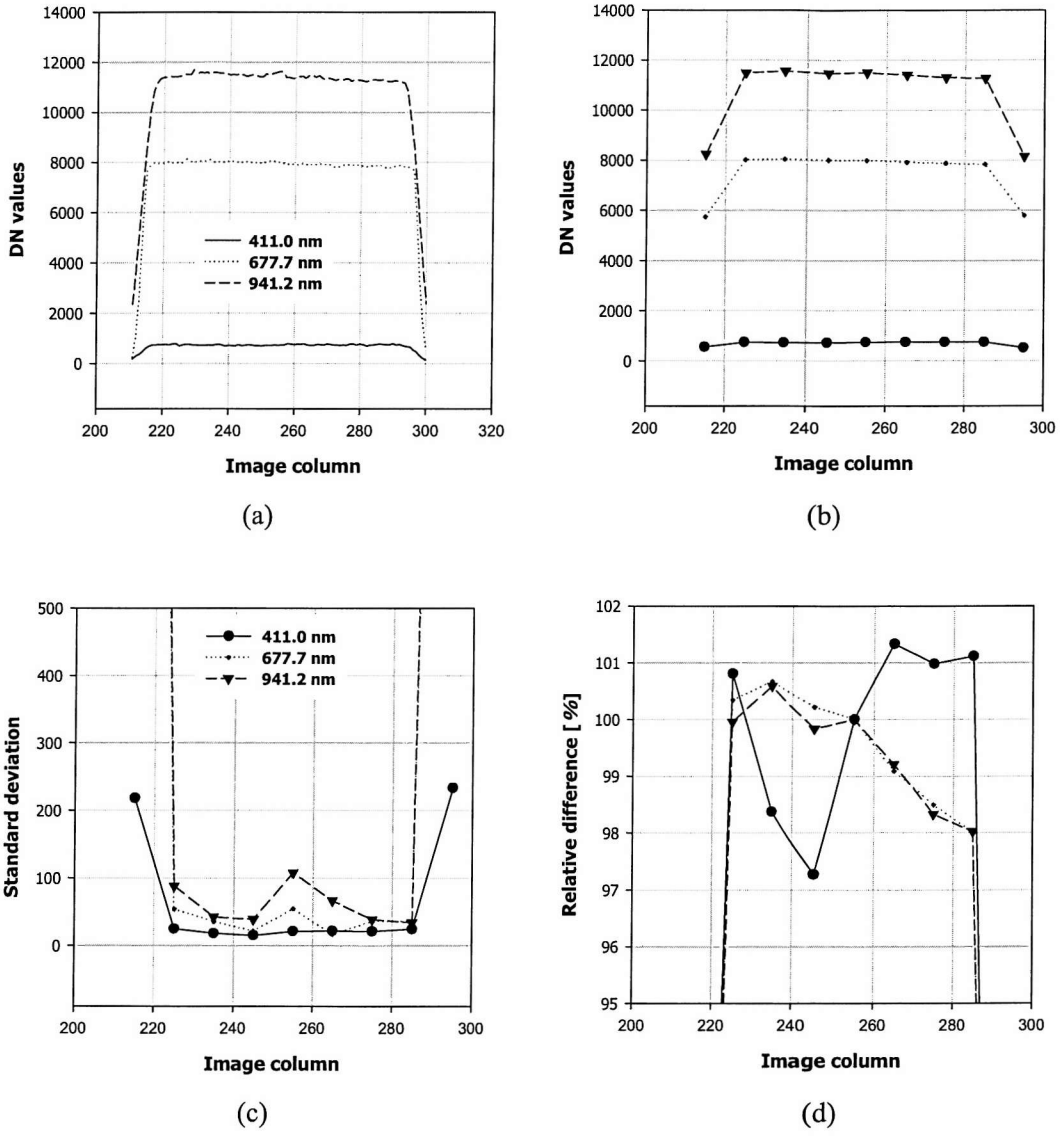

Figure 4-26. RSC verification data in spatial mode with selected three bandset (411.0, 677.7, and 941.2 *nm*). The original data subset in the centre image (*a*) are segmented every 10 columns and averaged (*b*). Standard deviation of each mean point is in (*c*). The relative differences (*d*) are calculated with the same way as shown in Figure 4-25.

The effect of non-uniformity in the RSC, as a result of spatial variation of the intensity source, influences the radiance output as shown in Figure 4-20 and Figure 4-21. This was tested

by using the RSC verification data in spatial mode. The data were obtained at the end of the CASI-2 calibration procedure, that is, measured against the same radiometric source (integrating sphere) under laboratory conditions. Due to the limited exit port size, only a small portion of spatial columns were illuminated around the image centre (Figure 4-26*a*), as with absolute radiometric data acquisition (Appendix A.5.1). The range of columns exposed to the illumination source were segmented and averaged every 10 pixels in order to reduce high frequency fluctuations. The positions of the mean values appear uniform across the column range (Figure 4-26*b*), but their standard deviation plot shows relatively larger values in the centre column of the image suggesting that there is greater variation of the radiance value in that region, possibly due to non-uniformity steps in the RSC (Figure 4-26*c*). The relative radiometric values of the mean points are represented in Figure 4-26*d*, as the same as Figure 4-25. Apart from the data in short wavelengths, the normalised differences from the image centre decrease from left to right in the image columns. Despite the same trend, the magnitude of relative difference is however greater than that of the integrating sphere, between ~+1.0 and ~-2 %. This results in non-uniform pixel values in the centre of the image due to the spatial variability of the sphere and non-uniformity of the RSC values. With comparison of relative difference figures, it can be concluded that the non-uniform uniformity data plays an important role in the inconsistent radiance pixel values across the image.

Consequently, the discrepancy of two uniformity data at short wavelength region, which would mainly cause RSC steps in the centre of the image, is a known issue for CASI-2 with wider than standard FOV (Figure 4-27). However, this problem could be minimised with a spatially uniform stable light source, and equally it is important to monitor the non-uniform RSC, which is not currently achieved during the routine laboratory calibration.

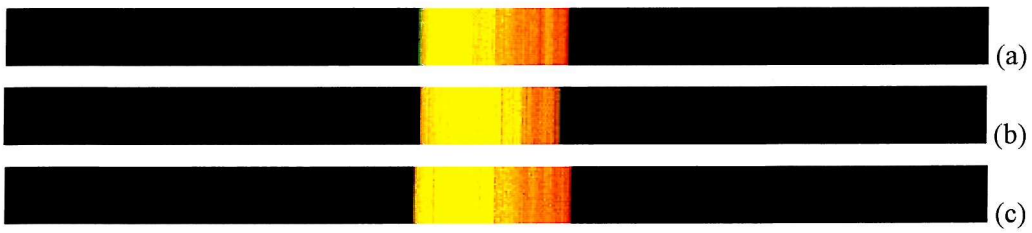

Figure 4-27. RSC verification data in spatial mode (Band 7 in filter.ccf; Rows 141-144) using Hoffman integrating sphere, from NERC28 (a), NERC 28a (b), NERC 29 (c). The pixel values in all pictures have been manually stretched in order to see their variations more clearly.

4.6. Summary

The RS data acquired by a state-of-art imaging spectrometer are meaningless without calibration to physical units in order to compare them with other environmental variables. Monitoring instrument performance through laboratory calibration maintains not only high quality data, but also the quality of data conversion from electronic signal to physically meaningful information in the image. Thus, the calibration process is an essential part of pre-processing for successful RS application, and should offer sufficient accuracy and reasonable uncertainties with available resources.

The calibration procedure of the NERC owned CASI-2 system follows the guidelines suggested by its manufacturer. It has fulfilled user's expectations in many applications of CASI-2 data to a large extent. However, at the same time, there are still susceptibilities and limitations of the CASI-2 output product due either to trade-offs between available resources and required details of the calibration results or to the calibration method or procedure itself. In this chapter, the spectral and spatial characteristics of the CASI-2 system, which cannot be tested with the conventional laboratory calibration procedure, are reviewed and their effects on the final output of the sensor are tested. Moreover, a method was developed to retrieve new information about the CASI-2, which has the potential to improve knowledge of the sensor system and enhance the usability of the data product.

The spectral properties of CASI-2 are determined by the wavelength calibration procedure. Currently, only limited samples are used for the wavelength calibration and the result is applied over all the detector elements with an assumption that there is little spatial variability of spectral response. The spectral emission lines, as wavelength standards, illuminate entire detector elements and are recorded in full-frame mode. Sub-pixel positions of the emission lines suggest that as expected there are systematic optical distortions across the image, known as optical smile. The reason for this could be partly due to optical distortions (i.e. 'smile' feature) or the nature of calculations of weighted average as described earlier. The smiling effect is wavelength dependent, i.e. it is less in the mid wavelength range and greater at both ends of the CCD array, although it is not clearly observed in the upper and lower limits of spectrum due to increased noise. Such variable sub-pixel positions results in uneven wavelength values of the corresponding pixels in cross-track image. The estimated wavelength uncertainty from the full-

frame wavelength calibration is ~1.0 *nm*, which is greater than the specification supplied by the manufacturer.

Even small errors in wavelength calibration can give completely different results in many image analyses. Mistakenly replaced G-numbers produced wrong atmospheric absorption features over an entire image, and gave incorrect information to the atmospheric correction model. This case study implies that spatial variation of wavelength value across an image could affect different pixel spectra and users must be aware that levels of spectral uncertainty vary in different parts of the image.

The effective wavelength range per detector element provides useful information when comparing CASI-2 data with other spectrometers that have a different number of detector elements or sensors. Unfortunately, conventional CASI-2 calibration does not include a procedure for measuring the spectral response (SRF) of each detector element. An iterative model was developed for the CASI-2 SRF, on the basis of using a spectral emission line as a wavelength-width standard. Despite the limited number of emission lines, the model results are of the same order of magnitude as generally used FWHM values of CASI-2, and show that estimates of the CASI-2 SRF could be achieved with minimal extra data.

As well as the susceptibility and sensitivity of wavelength calibration of CASI-2, the repeatability of accurate radiometric calibration was tested using replicated calibration data. For the NERC owned CASI-2, the main difficulty of calibration data acquisition is due to merging two-sided uniformity data. The comparison of the uniformity data and spatial variation of illumination source shows that the uncertainties of radiometric calibration are derived from the alignment changes between the SHU and integrating sphere for the uniformity pair and non-uniform illumination source. These error sources could possibly be reduced by using a more precise mount controlling the position of the instrument and a more uniform spatial distribution radiometric standard.

Chapter 5

Investigation of the CASI-2 downwelling irradiance sensor

5.1. Introduction

One of the approaches associated with correcting for atmospheric effects in airborne remote sensing systems is to measure the downwelling irradiance using ancillary instruments on a sensor platform. Several types of sensors for airborne radiometric observation have been tested by a number of authors for reflectance calibration (Milton *et al.*, 1994; Shepherd *et al.*, 1995; Piekutowski *et al.*, 1996; Gray *et al.*, 1997), as well as for atmospheric research (Foot *et al.*, 1985; Kilsby, 1986; Bannehr and Schwiesow, 1993).

Acquiring high quality data from airborne radiometers is not a simple task since most instruments of these types are designed for ground-based operations on stable and levelled platforms. Techniques have been developed to overcome these problems (Bannehr and Schwiesow, 1993; Piekutowski *et al.*, 1996), but none of these is suitable for practical applications without accurate sensor calibration and knowledge of its radiometric characteristics.

The Incident Light Sensor (ILS) is a typical downwelling irradiance sensor, which operates with the Itres CASI-2 airborne imaging spectrometer as a sensor system option. The diffuser head is mounted on top of the aircraft and is directly connected to the sensor system by a fibre optic cable. The most important advantage of the ILS is that downwelling irradiance is sampled coincidentally in the same spectral bands, as those imaged from the scene.

Unfortunately, the sensor characteristics of the ILS are less understood than other irradiance sensors, except for its specification from the manufacturer. Shepherd *et al.* (1995)

have analysed the errors from a rooftop-mounted incident irradiance sensor fitted to the Itres Instrument CASI, recorded during the flights. They applied a simple error analysis to the ILS data and concluded that it is feasible to measure downwelling irradiance from the ILS in a useful way over most of the spectral region.

The objective of this chapter is to characterise the properties of the ILS prior to its further application as an irradiance spectroradiometer. The description of the ILS and its integration with the Itres CASI-2 system is followed by laboratory experiments to determine its radiometric and geometric sensor attributes. The results will be used in a later chapter to develop a method of retrieving atmospherically standardised airborne images of sufficient accuracy for practical applications.

5.2. Experimental design for the ILS investigations

The conventional CASI-2 calibration procedure involves investigation of the mechanical and optical variations and characteristics to make the CASI-2 measurements independent of the instrument. Currently, the standard manufacturer's calibration procedure for the ILS only includes radiometric calibration and generates the radiometric sensitive coefficients (RSC) matrix (see Appendix A). More detailed tests, such as error ranges and angular response, are not required. Although several extra datasets from ILS are collected other than the ILS calibration, no verification is carried out as part of the manufacturer's standard calibration procedure.

There are also possible errors involved even during the ILS data collection for the calibration process. As a result, the standard calibration procedure of the ILS has been found to contain problems with practicality and consistency, and a better way is being investigated and developed with the manufacturer (personal discussion with Itres Research). The instrument setting is rather complicated and takes as much time as the radiometric calibration of the CASI-2. Two specific problems are still unanswered as stated below.

- The fibre optic cable between the ILS and the SHU is not only susceptible to errors caused by bending and twisting, but is also often less than a perfect light guide, especially for the short wavelength region. Non-linear behaviour under various illumination conditions might be expected due to the interaction or entrapment of light as it passes through the optic cable.

- The angular properties of the ILS have not been tested during conventional laboratory calibrations; it is assumed to be a perfect cosine receptor.

In order to investigate these problems, laboratory experiments were set up for both NERC and EA CASI-2 systems with the measurements detailed in Figure 5-1. The Hoffman integrating sphere replaced the videolamp used in the conventional ILS calibration as a luminance source. Direct measurement between the integrating sphere and the ILS reduced the time for setting the instrument up and provided the benefit of a stable and accurate standard radiance source, i.e. highly uniform radiance distributions and an adjustable illumination level

of the integrating sphere. Simple conversion of the ILS DN values into irradiance units make it easier to compare with a known reference of spectral intensity to the ones at other illumination levels.

	NERC CASI-2	EA CASI-2
Date	**7 Nov 2001**	**17-18 Dec 2001**
Data availability from the conventional ILS calibrations	✓	×
Measurement types		
• Radiometric measurement (Hoffman Engineering Integrating sphere; LS-64-8D)	✓	✓
• Angular measurement (Collimator from Oriel)	✓	✓
Directional test	×	✓
Starboard to port	n/a	✓
Nose to tail	n/a	✓
Uniformity test	✓	×

Figure 5-1. A list of measurements conducted for CASI-2 systems owned by NERC and EA.

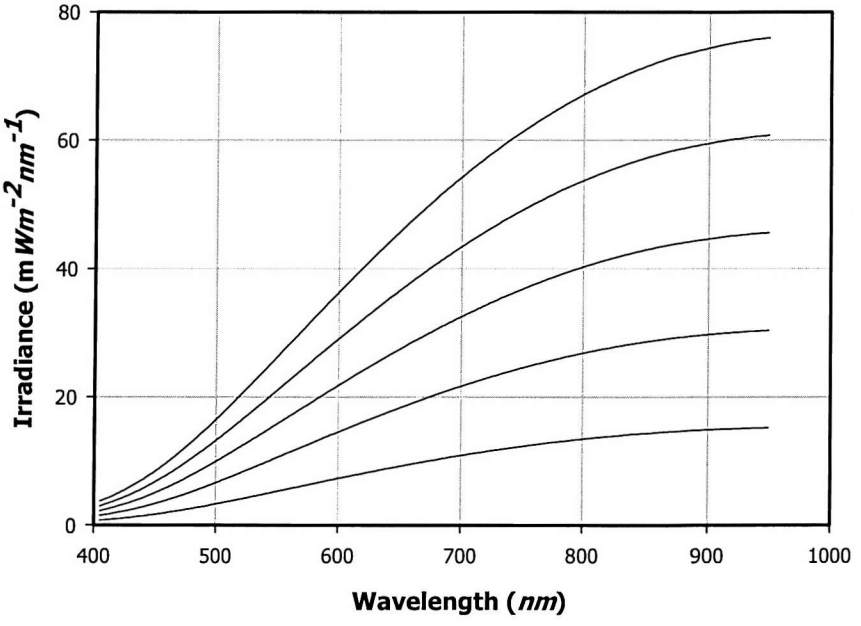

Figure 5-2. The irradiance spectra of Hoffman integrating sphere. Polynomial coefficients for radiance values in 1000 *fL* are used in the CASI calibrations (the curve with the largest values) (data provided by NERC EPFS). The rest of the other curves represent estimated spectral radiances that decrease proportional to the values with interval of 200 *fL*.

The angular response of the ILS was tested using a collimator that projected a parallel beam of light on to the ILS. This enabled a test of how close the ILS behaves to an ideal cosine receptor. In addition, the effective angular range over the sky dome of the ILS could be found from the various angle measurements. Directional variation of the angular response (azimuthal angles) was also measured.

For the NERC CASI-2, the angular properties of the ILS were tested, but with no directional angular response (left-right and nose-tail) since there is no marking on the diffuse sensor head to indicate its orientation in the airframe. Instead, a uniformity test of the collimator was carried out to measure the quality of the collimated light. The measurement details of the EA ILS omitted the uniformity test for collimated light. A pair of directional angular tests were done over the flight direction (nose to tail) and the aircraft wing direction (left-right).

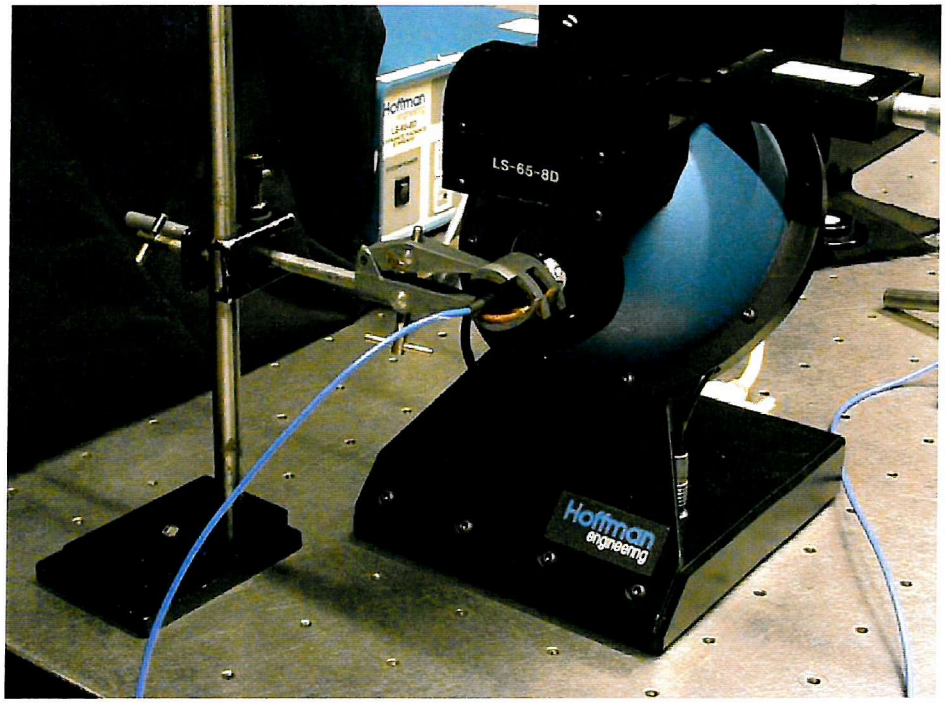

Figure 5-3. ILS setting with Hoffman integrating sphere.

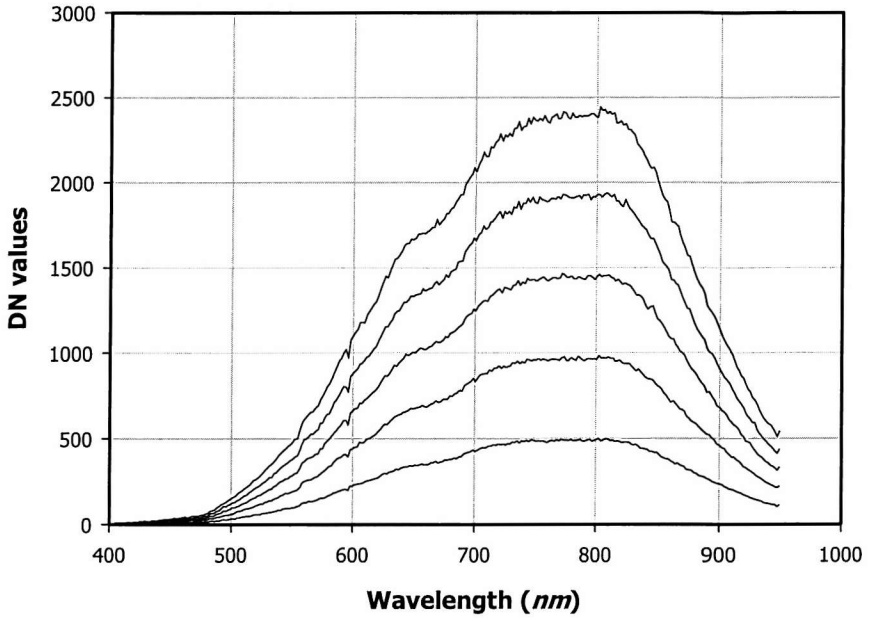

Figure 5-4. DN values of ILS at five luminance settings of the integrating sphere.

5.2.1. Linearity measurements

A Hoffman Engineering integrating sphere (Model number LS-64-8D) was used as a radiance source for the experiment, which is the same luminance standard as used for the CASI-2 calibration recommended by Itres Research Ltd.

S-coefficients (as shown in Table A.1 in Appendix A) were used to generate spectral radiance curves at the Hoffman integrating sphere setting of 1000 *fL* with 3.195*A* as calibrated in the NPL. Four other intensities with intervals of 200 *fL* were selected for the measurements, and their spectral radiances were estimated with an assumption that the radiance values of the sphere were linearly proportional with its luminance change across the wavelengths. Hence, for example, the radiance value at 800 *fL* is 80 % of the radiance from 1000 *fL*. Figure 5-2 shows the spectral radiance curves for five intensities for the ILS measurements.

The ILS sensor head was placed in front of the sphere's exit port looking inside a hollow sphere, so that an entire area of sky dome of cosine receptor received uniform light from

the sphere (Figure 5-3). The lamp current and luminance were initially at a default setting (3.195 *A* and 1000 *fL*, respectively). In CASI, pixel values in the ILS centroid column were displayed to determine the sampling integration time (2500 *ms* in this case) for a maximum value at around 2500 *DN*. Dark current measurements were obtained at the beginning and the end of the ILS data collection. Henceforth, the ILS data means the mean of dark currents subtracted from the raw DN values.

5.2.2. Angular measurements

5.2.2.1. Collimator

A collimator was built in NERC EPFS, University of Southampton. It uses a quartz tungsten halogen lamp stabilised by an Oriel power supply. The lamp provided enough brightness at 11*V* throughout the experiments. The lamp housing (manufactured by Ealing Electro-Optics Ltd.) was aligned with a collimator lens on a metal panel. The light focus was controlled in the back of the housing by adjusting the position of a paraboloidal reflector attached with a bulb. For height adjustment, two lab jacks were placed underneath the collimator (Figure 5-5(a)).

The area of the collimated beam was reduced by controlling an aperture of an iris diaphragm so as to illuminate only the diffused glass on the ILS sensor head (Figure 5-5(b)). The ILS was mounted on a stand with a rotating positioning stage. The mount provided a smooth, continuous horizontal rotation of the ILS over a range of ±90° with respect to the collimated beam direction. The ILS mount was designed to correct the sensor position in backward and forward motion, and hence the cosine receptor was placed exactly on the rotating axis of the rotary stage.

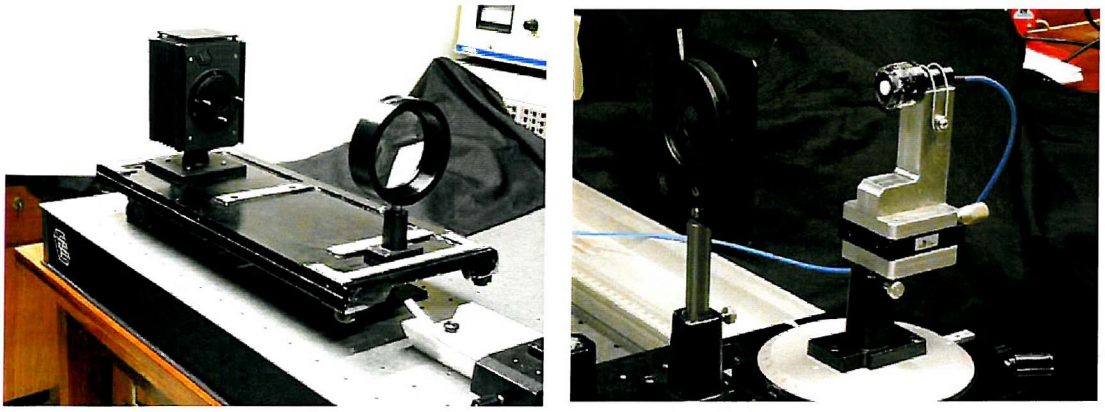

(a) (b)

Figure 5-5. A collimator is laid on two lab jacks for the height adjustment (a). The ILS mount is placed in front of an iris diaphragm to illuminate the diffuser of the ILS (b).

5.2.2.2. Performance check

The performance of the collimator was tested by measuring the uniformity of beam intensity during the ILS measurement of NERC CASI-2 (7 November 2001). The beam of collimated light was roughly focused by visual inspection (checking with a white sheet at the ILS position), however, a more accurate test of the collimation is important for the quality of the collimated beam. This was achieved using a fibre optic cable with a narrow FOV connected to a spectrometer (USB2000 Miniature Fibre Optic Spectrometer, Ocean Optics Inc.) which was placed on the ILS mount, and a series of measurements were taken horizontally across a beam diameter.

The position of the collimator was slightly displaced from the axis of the iris diaphragm for the NERC ILS measurements (Figure 5-6a). If the distribution of the light intensity were homogeneous, such misalignment would not be affected by the uniformity of the light reaching the ILS. The diameter of the beam of light passing through the iris diaphragm was approximately 20 *mm* (Figure 5-6b).

From the left end, 22 measurements were taken across a diameter with 1 *mm* interval. At each reading, the number of spectral samples was 2048 with a range between 518.43 and 1161.51 *nm*. Data from the fibre optic cable were DN values with no spectral units, and it was

not necessary to convert them into radiance units since only their relative values were to be compared.

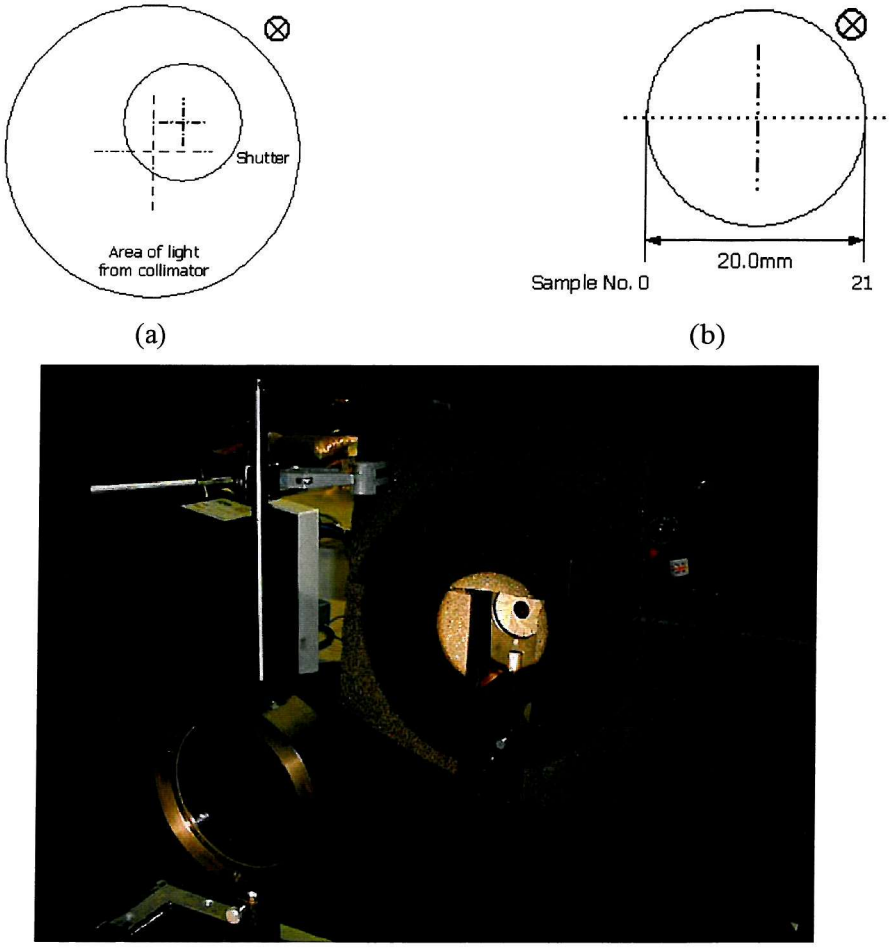

(a) (b)

(c)

Figure 5-6 Diagram of iris diaphragm alignment with respect to the collimator beam for NERC CASI, 7 November 2001 (a), and positions of a fibre optic probe for collimation uniformity check (b). A mark ⊗ on both diagrams represents that light travels away from the reader's point of view. Several black boards surround the Iris diaphragm shown in Figure 5-5b in order to prevent scattered light falling upon the ILS (c).

The mean spectral radiance in each sampling position was normalised with respect to that in the centre of illuminated area. Figure 5-7 shows that the intensities on the left side of the area (~103 %) tended to be larger than the other side (~85 %). It means the beam of light from the collimator was relatively stronger towards its centre, whereas the intensity decreased away from the centre. Percentage differences within the area vary more or less than 18 % across the region. However, as the effective area for a diffused sensor head was less by 1 *cm* across the

beam area, maximum intensity differences were expected to be below ±5 % for both NERC and EA ILS measurements. A vertical profile of uniform collimation was not necessary in this case because angular measurements of a cosine receptor were only required in the rotating horizontal plane.

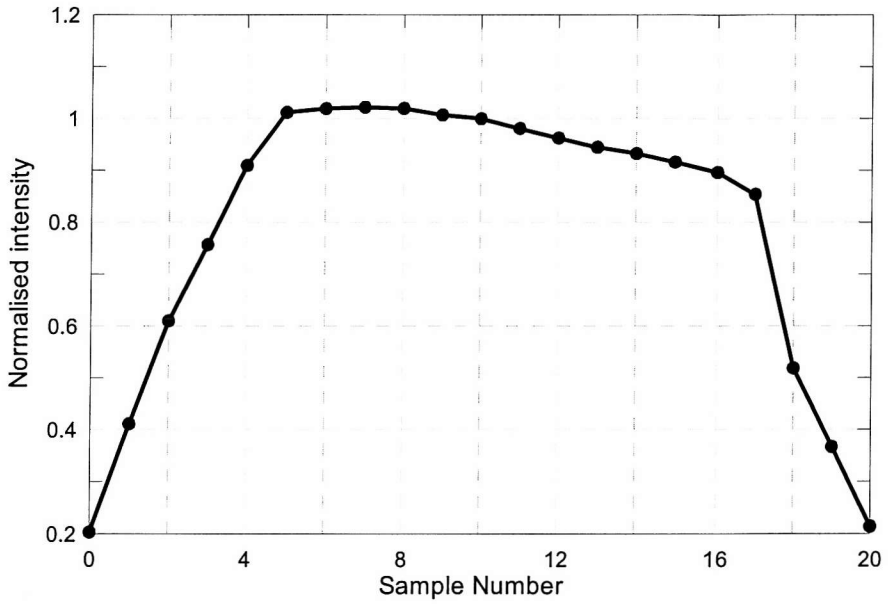

Figure 5-7. Normalised intensities of collimated light across a horizontal transect across the ILS. The integrated spectrum of each record is divided by that of sample number 10, as a centre of illuminated area. X-axis of the plot represents a diameter of collimated light, i.e. 20 *mm*.

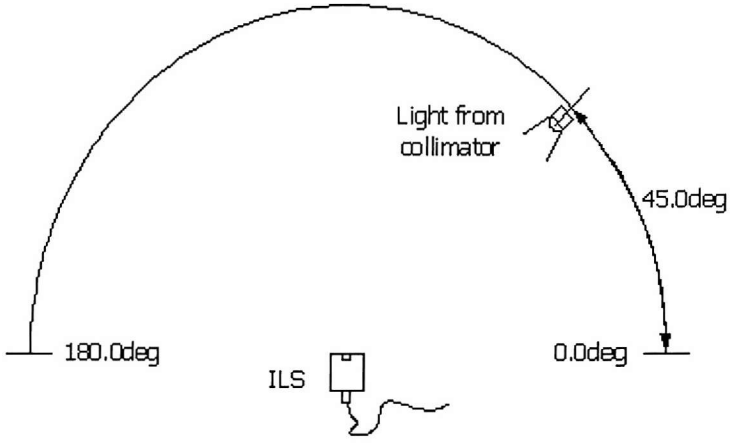

Figure 5-8 A diagram of angular spectral response measurements of ILS. During the experiments, however, the sensor position moved, while the light position was fixed.

5.2.2.3. Angular response of the ILS

The cosine receptor of the ILS was mounted on a specially designed rotary stage on an optical table as shown in Figure 5-5(b). In order to minimise light being reflected by objects nearby into the ILS (i.e. scattered light), a barrier covered by Cordelan fabric at the iris diaphragm allowed the light through its aperture. Hence, the collimated light only reached an area of a diffuse probe of the ILS. The rotating axis of the rotary stage was located exactly on top of the ILS sensor head by a sensor positioning knob in the ILS mount, with the intention that the ILS took as much light as possible at any angular location.

The angular responses of the ILS were obtained at 10° intervals between ±90° from the centre of the ILS position where the sensor looks straight into the collimator, while a position locking knob secured each position. The data recording started from when the light reached at 90° on the right side of ILS (0° in Figure 5-8) to the other side (180°). In order to minimise variations of the collimator intensity during the measurements, ILS data were recorded at 30° intervals over the range of angles, then filled in with the other angles at 10° intervals.

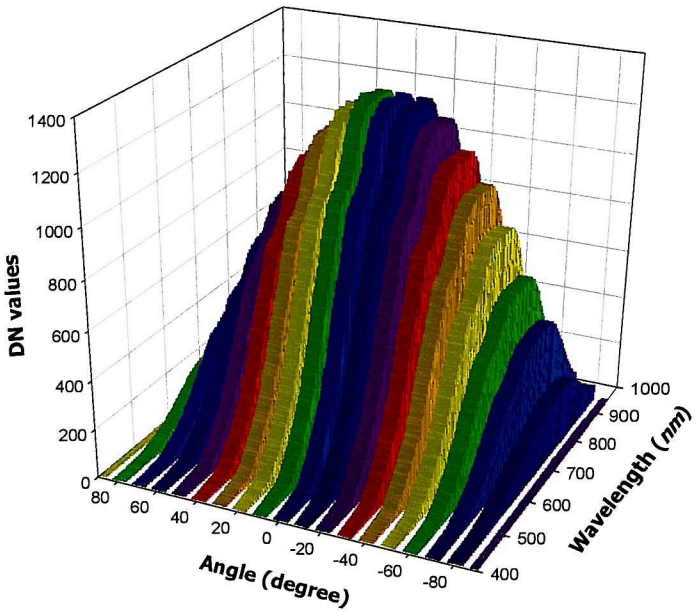

Figure 5-9. Raw DN of the ILS from directional variations (NERC CASI-2). The legends are identical to the ones in Figure 5-10. The ILS position in each angle is represented in Figure 5-8.

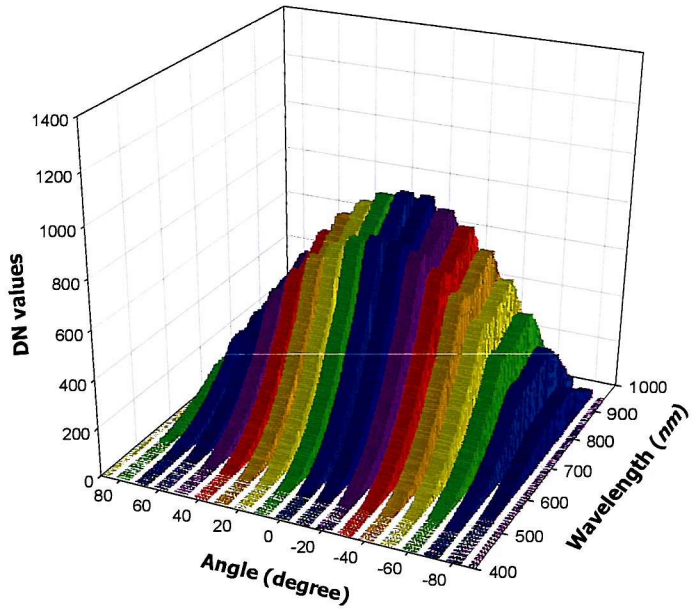

(a)

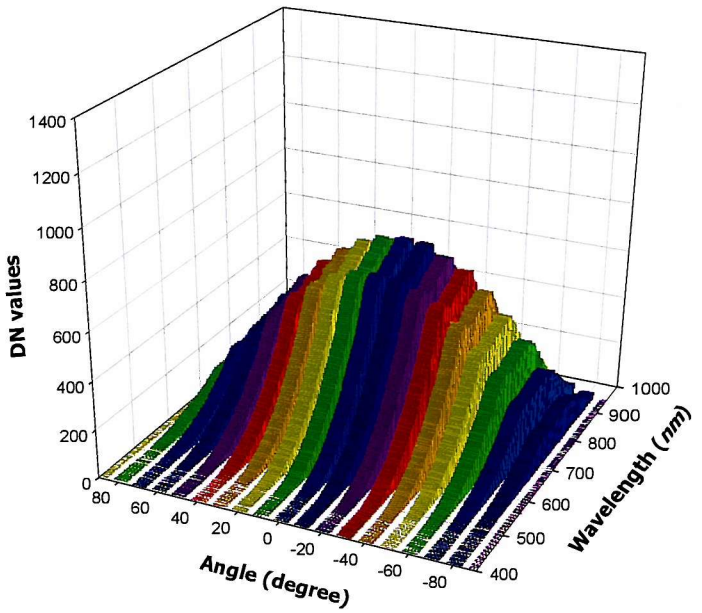

(b)

Figure 5-10. Raw DN of the ILS during directional variations (EA CASI-2). The scales for both plots are identical to the ones shown in (b). The angles shown in (b) are from left (-90 degree) to right (90 degree) of the aircraft, whereas those in (a) are from tail (-90 degree) to nose (90 degree; the flight heading) (b).

The ILS from the Environment Agency was always installed in the same direction every time when mounted in the aircraft, although the sensor is designed to have no directional dependencies. For the test of its directional dependency, two sets of angular data were collected, i.e. the angular measurements in the directions of left/right wing and nose/tail of the aircraft. The mean of two dark currents of ILS before and after the main measurements were subtracted from raw DNs of the ILS in order to minimise systematic errors from CASI-2.

Raw DN values from the angular measurements are depicted in Figure 5-9 and Figure 5-10. Both ILS from NERC and EA show similar spectral responses. Each group of spectral curves between symmetrical angles, e.g. 60 and 120 degree, are very similar to each other, but the differences may indicate that either the spectral response of ILS is not perfectly symmetrical or the collimated light is not spatially uniform. The spectral differences between pairs of symmetrical angles decreased for the left/right measurements of EA ILS (Figure 5-10b). This is partly because the radiometric resolution of the ILS is possibly degraded, as DN values are generally reduced; otherwise there are real differences between left/right and nose/tail.

5.3. Linearity check

The laboratory experiments measured the ILS signals from five levels of radiance intensities using the integrating sphere. Integration time of the CASI-2 was adjusted until the maximum DN values in the ILS column were greater than 600.

The DN values from ILS were converted to irradiance in order to compare the ILS measurements with the estimated sphere irradiance. The conversion coefficients were computed by using the same equation used for the ILS RSC ($DN\ [\mu Wcm^{-2}nm^{-1}]^{-1}\ ms^{-1}$; see Appendix A).

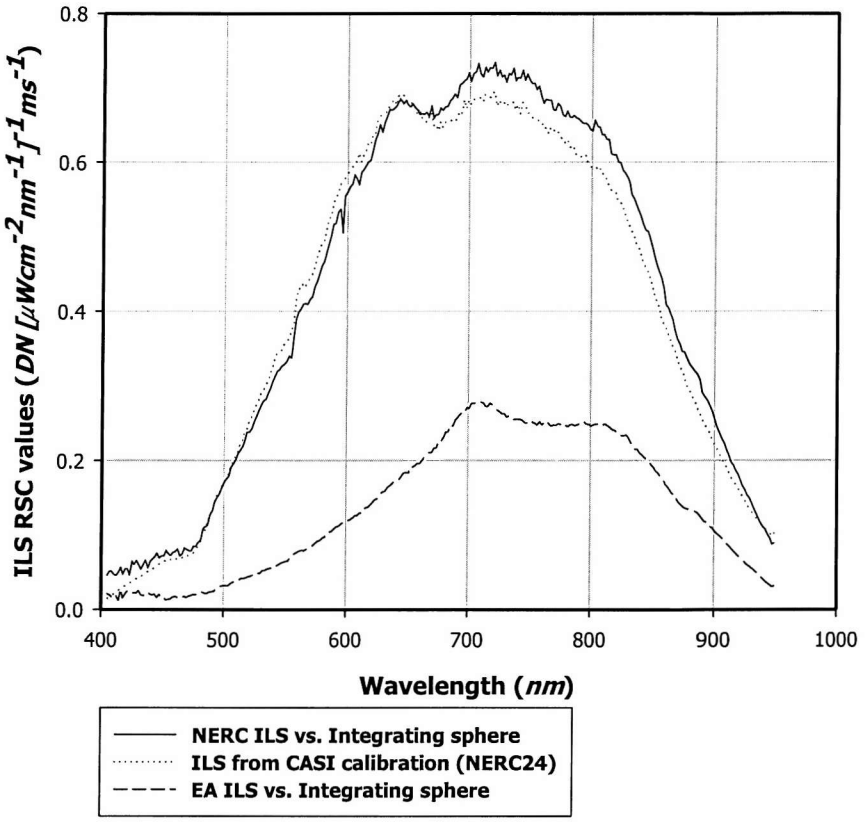

Figure 5-11. RSC coefficients values of ILS generated by the direct measurement with a Hoffman integrating sphere during the CASI-2 calibration (NERC24) and the measurements of EA ILS.

The comparison between the ILS RSC from the CASI-2 calibration and the one from the integrating sphere was only possible with the NERC ILS since RSCs from the EA were not available. The conversion equation requires integration time and ACR (Absolute Correction Ratio) that is defined as the ratio of corrected absolute DN to corrected uniformity DN. The ACR from the NERC CASI-2 calibration was used for both NERC and EA ILS, since the uniformity of spectral response is assumed to be fairly similar for each individual CASI-2 system. The radiance unit ($mWm^{-2}sr^{-1}nm^{-1}$) of the sphere is multiplied by 2π for irradiance ($mWm^{-2}nm^{-1}$) over the sky dome, as well as the ILS RSC is divided by 10 for the unit conversion between $DN\ [mWm^{-2}nm^{-1}]^{-1}$ ms^{-1} and $DN\ [\mu Wcm^{-2}nm^{-1}]^{-1}$ ms^{-1}.

The conversion coefficient curve for the NERC ILS (Figure 5-11) shows a similar trend to the ILS RSC from the NERC CASI-2, while it is quite different from the one from EA CASI-2, indicating that the spectral responses are different between the two CASI-2 systems. The difference of the RSC values between the ILS test measurement for this chapter and the routine CASI-2 calibration is not surprising as the standard manufacturer's calibration procedure for the ILS is found to be susceptible to errors from the previous calibration history. There are still a couple of factors to be carefully considered before the direct calibration method of the ILS used here, such as secondary (or higher) order reflection effects from the ILS sensor head itself when it is nearly inserted inside the integrating sphere, or the uncertainty of the sphere uniformity. In other words, the disagreement of the conversion coefficients of the NERC ILS may be because the light coming into the diffuse sensor head did not completely cover the sky dome and/or because the light reflecting back into the sphere's exit port from the ILS sensor head altered the ILS signal. Nonetheless, this new direct method makes much more consistent calibration results with the integrating sphere, the stable illumination source.

The RSC values from EA ILS show quite different trend as with NERC ILS. This is a known issue that the manufacturer replaced the ILS sensor head and its fibre optic cable in 2000 for better radiometric resolution, as a result of which the radiometric sensitivity of the ILS has been increased by a factor of 2 for NERC CASI system. On the other hand, the EA system kept the same as the manufacturer's original ILS specification which has relatively lower RSC values. According to the irradiance conversion equation of the ILS (Equation A.26 in Appendix A), it is expected that NERC ILS provides around double the radiometric resolution of downwelling irradiance than the EA CASI.

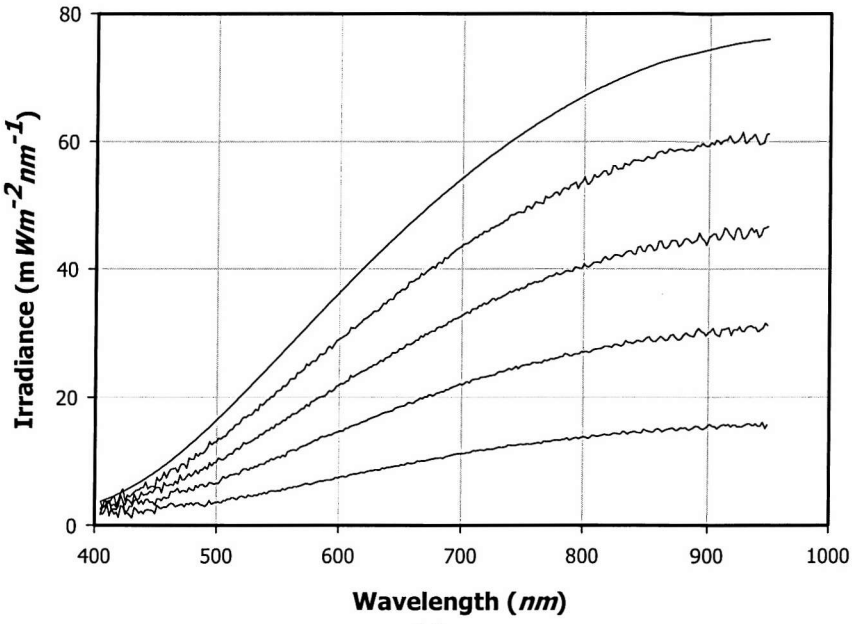

(a)

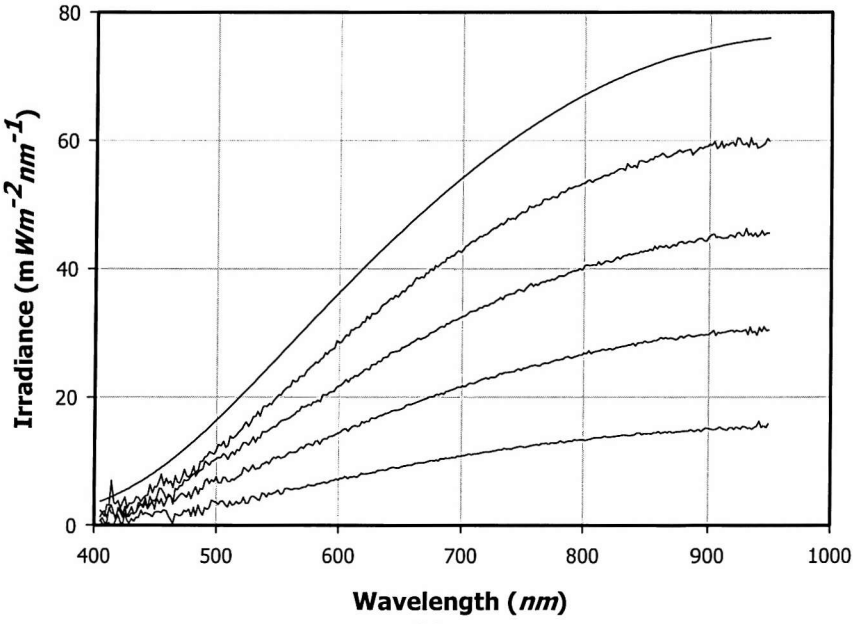

(b)

Figure 5-12. The measured irradiance spectra of the ILS transformed by the ILS conversion coefficients against the various intensity settings of the integrating sphere. NERC ILS (a) and EA ILS (b). The plot formats are identical to the one in Figure 5-2.

The raw ILS DNs from both CASI systems were converted into irradiance values to compare them with the estimated irradiance spectra of the integrating sphere as shown in Figure 5-4. Although there are some variations with relatively high frequency noise in both ends of spectra, all plots tend to follow the estimated sphere irradiances. Note that the spectrum at 1000 *fL* in Figure 5-12 is identical to the one shown in Figure 5-4, i.e. RSC values were derived by using the ILS data at 100 *fL* as a reference intensity and its irradiance conversion (inverse) does give the same irradiance values.

For more detailed assessment, each spectrum from the RSC conversion was compared with its corresponding irradiance spectrum from the integrating sphere. Again, data recorded at 1000 *fL* are not taken into account in this processing. Scatter plots in Figure 5-13 show that the RSC values for NERC ILS yield sensible irradiance values over various ranges of illumination conditions. Although there are small degrees of scattered data points at lower irradiance signal, especially in 400 and 200 *fL*, data points on the whole follow a straight line that matches equivalent irradiance values. Moreover, the prediction boundary from statistical analysis (with 99 % confidence limit) shows the irradiance from the ILS is expected to follow the same trend even with the values that are out of the data range measured. The results from the same analysis for the EA ILS dataset are depicted in Figure 5-14. The data points are again positioned on a line passing through the equivalent irradiance values for both axes. However, scattering behaviour in lower irradiance values tends to be greater than those in NERC ILS, resulting that the statistical prediction boundaries become greater and the linear regression lines may not pass through the origin (Figure 5-14a) or to give probable deviations as it extends toward the much greater irradiance values (Figure 5-14d).

The problem of relative inconsistency at lower irradiances remains to be investigated. Its significance depends upon the characteristics and the origin of the problem, and two possible sources are identified. First, the ILS signal could become relatively unpredictable, as the finer radiometric resolution might be necessary to represent the small changes. If this error is dominant, this will be considered as a limitation of the ILS or could be ignored since the problem affects mostly on the short wavelength spectra where the downwelling solar irradiance in reality is greater than longer wavelength region. Second, the problem may be wavelength dependent. Spectra shown in Figure 5-12 indicate that the fluctuations are also observed at longer wavelengths, as well as in the short wavelength region. Similar features have been noticed in several field spectroradiometers from my previous experience, which were either due

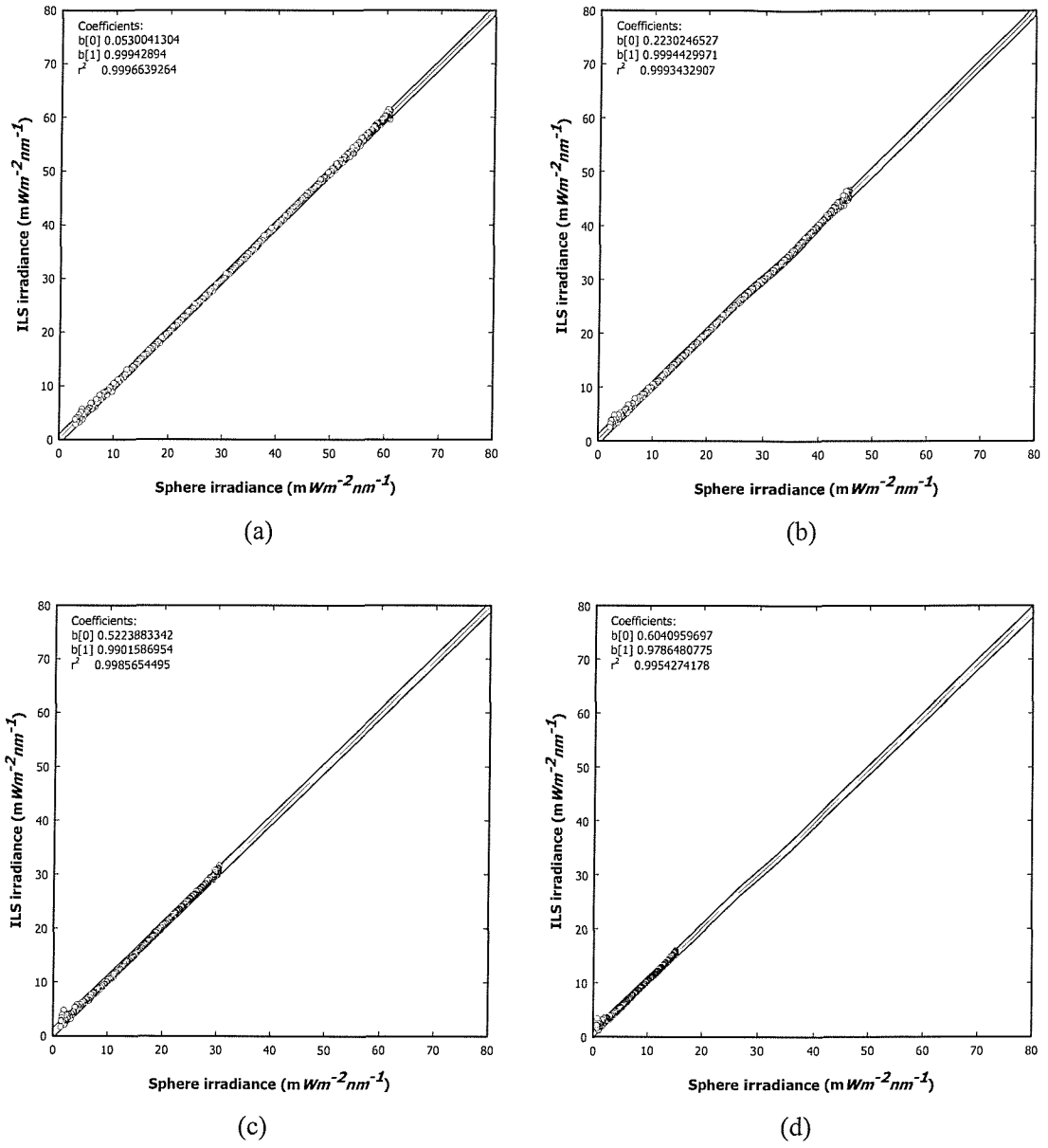

Figure 5-13. Comparison of irradiance values between the integrating sphere and conversion of NERC ILS measurements. As the measurement at 1000 *fL* is used as a standard illuminance level, only 800 (a), 600 (b), 400 (c), and 200 *fL* (d) are presented here. Each plot also includes a linear regression line and upper and lower prediction boundaries with 99 % of confidence limit. The coefficient b[0] represents the intercept of the regression line, whereas b[1] for its slope. Although irradiance values decrease with intensity levels, scales of the plot axes are kept the same in order to show the predictability of the regression models, especially, out of the data range.

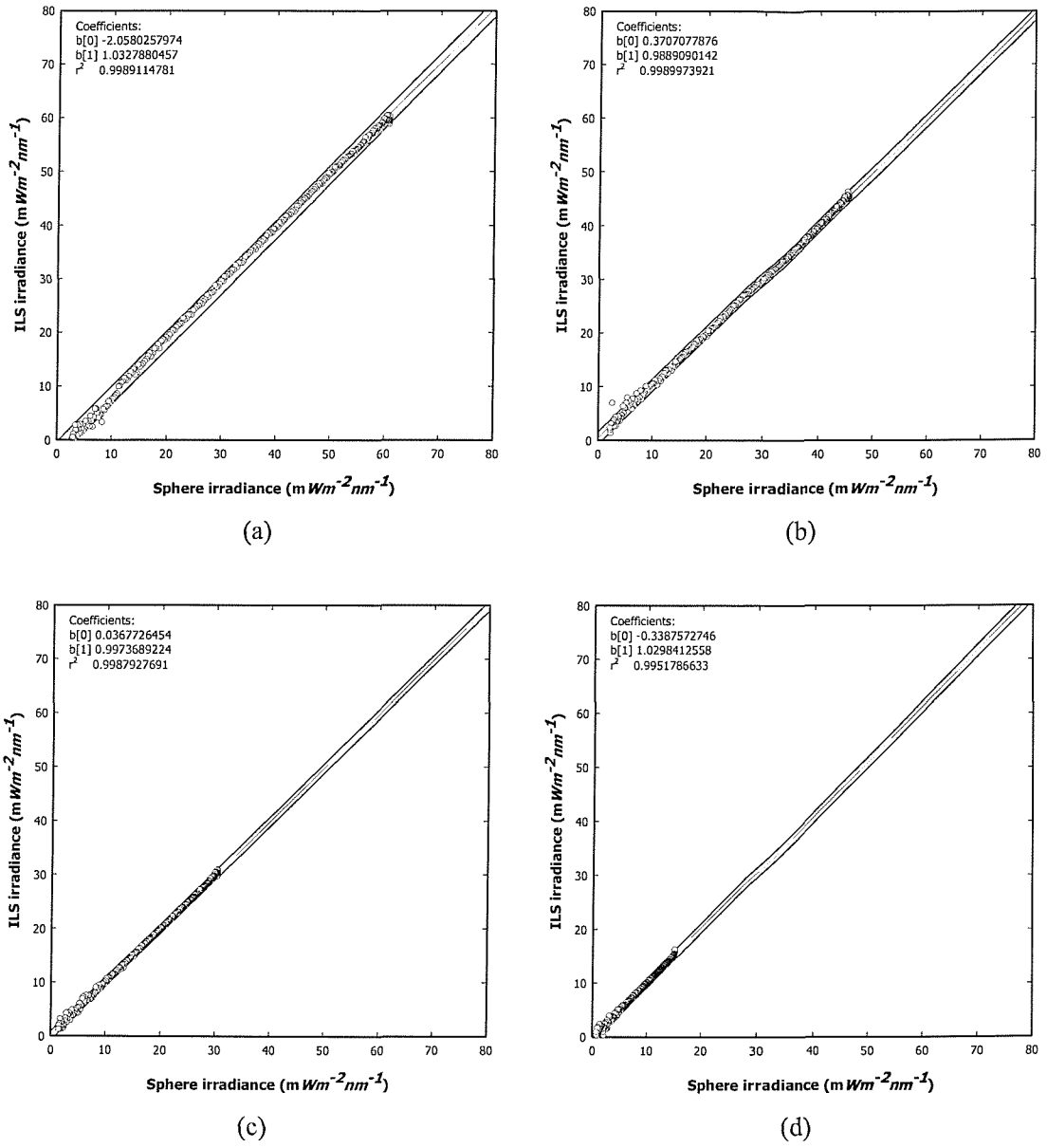

Figure 5-14. The same type of plots shown in Figure 5-13, but with the data from EA ILS.

to their own detector properties or due to their optic systems. The latter reason may be more difficult to identify because it is a kind of mixture of random and systematic errors.

One of the possible sources of error is because of the limitation of the light source used. The irradiance values of the integrating sphere are quite low in the short wavelength region and increase dramatically along with wavelength, contrary to the solar spectrum. The signal-to-noise ratio of the data as a result may be reduced at short wavelengths. Consequently, it is important to notice that the signal-to-noise ratio at short wavelengths could be relatively poorer than that in the NIR region.

There is also a known systematic error of the CCD array in the CASI-2 SHU. Previous experience of CASI-2 calibrations showed that the spectral profile of the CCD array was most sensitive between row numbers 120 and 200, i.e. roughly between 720 and 570 *nm*. In other words, the signals outside the region possibly have a less signal-to-noise ratio.

The amount of error over the irradiance spectra, independent from the mean irradiance curves, was compared by using the normalised difference between estimated and measured irradiance data (Figure 5-15 and Figure 5-16). It is a proportional difference between estimated and measured spectral irradiance, and tends to ignore influences from different spectra between illumination of the integrating sphere and that from the Sun.

Similar experiments on the ILS were performed by Shepherd and Xu (1993). They tried to establish the possible error ranges for the conversion of radiance images to reflectance CASI images, since large errors associated with reflectance values derived were likely to be a potential problem with using the ILS data. The real ILS data were simultaneously collected with the CASI image and were used for the reflectance calculation as an incident solar irradiance. Of the total error in the at-sensor reflectance, nearly the entire portion (99.3 %) was generated by the ILS even after using a moving average along with the CASI scans. Particularly, errors in short wavelengths were substantial (greater than 10 % of reflectance error at shorter than 450 *nm*), and exponentially decreased with wavelengths. The similar results were found in my experiment (Figure 5-15 and Figure 5-16), though much lower values, possibly due to the more controlled laboratory condition with stable light source.

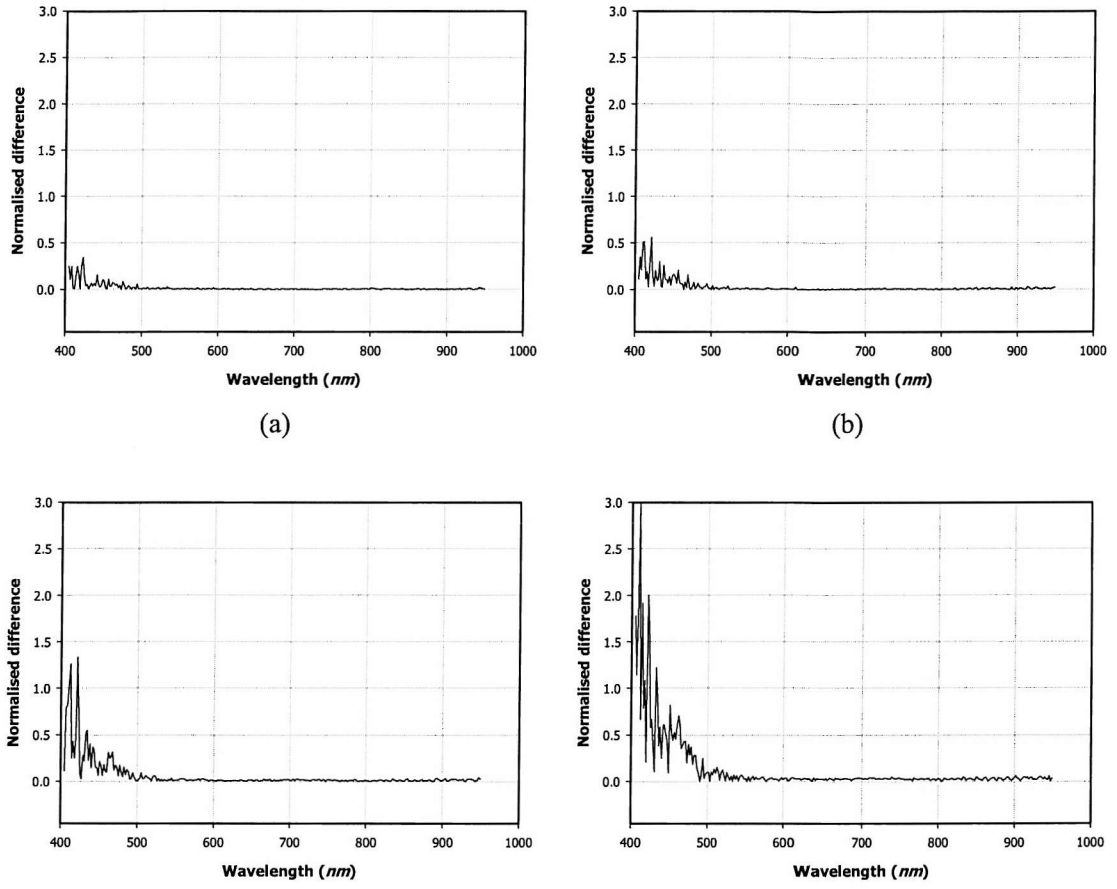

Figure 5-15. The spectra of normalised differences in four intensity levels from NERC ILS (as in Figure 5-13): 800 (a), 600 (b), 400 (c), and 200 *fL* (d). Y-axis scales are identical for all plots.

The error in the visible wavelength may be due to a '*multiple modal problem*', which is induced by the fibre optic cable (personal communication, Dr. Lee, J., Optoelectronic Research Centre, University of Southampton). It is one of the important characteristics of fibre optic cables that electromagnetic energy of different wavelength is likely to suffer interference, especially at shorter wavelengths. Although optic cable is theoretically capable of passing light from one end to the other with little or no energy loss, there might be some degrees of energy loss or interaction between the photons with different wavelengths. These can result in a non-linear response of intensity to the signal detected by the ILS CCD arrays.

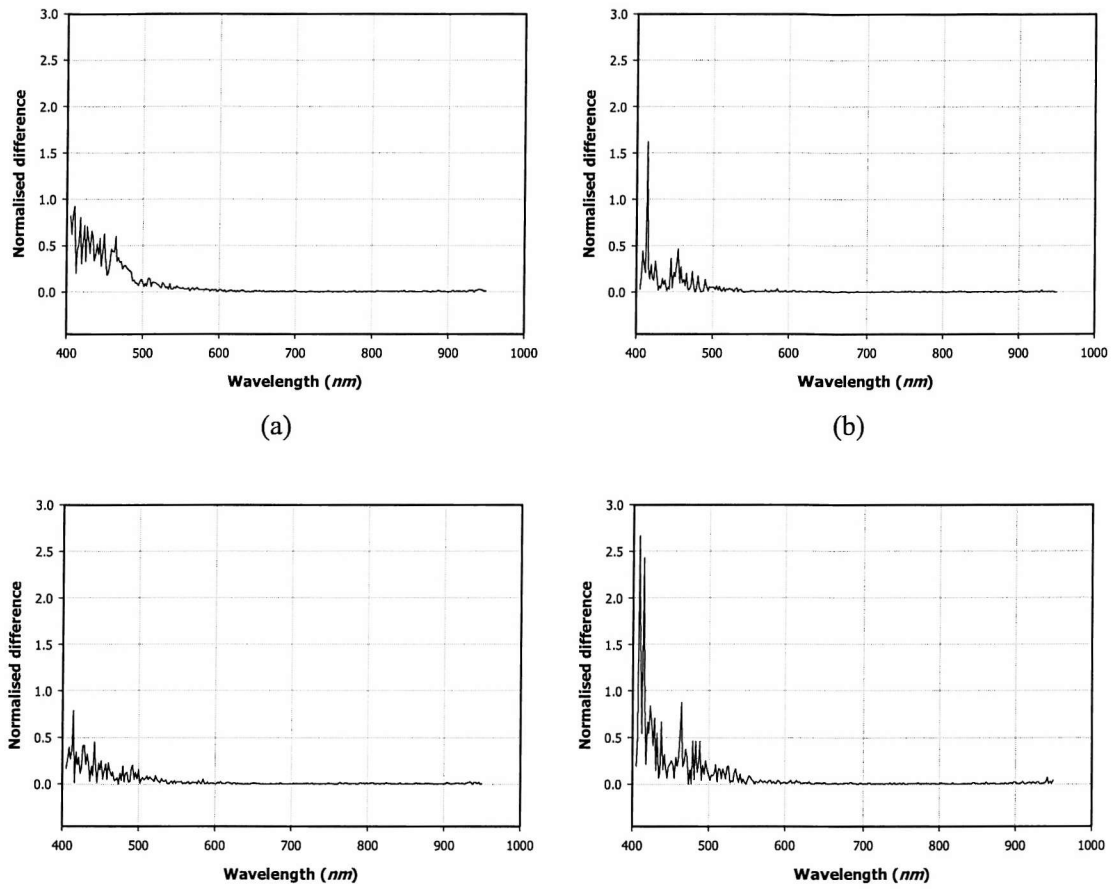

Figure 5-16. The same type of plots shown in Figure 5-13, but with the data from EA ILS.

The RMSE (Root Mean Square Error) values were calculated using the normalised differences significance in order to verify the three error sources described (Figure 5-17). The systematic errors, such as, those due to the poor sensitivity of the CCD array are expected to have an intensity dependence. In other words, the signal detected by the CCD array decreases while the amount of the instrument derived noise remain the same, resulting that the signal-to-noise ratio decreases with low intensity light. An error from the '*multiple modal problem*' in the fibre optic cable, on the other hand, tends to appear randomly (or non-linearly). The RMSE values in five different intensity levels indicate that the magnitude of the ILS error is mainly due to the properties of the fibre optic cable, although the systematic error still cannot be ignored.

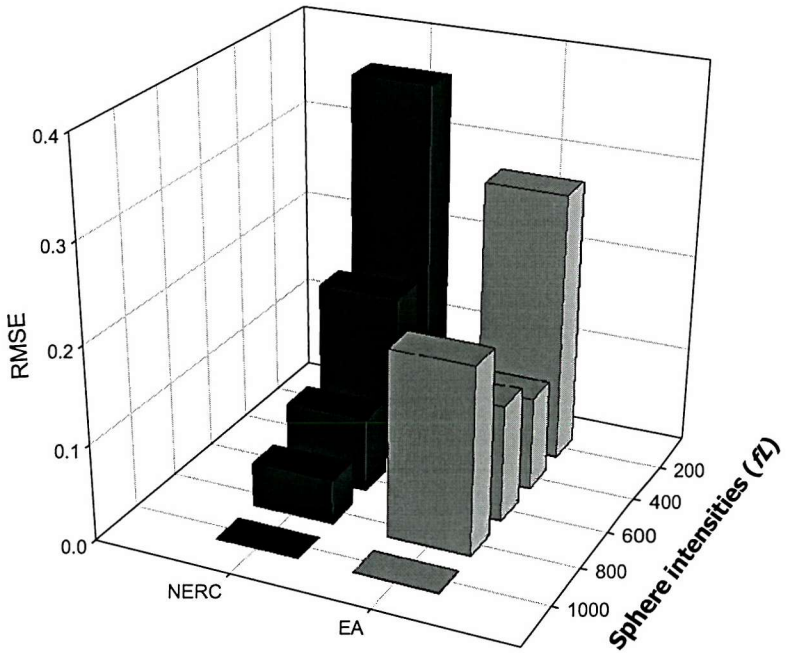

Figure 5-17. Comparison of integrated RMSE over the available wavelength range for five different intensities with NERC and EA ILS.

Total RMSE values for each intensity setting, therefore, indicate a contribution to systematic and random errors in the ILS measurements (Figure 5-17). The RMSE plot tends to show a gradual increase in NERC's ILS as the intensity is lower, whereas those from EA, within the similar magnitudes, have random distribution with various intensity levels. Having said that the fibre optic cable of the EA ILS is much longer, random error is thought to be relatively more dominant in EA system than that in NERC's, i.e. there are more chances of short wave interruption in the longer fibre optic cable. However, there is still a possibility of different fibre optic properties or different cable connector conditions.

One of the other tests determined how much the error is affected by non-linearity of the spectral response of the ILS. Linear regression analysis was carried out with averages of the ILS spectra (Figure 5-12) over the available wavelength range, as a function of the sphere intensity levels.

The intercept of the regression line was expected to pass through the origin, with an assumption that irradiance would become zero as the sphere intensity reached zero. The upper and lower ranges of the intercept include the origin within the confidence limits in EA ILS (between 0.692 and -0.668), while the NERC ILS does not. Such differences may be related to the RMSE values. NERC ILS with more control over systematic error has a tendency towards a changing mean of spectral irradiance proportional to various intensities. It could result in a better R-square than EA ILS and lift a regression line away from the origin. On the other hand, the EA ILS random errors cause a lower R-square, but does not affect the entire regression line position. Despite there being some degree of non-linearity in the system, statistical analysis suggests that the spectral response of the ILS can generally be treated as a linear system.

Stat. Tests		NERC	EA
R-square		1.000	0.999
Slope	Mean	0.045	0.043
	Upper limit	0.045	0.041
	Lower limit	0.046	0.049
Intercept	Mean	0.537	0.012
	Upper limit	0.761	0.692
	Lower limit	0.313	-0.668

Figure 5-18. Linear regression results of linearity test for the NERC and EA ILS. Both ranges in slope and intercept are with 99% confidence limits.

5.4. Angular response of the ILS

An angular response test of the ILS was performed to check how closely the diffuse sensor head behaves as a cosine receptor. If so, the amount of collimated light reaching the ILS theoretically depends upon its angular position and follows a simple cosine rule. Another thing to verify in angular measurements was the effective zenith angle of the ILS. A true cosine receptor for irradiance is expected to have a 90 degree effective angle to be able to measure the entire sky dome over the sensor.

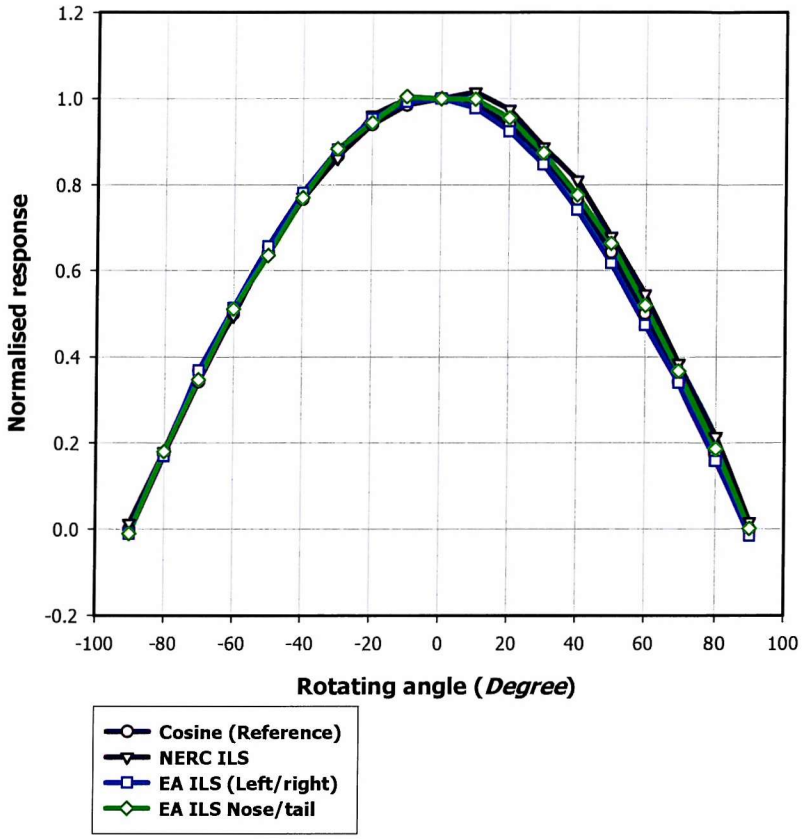

Figure 5-19. Angular response curve is superimposed with the ideal cosine curve.

The raw ILS measurements were recorded on a rotating mount with a parallel beam of light source. The position of the light started from zero degree where the ILS was looking 90 degree to the left hand side, then at increased angles before it reached 180 degrees (on the other

side of the ILS). In order to minimise variations of the collimator intensity during the measurements, ILS data were recorded at 30 degree intervals over the range of angles, then filled in with other angles at 10 degrees intervals.

Each angular measurement was spectrally averaged and normalised with the one at zero degree, i.e. the ILS is looking straight into the collimated beam (Figure 5-19). This gave a relative response at a certain angle with respect to the maximum light into the sensor. Normalised response plots were compared with a cosine curve as a reference. All angular measurements tend to follow the reference cosine curve, indicating that the ILS is a cosine receptor. Moreover, the fact that such trends are extended at both ends of the curve (+/-90), means that the effective zenith angle is 90 degrees for both ILSs.

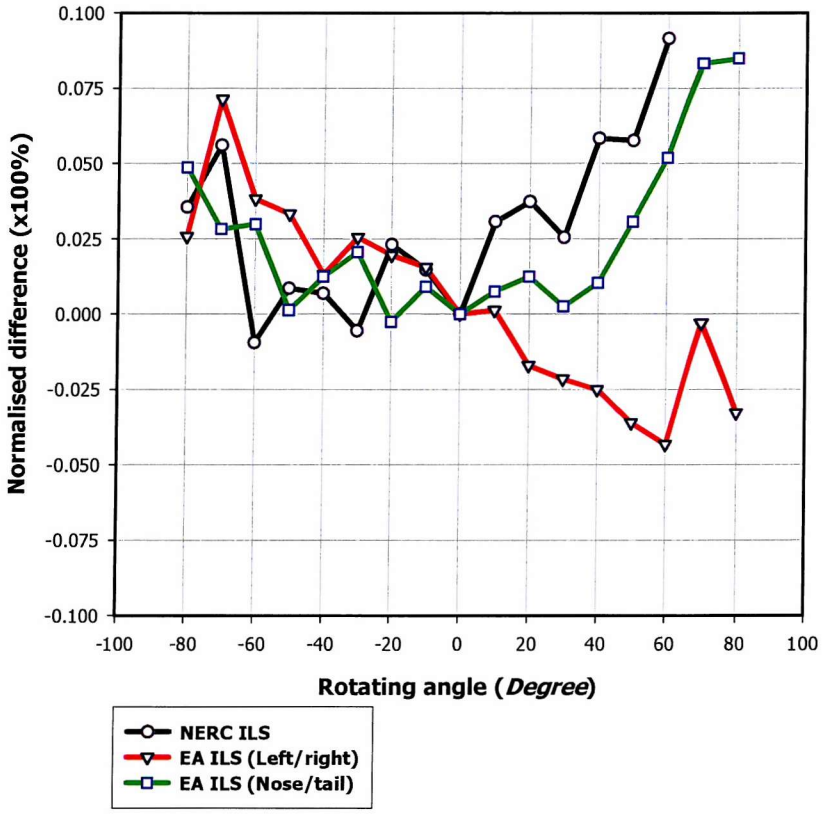

Figure 5-20. Normalised difference of angular response measurements with respect to the ideal cosine curve.

The normalised difference shows relative differences between a true cosine and the measured angular response. For an interpretation of the normalised difference of angular response, collimator uniformity, that was described in earlier section (see section 5.2.2.1), needs to be considered, since the uniformity test during the experiments of the NERC ILS showed its asymmetric distribution across the beam diameter. Such effect is also reflected in the angular measurements (Figure 5-20), i.e. normalised differences are greater in left than the right side of the ILS angle. It shows that the divergence (or skew) of the angular response from the cosine curve is mainly due to the inconsistency of the spatial distribution from the collimator, not from the ILS itself.

Although there was no actual testing, angular measurements for the EA ILS paid more attention to the instrument setting and resulted in much improved normalised differences with only a little non-uniformity. Overall, the error range was less than 10%, but could be less than 4% if one takes into account the range of angles +/-60 degrees (the zenith angle greater than 60 degree is a rather extreme case in the real world).

The variation in normalised differences shows a small difference in the two datasets. The normalised difference in the nose/tail case slightly increases as the ILS looks away from the light in both directions, whereas in the starboard/port direction it continuously decreases as the ILS rotates from right to left. In other words, the ILS responses overestimate at both sides in nose/tail case, but the right side of the receptor overestimates while the left underestimates. The angular response curve in the left/right case is hence skewed with respect to the ideal cosine curve. For the EA ILS, moreover, angular responses between the left/right and nose/tail show systematic differences but small enough to be ignored, since the normalised difference shows less than 4% in most probable positions, i.e. zenith angle of ±60°. However, such differences could be reduced by taking into account collimator non-uniformity.

5.5. Summary

A series of laboratory measurements were carried out to verify the radiometric and physical properties of a cosine receptor that simultaneously operates with the Itres CASI-2 system. Laboratory experiments were designed to characterise the spectral linearity and angular response of the downwelling irradiance sensor. A stable and accurate integrating sphere was used for the establishment of possible source of errors in the ILS using the irradiance conversion coefficients, and the uniformly collimated light was used for the angular response of the ILS that was compared with the theoretical cosine curve.

The irradiance conversion coefficient was found using direct measurements of the ILS with the integrating sphere assumed to be a stable light source. It was applied to the ILS DN measured at a total five different intensity levels for irradiance units. The transformed values were compared with the estimated sphere irradiance. The differences are considered as an error in the ILS. Whilst the measured spectra are generally quite similar to the references, they tend to be unstable at both ends of the spectra in every intensity level. The possible sources of the problem are either from optical fibre cable, the CASI-2 SHU, or both. The ILS probe is not of interest here because it is only a receptor collecting light to an optical fibre optic cable and not a device that affects the spectral signal. Instead, the sensitivity of the CCD array in the CASI-2 SHU is one possibility, as it is relatively ineffective in the same spectral region as here. It is a kind of systematic error that supposedly remains the same. However, the normalised difference shows that its significance only occurs in the visible area and its magnitude at different intensity levels varies in a rather random fashion. The results suggest the fibre optic cable as another source of error. 'Multiple modal problem' is a known property of the fibre optic cable, which amplifies or diminishes the low wavelength signal as it passes through the cable, and 8.5 *m* of ordinary fibre optic cable for the EA CASI-2 would be sufficiently long for this phenomenon to occur. Most fibre optic cable manufacturers quantify a 'cut-off wavelength', i.e. a wavelength of acceptable signal-to-ratio starting when light passes through the fibre optic cable. Further evidence should be sought from Itres in order to provide specific information on the cable used in the CASI-2 system.

Despite lots of advantages in the laboratory experiments, the limitations also need to be addressed: the spectrum of the integrating sphere is very different from that of the Sun. Much

greater signals in solar visible spectra mean a better SNR than those from the integrating sphere. Outdoor measurements of the ILS are therefore recommended in order to test whether the intensity fluctuation is induced by a low signal or by properties of the fibre optic cable.

So far, direct measurements of the ILS with a stable light source have provided the spectral properties of two components of the ILS, i.e. the CASI-2 SHU and fibre optic cable. The characteristics of the ILS probe, as a third component, were tested by its angular response. A collimator was used to provide uniformly distributed light over the ILS, of which the angular variations were compared against those theoretically represented by a simple cosine response. Parallel light reaching the ILS simulates direct incident solar irradiance with no diffuse radiation. Two sets of data, starboard/port and nose/tail, show a reasonably close cosine response, indicating that the ILS is considered as a true cosine receptor. The effective zenith angle of the probe is +/-90 degrees. The results show that the variations in the ILS signals fitted on top of the aircraft are mainly due to the aircraft attitude.

Continuous monitoring and calibration of the ILS is suggested for its application in operational airborne surveys. Since the ILS is supplementary equipment of the CASI-2 system connected via a fibre optic cable, care is needed in order to avoid unforeseen errors (e.g. during these experiments, one of the angular response measurements had to be repeated several times until a loosened fibre optic cable connection was noticed). The spectral properties of the ILS, particularly at visible wavelength region, deserve further investigations in the future.

Part II.

Operational pre-processing methods: Investigations into the effect of the atmosphere upon remotely sensed data.

The next two Chapters focus upon the effects of the atmosphere and the conditions of data acquisition, and how these influence the remotely sensed signal.

Chapter 6 reviews the literature in this area, focusing in particular upon numerical models developed to characterise the sky radiance distribution and practical methods of atmospheric correction. Chapter 7 describes a series of experiments designed to investigate the natural variability arising from clouds and water vapour in the atmosphere. Temporal variations in atmospheric clarity are used to emulate spatial variations typical of RS image data in a highly controlled way, prior to extending the analysis to multispectral image data. From these studies a conceptual model is produced to explain the variation in RS data caused by cloud shadows, and a method proposed to reduce or remove the influence of cloud shadows.

Chapter 6

Atmospheric and surface interactions in remotely sensed images

6.1. Introduction

In some basic applications of image processing, calibration of DN values to radiance is sufficient for inter-comparison between bandsets in the same image or for simple assessment (such as visual inspection) of images from different sensors. However, often more complicated processing is often necessary, especially when physical models or *in situ* measurements are incorporated with a RS image. The signal detected by an optical RS systems consists not only of the spectral signature of the object of interest, but is also controlled by variations due to Sun-target-sensor geometry, seasonally variable Earth-Sun distance, and dynamic atmospheric conditions (Slater, 1980; Vermote *et al.*, 1997; Moran *et al.*, 2001). Inconsistent sensor/target geometry and the interactions of incident (or target reflected) electromagnetic energy with atmospheric constituents, limits the direct use of RS images. These factors cause discrepancies between inherent target radiance and radiance detected by the sensor.

Under such circumstances, it is necessary to go beyond the basic radiometric calibration in order to obtain physically meaningful data related to intrinsic properties of the object of interest. The same is true for long term or seasonal monitoring, which is a key scientific issue in environmental remote sensing for the extraction of physical and bio-geophysical variables and hence improving our understanding of the environment with the information either in its own right or by assimilation into models, such as the physical behaviour of terrestrial surface processes (Plummer *et al.*, 1995). The surface reflectance factor, or spectral reflectance, is the most common parameter in optical RS. It represents an inherent property of an object

independent of atmospheric and isolation variations, and surface reflectance has become the fundamental measurement for most RS algorithms and biophysical models.

Retrieval of at-ground intrinsic target properties from remote sensing systems has long been a focus of interest in the optical RS community, and is increasingly of great importance in order to achieve the ultimate goal of accurate remotely sensed data from both spaceborne and airborne platforms. Without consideration of radiance modification, mainly introduced by atmospheric effects, the usability of remotely sensed data for information extraction is necessarily reduced in terms of nearly every application of RS techniques (Slater, 1985). For example, more than three decades of continuous Landsat TM program (which is still continuing) have provided the potential for long-term studies of natural resources, but it will be impossible to achieve the goal without operational atmospheric correction method. Not every image, particularly old archives, contains a record of the atmospheric condition at the time of the image collection, so that estimation of physically meaning comparable values for the surface is difficult for monitoring interannual or even seasonal plant soil conditions (Moran *et al.*, 2001).

Research and technology development in the last decade has resulted in a number of creative approaches to address or circumvent these issues to account for the influence of illumination and the atmosphere on sensor recorded radiance. There are three main approaches depending on the types of data they require: direct methods from ancillary measurements (e.g. Milton and Webb, 1987; Steven and Rollin, 1986), image based methods (e.g. Schott *et al.*, 1988), and the method using radiative transfer models (e.g. Zagolski and Gastellu-Etchegorry, 1995). The comparisons of performance and characteristics of these models have been studied by a number of authors (e.g. Roberts *et al.*, 1986; Ferrand *et al.*, 1993; Clark *et al.*, 1993; Dwyer *et al.*, 1995; Ferrier, 1995, Song *et al.*, 2000). Despite the fact that to date none of the methods are perfect, Slater (1985) suggested that in general the acceptable uncertainties from the atmospheric methods are of a few percent, while the instrument induced uncertainty is normally within about 1%.

This chapter introduces some of the concepts of optical remote sensing considered important for understanding their applications to retrieve environmental variables of interest. The characteristics of solar radiation, as the energy source of optical remote sensing (visible and NIR region of the electromagnetic spectrum; 400-1600 *nm*), is briefly described, followed by a consideration of its variations due to atmospheric constituents. The review of optical remote

sensing fundamentals provides an overview of various attempts to connect the indirect relation between the signal detected by remote sensors and environmental variables in three dimensions of remotely sensed data (spectral, spatial, and temporal).

6.2. Radiance source in optical remote sensing

Remote sensing is a technique that indirectly detects and records electromagnetic radiance (EMR) energy emitted by an object. Every object has its own EMR or absorbs/reflects radiation from other objects. In environmental RS, only a small portion of the electromagnetic spectrum is used depending upon its spectral characteristic of interest. Among these, the radiation from the Sun is the primary source of energy in passive RS, as it is not only containing wavelengths visible to human eye, but also plays an important role in controlling biophysical interactions of the life on Earth.

The solar radiation is generated by nuclear reactions within the Sun producing an entire spectrum of EMR. Just below the Sun's photosphere (i.e. the apparent surface of the Sun), the presence of an optical boundary tends to trap radiant flux generated from the core of the Sun. While a small concentration of negative hydrogen ions in the boundary keeps hold of energy by absorption, the temperature buildup as a result of the absorption induces convection current that transports the energy into the outer boundary, the photosphere. Consequently, the transparent gases in the photosphere re-radiate EMR into the space. Despite some degradation of the EMR energy after leaving the Sun, most of it is transmitted through space until it arrives at the Earth's atmosphere (Figure 6-1).

The irradiance curve at the top of atmosphere follows approximately a 6000 K blackbody source, while individual wavelengths may be equivalent to the range 4500 to 9500 K (Slater, 1980). More accurate figures are occasionally released, as the solar constant is directly related to the Sun's condition, such as sunspot activity in an 11-year sunspot-cycle. However, radiometric calculation can be simplified significantly by establishing a relationship between the solar radiance outside the Earth's atmosphere and the equivalent blackbody temperature of the Sun.

Once solar EMR enters the Earth's atmosphere, it experiences complicated interactions with atmospheric constituents before reaching the Earth's surface. As a result, the spectral intensity reflected from targets is altered, making it a complex task to retrieve spectral property of the target from remotely sensed data (Danson *et al.*, 1995). The following paragraphs will focus on the radiantion interaction within the Earth's atmosphere.

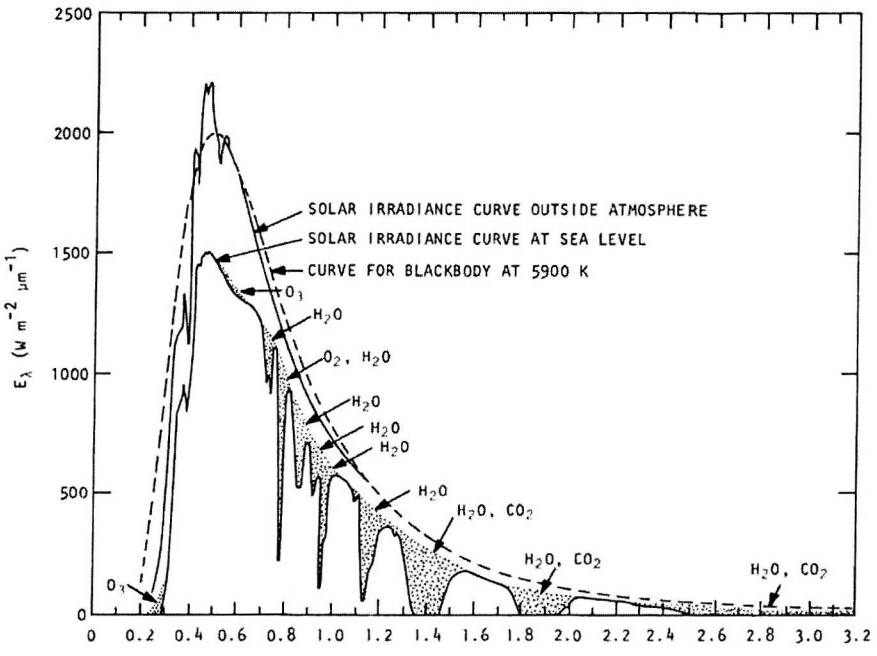

Figure 6-1. Spectra of solar irradiance for the flux at the top of the atmosphere, the flux at the sea level, and a blackbody source equivalent to 5900 K outside the Earth's atmosphere (after Valley, 1965; cited in Slater, 1980).

6.2.1. Interactions with the atmosphere

In an ideal world, solar radiation would illuminate the Earth's surface without interference from the atmosphere, and the radiance reflected from the surface would be transmitted perfectly to space. However, in reality, radiation undergoes significant interaction in the Earth's atmosphere before it reaches the satellite sensor. This interaction with the atmosphere can be severe, as in the case of cloud contamination, or minor, as in the case where there is essentially a clear sky field of view (Schott and Henderson-Sellers, 1984). For example, only approximately 80% of reflected radiance at 850 *nm* and 50 % at 450 *nm* reaches the satellite remote sensor (Vermote *et al.*, 1997). Regardless of the type of analysis that is performed on the remotely sensed data, it is important to understand the effect the atmosphere has on the radiance responses.

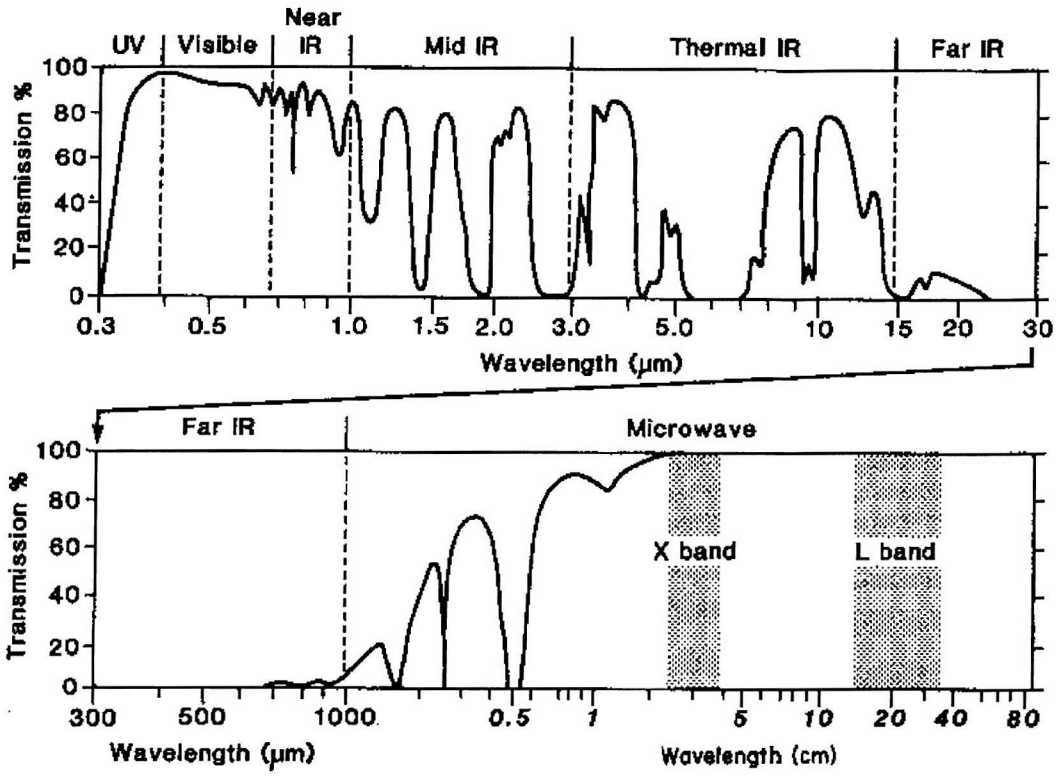

Figure 6-2. Electromagnetic spectrum associated with spectral bands with spectral groups. The curve represents spectral transmission, i.e. the larger the transmittance percentage, the less the atmospheric interactions (Mather, 1999).

The EMR reflected from the surface is reduced as radiation travels through the atmosphere, but the magnitude and characteristic of the atmospheric effect varies depending upon wavelength (Figure 6-2) (although radiance reflected from the atmospheric components may be important data for meteorological studies, the discussion here is focused on features on the Earth's surface). There are two main processes affecting the radiance change: *absorption* and *scattering*.

Although both alter the propagation of electromagnetic radiation through the atmosphere, they have fundamentally different characteristics, that is, changing intensity and its direction. As soon as radiant energy enters the top of the atmosphere, absorption starts due to the atmospheric constituents and some of that absorbed energy is then re-emitted at different wavelengths depending upon the type of object. On the other hand, scattering is only associated with directional changes (i.e. diffusion) of radiation by small particles in the atmosphere, and is a function of particle density, size, and radiation wavelength (Schott and Henderson-Sellers,

1984). Among various constituents in the atmosphere, aerosol particles (e.g. micrometre size dust particles or sub-micrometre pollution particles suspended in the air) are the most important for optical RS data (Kaufman and Tanré, 1996).

The following subsections give brief descriptions of atmospheric absorption and scattering which affect optical RS data.

6.2.1.1. Absorption

The loss of reflected radiance is normally affected by the absorption of energy to atmospheric constituents at a given wavelength. Atmospheric gases play an important role in absorption, the most primary components being ozone (O_3), carbon dioxide (CO_2), and water vapour (H_2O). The absorption of these gases tends to be effective in specific wavelengths (e.g. Tanré *et al.*, 1992), resulting in a strong influence on remotely sensed data (Kaufman and Tanré, 1996).

Ozone is present at an altitude of around 20~30 *km* in the atmosphere, and has an effect mainly on the ultraviolet spectrum. Carbon dioxide, well known as primarily responsible for changes in the greenhouse effect, is mostly present in the lower atmosphere with a relatively uniform distribution. It absorbs radiation in the mid- and far-infrared spectrum (effectively between 400 and 2000 *nm*), which can be detected by SWIR or TIR sensors. Maximum concentrations of water vapour are generally found at altitudes below 10 *km*, and its efficiency in absorbing radiation in terms of quantity and spectral distribution is several times more than those of all other atmospheric constituents combined. Also, unlike ozone or carbon dioxide, the spatial variation of water vapour changes frequently in time and space, e.g. presence of clouds or fog.

Since the presence of absorption in given wavelengths, *absorption bands*, is well characterised, most remote sensing systems are designed to avoid specific wavelengths of absorption unless properties of these atmospheric gases are needed (e.g. BenDor and Kruse, 1996) or they are used as a correction factor for atmospheric correction of remotely sensed data (e.g. Ouaidrari and Vermote, 1999).

6.2.1.2. Scattering

Scattering is the result of EMR redirection or attenuation by particles suspended in the atmosphere or by large molecules of atmospheric gases (Campbell, 1996). The effect of scattering is influenced by the size of particles and their abundance, wavelengths, and the distance which the EMR passes through the atmosphere. It primarily affects the short wavelength region (typically, 200 – 400 *nm*) with four different types of scattering: *Rayleigh*, *Mie*, *Raman*, and non-selective scattering. Of these, the most significant types in optical RS are Rayleigh and Mie scattering, which affect the visible wavelengths as a result of aerosols in the atmosphere, such as haze. For example, scattering in the green band of Landsat MSS data is four times greater than that in the NIR band (Jensen 1996). The relative proportion of Rayleigh and Mie scattering is determined by the relative particle size in the atmosphere in relation to the wavelength of radiance. The sky is full of scattering centres, and Rayleigh scattering is generally more dominant under most atmospheric conditions, although Mie scattering becomes important under cloudy or overcast conditions (Lillesand and Kiefer, 1994).

Rayleigh scattering is associated with molecules or microscopic particles whose size is similar or smaller than the wavelength of the interacting radiance. As the amount of scattering is inversely proportional to the fourth power of wavelength, scattering is greater with shorter wavelengths, and *vice versa* (Kaufman and Tanré, 1996).

Particles which are comparable in size to the wavelength of interacting radiance result in Mie scattering (Drury 1987). In most cases, water droplets or dust, which have a greater size than molecular particles, are the main cause of Mie scattering. The relationship between particle size and wavelength is basically the same, but its exponent varies from 0.7 to 2.0. Hence, Mie scattering tends to play a more important role in longer wavelengths than Rayleigh scattering.

6.2.2. Various paths of radiance

The interaction between EMR and atmospheric constituents attenuates the magnitude of radiation reaching the target object after redirection and some degree of extinction through the atmosphere. Incoming solar radiation is affected by atmospheric absorption and scattering,

through the atmosphere and interaction with the Earth's surface, until it reaches the sensor. Various paths of radiance in the atmosphere are considered as a function of successive orders of radiation interactions in the coupled system between the atmosphere and the Earth's surface (Vermote *et al.*, 1997). They are divided into two groups, incoming and reflected radiances. In addition to the fact that only a small portion of EMR reaches the ground targets, an even smaller portion of reflected radiation is detected by the RS sensor due to a combination of the following three causes,

1) The intrinsic radiance is reflected by the object of interest and transmitted directly through the atmosphere.
2) The radiant energy is scattered diffusely while travelling toward the detector.
3) The diffused radiation interacts further with the target background.

The signal of the first category carries the spectral signatures from the target, while the other two sources result in a combined error effect. These additional atmospheric interactions often cause discrepancy between observed RS data and *in situ* measurements on the ground and, as a result, any image analysis technique for the relative spectral response of different spectral bands or requiring quantitative studies is affected by the atmospheric composition at the time of data acquisition.

The incoming radiance illuminates the Earth's surface by means of three different paths (Figure 6-3). First, solar radiation directly hits the surface while some amount is lost due to absorption (*transmission*; ①). Second, the radiation at the surface is a result of scattering. The scattered light reaching the Earth's surface is termed *diffuse* irradiance (③). Theoretically, there may be a near infinite number of scatterings occurring with loss of its energy quite quickly. Single scattering is possibly enough to represent the entire scattering in the atmosphere (Singh, 1988). Lastly, the radiation reflected from the surface near the target may be scattered back to the target, due to a trapping mechanism (⑤). These successive reflections and scattering between the surface and the atmosphere are called the 'adjacency effect' and, again, the number of interactions would be more than one.

The radiation reflected by the surface is also affected by several types of atmospheric effects. The three types of radiation sources mentioned earlier are illustrated in Figure 6-3. First, the reflected radiance directly reaches the sensor with some amount of atmospheric

transmittance (①+③+⑤), i.e. absorption. Secondly, the radiance recorded by the sensor may include the reflected (or scattered) radiance without having made contact with the Earth's surface (②). This type of radiance path is known as atmospheric *path radiance*, and causes 'haziness' of the remotely sensed data. Third, the radiance at the sensor is possibly the contribution from the radiance reflected from the adjacent surface (④). This type of atmospheric interaction is generally assumed quite small and often ignored, but may contribute significantly in a heterogeneous environment, such as urban areas (Milovich *et al.*, 1995).

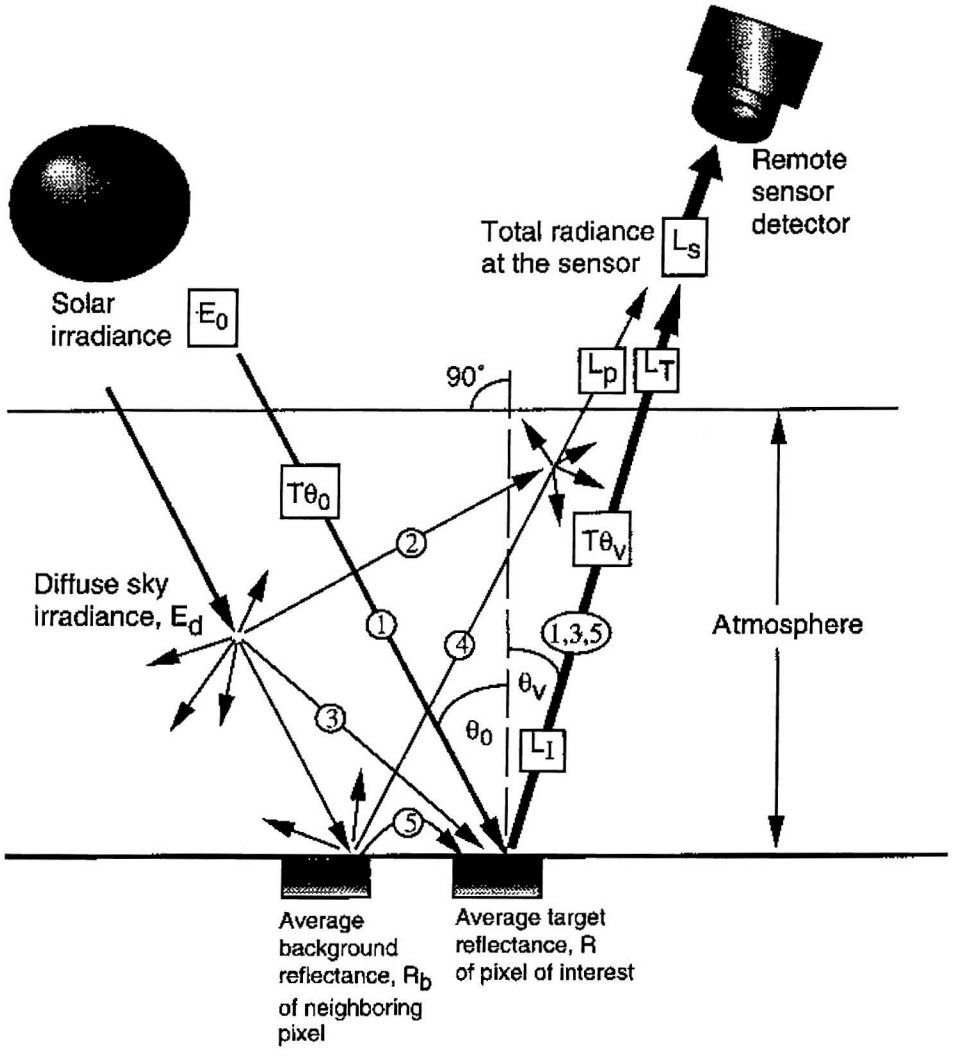

Figure 6-3. Various paths of radiance received by the remote sensing system (Jensen, 1996).

The analytical approaches of radiance paths are thoroughly derived by Vermote *et al.* (1997). The relationship between the radiance received at a sensor and the radiance reflected from the Earth's surface is shown in [6.1] on the basis of the various radiance paths described above.

$$L_s = \frac{1}{1-\rho_t \cdot s} \cdot L_t \cdot T(\theta_0) \cdot T(\theta_v) + L_p \qquad [6.1]$$

where,

L_s	Radiance measured by a sensor $[mWsr^{-1}m^{-2}nm^{-1}]$
L_t	Radiance of ground target $[mWsr^{-1}m^{-2}nm^{-1}]$
L_p	Atmospheric path radiance $[mWsr^{-1}m^{-2}nm^{-1}]$
T	Normalised total transmittance at incoming (θ_0) and radiance-reflected (θ_v) directions
ρ_t	Reflectance of ground target
s	Spherical albedo of the atmosphere

The amount of incoming radiance is directly related to the transmittance in the atmosphere ($T(\theta_0)$) and the radiance reflected from the surrounding surface, $1/(1-\rho_t s)$. The radiance due to the adjacency effect is an infinite series of successive reflections, $\sum_{n=1}^{\infty}(\rho_t \cdot s)^n$. The radiance reflected from the Earth's surface is decreased (transmitted) by absorption and scattering until it reaches a sensor, as incoming radiance. At the same time, additional radiance directly scattered by the atmosphere is also taken into account.

The normalised total transmittance is a ratio of atmospheric transmittance ($e^{-\tau/\mu x}$) and diffuse transmittance factor ($t_d(\theta_x)$) to the solar radiance at top of the atmosphere (E_0). Atmospheric transmittance is a ratio of solar radiation at the Earth's surface to that at the top of the atmosphere, representing the proportional loss of incoming radiance due to absorption and scattering. On the other hand, the diffuse transmittance factor is the quantity of diffuse radiance added due to scattering from any direction in the sky dome with respect to the solar radiation at the top of the atmosphere.

$$T(\theta_x) = e^{-\tau/\mu_x} + t_d(\theta_x) \qquad [6.2]$$

where,

τ	Optical thickness
x	Annotation of incoming (o) or reflected direction (v)

μ	$\mu_x = \cos(\theta_x)$ where θ_x is the zenith angle of either incoming or reflected direction
t_d	Diffuse transmittance factor

Consequently, the incoming radiance at the Earth's surface is composed of direct and diffuse radiances, and the normalised total transmittance can be rewritten,

$$T(\theta_0) = \frac{E_s^{dir} + E_s^{diff}}{\mu_0 \cdot E_0} \qquad [6.3]$$

Where,		
	E_s^{dir}	Direct solar radiance at the Earth's surface
	E_s^{diff}	Diffuse solar radiance at the Earth's surface
	E_o	Solar radiance at the top of the atmosphere

The normalised total transmittance reflected from the surface ($T(\theta_v)$) represents the radiance loss of the radiance at the sensor from the surface leaving radiance.

For the quantitative measurement of the Earth's surface, the reflectance of the surface (ρ_t) is defined as the proportion of incoming radiance that is reflected. With known surface reflectance, the radiative transfer equation [6.1], the relationship between the radiance measured at surface (L_t) and the surface reflectance (ρ_t), becomes,

$$L_t = \frac{\rho_t \cdot E_o}{\pi} \qquad [6.4]$$

These equations are a reasonably simplified form of most primary atmospheric interactions. Depending on the accuracy of atmospheric corrections demanded by users, some processes in the equations are either ignored or simplified further. Henceforth, the discussion will be restricted to the processes shown in the equations.

6.2.3. Interactions with ground objects

Solar radiation entering the Earth's atmosphere interacts with the objects in the natural environment. RS sensors then receive a portion of the reflected radiance energy which is interpreted as diagnostic to a greater or lesser extent of the characteristics of the objects. Among

the variety of elements in the natural environment, there are three broad areas where optical remotely sensed data are routinely applied: atmospheric research, land use/cover, and oceanic applications. Apart from atmospheric applications, many applications of optical remote sensing are associated with vegetation related analysis: this is the centre of discussion here.

For vegetation, several types of information can be retrieved in addition to the simple colour information as follows (Goel, 1989),

1) The distinctiveness of the vegetation (visual interpretation)
2) The phenological stages
3) The vegetation stress
4) The biomass of vegetation elements
5) The canopy structure.

Because the optical region of the electromagnetic spectrum is affected by of more than one biophysical property of vegetation, it is important to understand the underlying processes that contribute to the variation of the spectral characteristics different regions of the electromagnetic spectrum (Asrar *et al.*, 1989).

All living vegetation on the Earth's surface and in water have their own radiance spectra. They are chemically active through photosynthesis. This process is dominated by chlorophyll – a (generally) green pigment responsible for the green colour of vegetation. In the visible portion of the spectrum, chlorophyll molecules mainly absorb blue and red wavelengths for photosynthesis and absorb relatively less in green wavelengths (Gates *et al.*, 1965). The sudden drop of absorption in the NIR gives typical reflectance plateau for vegetation. Early studies showed that cell wall and air interfaces within the canopy leaf are primarily responsible for this pattern (Gausman *et al.*, 1969; Allen *et al.*, 1973; Kumar and Silva, 1973). Water content in leaves is also generally distinguishable in the SWIR region. There are four distinctive absorption features within the NIR and SWIR, i.e. at 970, 1190, 1450, and 1940 *nm* (Curcio and Petty, 1951; Knipling, 1970; Woolley, 1971). As moisture stress or natural maturity of vegetation is often associated with failure of the cavity functioning due to the deterioration of cell wall rather than physical change in the spongy mesophyll tissue itself, radiance changes in NIR may be used to represent vegetative vigour, crop diseases (e.g. Malthus *et al.*, 1993), or insect infestations (e.g. Radeloff *et al.*, 1999).

In addition to leaf pigments and water contents, there are number of chemical, physical, and physiological processes that need to be considered in order to explain a particular spectral response in a given wavelength for characteristics or status of vegetation. Hence, parameters, such as green-leaf area, leaf angle distribution, green phytomass, chlorophyll density, plant water status, and the spectral contribution of non-green parts (e.g. lignin or cellulose) are employed to provide a realistic representation of the spectral response of vegetation.

6.3. Inherent vs. apparent reflectance of the surface

Complicated interactions between EMR and atmospheric constituents affect images from optical RS sensors, as shown in the previous section. The frequently changing properties of solar radiation directly affect the target reflected radiance detected by RS sensors. As a result, the inherent spectral signature of a ground object might be different to the pixel values in an image and the acquisition of quantitative information from RS data becomes problematic. For example, this can lead to misinterpretation if changes of the reflected radiation are considered to be due to changes of the surface while in reality only the distribution of the incoming radiation is different. Two main effects are widely accepted to explain this. First, scattered (diffuse) light in the atmosphere influences incident and reflected radiance on the surface, and second, natural surfaces tend to have non-Lambertian angular anisotropy of the reflectivity. The latter is important due to detection of reflected radiance within a narrow field-of-view by most RS sensors, but it can be less affected if an integrated value over the hemisphere is used, such as albedo.

Reflectance, which is defined as the ratio of the reflected radiant flux to the incident radiant flux, is a dimensionless value only in the interval 0 to 1 due to conservation of energy (Nicodemus *et al.*, 1977). It represents an inherent surface property and is supposed to be independent of radiation changes due to atmospheric conditions. Peddle *et al.* (2001) described the properties of reflectance as follows,

> *Reflectance is an inherent property of an object which, unlike radiance and irradiance values, is independent of the intensity and nature of illumination. As a result, reflectance is generally the standard unit in remote sensing when using information from different sensors, times, or locations, or when comparing spectral measurements against known reflectance properties of objects (e.g. mineral identification from spectral libraries, geologic exploration).*

Spectral reflectance from an image is widely used in remote sensing to characterise a ground feature, either estimated with a numerical model or measured with field spectroscopy. This value greatly improves results in many RS applications, but users must still allow for the atmospheric effect and the bidirectional properties of the ground object.

In this section, the components that change the inherent spectral properties of the surface are reviewed: anisotropy of radiance distribution due to aerosol scattering under clear to overcast sky conditions, adjacency scattering effect, and the contribution of surface bidirectional properties.

6.3.1. Anisotropy of sky radiance distribution

In an ideal world, without atmospheric interaction, the incident solar radiation reaching the Earth's surface would have a single source from the Sun's specific position. However, after its reflection, absorption, and transmission through the atmosphere, incoming radiation on the ground target in terms of directional distribution becomes non-uniform over the sky.

The anisotropy problem of sky radiance is caused by variations of the fraction of transmitted and diffuse sky irradiance resulting from atmospheric absorption and scattering. Sunlight with atmospheric particles and molecules, i.e. permanent gases, aerosol, ozone, and water vapour, is attenuated by single and multiple scattering which is determined by optical thickness. Such interaction is strongly dependent on wavelength in the visible and near infrared region. About 40 to 50 % of the global solar radiation in the Earth on a horizontal surface is in the form of diffuse radiation (Brunger and Hooper, 1991). Although the total fraction of diffuse radiation is controlled more by local meteorological conditions rather than regional factors (Hay, 1977), local variations, mainly due to tropospheric aerosols, play an important role in the Earth-atmosphere-ocean system (Deirmendjian, 1980; King *et al.*, 1999). Schwartz *et al.* (1995) discussed three major mechanisms of atmospheric aerosols,

1) Direct radiative forcing: scattering of shortwave radiation by aerosols increases the Earth's albedo, cooling the climate system. Absorption of longwave radiation leads to heating the atmospheric system.
2) Indirect radiative forcing: changes of aerosol density in the atmosphere alters the reflectance property of clouds, therefore cooling the climate system.
3) Interaction with atmospheric gases: chemical reactions with atmospheric gases influences the concentration of gas composition, resulting in modification of latent heat in the atmosphere only if the gas reflectance is induced by water vapour.

Because the concentration of atmospheric aerosols is highly variable, any instantaneous measurements on predictions of diffuse radiation are exceedingly difficult, especially when the radiation changes are due to aerosol size distribution and single scattering albedo. Various RS sensors, such as well-calibrated multispectral radiometers (including thermal channels), polarimeters, and multi-angle spectroradiometers, have been actively used to measure tropospheric aerosol properties to enhance quantitative understandings of the global distribution of aerosol characteristics. King *et al.* (1999) reviewed the advantages and disadvantages of currently operating RS systems for aerosol studies, and suggested collaboration with a comprehensive network of ground-based sun photometer and sky radiometers, in order to make RS systems provide unambiguous information.

In terrestrial RS applications that use solar radiation as an energy source, scattered light is one of the most significant sources of errors (i.e. differences between the measured value and the inherent value of the object) for obtaining inherent spectral signatures for the identification of ground targets (Milton *et al.*, 1995). Non-uniform distribution of aerosol scattering, i.e. angular anisotropy of incident light, leads to directional variable reflectance values, as well as the non-Lambertian target properties. About 85% of the variation in reflectance measurements could result from different angles of solar illumination, and under various angular configurations, this was also shown by Rollin *et al.* (1997) using a field portable spectroradiometer.

To an extent, changes in atmospheric aerosol density results in changeable illumination conditions from clear to overcast sky conditions. The ratio of daily total diffuse radiation to extraterrestrial solar radiation may be compared with the daily average of total transmittance (Liu and Jordan, 1960). The amount of diffuse radiation is low in both sunlit and overcast conditions. However, there is an optimum in between where non-opaque clouds diffuse the sunlight strongly but it is not fully transmitted (Brunger and Hooper, 1991). The maximum amount of diffuse radiation in the atmosphere is about 25% when total daily transmittance is about 0.40, which represents the sky condition under a thin deck of cirrus. With respect to radiance distribution, there is a maximum intensity in the region near the sun and an increase in intensity towards the horizon due to the increasing optical thickness of the atmosphere at increasing zenith angles (Page, 1986). Also, diffuse radiation is dominant under completely overcast conditions, whereas the fraction of direct solar radiance, is about 90%, in the clear sky as Rayleigh scattering is predominant (Liu and Jordan, 1960). For many general purposes, the

daily average of total transmittance is referred to as the cloudiness index. On the basis of this, irradiance models have been developed, which do not give radiance information, e.g. Bodmann *et al.* (1988); Klucher (1979). There have been attempts to derive radiance information from simple mathematical step-functions (Hay and Davies, 1980; Hay and McKay, 1985; Perez *et al.*, 1990, 1986), and sky radiance distribution models from irradiance measurements (Morris and Lawrence, 1971; Page, 1986). Several sky radiance models are available, e.g. Harrison and Coombes (1988), some have taken advantage of a sky luminance distribution model, for instance, the model developed by Kittler (1965; cited in Brunger and Hooper, 1993). Although the photometric distribution of sky luminance is quantitatively different, i.e. a different measurement unit than radiance, they have proved to be qualitatively similar (Kondratyev, 1969; Michalsky *et al.*, 1991).

Most models are, nonetheless, limited to representing sky radiance distributions only under either clear or overcast sky condition. When the amount of total radiation is small (overcast sky condition), the source of incident radiation is dominated by diffuse radiation (Liu and Jordan, 1960). The distribution is symmetric about the zenith (isotropic), as no dependence on solar position exists as a consequence (Siala *et al.*, 1990). On the other hand, there is a greater variety of models for clear skies than for the overcast skies. Unlike overcast sky distribution models, the measurements upon which they are based were conducted rather differently depending on meteorological conditions, such as air mass, and atmospheric turbidity (Gueymard, 1986, cited in Brunger and Hooper, 1993). There are also problems because of two limiting assumptions, leading to substantially different results, in defining the origin of the diffuse radiation; the one assumes all sky diffuse radiation coming from direction of the Sun (heliocentric), the other uniformly from over the sky (isotropic) (Hay, 1978). The heliocentric model is an extreme sky model as opposed to the isotropic model and the least scattering of radiation (Siala *et al.*, 1990). It is a function of the solar zenith and azimuth angles. The fixed combinational model combines the isotropic and heliocentric assumptions, as with most of the published models (Morris and Lawrence, 1971; Weiss and Löf, 1980; Hooper *et al.*, 1987).

As the sky radiance model is capable of simulating the complete range of sky conditions from clear to dark overcast, the model requires more atmospheric parameters than are sometimes available operationally (Perez *et al.*, 1993a). Although several empirical measurements have tabulated distributions of average sky luminance over various sky conditions (Kimball and Hand, 1922, as cited in Hooper and Brunger (1980); Liu and Jordan,

1960), many numerical models using continuous functions are not consistent (Pokrowski, 1929, cited in Steven, 1977; Hopkinson, 1954, cited in Hooper and Brunger, 1980). On the other hand, some models produce physically realistic sky radiance distribution by using the weighted sum of the irradiance from clear and cloudy skies (Gueymard, 1986, cited in Brunger and Hooper, 1993; Page, 1986; Harrison and Coombes, 1988). The sky radiation distribution under partial cloud cover is still unclear. The influence of radiation reflected by clouds is complex, neither purely diffuse, nor purely specular, nor any simple combination of these. The time scale of its change is also too short to define a typical spatial distribution of diffuse radiance across the sky. The amount of cloud is parameterised as a function of diffuse fraction, atmospheric transmittance, and the position of the Sun in the sky (Brunger and Hooper, 1993). Their model describes the directional origin of the sky diffuse insolation under a complete range of sky conditions as observed by Brunger and Hooper (1991) and Liu and Jordan (1960).

In summary, the fractions of diffuse radiance and direct radiance are highly variable depending on clouds. Its variation is represented by the superposition of several independent components; isotropic, circumsolar, and horizon brightening. The weight of each component is determined by field measurements, and dependent on sky conditions, i.e. sunlit, overcast, or partially distributed clouds. A list of sky diffuse models currently and widely used is listed by type and applicable sky conditions in Table 6-1.

Model type	Sky condition	Name	Description	References
Diffuse irradiance	Clear sky	Heliocentric model	The limiting case at the opposite extreme from the isotropic model.	Hay, 1978
	Mid-sky condition	Fixed combinational model	Combination of the isotropic and the heliocentric assumptions.	Hay, 1978
	All weather	Variable combinational model	Overall refinement to the fixed combinational model.	Hay, 1978
		The Hay model	The weight index between isotropic and heliocentric components is determined by a ratio of irradiance on a horizontal surface (G_b) to the horizontal extraterrestrial irradiance (G_o).	Hay, 1979
		The Reindl model	Adding a horizontal brightening diffuse term to the Hay model above. The index is derived by a ratio of irradiance on a horizontal surface (G_b) to the global irradiance (G).	Reindl *et al.*, 1990
		The Klucher model	The heliocentric and horizontal brightening terms are controlled by the following modulation function, F, $F = 1-(Gb/G)^2$	Klucher, 1979
		The Perez model	The weight index between isotropic and heliocentric components is determined by functions of sky clearness, sky brightness, and the solar zenith angle.	Perez *et al.*, 1990
	Overcast	Isotropic model	Diffuse radiation originates uniformly from all over the sky.	Kondratyev, 1960
Diffuse radiance	Clear sky	Clear sky model	This type of model basically uses three parameters for the distribution of clear sky radiance, according to the formula introduced by Pokrowski (1929): scaling factor, empirical constant, and scattering coefficient. Although the value of second and third terms varying by several authors did not make significant difference, in general, none of the fits was found to be particularly satisfactory.	Hopkinson, 1954 (cited in Siala *et al.*, 1990); Steven, 1977; Pokrowski, 1929 (cited in Walsh, 1961)
	All weather	Three-component continuous distribution model	Hooper and Brunger (1980) proposed the three-component continuous distributions (TCCD) model. Each model component represents isotropic, horizontal brightening contribution, and circumsolar contribution. The model coefficients were derived after 127 scans of field measurements in Toronto, Canada.	Hooper and Brunger, (1980)
		Kt-K based continuous distribution model	Continuous distribution model developed by Brunger and Hooper (1993). The model is based on author's previous TCCD model, but this model is improved to provide enough flexibility for the model to represent the full range of diffuse radiance distribution. The model parameters require the clearness index (K_t) and the diffuse fraction (K), which are used to parameterise the sky conditions.	Brunger and Hooper, 1993; Coombes and Harrison, 1988; Rosen *et al.*, 1989

		Cloud cover-based	Weighted combination of models proposed previously by the same authors for completely clear and for overcast skies, i.e. similar to the variable combinational model. The weighting factors are determined from a measure of the cloud cover derived from long-wave radiation measurements, where aerosol density is determined. A satisfactory agreement between the radiance values predicted by the model and the corresponding measured values.	Harrison and Coombes (1988)
		Semi-empirical	The model is based on a mixture of physical and empirical reasoning, i.e. regression-type model with the form of the base functions derived from the analytical solution of the monochromatic equation of transfer which is obtained using the single scattering approximation in a plane-parallel atmosphere. It has been known that, for higher than first order scattering, the model becomes tremendously complicated, yet increase little in accuracy.	Siala *et al.*, 1989
		Three discrete radiance component	The model has been developed mainly for the short-term changes of diffuse radiance distribution over a partly cloudy sky. It consists of three discrete radiance components (TDRC), and represents both the instantaneous and time-averaged distributions of diffuse sky radiance. Each component is simulating direct, scattered, and reflected radiance.	Rosen and Hooper, 1987
		Stochastic model	The nature of diffuse radiance distribution is predicted by statistical approach. It incorporates the underlying probabilistic law between the inherently statistical nature of the diffuse sky radiance and time, rather than using a non-deterministic model for a physical process	Siala and Hooper, 1987
	Overcast	Overcast sky model	Steven and Unsworth (1979) summarised the attempts of several authors. Although a commonly using parameter in the equation for opaque overcast skies was varied, overall, the fit of the observed data was found to be very good.	Steven and Unsworth, 1979
Sky luminance	All weather	The Perez-CIE (Commission Internationale de l'Eclairage) sky model	The linear variation of sky conditions between isotropic and heliocentric is determined by sky clearness and sky brightness, which were introduced in the Perez model above. The model consists of four CIE formulations: the CIE overcast sky, the CIE clear sky, the Gusev turbid clear sky, and the intermediate sky.	Perez *et al.*, 1990
		The Perez all-weather sky model	The Perez's all-weather model requires five coefficients that are obtained by sky clearness, sky brightness, and solar zenith angle, as shown in other Perez's models.	Perez *et al.*, 1993a

Table 6-1. A list of sky diffuse radiance/irradiance models.

6.3.2. The adjacency effect

Target radiation reaching the RS sensor is affected by surrounding ground objects. There are two ways in which this can happen. One is that some proportion of the reflected radiance bounces back to the nearby target surface due to the atmospheric reflections and scattering after successive trapping mechanism between the surface and atmosphere. This is an additive radiation source with downwelling radiation, and is a function of the spherical albedo of the atmosphere. Second, the target-leaving radiance interacts with that from the adjacent surface while travelling toward the RS sensor. It affects the atmospheric diffuse transmittance which interacts with the atmospheric constituents, and which is considered as additional atmospheric diffuse transmittance. For definition, such environment reflectance (or adjacency effect) is described as the atmospheric crosstalk that modifies the radiance of nearby surfaces of different radiance (Slater, 1985).

The adjacency effect had not been realised until Pearce (1977; cited in Slater, 1985) and Dave (1980) analysed it using a Monte Carlo simulation. Dyche (1983; cited in Slater, 1985) confirmed the existence of adjacency effect even under clear sky conditions, although it was difficult to detect with *in situ* measurement. Several other attempts demonstrated that the addition of reflectance due to the adjacency effect was around 10-20 % of the theoretical values (laboratory simulation by Mekler *et al.*, 1984; airborne experiment by Kaufman *et al.*, 1983 – as cited in Slater, 1985). Numerical simulation by Pearce (1977) showed that the adjacency effect could extend over large distances. However, the significance of lowest-order adjacent effects was relatively less in coarse spatial resolution images, such as AVHRR (Singh, 1988). The effect was small enough to ignore in its NDVI product when multiple reflection was not considered in the atmospheric correction algorithm. Such effects are nonetheless still important for scene reflectance analysis, such as classification.

Verifying the adjacency effect is not straightforward. The magnitude of multiple reflections in a scene depends on the spatial uniformity of the ground target, the reflectance difference of surrounding area, and the atmospheric conditions. If there is intense atmospheric scattering over a relatively dark surface surrounded by a brighter area, the pixel values of the target in the image are more likely to be contaminated by atmospheric adjacency effect (Slater, 1980; Otterman, 1984). Thus, care is needed when the user selects ground targets for vicarious

calibration, for example (Moran *et al.*, 2001). More variable factors for the atmospheric adjacency effect were discussed by Otterman (1984): solar zenith angle against the terrain surface and directional property of the target.

The methods for minimising the adjacent effect were discussed by Tanré *et al.* (1981) and Kaufman and Fraser (1984), and using a multi-view sensor was proposed to determine its effect for atmospheric correction of remotely sensed images (Diner and Martonchick, 1985; Slater and Martinek, 1979; O'Neill *et al.*, 1997).

6.3.3. Target BRDF

All reflectance measurements either in the field or from RS sensors are intrinsically directional because the Sun is always in a specific position and because every pixel in the image necessarily has a particular view angle (Pinty and Verstraete, 1991). The position of the observer relative to the target changes the reflectance of natural surfaces, i.e. anisotropic or non-Lambertian. Such reflection characteristics of a surface are represented by the bidirectional reflectance distribution function (BRDF) (Campbell, 1996). Many investigations of reflectance assume the target to be Lambertian, which simplifies the analysis but limits the validity of results. It is necessary to take bidirectional effect into account, especially when comparing multitemporal data acquired at different viewing and/or illumination geometries.

Theoretical investigations reveal that directional variations of the surface result from the shadowing induced by the internal structure of the scattering medium (Pinter *et al.*, 1985; Verstraete *et al.*, 1990; Pinty *et al.*, 1990; Gilbert and Melia, 1993). As the proportion of shadow from target structure increases due to either low sun elevation or low viewing angle, the bidirectional reflectance distributions of the targets are often 'absorbed' and weakened in terms of the large fraction of diffuse radiation (Deering and Eck, 1986). On the other hand, when a sensor views a target in the same direction as the Sun, i.e. all of the objects in a scene are illuminated, the reflectance increases considerably across all wavelengths, this is called the 'hot spot' or 'backscatter'. When the sensor is directly opposite the Sun, or 'forward scatter', the reflected signal does not significantly decrease because the shadowing of the objects by others appears to be countered by the increased reflectance from light reflected speculaly (Cierniewski and Karnieli, 2003).

The anisotropy of a surface is also scale-dependent, and is related to the ratio of a roughness parameter, representative of the structural inhomogeneities of the scattering medium, over the linear size of the pixel viewed by the sensor (Hapke, 1984). Hence, anisotropic distribution of reflectance is mainly caused by the topography when using low resolution sensors, whereas, for small areas from higher resolution sensors, factors such as canopy cover and canopy structure are dominant. Analytical models over homogeneous targets of relatively small area have been found to be difficult to apply directly to remotely sensed data with far greater area. This is not only because sensor data often contains a heterogeneous mixture of bare soils and vegetation canopies, but also because, since the number of available observations in any given time period is smaller than the parameters the model needs, any statistical adjustment cannot be verified (Pinty and Versatraete, 1992). A smaller number of parameters are used in empirical models (Minnaert (1941) as in Smith *et al.* (1980); Walthall *et al.*, 1985; Shibayama and Wiegand, 1985); however, they are too simple to reproduce many of the bidirectional characteristics seen in nature. Moreover, as described, the occurrence of shadowing due to internal medium structure as the pixel size increases causes a failure of conventional radiative transfer models for representing BRDF in natural media such as vegetation canopies (Dickinson *et al.*, 1990).

Kernel-driven models, sometimes called hybrid models, approach BRDF as a linear superposition of a set of kernels (Pinty and Versatraete, 1992; Wanner *et al.*, 1995). They are normally a combination of a radiative transfer-based volume scattering and a geometric optics-based surface scattering (Pinty and Versatraete, 1992). Each kernel component describes BRDF shapes with or without physical parameters (Roujean *et al.*, 1992; Wanner *et al.*, 1995). These semiempirical models, as approximations to physical models or empirical functions, are mathematically quite simple but still retain BRDF characteristics, which aim to overcome the difficulties mentioned above (Strahler, 1994).

6.4. Minimising of atmospheric effects

As the incident solar radiation passing through the atmosphere reaches the Earth's surface, it is reflected, absorbed, or transmitted, and the same is true for target reflected photons. Such interactions change inherent spectral signatures of the ground and are clearly unstable in time and space, which often limits temporal studies in environmental sciences (O'Neill *et al.*, 1995). The ratio of the reflected energy to the incoming radiation has been widely accepted for the RS community to identify inherent properties of the object of interest (Barnsley *et al.*, 1994). However, the fact that, as shown in previous sections, there are many factors affecting reflectance values suggests that most users are estimating apparent (as opposed to inherent) surface reflectance values from uncorrected RS data.

There are numbers of methods available to reduce the atmospheric effects on radiance recorded data from, in particular, optical RS sensor data (e.g. Crippen 1987): (i) empirical relationships between pixel values and known reference reflectance value(s) from ancillary measurements or the comparison of multiple observations of the same area by multi-altitude or multi-angle scene acquisition, (ii) standardisation of image either from supposedly spectrally flat targets or from the scene average, and (iii) radiative transfer models as theoretically derived numerical simulations of the interaction of radiation with the atmospheric constituents and the surface. A number of performance comparisons of these different methods have been presented in the literature, such as Roberts *et al.*, 1986; Moran *et al.*, 1992; Ferrand *et al.*, 1993; Clark *et al.*, 1993; Dwyer *et al.*, 1995; Ferrier, 1995; Song *et al.*, 2001).

The selection of the atmospheric correction method is entirely dependent on the level of accuracy required and the availability of extra data, e.g. aerosol density in the atmosphere for radiative transfer models.

Mather (1999) summarised the RS applications that require atmospheric correction algorithms as follows,

1) Multispectral analysis: It may be desirable to compute a ratio of the values in two bands of a multispectral image. The effect of scattering increases inversely with wavelength, so

the two channels are affected differentially by scattering. The computed ratio will thus be a biased estimate of the true ratio.

2) Reflectance-based physical models: A researcher may wish to relate upwelling radiance from a surface to some property of that surface in terms of a physically-based model. To do this, the atmospheric component present in the signal recorded by the sensor must be estimated and removed.
3) Multi-temporal scene monitoring: Results or ground measurements made at one time are to be compared with results achieved at a later date. Since the state of the atmosphere will undoubtedly vary from time to time it is necessary to correct the radiance values recorded by the sensor for the effects of the atmosphere. In addition, it may be necessary to correct multispectral data for atmospheric effects even if it is intended for visual analysis rather than any physical interpretation.

The calibration of remotely sensed data is becoming increasingly important, as the applications of the remote sensing (RS) require more accurate information. In addition to the basic radiometric calibration, atmospheric correction is often essential for multi-temporal RS applications, for those focusing on dark targets, or for those in which physically meaningful units (e.g. spectral radiance, reflectance or albedo) are required. Incomplete or inaccurate atmospheric correction often results in failure of the most common uses of image data, such as mapping land-cover and land-cover change (Song *et al.*, 2001).

Despite this variety of scene reflectance retrieval methods, operational correction of the atmospheric effects of the surface, especially over the land is still an unresolved challenge (Kaufman and Tanré, 1996). Rapid development of new sensing techniques with better and more numerous spectral channels over wider wavelengths, with finer spatial and spectral resolution, and the sensor maintenance and calibration performances for precise pixel values cannot improve our knowledge from RS without accounting for the deficiencies of data sources in terms of the information sought, as there are many factors in atmospheric interaction with hard-to-predict effects.

6.4.1. Direct method from empirical measurements

Direct reflectance calibration methods use some means of ancillary measurements, in addition to the corresponding scene data. The extra dataset would be obtained either with a field spectroradiometer (or sunphotometer; e.g. Rollin *et al.*, 2002) on the ground target at the time of image acquisition or at the RS sensor, or by multiple scene acquisition over the identical area with different altitudes or viewing angles. Generally, these techniques have long been preferred in the RS community, as the methods work relatively easily in most circumstances and the results are reasonably accurate. The disadvantage of this kind of approach is that one needs to collect a near-instantaneous additional dataset. Field measurements also limit to operational usability of the direct methods in terms of financial and temporal limitations. Although there were proposals to set up a global scale network of automatic Sun/sky radiometers for the validation of atmospheric correction methods of satellite RS and for the study of aerosol climatology (Kaufman and Tanré, 1996; Kings *et al.*, 1997), these are still not feasible for operational reflectance calibration in ordinary circumstances. Even with the highest precision for the specific location of the spectroradiometer, to account for the entire spatial radiation over the surveyed area from the additional measurements always needs precaution, for example for the possibility of anisotropic sky radiance distribution due either to the property of the object or to the terrain slope that leads to a bidirectional problem of the target leaving radiance. New techniques and modified methods have been suggested to circumvent some of these problems (Moran *et al.*, 2001).

There are three main approaches to achieve reflectance calibration by using additional measurements: empirical measurements at the ground, those at the RS sensor level, and multiple scene acquisition over the same area. The following subsections will describe the advantages and disadvantages of each category of direct reflectance calibration methods.

6.4.1.1. Ground based: Empirical line methods

The empirical line technique is a relative atmospheric correction method based on the assumption that the atmospheric effects are an additive and multiplicative (linear) term (Song *et al.*, 2001). It basically normalises entire pixels in the scene data to one or more known field areas of known reflectance within the image. Thus, it effectively removes the changes of

illumination and atmospheric path radiance which affect the radiance measured by RS sensors (Kruse *et al.*, 1990). A linear regression is aligned on measured ground reflectance of each spectral band in turn against the corresponding pixel values of the image. The intercept value of the 'best fit' line determines the atmospheric effects, whereas the slope of the plot is proportional to the ground target reflectance (Crippen, 1987).

Although the empirical line method has been recognised as one of the most simple and effective atmospheric correction method for reflectance calibration of remotely sensed data, there are certain conditions and qualifiers for validating this methodology. Firstly, reference spectra are obtained from the ground at the same time of the flight. Secondly, it has been suggested that number of ground reference targets affects the magnitude of errors of the method's results. Although there have been attempts of using a single target, they failed to produce consistent results under various sky conditions (Freemantle *et al.*, 1992; McArdle *et al.*, 1992). Many studies showed that increasing number of reference targets improved the quality of output from the empirical line method (Kruse *et al.*, 1990; van der Meer, 1994; Dwyer *et al.*, 1995; Ferrier and Wadge, 1996 for two targets; Emery *et al.*, 1998 for three targets; Price *et al.*, 1995; Ferrand *et al.*, 1994 for four targets). Residual errors in empirical line calibration are reduced to less than ~1 % with three or more calibration targets (Emery *et al.*, 1998; Smith and Milton, 1999). Thirdly, a large spectral contrast between reflectance targets is required (Freemantle *et al.*, 1992). The optimum size of ground target is directly related to the spatial and spectral resolution of the sensor system, atmospheric condition of the time of the data acquisition, and the contrasting reflectance of surrounding surfaces (Slater, 1980). The selection of the target pixels in the image should also take account of the surface adjacent effects when there is high atmospheric scattering over high contrast target. Lastly, ground targets should minimise bidirectional effects, be spatially homogeneous with a reasonable size, and spectrally uniform. If the reference targets are acquired on spectrally stable calibration sites, the resulting calibrations are quite smooth and free of artefacts.

As it is a fundamentally simple approach, the empirical line method has its own limitations. Not all scene pixels can be calibrated by ground target measurements. As the atmospheric conditions that affect the remotely sensed image vary through time and are not spatially uniform, the results of the empirical method for each individual pixel remain in question. The viewing angle of each image pixel is different in a scene (for airborne sensing, the differences are even greater than those from the space due to generally wider FOV). Solar

angles also vary depending on the time of data acquisition. Milton and Webb (1987) showed that the Sun-sensor geometry can resulted in enhanced surface bidirectional features of soil area, leading to potential problems with applying the empirical line method. Even in specially allocated homogeneous natural test sites under clear weather conditions, surface BRDF as a result of solar angle changes yielded inconsistent estimation of the target reflectance, around 30 % in backward scattering and 13 % in forward scattering (Wu *et al.*, 1997). Moreover, suitable ground targets are not always available in the area covered. It is common to use either/both man-made materials (e.g. water tanks, McCardle *et al.*, 1992; asphalt or concrete, Freemantle *et al.*, 1992; roofs, Moran *et al.*, 1997), or a dark deep water body (e.g. lake or river) as ground targets, but in some cases, these cannot be found in a scene of, say, a forest area. Moran *et al.* (1997) suggested that the minimum requirement of the target size is represented by a ratio of sensor resolution to target size of 1:8 for at least four pixels unaffected by adjacent effects. For example, a necessary target size for the Landsat TM sensor (30 *m* of pixel resolution) is around 240×240 *m*, this also limits the target selection.

Even favourable materials can produce errors. For instance, changes in spatial resolutions due to varying altitude of airborne survey caused up to 12 % in reflectance differences after a spectral mixing effect on an asphalt parking lot with painted road markings (Milton *et al.*, 1997). An intensive ground target measurement programme of asphalt and concrete surfaces by Anderson *et al.* (2003) showed that changes of target reflectance were subject to the variable relative proportion of diffuse irradiance (due to changes of atmospheric conditions, e.g. aerosol content), and therefore, it was suggested that any temporal delay in ground measurement could result in increasing uncertainty for the empirical line atmospheric correction method. Also, more importantly, the accuracy of the measuring instruments both on the ground and in the RS platform are also important in maintaining accurate reference spectra in order to get absolute reflectance (Kollewe, *et al.*, 1996; Milton *et al.*, 1995).

6.4.1.2. Multiple observations over the same area

While the empirical line method involves extensive field measurements, atmospheric transmission and path radiance between the RS sensor and the surface can be directly derived by multiple image acquisitions over the same target area. This multiple observation technique is based on the retrieval of the atmospheric effects by using several different Sun-target-sensor

geometries. Thus, the near-simultaneously obtained images, which contain different representations of atmospheric conditions from the same ground objects, are considered as a new ancillary dataset for the retrieval of the atmospheric variables. A couple of assumptions are made with this method. First, the major contribution of atmospheric effects in the radiance reaching the sensor is Mie, or aerosol, scattering. As described in the previous section, aerosol distribution in the atmosphere is highly variable both in quantity and type and plays a significant role of the atmospheric path radiance. Second, these broad-band scattering processes behave linearly, as described in the empirical line method. Thirdly, if simultaneous measurements are not available, temporal uniformity in atmospheric conditions is assumed to be a quasi-invariant state between the data acquisition. Last, co-registration between images is assumed to have a reasonable accuracy.

This method can be approached in two ways: multi-angle and multi-height methods. The multi-angle technique uses the RS sensors at the same (or similar) altitudes, but with different view angles for each observation of the same area. This provides different atmospheric path length for transmission and path radiance, resulting in different atmospheric contribution to the scene images. The multi-view (or multiple window) approach was originally developed by Anding and Kauth (1970) for atmospheric correction of SST estimation, and its multispectral application by McClain (1981) was later adopted for NOAA's operational sea surface temperature (SST) product with a more reliable sensor in the series, NOAA-7 data. Two different types of sensors, NOAA-5 AVHRR and GEOS-1 VISSR, were used to correct SST (Hoyler, 1984), and similarly Sun and Minnett (1984) proposed the chlorophyll estimation method using nadir and off-nadir CZCS images. Their results, however, showed that the temporal intervals between two sensors might have been too large to apply this method for frequently changing atmospheric conditions. Later the success of these multiple satellite atmospheric correction technique inspired 'dual-view' sensors, such as ATSR (Along Track Scanning Radiometer) series and POLDER (POLarisation and Directional Earth Radiation), which has only a short period between multiple observations. Although application of the multi-sensor method for land surface studies was limited to the surface BRDF (e.g. Danson *et al.*, 1999; Leblanc *et al.*, 1999), Veefkind *et al.* (1998 and 2000) showed that atmospheric aerosol optical depth and its spatial distribution were successfully separated from the ground reflected radiance using the dual-view algorithm. For airborne optical RS, there has been attempt to use a side-overlapping area within more than two airborne images that were considered to have two different viewing angles and therefore different atmospheric path lengths (Steven and Rollin,

1986). With an assumption of isotropic surface reflectance, a linear relationship between the two different viewing angles was applied. The authors failed to show reasonable accuracies of the estimation of the atmospheric correction parameters, and concluded that relatively complicated scattering phase functions in VNIR and bidirectional properties of the surface reflectance would have caused considerable inaccuracies. A similar, but simpler approach with selective ground features, tends to have better results combined with the empirical line calibration.

The surface BRDF problem of land surfaces for the multiple-view method tends to be minimised by vertical multiple observations with near-nadir or similar viewing. The multi-height atmospheric correction method has been developed for airborne multispectral images which tend to have more flexible altitude changes (Steven *et al.*, 1984; van Stokkom and Guzzi, 1984; Steven and Rollin, 1986), and later extended to satellite sensors using simultaneous acquisition of airborne (and ground) measurements (Holm *et al.*, 1989). For example, the MSS-82 multi-height experiment was undertaken by Steven *et al.* (1984) in order to improve the radiative transfer models (e.g. ATREM) that often show deviations in strong atmospheric absorption bands from the reference spectrum due to an approximated model. The multispectral imagery, MSS 11 channel, was taken at six altitudes from 500 to 3000 *m* on a hazy day. Six areas were used as ground target points, and were chosen close to the nadir to minimise the difference in path length to the sensor. Attenuation coefficients, k, at each layer were applied to *in situ* data for the scattering coefficient (using Beer's law: exponential decrease of radiance attenuation with path length). The airborne data were extrapolated to the ground and calibrated using the reflectance of a ground reference target. They found that a high attenuation layer existed at an altitude of 1000~1500m (Mie scattering dominant), and suggested that this technique could be used for correcting atmospheric effects by direct measurements. More recently, Rollin *et al.* (2002) successfully applied multi-height atmospheric correction method for mid-season on-board calibration of the CASI-2.

The multi-altitude method tends to eliminate the integrated calibration issues between the RS system and other instruments, such as field spectroradiometers, to minimise the scale sampling problem normally linked with the ground based measurements, and to be more flexible in terms of selection of suitable ground targets for the ground techniques (O'Neill *et al.*, 1997). The success of this technique is dependent on to carefully selected ground target areas and a physically reasonable multi-altitude regression for simultaneously extrapolating the

acquired images to zero altitude. The target areas should be, first of all, identified on each image, which are usually natural boundaries that are highly uniform and reasonable in size in order to avoid bidirectional and adjacency effects. These criteria are particularly important since the spatial resolution of each image is proportionally different depending on altitude. Despite acceptable successes of the multi-altitude method (after several assumptions), the spatial and temporal variations of atmospheric conditions resulting in radiation changes in each image are thought to be the main limitation of this method (Steven and Rollin, 1986). Moreover, multiple surveys over the same area could decrease the possible area covered within the limited flight time and data storage. Nonetheless, the atmospheric optical information in addition to the surface reflectance derived from this method is useful for homogeneous areas, for example, forest or desert areas.

6.4.1.3. Ancillary measurements at sensor level

Atmospheric correction of RS data from spaceborne sensors has been relatively well understood for many years, since it is simpler than that of airborne data. The relatively small field of view due to high altitudes means less directional effects in reflected radiance from the ground, and more importantly, the radiantion travels twice the complete thickness of the atmosphere between sensor and the ground target, and the solar irradiance at the top of the atmosphere is known. In airborne sensing, flying in the middle of the atmosphere, estimating atmospheric conditions is much more complicated than for spaceborne RS data. The altitude and direction of the flight are not always the same, resulting in changes in the Sun-target-sensor geometry (Wilson, 1995). These result in variations in incident radiation and in the amount of atmospheric scattering above the sensor level (van Stokkom and Guzzi, 1984). Most airborne platforms acquire ground leaving radiance within the troposphere (up to ~10 *km* of altitude in mid latitude; Schmidt *et al.*, 1990). As this lowest layer of the Earth's atmosphere contains around 75 % of atmospheric mass and 99 % of water vapour in the atmosphere, most interactions from atmospheric constituents appear in this layer. The fact that, for example, NERC CASI normally operates lower than altitude of ~3 *km* (~10,000 *ft*) suggests that majority of atmospheric transmission is occurring above the airborne RS sensor.

As shown earlier, the multi-height method has limitation of spatial and temporal variations of radiation change, and Steven and Rollin (1986) suggested that simultaneous

incident irradiance measurements with an airborne sensor are required for atmospheric variations in each scan of the image and for extending the atmospheric correction capability toward non-clear sky conditions, i.e. cloudy or overcast. The feasibility of using an airframe mounted spectrometer to measure spectral irradiance at the sensor was investigated by Milton *et al.* (1994) using a Spectron Engineering SE-590 spectroradiometer. Two identical instruments, one with a cosine-corrected receptor for downwelling irradiance and the other with a nominal 1° field-of-view for upwelling radiance, were mounted outside the cabin of a Bell Jet Ranger helicopter. Multi-height measurements over uniform targets showed residual atmospheric effects in the reflectance spectra measured, which varied depending upon the thickness of atmosphere beneath the platform. The systematic nature of these variations suggested that an airframe-mounted irradiance sensor would be a useful addition to an aircraft sensor for atmospheric correction purposes, allowing the calculation of at-sensor reflectance and the temporal and spatial variability of the incident irradiance (Gray *et al.*, 1997).

However, the usability of data from a rooftop irradiance sensor is seriously compromised if fixed-wing platforms are used due to variations in downwelling irradiance signals caused by pitch, roll, and yaw motion of the platform. Uncorrected irradiance sensor position limits its usability. Milton *et al.* (2001) attempted to use only selected scans of the CASI's ILS measurements when the roll angle was less than 0.01 degree assuming that the ILS position was close to the horizontal on these occasions. The mean ILS value for each flightline showed that the temporal variation did not correspond to the ground based irradiance measurements. Shepherd *et al.* (1995b) have analysed the errors involved in using data from a rooftop-mounted ILS fitted to the CASI to calculate the reflectance of ground targets. An error analysis of the CASI ILS conducted by Shepherd and Xu (1993) showed a low signal-to-noise ratio in particular at short wavelengths, and concluded that at-sensor apparent reflectance could be derived with a precision of better than 5 % at 550 *nm* despite the fact that atmospheric effects underneath the aircraft were still important for at-ground reflectance. The performance comparison with three other atmospheric calibration methods demonstrated that the ILS derived apparent reflectance was best overall while radiative transfer method using PIF image features (featured by Freemantle *et al.*, 1992) yielded the best results for a vegetated area (Shepherd *et al.*, 1995).

Piekutowski *et al.* (1996) attempted to correct for variation in aircraft attitude on data from an incident light sensor fitted to the MEIS-II (Multispectral Electro-optical Imaging

Scanner) (Piekutowski *et al.*, 1996). For variations in aircraft attitude, their attitude correction still needed the 5S radiative transfer model to estimate the ratio of direct to diffuse irradiance at altitude. A similar attempt was conducted by Bannehr and Schwiesow (1993). The authors concluded that the aircraft motion correction of ±2° for the irradiance sensor on top of the aircraft improved its accuracy by ±12 % at low solar altitude, such as 70° of solar zenith angle. Also, they suggested that the successful determination of navigational uncertainties required at least three triangular headings at the same altitude.

6.4.2. Image-based methods

Atmospheric information at the time of data collection is not always available from ancillary measurements due to limitations of resources. The method above generally involves additional data from the field or laboratory thus imposing large cost and effort in order to identify true spectral signatures on the ground and to interpret them as biophysical variables for the environmental applications with high accuracy. Therefore, it is necessary to circumvent the required information of atmospheric conditions at the time of image acquisition. One of the alternative options is to derive the conditions about the atmosphere from the image itself in order to retrieve at-ground reflectance calibration. The direct estimation of radiances without *in situ* measurements was also suggested by Markham and Barker (1987) who noted the difficulties of atmospheric correction/calibration. A number of techniques, however, have been developed in an attempt to compare multidate and multisensor images, e.g. Badhwar *et al.* (1982); Schott *et al.* (1988); Hall *et al.* (1991). Such image-based methods are generally known as the simplest and quickest atmospheric correction method. However, it can sometimes provide the least accurate results or non-physical unit conversions (in image normalisation). Badhwar *et al.* (1982) tested non-scene dependent reflectance, and determined the analytical description of spectral response, i.e. 'spectral profile' as a reference. However, it required a large degree of human interaction and decision making to use as a reference. Many other techniques rely on in-scene or ground truth elements to independently normalise the variations of individual multitemporal images. In general, image-based methods have proved to be operational and automatic for multi-temporal analysis of remotely sensed images with acceptable accuracy (Kaufman and Sendra, 1988; Hill and Strum, 1991; Gilabert *et al.*, 1994; Liu *et al.*, 1996).

Multispectral remote sensing data allows three ways to assess such information, i.e. spatial domain, spectral space, and feature space (Curran *et al.*, 1998). The image-based atmospheric correction assumes that the radiance measurement of an image pixel is the summation of target radiance and contribution from atmospheric effects. Thus, results from any type of scene model are eventually affected by the effects of the atmosphere. This section is focused on the review of atmospheric correction methods that is based on each scene model.

6.4.2.1. Image Space Based

The image space is the most primitive interpretation method of remotely sensed data and is natural to a human interpreter. RS data acquired on different dates have different atmospheric effects on each image, and thus the reflected radiance values of the same surface result in non-identical pixel values due to changes in illumination, topographic shadows from different sensing geometry, and changes in sensor response.

With either no knowledge of atmospheric conditions provided separately or no *in situ* ground measurements, ground reflectance calibration with more than one image of the same area from different dates is straightforward. A comparison of a set of images can be achieved by normalisation. It corrects images containing a common scene in a relative, instead of an absolute sense. Chavez (1975) showed a direct method for adjusting digital values for atmospheric degradation, called histogram minimum methods (HMM). This procedure assumes an assumption that the minimum pixel value within a scene would be zero if there is no (or minimal) atmospheric scattering as an additive path radiance and it is supposed to be the same for normalising multi-date images. Despite its simplicity and wide applicability, the method ignores the changes of histogram shape (i.e. all pixels are uniformly illuminated) and the spatial position of the darkest pixels (i.e. different sensing geometry is not taken into account).

Extending the idea of the HMM in multispectral data, Chavez (1988) developed a Rayleigh scattering model that represents the amount of haze in the atmosphere. The Rayleigh scattering, a function of n-th power of the wavelength, is used to match the minimum histogram values in a certain waveband, and then extrapolate it to the rest of wavelength range with respect to the Rayleigh-to-n relationship. Later, this method was been modified to enhance its performance (Chavez, 1996).

6.4.2.2. Spectral domain based

Rather than attempting to apply entire scenes as above, here the atmospheric effects on the image are considered with more than one reference spectra derived within the scene. The result and its accuracy between image normalisation (relative comparison between multi-date images) and ground reflectance calibration (closest to the absolute correction). With known (or guessed) ground information, the procedure is similar to the empirical line methods, except that the selected pixel spectra are considered as input parameters in the RT-modelling. The following paragraphs represent the variety of spectral selection methods, which tend to have consistency and reliability in their application, especially for multitemporal studies.

One of the simplest approaches is to use a single reference spectrum and to subtract or divide it by each pixel value of the image. The Internal Average Relative Reflectance (IARR) method was developed and produces good results for dry areas with no vegetation or when there is no or little ground information available (Conel *et al.*, 1987). The reference spectrum is found by averaging the entire scene, but, in general, it is not a powerful enough tool to calibrate reflectance of images (ENVI User's Guide, 2002). Instead, an area of known 'flat' reflectance, i.e. spectrally uniform, is selected and is used to normalise images, known as the Flat Field method (Roberts *et al.*, 1986). This process requires in-scene ROIs to effectively reduce imaging spectrometer data to 'relative reflectance' (ENVI User's Guide, 2002). Like the irradiance measurement method, the ROIs are used as the reference spectrum, and its average is then calculated to find the fraction of the spectrum at each pixel of the image. The selection of ROIs within the image should be both geometrically and spectrally flat areas. Soil on a geomorphologically flat field, therefore, is reasonably suitable for the flat field method, although there is evidence showing that it may not have Lambertian properties depending upon viewing angle (Milton and Webb, 1987). As a result, the flat field method is only useful when there is an area in the image containing materials of flat reflectance.

With more careful selection criteria, radiometric scene normalisation has been developed to minimise atmospheric effects by using pseudoinvariant features (PIFs), as

reference spectra, with other series of images, so that it permits scene-to-scene normalisation by implementing a set of radiometric transformations (Schott *et al.*, 1988; Hall *et al.*, 1991). Typical PIFs must be spatially well-defined and uniform and spectrally stable in terms of consistent reflected radiance. Schott *et al.* (1988) approached fundamental radiation theory, and applied a linear function to PIFs in both images, i.e. estimation of the slope and intercept of the linear relationship from the average and standard deviation of the PIF pixels. NIR-to-red band ratio and mid-infrared band were used to isolate PIF masks which were then used to segment the image, although this was scene-dependent. Then a standard technique for histogram matching was used to check the linear transform method. Although averaged error was approximately less than 1 % of a reflectance unit, the segmentation process was interpreter dependent, and has insufficient refinement for wider application.

For more than a decade, the PIF method has been improved in terms of the target selection strategy and used in wide applications such as temporal image normalisation with various RS sensors. For example, five independent image normalisation methods using ground truth data for temporal variations, were compared by Gerson and Fehrenbach (1983), and they concluded that the normalisation using black and white land targets reveals the best result. A later study by Hall *et al.* (1991) extended the two-extreme-brightness PIFs in the spectral transformation for a more sustainable image normalisation method. On the other hand, Ahern *et al.* (1979) used clear water bodies to extract path radiance information, the work was extended by Kaufman (1988) and Ahern *et al.* (1977). Landsat TM images acquired in 1984 and 1990 were standardised using 1986's TM image and successfully monitored changes of forest cover (Coppin and Bauer, 1994). They collected aerial data for five in-scene PIF targets: a clear deep lake, dense vegetation, a large asphalt roof, gravel, and a concrete parking area. By using a deep water body and a bright sand area, atmospheric normalisation of ten multi-temporal TM images was performed for agricultural lands (Lenney *et al.*, 1996). With multi-date SPOT images, Michener and Houhoulis (1997) assessed the impact of flooding over forest area.

Rather than image normalisation with PIF technique, there have been attempts to achieve absolute ground reflectance calibration by combining in-scene data and knowledge of the interaction between the Earth's surface and atmospheric constituents. This is based on the dark object subtraction method (DOS), which is one of the simplest yet most widely used image-based atmospheric correction methods particularly for change detection and land cover classification. As a successor of the HMM (Chavez, 1989), many studies showed that DOS was

effective to minimise atmospheric contribution from the detected radiance signal (e.g. Spanner *et al.*, 1990; Ekstrand, 1994; Jakubauskas, 1996; Huguenin *et al.*, 1997). The dark pixel is assumed to have a zero ground reflectance such that its radiometric value represents the additive effect of the atmosphere (Crippen, 1987). Kaufman and Tanré (1996) demonstrated that the aerosol single scattering or the aerosol optical thickness was most distinctive as additive radiation over dark pixels in the image, whereas bright target in a scene was more sensitive for atmospheric absorption. However, DOS alone is inclined to suffer greatly from noise within the dataset as it greatly simplifies the atmospheric correction procedure, and the technique requires suitable dark pixels to exist somewhere on the image. The application of DOS has, nonetheless, been enhanced to estimate atmospheric path radiance and to give a high level of reflectance accuracy when integrated with a RT-model (e.g. Teillet and Fedosejevs, 1995). This combined method has been accepted by the Canada Centre for Remote Sensing (CCRS) Image Analysis System as an operational atmospheric correction method (Teillet, 1986).

6.4.2.3. Feature Space Based

The feature space of multispectral images is an essential link between image space and spectral space (Curran *et al.*, 1998). In most multi- or hyper-spectral remote sensing studies, multi-band processing supposedly gives greater spectral information of the Earth's surface than using a single band image. Increasing the volume of data per unit area in spectral dimension certainly provides an opportunity for retrieving more information, but at the same time, new methodologies are required to handle such data easily. Feature space not only overcomes the limitations of data presentation in image space (up to three RGB colour composition) and spectral space (only small number of spectra in a plot), but also can entire scene data be expressed by orthogonal space with unlimited number of spectral bands. Although spatial information has to be a trade-off, particular data models may be created in this *n*-dimensional space for RS application. Like any other types of data space, image processing in feature space also affects the atmospheric effects.

The data model has been developed in two main fields in this kind. First, Principal Component Analysis (PCA) is used to discriminate multi-temporal variations of the terrestrial materials from various atmospheric conditions. PCA technique normally reduces the dimensionality of multispectral data in feature space that are often difficult to handle with

conventional image processing facilities, especially when spectral dimension increases from multispectral to hyperspectral data. The method uses image data statistics to define a rotation of the original image in such a way that the new axes are orthogonal to each other and point in the direction of decreasing order of variance (Campbell, 1996; Lillesand and Kiefer, 1994). There are two different statistical approaches of PCA; unstandardised and standardised PCA. The former has long been used as a data compression tool as its transform coefficients are derived by computing the principal eigenvectors of the variance/covariance matrix (Lillesand and Kiefer, 1994; Richards, 1984). Singh and Harrison (1985) described that the transform coefficients of standardised PCA find the eigenvectors from the correlation matrix, i.e. each bandset has equal weight, once the new component is derived. Not only has PCA been applied to an extensive interband correlation method of multispectral image data, but also there is an example of an application for land classification using standardised PCA (Tucker *et al.*, 1985; Townshend *et al.*, 1987; Dwivedi and Sankar, 1992). In this manner, the standard method of PCA has been applied as a more efficient feature extraction method in remote sensing. The main axis of eigenvectors tends to optimally align in the predominant classes in the feature space and the rest of PCA components represent the prioritised classes from the centre of the main vector (Kauth and Thomas, 1976; Jackson *et al.*, 1983). Simultaneously, as it generally assumes relatively high signal-to-noise ratio of the sensor system, the smallest variations in the scene with the lower-order PCA components are considered as white noise from the RS instrument. Green *et al.* (1988) defined it as the 'maximum noise fraction' or MNF, and used PCA as a noise reduction algorithm for multispectral RS data.

More recently, Li and Yeh (1998) presented the monitoring of rapid urban expansion by using a combination of PCA and supervised image classification. The possible application of PCA in analysing multi-temporal image data sets was introduced by Fung and LeDrew (1987), and extended by Eastman (1992). Both studies also announced that standardised PCA is more efficient than non-standardised PCA in multitemporal image analysis. With an assumption of atmospheric effects as substantial sources of variation, Fung and LeDrew (1987) demonstrated change detection by circumventing explicit atmospheric correction. Eastman (1992) examined the potential of using PCA with standardised components, and showed the ability to identify seasonal elements and isolated monthly NDVI from AVHRR for 4 years. The modification of the standardised PCA for a larger number of images was analyzed for a 36-month sequence of NDVI data for the African continent (Eastman and Fulk, 1993). Each component was checked by examination of the graphs of the component loadings which are considered as the correlation

between the original images and the derived components. The first component represents the major element of spatial variability in NDVI over the whole season, while the rest are related to seasonal changes including sensor-related drift and the El Niño Southern oscillation event, which appears as a lower component due to a smaller change than seasonal variation. They concluded that the PCA is a strong tool for isolating both seasonal variation and long-term change events. Change detection technique for longer time series, but a smaller number of images, was tested by Guirguis *et al.* (1996). Three Landsat-MSS images were selected about 8 years apart. They compared the results from PCA and two other change detection methods, and confirmed that standardised PCA exhibits a better performance than unstandardised PCA for change detection as mentioned above. Moreover, the first three components from PCA were the most useful for them to determine the change detection for the time period. Yet no application of PCA for atmospheric correction has been done. PCA may possibly be used to isolate atmospheric contamination in a set of multitemporal images.

A second category of scene models, which is related to the atmospheric correction in feature apace, is a scene mixture model. When the cloud of data from the image is placed in the feature space, the positions of individual data points are characterised in the minimum size of spectral dimensions, i.e. intrinsic dimensionality. And these data points are expressed as mixtures of more than one reference spectrum (i.e. spectral endmember) within the space. All applications of spectral mixing presuppose a model of the scene being imaged (Milton, 1999). Spectral mixing is most meaningful when applied to a data set calibrated to physical units and for which the reference endmembers are known and characterised, both in physical terms and in their spectral properties. In order to maintain its simplicity, it has been assumed that the spectral characteristics due to spectral mixings are linear, i.e. more than one sub-pixel ground targets are mixed as a simple addition of individual target spectra.

Spectral endmember analysis is a technique that is commonly applied to hyperspectral data, but, as Adams *et al.* (1989) point out, it also has a role to play in global land cover mapping using data from conventional multispectral sensors with relatively few spectral bands, such as Landsat TM or NOAA AVHRR. The reason for this is that, although the size of intrinsic dimensionality in Landsat TM or other multispectral sensors may be small for vegetated scenes (typically band 2 or 3), this is sufficient to capture the important features present, such as the proportion of green vegetation within a pixel. Further information is possibly neither required nor desirable for many global scale applications due to the volume of data involved. The

simplest and yet most well-known feature extraction is the simple ratio and the normalised difference vegetation index (NDVI; Rouse *et al.*, 1974), which measures the angle of a pixel in feature space from the shadow endmember, the origin of two-dimensional feature space. A variety of vegetation indices, or similar, are widely used as tools of measuring vegetation vigour due to its relation to the biophysical properties of plants, such as LAI (e.g. Wardley and Curran, 1984; Weiser *et al.*, 1986; Peterson *et al.*, 1987; Baret and Guyot, 1991; Gong *et al.*, 1995). A variety of atmospheric interactions between this low- or high-order spectral transformation and biophysical information has long pervaded the remote sensing literature in terms of separating spatially and spectrally mixed scene components. For example, shadows in association with canopy structure and varying solar angle (e.g. Ranson and Daughtry, 1987; Leblon *et al.*, 1996), regional illumination changes due to atmospheric aerosol density (e.g. Roberts *et al.*, 1997; Hope *et al.*, 1999; Gao and Li, 2000), and the surface BRDF (e.g. Lee and Kaufman, 1986; Gemmell and Varjo, 1999; Huete *et al.*, 1992; Shepherd and Dymond, 2000).

Minimisation of the effect of the atmosphere in the spectral transformation was originally examined by Kauth and Thomas (1976), and extended by Crist and Cicone (1984), though these transformations are not accurate enough to distinguish significant levels of image-to-image variability. Hall *et al.* (1991) used a two-dimensional non-vegetated Kauth-Thomas (KT) greenness-brightness distribution function for a radiometric control set selection. This distribution indicated that some of the elements had nearly constant reflectance over time, and the only differences between images, due to varying sensor calibration and atmospheric conditions, introduce linear differences in the radiance (Conel, 1990). This results in less than 1 % of relative reflectance between 2-year apart images. Although the procedure of selecting a radiometric control set is more user-dependent than that the dark subtraction method developed by Schott *et al.* (1988). Its error range can be minimised by tightening the number of pixels of the control set in order to reduce the quantisation error term. The errors they found in the mid-infrared band are due to differences in humidity, a reported sensor fault and failure of atmospheric correction.

The application of feature space transformation has been advanced from image normalisation by more sophisticated algorithms deriving atmospheric optical properties from the scene. That is, separating the atmospheric contribution in the scene model from available information in the image itself (or supplied from external sources), rather than estimating inherent spectral reflectance of the surface after the atmospheric correction methods (e.g.

Jacquemoud *et al.*, 2000). Kaufman *et al.* (1996) suggested two main atmospheric aerosol corrections for remote sensing, direct and indirect image based methods. Like the spectral-domain-based method, the direct method derives the aerosol loading using a single (or multiple) PIF (e.g. Ahern *et al.*, 1977) or an atmospheric absorption or scattering channel inherent in the multispectral image (e.g. Salomonson, *et al.*, 1989; Veefkind at al, 1998), followed by an appropriate radiative transfer model. Of these direct corrections, Kaufman *et al.* (1997) proposed an algorithm using Dense Dark Vegetation (DDV) over a land surface for estimating atmospheric aerosol optical depth (Richter, 1996; Liu *et al.*, 1996). DDV is a similar concept to deep water or dark objects, but is considered as a more controlled dark surface (Kaufman and Sendra, 1988). In addition to the fact that the dark surface is generally more sensitive to aerosol scattering (Fraser and Kaufman, 1985), DDV tends to show reasonably stable low reflectance in visible wavelengths whereas aerosol scattering is relatively greater than in longer wavelengths. Kaufman and Sendra (1988) developed an atmospheric correction algorithm using DDV: Appropriate DDVs were selected using NDVI, the aerosol optical thickness was computed using a radiative transfer model, and the positions of multiple DDVs were interpolated to estimate spatial distribution in the scene if sufficient number of DDV exists in the image. Liang *et al.* (1997) applied the DDV method to correct Landsat TM images on a pixel-by-pixel basis. The DDV method was particularly effective for forested areas, such as in the Boreal forest (Zagolski *et al.*, 2000). The main disadvantage of the DDV-based aerosol retrieval is that even with carefully selected DDV it is still sensitive to the surface reflectance (Miura *et al.*, 2001), in particular, with low aerosol density (Kaufman and Tanré, 1996). As an alternative, Kaufman and Remer (1994) replaced the aerosol contaminated red waveband with a mid-IR channel in AVHRR and EOS-MODIS, which is much less sensitive to atmospheric aerosols. As a selection criterion for DDVs in the image, a stable relationship of radiance between mid-IR and visible spectra suggested the atmospheric corrected vegetation index as an indirect image based method, i.e. Atmospherically Resistant Vegetation Index (ARVI): self-correction process for the atmospheric effect, yet providing similar dynamic range to the NDVI (Kaufman and Tanré, 1992). The authors demonstrated that a comparison of ARVI with the RT-model simulation showed an operational and effective atmospheric correction method for most RS systems. ARVI is currently used as one of the operational MODIS algorithms over the land surface for optical aerosol thickness.

6.4.3. Radiative Transfer Model-Based Methods

The propagation of electromagnetic radiation through the atmosphere has been well characterised by Chandrasekhar (1960). Based on this theoretical approach, which establishes rigorous interactions through the column of atmosphere for the radiation reaching the RS sensor, a number of radiative transfer codes have been developed to simulate atmospheric effects on RS images. Applications of the RS-models are often used in atmospheric and Earth's energy budget research due to their high accuracy and precise results. Moran *et al.* (1992) demonstrated that error ranges of Landsat TM reflectance for all spectral bands were ±0.01 after running the RT-model with on-site atmospheric optical depth and water vapour measurements. Better results however always come with a price. To obtain an accurate radiance-to-reflectance conversion for remotely sensed images, the model requires detailed atmospheric parameters to be made at the time of the image acquisition, and variables required for the radiative transfer equations mean a series of detailed calculations in order to provide an estimate of the atmospheric scattering, as well as a well-calibrated sensor (Crippen, 1987; Moran *et al.*, 2001).

Most RT-models used in RS images are designed to simulate radiation interaction between photons and atmospheric constituents, such as gaseous absorption and scattering by molecules and aerosols as realistically as possible. In many RT-models, the successful simulation of these involves atmospheric information, for instance, vertical and horizontal distribution of atmospheric gases, density of aerosols, the target properties, its spatial uniformity and so on. Although the assumption of Lambertian surface simplifies the model dramatically, some models include the functionality of the surface BRDF (Tanré *et al.*, 1990; O'Neill *et al.*, 1995). Usually, more input parameters are required for the surface BRDF in order to take into account the radiance perturbation due to the surface properties. The variables are, for example, geometrical conditions, the atmospheric model, the aerosol characteristics, the spectral band observation and the ground reflectance.

One of the problems with the direct usage of the RT-models is that such input data are not always available. In real conditions, it is virtually impossible to obtain a snapshot of the atmospheric condition of the surveying area at the time of image acquisition. Several methods have been attempted to circumvent such difficulties. Some use approximated atmospheric

conditions categorised by several distinctive regions, while inversion of the RT-models with image-based or laboratory-based reference data estimates essential information for the atmospheric correction over the entire image. Also, statistical methods applied to spectral bandsets provide approximations of atmospheric effects according to the prerequisite meteorological data. Lastly, the combination of the RT-model with the ground measurements would compensate for the limitations of each approach. The following list shows the types of RT-model application for atmospheric corrections

1) Generalised atmosphere standard (e.g. Moran *et al.* 1992)
2) Iteration of inverted RT-model (e.g. Zagolski and Gastellu-Etchegorry, 1995)
3) Statistical method from different viewing or a specific waveband (e.g. Berk *et al.*, 1989; Veefkind *et al.*, 2000)
4) Hybrid model: Combination of radiative transfer equations and the ground measurements (Moran *et al.*, 2001)

For the first category of the RT-model methods, the 6S code, as a successor of 5S, uses an approximation technique to model aerosol scattering that could be a few percent in reflectance units in some cases (Vermote *et al.*, 1996). In regions of high atmospheric transmission or highly turbid atmospheric conditions, there are anomalous features in the RT-model compared to the laboratory spectrum. ATREM (Atmospheric REMoval Program: Gao *et al.*, 1992) or LOWTRAN, which uses predetermined solar spectra, often result in a certain magnitude of discrepancies due to possible changes of the solar spectrum depending on the Earth-Sun distance and variable strength of incident solar radiation at the top of the atmosphere and/or in the accuracy of the instrument's radiometric calibration.

The modelled atmosphere consists of different simulated atmospheres, aerosol types, solar zenith angle, and ground altitudes. The general model atmosphere could be the U.S. Standard Atmosphere varying with geometric position and seasonal variability and the model for the specific area constructed by field measurements and/or localised atmospheric composition. Furthermore, Richter (1990) showed that the adjacency effect on a RS image could be estimated using a $n \times n$ pixel window and approximate weighing functions for surfaces with different reflectance. Although these catalogues of atmospheric conditions increase the processing time especially when there are no supplementary atmospheric data available, they

are not always applicable and can cause error in the atmospheric correction of RS images (Cartalis and Retalis, 1996).

In addition to estimation of the surface BRDF property, one of the significant sources of error from using a modelled atmosphere is the adjacency effect, which is a function of diffuse radiation in the atmosphere and spatial pixel resolution of the RS system (see Section 6.3.2). Usually, RT-model based methods assume an extended homogeneous ground area. It means that no (or little) spatial variability due to the adjacency effect which is mainly due to multiple reflections, i.e. scattering, is expected from the surrounding targets at ground level (Tanré *et al.*, 1992; Singh, 1992). Verifying the adjacency effect is difficult from *in situ* measurements and RT-models are the only viable method for this purpose. Due to the nature of multiple scattering in the atmosphere, various input parameters are necessary for its accurate estimation, such as the atmospheric albedo, atmospheric optical depth, gaseous transmittivity, and the total and diffuse transmission coefficients. Since the use of modelled atmospheric data often contributes to increasing the magnitude of errors, an alternative method has been developed to minimise the uncertainties despite the limited available input data. Zagolski and Gastellu-Etchegorry (1995) conducted an iterative method using Gauss-Siedel's principle, which is based on the inversion of 5S model. Inter-relations between the number of variables for the atmospheric correction of the RS image and the surface adjacent effect were grouped. Three look-up tables were created using visible multispectral bands, which simplifies the iteration processing for the adjacent effects. This pixel-by-pixel computation resulted in less than ~0.01 of reflectance value for all of the multispectral bands (although the results were obtained with help of *in situ* vertical atmospheric measurements using radiosonde). The authors concluded that the adjacency effect on a heterogeneous surface should be taken into account, especially in the optical spectrum.

The third approach to retrieve required atmospheric variables for the RT-model is to use in-scene spectral information from the multiple bandset. As already shown earlier, this is based on the Chavez method (1988) of simple estimation of Rayleigh scattering from a reference spectral band. The ATmosphere REMoval program (ATREM) is a similar technique with more detailed radiative transfer functions, especially suitable for hyperspectral RS images. For atmospheric absorption, the ATREM approximates atmospheric transmittance of seven gases using the Malkmus narrow band model and a pressure scaling estimation method. Some atmospheric scattering codes have been adopted from 6S. However, spatial distribution of atmospheric aerosol, as a source of scattering, is accomplished by two water absorption bands

(940 and 1140 *nm*) with a three-bandset ratio technique. Because aerosol information is obtained from the image itself, pixel-by-pixel correction is possible. Such atmospheric data are employed in radiative transfer equations, and provide the effect of water vapour absorption/scattering effects in 400~2500 *nm* region. Similar techniques have been attempted with other spectral bands. Veefkind *et al.* (2000) demonstrated the separation of atmospheric aerosol from an image acquired by a spectrometer onboard the ERS-2 satellite that operated in UV-VIS-NIR wavelength regions (240~790 *nm*). On the basis of the fact that surface reflectance in the UV is relatively small, the authors developed an aerosol retrieval method using the UV band. This method resulted in less than 0.1 of optical depth and illustrated that large aerosol plumes over Belgium and France originated in the industrialised regions in Germany and Belgium.

Although ATREM (and similar programs) have performed successfully with many hyperspectral RS dataset (e.g. Ferrier, 1995), there are limitations to be considered. Firstly, there must be water absorption bands in the image. Secondly, the statistical RT-model normally assumes a Lambertian surface in the horizontal plane, although topographic effects could be taken into account. Thirdly, multiple atmospheric scattering is not considered (Gao *et al.*, 1992). Lastly, as Berk *et al.* (1989) highlighted, the spectral interpolation for the atmospheric parameters may introduce error.

One of advantages in running a RT-model for atmospheric correction is relatively quick and easy processing in comparison to methods requiring ancillary data. On the other hand, despite the theoretical basis of RT-models, field-based calibration methods often provide better accuracy, especially they use on-site atmospheric information at the time of the image acquisition. Many studies have been conducted to compare various types of atmospheric correction methods (Roberts *et al.*, 1986; Clark *et al.*, 1993; Ferrier, 1995; Song *et al.*, 2001), and the most accurate results have been attained when RT-models were combined with field measurements. This, so called the *radiative transfer ground calibrated* (RTGC) or *hybrid* method, tends to compensate limitations of each method and, at the same time, take advantage of both approaches. Clark *et al.* (1999) showed that even a minimum effort on the ground (i.e. a couple of people taking a few ground target measurement) could greatly improve the reliability of the RT-model.

Another attempt at a hybrid method was developed by Moran *et al.* (2001). This is based on an image-based empirical line method: at least two PIFs (normally having high contrast between them) are used to fit a regression line to a plot of pixel values against apparent reflectance on the ground. The accuracy of this method is highly dependent on the selection of PIFs, particularly in dark area where aerosol scattering is mostly affected (Schott *et al.*, 1988). Moran *et al.* (2001) adopted the RT-model in order to refine the spectrum of the dark target. The refined empirical line (REL) method improved the accuracy of the target area to 0.01, whereas typical error range was more than 10 % (Caselles and García, 1989). They concluded that the REL method had great potential for reflectance calibration for long-term monitoring. In particular, the method had an advantage of needing only a single in-scene area, but not requiring the existence of vegetation, bi-directionality, and spatial uniformity.

Chapter 7

Empirical measurements of short-term temporal variability of the atmosphere and development of a conceptual model

7.1. Introduction

Atmospheric effects are considered as an important factor on remotely sensed images because multispectral data recorded by spaceborne or airborne optical sensors are taken under different illumination conditions and observation geometries. These variable conditions are mainly due to the interaction of the solar spectrum with atmospheric constituents. The VNIR spectrum from the solar radiance is scattered and absorbed by atmospheric gases, aerosols and clouds. They eventually alter the radiance reflected from the object by means of its attenuation, spatially variable distribution, and bidirectional radiation distribution. Thus, these mixtures of atmospheric effects mean that the radiation detected by a RS sensor is wavelength dependent (Kaufman, 1985 and 1988), temporally variable (Peterson *et al.*, 1981; Kaufman and Fraser, 1983), and spatially non-uniform (Husar and Holloway, 1984).

Difficulties in understanding the atmospheric effects on RS images arise because they are only partially predictable. Hence, as described in the previous chapter, most efforts of atmospheric correction are devoted either to a broadly defined estimation of scattering and absorption by aerosol particles and molecules or to averaged direct measurements for pixels in an image, such as, from ground based sky or sun radiometers. These approaches yield inevitable limitations in terms of accuracy and precision (i.e. uncertainty) of atmospheric conditions in space and time. This drawback makes it difficult to compare images acquired on different dates and places.

In this chapter, the effects of atmospheric variability in the spectral domain of remotely sensed data are addressed. An experiment was designed to investigate short-term temporal changes in the atmosphere as these place a fundamental limit on every method of atmospheric correction (see Chapter 6). With an assumption that aerosol scattering of solar radiation is dominant for the changes of spectral signature across the entire range of the VNIR region (Kaufman and Tanré, 1996; Tanré *et al.*, 1992), the spectral changes when clouds pass through the direct solar beam would represent the variation of the atmosphere and provide an insight into the variation caused by sub-visual clouds, such as patches of water vapour. A field spectrometer was set up on various ground targets on different dates and continuously recorded the ground leaving radiance under illumination changes due to patches of clouds passing over the sites. Results from the field experiments are compared with a linear model using radiative transfer equations, which will give the importance of atmospheric corrections of RS image for spectral domain processing.

7.2. Field data acquisition

7.2.1. Instruments

For the purpose of this analysis, data were acquired using an Analytical Spectral Devices (ASD) FieldSpec™ Pro high performance field spectroradiometer comprising the spectrometer unit, a notebook computer for instant feedback and storing measurements and an interconnecting fibre-optic cable (Figure 7-1). At the end of the fibre-optic cable, a pistol grip was attached with a fore optic designed to reduce the instrument's field-of-view (FOV) with 8 degrees.

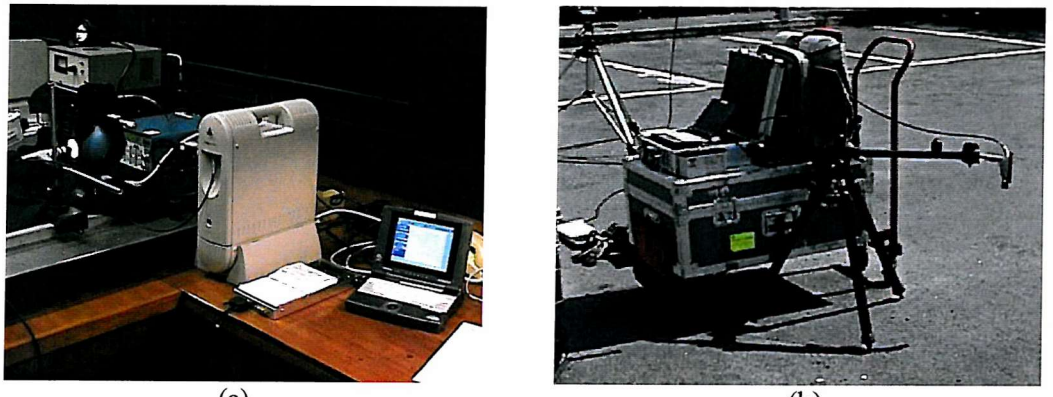

(a) (b)

Figure 7-1. ASD FieldSpec Pro setting in EPFS Laboratory (a) and in the field experiment on 29 July 2000 (b). In (a), although there are some other instruments in the scene, the main body of the ASD and its attached notebook are seen. The ASD is protected in backpack during the field experiment (b).

The data from the ASD provide high spectral resolution and high accuracy. The ASD measures over the visible to short-wave infrared wavelength range (350 ~ 2500 *nm*) with 10 *nm* spectral resolution. The entire spectrum range is measured by three spectrometers: a photo diode array spectrometer for 350 to 1000 *nm* (UV/VNIR), and two fast scanning detectors with diffraction gratings for the spectral range of 1000 ~ 2500 *nm*. The light travelling through the fibre-optic is separated into each of the three spectrometers in the instrument.

The signals detected by each spectrometer overlap at around 725 and 1950 *nm*, at which radiance spectra may show an offset, possibly due to a temperature dependence function. This

discrepancy is normally greater at the VNIR/SWIR1 overlap than at the SWIR1/SWIR2 overlap, and was minimised by warming-up the instrument for more than 90 minutes.

The spectrometer unit outputs 16 bit encoded raw DN values and the notebook computer attached to the ASD instrument controls and stores all the data acquisitions and produces real-time displays. Data type can be selected as raw DN, reflectance, radiance, or irradiance with various automatic sampling rates (> 1 second).

For the purpose of the experiments, raw ASD data in binary format were converted into radiance and stored in ASCII format. The routines used for this procedure are depicted in Figure 7-2. The raw data are converted to radiance using *Rcalc.exe* that uses previously calibrated standard lamp data provided by the manufacturer. *Portspec.exe* converts a spectrum from ASD binary format to ASCII and appends the header information.

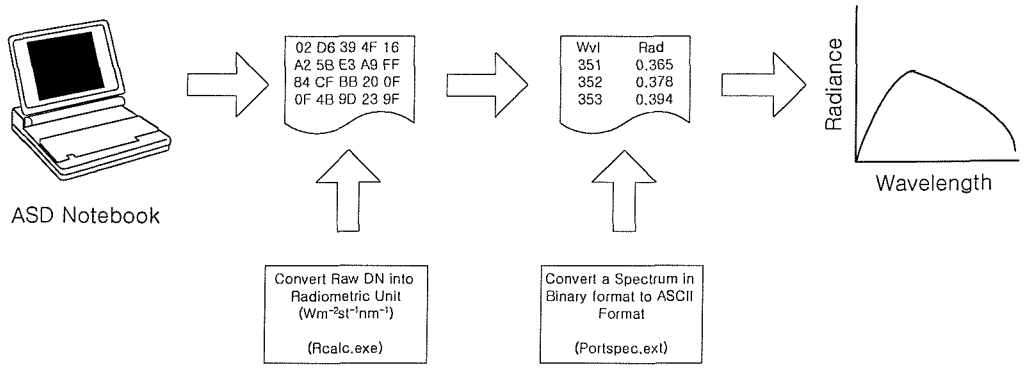

Figure 7-2. Flow diagram of data processing procedure of ASD.

In some occasions when ASD was not available, simpler instruments were used to enhance portability of measurements under quickly changing atmospheric conditions. The MMR (Milton Multiband Radiometer) is a simple radiometer designed for measuring reflectance in the first four Landsat TM bands (Milton, 1980). There are two MMR sensor heads – one for the reference panel and the other for the ground target, a meter unit, and a data logger (Figure 7-3). LI-1000 manufactured by LiCor™ was used as a data logger and this offers the choice of automatic data sampling interval (≥ 1 minute), and manual operation. For some of the work a new data logger (EPE) developed in the Geography department, University of Southampton (UoS), was used because it can collect data as short as every half second automatically. The LI-1000 has 8 bit resolution and presets the data as real numbers whereas the UoS EPE logger has 12 bit resolution and presets the data as integers.

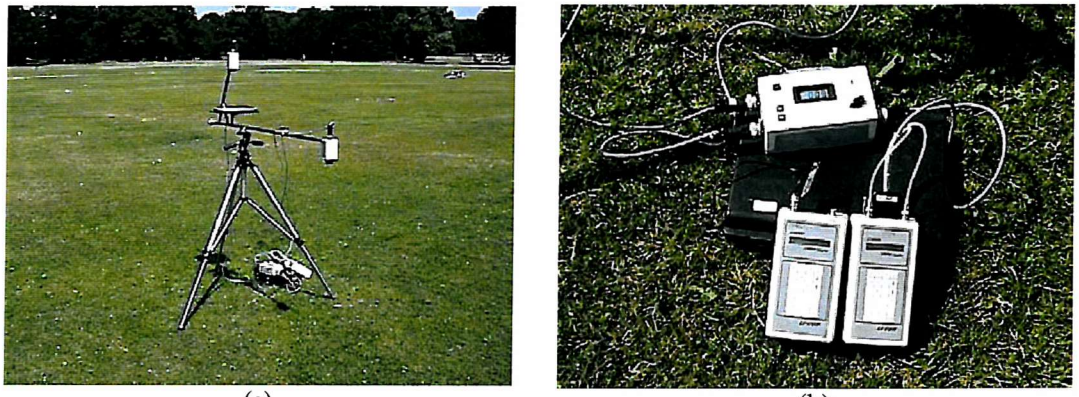

(a) (b)

Figure 7-3. Tripod-mounted MMR in field measurement (a) and close look of data logger (b).

Each MMR head uses four silicon photodiodes. Standard gelatin filters are used to produce approximate the Landsat TM bands. The reference number of MMR heads in this experiment is Log01 (YYY93; reference panel) and Log02 (BAL97A; target). Spectral response functions for each MMR band were measured using a monochromator with 5 nm sampling intervals over the region 400 – 1200 *nm* (Figure 7-4). The plots for two MMR heads show that most corresponding bands are filtering nearly in the same spectral region and range. The curves in band 4 are not however quite the same: the curve for Log01 starts at 800 nm, whereas Log02 from around 750 *nm*. Relatively small responses of band 4, little spikes less than 0.1, occur along visible wavelength region. They are considered as a random error and ignored in later processing. Since the spectral response functions between the two MMR heads are not identical, they would normally be used to be matched pairs for measurements of reflectance using the dual-beam method.

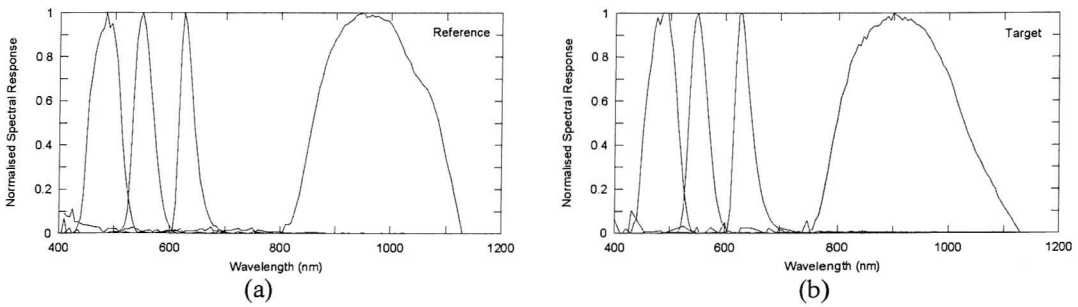

(a) (b)

Figure 7-4. Spectral response function curves of MMR head for Log01 (a) and Log02 (b). In each plot, peaks are in band 1, 2, 3, and 4 from the left.

7.2.2. Field measurements with the ASD and MMR

There were four different terrestrial targets and one artificial target which was used to measure incident solar radiance. For the incident radiance, a Spectralon™ reference panel reflected the direct solar beam into the nadir viewing ASD probe. The recording intervals of the ASD were fixed at 1 second, and the period of the measurements varied depending on the sky condition. A full description of each ASD data set used is shown in Table 7-1.

Target	Date	Description
Grass 	26 July 2000	The target was located in The Common, Southampton, UK. A typical grass field. It was mowed three days before the measurements, so was fairly short and regular. Although there were some patches of dried grass around the target, the field of view of the ASD is only covered the grass area.
Dried grass 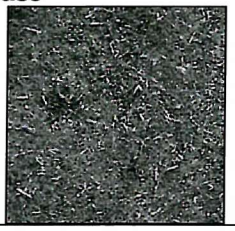	26 July 2000	The same location was used as for the grass. The dried grass target was about 10 m apart from the grass target area above. It was nice pile of uniform dried grass and no soil background could be seen.
Asphalt 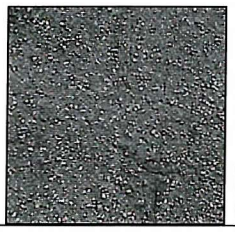	29 July 2000	Worn-out asphalt target in the car parking on the University of Southampton campus. It was relatively finer in texture than that on the ordinary road. Hence much less bi-directionalities were expected.
Concrete 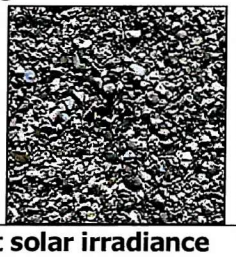	28 July 2000	The individual size of the concrete blocks in the pedestrian street were about 30×50 *cm*, the field of view of the ASD was smaller than this. It was ensured that the building adjacent to the site was on the opposite side of the Sun.
Incident solar irradiance	16 September 1998	The same site as the concrete target. Pedestrian concrete blocks at Geography department building.

Table 7-1. The description of the reflected radiance from four ground targets and a measurement of incident solar irradiance using the ASD. The measurements were taken in the various places, Southampton, UK.

The measurements from each target were performed on different dates, except for the two grass targets. During the measurements, the sky conditions were changeable in terms of cloud thickness and density. The time series plots show the frequency and length of the cloud shadows during the data collection under the illumination changes (Figure 7-5). Even under sunlit conditions, the intensity varied constantly, which indicates that atmospheric conditions were unstable and involved spatially non-uniform invisible aerosols. Many sharp peaks occurred when there were small clouds and gaps between clouds. Small and thick patches of clouds passed frequently during the data collection for incident radiance (Figure 7-5e), and sometimes it was necessary to wait for cloud shadows to pass as long as for 5 minutes (Figure 7-5b).

In order to see the characteristics of the sunlit and shadow boundary (SSB), an automatic SSB selection routine was developed. The entire spectral range of the ASD (350 ~ 2500 *nm*) was integrated as shown in Figure 7-5. Temporal variation, v, of radiation in each dataset was investigated by the difference of adjacent readings.

$$v = \left| \frac{rad_{m+1} - rad_{m-1}}{t_{m+1} - t_{m-1}} \right| \qquad [7.1]$$

where, v Rate of incident radiance change in given time period $[W\,m^{-2}\,sr^{-1}\,t^{-1}]$
rad Radiance $[W\,m^{-2}\,sr^{-1}]$
t Time [*second*]
m Data recording interval

The thresholds, v, for selecting the SSB were generally greater than 1 for targets and 5 for the incident solar radiance in the region of more than 8 continuous scans (i.e. longer than 8 seconds of continuing illumination changes at the edge of clouds). This procedure picks out long enough radiance changes with sufficiently large drops or increases of illumination changes. The routine chose 5 to 8 SSBs for each target (grey drops in Figure 7-5). The periods of the selected SSB, as a result, also vary, as well as the ranges of intensity changes due to changing opacity and speed of clouds. The number of selected SSBs were 6, 7, 7, 5, and 8, for targets of grass, dried grass, asphalt, concrete, and incident radiance, respectively.

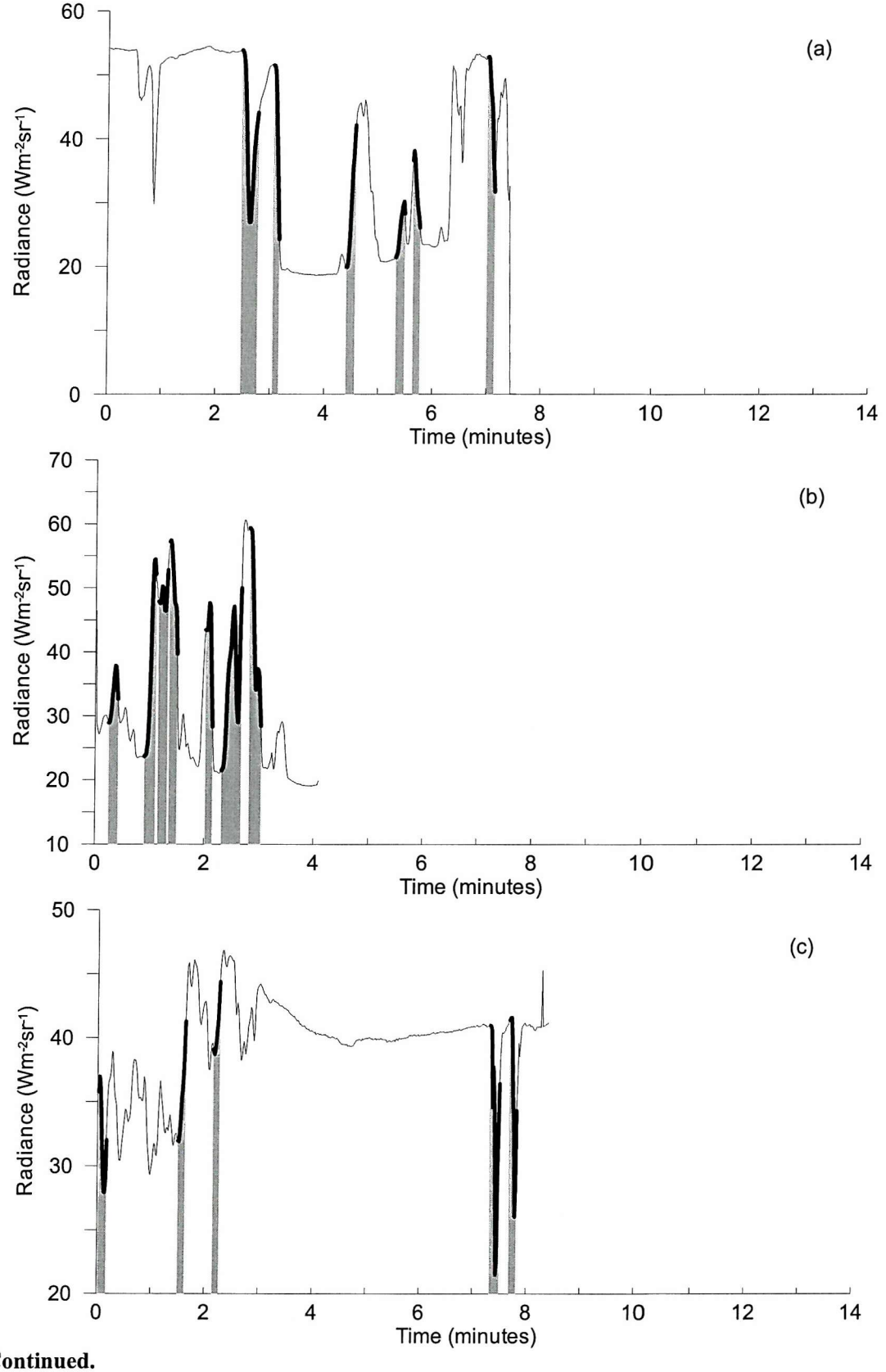
(a)
Radiance (Wm-2sr-1)
Time (minutes)
(b)
Radiance (Wm-2sr-1)
Time (minutes)
(c)
Radiance (Wm-2sr-1)
Time (minutes)

Continued.

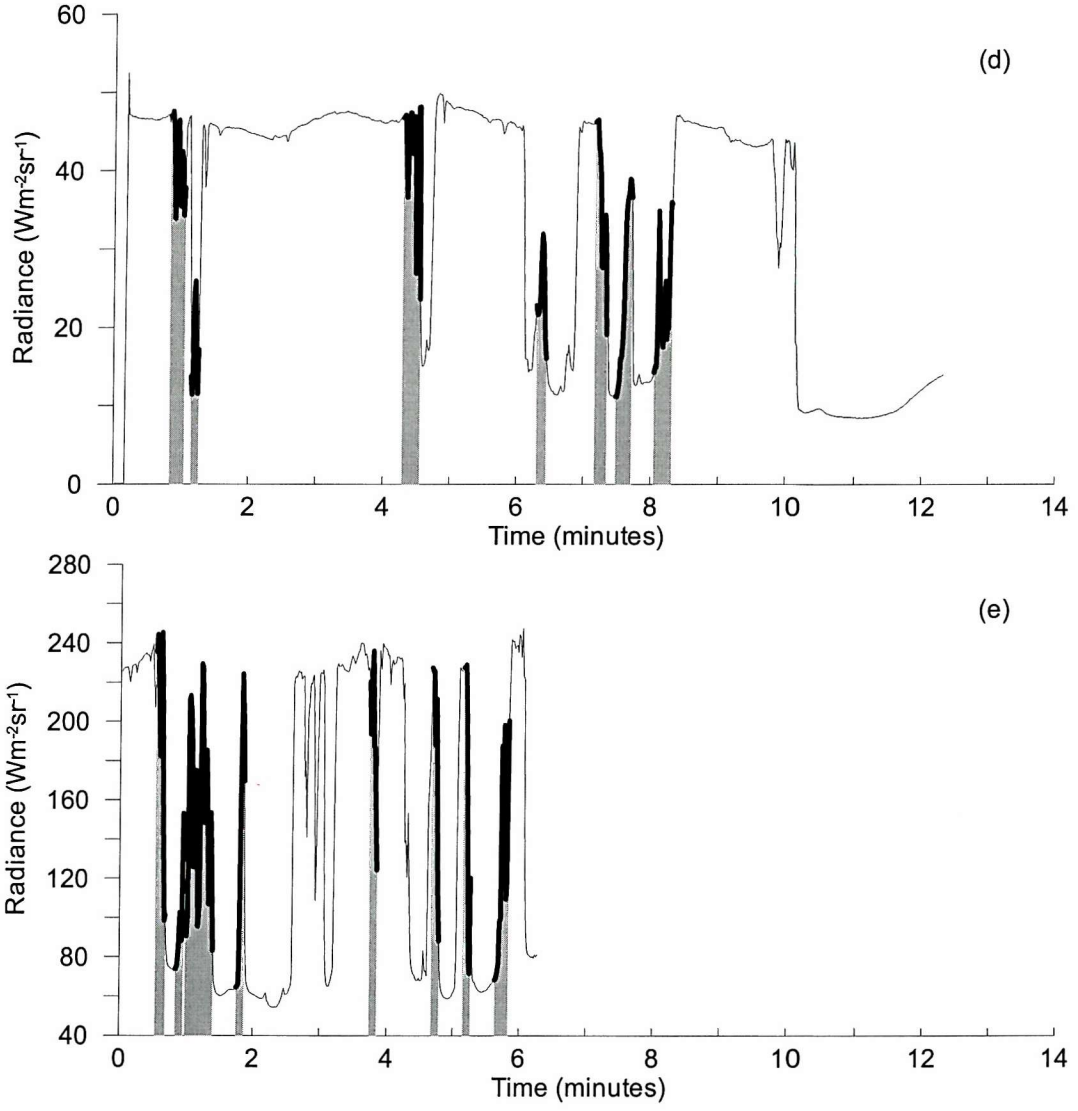

Figure 7-5. Time series plots of ASD field measurements, using integrated radiance on graphs between 350 and 2500 *nm*. They are grass (a), dried grass (b), asphalt (c), concrete (d), and Spectralon panel radiance (e), respectively. The grey bars represent selected sunlit-shadow boundary cases. Incident radiance measurement was conducted in September 1998, whereas the rests were in July 2000.

7.2.3. Spectral variations under sunlit and shadow boundaries (SSB)

There were in total 33 SSBs from four different terrestrial targets and one with the reflectance panel. The spectral plots of the example spectra show an overall radiance decrease

but with different magnitudes when the intensity reduces due to cloud shadows (Figure 7-6). It is important to notice that, except the spectral regions near 1400 and 1900 *nm*, no spectra were found to have zero values, i.e. no true darkness, even under the darkest shadows during the measurements.

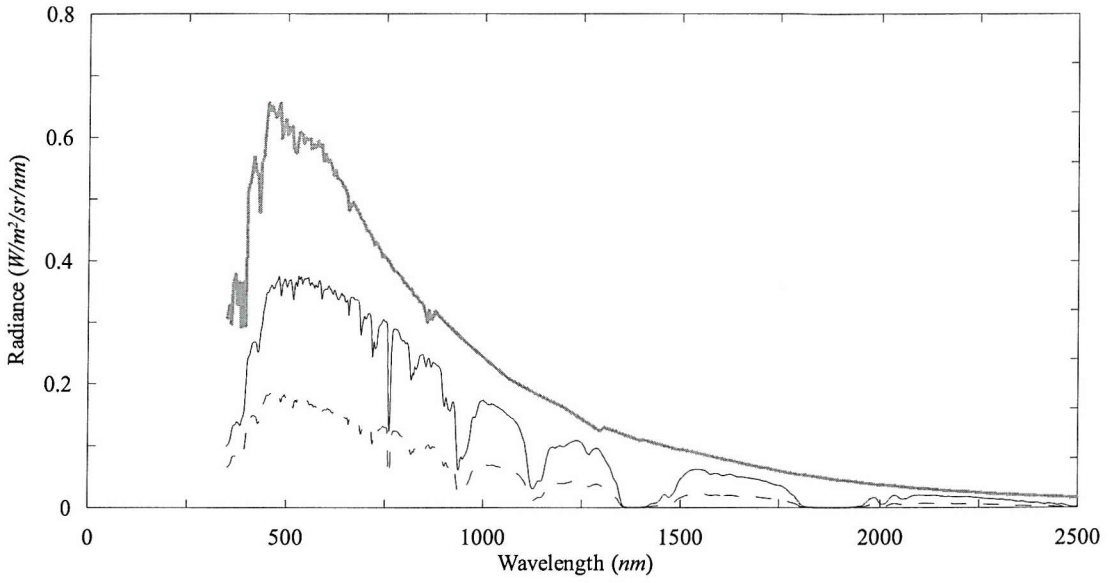

Figure 7-6. A plot of typical spectra of incident solar radiance under sunlit (solid line) and shadows (dotted line). The data were taken on 16 September 1998. The grey line is the radiance at the top of atmosphere calculated from 6S (Vermote *et al.*, 1997) on the same date as the others.

In the two-dimensional feature space, the radiation changes in each SSB follow a line directed near to the origin. Figure 7-7 shows typical examples of scatter plots for each target in 640 *nm* (red; *x*-axis) and 800 *nm* (NIR; *y*-axis). The linear regressions on the data have r^2 value of greater than 0.9, and the ranges of 95% confident limits are fairly narrow. It is important to notice that no intercepts of the regression analysis pass exactly through the origin. The slope and intercept values seem to be different even amongst individual SSBs of the same target. Further tests of this phenomenon will be performed later in this chapter.

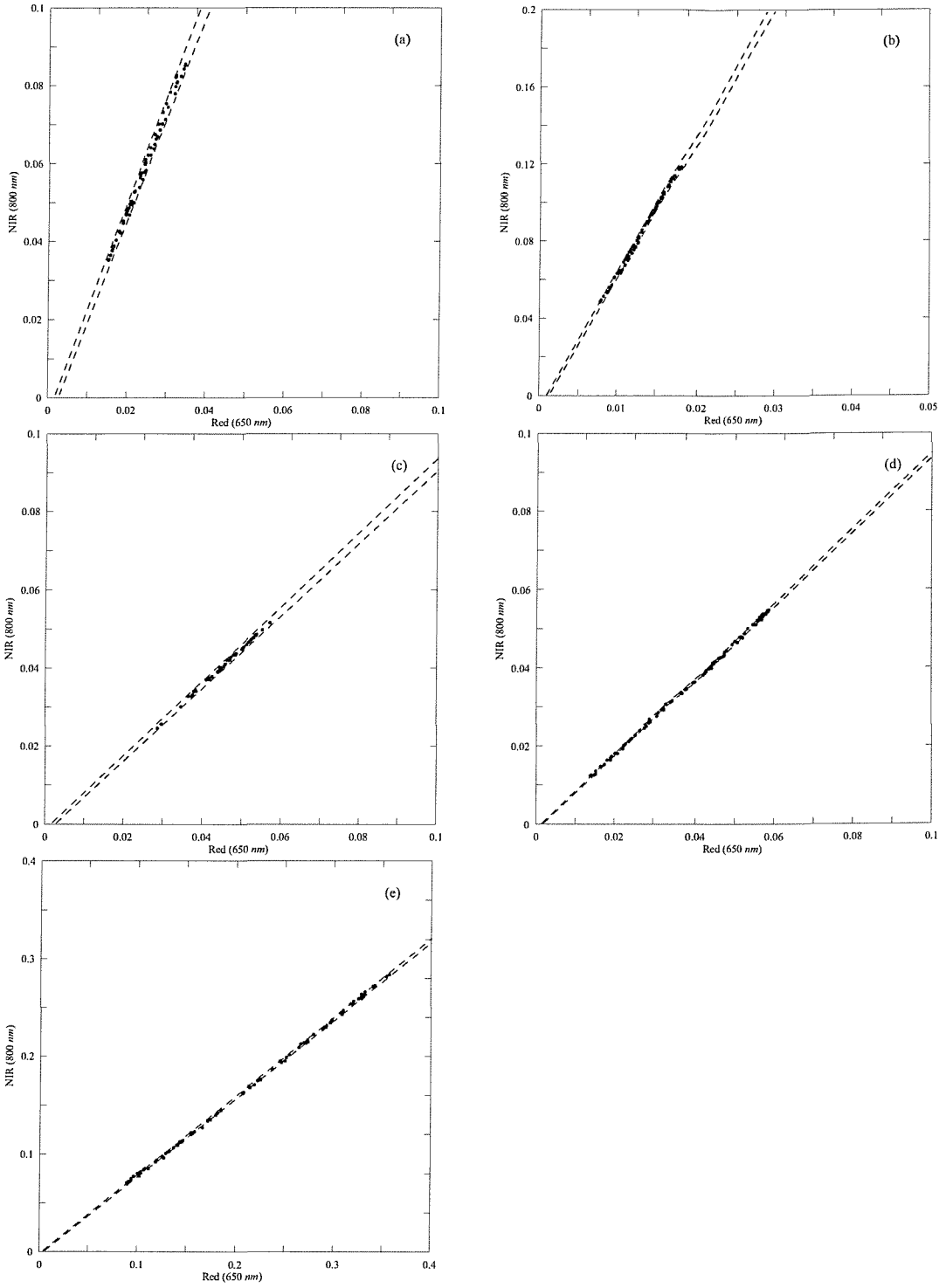

Figure 7-7. Plots of the ASD data measured from the targets of grass (a), dried grass (b), asphalt (c), concrete (d), and reflectance panel (e). Two wavebands were selected; 650 and 800 *nm* as *x*- and *y*-axis in the plots, respectively. The black dots represent the ASD data from the files of SSBs. Two dotted lines in each plot shows the 95% confidence range from its linear regression.

7.3. Slope and intercept of linear regression

Linear regression was applied over wavebands measured by the ASD, and it was in the form of,

$$Y = aX + b \qquad [7.2]$$

where, Y Dependent variable; Arbitrary waveband from ASD
X Independent variable; a waveband from ASD that is always greater wavelength than that of Y.
a Slope
b Intercept

For the purpose of this analysis, the waveband 1600 *nm* was used as the dependent variable Y, while the spectral signal in wavelengths shorter than 1600 *nm* was treated as the independent variable X. The reason for choosing 1600 *nm* as the reference wavelength that was relatively unaffected by atmospheric absorption/scattering, yet its radiometric signal was sufficiently large to provide a reasonable signal-to-noise ratio. For wavelengths greater than 1600 *nm*, x-axis was fixed as the reference waveband, while the y-axis was changed. Two ranges of wavelengths were not considered in the calculation: 1300~1500 and 1800~2000 *nm*, because of the zero signal shown in Figure 7-6.

The spectral variations of the slopes from the linear regression are depicted in Figure 7-8. The most distinctive feature in the plots is that the slope values in the short wavelength region increase exponentially depending upon the ground target, whereas the slopes at longer wavelengths are quite similar, and independent of target type. Since the ranges between 25 and 75% quartiles in each plot are narrow, the slopes for the different targets are thought to be dependent on target, e.g. large slopes at shorter wavelength region for grass and dried grass. Two peaks from water absorptions at around 900 and 1150 *nm* (Figure 7-6) appear in all of the plots, there are also fluctuations around 2500 *nm* due to instrument error.

The intercept is another coefficient determined with a linear regression function. It determines the dependent variable Y when the independent variable X equals zero. The intercept in the ASD measurements under SSB means the smallest value in the wavelength of Y-axis, as the radiance in X-axis becomes zero (see Section 7.5). In ideal world, the linear regression

functions over radiance decrease due to shadows are expected to have zero intercept, i.e. the ratio of reflected radiance energy under sunlit to shadow is to be expressed by that of direct solar radiances. This is true because the radiance energy becomes zero under complete darkness.

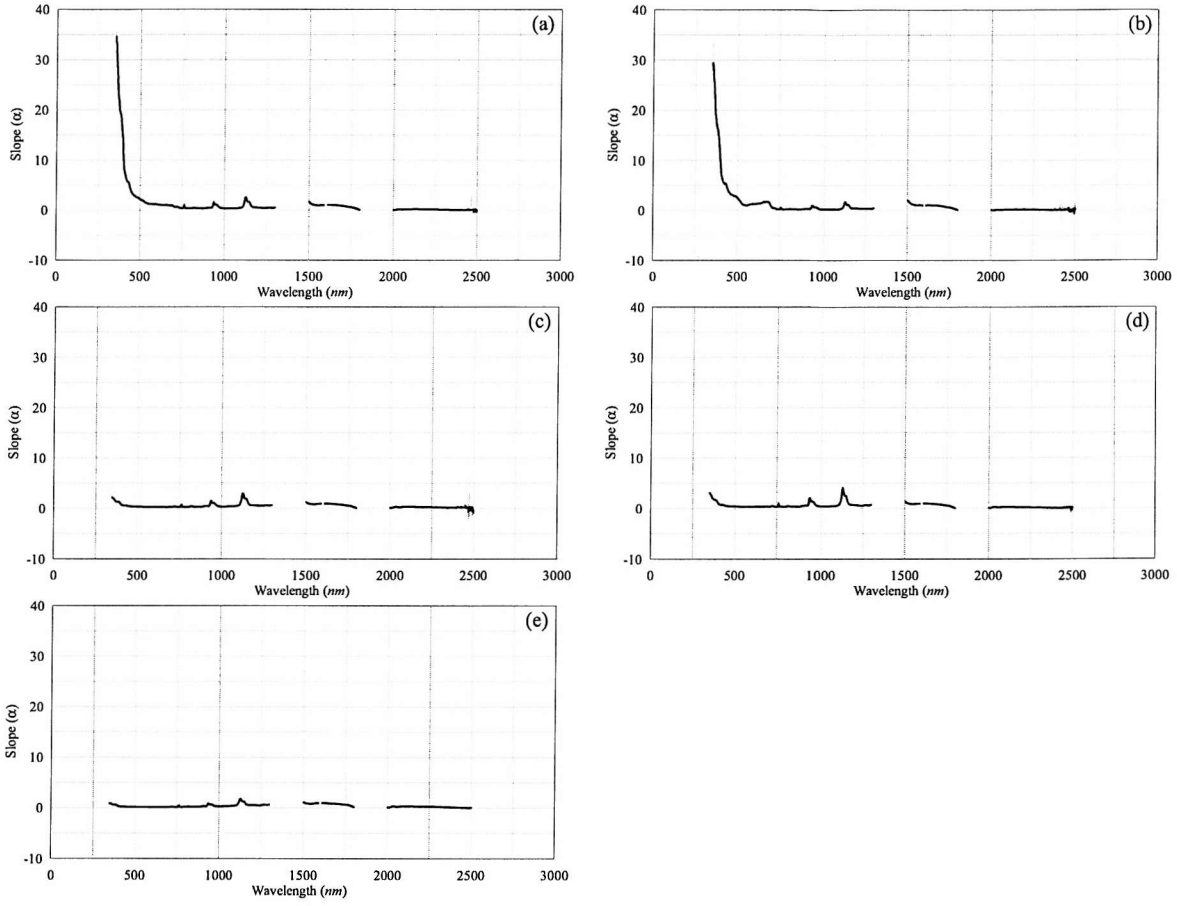

Figure 7-8. Plots of slope from linear regression of data record reference at 1600 *nm* measured in the targets of grass (a), dried grass (b), asphalt (c), concrete (d), and reflectance panel (e).

The plots in Figure 7-9 illustrate that the intercepts from the linear regressions move away from the origin as the wavelength decreases. The intercepts tend to decrease exponentially, although the gradient of the exponential curves vary depending on the type of ground target. Such relationships are shown in all targets though the magnitudes vary. The intercept values are so small that this spectral change may look like a function of slope increase, but they have different spectral characteristics as their exponential gradients are not the same. Although there are signs of atmospheric water absorption at around 1000 *nm*, there is an obvious relationship between the intercept and wavelength. The lowest negative intercept value is at start wavelengths but this increases gradually through to the longer wavelength region.

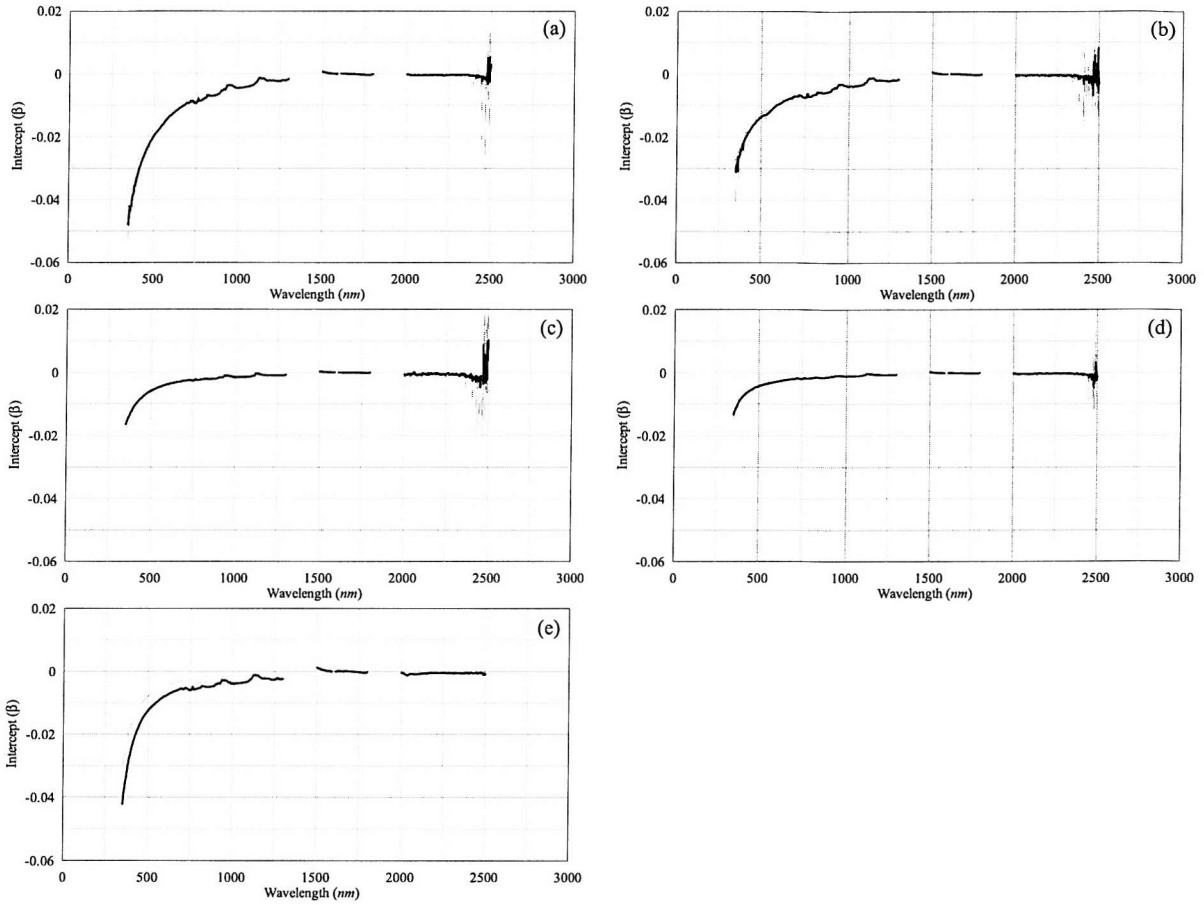

Figure 7-9. Plots of intercept from linear regression of data measured in the targets of grass (a), dried grass (b), asphalt (c), concrete (d), and reflectance panel (e), respectively. The annotations are the same as shown in Figure 7-12.

7.4. Linearity test

The quality of linear regression lines is investigated using the coefficient of determination, symbolised by r^2 (Figure 7-10). The r^2 values for wavelengths below 2000 *nm* show consistent values very close to 1, indicating that the linear regression lines represent radiance change under shadows. Since the r^2 for wavelengths below 2000 *nm* is generally greater than 0.98, more than 98 % of the variation of Y is explained by the variation of X. The decrease of the r^2 at wavelengths greater than 2000 *nm* tends to have different shapes depending on the targets. The reason for this would be due to low radiance value at the wavelength region or due to low SNR (i.e. the variations of radiance under SSB are subject to the instrument error). The curve for the incident radiance (e) is relatively smooth because the radiance values are higher than for the other surfaces.

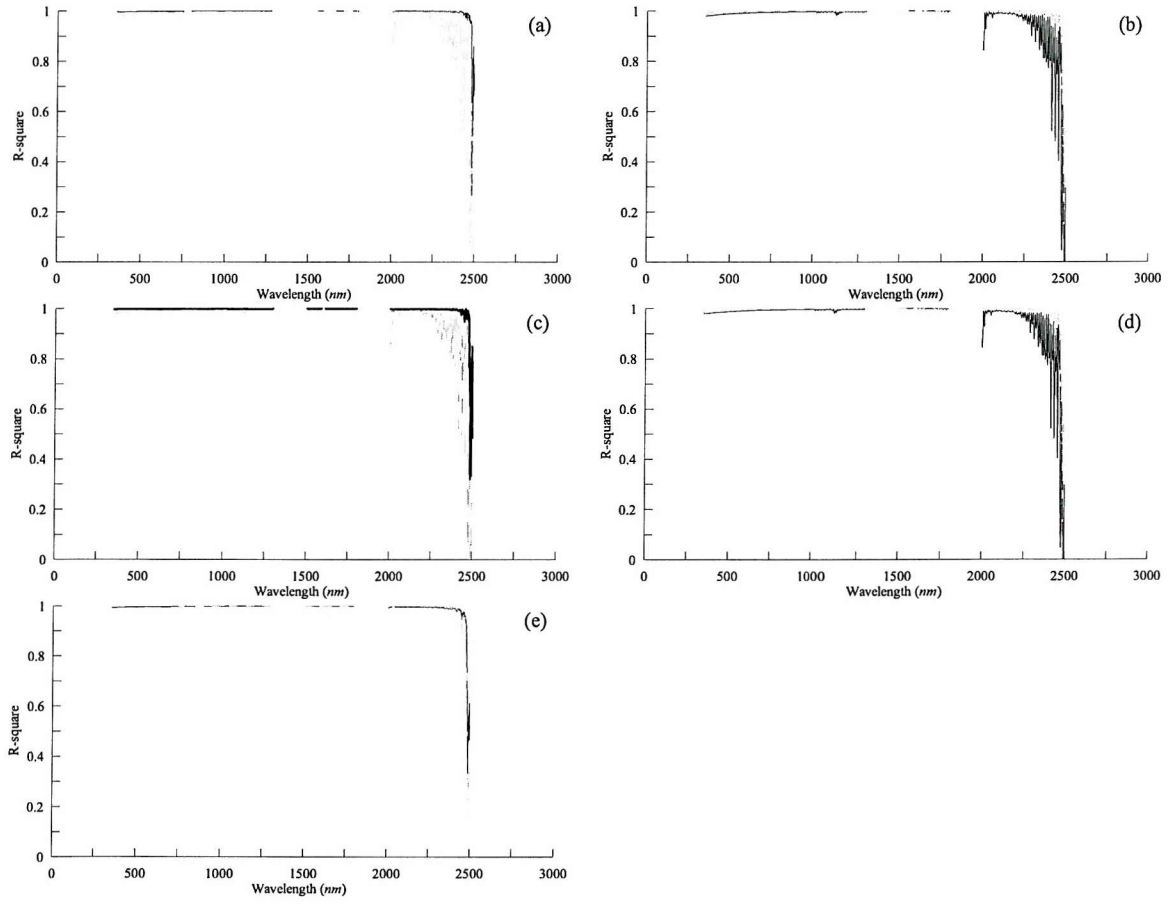

Figure 7-10. Plots of r^2 from the linear regression of data measured in the targets of grass (a), dried grass (b), asphalt (c), concrete (d), and reflectance panel (e). The annotations are the same as shown in Figure 7-12.

Although the coefficient of the r^2 shows that the SSB data are explained very well by the linear relationship, extended statistical analysis is necessary. A further test will involve the form of the relationship of data cloud in two-dimensional feature space to test the extent to which it has a curvilinear shape. Previous studies have shown that the radiation interaction between vegetation and background soil is possibly a cause of nonlinear mixing in spectral feature space (Law *et al.*, 1994; Ray and Murray, 1996).

A simple examination using r^2 values: the change in r^2 values from linear and polynomial regression gives an idea of whether increasing polynomial order contributes more accurate prediction. The computation reveals that there is little increase, < 0.01, on r^2 using a second-order polynomial equation. Since the r^2 from linear regression is already close to 1, the r^2 anomaly analysis does not resolve the comparison between linear and higher-order regression.

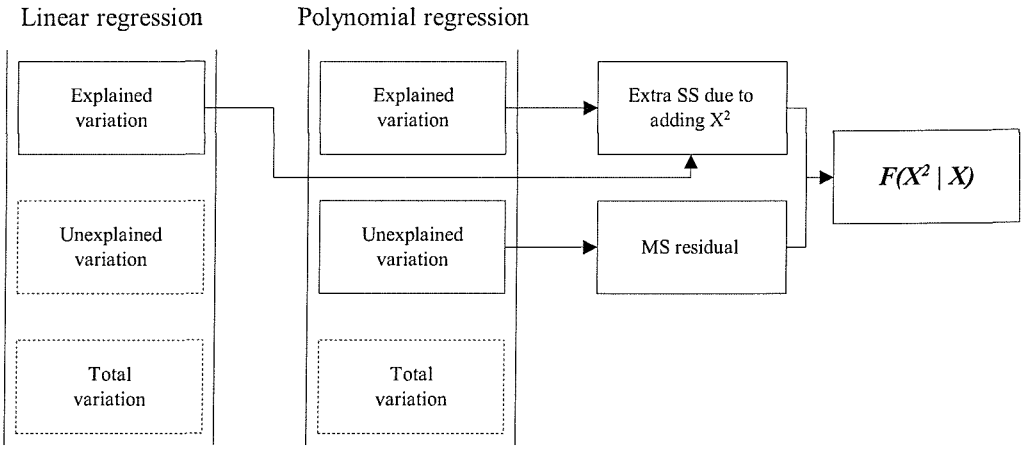

Figure 7-11 A schematic diagram of the linearity test (linear and secondary polynomial regression) using *ANOVA* (Kleinbaum *et al.*, 1998).

The other statistical test for the linearity follows the method described in Kleinbaum *et al.* (1998) (see Figure 7-11). It basically compares the analysis of variance (*ANOVA*) from both linear and polynomial regression lines. Each *ANOVA* from the regressions partitions express explained and unexplained variations. The differences between the predicted independent value Y and its original Y are determined by the sum of squares (*SS*) from both sources of variation. The explained variation presents the portion of *SS* that can be predicted by the regression equation, while the unexplained variation is the residual variation that it is still not able to explain after the regression analysis. The explained mean square (*MS*) is based on one degree of

freedom (*df*), and consequently *df* of *n-2* remains for the residual *MS*. The significance test, *F*, is the ratio of explained to unexplained *MS*, and describes the statistically significant portion of the variation of *Y* as explained by regression on *X*.

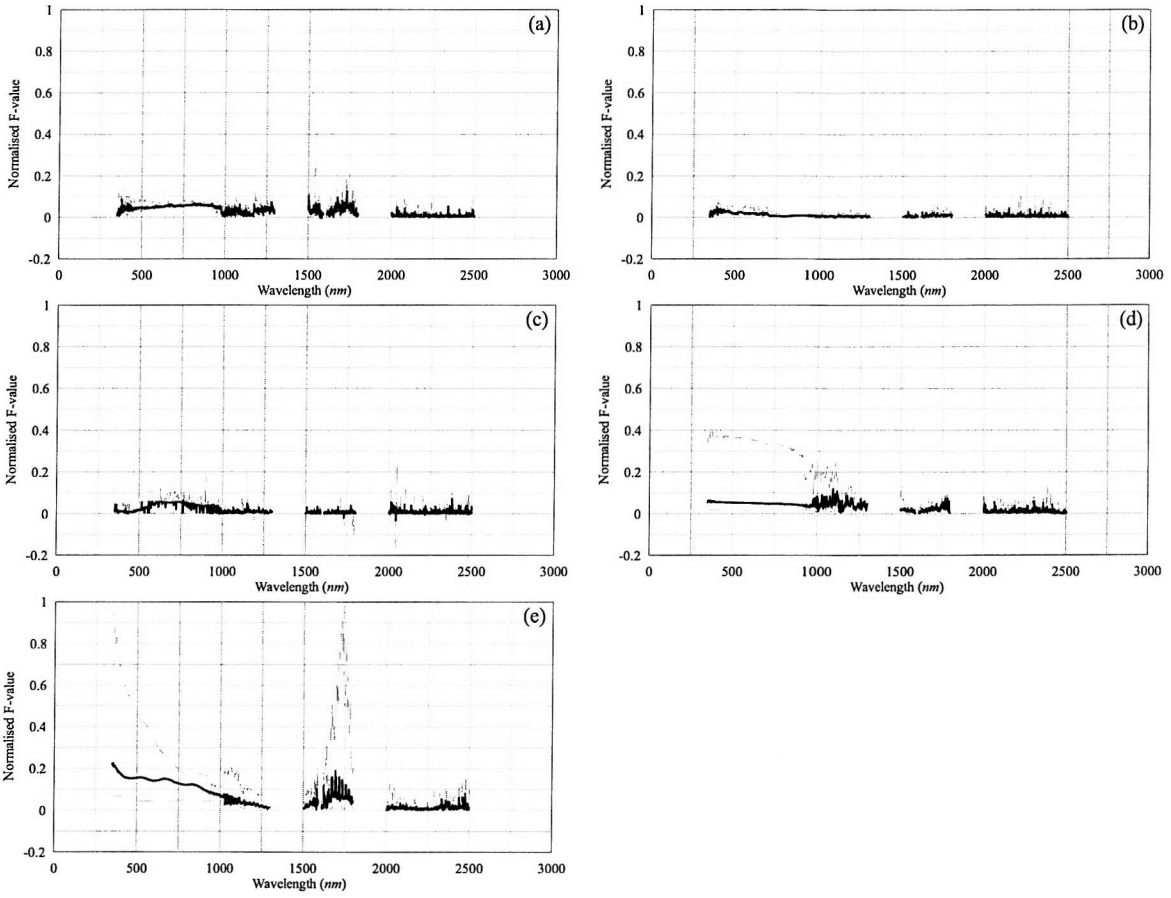

Figure 7-12. Plots of normalized F-value measured in the targets of grass (a), dried grass (b), asphalt (c), concrete (d), and reflectance panel (e). The dark solid line in each plot represents median and lower and upper grey lines are 25 and 75% quartiles.

There are two regressions to be compared to each other; one is a straight line and the other is second-order polynomial line that adds X^2 to the former. Since the latter is generally expected to give more accurate prediction, the added *SS* on top of the linear regression is compared to the residual *MS* from the secondary polynomials. Thus it tests whether the regression after including an extra term X^2 is statistically more significant than the simpler form of regression. In order to explain about increased predictive power, the null hypothesis, H_0, is performed for a partial *F* test, i.e. the addition of the X^2 term to the straight-line model does not significantly contribute more accurate prediction of *Y* over and above that achieved by the straight-line model itself. The layout of the method is outlined in Figure 7-11.

The method for the linearity test was applied to the ASD data from SSB. Since the different number of measurements in each SSB means different *df*, the critical F-values for the hypothesis test, that is a function of *df* and probability of occurrence, vary so that comparison of the results is complicated. In order to normalize them, the F value, here with probability of 0.01%, divides the corresponding critical values of F. Hence when the ratio is greater than one, the *F* value is larger than its critical and the null hypothesis is rejected.

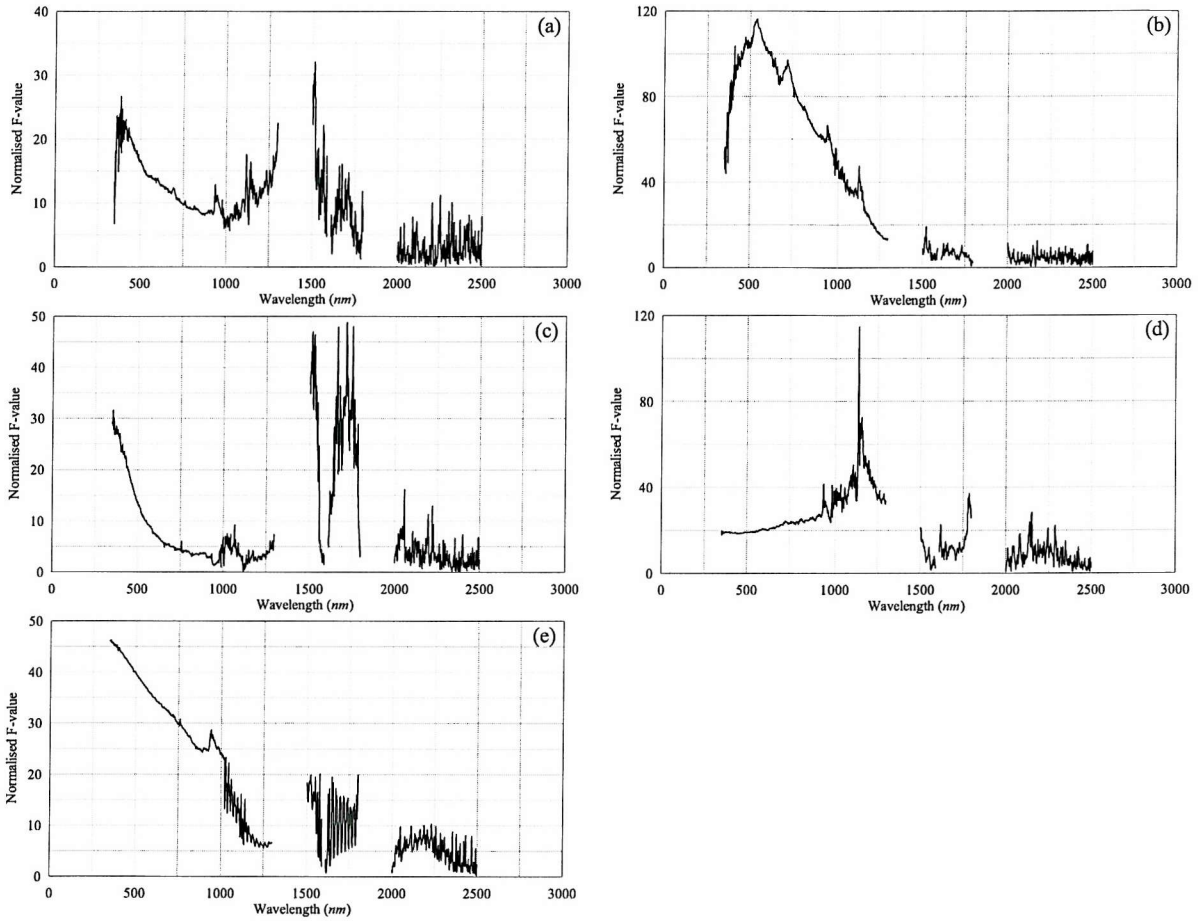

Figure 7-13. Plots of normalized *F*-values of linear regression of data measured in the targets of grass (a), dried grass (b), asphalt (c), concrete (d), and reflectance panel (e). The annotations are the same as shown in Figure 7-12.

The normalized *F*-values are shown in Figure 7-12. As shown in the previous plots, 25 and 75 % quartiles of the normalized F-values, in dotted grey lines, show the variations of normalized F-values with respect to their median. Regardless of the trend in the plot, an important factor is whether the normalized F-values are less than 1. In all targets, normalized F-

values over wavelength covered by the ASD show that the linear regression explains the radiance changes under SSBs sufficiently in two-dimensional space. The F-values at lower wavelengths are normally greater than those in the rest of the wavelength region. The variations of the normalized F-values within SSBs are larger for the concrete target and for the incident solar radiation. However, they are still less than the critical F-value, i.e. regardless of types of clouds and different targets, illumination changes due to shadows are linear in any wavelength. Such differences and variations may be mainly caused by frequent changes of clouds in shape and position.

Statistical analysis shows that there is a linear relationship in SSBs between wavebands. Deviations of data points from the linear line are very small, and there is no sign of spectral patterns (Figure 7-12). Since each SSB condition is assumed to have different distributions and types of clouds, it is interesting to find that different sky conditions yield different linear relationships between wavebands. In order to test more than one regression line from SSBs of each target for the slope consistency, a method for comparing regression lines was adopted from an analysis of covariance (*ANCOVA*) (Sokal and Rohlf, 1995). Quality test of more than a single regression coefficient (i.e. slopes of linear lines), a *SS* of a group of regression coefficients is required from a mean of the slope values. A sum of unexplained *SS* is used to derive a weighted average of unexplained *MS* – because each group of SSB has a different amount of data. As introduced earlier, explained *MS* divided by unexplained *MS* defines the *F* value.

As linear regression analysis was applied to the entire spectral bandset of the ASD, the results of this statistical test have the same spectral resolutions. Again, normalized F values are defined in order to compare homogeneity of regression slopes for different targets. The results show that normalized F values in most of the waveband are greater than 1 (Figure 7-13). Although some are less than 1 in the wavelength greater than 2000 *nm*, these are likely to be due to instrument error or low radiance as shown in Figure 7-8 and Figure 7-10. The fact that the normalized F value is greater than 1, indicates heterogeneity among groups of SSB. In other words, the regression lines among groups of SSB for a target are statistically different. Consequently, the measurement of the spectral signature on a ground target is not invariant, and its time scale is less than an order of minutes. The differences may be influenced by different atmospheric conditions and cloud types and heights even for the same target.

7.5. Shadow-line model in 2D feature space

From the earlier field experiments it was found that linear regression explained the behaviour of data clouds in feature space, collected under radiation changes due to variable aerosol density in the atmosphere. A single linear relationship (i.e. slope and intercept values) from one SSB was statistically different from the others even for the same ground targets. It was suggested that varying factors of these modifications would be mainly due to temporal variations of atmospheric conditions.

In this section, a linear model is developed on the basis of radiative transfer (RT) equations. The model will be used both to give an insight into the properties of the data clouds (i.e. following linear regression) from empirical analysis and to estimate the significance of atmospheric effects in spectral feature space.

A similar attempt to determine atmospheric radiation and transmittance was made using scene shadows, as a spatial variation of illumination condition (Piech and Walker, 1974; featured in Slater, 1980). With an assumption that a secondary scattering induced by adjacent effect is ignored (i.e. the spherical albedo is believed to be much smaller than illumination change due to patchy cloud shadows), a combination of two RT equations for sunlit and shadow areas eliminates the apparent ground reflectance and atmospheric transmittance from both equations and leaves a straight line with coefficients of the direct-to-diffuse term. The difference between their study and the present case is that the radiation changes in the time domain rather than in the spatial domain, as the ground target was fixed during the cloud shadow passing.

A pair of total radiance under sunlit (○) and shadow (●) areas is defined in Equation [7.3]. The radiance detected by the radiometer is a sum of the reflected irradiance with atmospheric transmittance and atmospheric path radiance.

$$L^{\circ} = \frac{E^{\circ} \cdot \rho \cdot T_v}{\pi} + L_p$$
$$L^{\bullet} = \frac{E^{\bullet} \cdot \rho \cdot T_v}{\pi} + L_p \qquad [7.3]$$

where, L_s and L_d Irradiances due to sunlit and shadow conditions

E° and $E^{\bullet}$	Total incident solar irradiances under sunlit, ○, and shadow, ●
ρ	Reflectance of target
T_v	Atmospheric transmittance from the surface to the sensor
L_p	Atmospheric path radiance

As the ground target and sensor position remain unchanged during illumination changes, the term $\rho T_v/\pi$, is eliminated as shown in Piech and Walker (1974) and the equations become,

$$L^{\bullet} = \frac{E^{\bullet}}{E^{\circ}} L^{\circ} + L_p \left(1 - \frac{E^{\bullet}}{E^{\circ}}\right) \qquad [7.4]$$

As the viewing target is covered by clouds, incoming illumination is decreased by the ratio of incident solar irradiance (direct-to-diffuse) and atmospheric effects; the first and the second terms in Equation [7.3]. With this equation, we distinguish the two wavebands by the subscripts R and N as red and NIR bands, respectively. These terms, however, can be used with any bandset. When rewritten,

$$\begin{aligned} L_r^{\bullet} &= R \cdot L_r^{\circ} + L_{pr}\left(1 - R\right) \\ L_n^{\bullet} &= N \cdot L_n^{\circ} + L_{pn}\left(1 - N\right) \end{aligned} \qquad [7.5]$$

where $R = E_{dr} / E_{sr}$ and $N = E_{dn} / E_{sn}$. The atmospheric path radiance (L_{pr} and L_{pn}) is an additional electromagnetic energy term from other than direct radiation detected at the sensor. Since in the field experiments the distance between the sensor and the target was much smaller than that between the Sun and the target, the atmospheric path radiance is assumed to be zero. Hence the ratio of the illumination changes due to cloud shadows is represented by that of the incident solar radiance.

The shadow effect can be expressed in two-dimensional feature space using Equation [7.5]. It is the simplest case and easily extendable to n dimensions. The illumination change in the feature space is assumed to be linear, and it is expressed as,

$$L_n = aL_r + b \qquad [7.6]$$

In Equation [7.6], a is the slope and the intercept, b, is the offset value of L_n when L_r become zero. The slope is the ratio of the sunlit/shadow difference in two wavebands. When

there are two points, under sunlit and shadow conditions, respectively, they join with the line from Equation [7.6] (Figure 7-14).

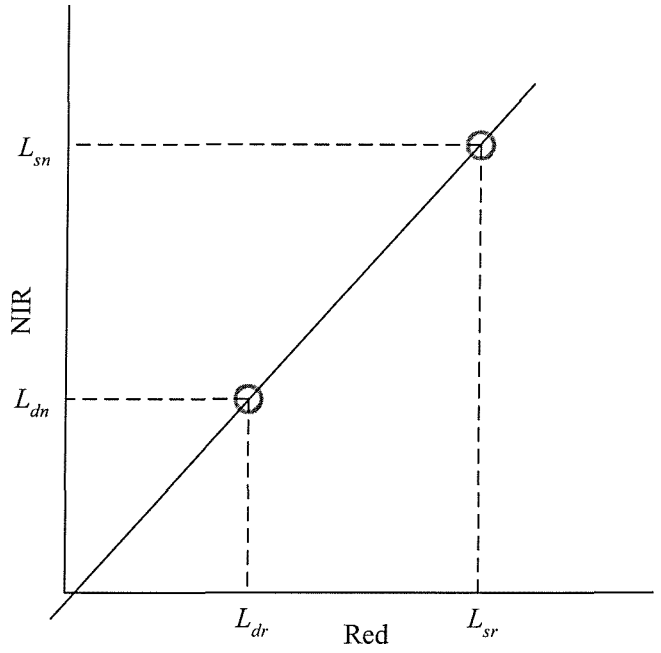

Figure 7-14. A plot of two-dimensional feature space. Two circular points represent the radiometric measurements under sunlit and shadow conditions.

The slope, α, can be rewritten by substituting Equation [7.5],

$$a = \frac{\Delta L_n}{\Delta L_r} = \frac{L_n^{\circ} - L_n^{\bullet}}{L_r^{\circ} - L_r^{\bullet}} = \frac{L_n^{\circ} \cdot (1-N)}{L_r^{\circ} \cdot (1-R)} \qquad [7.7]$$

Thus the slope becomes a function of radiance in two wavebands under sunlight and a ratio of solar irradiance in shadow to that in sunlight. The electromagnetic energy reaching the ground under sunlit and shade areas are,

$$E^{\circ} = E_o \cdot \mu \cdot T_i^{\circ} + E_d^{\circ}$$
$$E^{\bullet} = E_o \cdot \mu \cdot T_i^{\bullet} + E_d^{\bullet} \qquad [7.8]$$

where,
- E_0 Solar flux at the top of the atmosphere
- μ $Cos(\theta_0)$ where θ_0 is the Sun zenith angle
- T_i Atmospheric transmittance from the Sun to the surface
- E_d Diffuse irradiance

Under the shadows, it is understood that diffuse radiation is the only source of light. Thus, direct atmospheric transmittance in shadow, $T_i^{\bullet}$, is assumed to be near zero (Pearce, 1985). The term, $E^{\bullet}/E^{\circ}$, in Equation [7.4] corresponds to the ratio of diffuse to total irradiance if the shadow is dark enough.

From Equation [7.7], the intercept, b, is defined as,

$$b = L_n - \frac{\Delta L_n}{\Delta L_r} L_r \qquad [7.9]$$

If L_r and L_n are replaced with $L_r{}^{\circ}$ and $L_n{}^{\circ}$, b can be rewritten,

$$b = \frac{L_n^{\circ} L_r^{\circ} \cdot (1-R)}{L_r^{\circ} \cdot (1-R)} - \frac{L_r^{\circ} L_n^{\circ} \cdot (1-N)}{L_r^{\circ} \cdot (1-R)} \qquad [7.10]$$

$$b = L_n^{\circ} \left[1 - \frac{(1-N)}{(1-R)} \right] \qquad [7.11]$$

$$b = L_n^{\circ} \cdot \left(\frac{N-R}{1-R} \right) \qquad [7.12]$$

In Equation [7.11] and [7.12], the intercept b is a function of NIR irradiance in sunlight and diffusion ratios in red and NIR wavebands. Since the irradiance $L_n{}^{\circ}$ is non-zero, b can become zero only if the direct-to-diffuse ratios in two different wavebands are equal (also, direct-to-diffuse ratio cannot become one).

The above slope and intercept derived by RS equations correspond to the results shown in the field measurements and are tested in the following sub-sections in terms of various characteristics of the shadow-line. The main investigations will focus on how atmospheric conditions affect the shadow-line, whether illumination changes have linearity in two-waveband space, and whether the regression lines pass through the origin, i.e. $b = 0$.

7.5.1. Attributes of shadow-line with temporal variation of atmospheric conditions

It was observed that the variation of illumination over a ground object follows a narrow linear trend (shadow-line) in spectral feature space. However, the position and angle of the shadow-line varies with type of ground targets and atmospheric conditions. These properties of the shadow-line are also explained by the analytical equations derived earlier.

The theoretical expressions of both slope and intercept of shadow-line (Equations [7.7] and [7.11]) contain the identical relative amount of direct-to-diffuse ratios between two wavebands, $\Re$, defined as,

$$\Re = \frac{1-N}{1-R} \qquad [7.13]$$

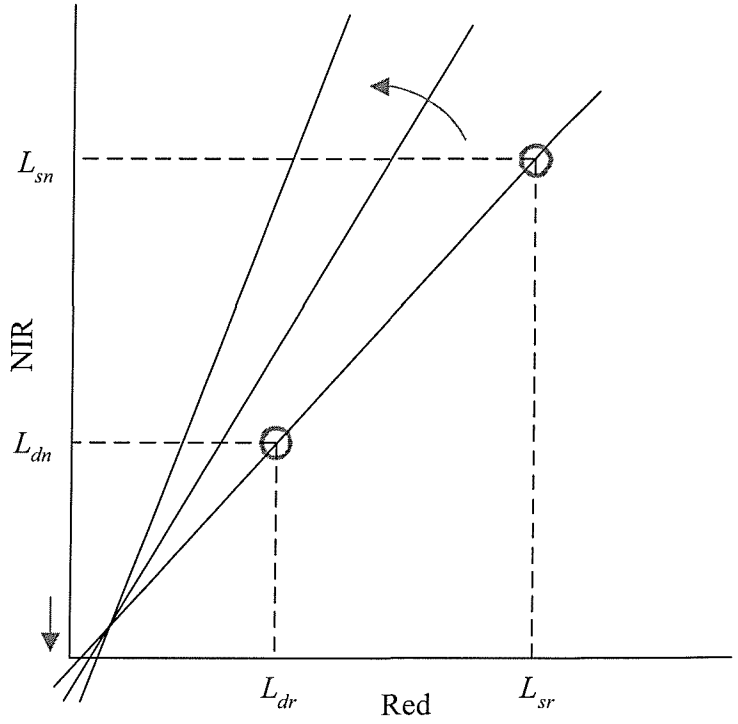

Figure 7-15. A schematic diagram of relationship between slope and intercept of a shadow-line due to the variation of $\Re$.

Since the slope of shadow-line is always positive due to the fact that entire spectrum decreases with a decrease in illumination, i.e. $a > 0$, and that all radiances are positive values, the term $\Re$ should be greater than zero. In addition, the intercept β over a range of wavelengths is less than zero (Figure 7-9). The negative b is obtained by $\Re > 1$ (see Equation [7.11]). If the $\Re$ increases, the slope of the shadow-line increases while the intercept decreases. Figure 7-15 illustrates the relationship between the slope and the intercept of shadow-line due to variations of $\Re$. From the field data acquired under patches of cloud shadows, the inverse relation between the slope and the intercept is shown in Figure 7-16. Equation [7.14] below is derived by a combination of slope (Equation [7.7]) and intercept (Equation [7.11]).

$$b = -L_r^{\circ} \cdot a + L_n^{\circ} \qquad [7.14]$$

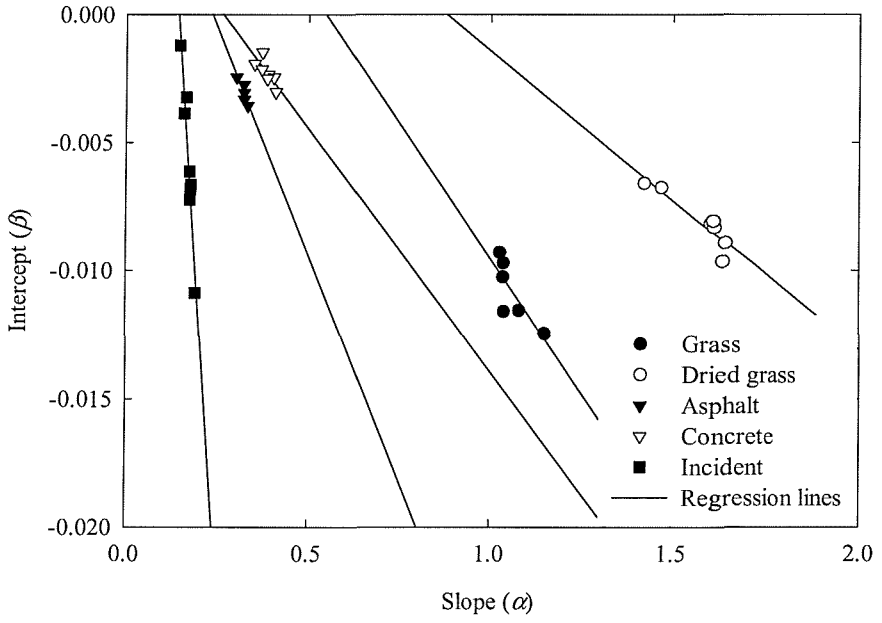

Figure 7-16. Plots of intercept values against their slope. A single SSB from each target is selected.

The radiance measurements under SSBs are influenced by several atmospheric effects. The main atmospheric effects on the series of ASD measurements are the atmospheric transmittance in terms of cloud shadows and scattering and absorption by aerosols in clouds and/or through the Earth's atmosphere. Thus the ratios of direct-to-diffuse, R and N, consist of two atmospheric terms: incident atmospheric transmittance between the Sun and the ground

target, T_i, and downwelling diffused radiance, E_d. (see Equation [7.8]). If substituted into Equation [7.13], Equation [7.8] can be rewritten $\Re$,

$$\Re = \frac{\left(\frac{E_{on}\mu\left(T_{in}^{\circ} - T_{in}^{\bullet}\right)}{E_{on}\mu T_{in}^{\circ} + E_{dn}}\right)}{\left(\frac{E_{or}\mu\left(T_{ir}^{\circ} - T_{ir}^{\bullet}\right)}{E_{or}\mu T_{ir}^{\circ} + E_{dr}}\right)} = \frac{\left(\frac{T_{in}^{\circ} - T_{in}^{\bullet}}{T_{in}^{\circ} + E_{dn}/E_{on}\mu}\right)}{\left(\frac{T_{ir}^{\circ} - T_{ir}^{\bullet}}{T_{ir}^{\circ} + E_{dr}/E_{or}\mu}\right)} \qquad [7.15]$$

where $E_n^{\circ} = E_{0n}\mu T_{in}^{\circ} + E_{dn}$, $E_n^{\bullet} = E_{0n}\mu T_{in}^{\bullet} + E_{dn}$, $E_r^{\circ} = E_{0r}\mu T_{ir}^{\circ} + E_{dr}$, *and* $E_r^{\bullet} = E_{0r}\mu T_{ir}^{\bullet} + E_{dr}$. It is important to notice that the diffuse radiance in a certain wavelength is the same under sunlit and shadow. When clouds are dark enough to obstruct direct solar incident radiance, the atmospheric transmittance, $T_{in}^{\bullet}$, and $T_{ir}^{\bullet}$, is assumed to be near zero. Hence atmospheric transmittance and diffuse radiance determine the value $\Re$.

The seesaw movement of the shadow-line as $\Re$ changes is therefore responsible for the statistically different shadow lines in a group of SSBs on a ground target as shown in Section 7.4. This variation is increasingly important when the radiance values in two wavebands, L_r° and L_n°, are similar, i.e. a ground object with relatively uniform spectral signature like asphalt or concrete. However, ranges between 25 and 75% quartile boundaries of the intercept in short wavelength regions are greatest for solar incident radiance and are greater for vegetation than for artificial targets (Figure 7-9). This may be directly related to the temporal variation of atmospheric conditions during the field data acquisition. Time series plots of the field experiments show that patches of clouds appeared most frequently during the measurements of solar radiance (Figure 7-5e) and conditions were comparably stable during measurements of asphalt and concrete targets (Figure 7-5c and d). Consequently, shadow-line changes are dominant in the atmospheric conditions, but the term $\Re$ is not the only factor that contributes to the shadow-line.

Without atmospheric scattering (i.e. diffuse radiance), it is expected that the intercept value becomes zero, i.e. the shadow-line would pass through the origin as $\Re = 1$. In other words, we consider that $\Re = 1$ if E_{dn} and E_{dr} equal zero in Equation [7.15]. This is often acquired under controlled environment such as in the laboratory. Figure 7-17 is a typical

example of various illuminations in spectral feature space. With statistical confidence, a straight line through the data points passes through the origin, i.e. the intercept equals zero.

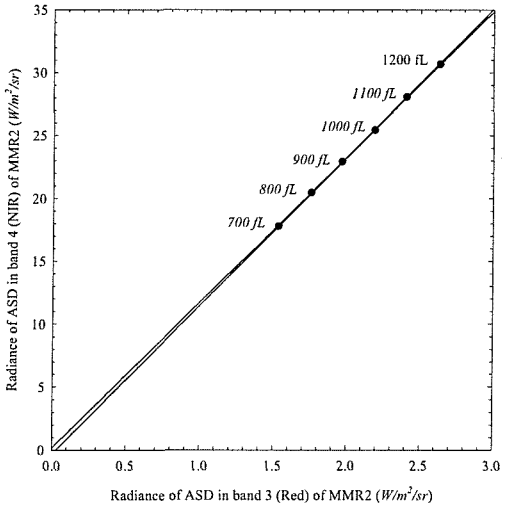

Figure 7-17. A plot of the ASD measurements in the laboratory (29 September 2000). The light source used was an integrating sphere manufactured by Hoffman Engineering™. 6 steps of the brightness were set from 700 to 1200 *fL*. The ASD data were integrated. The upper and lower confidence lines (95%) are depicted from regression analysis.

Although the assumption that there is no diffuse radiance from the atmosphere eliminates the intercept coefficient of the shadow-line, the slope term is explained in a different manner. The slope, a, is a ratio of two reflected radiances in different wavebands (Equation [7.7]). If Equation [7.3] and [7.8] are substituted into the slope equation, a becomes,

$$a = \frac{L_n^{\circ} - L_n^{\bullet}}{L_r^{\circ} - L_r^{\bullet}} = \frac{\rho_n E_{on}\left(T_{in}^{\circ} - T_{in}^{\bullet}\right)}{\rho_r E_{or}\left(T_{ir}^{\circ} - T_{ir}^{\bullet}\right)} \qquad [7.16]$$

The atmospheric transmittances, $T_{in}^{\bullet}$, and $T_{ir}^{\bullet}$, are again ignored ($\sim$ 0) if under complete shadow. If the slope value changed during the field experiments, it is either because of different ground target (reflectance, ρ_n and ρ_r) or because of the temporal variation of atmospheric transmittance. The solar irradiances at top of the atmosphere, E_{on}, and E_{or}, are assumed to remain the same, since each session of measurement was too short to be affected by Sun angle changes.

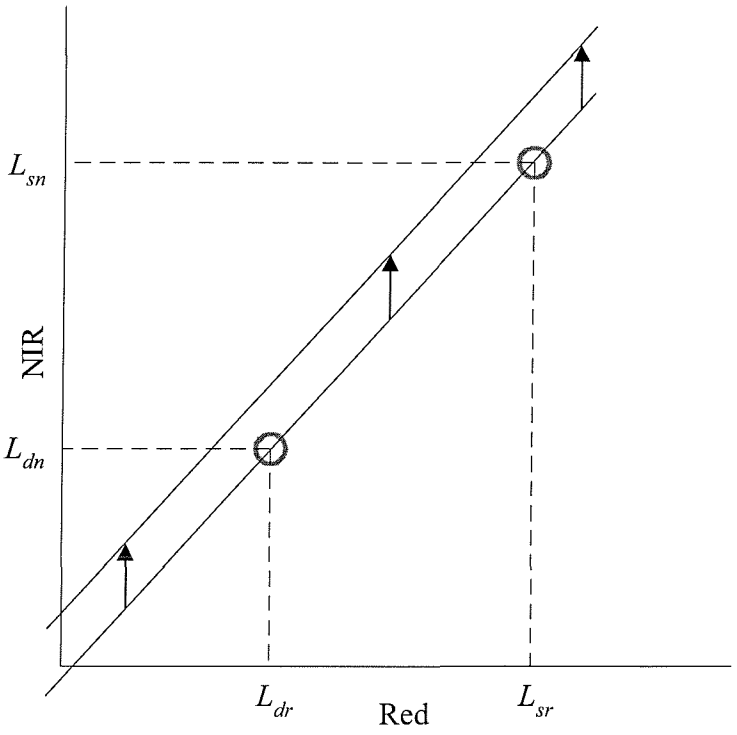

Figure 7-18. A schematic diagram of shadow-line changes due to temporal variation of diffuse irradiance.

Figure 7-18 shows the changes of shadow-line due to the effect of diffuse radiance. If atmospheric transmittance remains the same, the temporal variation of diffuse radiance causes only intercept changes with the fixed slope, i.e. only up-down movement of the shadow-line in the spectral feature space. These explain the relatively smaller variations of the slope value (Figure 7-8) than those of the corresponding intercept in the short wavelength region (Figure 7-9). Also, the variable ranges of 25 and 75% quartile boundaries of the intercept over different ground targets are determined by the magnitude of diffuse radiance which is directly related to atmospheric turbidity.

As a conclusion, the shadow-line in spectral feature space changes due to temporal variations of atmospheric conditions. Of these, the magnitude of diffuse radiance contributes only to the intercept of shadow-line, whereas atmospheric transmittance affects both the slope and the intercept.

7.5.2. Nonlinearity of the shadow-line

Theoretically, nonlinearity in spectral feature space is mainly induced either by interactions between subpixel elements (Law *et al.*, 1994; Ray and Murray, 1996) or by addition of radiation from surrounding targets (Tanré *et al.*, 1987; Zagolski and Gastellu-Etchegorry, 1995; Vermote, *et al.*, 1997). The former was ignored during the statistical linearity test due to the nature of the ground targets used for the field experiment (see Section 7.4), the latter, known as adjacency effects or secondary scattering, is investigated in this section.

In RT models, such as 6S, the adjacency effect term becomes more important when the surface reflectance is not uniform. A secondary scattered flux consists of the trapping mechanism, and is related to the successive reflections and scattering between the surface and the atmosphere. The total radiance detected by the sensor is rewritten below from Equation [7.3] with secondary scattering,

$$L = \frac{E_s \cdot \rho_c \cdot T_v}{\pi \cdot (1 - s \cdot \rho_e)} + L_p \qquad [7.17]$$

where,

L	Radiance detected by the sensor
E_s	Total incident solar irradiances
s	Spherical albedo
ρ_c	Reflectance of target
ρ_e	Reflectance of adjacent target
T_v	Atmospheric transmittance from the surface to the sensor
L_p	Atmospheric path radiance

The atmospheric path radiance, L_p, is assumed to be ~0. When the radiance equation in Equation [7.17] is applied to the slope coefficient in Equation [7.7],

$$a = \frac{\Delta L_n}{\Delta L_r} = \frac{L_n^{\circ} \cdot \left\{ 1 - N \cdot \left(\frac{1 - s_n^{\circ} \cdot \rho_{en}}{1 - s_n^{\bullet} \cdot \rho_{en}} \right) \right\}}{L_r^{\circ} \cdot \left\{ 1 - R \cdot \left(\frac{1 - s_r^{\circ} \cdot \rho_{er}}{1 - s_r^{\bullet} \cdot \rho_{er}} \right) \right\}} \qquad [7.18]$$

Spherical albedo (s) is a function of the optical thickness of the atmosphere, noted as τ, (Vermote *et al.*, 1997). Since there is a second-order relationship between τ and s, it affects the

slope coefficient in Equation [7.18]. The slope coefficients with secondary scattering are simulated with typical radiative conditions. Optical thickness, τ, varies from 0.1 to 0.9, equivalent to atmospheric transmittance of around 0.4 to 0.9, while all the other variables are invariant, i.e. $L_n^{\circ} = 0.60$, $L_r^{\circ} = 0.57$, $\rho_{en} = 0.50$, and $\rho_{er} = 0.30$. The slopes calculated from the variables are illustrated in Figure 7-19. The slopes without spherical albedo are, as expected with the given conditions, constant through various transmittance in terms of darkness of shadows.

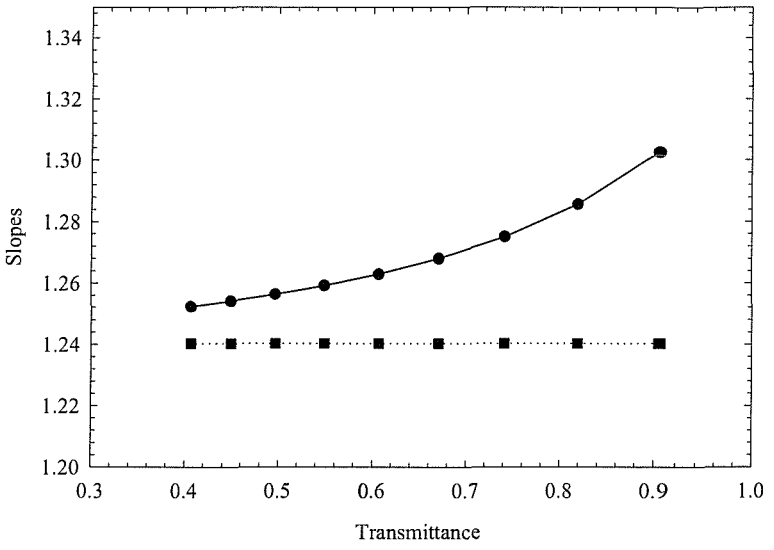

Figure 7-19. A plot of the slope changes with atmospheric transmittance. The slope increases as the effect of the spherical albedo increases (•), while it is invariant without adjacency effect (■).

On the other hand, adding a term for spherical albedo produces slope changes in second-order polynomial curves. As a result, the radiance changes with increasing or decreasing illumination tend to have curved shapes within two-dimensional spectral feature space as shown especially in the lower wavelength region. However, such non-linearity occurs in only a few cases of SSBs, this suggests that the adjacency effect is very small, compared to the shadow illumination changes and can be ignored. In addition, when one considers multiple scattering (i.e. the target reflected radiation scattered underneath clouds and back to the target), the estimation would be more complicated due to irregular formations of clouds. These non-linearity factors, however, do not seem to affect the data used in this chapter. It implies that such effects might be ignored in the further studies.

7.6. Dark Point Virtual Endmember (DPVE)

The previous sections were devoted to investigating characteristics of a single shadow-line. The position of a shadow-line in spectral feature space is determined by the target reflectance and atmospheric conditions. Shadow-line analyses in the time domain on the ground, however, cannot be extended to the spatial domain unless more than one instrument is employed simultaneously. A remotely sensed image is a snapshot of scene that often contains several shadow-lines that are due to topography and/or non-uniform distributions of atmospheric constituents, such as clouds. It is hypothesised that the shadow-lines in a scene would have a pattern in spectral feature space and that more information could be retrieved from them.

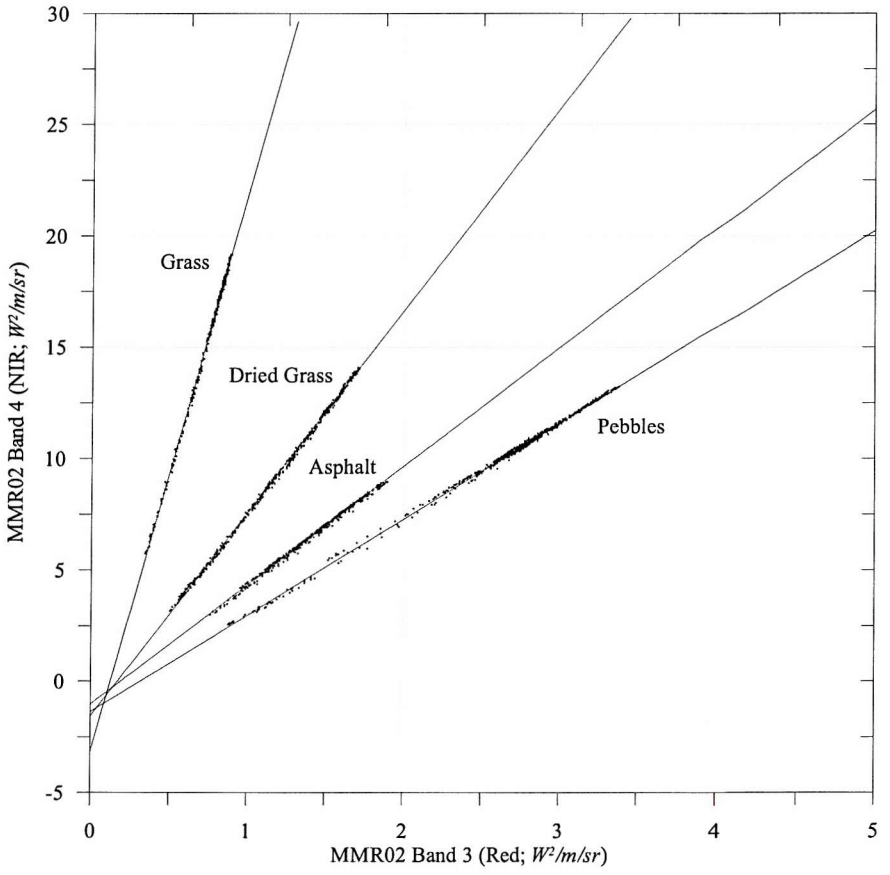

Figure 7-20. Shadow-lines of data acquired by 4-channel radiometer (MMR)[††] during the field experiments.

[††] MMR was used for this experiment only because ASD was not available.

All shadow-lines pass close to the origin, and their intercepts alter with variations of atmospheric conditions. The point where more than two different shadow-lines converge is defined as the dark point virtual endmember (DPVE) for the data set. It is important to note that the DPVE identified in this way is 'darker' than any of the data points present in the scene. It is closer in concept to a virtual endmember as described by Tompkins *et al.* (1997) or to the 'point of all shadow' (Kauth and Thomas, 1976) than to a dark object present in the scene. Figure 7-20 shows the shadow-lines acquired during field measurements on different dates, pass close to the origin.

7.6.1. A pair of shadow-lines

The position of the DPVE, (L_r^{dpve}, L_n^{dpve}), in two-dimensional spectral feature space is derived by using two shadow-lines,

$$\begin{aligned} L_n^{dpve} &= a_1 \cdot L_r^{dpve} + b_1 \\ L_n^{dpve} &= a_2 \cdot L_r^{dpve} + b_2 \end{aligned} \qquad [7.19]$$

where,

L_r^{dpve}	DPVE point in x-axis [radiance]
L_n^{dpve}	DPVE point in y-axis [radiance]
a_1, b_1	Shadow-line slope and intercept of the first ground target, respectively
a_2, b_2	The second shadow-line slope and intercept, respectively

The DPVE points from Equation [7.19] are,

$$\begin{aligned} L_r^{dpve} &= -\frac{b_1 - b_2}{a_1 - a_2} \\ L_n^{dpve} &= \frac{a_1 \cdot b_2 - a_2 \cdot b_1}{a_1 - a_2} \end{aligned} \qquad [7.20]$$

The slope (Equation [7.7]) and intercept (Equation [7.11]) of two shadow-lines are substituted into the position of the DPVE, and rewritten Equation [7.20],

$$L_r^{dpve} = \left[\frac{L_{r1}^{\circ} \cdot L_{r2}^{\circ} \cdot \left(L_{n1}^{\circ} - L_{n2}^{\circ}\right)}{L_{r1}^{\circ} \cdot L_{n2}^{\circ} - L_{n1}^{\circ} \cdot L_{r2}^{\circ}}\right] \cdot \left[\frac{1}{\Re} - 1\right]$$
$$L_n^{dpve} = \left[\frac{L_{n1}^{\circ} \cdot L_{n2}^{\circ} \cdot \left(L_{r1}^{\circ} - L_{r2}^{\circ}\right)}{L_{r1}^{\circ} \cdot L_{n2}^{\circ} - L_{n1}^{\circ} \cdot L_{r2}^{\circ}}\right] \cdot [1 - \Re] \qquad [7.21]$$

As two shadow-lines are not identical (i.e. $L_{r1}{}^{\circ} \neq L_{r2}{}^{\circ}$ or $L_{n1}{}^{\circ} \neq L_{n2}{}^{\circ}$), $\Re$ should equal 1 for the DPVE at the origin, meaning that there was no diffuse radiance from the atmosphere.

The RT driven DPVE model was tested with the SSB data from the field measurements. In Figure 7-21, the diffuse ratios, $\Re$, from all possible combinations of the available ground targets with the DPVE model (Equation [7.21]) are compared to those from the slopes and intercepts of each shadow-line (Equation [7.7] and [7.11]). The values of $\Re$ from the first equation, L_r^{dpve}, of the DPVE model show large variations, whereas those in L_n^{dpve} are relatively consistent. Comparably, the $\Re$s from an individual shadow-line are more stable for all targets.

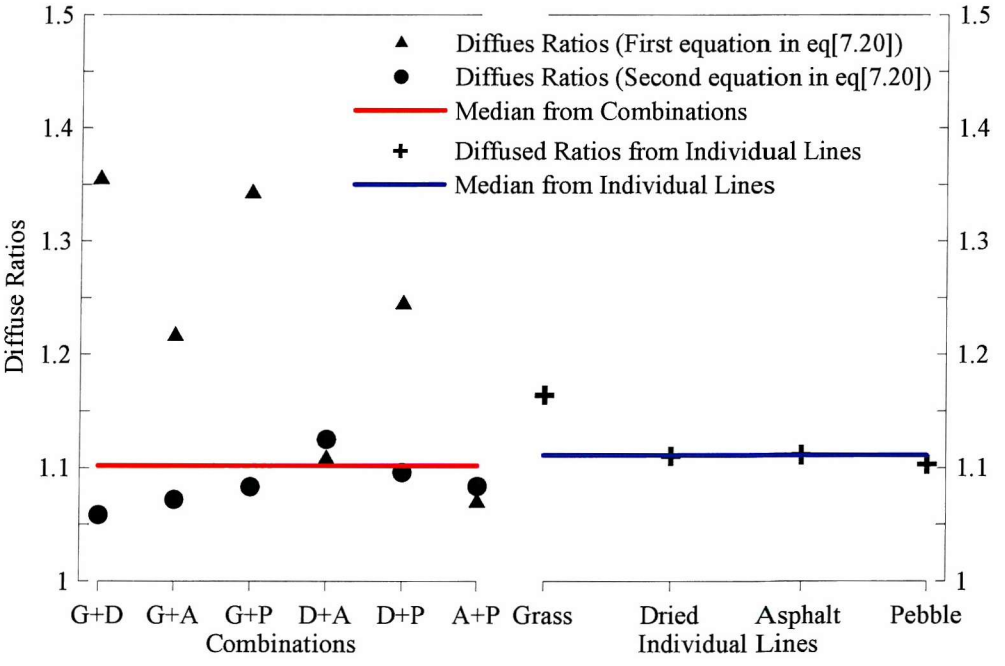

Figure 7-21. Comparisons of $\Re$ from the DPVE models and the shadow-line model by using the SSB measured on the ground. Since the DPVE model requires two shadow-lines, all possible combinations from available targets (G: Grass, D: Dried grass, A: Asphalt, and P: Pebbles) were applied in the left side of the plot. Each symbol in the plot represent $\Re$ from L_r^{dpve} (▲), L_n^{dpve} (●), and each individual shadow-line (✚).

Strictly speaking, the comparison of the $\Re$s between different targets is meaningless, since measurements were carried out under different atmospheric conditions and hence different $\Re$s. Figure 7-21 is nonetheless still important for the performance checks between the models. The $\Re$s from each model are assumed to be represented by the median of the $\Re$ as if all data were obtained simultaneously, under the same atmospheric conditions. The median is appropriate due to the fact that the atmospheric conditions of our samples do not follow standard distributions (i.e. not suitable to use normal distributed). Despite relatively large variations, the median $\Re$ in the DPVE model (red) is close to the one from the individual shadow-line model (blue).

7.6.2. More than two shadow-lines: The SVD

The limitation of the DPVE model developed using the RT equations above is that the formula would become too complicated if more than two shadow-lines were to be used. An alternative approach to find the DPVE from n shadow-lines is to use singular-value decomposition (SVD). The SVD is one of the most common solutions for simultaneous linear equations. In the RS community, the SVD is mainly used for the linear spectral mixing models (e.g. Boardman, 1989). If multiple shadow-line equations for the DPVE are transformed into the matrix equation of $A \cdot x = b$, where A is a matrix of multiple regression coefficient, x is a DPVE of two-dimensional space, and b is a column vector matrix of n number of regression constant,

$$\underset{A}{\begin{bmatrix} 1.0 & -a_1 \\ 1.0 & -a_2 \\ \vdots & \vdots \\ 1.0 & -a_n \end{bmatrix}} \cdot \underset{x}{\begin{bmatrix} L_n^{dpve} \\ L_r^{dpve} \end{bmatrix}} = \underset{b}{\begin{bmatrix} b_1 \\ b_2 \\ \vdots \\ b_n \end{bmatrix}} \qquad [7.22]$$

The matrix A is defined by the SVD as follows,

$$A = U \cdot W \cdot V' \qquad [7.23]$$

where, U The product of an $m \times n$ column-diagonal matrix

W The $n \times n$ singular value array
V' Transpose of an $n \times n$ matrix of orthogonal columns

The column matrix x can then be found by,

$$x = V \cdot W \cdot U' \cdot b \qquad [7.24]$$

The DPVEs derived from the RT driven model (Equation [7.21]) using in total 6 combinations of pairs of ground targets developed in the previous section were compared with the real DPVEs, that is, the point where two shadow-lines converge (Figure 7-22). Although the DPVE positions from both methods are close, the differences might be due to the deviations of the data points from the linear regression line. The DPVE applied with the field data shows that the SVD DPVE is placed quite close to the median DPVE. This indicates that the SVD would be an alternative viable means of finding the DPVE with the advantage that it can cope with any number of shadow-lines extending its usability to the scene data, such as multispectral RS images. The application of the DPVE in a remotely sensed dataset is introduced in Chapter 8.

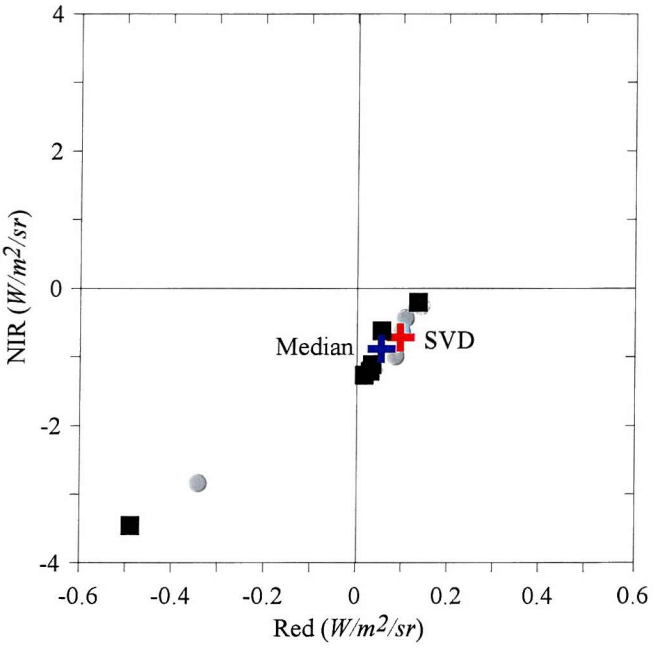

Figure 7-22. The scattering plot of the DVPEs in two-dimensional feature space. The axes scales are not matched. With the all-available combinations of the shadow-line pair, the points with ● represent the real shadow-line cross position, whereas dots with ■ is the results from the DPVE model with a pair of shadow-lines. The median (✚) and the SVD (✚) of modelled DPVEs are also shown.

7.6.3. The DPVE and the atmospheric effects

The existence of the DPVE means that simultaneous shadow-lines in the feature space have identical $\mathcal{T}$s, i.e. the same atmospheric transmittance and diffuse irradiance for the shadow-lines (Section 7.6.1). The mathematical form of the DPVE shows that its position is determined by the magnitude of atmospheric effects and that the convergence point moves toward the origin if there is no aerosol scattering in the atmosphere.

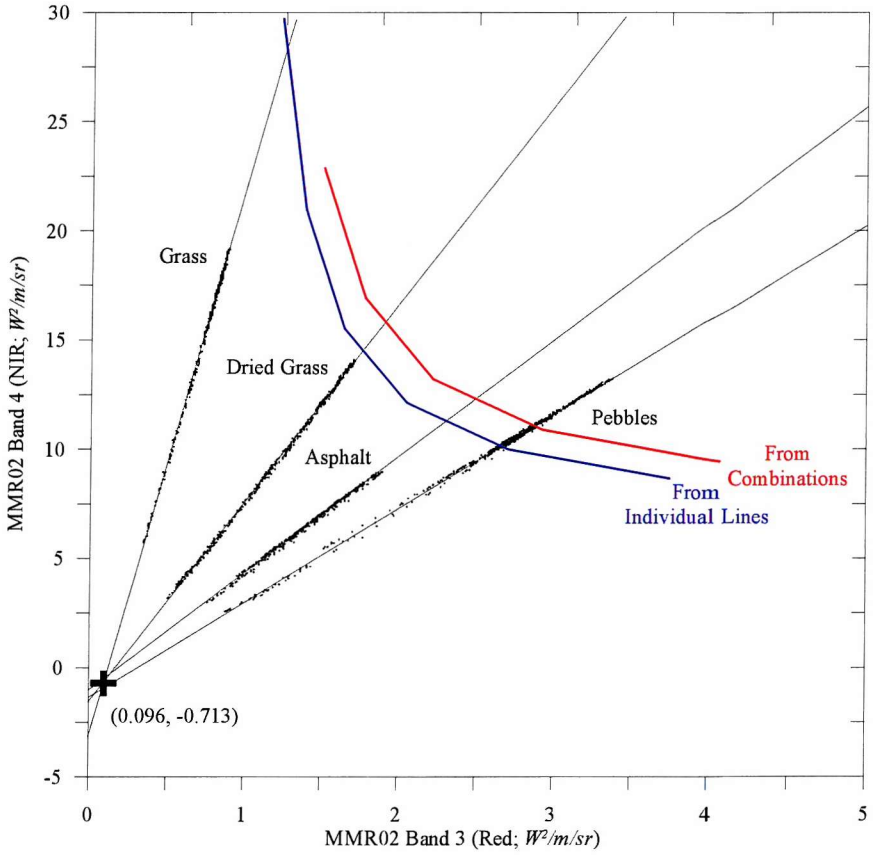

Figure 7-23. Shadow-lines of data acquired with a 4-channel radiometer (MMR) during the field experiments. The point with a symbol ✚ represents the SVD DPVE with its coordinate in the brackets. More details are provided in the text.

With an assumption of a single DPVE from our field data, characteristics of the DPVE in relation to the variation of the atmospheric condition are examined. Theoretically, the maximum radiances for the corresponding shadow-lines can be defined by a single DPVE. This is derived by substituting Equation [7.11] into Equation [7.6].

$$L_r^{\circ} = \frac{b \cdot \Re}{a \cdot (1 - \Re)}$$
$$L_n^{\circ} = a \cdot L_r^{\circ} + b \qquad [7.25]$$

For Equation [7.25], as defined earlier, $\Re$ should be greater than 1, so that both L_r° and L_n° are positive values.

Two DPVEs from median and SVD of multiple shadow-lines acquired by the field measurements were applied to find the maximum radiance values for each shadow-line using Equation [7.25]. The continuous maximum radiance lines are superimposed on the feature space for the field data (Figure 7-23). The two curves shown in Figure 7-23 were computed from two different positions of DPVEs shown in Figure 7-22, respectively. It implies that the variation of the DPVE position presumably due to atmospheric effects determines the changes of the maximum radiance points and hence results in different shapes of the data cloud in spectral feature space. From this plot, the maximum radiance lines pass through the middle of the largest points of the measured radiances. For example, the data points of the grass shadow-line are under-sampled, whereas those for pebbles are over-sampled. The reason for this is that the data were collected under different atmospheric conditions.

7.7. Summary

The two main objectives of this chapter were: (i) to quantify the fundamental uncertainty introduced by the atmosphere, and (ii) to provide a conceptual model in order to explain how the uncertainty changes under different illumination conditions. Although the effect of the atmosphere at any one instant in time is difficult to determine, the overall trend of illumination changes as a result of variations in atmospheric conditions is predictable and can be modelled.

A series of field measurements were designed to obtain spectral signatures of several targets while radiation reaching the ground varied mainly due to the changes in aerosol density in the atmosphere. The variety of cloud patches that passed during the data acquisition indicates that the magnitude of aerosol scattering changed rapidly over a relatively short period. A group of sunlit and shadow boundaries (SSB), which had sudden illumination change of spectral radiance within short period (i.e. it was assumed to represent instantaneous atmospheric conditions), was selected from each target measurement. It was shown that diffuse radiance scattered by the atmospheric constituents exists even if there is no direct solar radiation due to thick dense cloud, as the minimum data value in each SSB is never close to the origin in the feature space.

The data plot of simple two-dimensional spectral feature space reveals that spectral variation due to illumination changes follows a regression line, which is defined as a 'shadow-line'. The properties of each shadow-line have a specific spectral pattern: the slope value decreases exponentially with wavelength, while the increasing intercept value is always less than zero. With respect to its position, any shadow-line should ideally pass through the origin in the feature space, since no signal is received under complete darkness in any wavelength. In addition to the visual examination of the shadow-line, statistical analysis was performed in order to test whether conditions, the non-zero intercept value was due to instrumental error. A linearity test resulted in the following,

1) It is unlikely that any single shadow-line would pass through the origin,
2) Non-linearity in the shadow-line, i.e. additional source of radiation from adjacent ground objects, can be ignored, and

3) The position of the shadow-line does not remain constant even for the same ground target.

Consequently, it was hypothesised that the variations of shadow-line are caused by the effects of the atmosphere and that, as a result, its magnitude influences uncertainty in RS data.

In order to test the hypothesis, conceptual models derived from radiative transfer equations were developed. In terms of the design of the field experiment, the distribution of radiances for sunlight and shaded conditions were simplified by several assumptions:

1) The angle of incident solar radiation was assumed to remain the same for each SSB because the speed of cloud patches are much faster than Sun position changes,
2) Atmospheric transmittance between ground objects and the sensor was ignored, as its distance is much smaller than that of the entire atmosphere, and
3) After statistical analysis, higher order scattering was not considered.

The mathematical expressions of slope and intercept contain the ratio of normalised atmospheric transmittance, $\mathcal{R}$ (as shown in Equation [7.15]), in which both apparent transmittance and diffuse radiance terms are included. The term $\mathcal{R}$ represents the effect of the atmosphere, and plays an important role in determining the characteristics of the shadow-line in feature space.

The significance of two variables that represent atmospheric conditions, i.e. transmittance and diffuse radiance, is examined using the shadow-line model. The inverse rotational relationship between the slope and intercept of the shadow-line suggests that the position of the shadow-line has a rotational movement in two-dimensional feature space, which leads to statistically different shadow-lines in the same group of field data as shown earlier. Further investigation of the shadow-line model reveals that the slope is only a function of atmospheric transmittance, whereas the intercept is still affected by both variables. Thus, we can assume that if there is no variation in transmittance, the intercept of shadow-line will change but not the slope.

The results showed that the properties of a shadow-line from any ground object are affected by changes in the atmosphere. It is therefore hypothesised that more than one shadow-line under simultaneous atmospheric conditions converge into a certain point (defined as the

dark point virtual endmember, or DPVE) in spectral feature space, as the same magnitude of atmospheric effects applies identically to all shadow-lines and move them away from the origin. This idea is associated with dark endmember used in spectral mixing (or unmixing) models. In conventional studies, it is often assumed that data points in changing illumination are passing the origin in feature space. However, it should be carefully selected as many shadow-lines do not pass through the origin.

The DPVE with a pair of shadow-lines was derived using the shadow-line model. The atmospheric effect term, $\Re$, still plays a significant role in the definition of the DPVE (Equation [7.21]), representing that the DPVE characterises the effect of the atmosphere for the corresponding shadow-lines. This was tested by the comparison of the term $\Re$ between the DPVE and a single-shadow-line model, and it showed quite close results. The DPVE model with more than two shadow-lines was achieved by using the singular-value decomposition (SVD) method that is one of the powerful tools not only to increase the number of shadow-lines but also to expand the dimensionality of feature space.

The existence of the DPVE was checked by the modification of shadow-line model. The maximum radiance of a shadow-line was considered as the upper bound to the data cloud in spectral feature space. The estimated maximum boundary was determined by, again, the term $\Re$, and was found to move away with the minimum value of $\Re$ (i.e. $\Re > 1$) and vice versa. Thus, the boundary will be infinite with no atmospheric effects (i.e. no diffuse radiation), whereas the range of maximum data points becomes closer to the DPVE with increasing amount of atmospheric scattering (under thick hazy condition due to dense aerosol contents, it difficult to recognise objects). This is related to the fact that a scene image is blurred with a higher density of aerosol in the air, such as an appearance of haze.

The position of the shadow-line is sensitive to the effect of the atmosphere, and should be taken into account in image analysis based on the spectral feature space. The changes in data plots due to the variation of atmospheric constituents are a major source of uncertainty and will influence the subsequent data analysis.

Part III.

Contribution of the research to operational airborne remote sensing

The final two chapters of the thesis build upon the experimental and theoretical work of the earlier chapters to present two novel practical methods to correct for the effect of atmospheric variability on airborne RS data.

The first (Chapter 8) is an image-based method which can be used to achieve a qualitative improvement in image quality, a reduction in scene noise where this is due to shadowing, and an improvement in the accuracy of multispectral ratios.

Chapter 9 describes an innovative way to use the data on downwelling irradiance measured by a roof-mounted sensor to correct for irradiance radiation affecting RS data. This method also has the potential to provide data on the sky irradiance distribution at the time of sensing.

Chapter 8

Image-based method: Sensing in shadows

8.1. Introduction

Shadow:

I. *Comparative darkness.*

1. a. *Comparative darkness, esp. that caused by interception of light; a tract of partial darkness produced by a body intercepting the direct rays of the sun or other luminary. Cf. sense 11.*

II. *Image cast by a body intercepting light.*

4. a. *The dark figure which a body 'casts' or 'throws' upon a surface by intercepting the direct rays of the sun or other luminary; the image (approximately exact or more or less distorted) which this figure presents of the form of the intercepting body.*

- Oxford English Dictionary -

In an ideal world, the intensity and direction of radiation in a RS dataset would be uniform. One could then assume that differences in reflected radiance signals are solely due to different spectral characteristics of ground targets. In reality, the direction and magnitude of incident radiance is not always uniform due to atmospheric conditions and/or target geometry, the spectral signatures of ground targets are therefore altered. Of these temporal and spatial non-uniformities in illumination, there is the special case presented by 'shadow', which is defined as the target leaving EMR with no (or little) direct solar radiation. Shadows cast on the target surface affect the reflected flux in three ways. First, its intensity will be reduced including changes in illumination geometry; second, its spectral character will be changed; and third, its angular distribution will be altered.

The appearance of shadows in a scene is a benefit for some applications of RS. As a primary element of visual interpretation for both photogrammetric and computer vision

communities, scene shadows provide textural (three-dimensional) information of an object which is illuminated at an angle, which may otherwise be invisible or appear unrealistic. It also plays a significant role in image enhancement and pattern recognition for object identification, terrain classification, and geological mapping (Curran, 1985; Campbell, 1996). Shadows in a scene carry information concerning the irregular surface of the Earth's terrain. These variations in image brightness have long been an important subject for photoclinometrists who retrieve topographic information, on the basis of bi-directional effects, from the brightness of an image (Campbell, 1996) and photogeologists who have studied the moon's surface since the 1940s. Techniques for mapping terrain elevation using shade from coarse spatial resolution Synthetic Aperture Radar (SAR) images (e.g. Guindon, 1991) have been applied to multispectral spaceborne sensors, such as SPOT (Shettigara and Sumerling, 1998), for height estimation of buildings, despite the fact that their spatial resolution is much coarser than that of aerial photos (Kim and Muller, 1998). Similar methods have been used in atmospheric and meteorological research, for example, to determine the presence of clouds for mesoscale temperature gradients and the energy and moisture fluxes in the atmosphere (i.e. the energy balance at the Earth's surface). Studies on this topic were reported on cloud detection and/or recognition (Hutchison and Choe, 1996; Shin *et al.*, 1996) and estimation of its shadow projected on the Earth's surface (Simpson *et al.*, 2000; Berendes *et al.*, 1992; Gurney, 1982, 1983).

In many other applications of RS, however, shadows are a frequent problem affecting multispectral optical airborne and satellite data for spectral, spatial, and temporal applications. A human interpreter looking at, for example, an aerial photo affected by (completely or partially cast) shadows is often able to make sense of the scene because the field patterns are still visible, but conventional computer-based image classification methods often fail because the spectral properties of the object may have been altered under the shadow. In early studies, the assumption that the target surface is a diffuse reflector, i.e. Lambertian surface, with a uniform reflectance, greatly simplified the analysis of the observations. It works reasonably well for some extraterrestrial surfaces, but in some surfaces on the Earth such an assumption is difficult to accept because mixture of surface materials (e.g. vegetation) often confuses interpretation of, say, the soil itself. Also, they severely limit the value of such images for quantitative study (e.g. determination of surface BRDF). Shadows are a frequent problem when images should be acquired during a critical temporal period due to scientific, logistical or financial reasons. In addition to topographically induced shadows, the appearance of which is associated with Sun angle and object dimensions, atmospheric shadows are difficult to predict in spite of the area

that they cover and their frequency, i.e. approximately 50 % of the entire surface of the Earth is covered by clouds at any time and location (Hughes and Henderson-Sellers, 1985; Stowe, 1984). The practical application of spaceborne and airborne remote sensing could therefore be greatly limited unless data that are completely shadow free are available (see Section 2.1.1). An operational cloud shadow correction method would enable data collection flights to go ahead in what are currently considered suboptimum conditions.

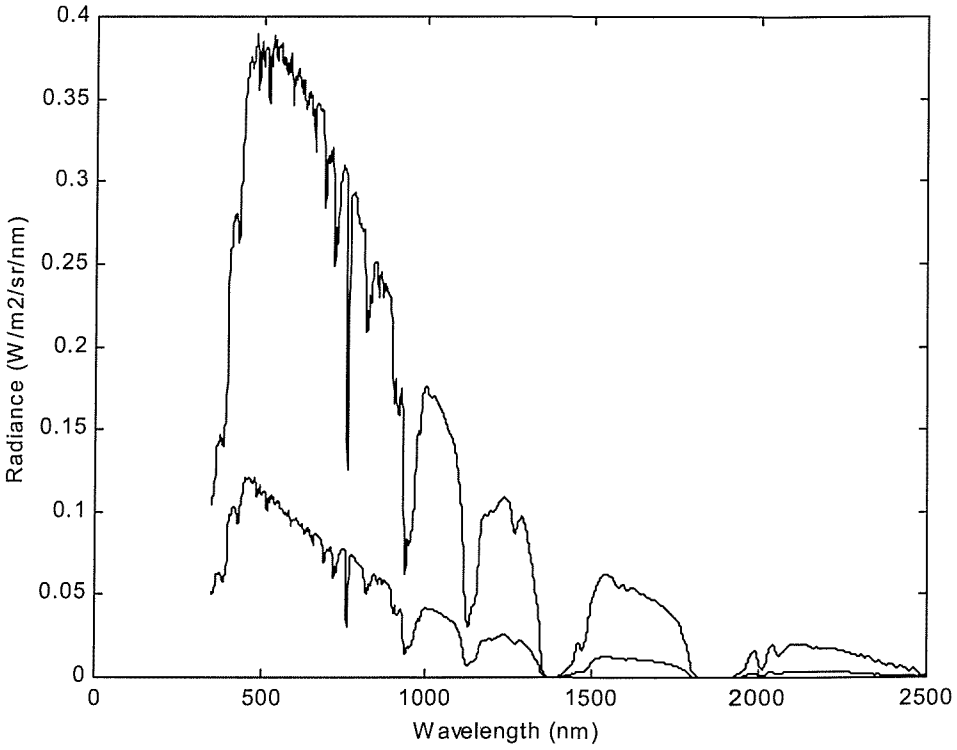

Figure 8-1. Plots of typical radiance from a reflectance reference panel under sunlit and cloud shadow. The data were collected using an Analytical Spectral Devices FieldSpec FR Spectroradiometer at 11:34 BST on 16 September 1998.

In this chapter, shadow in the scene is considered as an indicator of atmospheric conditions to facilitate atmospheric correction of a RS image. As shown in the previous chapter, if a cloud casts a shadow on the ground, issues of atmospheric effects arise; the dense aerosols prevent direct radiation reaching the area that is shadowed, it is therefore only illuminated by diffuse radiation (Figure 8-1). Shadows in RS images are a frequent problem that causes analysis error in many image processing methods. In turn, the shade area may contain valuable information on the nature of atmospheric effects at the time of the image acquisition, which the

directly illuminated area cannot show. Reviews about shadows in remotely sensed data are discussed in the next section, following conventional cosmetic shadow suppression methods. Developing an image standardisation method will be presented in later sections by extending the idea of DPVE described in the previous chapter.

8.2. Data sets used

Three image data sets with strong and distinct cumulus cloud shadows were used in the study: one collected with a Daedalus AADS1268 Airborne Thematic Mapper (ATM) and two collected with an Itres Instruments Compact Airborne Spectrographic Imager (CASI) (Table 8-1). The airborne scanner data were first calibrated to in-band radiance measured at the sensor using the gain and offset values provided, and subsets of 400 lines × 400 columns were extracted from each of the calibrated data sets.

		Rural Area		**Coastal Area**
Name		**Rural 1**	**Rural 2**	**Coast 1**
Area		West Sussex	Hertfordshire	Chichester harbour
Sensor		ATM	CASI	CASI
Number of bands		11	4	10
Flying height (m)		800	1,280	1,200
Bandset		ATM	TM	CASI default
Centre wavelength (*nm*)	**1**	435	485	450
	2	485	560	490
	3	560	660	552
	4	615	830	670
	5	660		700
	6	723		710
	7	830		740
	8	980		750
	9	1,650		762
	10	2,215		780
	11	10,750		

Table 8-1. Summary characteristics of the data sets used.

An airborne platform was used because it provided high spatial resolution and because it offered flexibility in flight timing and the area covered. The three sites were the South Downs east of Petersfield, an area north of St Albans, and Thorney Island in Chichester Harbour. The first two scenes are rural areas with landscapes typical of southern England: small agricultural fields, hedgerows, small stands of woodland, various types of lowland grassland, and some artificial surfaces (roads, buildings etc.). On the other hand, Thorney Island is a disused military airfield, where some large buildings (e.g. hangers and oil tanks) are located.

Most bands were in visible and near infrared (NIR) wavelengths, and the CASI sensor (in CASI-2 default mode) had a number of bands located close together around the vegetation red-edge (690–750 *nm*). The ATM had generally broader bands distributed throughout the visible, infrared and thermal wavelengths. For the second rural area the CASI was programmed for four spectral bands similar to Landsat TM bands 1, 2, 3, and 4. All the images were partly contaminated by cloud shadows that distorted the colours on colour composites and masked boundary features, making visual interpretation difficult and automated classification impossible.

8.2.1. Image Descriptions

1) South Downs

These data were collected on 19 September 1984 as part of a project studying the application of remotely sensed data for soil survey (Milton and Webb, 1987). The particular flightline used for this study was excluded from the earlier work because it was severely affected by cumulus cloud shadows. The data were converted from digital numbers to in-band radiance using the gain and offset values provided in Wilson (1988). Topographic shadow is cast along the north-facing escarpment of the South Downs, and within the many bare soil fields in the area. Vegetation shadows are seen within the stands of woodland and there are many ephemeral shadows from cumulus clouds.

2) St Albans

These data were collected on 1 May 1996 in order to provide a test data set for the application of per-parcel based methods of land cover classification (Aplin *et al.*, 1999), but were also severely compromised by the presence of cloud shadows. The data were provided by Atlantic Reconnaissance and were calibrated to in-band radiance by the supplier. In the image, ephemeral shadows can be observed from cumulus clouds, and moderate amounts of topographic and vegetation shadows, cast within the agricultural crops growing in many of the fields, are visible.

3) Thorney Island

The CASI data were collected on 1 May 1994 and were converted to in-band reflectance using the empirical line method (Roberts *et al.*, 1986). Further details of the data set

and its pre-processing to compensate for the motion of the aircraft are provided in Milton (1999). Topographic shadow is shown down-Sun of buildings, vegetation shadows are evident within tree canopies, but there is no geometric shadow due to topography because of the flat nature of the terrain. There are no ephemeral shadow and minimal skylight infill due to the clear skies during data acquisition.

8.2.2. Shadows in the sample images

Shadow in remotely sensed images may be classified according to origin and significance. Shadow originating from the interaction between the source(s) of illumination and the geometric arrangement of objects in the scene may be termed 'geometric shadow', whereas that which is caused by short-term disturbance to the illumination distribution (e.g. cloud shadows) may be termed 'ephemeral shadow'. As to its significance, this is a continuum from, at the one extreme, deep shadow formed by opaque objects and not illuminated by scattering from the surroundings to, at the other extreme, filtered shadows cast by translucent objects and illuminated by scattered light from surrounding objects. The amount of energy transmitted through translucent objects and the degree of scattering from surrounding objects are wavelength dependent, hence filtered shadows are not uniformly black but have a spectral response. Even deep geometric shadows are illuminated by skylight, which varies in intensity with wavelength and with the amount of scattering by the atmosphere.

In practical terms, assuming no scattering from the surroundings (i.e. flat terrain), the major distinction on images collected in VNIR wavelengths is between shadows within vegetation canopies (which are likely to be a mixture of deep, cast shadows and filtered shadows), and those within bare soil surfaces (which are illuminated only by skylight). The three test data sets thus provide a range of the types of shadow likely to be found on remotely sensed images.

8.2.2.1. Geometric shadow

The CASI data from Thorney Island shows the importance of spatial resolution in the identification of the shadow point when the image only contains small areas of geometric

shadow. The intrinsic dimensionality of the CASI data was determined to be three using an MNF transformation (Green *et al.*, 1988) and the 'purest pixels' in this reduced three-dimensional feature space were determined using the Pixel Purity Index (PPI) method described by Boardman (1993). The image data were then sub-sampled to reduce the spatial resolution from 4m to 36m, in order to match that offered by systems such as Landsat TM which would be more likely to be used for large-area survey in the UK.

The results of this are shown in Figure 8-2 in the form of a scatter plot of the first two MNF bands of the purest pixels at 36 *m* spatial resolution located within the envelope defined by the purest pixels at the higher spatial resolution. As would be expected, the mixing space at the coarser resolution is much reduced, but the most important point is that the pure shadow endmember is not present in the 36 *m* data set. At this coarse spatial resolution, shadow is only present as a mixture with other objects in the scene, and techniques to identify image endmembers such as the PPI would fail to detect the true shadow point. In a situation like this it is necessary to adopt a method which can find 'reference' or 'virtual' endmembers by extrapolation from the image endmembers. Boardman (1993) describes such a technique based upon the principles of convex geometry and this was explored further for the Thorney Island data set by Milton (1999).

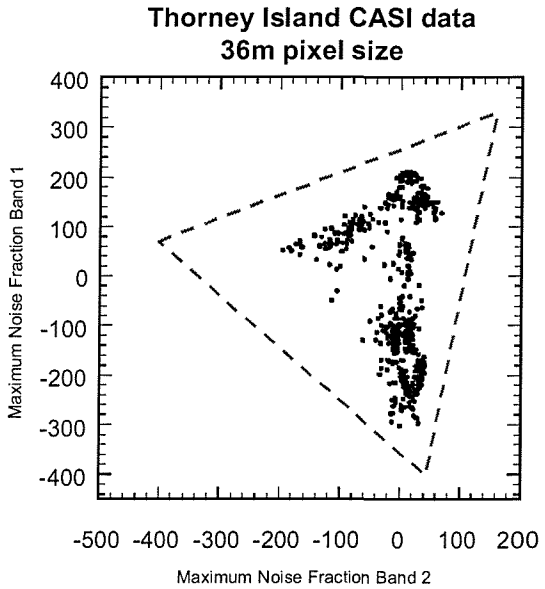

Figure 8-2. MNF plot of the purest pixels in the 36m data (dots) in relation to the envelope defined by the purest pixels in the 4m data (dashed line) (Milton, 1999). The shadow endmember (top-right) is absent from the coarser resolution data.

8.2.2.2. Ephemeral shadow

The aim of this part of the work was to remove the effects of ephemeral cloud shadows upon vegetation indices, specifically NDVI, through translation of the origin of the feature space to an accurate shadow point. The remaining two data sets were used for this work as both were seriously affected by cloud shadows and they were collected by different airborne sensors (Table 8-1). The effects of cloud shadows upon data collected in visible and NIR may be summarised as follows:

1) Reduction in the level of irradiance (expected to be the dominant effect)
2) Change in its spectral distribution, due to scattering and absorption within the cloud
3) Change in the direction of illumination, from direct plus skylight to primarily skylight

For near-Lambertian surfaces imaged in wavelengths relatively unaffected by spectrally selective water absorption, a systematic reduction in irradiation would be expected depending upon the thickness of the cloud. Enhanced forward scattering, especially around the edges of thin clouds complicates matters, but this is a minor effect in comparison to the overall reduction in the level of illumination.

8.3. Conventional shadow suppression methods

Few studies in remote sensing consider seriously the validity of the results of either simplifying or removing the effect of shadow. As some methods to avoid shadowing effects have been suggested in order to separate the sources of brightness change caused by different surface material and topography, band ratioing is one of these. By dividing a pair of pixels into separate bands, the quotient is supposed to show pure reflectance information without the effects of topography. This has been used extensively by geologists in remote sensing, and resulted in useful lithological information (e.g. Goetz *et al.*, 1975; Vincent *et al.*, 1984). The ratios are also effective in enhancing or revealing latent information when there is an inverse relationship between two spectral responses to the same biophysical phenomenon. This method is the simplest form of vegetation index, that is, that the combinations of several spectral values are used to derive a single value representing quantitative measures of biomass. Basically, the relationship between the absorption of red light by chlorophyll and the strong reflection of NIR radiation by mesophyll tissue yields distinguishable vegetation brightness regardless of illumination effect (Campbell, 1996).

This shadow suppression approach in a scene is based on the fact that the reduction in intensity is the dominant effect, rather than any changes in the spectral quality of the light reaching the ground. It is therefore reasonable to expect that other multispectral transforms that separate intensity from hue should behave similarly. There are a number of candidate transforms, including ratio-based vegetation indices such as the NDVI (Rouse *et al.*, 1974) and TSAVI (Baret *et al.*, 1989), many of which have been shown to be functionally equivalent by Perry and Lautenschlager (1984), and those based on the measurement of angular separation in n-dimensional feature space, such as Spectral Angle Mapper (SAM) (ENVI User's Guide, 2002). All of these have the potential to reduce the effect of cloud shadows, however, before they can be applied for this purpose it is essential that the data are converted to apparent reflectance, or to a directly related quantity, such as apparent radiance. These are the reflectance or radiance values that would be measured at ground level, scaled by a multiplicative factor to account for the effect of topography or shadowing.

Two conventional approaches to suppressing shadows are reviewed and will be tested for their effectiveness for cloud shadows. The methods used here are based on band ratioing in feature space.

8.3.1. RGB-HSI transformation methods

Liu and Moore (1990) used RGB space transformation to suppress partly shaded image data. They assumed that illumination effect was the only factor which affected shadows, and used RGB-IHS (red, green, and blue to intensity, hue, and saturation) transformation in three dimensional Cartesian-polar co-ordinate systems (Figure 8-3). Within a colour cube of a three band colour composite, the diagonal line from the origin is called the grey line, and represents brightness. The distance of a point from the grey line is saturation, purity of colour. Hue, spectral range, is the azimuthal angle around the grey line. It is theoretically proved that illumination change does not affect the hue value and that the ratios of irradiance in shadow to that under sunlit tend to be consistent.

Liu and Moore (1990 selected three band triplets from a Landsat TM image. Spectrally adjacent bands from the image were used, so that they could assume the atmospheric effects were almost the same. RGB-IHS transformation was performed on each band triplet, and the hue components were extracted from each. These were independent of the illumination effect. The hue image RGB false colour composite with three hues was shown to be shadow free and more detailed in spectral classification. The result was promising for lithological classification and rock discrimination.

Another attempt was to use the thermal band of ATM into the RGB-IHS-RGB transformation (Liu and Moore, 1993). The variations in the thermal band were different from other bands, because it is assumed not to be affected by the shadows of a moving patch of cloud. In order to take advantage of this, the result of RGB-IHS had to be transformed into RGB again. In this case, illumination change was replaced by the thermal band used as a pseudo intensity component. Moreover, image differencing was used on each composite of RGB during pre-processing, since saturation is also affected by the presence of shadow (Schowengerdt, 1983). The differencing of subtracting the same band from each RGB, tends to increase the colour saturation and balance it among different illuminations, whereas the intensity decreased. A

colour composite of ATM band 9, 4, and 2 was chosen for a RGB colour cube, this band combination is often used for lithological surveys. Band 8 was used as a subtractor, it is supposed to have low correlation to the RGB colour combination.

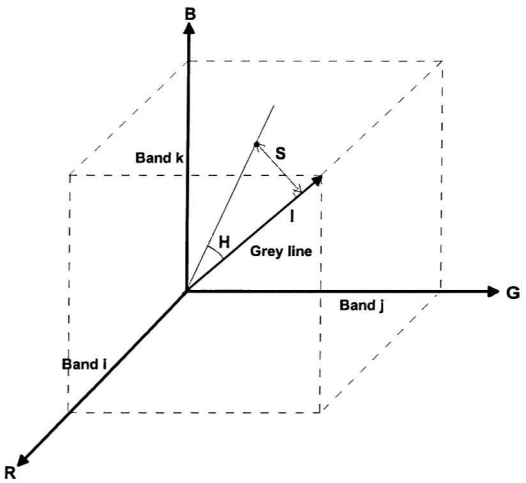

Figure 8-3. Three-dimensional RGB-IHS space.

Using either method, RGB-IHS transformation is an effective tool in the suppression of shadows in an image. The same procedure as that introduced by Liu and Moore (1990 and 1993) was followed for the South Downs image. The results are depicted in Figure 8-4 and Figure 8-5, and show flow-charts of both methods. Both RGB-IHS-HRGB and RGB-IHS-RGB methods, however, did not produce shadow free images for the South Downs, especially when shadows were present over vegetation. The main reason for the failure is that unlike the hypotheses made above, hue components are not able to suppress the cloud shadows in vegetated areas, bearing in mind that Liu and Moore applied their methods to an image of a semi-arid area with little vegetation. The final outputs of the methods using the South Downs image shows that the shadow still exists on vegetated areas whereas shadow is effectively suppressed in bare areas. This suggests that hue (spectral range) does not move parallel to grey line, i.e. the diagonal line in the colour composite cube. On the other hand, the spectral variation of bare soil is relatively closer to the grey line in 3-D space than that of vegetation, so that the variation of illumination on the bare soil area was removed effectively in the colour composite triplet of adjacent bands.

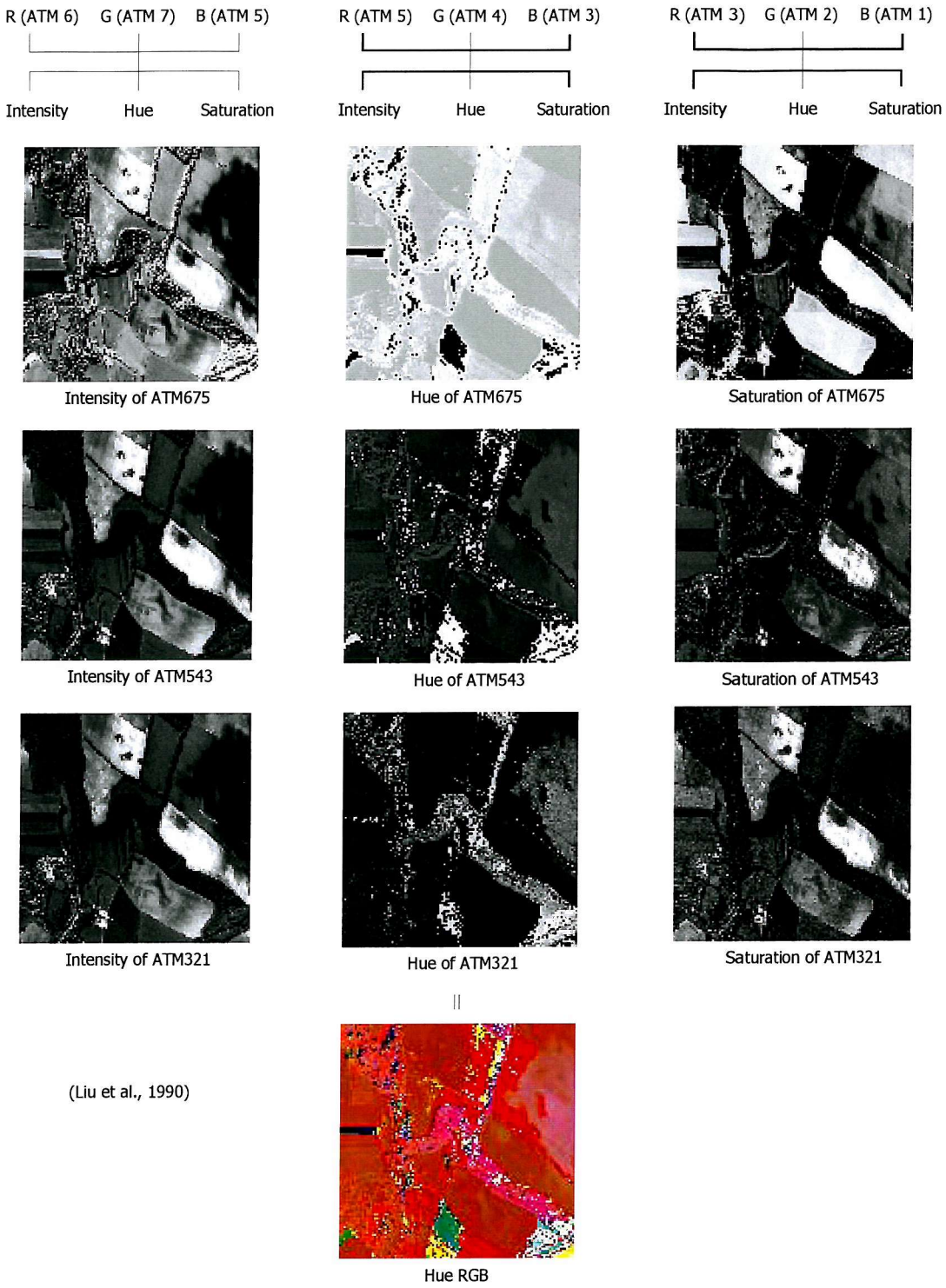

Figure 8-4. Shadow suppression procedure of RGB-IHS-HRGB, developed by Liu and Moore (1990).

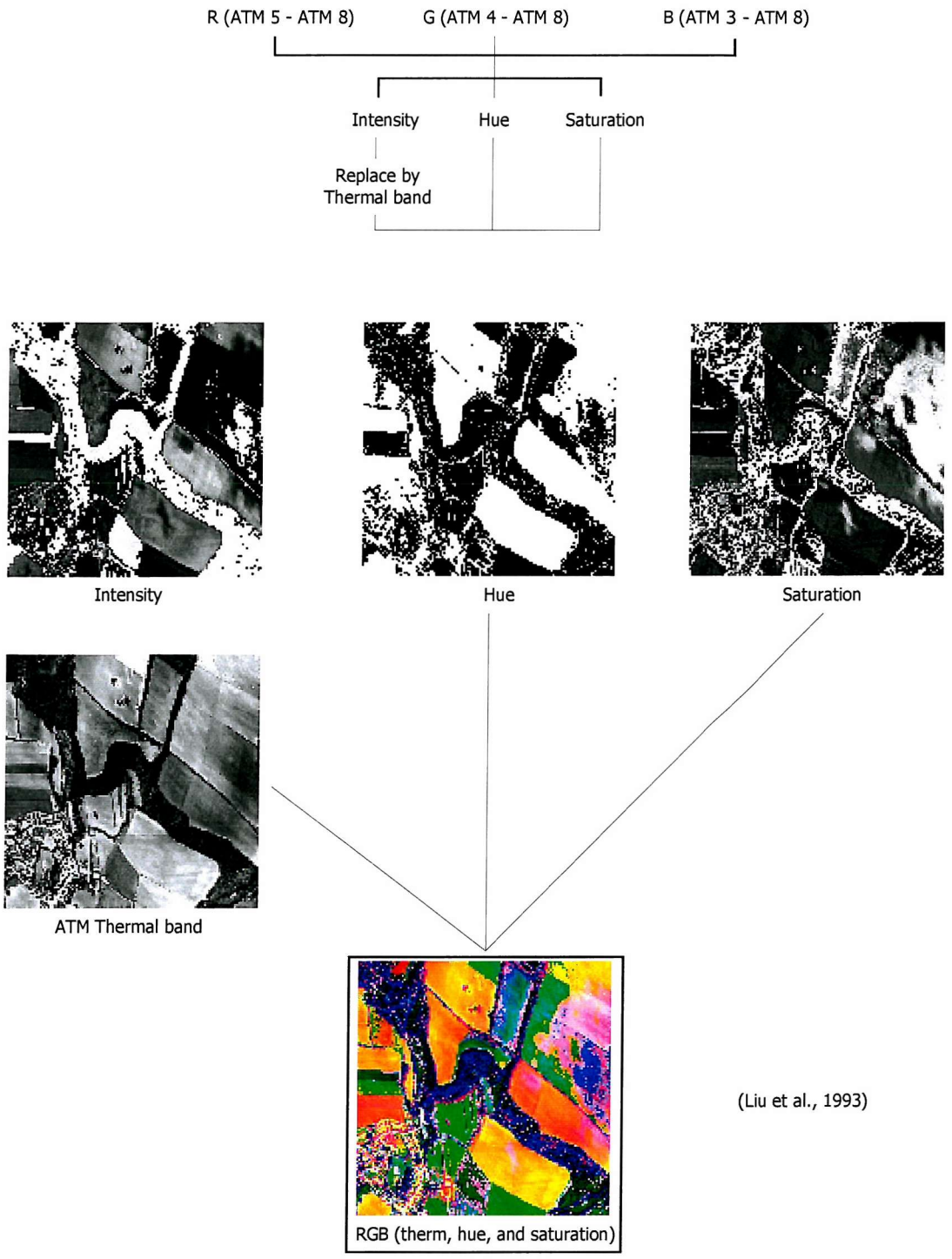

(Liu et al., 1993)

Figure 8-5. Shadow suppression procedure of RGB-IHS-RGB, developed by Liu and Moore (1993).

8.3.2. Spectral Angular Mapper (SAM)

In Liu and Moore's method, a triplet of ATM bands for HRGB transformation is needed and the thermal band is also necessary for RGB-IHS-RGB transformation. They only worked on soil and rocky areas, in terms of position of the pixels on a diagonal line. Spectral angle mapper (SAM) is based on a similar concept of determining spectral range, i.e. hue component, as in RGB-IHS transformation. In this case, one can determine a reference spectrum within an n-dimensional space, and therefore a vector of intensity component within varies depending on the selected spectral library or ROIs from the image. SAM was originally developed for geological survey to eliminate illumination effect on images corrected to apparent reflectance (Figure 8-6). Notice that the angle between the vectors is the same regardless of the length.

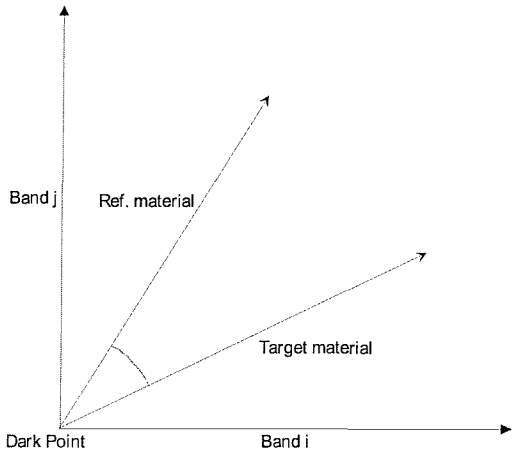

Figure 8-6. Two-dimensional example of SAM. The angle between reference and target in the feature space represents the spectral angle.

The method is insensitive to the unknown gain factor because it uses only the 'direction' of the spectra and not their 'length'. The length of the vector relates only to how fully the pixel is illuminated, so that all possible illuminations are treated equally and poorly illuminated pixels will fall closer to the origin. The method is to treat 'spectral angle' as vectors in a space with dimensionality equal to the number of bands (not only two dimensional space, such as vegetation index using red and NIR radiation), once data are assumed to be correct to physically meaningful values. The 'brightness' of the SAM is defined by the direction of its unit vector, as it is in various types of vegetation indices. SAM calculates the spectral angle, α_{sam}, between the reference and a line of zero-crossing dark point by applying the following equation:

$$\alpha_{sam} = \cos^{-1}\left(\frac{\sum_{i=1}^{n} t_i \rho_i}{\left(\sum_{i=1}^{n} t_i^2\right)^{\frac{1}{2}} \left(\sum_{i=1}^{n} \rho_i^2\right)^{\frac{1}{2}}} \right) \qquad [8.1]$$

where n is a number of bands, t is a target spectrum and ρ a reference spectrum. A 5×5 window of bare soil ROI of South Downs image with no shadow was selected as reference spectraum Figure 8-7 shows result of SAM calculation of the ATM bandset excluding the thermal band. The result shows that SAM is also unable to suppress vegetated shadow areas, which is the same result as with the RGB-IHS transformation method described earlier.

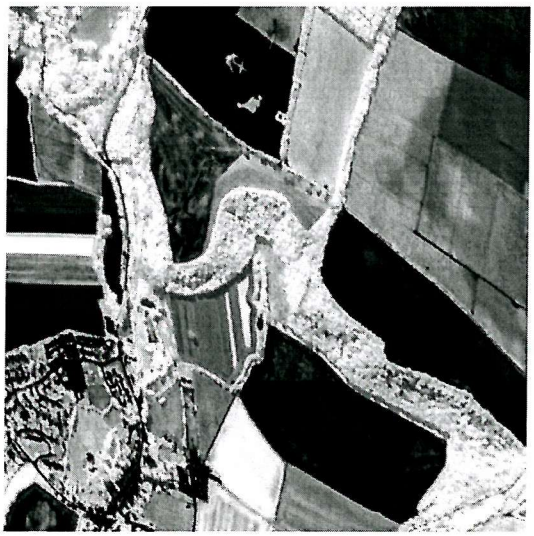

Figure 8-7. Result image of South Downs image from SAM

8.4. Application of the DPVE on the Scene Shadows

The conventional shadow suppression methods introduced in the previous section have been proposed for this task, but ratio-based vegetation indices or colour space transformations calculated by these methods were only partly effective for the shadows on vegetation. It is assumed that these methods only work effectively if the image data are firstly aligned to the hypothetical 'dark point virtual endmember' (DPVE) in the multispectral feature space. The DPVE may lie outside the cloud of points forming the image data, so it is not sufficient to simply subtract the digital number of the darkest pixel in each band. In this section, we identify the DPVE on a number of images by the convergence of shadow-lines in, first of all, a two-dimensional feature space and later extending it toward *n*-dimensional space. These lines are derived from regions-of-interest that straddle the boundary of sunlit and cloud shadow areas on bare soil and green vegetation. DPVEs are identified in each of the data sets in a similar way and the origin of each feature space shifted accordingly. Aligning the data set to an accurate DPVE in this way is shown to greatly enhance the ability of the simple NIR/Red ratio to suppress shadows from clouds as well as those from buildings and within forest canopies.

8.4.1. Attributes of the DPVE in image

Precise identification of the shadow point in spectral feature space is important because many multispectral transformations are based on the assumption that variation in brightness (as opposed to colour) is expressed by the angle of radial lines from the origin of the feature space (i.e. a ratio of two radiances in different wavelengths is independent of illumination variation). This is only true if the shadow point of the data is aligned with the origin of the feature space. Any displacement of the shadow point from the origin will introduce an error into ratio-based pre-processing techniques such as those commonly used for topographic removal and cloud shadow suppression. Ratio-based vegetation indices have been similarly shown to be affected by data calibration (Crippen, 1988).

It is evident from Figure 8-8b that the transect data from the vegetated field do not fall neatly along a radial line from the origin of the feature space, whereas those from the bare soil field do. The main variation in both the bare area and the vegetated area is brightness rather than

colour which has caused scatter around the radial lines. However, it is also apparent that the point of intersection of the lines from the two surfaces is displaced from the origin of the feature space. All the bare soil points lie approximately on a line radiating from the origin but those from the vegetated area cross the line from the origin, meaning that their vegetation index calculated with reference to the feature space axes would vary, depending on whether or not the pixels were in cloud shadow. The data had been corrected for sensor gain and offset, so the most likely cause of the displacement from the origin is scattering in the atmosphere introducing a path radiance contribution. Most importantly, the intersection of the two transect lines in the feature space defines a true shadow point for this data set which is outside the existing cloud of data points. It is thus analagous to a virtual endmember as described by Tompkins *et al.* (1997). Parallels can be drawn with the modified dark object subtraction method of atmospheric correction described by Chavez (1988), in that the procedure described here has identified a point in n-dimensional feature space which should represent the atmospheric scattering component in each band of the sensor.

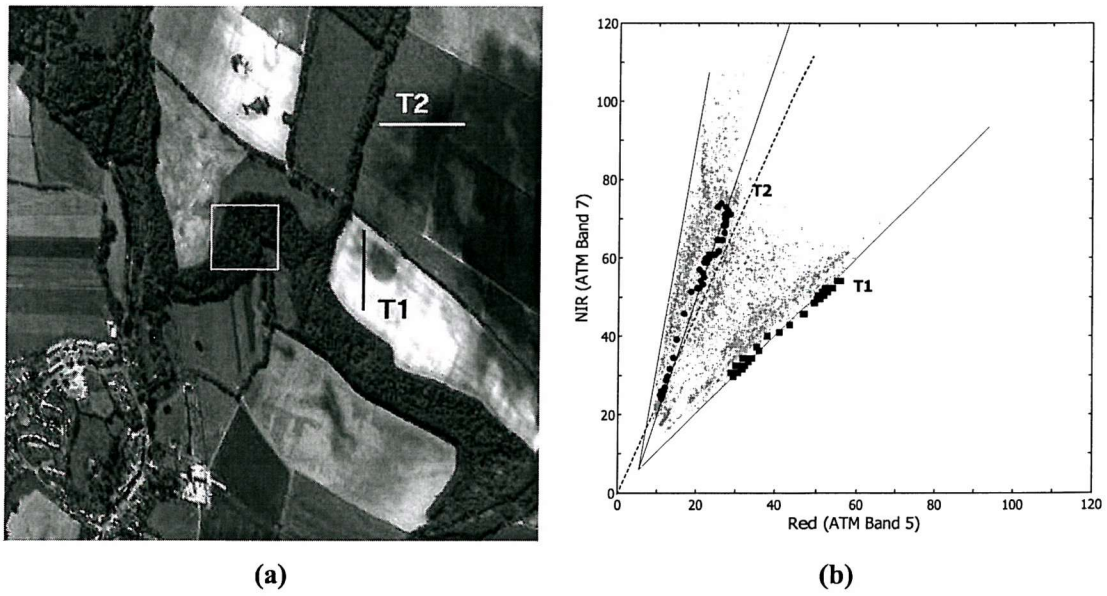

(a) (b)

Figure 8-8. Daedalus ATM Band 5 image from the South Downs showing ephemeral cloud shadow (a). Feature space plot (b) of ATM bands 5 and 7 showing the data from the two transects marked on the image. TI: bare soil, T2: vegetated.

8.4.2. Shadows in 2-D feature space

Figure 8-9 shows a comparison between a calibrated, but uncorrected NDVI image and one which has been aligned to the correct shadow point after conversion to in-band radiance. The DPVE correction was made as described in Section 8.4.1 (Figure 8-8b). Cloud shadows are still evident in the uncorrected NDVI image, and intra-canopy shadows are still evident in the belt of trees in the uncorrected image. As a result, cloud shadow affects the accuracy of vegetation estimates as well (Simpson *et al.*, 1998). These estimates are important because terrestrial vegetation, the main component of continental biomass, affects the climate system over a broad range of time and space scales by modifying the surface energy balance and by influencing the exchanges of water and carbon dioxide between the land surface and the atmosphere. Early studies emphasised that dust, aerosols, Rayleigh scattering and small clouds tend to increase the visible reflectance, with respect to the NIR, and thus reduce the NDVI estimates of vegetation. Until recently, however, relatively little attention had been paid to the effects of (cloud) shadow on NDVI, although Pech *et al.* (1986) showed that, in general, vegetation and greenness indexes are compromised because the near infrared has a greater influence than the visible. Viovy *et al.* (1992) also recognised the noise characteristics that undetected shadow imparts on NDVI.

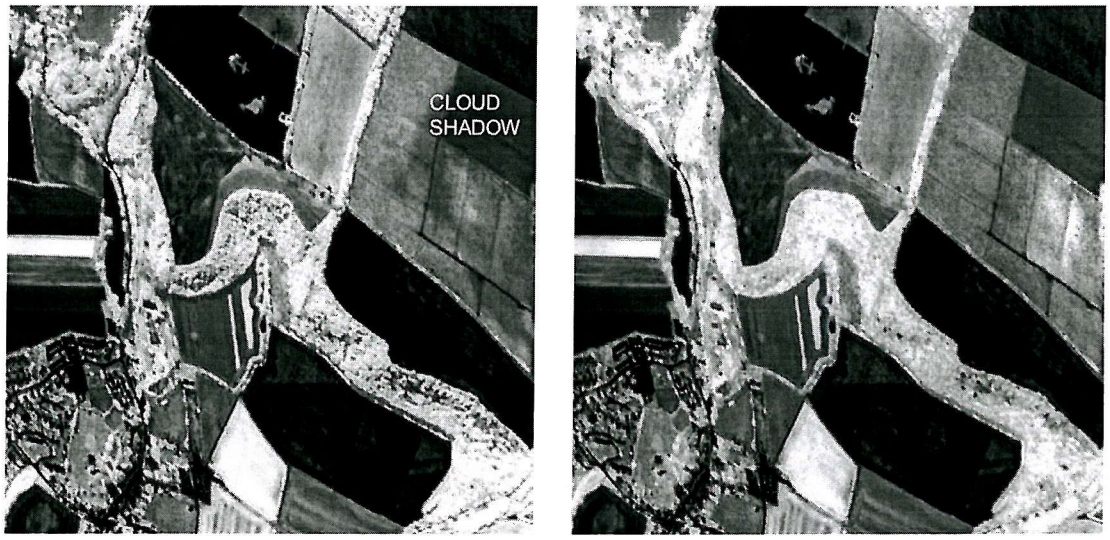

(a) (b)

Figure 8-9. NDVI images from the South Downs before (a) and after (b) shadow point correction.

The shadow point corrected image has suppressed both cloud shadows and canopy shadows. Ironically, intra-canopy shadows are also an important source of information in forest classification, so this shadow suppression technique must be used wisely if it is to be of general benefit in land cover classification. DPVEs were identified from each of the data sets using the method described above, and a simple vegetation index calculated from the corrected data to illustrate the ability of the technique to suppress cloud shadows. Images in the right column of Figure 8-12 shows three images of *Offset Corrected Vegetation Indices* (OCVI) created using two bands (Red and NIR) for the three images described in Table 8-1. These were calculated as:

$$OCVI = \frac{(DN_{NIR} - Off_{NIR})}{(DN_{Red} - Off_{Red})} \qquad [8.2]$$

where Off_{Red} and Off_{NIR} are the offset values of the DPVE. The results show shadow free images which, in qualitative terms, are much better than NIR/Red images created from either the raw data or the radiance calibrated data without offset correction.

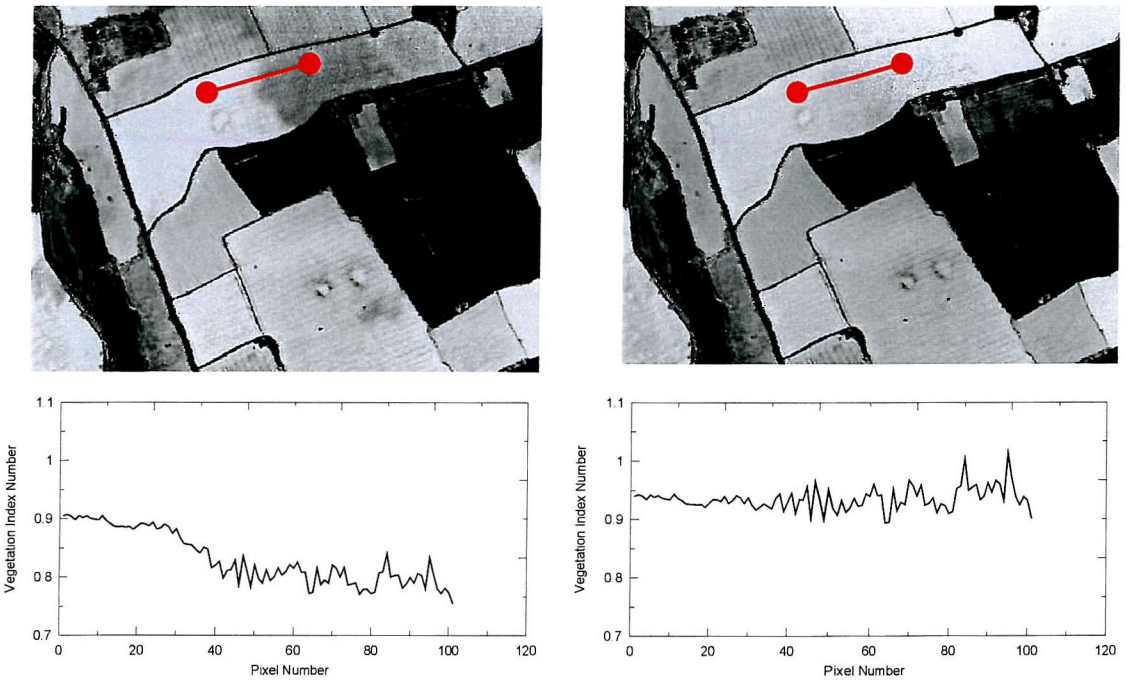

(a) (b)

Figure 8-10. NDVI images from Rural Site 2 near St Albans in Hertfordshire before (a) and after (b) shadow point correction using OCVI. Transect plots of NDVI are shown under each image.

The left-hand image in Figure 8-12 shows the thermal band for Rural Site 1 (A1) which is unaffected by cloud shadows and the red bands for the other two sites, both of which are badly affected by cloud shadows. Daytime thermal imagery is rarely used in land cover classification but it is useful in the present context for two reasons. First, it is unaffected by cloud shadows, and second, some land parcel boundaries are more clearly shown on thermal images than on the OCVI image. An alternative measure of the improvement gained through OCVI is shown in Figure 8-10 which shows values of OCVI from the bare soil transects compared with NDVI calculated without any adjustment of the data to account for the DPVE.

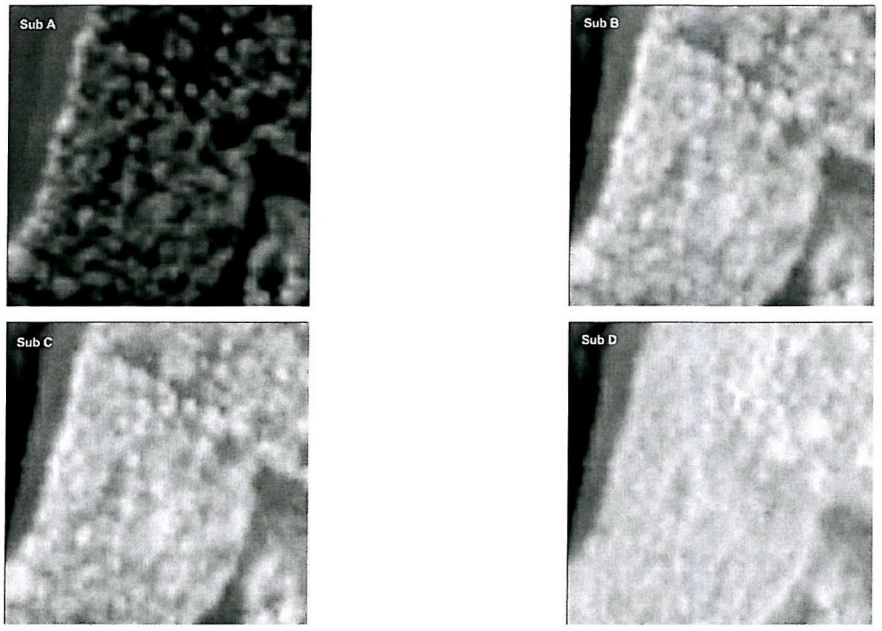

Figure 8-11. Close-up of the area of woodland outlined in Figure 8-8a showing the suppression of intra-canopy shadow achieved by OCVI compared with vegetation indices derived from data which have not been offset-corrected. NIR (A), NDVI (B), PVI (C), and OCVI (D).

The same procedure was conducted to calculate OCVI images for Rural Site 2 and Coast Site 1 (B and C in Figure 8-12). The technique was particularly effective for the Coast Site 1 image, suppressing both a large area of cloud and the shadows associated with buildings (Figure 8-12, C1 and C2). The ability of the technique to suppress other shadow features, apart from cloud shadows, is also seen in the reduction in intra-canopy shadowing evident in Figure 8-11 which enlarges the area of woodland outlined in Figure 8-8a. The technique was less effective for Rural Site 2 because the image was dominated by vegetation and it was therefore difficult to define a precise soil line, but the result was still a significant visual improvement on the uncorrected data.

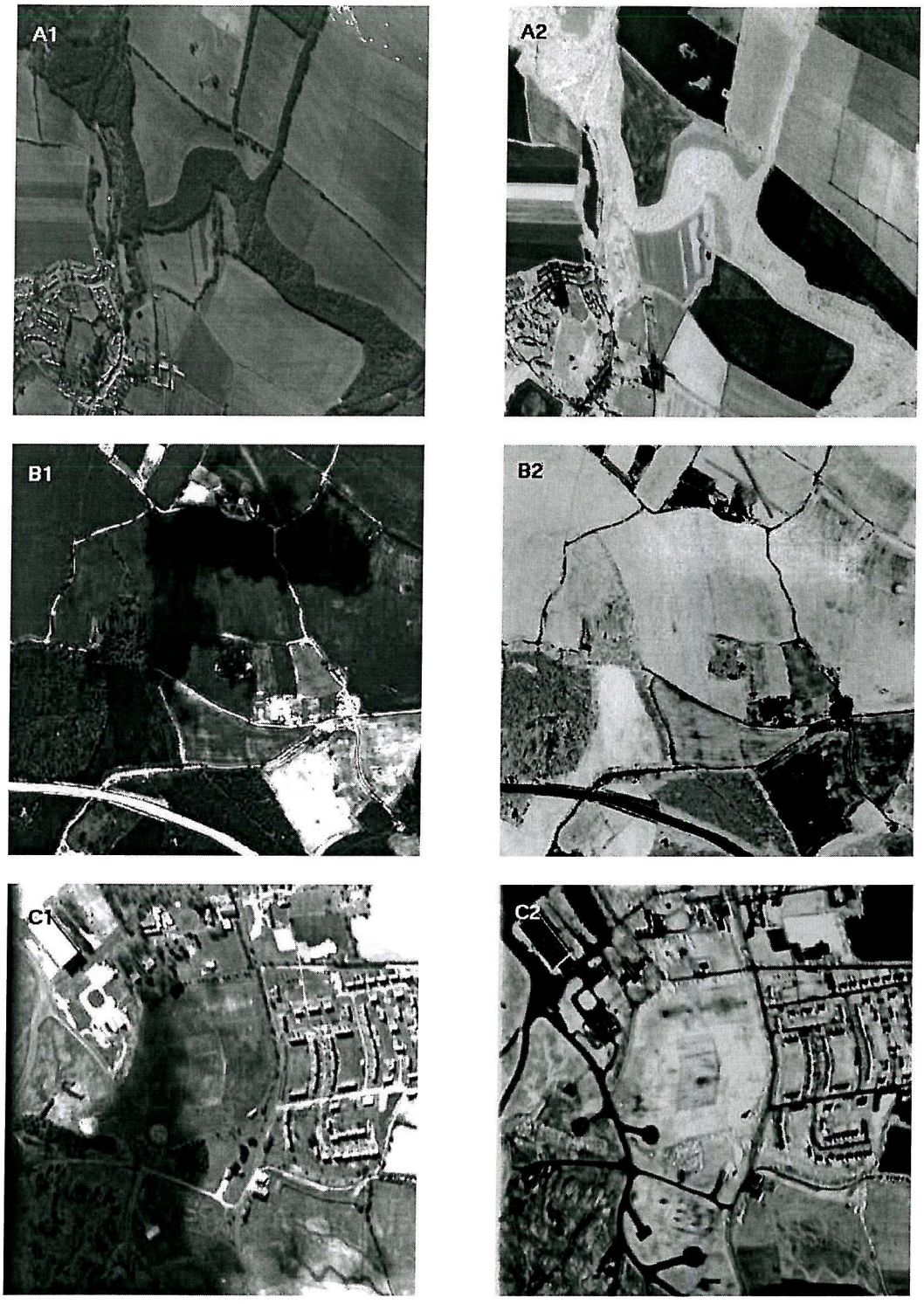

Figure 8-12. Left-hand side shows ATM thermal band for Rural Site 1 (A1); ATM red band for Rural Site 2 (B1); CASI red band for Coast Site 1 (C1). Right-hand side shows OCVI images for the same areas (A2, B2 and C2).

8.4.3. Shadows in *n*-dimensional space

The efficient shadow suppression in 2-dimensional feature space by using the DPVE alignment suggests that a simple technique could be useful for vegetation survey and land cover mapping under various sky conditions. The technique does not rely on any ground data or detailed knowledge of the area and is readily adapted for use with any calibrated multispectral sensor. It was hypothesised that the DPVE correction attributes could be used to convert radiance values of a scene to truly apparent reflectance values or standardised radiance values. The apparent spectral values are often measured at ground level and remove the atmospheric effect, especially an additive effect of path radiance that would otherwise give erroneous spectral reflectance values. The first objective of DPVE in *n*-dimensional space is to see if there is any relationship between DPVE and atmospheric effects. And the second is to see whether a linear change in illumination can also be applied to *n*-dimensional space, as well as to determine if a DPVE exists in *n*-dimensional space.

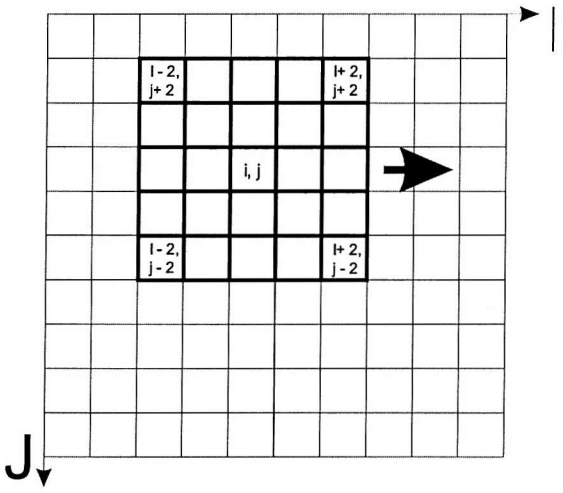

Figure 8-13. Overlapping moving windows for moving summary statistics.

In the previous section, DPVE in 2-D feature space was determined by two steps, defining at least two regions of sunlit/shadow boundaries over uniform surface and applying linear regression lines, i.e. shadow lines, respectively. To extend 2-D DPVE to higher dimension of feature space (where, $n > 3$), whole processing needs to be automatic because of the following reasons. First, finding DPVE is becoming difficult by using a simple plot of data cloud, as shown in Figure 8-8. As data visualisation in high dimension is very difficult, more

generalised sunlit/shadow decision method is required. Second, minimum number of sunlit/shadow regions should be greater or equal than number of multispectral bands. For example, at least two shadow lines are necessary for DPVE in 2-D feature space. Therefore, DPVE method for *n*-D feature space uses more efficient approaches to find a point where all the linear regression lines from the boundary areas pass in *n*-dimensional space.

The procedure is designed to select sunlit/shadow boundary at least in a semi-automatic way, as the visual decision of the boundary ROIs in a scene becomes increasingly difficult with increasing spectral dimensionality, i.e. number of bands. In order to find the ROIs of sunlit and shadow boundary, a moving window technique was used, this scans through whole scene with an appropriate sized ROI (Figure 8-13). The moving window is widely used to investigate summary statistics in geostatistics (e.g. Isaaks and Srivastava, 1989), spectral mixing (e.g. Mather, 1999) and image processing (e.g. Castleman, 1996). The size of the segment window varies depending on the spatial pixel resolution and mean area of interest: in this case, the size of sunlit/shadow boundary. After several test runs of the model, a 5×5 pixel square window was determined as the most appropriate for the sample images. For thorough scanning, the window is overlapped while scanning through the entire image.

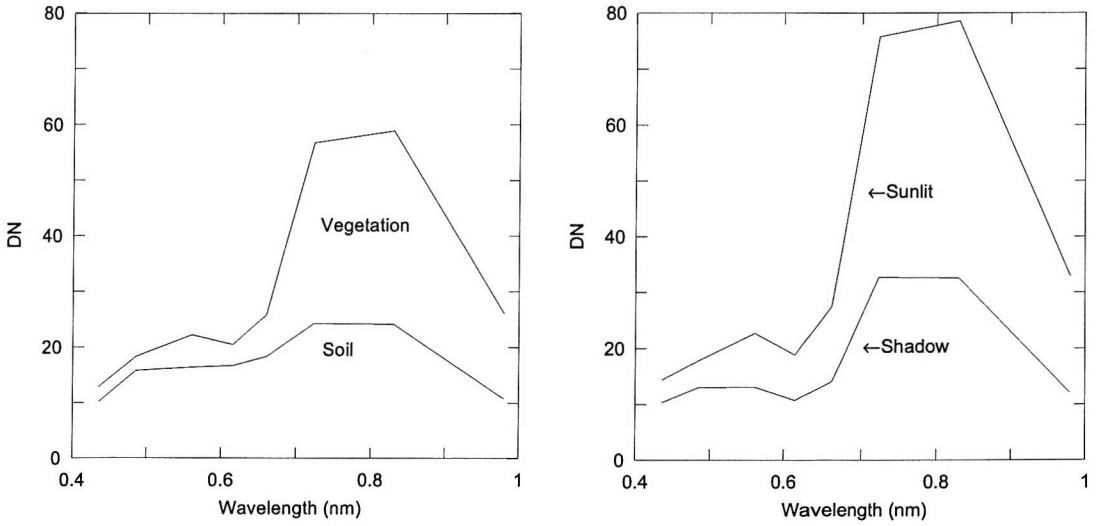

Figure 8-14. Comparison of spectra between spectrally mixing ROI (a) and sunlit/shadow boundary (b).

During each scan of 5×5 pixels, a total of 25 spectral values are compared in order to determine if the group of pixels represents a sunlit/shadow boundary. Despite its relatively small size, sunlit/shadow boundary selection considers not only spatial variations in the group

of pixels but also spectral variations. One of the challenges for this task is that, using available wavebands, illumination changes over a uniform ground target should be effectively distinguished from those due to the target brightness changes, such as a boundary between wet and dry soils (Figure 8-14). An instant decision could be made using visual interpretation as surrounding textual information could be considered, however, this would be a time consuming process, especially when there are a large number of pixels in an image. When using a computer programming algorithm, more detailed information might be necessary to get satisfactory results. The hypothesis of linear behaviour of illumination changes in spectral feature space, which was shown in Chapter 7, is necessarily extended in *n*-dimensional space. The data points will align linearly in *n*-dimensional space if a group of selected pixels (after sensor's radiometric calibration) are a sunlit/shadow boundary over uniform surface, otherwise a rather scattered trend is evident. Multiple linear regression lines were initially applied, but these failed to recognise sunlit/shadow boundary. The reason for this was that goodness-of-fit test of the multiple regression was not able to distinguish between the area with different target brightness and that of sunlit-shadow.

ROI	No. of pixels	Description
V1	98	Vegetation, shadow in the right half
V2	62	Vegetation, shadow in the left half
B1	317	Bare, randomly distributed shadows
B2	62	Bare, shadow in the upper half, and weak shadow on the left

Table 8-2. Summary information of ROIs from South Downs.

PCA Factors	Eigen values			
	V1	V2	B1	B2
1	*9.909*	*9.933*	*9.751*	*9.955*
2	*0.069*	*0.037*	*0.209*	*0.026*
3	0.017	0.024	0.029	0.012
4	0.003	0.004	0.006	0.005
5	0.001	0.001	0.004	0.001
6	0.001	0.000	0.001	0.001
7	0.000	0.000	0.000	0.000
8	0.000	0.000	0.000	0.000
9	0.000	0.000	0.000	0.000
10	0.000	0.000	0.000	0.000

Table 8-3. The list of loading values resulted from standardised PCA of each ROI defined in Table 8-2.

An alternative statistical method was used: standardised Principal Component Analysis (PCA). It was originally developed to find how many variable factors are affected by radiation change under clear and cloudy skies. Here PCA was expected to separate the effects of illumination changes under shadows from other sources, e.g. bidirectional properties and spatial non-uniformity of the surface. Four regions of interest, assumed to be shadow boundary areas near to T1 and T2 in Figure 8-8a, have been chosen in total from the South Down images in order to test whether PCA picks up sunlit/shadow boundaries (Table 8-2). Each region of interest (ROI) was assumed to be a uniform ground surface with sunlit and shadow being the only variable. Spectral differences between sunlit and shadowed areas vary depending upon the ground surface, and the spectral variations continue through the shadow boundary, i.e. there is a gradual decrease in DN values from sunlit to shadow areas. Using only visual interpretation it is not clear whether the illumination change in 'B1' is caused entirely by shadow or if BRDF is a factor. The PCA results show that there is a high level of confidence that the other 3 ROI are affected entirely by shadow.

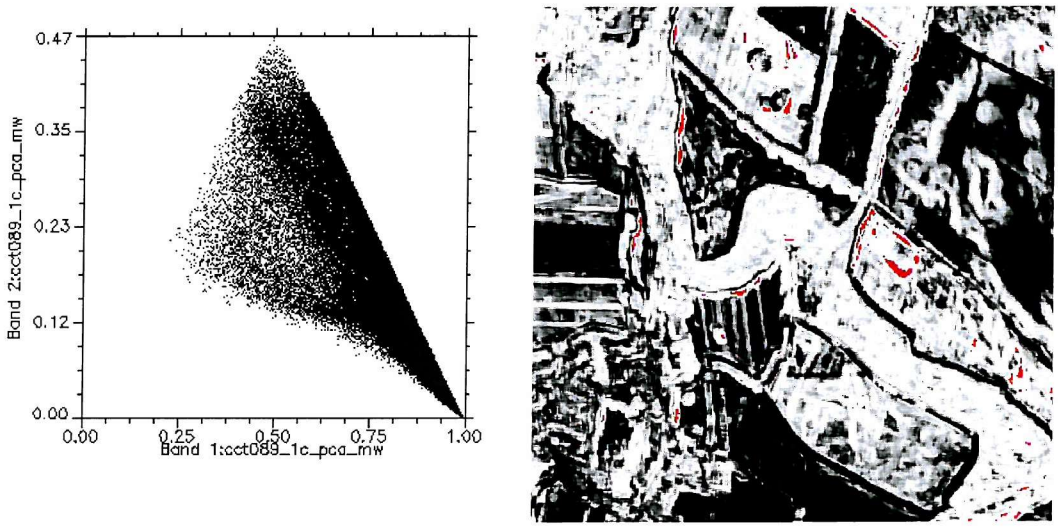

Figure 8-15. First vs. second component plot from result of PCA (a) and Image of first component (b). In (b), ROIs of sunlit and shadow boundary are presented in red.

The Eigenvalues from the standardised PCA indicated that nearly 97 % of variation is in the first component, i.e. dominant of illumination change (Table 8-3), while the area of different target brightness had more or less 80% of variation in the first component. Although PCA does not give 'directional' information within the feature space, it is assumed that such a high value in the first component of PCA can exist only in a SSB over uniform ground surface. The PCA

analysis has proved the most efficient method to determine SSBs in the scene. The following spectral Eigenvectors were small but varied depending on the type of ground targets. It might have been a function of the angular distribution of radiation or of the surface BRDF. However, further investigation will also be required to establish the properties of the shadows within the vegetation canopies.

The first and second components of PCA from overlapped moving windows are dominant in the South Downs image (Figure 8-15a). As the first component is close to 1 (~100 %), the second and the rest of components become nearly none. A value of 90 % or greater in the first component is generally assumed to be in the shadow boundaries. The correct threshold may be decided manually, as it would depend on how large an area was affected by shadows in a scene. 98.7% or more of first component is found to have reasonably well covered shadow boundaries (Figure 8-15b). Overall 980 of ROIs were selected of cloud shadow and geometric shadow boundaries (mainly due to trees and fences). However, it should be noted that the deep cloud shadow in the upper right of the image does not seem to have appropriate shadow boundaries.

With the selected shadow boundary area, the DPVE in n-dimensional space was computed using an overdetermined linear matrix solution, which has more linear equations than unknowns. It is expected to align closely to DPVE. They are expressed as a matrix,

$$A \cdot x = b \qquad [8.3]$$

where A is a matrix of multiple regression coefficient, x is a DPVE in n-dimensional space, and b is a column vector matrix of multiple regression constant. The size of A is $m \times n$: m is the number of ROIs selected and n is the number of bands. Of course, the number of components of b have to be the same as m. Since matrices A and b are results from spectral pixel values, the vector b is expressed as a linear combination of the columns of A in order to have a solution especially when A is not a square matrix, i.e. more matrix elements than is required with respect to the unknown variables. An array inversion ($x = A^{-1}b$) is the simplest approach but involves heavy computations and relatively large round-off errors. Instead, Singular Value Decomposition (SVD) was used to find a solution. The number of selected ROIs, assumed to be in sunlit and shadow boundary over a uniform ground surface, have to be equal or larger than the number of bands. In other words, m has to be larger than n, i.e. the system is overestimated.

A unique solution is impossible in either overestimated or underdetermined systems, although an orthogonally projected or minimal norm solution - minimum length of possible solution - is possible. The solution has the property of minimizing the residual (least-square) error, ε,

$$\varepsilon = \frac{\sum_{i=1}^{m} \sqrt{\left(b_i - \sum_{j=1}^{n} A_{i,j} x_j \right)^2}}{m} \qquad [8.4]$$

In order to achieve the smallest error value, the selected ROIs have to have only illumination change over uniform ground surface, and they should be as many as possible for greater statistical confidence (i.e. there should be at least as many as the number of bands of the image). The result from the SVD produces n-dimensional DPVE with an error, ε, of 0.12 [*DN*].

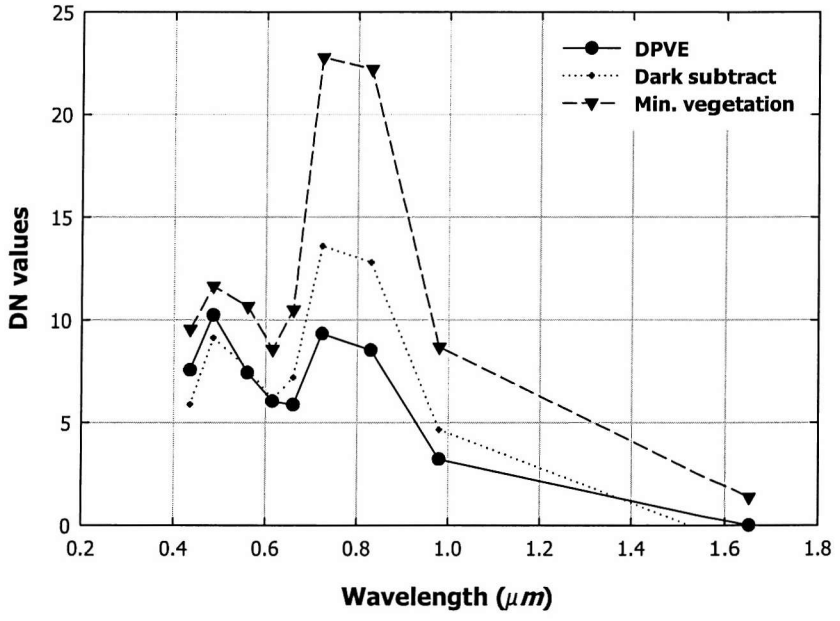

Figure 8-16. Comparison of multispectral DPVE, minimum pixel values for dark subtraction (using ENVI), and dense dark vegetation in ATM bands between 1 and 9. The negative DN value at band 9 for dark subtraction may be due to the sensor calibration error.

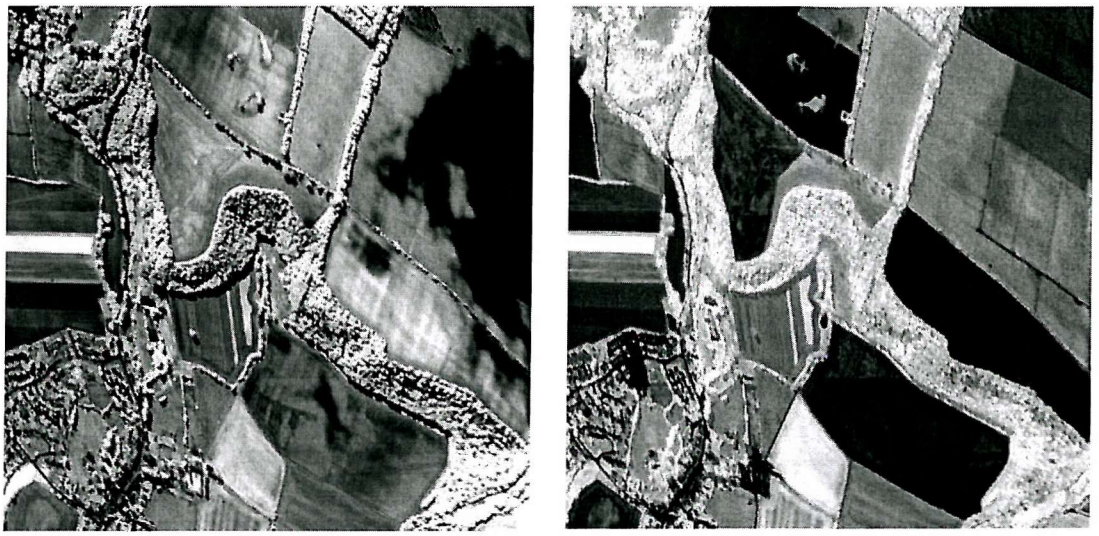

Figure 8-17. Uncorrected ARVI (a) and dark subtracted SAM (b)

As defined earlier, the multispectral DPVE from SVD is also darker, i.e. smaller, than any other image based standardisation methods using dark values in a scene. Figure 8-16 illustrates the comparison of DPVE with the minimum pixel values for dark subtraction and with the manually chosen dense dark vegetation (DDV) for atmospheric resistant vegetation index (ARVI, developed by Kaufman and Tanré, 1992). The DPVE in short wavelengths is slightly greater than the spectrum for dark subtraction, which is probably due to relatively small variations of pixel values under the range of illumination change. The processed images with the reference spectra applied are shown in Figure 8-17. Shadows in dark subtracted SAM image remain the same as in the uncorrected one. There is a slight improvement in shadow suppression in the uncorrected ARVI compared to the uncorrected SAM, although there are still traces of shadows in the ARVI image.

The *n*-dimensional DPVE corrected SAM shows quite similar results to the one in Section 8.4.2 (Figure 8-17b). They are not identical, however, because *n*-dimensional SAM has more dimensionality to measuring spectral angles than 2-dimensional space. The plot of DPVE, Figure 8-16, has an impression of typical atmospheric path radiance (Campbell, 1996), though with some irregularity.

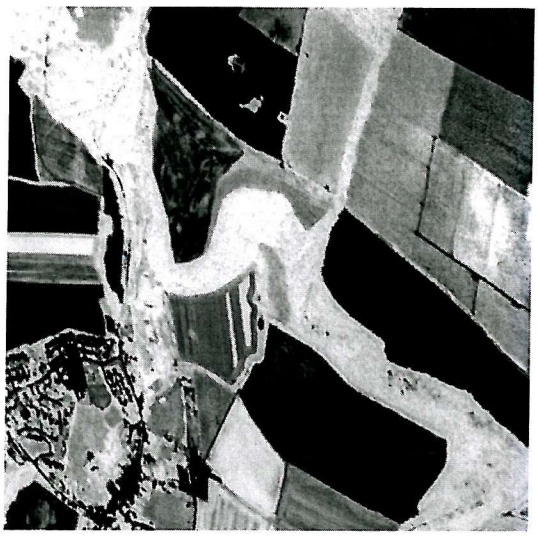

Figure 8-18. *n*-dimensional DPVE corrected SAM.

8.5. Summary

For conventional image-based atmospheric correction (or normalisation) methods, dark ground PIF targets have been widely used, as they normally represents the magnitude of atmospheric aerosol scattering without much effect from the target spectrum signature (Schott, 1988; Fraser and Kaufman, 1985). This dark surface correction has been used as an alternative method when ground measurements were not available. However, it may not be considered as a true operational image calibration method, because an appropriate dark surface does not always exist in a scene and because the quality of the results is highly dependent on how well the signal from the target area represents the pure atmospheric conditions (Moran *et al.*, 2001). Examples of the most favourable dark targets are deep water bodies, (such as a lake or sea water), asphalt, and dense dark vegetation (DDV).

Scene shadows are often used as a dark area in an image. Shadow appears when incident radiation is blocked by other objects, while the path between the target and sensor is not. Although there are many types and sources of shadows in nature, they can generally be grouped into two categories in terms of source: geometric and ephemeral shadow. Geometric shadow is generally caused by fixed objects on the ground, e.g. trees or leaves, topographic changes, or buildings, whereas ephemeral shadow is caused by unexpectedly changing atmospheric conditions, i.e. cloud as a form of dense water vapour in the atmosphere. Studies considering the difficulties of acquiring suitable RS data have highlighted cloud and cloud shadow as the major constraint – this is especially true in mid-latitude regions (Gastellu-Etchegorry, 1988; Cushnie, 1988; Legg, 1991; Fuller *et al.*, 1994; Marshall *et al.*, 1994; Read, 1999).

The appearance of scene shadow is frequently related to the errors in spectral, spatial, and temporal applications of multispectral remote sensing. In shaded areas in a scene textual and spectral information is often altered, while a human interpreter may be able to take this into consideration most computer based image processing algorithms will not be capable of distinguishing this. There have been several attempts to overcome these shadow problems: image fusion from the same type of sensor (Wang *et al.*, 1999) or from a different type of sensor (Nezry *et al.*, 1993; Hegarat-Mascle *et al.*, 1997), geometric segmentation (Simpson and Stitt, 1998), geostatistical interpolation (Rossi *et al.*, 1994), and colour space transformation (Liu and

Moore, 1990 and 1993). In most RS literature, scene shadows have been considered as dark masked regions, and have simply been abandoned or increased in pixel brightness to visually match the neighbouring area. These mostly cosmetic approaches may have improved the images visually, but could have increased uncertainties in the biophysical quantitative image analysis.

While most conventional shadow suppressions are focused on cosmetic improvement within the shadow, the first meaningful investigations of scene shadow were conducted by Piech and Walker (1974) and Piech *et al.* (1978). They took advantage of shadows as an important source of parameters for atmospheric correction. A series of ratios of radiative transfer equations between shaded areas and adjacent sunlit areas were theoretically, supposed from a straight line, with slope and intercept representing atmospheric path radiance at the time of image acquisition. Assuming that a pair of SSB areas from two different uniform targets was selected, the ratio reduces the dependency of target leaving radiance. The accuracy of atmospheric correction using scene shadows was improved using a hybrid RT-model, i.e. information from the shadow area provided input parameters for this RT-model (Reinersman *et al.*, 1998). The method was applied to seawater; the part of the image covered by cloud shadow, the adjacent areas were assumed to be spatially uniform. The results showed that the use of information in the scene shadows contributed to the atmospheric correction method and that it was especially suitable for applications requiring high accuracy output, such as sensor calibration.

It is interesting to note that conventional shadow suppression methods using feature space transformation only produce best results in semi-arid or non-vegetated areas. The transformation techniques developed by Liu and Moore (1990 and 1993) are identical to the feature space classification, SAM, originally developed for geological surveys, but with different spectral dimensions. Investigation of two-dimensional scatter plots of sunlit/shadow ROIs in the scene showed that the failure of shadow suppression in vegetated area was related to the position of DPVE, introduced in Chapter 7. The new DPVE for shadow suppression is in a rather different position to that shown in the previous chapter. This indicated that the addition of an atmospheric path radiance term might have resulted in the movement of the DPVE in feature space, and that in turn, the atmospheric effects in the image could be corrected using scene shadows.

The DPVE corrected vegetation index, OCVI, demonstrated that in various RS sensors and different spectral bandset, the decreased pixel values of a conventional vegetation index in shade areas disappeared over both soil and vegetation regions and that the image textures from OCVI were similar to the images in thermal band (in ATM sensor). Also, more importantly, shadows in vegetation canopies seemed to be minimised in OCVI.

The successful test of the relationship between the DPVE and the scene shadows led to the extension of the concept to higher dimensional image data. A semi-automatic shadow boundary selection method was developed in order to efficiently find as many shadow boundaries as possible. In fact, for overestimated linear systems (which generally give better results), a larger number of shadow boundaries are required than the size of the spectral dimension of the image. SVD computation using the selected shadow boundaries resulted in vegetation-spectrum-like DPVE values with a reasonable least-square error. Possible sources of error were non-uniform target materials and/or different viewing angles of each shadow boundary. The multispectral DPVE corrected SAM showed very similar results to OCVI (and even ARVI) with minimal shadow effects. The multispectral DPVE, as defined in Chapter 7, was darker than any other dark spectrum found in the image, while the overall spectrum shape was similar to that of vegetation.

Since this work was completed, a similar study of a reflectance correction algorithm using scene shadow, has been reported Portigal (2002). The shadow endmember, DPVE, was selected directly from the minimum shaded region of the scene, and it was subtracted before running the MODTRAN radiative transfer model to make the image spatially uniform with direct solar illumination, i.e. shadow-free. However, this method is susceptible to the particular shadow types in the scene. As an improvement, Adler-Golden *et al.* (2002) developed an iterative de-shadowing method. They applied a MODTRAN based RT-model prior to the actual shadow removal. Normally RT-models remove atmospheric path radiance, which is an additive parameter between the target and the sensor, and the scene shadows are dealt with separately. Both de-shadowing methods, Adler-Golden *et al.* (2002) and the DPVE method outlined here, remove scene shadows effectively from spectral mixing analysis (or similar type of feature space based method). DPVE could be the all-in-one solution for atmospheric correction of multispectral images in the absence of simultaneous ground data.

Chapter 9

Ancillary measurement based method: At-sensor downwelling irradiance

9.1. Introduction

One of the main benefits of airborne sensors is that they can be deployed at short notice to gather data on episodic or catastrophic events such as floods or pollution incidents. Inevitably, this often means acquiring data under partial or complete cloud cover, and standardisation of such data can be very difficult, leading to problems identifying suitable training sites for multispectral classification. Even if the sky conditions are perfect, there can be major differences between data collected on different flightlines if these vary in direction relative to the Sun, or if a large area is being surveyed. For these reasons, some form of standardisation between flightlines is normally attempted before classification.

A number of aircraft sensors have the facility to measure spectral downwelling irradiance using a sensor mounted on the roof of the aircraft. Application of at-sensor irradiance measurement with airborne imaging RS system is a feasible approach to overcome the operational limitations of airborne RS applications. A properly validated Incident Light Sensor (ILS) could play an important role in airborne RS, through the providing of additional information for image standardisation, and also as a means of monitoring atmospheric conditions, thereby improving the quality of the output image.

To date, these data are rarely used for atmospheric correction. Part of the problem is that the attitude of the airborne platform is always changing during data collection, even under moderately stable flight conditions, so that direct use of such data often introduces errors in the standardisation of atmospheric effects in remotely sensed images. Also, simplistic or unsuitable assumptions of sky conditions have prevented retrieval of sufficient information for

improvement of data quality. Several conventional attempts to use the ancillary measurements were reviewed and their usability and constraints were also discussed in Section 6.4.1.3.

In the CASI system, the incident light sensor (ILS) is a cosine-corrected receptor fitted horizontally in the roof of the aircraft. The sensor head is connected to the CASI via an optical fibre. Light from the ILS is imaged onto the hidden section of a two-dimensional CCD array, and recorded in spectral bands identical to those from the scene viewed by the CASI. With the CASI configured in spatial mode, the ILS data are recorded in column 512 in each line of image data. The data from the ILS are strongly affected by the direction of flight relative to the Sun, i.e. in flightlines away from the Sun ILS values are greater than those in opposite direction due to the nature of aircraft flight (nose up to maintain flight altitude).

The continual motion of the ILS is used to advantage here, as a means to fit a sky radiance distribution model developed by Brunger and Hooper (1993) to data from the Itres Instruments CASI ILS. The inclination of the ILS sensor, due to changing aircraft attitude, is considered as the slope plane in the model. The selected model coefficients correspond to parameterised atmospheric conditions and represent atmospheric transmission and the proportion of direct-to-diffuse flux.

Prior to employment of the model in enhancing usability of at-sensor incident irradiance, the following sections provide background information of the model development. This is based on the CASI-2 ILS, the characteristics of which were tested in Chapter 5. The synchronisation of the spectral irradiance data from the ILS with positional information of the airborne platform is described in detail before introducing and testing several sky irradiance models.

9.2. Attitude correction of the ILS

The continuously changing position of the ILS is directly affected by the unstable operation of an airborne platform, since it is mounted on top of the aircraft. Inevitably, the ILS is tilting with respect to the horizontal plane. This means that at any one time only a part of cosine receptor receives downwelling irradiance; leading to problems in usability of ILS data. Figure 9-1 shows a typical ILS data set and aircraft attitude records under fairly normal flight conditions. Pitch angle was consistently positive with an average of around less than 3° (aircraft fly nose-up in order to maintain speed and altitude), and the variation of roll angle was within ± 10° of horizontal. In addition to relatively slight changes of the flight heading (yaw), the overall flight attitude records show that there was no serious atmospheric turbulence. However, the ILS records show significant fluctuations throughout the flight line, and the variation is not often associated with the sky conditions above the atmosphere at the time of the flight. It is noticeable that in this particular example the first half of the record seems to have an inverse relationship with the aircraft's roll motion, while the rest of the data may represent an unstable atmospheric condition.

The aircraft motion is one of the most obvious reasons for defects in at-sensor irradiance measurement, unless the probe is mounted with an active gyro system that instantaneously corrects its position as if it was on a horizontal surface. The signals received by a cosine receptor on a tilted platform decrease available area of sky dome. In other words, the sensor's view region below horizontal plane, as a result of the sensor tilting, is no longer the downwelling signal. This results in different solar angles with respect to the probe and the signal changes. For example, if the cosine receptor is tilted toward the solar position, the magnitude of irradiance increases due to closer nadir Sun angle with respect to the probe, whereas it tends to reduce in the opposite direction.

Using data from the accurate on-board navigation system, which is common for most airborne RS platforms, means that the geometric offset above can be resolved relatively easily with several steps of calculations. In this section, the positional problem is approached mainly as two different problems: verifying the instantaneous position of the ILS and calculating the relative Sun angle (Figure 9-2). Finally, these are combined to yield accurate Sun-sensor geometry in respect of the inclination of the platform.

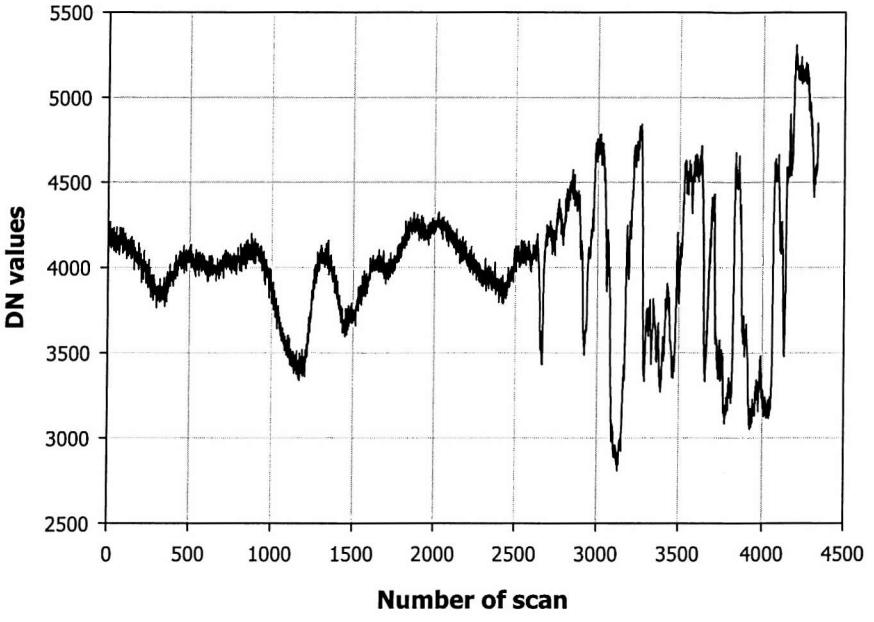

(a)

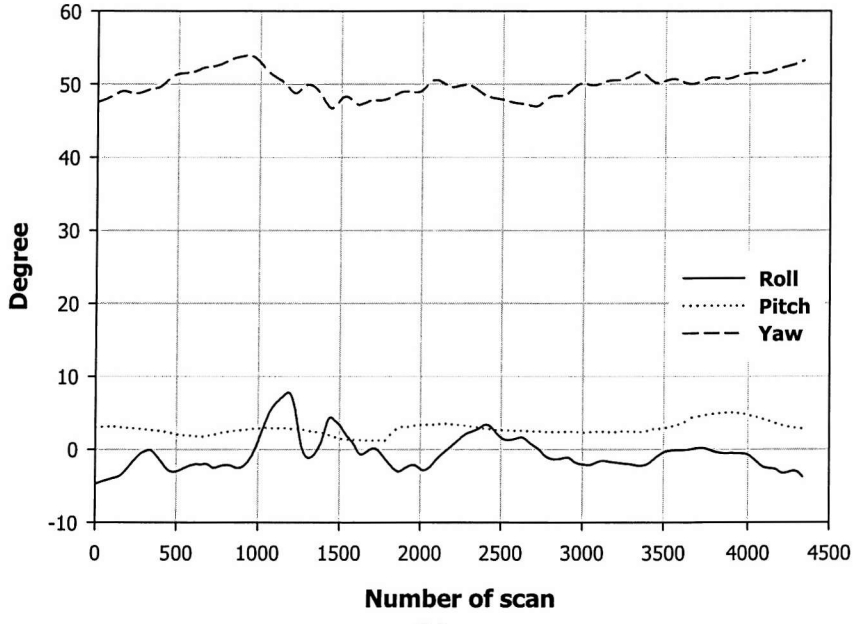

(b)

Figure 9-1. An example dataset of ILS (a) and fight attitude records (b). The ILS plot is band 5 out of 13 spectral band set. The data (ref. Imag5143) provided by the UK Environmental Agency were acquired on 25 August 2001, 11:05 GMT, over Coventry Airport (at 435254, 2742968 of the UK National Grid).

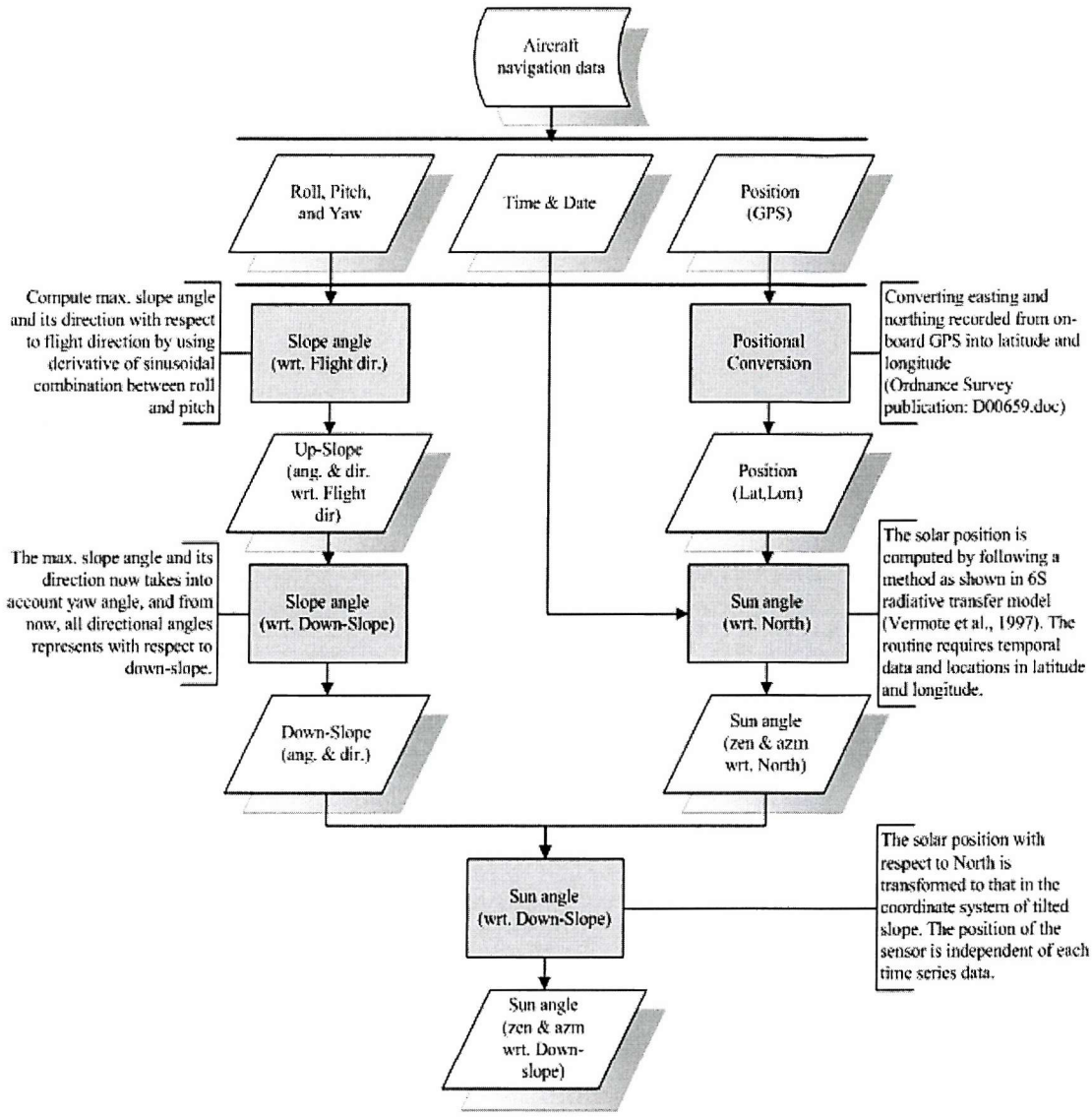

Figure 9-2. Schematic diagram of ILS attitude correction algorithm described in this section.

9.2.1. Attitude and navigation records: An example

The example data set presented in this section were provided by the UK Environment Agency (EA). The flight attitude data was provided by highly accurate POS/AV (Position and Orientation Solutions for Airborne Surveying and Remote Sensing), since the EA operates, as well as CASI-2, an airborne optical laser scanner (LIDAR) to measure the distance from the aircraft to the ground with higher than several centimetres precision. For real time measurements, the sampling rate of POS/AV is usually greater than that of the image scanning. Thus interpolation (rather than extrapolation) of the positional data results in a better quality, e.g. angles of attitude change with a precision of 1×10^{-4} degrees and the navigational data at least $1\times10^{-3}\,m$.

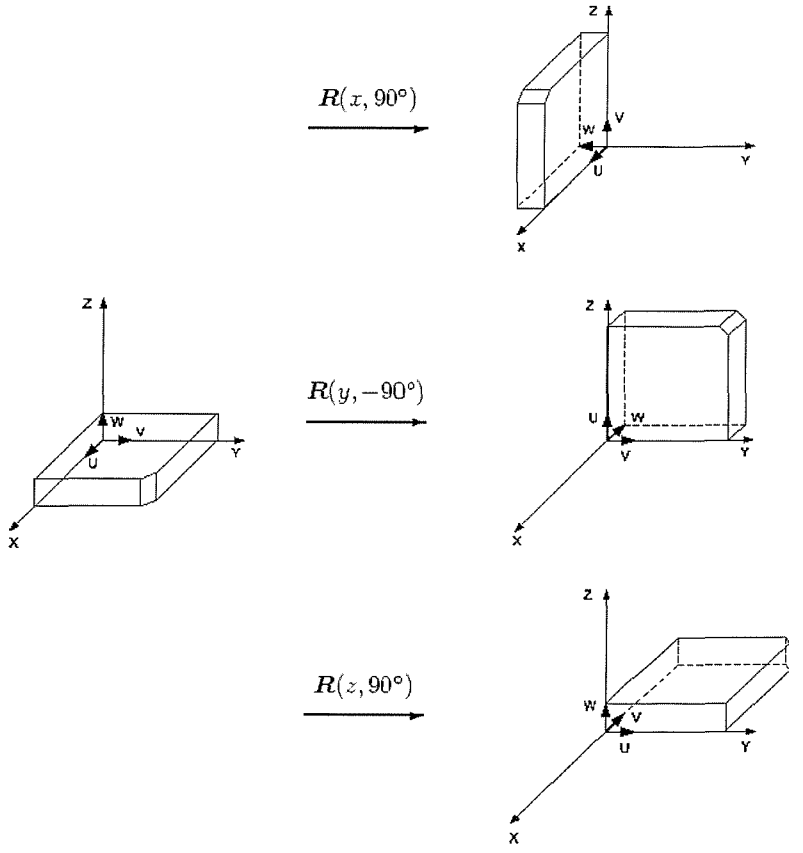

Figure 9-3. Base rotations of angle for aircraft attitudes.

R(x): Roll
R(y): Pitch
R(z): Yaw

The attitude data has rotating angles in the Cartesian coordinate system (x, y, and z-axis), where the flight direction is set by the *x*-axis (Figure 9-3). Each rotational component among three orthogonal axes is shown in angle of degree based on a fixed reference coordinate system. Roll is an angle in the *x*-axis in Figure 9-3, the deviation from level in the side-to-side axis. Positive roll, in this particular example, indicates a left tilt of aircraft with the left wing dropping below horizontal and the right wing rising above horizontal. Pitch is the slope of the aircraft in the nose-to-tail, y-axis. It is controlled mainly by variation of flight speed. Lastly, yaw is the rotational angle of the aircraft representing the *z*-axis. The combination of these can describe the aircraft position during the flight.

9.2.2. The Sun angle

The structure of the navigation data used by the UK Environment Agency consists of three components, the aircraft attitude, positional data recorded by on-board GPS in OSGB36 format (UK National Grid in metres), and the date and time of the flight. The sequence of the data are synchronised with the scanning lines of imagery from CASI-2, i.e. the number of data in the navigation file corresponds to those in the CASI image.

9.2.2.1. Flight navigation

Since the position of the flight over the Earth is a significant input for calculation of the Sun angle, the recorded GPS data are converted into latitude and longitude angles. The calculations are based upon data in 'A Guide to coordinate systems in Great Britain: An introduction to mapping coordinate systems and the use of GPS datasets with Ordnance Survey mapping', a report published by the UK Ordnance Survey (2001).

9.2.2.2. Computation of the solar angle

As the main purpose is to find solar positions relative to the aircraft attitude, there are two parallel procedures which are merged at the end. The first part involves calculating the Sun position with respect to North. A number of different routines were considered, but for reliability, the routine is derived from a subroutine (*Possol.for*) contained within the 6S RT

model (Vermote *et al.*, 1997), and re-coded for Mathcad. This computes the solar azimuthal and zenithal angles (in degrees) for a point over the globe defined by its longitude and its latitude (in decimal degrees) for a day of the year (fixed by number of the month and number of the day in the month) at any GMT.

9.2.3. Instantaneous ILS position

While the position and orientation of the aircraft are represented in a right-hand Cartesian coordinate system with three mutually orthogonal unit vectors, these cannot describe the actual slope of the ILS sensor. Moreover, since this coordinate system is referenced with respect to the instantaneous flightline, its position in a relatively larger stationary coordinate, such as the Earth's spherical coordinate system, keeps changing in each scan of the navigation record. Imagine a circular disk able to tilt in arbitrary direction and angle and its position is expressed only by roll, pitch, and yaw angles (see Figure 9-4). If both roll and pitch angles are positive as shown in the figure, for example, the maximum gradient of the disk appears in the first quarter of the circle with respect to looking down from the top of the zenith. The magnitude of the zenith angle of the slope top as a result of the motion is a combination of three attitude compositions.

Thus, coordinate transform, i.e. from the Cartesian to the sphere coordinate, is necessary, because our main interest here is the instantaneous maximum slope of ILS and its azimuthal angle with respect to either North or the flight direction. The conventional matrix based transformation, known as the collinearity equation, is widely used. This method is however inconvenient for our purpose since it produces negative angles depending on the quarterly azimuthal position (range from –90° to 90°).

The following subsections will describe a newly developed simple transformation method that uses derivatives of roll and pitch angles. This method is computationally efficient and provides continuous azimuthal angles, i.e. from 0° to 360°, which would be more convenient for comparison with the solar angle.

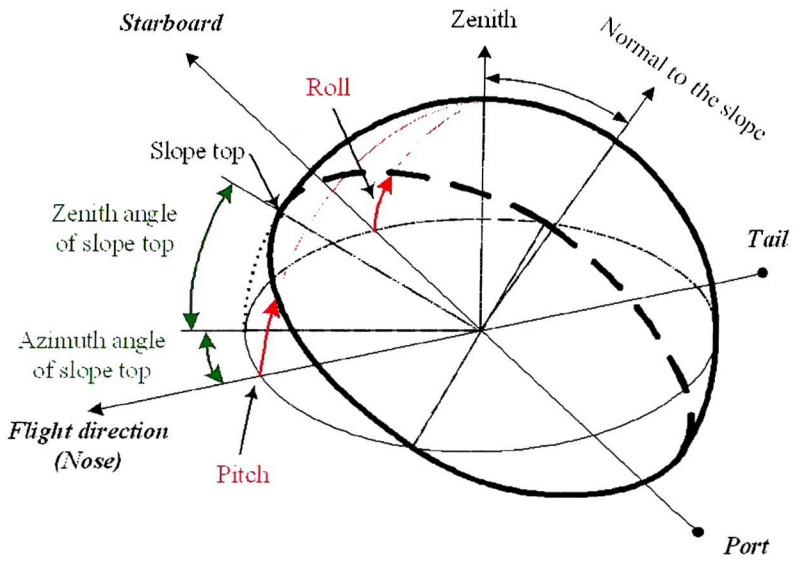

Figure 9-4. A schematic diagram of ILS position with respect to the aircraft attitude.

9.2.3.1. The maximum slope (zenith angle) of the ILS

The pitch angle is measured parallel to the axis of the aircraft motion, whereas the roll angle is cross axis to the flight direction. In other words, pitch and roll have a phase difference of 90 degree (Figure 9-4). The slope of the ILS at any point of azimuth angle is expressed by a trigonometric equation (amplitude of sine or cosine curve is corresponding pitch or roll angle). Figure 9-5 shows examples of slopes at any angular position of ILS with a certain pitch and roll angle, +10° and -5° respectively. The pitch angle (+10°) appears on the flight heading (an azimuth angle of 0°), and gradually decreases as it is away from it until its minimum at opposite direction (180°). On the other hand, the given roll angle (-5°) is shown 90° clockwise from the flight direction (if the positive value represents the right wing up) and has 180° phase for its opposed value. Therefore, slope from pitch angle is represented by a sine curve, whereas that from roll is a cosine.

The slope of the ILS probe is associated with both pitch and roll angles. Hence the ILS slope at any azimuthal point is represented by a sum of trigonometric functions with pitch and roll values,

$$\beta = \theta_r \cdot \cos(\phi) + \theta_p \cdot \sin(\phi) \qquad [9.1]$$

where, β Angle of slope due to the motion of aircraft [*degree*]
ϕ An arbitrary azimuthal point, between 0~360° [d*egree*]
θ_r Roll angle [d*egree*]
θ_p Pitch angle [d*egree*]

A sum of pitch and roll for azimuth angle provides the angle β (the thick solid curve in Figure 9-5). From the example values, a maximum slope of 11.18° appears at an azimuth angle of 333.50° (around 11 o'clock direction with respect to the flight heading).

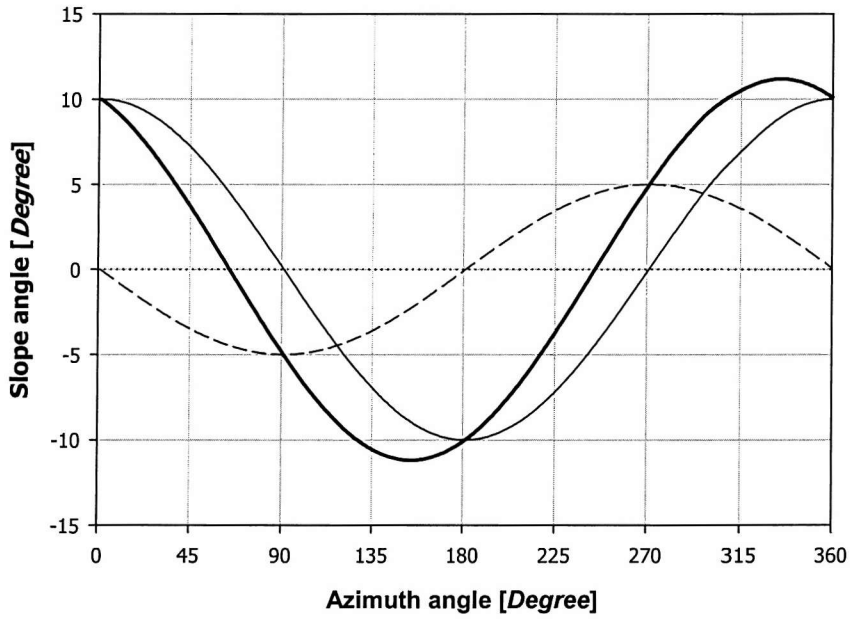

Figure 9-5. Slope angles surrounding edge of the ILS probe. Azimuthal angle is set to zero in flight direction. The angle created by pitch motion is shown by the thin solid line, whereas the dotted line is roll. The thick solid line represents the slope combined with pitch and roll.

9.2.3.2. Azimuthal angle of the ILS slope

The azimuth angle of the maximum slope of ILS in the previous section can only be found using a lookup table that is an array of α with a full range of azimuth angles (θ). This could be rather impractical and result in inaccurate azimuth angle of the slope since it depends on the intervals of θ, so a more efficient way is to use derivatives of Equation [9.1], this is expressed by,

$$\beta' = \frac{d\alpha}{d\theta} = -\theta_r \cdot \sin(\theta) + \theta_p \cdot \cos(\theta) \qquad [9.2]$$

As the derivative represents the gradient of its original curve, it will become zero when the sinusoidal curve reaches its peak or trough. According to the example angles used earlier, the derivative plot of the slope angle of ILS as a function of azimuthal angle is shown in Figure 9-6. As expected, the azimuthal angle at maximum or minimum value of the ILS slope has zeros in its derivative curve, while the transient points where the signal changes (negative or positive) of the ILS slope show the maximum absolute derivative values. Therefore for the azimuth angle for the maximum slope angle, set $\beta' = 0$ and this can be written as Equation [9.2],

$$\alpha = \tan^{-1}\left(\frac{\theta_p}{\theta_r}\right) \qquad [9.3]$$

where, α Azimuth angle at the maximum slope angle [*degree*]

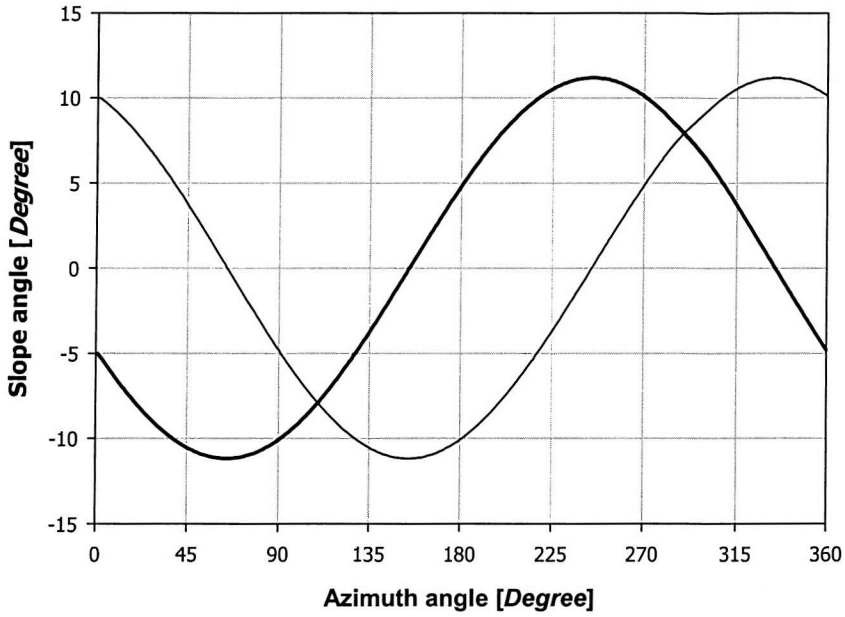

Figure 9-6. The comparison between the ILS slope due to aircraft motion (as shown in Figure 9-5) and its derivative, i.e. azimuth angle of the maximum slope.

9.2.3.3. Absolute slope position with real data

The above methods for the slope angle of ILS were applied to the real records of flight attitude shown in Figure 9-1. In order to improve efficiency of computational time, the azimuth angle of the maximum slope α from Equation [9.3] was substituted into Equation [9.1] for the slope angle.

The slope direction (azimuth slope) was set to the flight heading and its positive value meant that the maximum slope was placed on the right hand side of the flight direction and *vice versa*. The variation of the slope direction is much greater than that from pitch or roll records (Figure 9-7). The range of the variation is from -60° to +70° throughout the data scan. Such variation indicates that even under ordinary flight conditions the horizontal position of ILS changes dramatically.

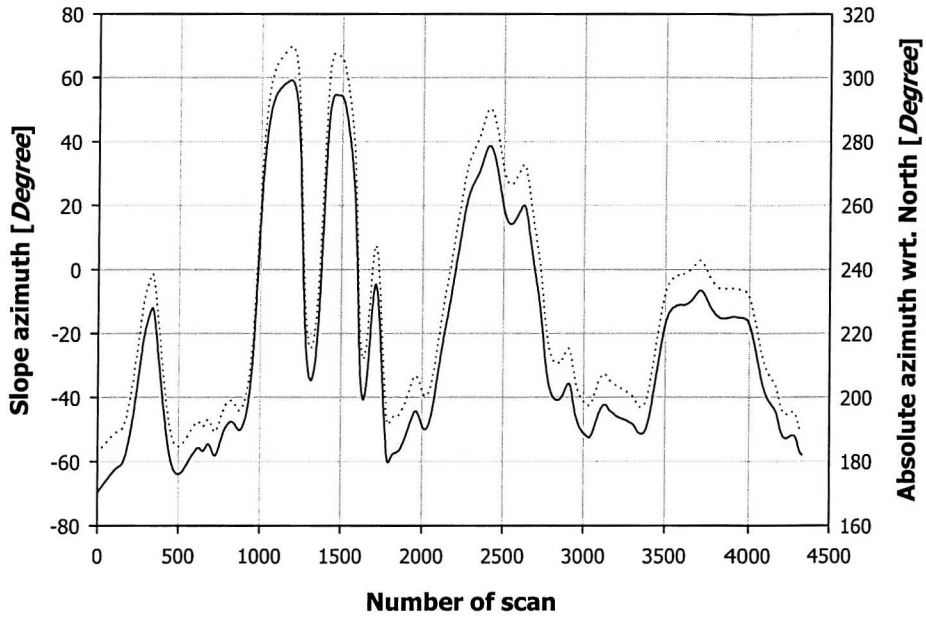

Figure 9-7. The maximum slope position of ILS (azimuth angle) along with the flight. The azimuth angle with respect to the flight heading is illustrated by the dotted line, and its direction from North is shown by the solid line.

The direction (azimuth angle) of the ILS slope should be considered with respect to North, in order to compare it with the solar angle. As slope angle, β, from Equation [9.1] is computed only by pitch and roll records with respect to the flight direction, the flight heading variation (i.e. yaw) is to be taken into account as follows,

$$\alpha_N = \alpha + \theta_y + 180 \qquad [9.4]$$

where, α_N Absolute slope direction of ILS with respect to North [*degree*]
θ_y Yaw angle [d*egree*]

With the conditions,

$$\begin{aligned} &if\ \alpha_N \geq 360, \\ &\qquad \alpha_N = \alpha_N - 360 \end{aligned} \qquad [9.5]$$

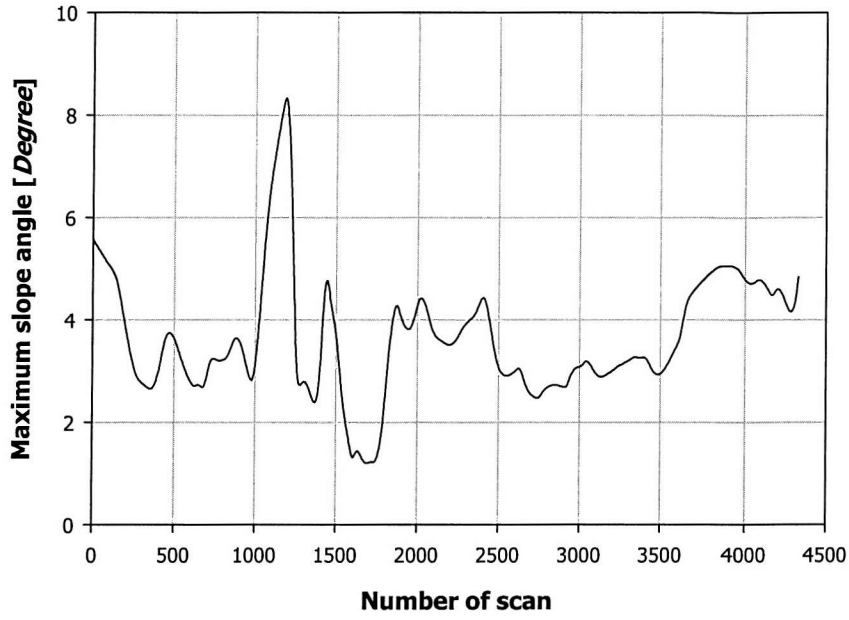

Figure 9-8. The ILS slope due to flight motion.

For later use, Equations [9.4] and [9.5] are used to compute the azimuth angle of the 'minimum' slope, i.e. down-slope direction. The result is compared with the azimuth angle with respect to the flight direction in Figure 9-7.

The maximum slope angle is calculated by substituting the slope direction α in Equation [9.1] (Figure 9-8). While the largest slope angle was just over 8°, the ILS position was always tilted throughout the flight (with a minimum slope of around 1.2°). The plot of the slope is likely to be quite different from any component of the attitude data, it is important to note that attitude records cannot be used directly to estimate the actual slope of the ILS.

9.2.4. The ILS position vs. solar angle

The solar angles found earlier were based on the horizontal plane with respect to North. With regards to the slope surfaces which represent the FOV of the cosine receptor, the relative solar angles are directly associated with the position of the inclined surface as found in the previous section. The conversion processing between a point (θ, ϕ) in horizontal plane and a

point (θ_s, ϕ_s) on an inclined plane is shown in Figure 9-9. The rotation of spherical coordinates tends to be more complicated than in Cartesian coordinates, i.e. simple trigonometric functions in three-dimensional space. In this section, the conventional sphere rotation problem will be introduced and the application of the method for our data will be examined.

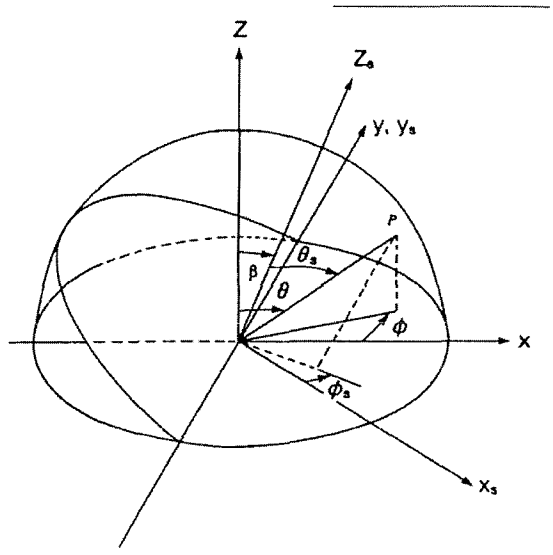

Figure 9-9. Interception of the diffuse radiation by an inclined, south-facing surface (Fig 1. from Siala *et al.*, 1993). θ, an angle between Z and arbitrary position P is measured in the vertical P-Z plane, while θ_s is measured in the inclined P-Z_s plane. ϕ is measured in the horizontal X-Y plane, while ϕ_s is measured in the inclined X_s-Y_s plane. β is measured in the vertical Z-Z_s plane.

9.2.4.1. Solar zenith on an inclined surface

The zenith angle always has its reference as the normal from a horizontal plane. Thus, a new solar zenith is basically an angular distance from the changed reference pointing due to the surface inclination to the original solar position with respect to the horizontal plane. The trigonometric value of the distance is converted into the angular difference between the two points. The relation is expressed by the following equation,

$$\theta_s = \cos^{-1}\left[\sin(\beta)\cdot\cos(\theta_{sun})\cdot\cos(\phi_{sun}-\alpha)+\cos(\beta)\cdot\sin(\theta_{sun})\right] \qquad [9.6]$$

where, θ_s The solar zenith in a slope plane [*degree*]
θ_{sun} The solar zenith in a horizontal plane [*degree*]

ϕ_{sun} The solar azimuth in a horizontal plane [*degree*]

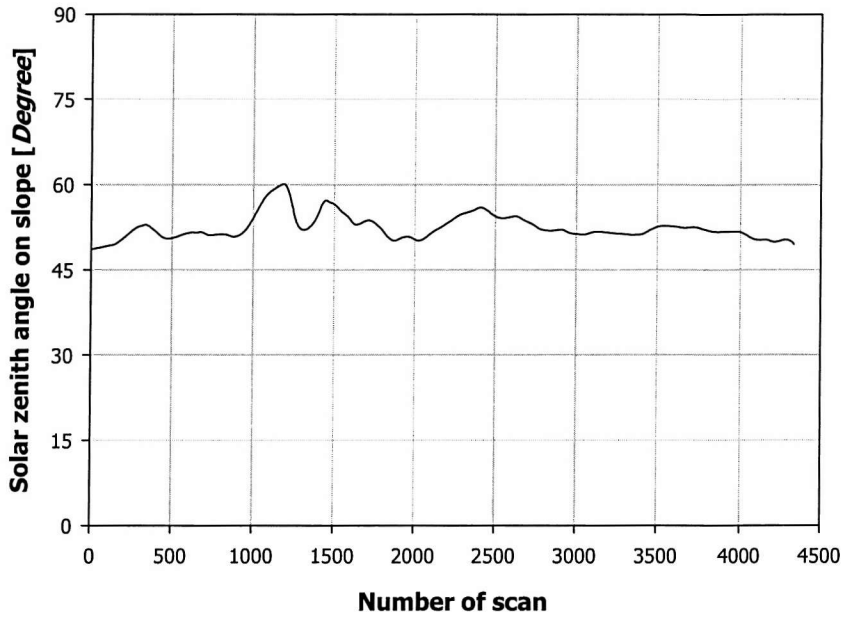

Figure 9-10. Variation of solar zenith angle with respect to the ILS plane, which is continuously moving during the flight.

The above equation was applied to the example dataset (Figure 9-10). The variation shows a range of around ±6°, there is a similar, although not identical, trend as the roll motion (see Figure 9-1), with an average of the mean solar zenith on a horizontal surface. The reason for this is that the roll angle has the greatest variation, the other angles are relatively stable during flight. According to the Equation [9.6], the solar zenith on the slope is mainly a function of the slope direction and its inclination. In this example, the relatively small magnitude and range of variation of the slope angle β results in a greater contribution to the second term of the right hand side of the equation.

9.2.4.2. Solar azimuth on an inclined surface

The simplest way to estimate the solar azimuth is a simple subtraction of the slope direction from the solar azimuth in a horizontal surface, i.e. ϕ - α. This would be true if the slope angle was small and/or greater the solar zenith (low Sun angle). In contrast, the difference

between ϕ and ϕ_s, in Figure 9-9, increases as the solar zenith decreases, i.e. becomes closer to the normal pointing to the surface. When this effect is taken into account, the relationship between the Sun angles on a horizontal surface and those inclined is,

$$\phi_s = \sin^{-1}\left(\frac{\sin(\phi_{sun} - \alpha)\cdot\sin(\theta_{sun})}{\sin(\theta_s)}\right) \quad [9.7]$$

where, ϕ_s The solar azimuth in a slope plane [*degree*]

Figure 9-11 shows the solar azimuth from the example dataset. The results from Equation [9.7] are compared with the ones from the simple subtraction method. There is ±5° or less difference between these outputs in some low Sun angle or solar azimuth angle away from the slope direction. In general, however, there is not much difference between ϕ and ϕ_s, but the slope factor should be considered for solar azimuth computation because of some particular conditions of solar angles with respect to the slope position.

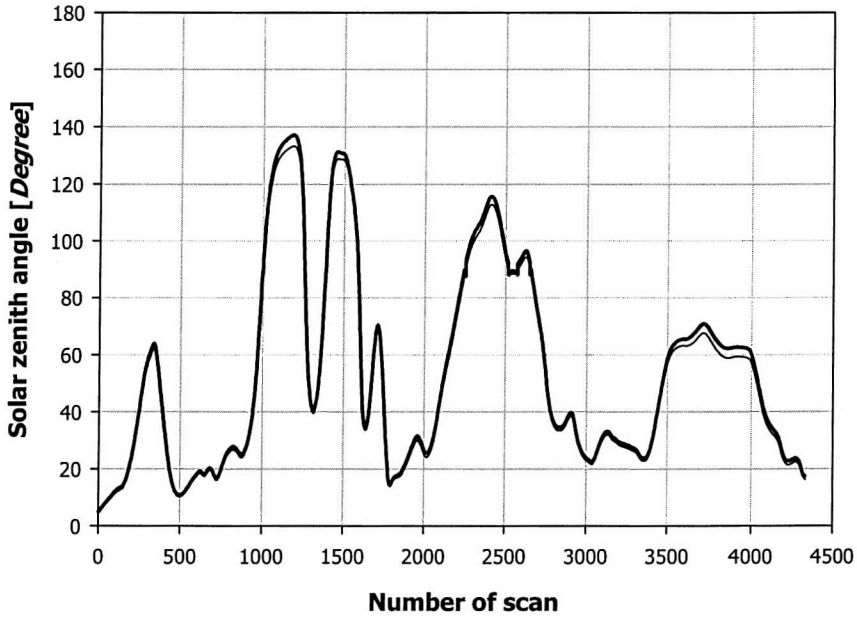

Figure 9-11. Solar azimuth angle relative to the ILS plane. It varies with aircraft attitude while flying. The thin solid line represents the solar azimuth variation from simple subtraction between the fixed solar azimuth and flight heading, while the thick solid line is the solar direction which takes into account the solar zenith angle derived in the previous sub-section.

9.3. Sky models for extreme sky conditions

The estimation of the ILS position due to aircraft motion provides the instantaneous solar angle with respect to the sensor on an inclined surface. In practice, the aircraft attitude is always tilting toward a certain direction during the flight. As a cosine diffuser is mounted parallel to the body of the plane, the slope of the probe is associated with the aircraft attitude. The irradiance on the cosine receptor inclined toward the sun is greater than that on the horizontal plane, and *vice versa*. Consequently, the varying relative solar angle on the ILS probe results in changes of irradiance signal, which would be different from a horizontally placed cosine receptor at the same level. The magnitude of the difference is determined by sky illumination conditions, i.e. the ratio of direct to diffuse downwelling irradiance. If the incident illumination consists of direct irradiance, the irradiance signal on the slope is represented by a simple cosine relationship, whereas under completely diffuse illumination condition (e.g. overcast sky), the irradiance differences between horizontal and sloped plane are only dependent on the slope angle.

In this section, because of the simplicity, these two extreme cases of sky conditions are examined for the estimation of the ILS data as if it were in the horizontal plane.

9.3.1. A single sky condition model

The simplest slope irradiance model basically assumes that the diffuse sky radiation is uniformly distributed over the sky dome. Under completely overcast skies, the dependence on solar position disappears as the maximum intensity in the solar zenith direction is uniformly distributed due to decreasing atmospheric transmittance. In this isotropic model the total irradiance is only a function of slope angle as follows,

$$G_{d,i} = G_d\left(1+\cos(\alpha)\right)/2 \qquad [9.8]$$

where, $G_{d,i}$ Diffuse irradiance on an inclined surface $[W\,m^{-2}\,sr^{-1}]$
G_d Diffuse irradiance on a horizontal plane $[W\,m^{-2}\,sr^{-1}]$
α Slope of the aircraft [*degree*]

The isotropic model using the above equation tends to underestimate the diffuse irradiance from clear sky conditions and approximates prediction of completely overcast conditions.

As for the another extreme sky condition, the entire diffuse sky radiation is assumed to come from the direction of the solar position, as well as the direct solar radiation. This is modelled by a heliocentric function in which the total irradiance is a function of the angular distance from the sun to a point in the sky,

$$G_{d,i} = G_d\left(\cos(\alpha)+\sin(\alpha)\cos(\phi)\tan(\theta)\right) \qquad [9.9]$$

where, ϕ Azimuth angle measured in radians clockwise in the horizontal plane from the North [*degree*]
θ Angular distance from the zenith in radians [d*egree*]

The heliocentric model normally overestimates the diffuse radiation in most real sky conditions and increases its magnitude as the slope inclines toward the sun.

Ratios of irradiance on an inclined surface to irradiance in the horizontal plane with isotropic and heliocentric models were computed using the sample ILS data, as shown in the previous section (Figure 9-13). Under isotropic sky conditions, the ratio values are close to 1.0, indicating that there is not much difference in irradiance between sloping and horizontal ILS position. On the other hand, the conversion coefficients in heliocentric condition show greater variations over a range of ILS values. The coefficient values follow a similar trend to the ILS signal until high frequent fluctuations appear due to appearance of cloud patches at the end of the flightline, which means that anisotropic distribution of diffuse radiance plays an important role of changes in the ILS readings, as well as true variation of the atmospheric conditions.

These correction coefficients were divided by the raw ILS data, so that the results are supposedly correct for irradiance changes due to non-uniform atmospheric conditions along the flightline. The ILS corrections with two extreme sky conditions (i.e. isotropic and heliocentric models) do not seem to remove attitudinal changes of the ILS data effectively. Using the overcast sky model (isotropic), the correction is hardly noticeable, indicating that the aircraft motion does not influence the ILS data changes (Figure 9-12a). The heliocentric model, on the other hand, simulates clear sky condition, i.e. it assumes minimum or no diffuse radiation

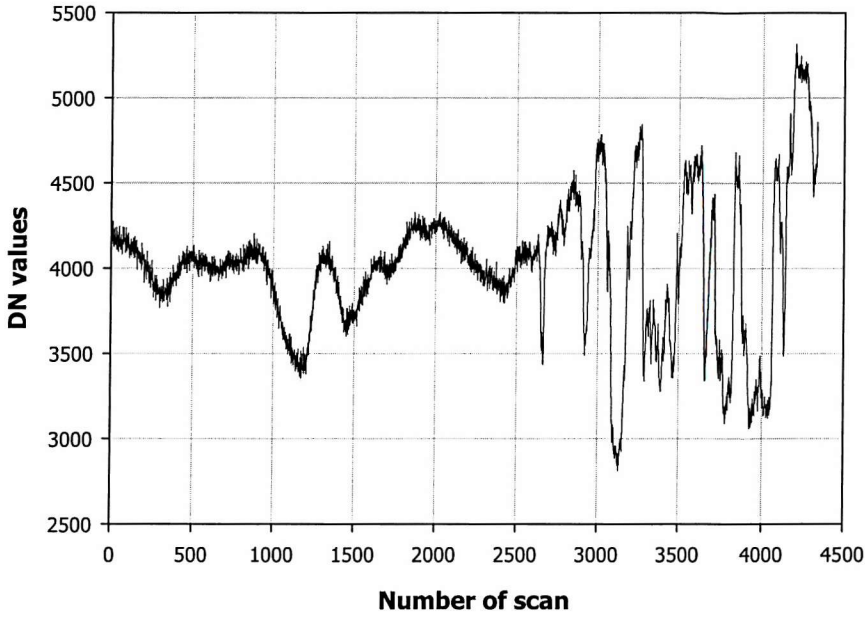

(a)

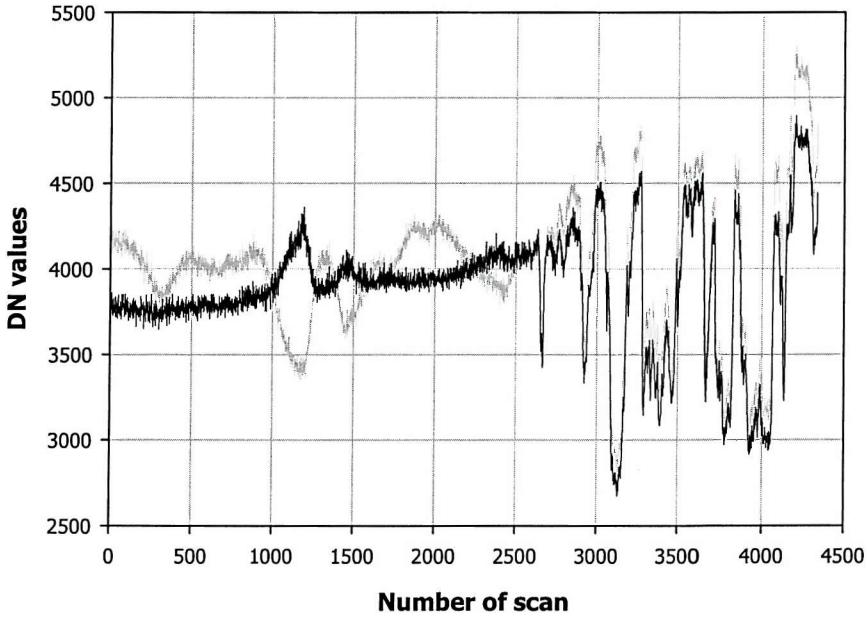

(b)

Figure 9-12. Corrected ILS data (dark plot) under the assumption of isotropic (a) and heliocentric sky conditions (b). Grey plots represent the original ILS data. The data used in this plot is the same as in the previous section. In plot (a), the original ILS data seem to be hidden because they are very similar to isotropic model output.

if overestimated the corrected ILS (e.g. the scan of around 1200 in Figure 9-12b), with generally decreased values in the atmospherically disturbed regions (i.e. the second half of the example data).

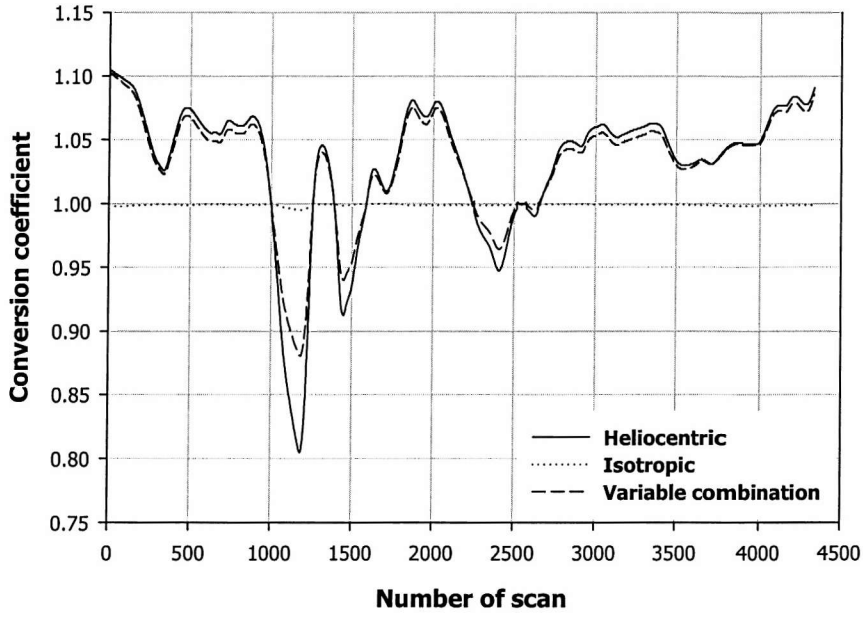

Figure 9-13. Ratios of irradiance on inclined surface to that in horizontal plane. If the conversion coefficient is greater than 1.0, the tilted ILS receives more irradiance than it is supposed to in its horizontal position, and vice versa.

9.3.2. Flexible sky condition model

The above two models were designed to simulate extreme cases of sky conditions and both models show rather unrealistic results. In order to make the model more practical, a combinational (or anisotropic) model is necessary (e.g. Hay, 1978). The simplest combinational model basically treats half of the total irradiance as uniformly distributed diffuse radiation and another half as direct flux from the Sun. Figure 9-14a illustrates the result of the fixed combinational model for the example ILS data. In its result, the overestimation shown from heliocentric model is greatly reduced, while there is an improvement from underestimated isotropic model. As above, the ILS correction is only effective in the ILS data under spatially uniform sky conditions.

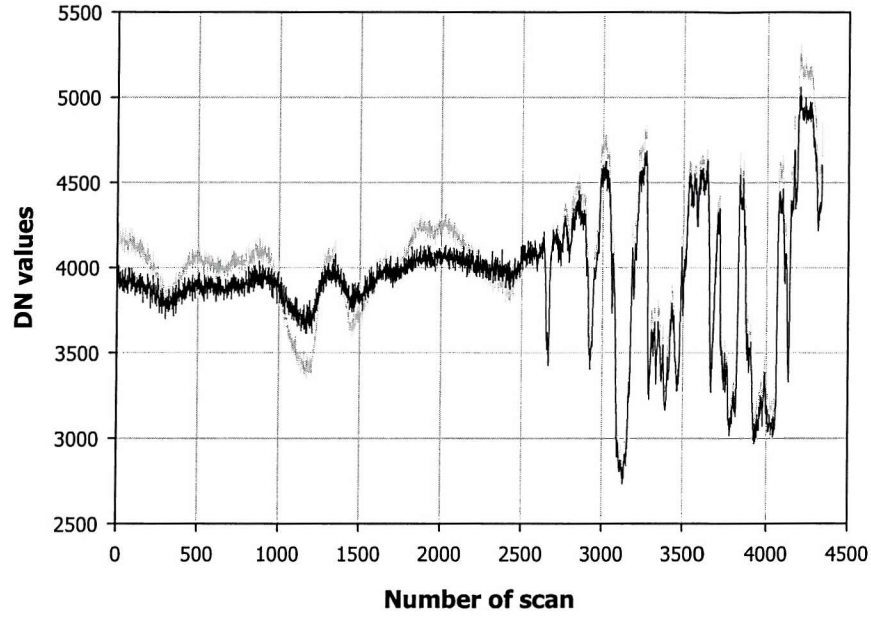

(a)

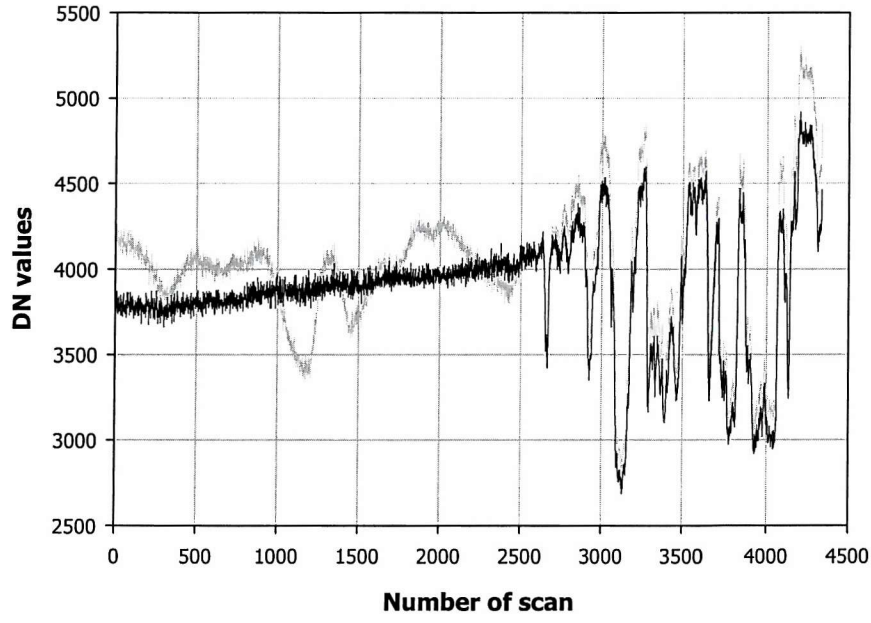

(b)

Figure 9-14. Corrected ILS data by using combinational model (50:50 of isotropic and heliocentric components) (a) and variable combinational model (18:82) (b). The data used in this plot is the same as in the previous section.

More flexible usage of the combinational model is to use a variable coefficient for both extreme models depending upon the sky conditions. As an assumption is made that the sky conditions are somewhere between these two extreme cases, this model uses a flexible irradiance model that gives weight between isotropic and heliocentric models (Figure 9-14b), as follows,

$$G^{f}{}_{d,j} = (1-c)\cdot G^{i}{}_{d,j} + c\cdot G^{h}{}_{d,j} \qquad [9.10]$$

where c is a combination weight with a range between 0.0 and 1.0. The flexible model represents an isotropic model when c becomes 0.0, and a heliocentric sky conditions with $c \sim$ 1.0.

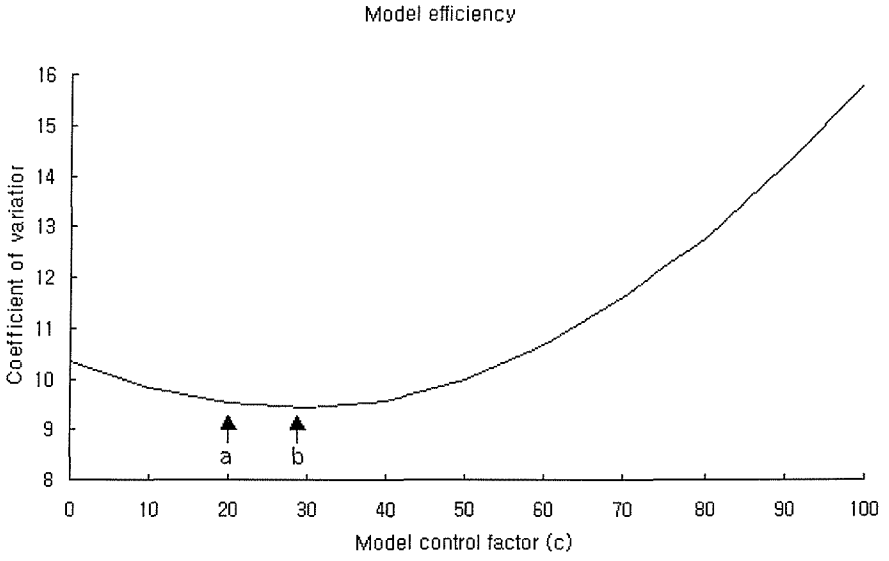

Figure 9-15. Model efficiency plot using coefficient of variation. A point *a* is the best combinations from the visual test of the model, while a point *b* is the smallest value decided by the coefficient of variation. The input data are imag5137. The whole range of the ILS data (band 8) is smoothed with a width of 99 data scans.

The coefficient of variation turns out to be the most suitable indication method for finding an appropriate ILS correction from the model automatically. It is a ratio of average to standard deviation of the ILS values within a selected range. The coefficient is used to help a user decide an appropriate combination between two sky conditions, but care should be taken as the real spatial variations of irradiance through a flightline may cause confusions with effectiveness of the model (Figure 9-15).

9.4. Sky models for all weather conditions

More sophisticated irradiance models on tilted surface have been developed using sky radiance distribution models (SRDM) in order to simulate any state of weather conditions. While the SRDMs reproduce anisotropic radiance changes over the sky dome, they normally require atmospheric parameters for the result with higher accuracy. Many authors have attempted to develop numerical models for prediction of various sky conditions, including Hooper and Brunger (1980 and 1987) (radiance model) and Perez (1993a, b) (luminance model).

The performance of these different models were compared by Vartiainen (2000), and Perez's model (Perez, 1993a and 1993b) was shown to have the lowest error range amongst five sky irradiance models and six sky radiance distribution models on slope. However, Brunger and Hooper's model (1993) was used in this study, as it is one of the few sky radiance distribution models that covers the complete range of atmospheric conditions.

For SRDM on an inclined surface, there have been a number of empirical and analytical studies (e.g. Brunger and Hooper, 1993; Gates, 1980), originally inspired for estimating the efficiency of solar panels to be used inclined on the top of buildings (Hooper and Brunger, 1980). The diffuse irradiance on the inclined surface is obtained by integrating the sky radiance distribution model over the sky dome visible to the surface with the horizontal global and diffuse irradiance measurements.

9.4.1. Brunger and Hooper's SRDM

Although there is evidence indicating that radiance (unit $W\,m^{-2}\,sr^{-1}$) and luminance (unit $lumen\ m^{-2}\ sr^{-1}$) distributions are qualitatively similar, the radiance distribution model is more sensible for RS applications. Another important feature of the model is that it is a function of two parameterised atmospheric conditions, the atmospheric clarity index (k_t) and diffuse fraction (k).

The model used in this study is based on the Three-Component Continuous Distribution (TCCD) model of Hooper and Brunger (1980) which comprises circumsolar ($a0$), horizontal

brightening (*a1*), and uniform background terms (*a2*). An extra coefficient (*a3*) is set as a linear term. The model calibration was undertaken by finding the parameters. A number of field experiments under a wide variety of atmospheric condition were sorted into bins defined by specific ranges of k_t and k. The set of measurements in each bin were statistically analysed for the model parameters.

Once the atmospheric condition had been selected, its corresponding parameters were used to calculate the radiance ($W\,m^{-2}\,sr^{-1}$) of the sky over the whole hemisphere (q,f),

$$L(\theta,\phi,\theta_s,\phi_s) = G_d\left[\frac{a_0 + a_1\cos\theta + a_2\exp\left(-a_3\Psi(\theta,\phi,\theta_s,\phi_s)\right)}{\pi\left(a_0 + 2a_1/3\right) + 2a_2 I(\theta_s,a_3)}\right] \qquad [9.11]$$

substitute,

$$I(\theta_s,a_3) = \frac{\left[1+\exp\left(-a_3\pi/2\right)\right]}{\left(a_3^2+4\right)}\cdot\Gamma(\theta_s) \qquad [9.12]$$

$$\Gamma(\theta_s) = \left\{\pi - \left[1 - \frac{2\left[1-\exp\left(-a_3\pi\right)\right]}{\pi a_3\left[1+\exp\left(-a_3\pi/2\right)\right]}\right]\cdot\left[2\theta_s\sin\theta_2 - 0.02\pi\sin\left(2\theta_s\right)\right]\right\} \qquad [9.13]$$

where,

	a_0, a_1, a_2, a_3	Parameters of assignable value that allow the sky radiance model to respond to the atmospheric radiation conditions
	G_h	Global solar irradiance on a horizontal surface [$W\,m^{-2}$]
	(θ_s, ϕ_s)	Coordinate of the direction of the sun [*degree*]
	L	Sky radiance at point (θ_s,ϕ_s) [$W\,m^{-2}\,sr^{-1}$]
	Ψ	Angular distance in radians between the direction of the solar disk and the direction (θ,ϕ)

and the angular distance in radians between (θ, ϕ) and (θ_s, ϕ_s),

$$\Psi(\theta,\phi,\theta_s,\phi_s) = \arccos\left[\sin\theta\sin\theta_s\cos\left(\phi-\phi_s\right) + \cos\theta\cos\theta_s\right] \qquad [9.14]$$

The distribution of radiance over the hemisphere on a slope was used to calculate the ratio of sky irradiance on the slope to that which would have been found on a horizontal surface, and to integrate the radiance over the sky dome visible to the surface.

$$G_{d,i} = G_d \frac{\int_{-\pi}^{\pi}\int_{\alpha_0}^{\pi/2} L(\theta,\phi,\theta_s,\phi_s)\cos\theta(\sin\theta\cos\alpha+\cos\theta\sin\alpha\cos\phi)\cdot d\phi d\theta}{\int_{-\pi}^{\pi}\int_{0}^{\pi/2} L(\theta,\phi,\theta_s,\phi_s)\cos\theta\sin\theta\cdot d\phi d\theta} \quad [9.15]$$

Depending on whether the position on the point over the sky dome is below the horizon or not, the limit of the inner integration is given by,

$$\alpha_0 = \begin{cases} 0 & \text{Where } -\pi/2 \le \phi \le \pi/2 \\ \arctan(-\tan\alpha\cos\phi) & \text{Otherwise} \quad 0 \end{cases}$$

9.4.2. Data Description

On 3 September 1999 the intertidal vegetation bordering the West Solent, Hampshire, UK, was surveyed using CASI from the Environment Agency (EA) on behalf of English Nature. Over 30 flightlines were flown at an altitude of 2,500 feet between 09:00 and 12:40. The CASI was configured in spatial mode using the intertidal bandset recommended by Thomson *et al.* (1998).

Image	Time (GMT)	Heading (Degree from the North)	Solar Azimuth (Degree from the North)	Relative sun angle (= heading– solar azimuth)
Imag4315	9:20:16 to 9:21:35	232	126	106
Imag4332	10:40:16 to 10:41:56	55	150	-95
Imag4349	12:13:36 to 12:15:44	175 (151)	184	-9
Imag4350	12:18:56 to 12:21:04	341 (331)	185	156
Imag4354	12:36:20 to 12:37:37	231 (331)	191	40

Table 9-1. Flight information overpass of the calibration site. Figures in brackets indicate information in *.inf file, which are suspected as being in error, based on the map provided and the image orientation.

During the period of the aerial survey, three flight lines (Imag4315, Imag4332, and Imag4354) passed over the Beaulieu Heath Calibration Site (BHCS; approximately N50° 50', W1° 25') where a Spectron SE-590 spectroradiometer was located and continuously measuring downwelling irradiance over the spectral range from 368 to 1114 *nm*. The data from the SE-590 were integrated over the spectral range and plotted for the series of measurements (Figure 9-16). The solar flux reaching the ground was modelled using the 6S code and superimposed on the ground measurements. The difference between them (grey region in Figure 9-16) increased slightly with time. Between around 09:00 and 10:45 the solar irradiance steadily increased as the early morning mist cleared, and there was an interval during which the solar irradiance changed rapidly as high level cloud passed over the area. Soon after such disturbances, the irradiance became stable, and remained so until the end of the survey.

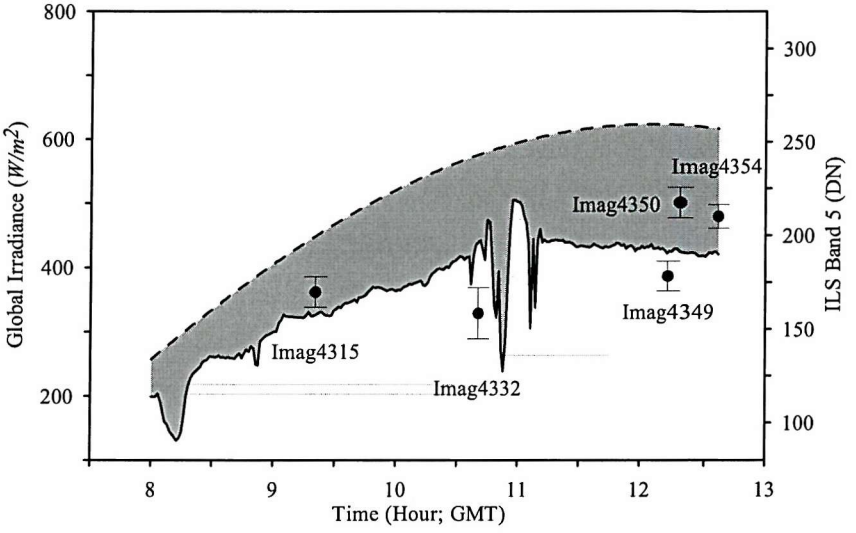

Figure 9-16. Global irradiance at ground in Beaulieu Heath calibration site (solid line), and the solar flux modelled by 6S (dashed line). The grey area between dashed and solid lines represents the difference between those two. The mean DN values of the ILS from three flights over the calibration site are superimposed with their standard deviation ranges, as are the mean DN values from the two test flightlines (Imag4349 and Imag4350)

The flightlines of Imag4349 and Imag4350 were selected in order to test whether the method could compensate for the effect of different flight direction on data from the ILS. These flightlines represent almost the worst case possible, with Imag4349 being flown almost directly into the Sun (relative solar azimuth -9°) and Imag 4350 being flown almost directly away from the Sun (relative solar azimuth 156°). The area covered by flightlines Imag4349 and Imag4350 was approximately 9km north of the site at which solar irradiance was measured at the ground,

and it is assumed that similar conditions prevailed at both sites. Figure 9-6 shows that the solar irradiance during the period of these flightlines was almost constant.

9.4.3. Results

Brunger and Hooper's model (1993) described above was applied to the ILS data. The model was originally developed in order to calculate the irradiance on a slope ($G_{d,i}$) from known atmospheric conditions (kt, k). In the case of the ILS data, on the other hand, the objective was to use the measurements made by the inclined sensor to calculate the irradiance in the horizontal plane at sensor altitude, as well as to determine the atmospheric conditions.

To achieve this result it was necessary to invert the model, although it is not a true inverse (Figure 9-17). A table of the model coefficients obtained by intensive field experiments over a wide variety of atmospheric conditions was used as input data. A total of 48 sets of model coefficients over specific ranges of k_t and k were applied to the model with solar positions (θ_s, ϕ_s), slope angle (α), and direction relative to the sun.

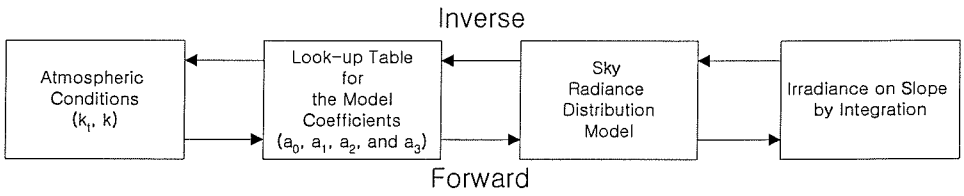

Figure 9-17. Schematic diagram of sequence of Brunger and Hooper's model.

The aircraft attitude data had to be pre-processed before it was applied to the model. To find the accurate degree of slope and its direction is significant as the model is sensitive to the inclined surface in relation to the Sun position. The aircraft attitude is expressed by pitch and roll with respect to the flight direction. Although pitch is greater than roll (see Figure 9-19) so that flight direction may be considered as fixed slope direction during the flight, line-by-line calculations using pitch and roll show variations of more than 10° in slope direction and ±5° in slope angle. Such variations in slope causes equivalent differences in Sun position.

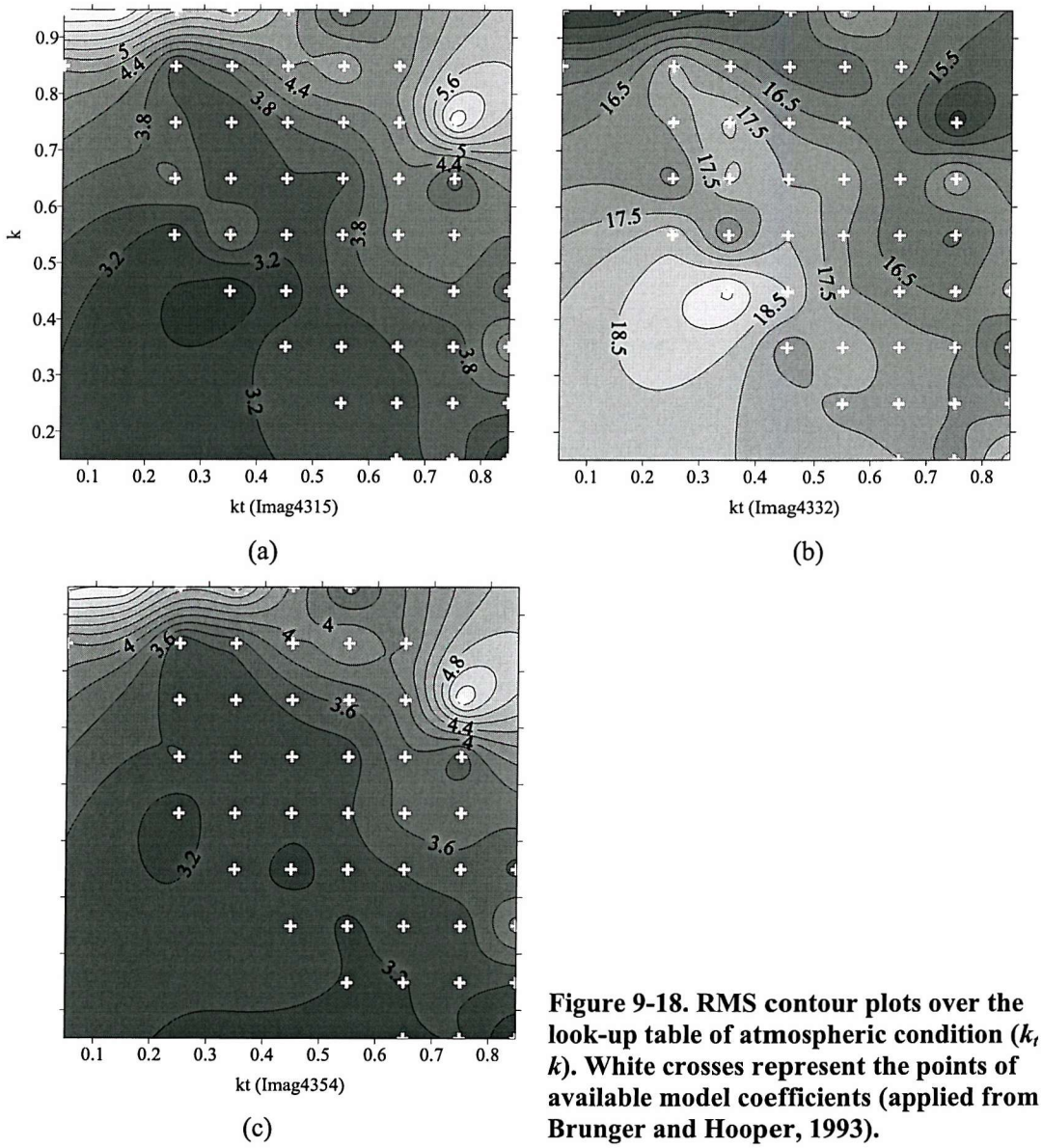

Figure 9-18. RMS contour plots over the look-up table of atmospheric condition (k_t k). White crosses represent the points of available model coefficients (applied from Brunger and Hooper, 1993).

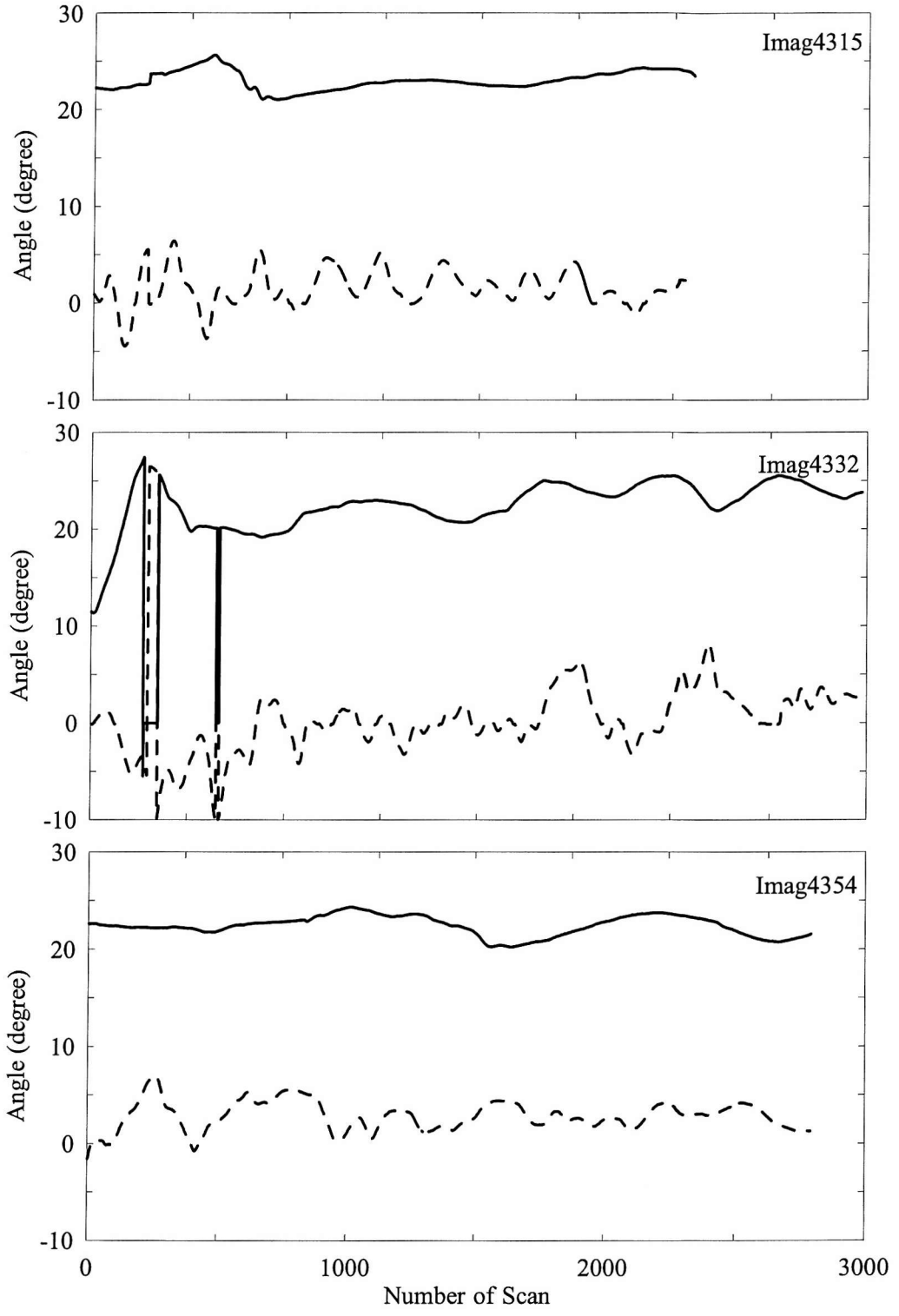

Figure 9-19. Plots of pitch (solid line) and roll (dotted line) in each flight line.

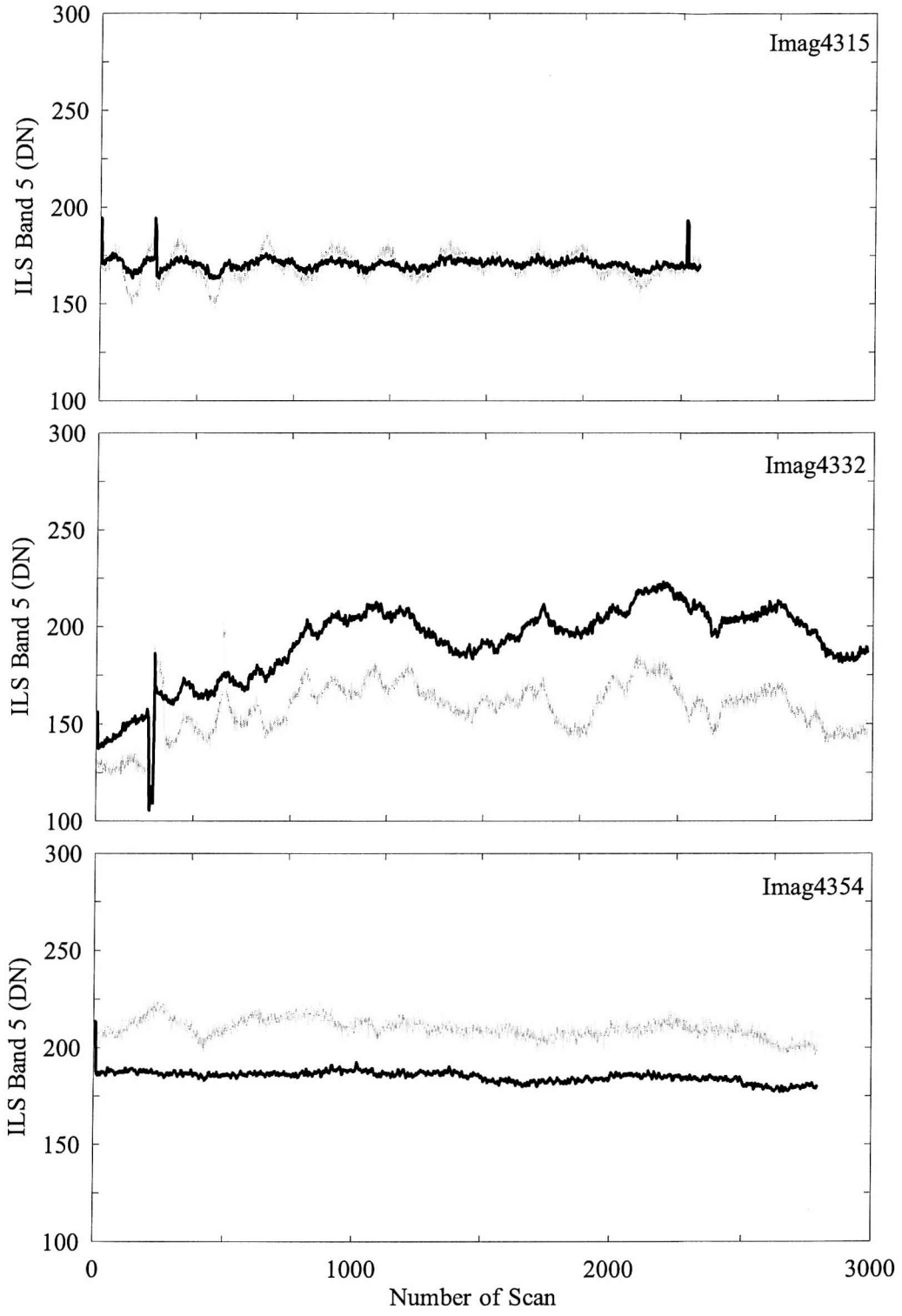

Figure 9-20. 7-moving-averaged raw ILS (grey) is superimposed on the model corrected ILS plots (black).

9.4.4. ILS data over a calibration site

Since each flightline took less than 2 minutes over a linear distance of less than 10 km, it was assumed that atmospheric conditions above at-sensor level were relatively uniform and constant. Therefore, the irradiance on the horizontal surface calculated from the model was assumed to be constant as well. The uniformity of the ILS signal corrected by the model was determined using the Root Mean Square (RMS) deviation as a convenient measure of the spread around the mean. The lowest region in the look-up table represented the most appropriate value for the ILS correction. The contour plots of RMS in each flightline show that the position of the lowest RMS region varied, indicating that atmospheric conditions changed during the survey (Figure 9-18). In comparison with the field measurements during the flights (Figure 9-16), Imag4315 was affected by the early morning mist and results show relatively low atmospheric clarity index (k_t = 0.35) with moderate diffuse ratio (k = 0.45). Imag4332 was collected just before the high level cloud (k = 0.75), while steady increases of irradiance was about to settle (k_t = 0.75). In the last flight (Imag4354), atmospheric conditions above the altitude of the flight became clear and stable. The atmospheric clarity index (k_t = 0.85) was similar to the previous flight (Imag4332) and the amount of irradiance at the ground in both flights was similar, though it was more unstable in Imag4332, but the proportion of diffuse irradiance with respect to the global irradiance was reduced (k = 0.15).

The model coefficients determined in each flight from the parameterised atmospheric conditions above were used for irradiance on a horizontal surface at sensor level (Figure 9-20). In order to reduce the high frequency errors and outliers, the ILS data were averaged over 7 scans. The effects of aircraft attitude on the ILS data were effectively minimised, and the corrected ILS values decreased in Imag4315 and Imag4354 while they increased in Imag4332. The mean values after correction follow the trend of irradiance changes at ground quite well (see Figure 9-16). The variations, still shown after the correction, may be due to errors in the ILS calibration or to actual atmospheric variations over the area. The ILS correction on Imag4332 gives relatively poor results, this may be due to unstable atmospheric conditions during this flightline, or possibly incorrect information on flight direction (E.M. Rollin, personal communication).

In addition to atmospheric characteristics and ILS correction from aircraft attitude, at-sensor sky radiance distributions were given by the model calculations (Figure 9-21). The radiance of the sky was calculated using Equation [9.11]. Stereonet plots of the sky radiance distribution during the acquisition of Imag4315 and Image4354 show a similar pattern whereas that from Imag4332 is similar to the radiance distribution under a cloudy sky. On the other hand, the magnitudes of the radiance are similar in Imag4332 and Imag4354, both being much larger than Imag4315 which has radiance concentrated in the Sun's direction.

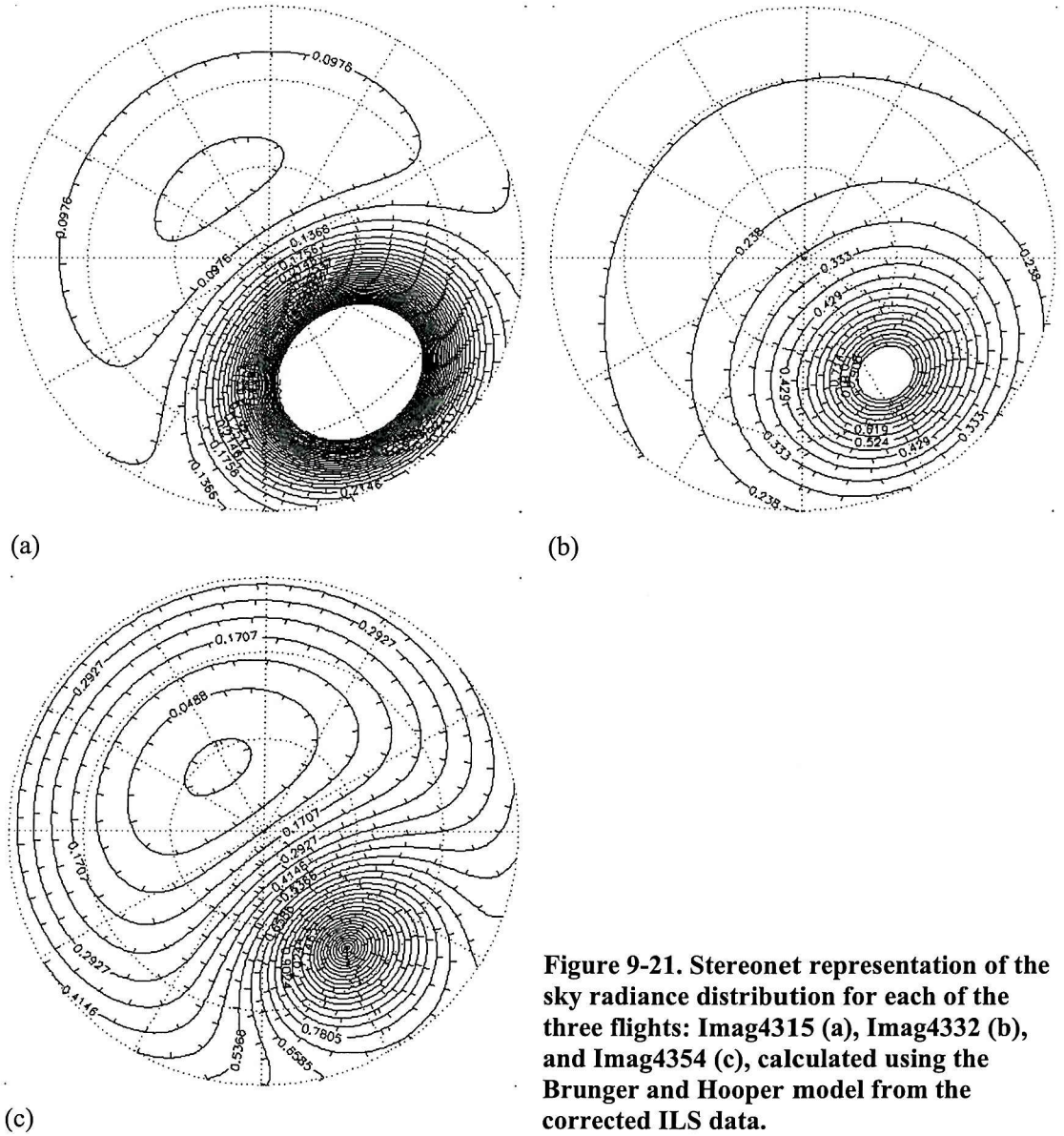

Figure 9-21. Stereonet representation of the sky radiance distribution for each of the three flights: Imag4315 (a), Imag4332 (b), and Imag4354 (c), calculated using the Brunger and Hooper model from the corrected ILS data.

9.4.5. Comparing ILS data in different flight directions

Since the variation of pitch is mainly responsible for the orientation of the ILS, the average flight direction shows how the Sun position changed relative to the slope of the receptor. From more than 30 flightlines during the flight campaign, two images were selected for testing the model. Imag4349 was flown into the Sun, whereas Imag4350 was in the opposite direction. The ILS data were greatly increased when the flight direction was away from the solar position, due to the receptor being tilted towards the primary source of illumination, and vice versa.

The model succeeded in correcting the mean spectral irradiance from the two flightlines, which is much closer than in the raw data, and is more representative of that measured on the ground at the calibration site (Figure 9-22). The failure of the model to correct for all the effects of aircraft attitude may be because the yaw direction was not recorded precisely (unlike pitch and roll). A small error in yaw would have a relatively large effect upon the ILS value at these extreme conditions of relative solar azimuth.

Figure 9-23a shows plots of aircraft attitude during the acquisition of Imag4349 and Imag4350. Like the others, pitch angles are generally larger than roll, and their means are greater than 20°. The comparison of the plane attitudes with the ILS show that changes of the ILS data correspond to changes in the orientation of the plane. The ILS data was again applied to the model and a correction derived. Figure 9-23b shows the results of applying the correction method to data from flightlines Imag4349 and Imag4350. As would be expected from the flight directions, ILS data from Imag4349 have increased, while those from Imag4350 have decreased. The results show some reduction in the effect of aircraft attitude, but not a complete correction.

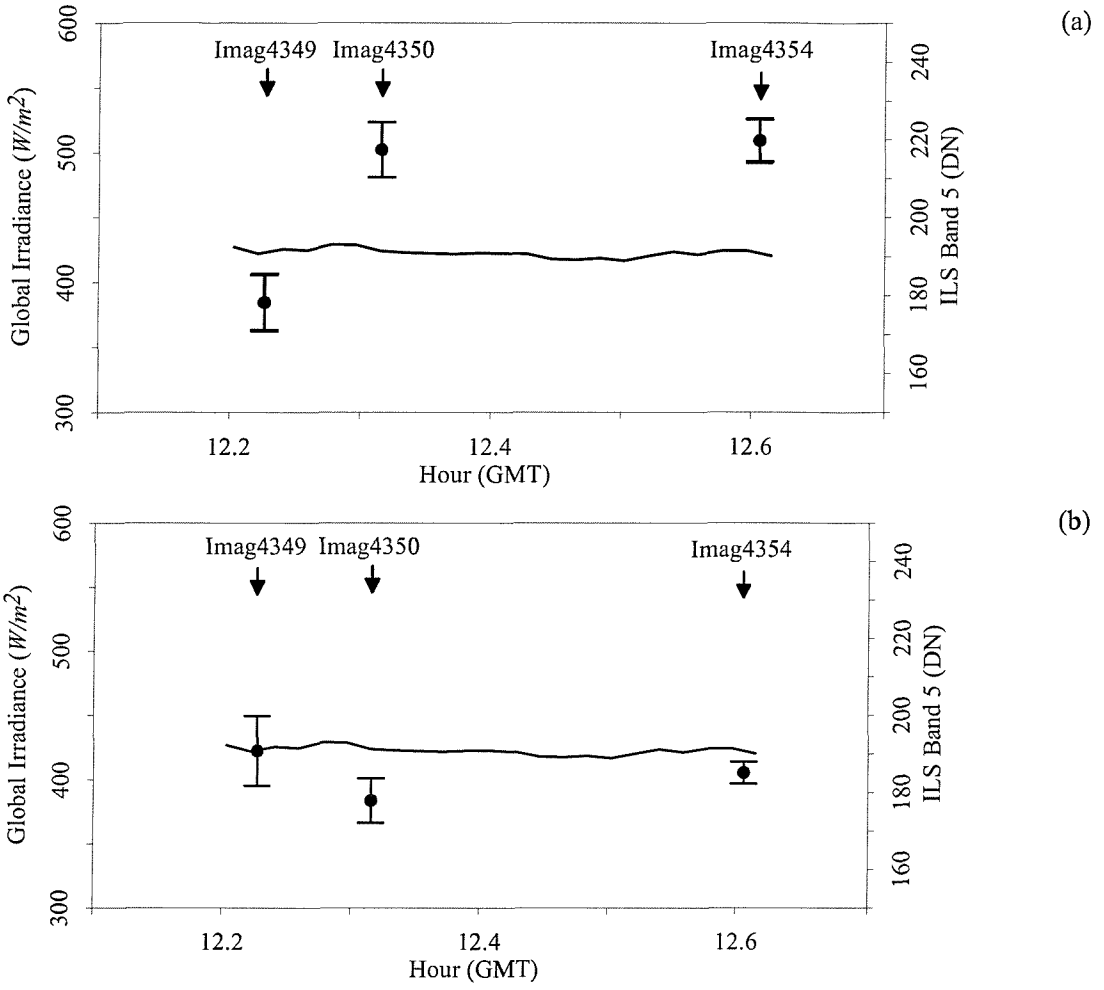

Figure 9-22. Comparison between mean DN values of ILS data from the two test flightlines (a) before correction and (b) after correction. The error bars indicate one standard deviation either side of the mean. Also there is a plot of the mean DN values of ILS data from flightline Imag4354 that passed over the calibration site shortly after the two test flightlines. The solid line in each plot represent irradiance measurements at ground level during the flight. Scales between global irradiance and ILS DN are the same as shown in Figure 9-16.

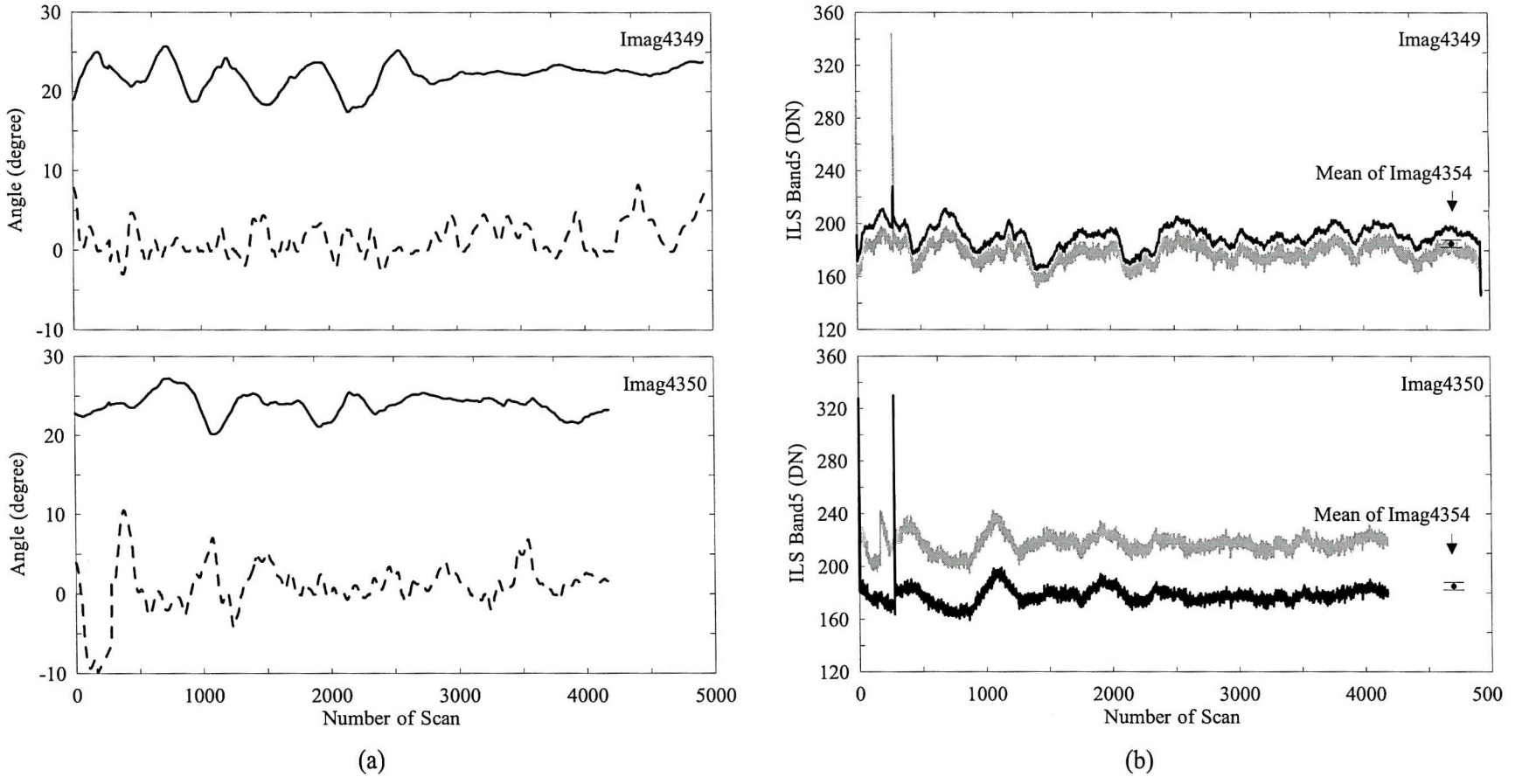

Figure 9-23. Plots of pitch (solid line) and roll (dotted line) in each flight (a). In (b), 7-scan-averaged raw ILS (grey) is superimposed on the model corrected ILS plots (black). The error bars in plot (b) represent the range of standard deviation of model calculation in Imag4354.

9.5. Summary

One of the main limitations of airborne RS is the need for the aircraft flight altitude and attitude to be taken into account for image standardisation or correction for atmospheric effects. Although the much lower sensor operation height of aerial RS means reduced atmospheric effects on target-leaving radiance, the troposphere is a well-known dynamic mixing boundary with highly variable (spatially and temporally) atmospheric aerosols that are generally one of the major contributors in altering the data from optical RS. Using an ancillary instrument simultaneously with the image data acquisition, it is possible to retrieve *in situ* atmospheric condition at the time of the flight. In particular, ground-based measurements are limited in spatial sampling for atmospheric correction of the corresponding RS image. At-sensor measurements provide continuous scans of the atmospheric condition at the position of the imaging sensor. Thus, although it does not provide information for the whole atmosphere, there is *in situ* data for a relatively wide coverage at the same altitude as the flight. Data from downwelling irradiance at the airborne imaging spectrometer potentially provides the atmospheric transmittance at the sensor altitude for image calibration, and with at-ground measurements or known targets, it is possible to estimate additive atmospheric path radiance between the target and the sensor using the empirical method (described in Chapter 6). In this study, CASI's Incident Light Sensor (ILS) was used, the specifications and characteristics of which were thoroughly investigated in an earlier chapter.

Direct use of ILS data, however, has been limited, mainly because of aircraft motion which causes the ILS signal to change. Even in the case of a very stable flight, the aircraft is rarely in a horizontal position, instead, it is continuously manoeuvred in order to keep the platform in the right position and direction. There has been an attempt to use a selection of ILS records with a near horizontal position of the ILS (Rollin *et al.*, 2001), but the fact that aircraft's positional effects still existed in the dataset made this method difficult to match with the ground-based measurements for the image standardisation. The precise flight navigation systems enable us to estimate the accurate instantaneous position of the ILS receptor with respect to the aircraft's motion, leading to a better understanding helping to establish the relationship between irradiance signal received by the ILS and the continuous changes of the ILS probe position.

The computation of precise ILS receptor position along with the aircraft motion only provides the sensor's geometric information with respect to the horizontal plane, so a sky irradiance model is also necessary in order to simulate changes of the ILS signal due to changes in attitude of the airborne platform. The model described basically considered the instantaneous ILS position as the receptor on a tilted surface, and yields normalised irradiance values on a tilted surface (i.e. ratio of irradiance on slope to that on the horizontal plane). The multiplication of the inverse model output with the original ILS values corrected for the ILS data for aircraft motion. A test of the two extreme sky condition models showed that these models were too unrealistic for real irradiance data, and that a combination of the two sky conditions resulted in more reasonable at-sensor irradiance values from the ILS.

A more complicated ILS correction method was performed using a sky radiance distribution model (SRDM), also known as an all-weather sky radiance model. While this theoretical-based simulation normally is expected to give more accurate results, it requires more variables or coefficients as a function of the environmental parameters. Brunger and Hooper's model was used and needed a set of four coefficients which are determined by the atmospheric transmittance and clearness of the sky. The continuous slope changes of the ILS sensor due to variations in aircraft motion and uncertainties in sky conditions during the flights cause problems in the direct use of the ILS data, but this helps in finding the optimum coefficients for the model when inverted. This method assumes that the spatial distribution of atmospheric conditions is nearly constant unless the changes are caused by an atmospheric disturbance, such as the appearance of clouds. In other words, a series of ILS measurements are treated as various slope angles of the ILS recorded under a spatially and temporally pseudo-invariant sky radiance condition, and the atmospheric variables which were originally input parameters for the model can be retrieved by the inverse procedure. These inverse model outputs have great potential as input data to the conventional radiative-transfer atmospheric correction algorithms. In summary, the inverse SRDM method gives the following additional information of the sky above the aircraft at the time of the flight,

1) Atmospheric parameters (k and k_t)
2) Sky radiance distribution over a flightline

The evaluation tests of the inverse SRDM method were conducted using the ILS data flown over ground calibration targets in New Forest, UK. The ground measurements showed

that three flightlines at different times of day in the same area, were distinctively affected by atmospheric conditions. Such sky conditions were directly reflected in the ILS signals, as is the effect of aircraft motion during each flight. The model results indicated that the predetermined set of coefficients from Brunger and Hooper's model (1993), which represented the various sky conditions, worked quite well with the sample dataset for the ILS correction. Moreover, the atmospheric parameters from the model were synchronised with the spectrometer data measured on the ground. As a second test, the ILS data collected in rather extreme cases of the flightlines, i.e. toward and away from the solar position, were selected. Since aircraft flying at relatively low altitudes (or slow speed) tend to fly with their nose up in order to maintain flight altitude, the datasets used here from parallel flights with different directions showed overall scans of the ILS higher (with flight away from the Sun) or lower (with flight toward the Sun) throughout the flight, with comparison to those from ideally horizontal flightlines (i.e. more dependent on the flight attitudes) with respect to the Sun's position. The deviation of the mean ILS values from the time series measurements at ground is mainly due to the problem with the geometry of flight direction with respect to the solar azimuth angle. The inverted SRDM method produced similar mean ILS values to the ground measurements, indicating that the flightline-to-Sun geometry effects were also minimised.

From the evidence presented above, the inverted SRDM method is expected to have great potential for operational ILS correction and, furthermore, for image standardisation. The flexible combination sky model presented here was applied as an image standardisation using the CASI data with multiple flightlines from the UK Environment Agency. Figure 9-24 is a mosaic image of the several CASI images over the Stonehenge area in the UK, after the ILS correction model processing. Illumination differences between the flightlines were diminished dramatically, although there are still traces of the mosaicing. Since the discrepancies between images are more distinctive in the vegetated areas, especially in the grass region, the problems were mainly caused by the target BRDF rather than the ILS correction itself.

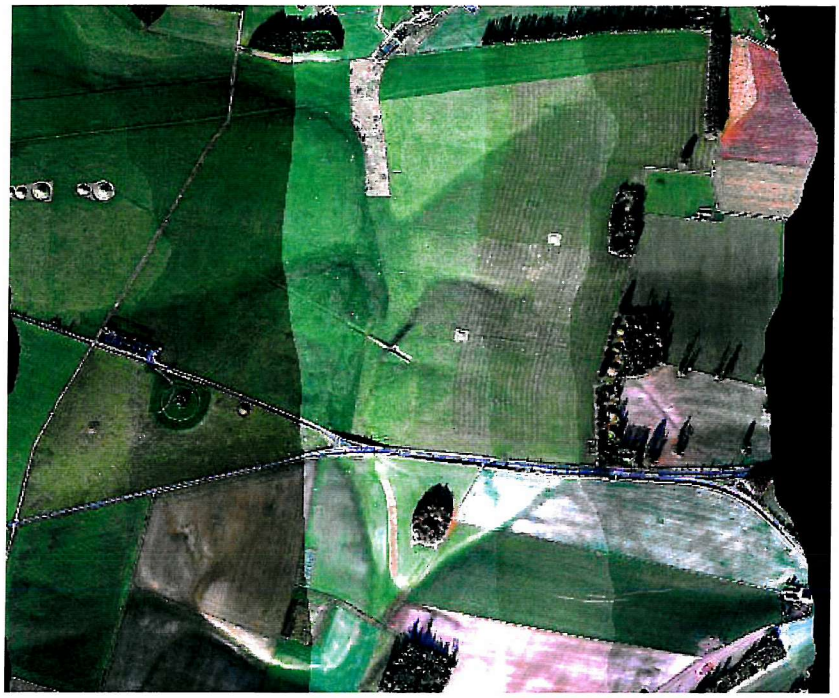

(a)

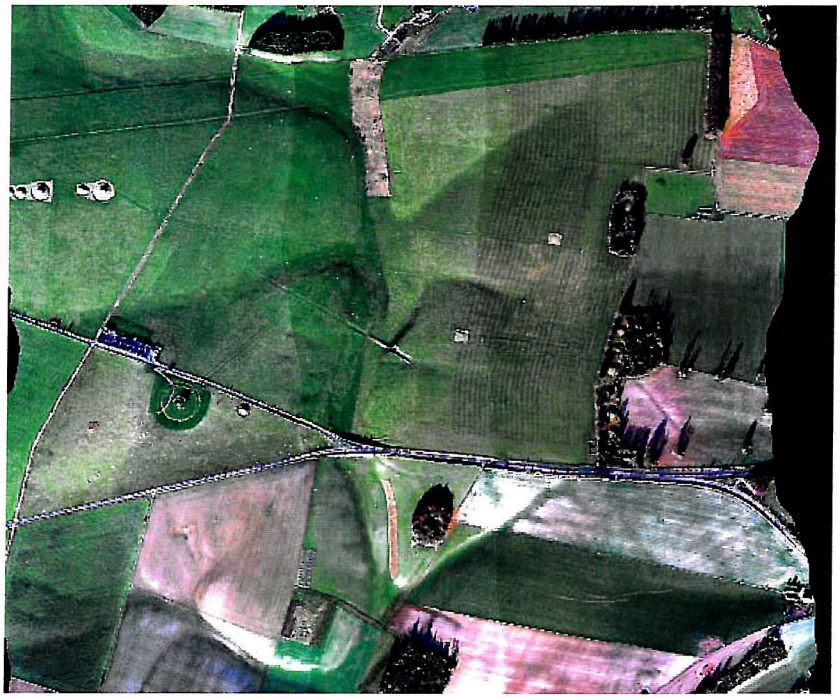

(b)

Figure 9-24. Mosaic of five images of the Stonehenge area, UK, with (b) and without (a) the ILS correction (the flexible combination model). Courtesy of the UK Environment Agency (2001).

Chapter 10

Conclusions

10.1. Introduction

For RS to be a truly useful technique in environmental science, it is necessary to obtain physically meaningful data values, so that data from different sensors or from different spectral bands of the same sensor can be compared. This is achieved through a series of pre-processing methods which convert electric signals from currently operating RS sensor systems into, for example, pixel values in radiance units that represent the spectral signatures of ground targets. In practice, the retrieval of physical quantities from a remote sensor is not a trivial task. Failure to complete even this lowest level calibration causes errors into even the simplest analysis (Crippen, 1988). Sensors operate in harsh environments, variations in atmospheric conditions and vibrations or shock during sensor operation can degrade data quality. Such errors even exist for state-of-the-art sensing systems. Therefore, the use of RS in various applications should go through at least some degree of data preparation before the image analysis processes. As the signal detected by multispectral optical remote sensing represents the biophysical properties of an object on the ground as well as other factors, such as instrument induced and/or atmospheric variation, the pre-processing of remotely sensed data leads to retrieval of 'information' from 'data'. Pre-processing in RS consists of three main processes: radiometric correction, atmospheric correction and geometric correction. The main focus in this thesis has been to investigate and improve image pre-processing techniques.

The principal objective here was to focus on radiometric calibration and atmospheric correction, which tend to increase uncertainties in pixel values if a certain level of accuracy cannot be obtained. As a result, the contents represented in the previous chapters are primarily divided into two parts, sensor calibration and atmospheric corrections/standardisation.

As a conclusion to this thesis, the previous chapters are grouped into two sections (based on source of errors and uncertainties within the image) and are summarised.

10.2. Sensor calibration and radiometric correction

All RS systems require a calibration procedure in order to characterise the sensor performance. Although most sensor specifications are determined at the design stage, the details, which are often required for producing accurate data (e.g. radiometric response properties), are not identical – they are unique to each sensor system. Laboratory calibration is specially designed to deliver this delicate information about the RS sensor, which normally consists of general sensor characteristics, radiometric, and wavelength calibration. This information changes frequently within a tolerance range due to the nature of platform and its environment, and hence the sensor calibration should ideally be performed every time an image is acquired (Winter *et al.*, 2001). However, in practice, this could introduce even more errors as a result of the sensor being dismantled and transported to the laboratory. For the NERC CASI-2 system, the current compromise is to perform three laboratory calibrations and one manufacturer's maintenance per a year.

Laboratory calibration procedures do not necessarily cover the entire sensor characteristics that are required for some RS applications, because the calibration results have to be a compromise due to time and cost limitations. The following paragraphs describe the CASI-2's characteristics investigated in this thesis, which are not included in the routine calibration procedure outlined by the manufacturer.

- **Spectral smile feature**

  The spectral smile feature is caused by optical distortion between the optical system in the sensor head and the array detector. Although it is minimised at the sensor design stage, the spectral alignment problem is inevitable due to the nature of this type of sensor. During the laboratory calibration, it is important to monitor its variations over the period of sensor operation. The conventional method has been designed to check the optical alignment using a simplified procedure, and no measurement is performed to test the variation of spectral distortions across the wavelength domain of the detector elements.

A more detailed experiment showed that the magnitudes of wavelength difference across the image pixels varied as a function of spatial and spectral position in the image (0.4 ~ 0.8 pixels; if it is assumed that the mean wavelength interval between adjacent detector element is ~1.9 *nm*). This figure is much greater than the acceptable spectral alignment (< 0.3 pixels) featured in the manufacturer's system specification, which supposedly applies over the entire detector elements for all CASI-2 systems. The variation of optical spectral alignment is also associated with the accuracy of wavelength calibration over the whole detector array.

- **Sensitivity of wavelength calibration**

Normally, the wavelength calibration coefficient is determined using the column of CCD pixels in the centre of the image. In addition to limitations of the wavelength standards, a single column calibration could simplify the procedure with minimal loss of accuracy and eventually save time. Spatially non-uniform (across the image) spectral responses shown above lead to the necessity of different wavelength calibration coefficients for each column of the detector array.

More importantly, the determination of the wavelength for each detector elements is a highly sensitive task. This is primarily due to the relatively weak intensity of the wavelength standards commonly available (i.e. low SNR) and known uncertainties in the method of finding the correct pixel number of the corresponding spectral emission (Section 4.2.2). A small error could result in a notably different wavelength calibration output. A case study (in Section 4.3) showed the possible errors introduced by using inappropriate G-numbers in a NERC CASI-2 dataset in which incorrect wavelength calibration data were used. The difference between the two sets of G-numbers was trivial. For example, the largest polynomial coefficients (G0) differ by only ~0.8 *nm*, which could happen in a routine calibration. These similar sets of coefficients showed dramatic deviation increasing in shorter wavelengths, up to 45 *nm* at column 288, which is unacceptable for applications of the image. This example shows that even small differences in the wavelength calibration coefficients result in large spectral differences in the collected image.

- **Estimation of spectral response function (SRF)**

Determination of the SRF of the CASI-2 system is not a part of the routine laboratory calibration, and has not been known to end-users, though it is an important intrinsic property of the system. Such information is particularly important for inter-comparison with other datasets. For example, when a multispectral CASI-2 image is compared with field spectroradiometer data with a narrower band for atmospheric correction (e.g. empirical-line method) or spectral endmember studies, the band response function of the CASI-2 should be used to transform the measurements from the spectroradiometer into the CASI-2's bandset.

A numerical model was developed to estimate SRFs for each spectral detector element. Measurements of wavelength standards (gas tube lamps) using a high spectral resolution optical spectrum analyser (OSA) were used as reference spectral responses. The model had several assumptions as follows,

- that FWHM of each emission peak of the wavelength standards is greater than that of CASI-2's detector elements,
- that the FWHM of each detector elements of the CASI-2 is greater than the spectral resolution of the OSA (0.1 *nm*),
- that the spectral response of the CASI-2 is expressed by a Gaussian curve,
- that adjacent detector elements surrounded by each emission peak in CASI-2 have the same FWHM values,

According to these assumptions, the signal of each CCD element at a spectral emission peak was determined by integration of emitted energy that is received within the range as a function of Gaussian SRF with a given FWHM. The model was a kind of inversion process, as it iteratively compared the spectral data measured by the CASI-2 with the simulated CASI-2's spectrum with an arbitrary FWHM. The results showed that the model had successfully provided FWHM values on spectral emissions with the same order of magnitude as those roughly estimated by the CASI-2's manufacturer. Any errors found may have been due to a non-Gaussian spectral response of CASI-2 and/or

variable FWHM within the spectral range of sampling CCD detectors around each emission line.

The estimation of SRF is normally obtained using a tuneable laser which is expensive and time consuming for regular check-ups. The model simulation showed the potential for reducing time and cost of the SRF measurements for a routine laboratory calibration with reasonable accuracy. There is, however, room to improve this preliminary model, for example by testing it with other SRF shapes (e.g. trapezoid; Hopkinson *et al.*, 2000) and comparing the model results with the true FWHM (e.g. measured by NPL, UK).

- **The effect of errors in the radiance standard**

Although the accuracy and consistency of calibration standards is beyond the scope of this thesis, the systematic characteristics of the radiometric standard were discussed in Section 4.5, as they are directly related to the calibration performance and image quality. For NERC CASI-2 system, the problem with radiometric calibration is introduced with the merging of calibration data for the two halves of CCD array, due to wider FOV of the objective lens than the size of exit port of integrating sphere (i.e. the radiance standard). Tests suggested that discontinuities in radiometric values across the image are caused both by inconsistent sensor alignment and by spatially non-uniform radiance standards.

- **Characteristics of the Incident Light Sensor (ILS)**

One of the unique features of CASI-2 is its ability to measure downwelling irradiance at sensor level simultaneously with scene data. The roof mounted Incident Light Sensor (ILS) is a cosine receptor directly connected to the CASI-2's SHU via a fibre optic cable. As the light received by the receptor is detected by the same detector array as the image data, the radiometric properties of ILS are similar to those of the imaging part in terms of calibration procedure. Conventional laboratory calibration of the ILS is, however, primitive, and only little is known about the performance of the ILS, which is partly the reason for its limited application by users (e.g. Shepherd and Xu, 1993).

As an irradiance spectroradiometer, two main characteristics of the ILS were investigated in Chapter 5: its radiometric properties and its angular response. The radiometric properties included irradiance conversion coefficients and a linearity check of the spectral response under variable illumination. Although the radiometric response of the ILS was shown to be linear, noisy signals in short wavelengths (< 500 *nm*, as similarly shown by Shepherd and Xu, 1993) indicated that there might be a 'cut-off wavelength' as an intrinsic property of the fibre optic cable. The angular response of the ILS was tested in order to verify if it behaves as a true cosine receptor. A collimator experiment with variable angular positions of the ILS showed that the relative response varied less than ~4 % from its nadir position, which is acceptable as a cosine receptor.

10.3. Influence of atmospheric variations on images

Another important task in pre-processing optical RS images is associated with atmospheric effects. When electromagnetic energy emitted from the Sun travels through the Earth's atmosphere, it interacts with atmospheric constituents in the form of scattering and absorption, before and after reflection from the target objects until it reaches the sensor. Consequently, the possibility of directly using remotely sensed data for retrieval of environmental variables is greatly reduced. While uncertainties from the sensor itself are monitored frequently and, in general, its magnitudes are relatively consistent within predetermined ranges (as shown in Part I), atmospheric effects on an image are often difficult to predict due to their spatially and temporally variable nature. This limits the operational ability of the RS technique as a true year-round tool for environmental sciences.

One of the main advantages of airborne optical RS is flexibility in time and space. Atmospheric effects can be minimised in that aircraft can fly under cirrus clouds or wait for suitable conditions. Data can also be collected when spaceborne sensors are not in a required location (e.g. in the event of oil spills, floods, or forest fires). On the other hand, there are difficulties to overcome with airborne sensing. First, the total atmospheric effect in airborne sensing may be less than spaceborne sensing as aircraft operate in the middle of atmosphere, but estimating its magnitude is more difficult because of the variable altitudes of aircraft (i.e. the constant air mass of incident and reflected radiation would make atmospheric correction relatively easier for spaceborne sensors). Moreover, the fact that the majority of atmospheric constituents exist in the troposphere, where most airborne sensors operate, means that there is only a limited reduction in atmospheric effects in airborne RS (Kings *et al.*, 1997). Second, airborne sensors normally have a wider FOV than satellite sensors, resulting in more surface BRDF effects. Thirdly, airborne sensors operate under an unstable platform environment, and therefore, Sun-target-sensor geometry in each pixel of the scene is highly variable depending on the aircraft's attitude.

A lot of work has focused on understanding the interaction between the Sun's electromagnetic energy and atmospheric constituents, not only for the atmospheric standardisation/correction of optical RS data, but also for atmospheric research itself. Techniques, which separate the atmospheric contribution from optical RS data, are divided into

three main categories: empirical model, image-based, and radiative transfer (RT) model-based methods. The selection of an appropriate method among these should be decided on the basis of the available dataset that represent the atmospheric conditions and the required accuracy of the result that is directly related to the robustness and computational resources available. Reviews of a variety of atmospheric correction methods in Section 6.4 concluded that the most satisfactory results normally came from the retrieval of *in situ* atmospheric information at the time of image acquisition. A RT-model with a thorough theoretical background resulted in the best quality output when *in situ* measurements were used as atmospheric input parameters (e.g. Clark *et al.*, 1999). Consequently, atmospheric information affecting an RS image (e.g. the magnitude of diffuse radiation associated with the abundance of atmospheric constituents) is most appropriately retrieved from the image itself or by independent measurements conducted at the time of image acquisition.

In Chapter 7, analysis from a ground-based experiment (i.e. there was no atmospheric path radiance between target and sensor) showed that frequently changing atmospheric conditions played an important role in the changing position of the data cloud in feature space. The variation was sensitive enough to directly affect accuracies in feature-space based analysis (e.g. spectral mixing or vegetation indices). It also determined a pattern and range of data plots available within the feature space, which would cause a certain magnitude of discrepancy for the use of laboratory-measured spectral endmembers (see Section 7.6.3). Another important factor to notice from this study, is that, even for ground-based field spectroradiometer measurements, radiance data are affected by variations in atmospheric conditions. Due to spectrally different atmospheric scattering, a shadow-line, which represents illumination changes while the target remains unchanged, is theoretically unable to pass through the origin of the spectral feature space, and the position of the shadow-line varies depending on the magnitude of diffuse radiation. This suggests that conventional feature space analysis methods (such as NDVI or SAM, all of which normally consider the origin as a reference point) should be expected to have systematic errors, as long as a diffuse radiation factor exists within the reflected radiance value. To an extent, an inaccurate dark point might also remain even after applying some atmospheric correction algorithms that only deal with atmospheric path radiance between the target and the sensor (e.g. empirical line method or image-based methods).

A new approach to atmospheric correction was described using shadows in the scene (as an image-based method) (Chapter 8). Shadows are generally caused by objects obstructing

direct incident light that would otherwise have reached the target object. Scene shadows have been a frequent problem in many applications of remotely sensed images, such as image classification or spectral mixing analysis. Radiometric properties of shadows, however, vary depending on a type and magnitude of atmospheric constituents, and could be possibly used as a source of information about the atmospheric condition. For example, if there were no diffuse radiation in the atmosphere, objects in shadow would not be seen, whereas a scene in shadows could be recognised when there is diffuse radiation, that is, coming from different directions. Therefore, radiation reflected from scene shadows is a spectral signature of target that is illuminated only by diffuse radiation.

This scene-shadow atmospheric correction method is based on the idea that diffuse radiation affects the characteristics of the DPVE (Dark Point Virtual Endmember) introduced in Chapter 7: when reflected radiation of any ground targets is under reduced illumination due to shading, the data plot converges into a single point in spectral feature space. A simple test showed that the DPVE of a scene exists in two-dimensional feature space, and its position is determined by a combination of diffuse radiation and atmospheric path radiance. Subtraction of DPVE values from a scene theoretically removes the contribution from the atmosphere for each pixel in an image. This was then extended to *n*-dimensional spectral bands. A PCA based semi-automatic shadow boundary selection method successfully selected the shade-only ROIs over a uniform target area, and SVD computed *n*-dimensional DPVE with an acceptable RMS error. The spectral DPVE were, as defined, generally darker than any other pixel spectrum in the scene, suggesting that the differences could represent the effect from diffuse radiation. As shown in two-dimensional DPVE correction, multispectral DPVE also resulted in an effective shadow suppressed image by removing atmospheric scattering from a scene.

The second atmospheric correction method explored used a downwelling irradiance sensor at the same level as the airborne sensor (Chapter 9). The CASI-2's ILS, the performance properties of which were examined in Chapter 5, has been used since the CASI-2 sensor was put on the market. The at-sensor irradiance sensor was developed on the basis that, if the total incident radiation at the sensor altitude is known, the magnitude of atmospheric effect for both incident and reflected radiation could be the same and simplify atmospheric correction algorithm. In fact, many attempts of atmospheric correction for spaceborne RS images have taken advantage of the electromagnetic energy travelling twice the complete thickness of the

atmosphere (i.e. the same amount of atmospheric transmittance both ways) and of relatively easy estimation of the solar irradiance at the top of the atmosphere.

Atmospheric correction methods using at-sensor irradiance measurements, however, have rarely been operational due to the nature of airborne platforms. The relative instability makes it difficult to keep the cosine receptor in a horizontal position, and the ILS signals tend to change depending on the aircraft's motion and flight direction with respect to Sun, as well as with the variation of atmospheric conditions above the sensor altitude. While estimation of the ILS position due to aircraft motion and the relative Sun angle can be obtained with the navigation system used for geometric correction, the correction of the ILS signal may be obtained by a sky irradiance model in order to retrieve at-sensor irradiation as if it was measured on a horizontal plane. The model considers each ILS scan at an instantaneous position as a cosine receptor on tilted plane. Results from two simple sky irradiance models (for clear and overcast conditions) showed that fixed models were not accurate enough to simulate downwelling irradiance under ordinary sky conditions. Instead, a variable fraction of these two models was more successful for ILS correction.

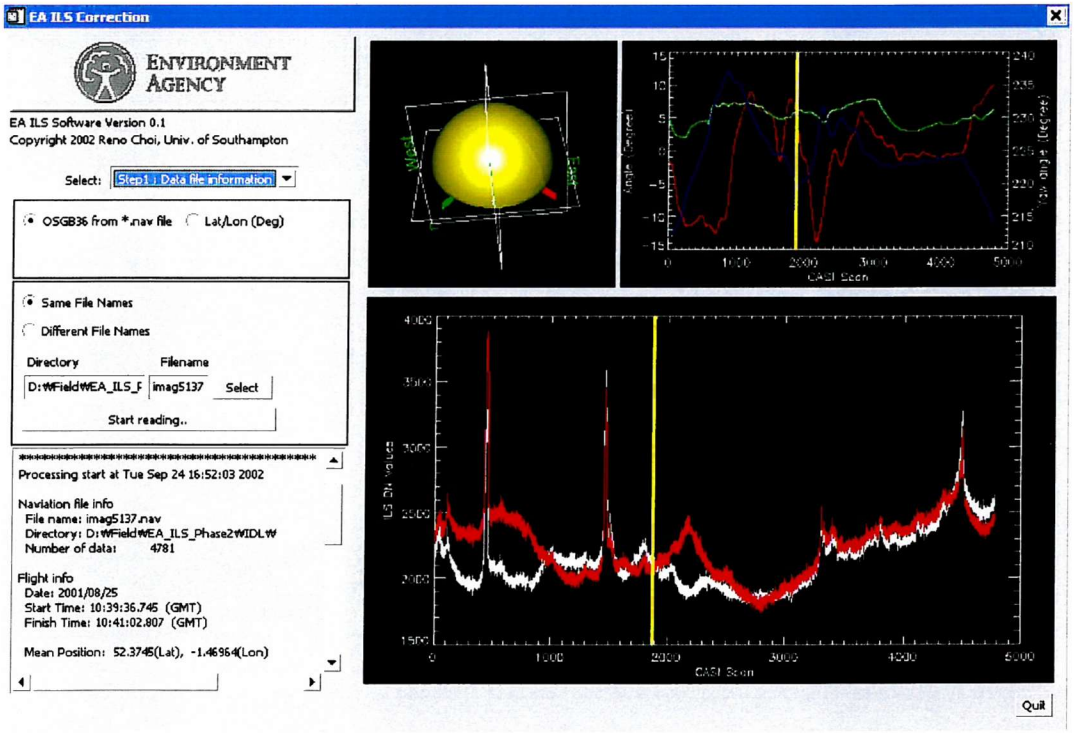

Figure 10-1. The main GUI (Graphic User Interface) window of SCILS (Standardization of CASI Incident Light Sensor).

A computer program called *SCILS* (Standardization of CASI Incident Light Sensor) has been developed for use with the Compact Airborne Spectrographic Imager (CASI) owned by the UK Environment Agency (EA) (Figure 10-1). In essence, the program uses a flexible combined sky irradiance model to recreate the irradiance that would have been measured had the aircraft been flying perfectly level. A correction can then be applied to the image data in order to standardise several flightlines prior to mosaicing or classification.

A more complicated (but possibly more useful) ILS correction has been attempted using an all-weather sky radiance distribution model (SRDM). Originally, SRDM on slope required several atmospheric parameters as input data, but inversion of the model means that such atmospheric information could be obtained if a series of instantaneous ILS positions were used as the model input. With an assumption that spatial distribution of atmospheric condition over an entire flightline is uniform, the minimum standard deviation of ILS's variation from the available group of model coefficients determined the most appropriate atmospheric parameters for the dataset. The model results for three example ILS datasets flown over the same ground reference site and two opposite (180°) flight direction datasets demonstrated that the inverse SRDM method standardised temporal and spatial ILS data successfully. As it is based on a SRDM, the model coefficients for a flightline could also be used to acquire a distribution of sky radiance over the sky dome, which could, potentially help estimate surface BRDF.

10.4. Concluding remarks and future studies

The various tasks described as 'pre-processing' are fundamental to the effective use of remotely sensed data. If RS is to take its place amongst the various scientific techniques available to study the environment it is essential that end-users have confidence in the data they are using, and are provided with accurate and meaningful statements about its precision and accuracy. In this thesis, two important aspects of pre-processing were discussed: sensor calibration and atmospheric correction.

Laboratory calibration does not always show every aspect of sensor performance, and it may be neither cost-effective nor even possible to determine complete knowledge of the sensor's performance in the laboratory alone. However, the research described here has shown how it is possible, with relatively limited resources, to go beyond the basic manufacturer's calibration and acquire information to address several important areas of concern for an array-based imaging spectrometer. The study focused on the Itres Research CASI-2 instrument, which is highly-regarded and used in many countries around the world. The study identified several aspects of the present calibration procedure recommended by the manufacturer, and its implementation by the NERC EPFS in the UK, that could be improved:

- The overall spectral calibration procedure could be improved if more was known about the 'optical smile' affecting the spectral calibration of the CASI system.

- The SRF of the CASI-2 was determined independently of the manufacturer for the first time, using an innovative numerical technique. Although this was just a preliminary investigation of this parameter, the results suggested that this would be a fruitful line of further enquiry as knowledge of the SRF is crucially important if CASI data are to be assimilated into physical models.

- Limitations of the spectral radiance standard recommended by the manufacturer were identified in relation to its spatial uniformity and the need to merge the two halves of the calibration image. To be fair to the manufacturer, this problem has only arisen since the sensor owner (NERC) replaced the original lens with one having a large field-of-

view. Clearly, enhancement of the system did not fully consider the impact of this upon the calibration procedure.

- Itres Research Ltd, manufacturer of CASI-2 system, is currently developing a new way of ILS data collection using all the CCD columns allocated for the ILS (approximately 30-40 columns) rather than a single column (Personal communication from Tyme Witterbrood, Itres Research Ltd, 2003). This, together with planned hardware improvements already in the pipeline, will greatly enhance the potential of data from the ILS, making it even more important that users are provide with the necessary tools and information to make use of this sensor.

Atmospheric effects on remotely sensed data were reviewed and the effects of atmospheric variability studied in terms of how this influences the remotely sensed signal. Temporal variations in atmospheric clarity (and by extension, spatial variations typical of RS image data), were shown to cause errors which also affected multispectral ratio-based analysis. Two novel practical methods of atmospheric correction were developed following a series of practical experiments and theoretical studies. The first was an image-based method which can be used to achieve a qualitative improvement in image quality, a reduction in scene noise due to shadowing, and an improvement in the accuracy of multispectral ratios. The second described an innovative way to use the data on downwelling irradiance measured by a roof-mounted sensor to correct for irradiance radiation affecting RS data. The method also had the potential to provide data on the sky irradiance distribution at the time of sensing. The following are suggestions for further studies which could extend the findings in this thesis.

- The relationship between DPVE position and atmospheric diffuse radiation suggests that spectroradiometer data collected in a controlled environment (e.g. laboratory) could be different from that in field-based or RS data. So, for example, failure to consider the diffuse radiation component could cause errors when laboratory-derived spectral endmembers are transferred to the field environment for use in spectral unmixing.

- An atmospheric correction algorithm using in-scene shadow would enhance the operational application of remote sensing. However, the possible differences between different types of shadows were not discussed in this thesis, and very few studies have addressed this, although Leblon *et al.* (1996) stands out in this respect. It may be

possible to improve the shadow removal technique developed in this research to discriminate more effectively between different types of shadow which could be very useful in some applications, e.g. tree species classification, where the transmission between leaves from different species is known to vary.

- The use of data from an at-sensor spectral irradiance sensor also has tremendous potential for further development. Undoubtably, this will be challenging and the research described here is only the first step towards making data from the CASI ILS more useful. However, it is an important first step and it begins to unlock the potential of what has up to now been a largely ignored source of data about the atmosphere and its influence upon the remotely sensed signal.

Appendix A

Sensor system: Laboratory Calibration of the CASI-2

A.1. Introduction

The main objective of optical passive remote sensing is to distinguish objects on the Earth's surface by detecting electromagnetic energy reflected by them. The signal received from a remote sensing instrument must therefore be converted into an appropriate radiant unit.

Sensor calibration is a process that characterises the sensor response with a sensible physical unit (Système International, SI) and makes its measurement independent of the sensor and conditions of measurement. The sensor calibration procedure often involves three stages: the sensor characterisation, the sensor output calibration, and the evaluation of the calibration results. These categories are tested in various ways, such as, in the laboratory, during the sensor's operation, or by using an internal calibration device.

The importance of routine calibration is particularly important due to the harsh conditions during sensor operation (Hildum *et al.*, 2001). Furthermore, as the sensor technology is progressing rapidly users demand higher quality data.

The CASI-2 follows the laboratory calibration procedure originally established when the CASI was first developed and that has later been modified by the manufacturer (Babey and Soffer, 1993; Itres Research Ltd, 1995). The CASI-2 operated by NERC ARSF is calibrated by NERC Equipment Pool for Field Spectroscopy (EPFS), at least two or three times a year.

The following sections describe the CASI-2 calibration procedure currently carried out by NERC EPFS that mainly consists of five parts.

1. Sensor characteristics
2. Wavelength calibration
3. Radiometric calibration
4. ILS calibration
5. Evaluation of the calibration results

A.2. Calibration Standards

A calibration standard is used to relate the signal output from an instrument to the appropriate physical unit. The standards are most often characterized as primary, secondary, or alternative standards. Primary standards are prepared from traceable materials by national standards organisations, such as the UK NPL, using precise methodologies and under controlled environmental conditions. Such near absolute standards are then compared with the secondary standards from a manufacturer (or an independent testing organisation). The secondary standards are calibration transfer devices, with traceability, to give instrument calibration results equivalent (within certain limits) to those obtained when an instrument is calibrated with a primary standard.

The standards employed during the CASI-2 calibration are secondary standards in the forms of a continuum luminance source, a variety of spectral emission line sources, and a ceramic tile for reflectance responsivity. For optimal calibration results, they are the CASI-2 manufacturer recommended standards and are routinely tested against primary standards from the UK NPL.

A.2.1. Radiance source

The radiance standard is a continuum illumination source that has a known intensity, and used for absolute radiometric calibration of spectrometers. The lowest calibration uncertainties of the radiance standard are achieved by considering stability, repeatability, and reproducibility (Hopkinson *et al.*, 2000).

Since a controllable luminance source with high stability and uniformity is required, an integrating sphere, as a widely used radiance standard, is used for the CASI-2 calibration. It is defined as a device that makes a spatial integration of luminous flux (or radiant flux) generated (or introduced) in the sphere (Ohno, 1999). The internal wall of the integrating sphere is coated with a white diffusing material of high reflectance (e.g. $BASO_4$, barium sulphate paint) acting as a secondary source, ensuring that ideally the amount of flux incident anywhere on the sphere wall will create an equal illumination (non-directional) on the exit port. The sphere normally provides much more degree of uniformity than a single plane diffuser, due to multiple reflections (equation [A.1]) of light in the sphere.

$$\Phi\left(\rho+\rho^2+\rho^3+\cdots\right)=\Phi\cdot\frac{\rho}{1-\rho} \qquad [A.1]$$

where, Φ Luminous flux from a light source $[W]$
ρ Reflectance inside a hollow sphere (0-1)

Hence, the sphere efficiency (E_d/Φ) becomes greater with multiple reflections than a single reflectance, as follows,

$$E_d=\Phi\cdot\frac{\rho}{1-\rho}\cdot\frac{1}{4\cdot\pi\cdot r^2} \qquad [A.2]$$

where, E_d Illuminance in a unit area after multiple reflection $[Wm^{-2}]$
r Radius of the sphere $[m]$

Equation [A.2] also indicates that small improvement of the internal reflectance yields large changes of the sphere efficiency. For example, the detector signal at ρ of 0.99 is twice greater than at ρ of 0.98. More importantly, the diffuser coating should be uniformly covered to maximise the uniformity of non-directional illumination.

Colour temperature is a function of current setting of the lamp, and may contribute large errors, particularly in the short wavelength region. It is the colour appearance of a light source (the temperature of a black body or Planckian radiator having the same chromaticity as the source Hopkinson *et al.*, 2000).

For the CASI-2 radiometric calibration at NERC EPFS, the radiance source used is a Hoffman Engineering integrating sphere (Model number of LS-64-8D). The interior of the sphere is diameter of 15 *cm* with an exit port diameter of around 4.6 *cm* that is larger than CASI-2's objective lens and that is supposed to fill entire standard FOV of the SHU. The inside of the sphere is coated with a 1 *mm* layer of high purity $BASO_4$ for diffuse reflectance.

The illumination source is a highly stable 100 *W* quartz-halogen lamp light from which is reflected on the wall before it exits the sphere. The level of illumination can be adjusted by a micrometer controlling an aperture at top of the sphere. Silicon detectors responsive to red and blue are installed inside the sphere, monitoring the sphere's colour temperature. The spatial uniformity of luminance is to be around ± 0.05 % over 2.5 *cm* of horizontally across diameter at the centre of the exit port and ± 0.1 % within 4 *cm* of diameter.

For accuracy of the spectral radiance, the sphere is sent to the UK National Physical Laboratory (NPL) after every 12 months or 100 hours of use. While the lamp lasts more or less 500 hours according to the manufacturer, the ageing process of lamp's filament and possible contamination of the sphere should be checked and re-calibrated more regularly. The error margin of radiance values over the entire wavelength of the sphere's specification during a routine calibration is ±2% in relation to US National Institute of Standards and Technology (NIST) standards.

k	S_k
0	-10.1549773594
1	32.3616830154
2	-12.2251629204
3	1.3564350703
4	0.1098269477
5	-0.039576337
6	$3.5658711442\times10^{-3}$
7	$-1.2788006239\times10^{-4}$
8	$1.2544121355\times10^{-6}$

Table A-1. The polynomial coefficients calculated for equation [A.3]. The radiance data for the coefficients are from the sphere calibration at May 2001.

The calibrated spectral radiance of the sphere is provided at a specific lamp current and luminance setting, 3.195 *A* and 1000 *fL*[‡‡], respectively, by the NPL. The result of routine calibration has spectral radiance values with 2*nm* intervals from 300 to 800 *nm* and 10 *nm* intervals from 800 to 2500 *nm*. The calibrated radiance values are interpolated to match the centre wavelengths of each channel of the CASI CCD array. Nine coefficients from the least square polynomial fit to the calibrated radiance values are used as below,

$$L(\lambda_j) = \sum_{k=0}^{8} S_k \cdot \left(\frac{\lambda_j}{1000}\right)^{2\cdot(1-k)} \qquad [A.3]$$

where λ_j Centre wavelength for the CCD row j [*nm*]
L Sphere radiance [$\mu W\ cm^{-2}\ sr^{-1}\ nm^{-1}$]
k Polynomial indices ($k = 0 \ldots 8$)
S_k Polynomial coefficient (S-coefficient)

The example list of the nine polynomial coefficients (S-numbers) is shown in Table A-1.

A.2.2. Wavelength standards

The wavelength calibration is performed to match the spectral features from wavelength standards to the spectral pixels of an array detector in a spectrometry. The wavelength standards normally used are either (or both) spectral emissions (from line sources) or spectral absorption features (from filters or tiles).

NERC EPFS owns a set of spectrum tubes, manufactured by Electro-Technic Products, Inc. (http://www.electrotechnicproduct.com/), for the wavelength calibration of the CASI. The spectrum tubes contain one or more types of elements as gaseous atoms or molecules at low pressure. With the Electro-Technic Model SP-200 Spectrum Tube Power Supply, electrodes at the both ends of the tube supply energy of electric field in a tube. Ions and electrons are then accelerated and collided generating kinetic energy. As excited electron becomes unstable and tends to release its own energy, a photon of energy is emitted simultaneously by a function of the wavelength of light. Depending upon the type of excited atom in a tube, characteristic wavelengths with distinctive emission vary, resulting a series of monochromatic emission lines. Spectrum tubes are carefully controlled to assure maximum clarity and brightness.

There are four different spectrum tubes for NERC CASI-2 calibration, e.g. Helium, Hydrogen, Mercury, and Oxygen. Unique emission or absorption lines of each tube for the CASI calibration are

[‡‡] Footlambert (*fL*) is a unit of photometric brightness ($cd\pi^{-1}ft^{-2}$, where *cd* is candela (luminous flux per steradian)). Since luminous flux can be expressed by radiant flux ($lm = 1/683\ W$), $fL \cong 5\times10^{-3}\ Wm^{-2}sr^{-1}$ between 380 and 760 nm.

shown in Table A-2. While the intensity of each emission is likely to vary as the longer the tube is in use, their centre wavelengths are not supposed to change.

The width of spectral emission line is assumed to be much narrower than the mean spectral bandpass of the CASI-2. However, the manufacturer of the spectrum tube was not able to provide the width of each spectral line and the wavelength uncertainty of the tubes.

Spectrum Tube	Spectral emission lines (*nm*)	CCD rows number @ ncol 335 (pixel)	Centroid (pixel)
Helium (He)	728.1	111 – 120	115.57
	706.5	122 – 131	126.89
	667.8	142 – 151	147.11
	587.6	185 – 194	189.30
	501.6	230 – 239	235.21
Hydrogen (H)	656.3	149 – 158	153.21
	486.1	239 – 248	243.11
Mercury (Hg)	546.1	207 – 216	211.24
	435.8	265 – 274	270.12
Oxygen (O)	844.6	51 – 60	54.65
	777.5	85 – 94	89.85

Table A-2. Gas tubes and their spectral emission lines chosen for CASI-2 wavelength calibration. CCD row numbers and centroid values are from the CASI calibration (NERC26) in 4 July 2002.

A.2.3. Reflectance standards

Reflectance standards are ceramic tile (or panel) type standards that provides spatially and spectrally homogeneous reflectance to verify linearity and responsivity of spectrometers. For a proper reflectance standard, it also has greater than 80 % of reflectance with wavelengths of UV through NIR, as well as a highly Lambertian spectral reflectance behaviour. Like any other calibration standards, reflectance standards need to have regular maintenance and should have calibration from primary or secondary standards.

Description	Value
Spectral range	200 ~ 2500 *nm*
Reflectance	98 ~ 99 *%*
Thermal stability	Up to 350 *°C*
Vacuum stability	No outgassing except for entrained air
Laser damage threshold	> 8.0 Jm^{-2}
General use	UV – VIS – NIR
Density	1.25 ~ 1.5 gcm^{-3}
Water permeability	< 0.001 % (Hydrophobic)
Hardness	20 ~ 30 Shore D
Coefficient of linear expansion	5.5 ~ 6.5 × 10^{-4} *°C*
Flammability	Non-flammable

Table A-3. Specifications of the Spectralon™ diffuse reflectance panel (Labsphere Inc., 2001)

In addition to their use in calibration, reflectance panels are often used in field spectroscopy. Simultaneous or sequential measurements of ground reflectance using spectroradiometer need both target reflected and solar irradiance, and reflectance panels are used for the reflection of incident irradiance so as to capture the diffused radiance into the radiometer's FOV for irradiance measurement.

The Spectralon™ diffuse reflectance panel used for the calibration of the CASI-2 ILS in NERC ARSF, has a dimension of ~5×5 *cm* composed of highly reflective (~99 *%*) pure polytetraflouroethylene (PTFE) powder. As it was originally designed for both laboratory and field applications that is normally exposed to harsh environment, the Spectralon® diffuse reflectance panel is compressed into a hard material with a barium sulphate ($BaSO_4$) coating on its surface for a relatively flat spectral response (< ~5 *%* of variation) in VNIR with near complete opaque reflectance.

The reflectance factor for the panel was measured by the NPL in April 2000. For two different geometry (0° and 45°) of its spectral characteristics, the random uncertainties of the reflectance factor measurements were estimated as less than 0.65 *%* within the spectral range between 320 and 800 *nm* and less than 2.3 *%* in 800-2000 *nm* region.

A.3. Spectrometer Characterisations

The calibration procedure of the CASI-2 starts with the characterisation of the sensor system to assure the sensor operation, called 'Pre-calibration'. This procedure involves the performance check within the limits specified by the manufacturer.

The tests carried out during the pre-calibration cover most items representing the sensor states and specifications shown in Section 3.4, otherwise pre-determined by the manufacturer (e.g. frame shift smear, scattered light). Tests for the CASI-2's operational parameters and hardware conditions are relatively straightforward in terms of data acquisition and their processing. In contrast, CASI-2's signal related pre-calibration tests may require background information and thereby are described in the rest of this section. Since spectral alignment check is carried out with the data acquired for wavelength calibration, it is shown in the next section (section A.4).

A.3.1. Dark current noise

The dark current noise has linear behaviour with the IT values (Table 3-5. in page 57). CASI-2's DC generation rate is defined as the slope of the line fitted to the DC values with their corresponding ITs, while its intercept represents electronic offset (EO). Both are sensitive to the temperature variation. With a pair of dark signal at different ITs, the DC generation rate is,

$$dcgr = \frac{s_1 - s_2}{it_1 - it_2} \qquad [A.4]$$

where
- $dcgr$ DC generation rate $[DNs^{-1}]$
- s_1, s_2 Dark signal for it_1 and it_2, respectively $[DN]$
- it_1, it_2 IT values for s_1 and s_2, respectively $[s]$

A.3.2. Sources of noise: Light Transfer Curve (LTC)

The level of noise generated in the CASI-2 data is quantified and categorised by the Light Transfer Curve (LTC) method introduced by Janesik *et al.* (1985). The procedure mainly consists of two parameters representing the noise level, image related (σ_{PT}^2) and non-imaging related ones (σ_o^2).

$$\sigma_T^2 = \sigma_{PT}^2 + \sigma_o^2 \qquad [A.5]$$

where
- σ_T^2 Total signal variance $[electrons^2]$
- σ_{PT}^2 Photo/thermal-induced signal variance $[electrons^2]$
- σ_o^2 Instrument-induced signal variance $[electrons^2]$

The non-signal related noises from various sources are represented by the system noise floor, whereas the errors induced by the measured pixel values are characterised by the system electronic gain (or system gain).

The magnitude of electrical signal as a response of captured photons is converted into DN values within the dynamic range of the instrument. Due to the nature of a quantisation process, the discrepancies are included in relationship between the number of electrons and DN values. It is normally generated by the signal nonlinearity (Hopkinson *et al.*, 2000).

$$ne = n \cdot G + Q_o \qquad [A.6]$$

where
- ne Number of electrons [*electrons*]
- n Quantisation value from a pixel [*DN*]
- G System gain [*electrons* DN^{-1}]
- Q_o Quantisation error (~0.3 $DN \times G$) [*electrons*]

Since the linearity of the CASI-2 generally is assumed by its manufacturer, the quantisation error is neglected in this processing. To investigate errors in electrical signal, equation [A.6] is used for the equation [A.5], and re-written,

$$S_T^2 \cdot G^2 = S_{PT}^2 \cdot G^2 + S_o^2 \cdot G^2 \qquad [A.7]$$

Where
- S_T^2 Total sample variance [DN^2]
- S_{PT}^2 Photo/thermal-induced sample variance [DN^2]
- S_o^2 Instrument-induced sample variance [DN^2]

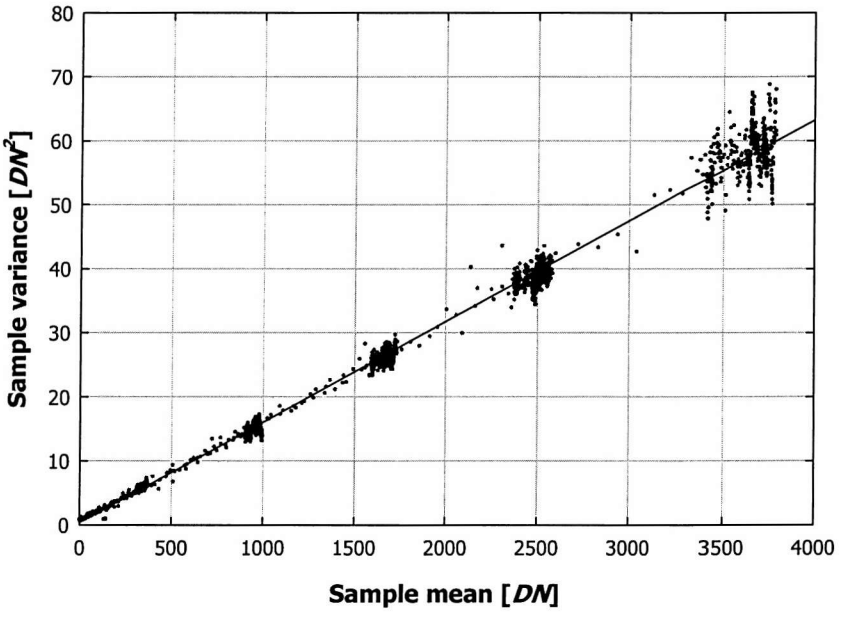

Figure A-1. A plot of sample variance against the sample mean (dotted) and linear regression line (solid) from a data collected during the NERC's CASI-2 calibration (February 2003).

To distinguish between photo/thermal-induced and instrument-induced electrons, it is assumed that the photo/thermal-induced signal is a Poisson process (Equation [A.8])

$$\left|S_T^2 \cdot G^2\right| = \left|\langle x \rangle \cdot G\right| \qquad [A.8]$$

Hence, equation [A.7] becomes functions of the sample mean ($\langle x \rangle$) and total variation (S_T^2), which are computed from the sample data, as follows,

$$S_T^2 = \langle x \rangle \cdot G^{-1} + S_o^2 \qquad [A.9]$$

And both system gain (G) and instrument-induced sample variance (S_o^2) can be computed by a linear regression line. Figure A-1 shows an example plot of the sample variance against the sample mean. From this plot, the system gain is an inverse of slope value from the regression line, while noise floor (*nfl*) can be obtained by using both slope and intercept values as the following equation.

$$G = \frac{1}{Slope} \qquad [A.10]$$

$$nfl = S_o \cdot G = \frac{\sqrt{Intercept}}{Slope} \qquad [A.11]$$

The ratio of signal to its corresponding total noise (σ_T) defines the Signal-to-Noise Ratio (*SNR*), which indicates the efficiency of true signal against magnitude of errors from various sources. Generally, maximum SNR is achieved at instrument's largest signal (Figure A-2), according to the equation below,

$$SNR_{\max} = \frac{\max(e_{total}) - e_{dark}}{\sqrt{\sigma_{PT}^2 + \sigma_o^2}} = \frac{G \cdot \max(\langle x \rangle)}{\sqrt{G \cdot \max(\langle x \rangle) + nfl^2}} \qquad [A.12]$$

Where
- SNR_{max} Maximum SNR from a measurement
- e_{total} Total electrons sampled [*electrons*]
- e_{dark} Sample electrons from DC [*electrons*]
- *Max()* Maximum value of variable inside the parenthesis [*DN*]

For the CASI-2's LTC test, the Hoffman integrating sphere illuminates the SHU in spatial mode with 6 spectral bands specified by Itres Research Ltd. The CASI-2 image is recorded for more than 5000 scan lines against the inherently stable and constant radiation source, hence variations from the data would represent the instrument's noise. Sufficient range of pixel values (within dynamic range) for the analysis (see Section 3.3.2) is acquired simultaneously in 6 spectral bands, since radiance spectrum of integrating sphere is gradually increasing with wavelengths. Each individual spatial pixels (512 columns) over the recorded scan lines is then used to compute the sample mean ($\langle x \rangle$) and total variation (S_T^2) for the processing shown above.

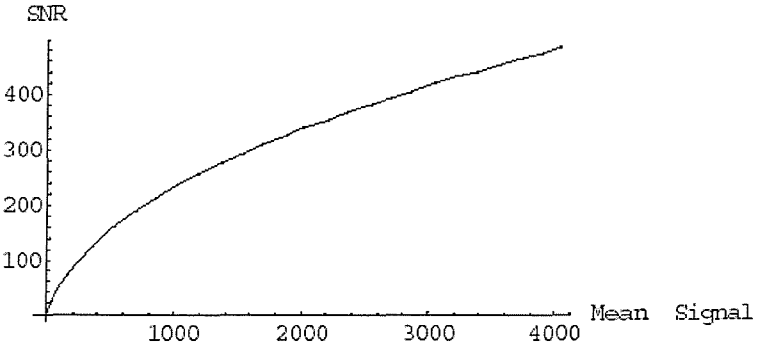

Figure A-2. The relation between SNR and signal levels (Itres Research Ltd, 2001). In this particular example, *G* of 60 [*electrons DN*$^{-1}$] and *nfl* of 1.4 [*electrons*] with a signal level of 4025 [*DN*].

It is important to note that the maximum SNR is the largest value that can be theoretically obtained. During CASI-2's real operation, SNR could decrease depending on the level of signal and due to the nature of the airborne platform (such as engine vibrations or shocks while flying). Nonetheless, Itres Research Ltd guarantees high enough SNR value even under low radiation conditions where normally the signal revel is adjusted by using IT or aperture settings at first. Typical values resulted from the LTC processing is listed in Table A-4.

Parameter	Value
System gain [*electrons DN*$^{-1}$]	63.63
Noise floor [*electrons*]	39.44
Maximum SNR	489.62
Measured offset [*DN*]	62.90
Saturation [*DN*]	3855

Table A-4. The results of LTC processing from NERC's CASI-2 calibration (February 2003).

A.3.3. Determination of ILS centroid

Only a single column among the range of the CCD array allocated to the ILS is considered as the ILS data in the CASI-2. The reason for this is that the fibre optic cable from the ILS is glued and its position varies depending upon the particular CASI-2 system. To establish its change was originally a part of the pre-calibration procedure, called ILS centroid determination test, but it has been no longer a routine check since the year 2002. The ILS centroid is given in the CASI initialisation file (casi.ini) with the others after every laboratory calibrations.

It is basically to measure DN values in the ILS region of the CCD array and find the most sensitive column. The ILS centroids along the column wavelength are calculated as in equation [A.13].

$$C_j = \frac{\sum_n (cs+n)\cdot ILS_{j,n}}{\sum_n ILS_{j,n}} \qquad [A.13]$$

where
- cs Start number of the ILS region ($cs = 30$)
- c_j The ILS centroid value
- n Number of columns in the ILS region ($n = 0 \ldots 10$)
- $ILS_{j,n}$ ILS values (DN)

As mentioned, the ILS centroid is a unique characteristic of the specific CASI-2 system. In Figure A-3, the centroid curves are different from the NERC and EA CASI-2. The curves are mainly on column 35 at lower wavelengths and gradually move toward column 37 with the increasing wavelength. Nonetheless, both instruments show that the ILS centroids are still within the ILS region of the CCD array. A single column number for the CASI setup file is an average of the spectral variations of the centroids by using the equation [A.14]. The ILS column is 35 for NERC (34.69) and 38 for EA CASI-2 (38.94) that is assumed to be the most responsive for the ILS signal.

$$\frac{\sum_j C_j}{288} \qquad [A.14]$$

The ILS data are also recorded within the CASI raw format data, regardless its operational mode. While the on-board processor of the CASI-2 computes radiometrically corrected pixel values of the scene, the spectral response of the ILS is also converted into irradiance units. During the post-processing, the ILS data are retrieved and saved within the image data (last column in each line), separately in a hierarchical data format (HDF; NERC CASI-2) or in a separate file (EA CASI-2).

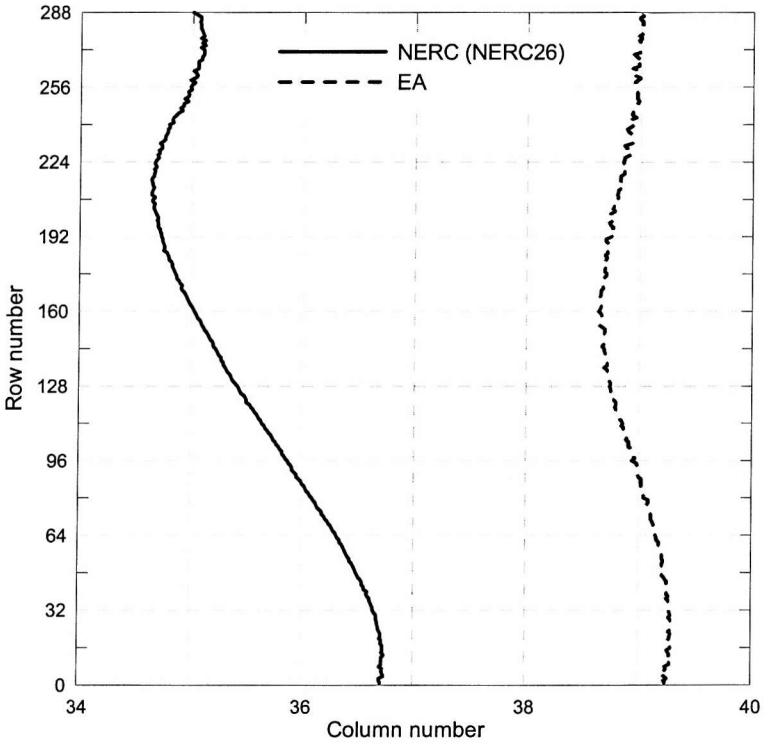

Figure A-3. The ILS centroid plot of NERC (Solid) and EA (Dashes).

A.4. Wavelength calibration

Wavelength calibration in the CASI-2 is to relate between CCD rows (spectral dimension of an detector array) and wavelength standards with known spectral features. This is a part of routine laboratory calibration procedure since the responsive wavelength for each individual CCD row varies due to many sources, such as the alignment change or contamination of the CCD array, diffraction grating, lenses, and entrance slit.

During the CASI-2's calibration, tests for the wavelength related properties consist of two categories. First, spectral properties and performance check due to physical changes on sensor system about spectral measurements are examined by spectral alignments. Second, the variations of centre wavelength assigned for each CCD row as a result of changes in spectral properties are tested by wavelength determination.

Four spectrum tubes, e.g. Helium, Hydrogen, Mercury, and Oxygen, are placed in front of an objective lens of the SHU with a diffuse glass attached in order to illuminate uniformly across entire width of slit (Table A-2). With aperture setting of 3, IT is individually adjusted for each spectral emission line in order to see a clear spectral feature in the wavelength region. Like many wavelength calibration of spectrometers, spectral resolution of emission features from the spectrum tubes are greater than that of an array detector output. The wavelengths of the emission lines are with an accuracy of 0.1 *nm*, and hence the pixel position of the CCD row for a spectral feature will be estimated within sub-pixel accuracy.

A.4.1. Determination of spectral alignment

To measure misalignment and contamination of the CASI-2's optical system and its array detector, the spectral alignment is performed. The CASI-2's manufacturer recommends comparing both ends of image swath (512 pixels) rather than the entire pixels across.

$$alignment = \left(\langle r \rangle_{135} - \langle r \rangle_{535}\right) \cdot \frac{512}{135 - 535} \qquad [A.15]$$

where $\langle r \rangle_c$ Mean row CCD number c [*pixel*]
alignment Spectral alignment [*pixel*]

Test of spectral alignment is made using an emission line of Hydrogen (656.3 *nm*), since it is close to the centre of the CCD row (~152 pixel out of 288 pixels). An acceptable spectral alignment is <0.3 pixels, i.e. ~16 % of pixel offset from the mean wavelength interval of ~1.9 *nm*. From the NERC CASI-2 calibration in February 2003, the spectral alignment value was recorded as 0.11.

One of the main objectives of the spectral alignment is to examine an effect known as optical smile on the spectral sampling of the CASI-2 (see Table 3-6). In many cases for the CASI-2 calibration, a simple two-point measurement is sufficient to realise the spectral misalignment if the arrangements between the sensor elements deviates like rotation or twist (i.e. right-down/left-up of the CCD array and vice versa). Result from the spectral alignment sometimes remains unclear with the spectral alignment test using just two points. Due to the smile feature, the mean row numbers in the centre of spatial columns are possibly lower or higher than those at both ends of the imaging swath, while the result from equation [A.15] becomes near zero (i.e. shifted in one direction).

A.4.2. Wavelength determination

The assignment of centre wavelengths over rows of the detector array is the main purpose of the wavelength determination processing. Although it was shown in the earlier section that wavelength

response in each row of the CCD array is not identical across its spatial column, the spatial variation of spectral response is ignored in this processing in terms of simplifying the procedure and operational.

Eleven selected spectral emission lines from low pressure gas lamps spread evenly over the spectral range of the CCD array are used (Table A-2). The same equation as in spectral alignment test (Equation [4.2] in p.76) is used to obtain sub-pixel position of each spectral line.

The CASI-2 setup is supposed to acquire the largest signals. The SHU is placed with the slit horizontal, while the spectral gas tube is set vertically. This instrument setting is to obtain a spot radiance from the lamp, although there is lack of spatial coverage. The CASI-2's SHU is placed in front of the lamp diffused by an opal glass in order to disperse the illumination across at least ± 10 spatial pixels from the CASI-2's optical axis (column 335). The signal recorded is *in situ* DC corrected, avoiding possible errors from the actual emission signal. Also emission lines with low SNR require more than one reading, which averages (and minimises as a result) random noise of an apparent shift in the row position of the emission line.

Sub-pixel positions acquired from spectral tubes with known wavelengths of emission lines are paired. The relation between the discrete data pairs provides a model for a continuous association between wavelength and each spectral pixel of the CASI-2. In an ideal condition, the sensor's optical system and an array detector make such relationship linear. However, the CASI-2's wavelength determination method is designed to take into account possible non-linearity, for example, as follows,

1) Misalignment between lens, slit, grating, and CCD array, like spectral smile features
2) Microscopic irregularities in the groove spacing of the grating
3) Imperfect size or spacing of the CCD elements

Because of these, a third order polynomial fitting is applied to represent the functional relationship between wavelength and the CCD row (Figure A-4). The coefficients of a polynomial regression are known as '*g*-numbers', and they are calculated by the following equation,

$$g_j = (A^T \cdot A)^{-1} \cdot A^T \cdot \Lambda \qquad [A.16]$$

where g_j Coefficients of a third order polynomial regression
A $A_{ij}=<r>_i^j$
Λ Spectrum line wavelength data set ($\Lambda=A \cdot g$) [*nm*]
i Index of the spectrum line data set (0...10)
j Index of the third order polynomial (0...3)

And estimation of centre wavelength for each row of detector array is

$$\lambda(r) = g_0 + g_1 \cdot r + g_2 \cdot r^2 + g_3 \cdot r^3 = \sum_{l=0}^{3} g_l \cdot r^l \qquad [A.17]$$

where λ Wavelength [*nm*]
r Row number of the CCD array [*pixel*]

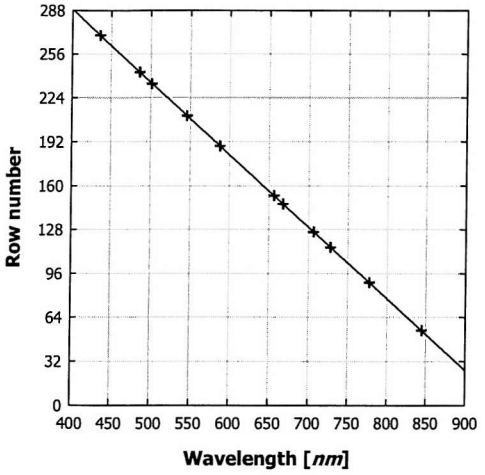

Figure A-4. Wavelength calibration for NERC CASI-2 (February 2003). Dots are from the measured sub-pixel position, whereas the solid line is the polynomial fit to the data.

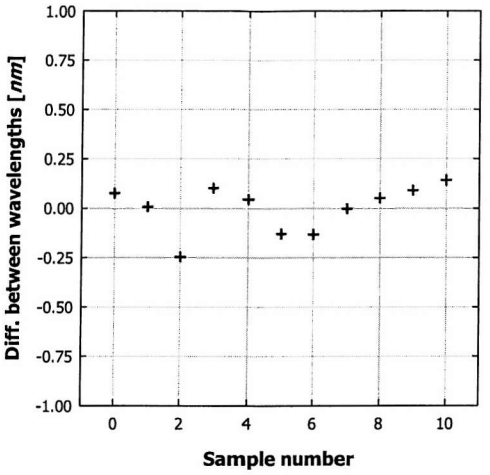

Figure A-5. A plot of differences between measured/poly-fit wavelengths for 11 data pairs. Data are from the same calibration event in Figure A-4.

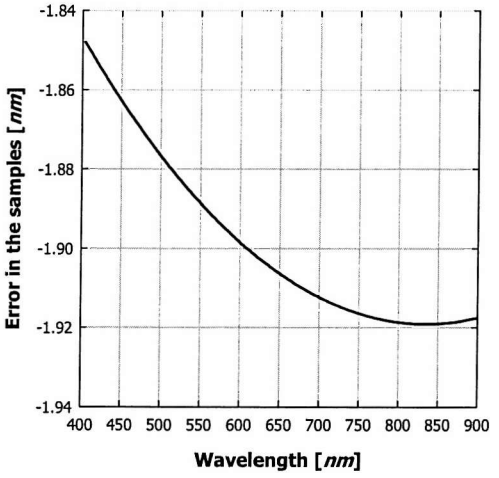

Figure A-6. Deviation of the sample position to the poly-fit line. Data are from the same calibration event in Figure A-4.

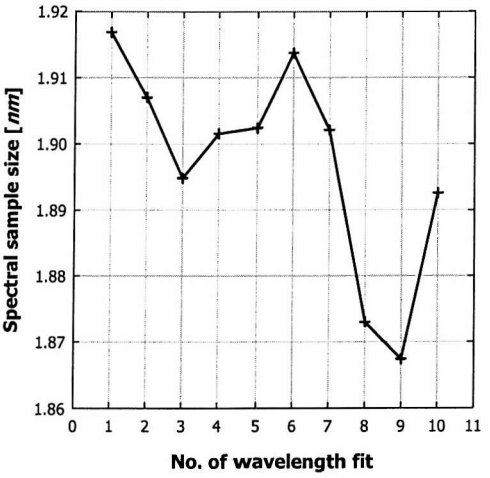

Figure A-7. The minimum spectral sampling interval (normally 1.9 *nm*). Data are from the same calibration event in Figure A-4.

The wavelength calibration results are verified by the goodness of fit of the polynomial to the data pair measured and the standard deviation of the difference between the fitted and true wavelengths for the measured sub-pixel positions. The residual error in the polynomial fit is no greater than ±0.2 *nm* for the NERC CASI-2 calibration in February 2003, the maximum uncertainty induced by the polynomial fit is around 10 % (on the basis of the estimated maximum band width is 2.2 *nm*) at the optical axis region (Figure A-5). The standard deviation (σ) of the estimates/measured difference indicates that the magnitude of their disagreement can be predicted as a probability of the error. From the same calibration

event, σ of 0.115 means that the error from the polynomial fit would be ≤ 0.115 *nm* with a probability of ≤ 68.26 % (at 1σ) or 0.230 *nm* with ≤ 95.44 % chance (at 2σ).

With the spectral alignment test, a total maximum uncertainty of the wavelength assignment for rows of the CCD array is 0.3 *nm* (0.2 + 0.1; ~14 % of a pixel). If the entire FOV and wavelength range are considered, the new total uncertainty would become 0.8 *nm* (0.2 + 0.6; ~36 % of a pixel) at the centre optical axis (column 335).

On the whole, wavelength calibration is the most sensitive procedure in the CASI-2 calibration. Sub-pixel position may vary depending on the number of samples and their starting row. There are also certain errors in the interpolation method, i.e. centre of gravity method. Moreover, sources of systematic errors, such as spectral alignment problem (optical smile feature) mainly induced by optical distortion, may contribute total errors in wavelength calibration. Complete verification of such problems are compensated with entire system performance and efforts involved during the instrument calibration. However, it is important to understand the sources of errors and significance on the spectral basis analysis with the CASI-2 data. As an example, one of the common mistakes that often occur in the image analysis is presented in Section 4.3.

A.5. Radiometric Calibration

In combination with the wavelength calibration, the laboratory radiometric calibration is to determine the relationship between physically meaning radiance units from the electrical signal of the instrument. For the CASI-2, as an array detector imaging spectrometer, radiometric calibration should be applied for each individual detector element. Thus, the following items are necessarily taken into account for conducting radiometric calibration of a detector array instrument.

1) Each CCD element is projected by uniform (or at least known) illumination in terms of maintaining the calibration accuracy.
2) Generally determined instrument-induced noises during pre-calibration are also taken into account as susceptible characteristics in a detector array.
3) The operational controlling factors, such as IT or aperture setting, should be considered as variables for the radiometric conversion.

The radiometric calibration procedure of the CASI-2 consists of two stages, calibration data collection and calibration data processing. During the collection of the calibration data a sum of multiple detector response is recorded under a reliable and traceable light source with known spectrum which is supposed to give uniform stable illumination over entire range of a detector array, i.e. both spatial (612 columns) and spectral area (between around 400 and 950 nm). For the NERC CASI-2 calibration at EPFS Hoffman Engineering radiance standard integrating sphere (LS-64-8D) is exploited throughout the radiometric calibration data collection. For the calibration data processing, then, a Radiant Sensitivity Coefficient (RSC) is computed for each detector and aperture setting as a function of IT. This will make DN values from each element into an absolute spectral radiance ($\mu W\ cm^{-2}\ sr^{-1}\ nm^{-1}$).

A.5.1. Data acquisition

The acquisition of the radiometric calibration data is a time-consuming procedure, since three sets of measurements in full frame mode over the entire imaging area of the CCD array for five aperture settings available to the CASI-2 are needed (from 1 to 5; Table), as follows,

1) Uniformity data
2) Absolute spectral radiance data
3) Dark data

The reason for collecting uniformity and absolute date for each aperture setting is to prevent additional illumination sources of errors other than the radiance standard affecting the calibration.

Prior to commencing the radiometric data collection, the appropriate IT for each aperture setting is determined so as to produce maximum signal of a 75 % (around 3000 DN) within the whole area of the CCD array. This is to prevent the signal saturation, and keep the same IT at a certain aperture setting over the series of data collection.

At least 512 frames (in full frame mode) are summed for each measurement in order to minimise statistical noise levels. With available on-chip memory, the processing can be speeded-up when using 16-bit summation. Hence, while every 16 of 12-bit full frames are summed in the ICU before writing into a storage media, thus a minimum of 32 summed frames are left to be stored (16×32 = 512) for each aperture setting.

The uniformity data should illuminate every detector element uniformly and normalise their response to the optical axis. This relative response of each detector gives the multiple effects of all instrument induced non-uniformity information, such as pixel-to-pixel response variation due to non-homogeneity in the CCD array and misalignment of the optical system (i.e. vignetting, spectral alignment, pattern noise or keystoning).

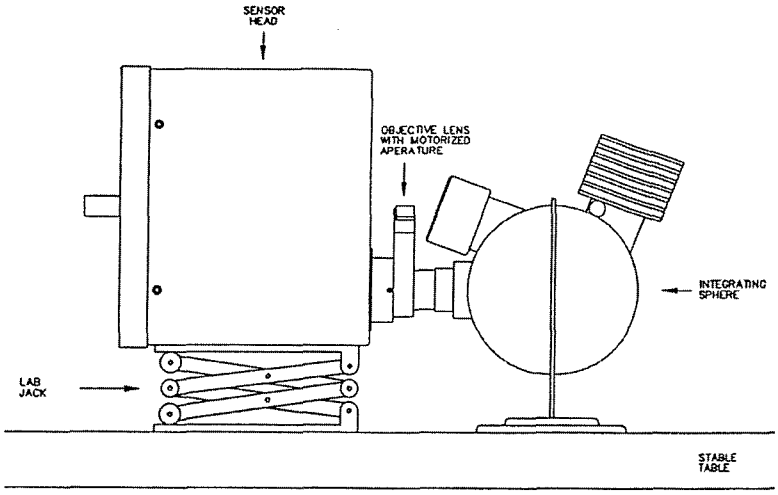

Figure A-8. Instrument setting for spatial uniformity calibration of CASI-2.

To reduce interruptions of a highly uniform source of light, the objective lens of the CASI-2 SHU has to be placed in close proximity to the exit port of the integrating sphere, so that entire FOV of the CASI-2 is illuminated uniformly (Figure A-8). Since NERC decided to increase the FOV to 54.4°, the exit port of the integrating sphere is no longer large enough to cover NERC CASI-2. Consequently two spatial halves of imaging part of the CCD array along the slit axis are collected in each aperture setting, i.e. left (columns between 82 and 335) and right sides (columns between 336 and 512).

The close position between the objective lens of the CASI-2 and the luminance source from the integrating sphere however causes secondary reflection from the lens into the sphere, resulting in invalid radiance received by the CASI-2 in spite of its uniformity. Hence the signal recorded during the uniformity data collection is not appropriate to be used as an absolute calibration and separate measurements are necessary.

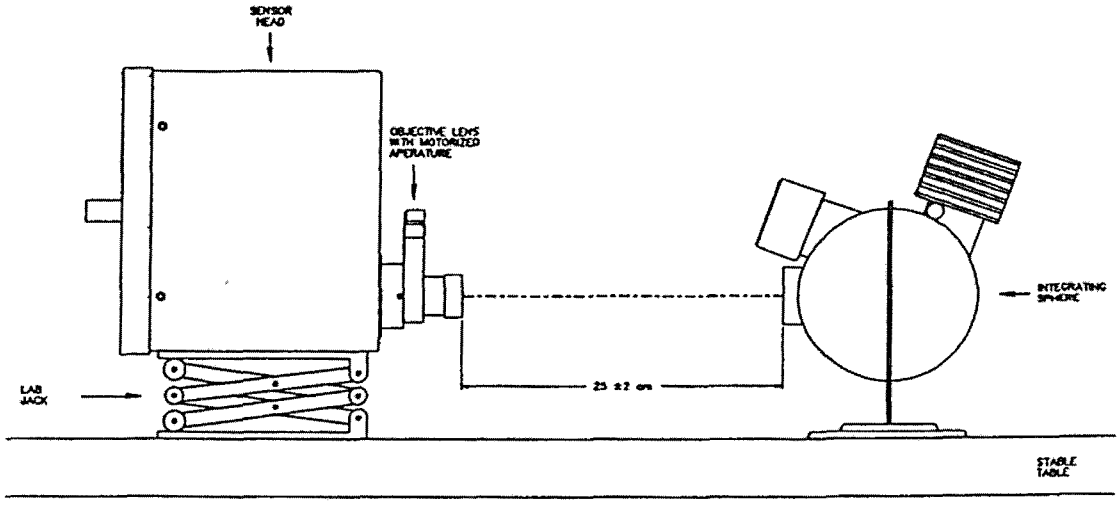

Figure A-9. Instrument setting for absolute radiometric calibration of CASI-2.

The absolute radiometric calibration data collection is designed to avoid such a reflected-back radiance problem during the uniformity data. The CASI-2's objective lens in the fore-optics and the integrating sphere's exit port are put apart in association with its optical axis. The distance between them

is decided to achieve at least ±50 pixels in the centre of optical axis (column of 335). Thus valid absolute spectral radiance data is only limited in the 100 spatial pixels across the CCD array due to instruments' distance.

It is also important to make sure that the alignment of instruments are parallel each other's viewing plane. For NERC CASI-2's absolute calibration data collection, an approximate distance is 25 *cm* (Figure A-9).

For the NERC CASI-2, an optical flat is set between the SHU and the integrating sphere. It is a plane glass lens that is installed on body of aircraft in front of the SHU to protect harsh condition during the CASI-2's operation. Its radiometric effect is expected to be similar to Eequation **[3.1]**.

The dark data, as DC generated due to the non-uniformity of the CCD array, are collected for each five IT settings with the aperture closed in the completely dark laboratory condition.

Typical plots of radiometric calibration dataset are depicted in Figure A-10.

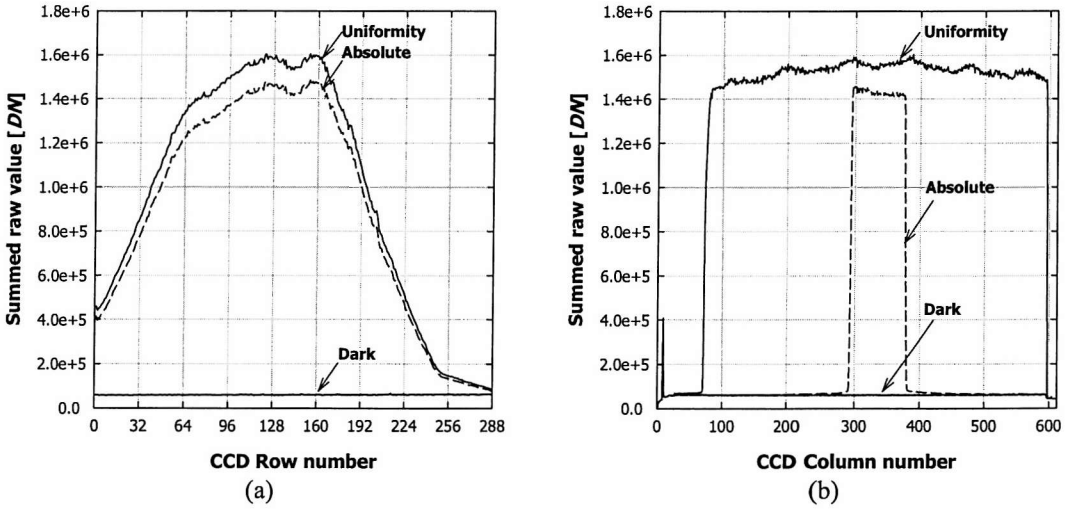

Figure A-10. A set of radiometric calibration data is plotted in a row (a) and column (b) transactions. The plots are selected at 335 column for (a) and 144 rows for (b) in Aperture 3. The data are collected during NERC CASI-2 calibration in February 2003.

A.5.2. Radiometric correction processing

Once a set of radiometric calibration files (uniformity, absolute, and dark) is obtained, the pre-processing of these data is carried out as follows,

1) The left and right sides of the uniformity data are merged to create a complete scene image of uniform detector response,
2) Dark signal is estimated for the constant electronic offset and thermal-induced dark current signal as a function of IT setting,
3) Frame Shift Smear estimation to compensate the transfer time of each detector element and the total IT, and
4) Scattered light estimation for secondary reflection within the CASI-2's optical system is estimated.

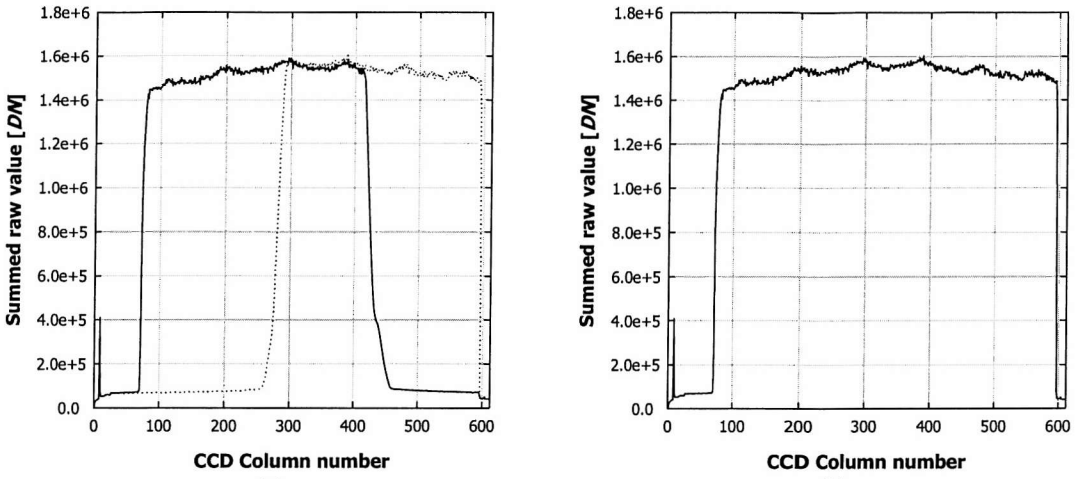

Figure A-11. A multiple plot of two haves of summed uniformity data (a) and a merged uniformity plot (b) from the data in (a). In (a), a solid line represents left side, whereas a dotted for right. The plots are selected at 144 rows in Aperture 3. The data are collected during NERC CASI-2 calibration in February 2003.

Two halves of spatial uniformity files per each aperture setting are merged into a single scene image. Software supplied by the CASI-2's manufacture cuts each side of uniformity data from a given column number that is normally a centre of optical axis (column 335), and then creates a new file containing the response of the entire detector array as if they are exposed to the same magnitude of illumination. A distinctive step might appear in a merging column if alignment between the SHU and the integrating sphere is altered during a pair of uniformity data. This could result inaccurate radiometric calibration, so consequently, it is important to maintain the viewing plane of the instrument in parallel to the exit port of the sphere for the data collection.

For radiometric correction process of the CASI-2, systematic noise induced by an instrument consists of DC, EO, FSS, and SL (see Section 3.4.1). These are to be discarded in order to acquire a true radiometric signal from a raw data (equation [A.18]).

$$P^{c}_{r,c} = P_{r,c} - \left(DS_{r,c} + FSS_{c} + SL_{r} \right) \qquad [A.18]$$

where

r	Row index
c	Column index
$P^{c}_{r,c}$	Corrected data value for pixel (r,c) $[DN]$
$P_{r,c}$	32-bit summed raw data value for pixel (r,c) $[DN]$
$DS_{r,c}$	Dark signal for pixel (r,c) $[DN]$
FSS_{c}	Frame Shift Smear for each pixel in column c $[DN]$
SL_{r}	Scattered light for row r at a given column c $[DN]$

The next several paragraphs present each error sources and its effect on the radiometric calibration procedure.

Dark signal ($DS_{r,c}$) recorded during the calibration data acquisition represents the constant EO and thermal-induced DC signal at a given IT setting. Although there is a masked area in the CASI-2's CCD array for retrieval of the dark signal (normally in the columns from 605 to 611, equation [A.19]), separate dark data are recommended to be obtained for a pixel-to-pixel variation of the DC generation. In

terms of data handling, a dark signal is simply subtracted from both associated uniformity and absolute dataset.

$$EO_r = \frac{1}{7} \cdot \sum_{c=605}^{611} P_{r,c} \qquad [A.19]$$

where EO_r Electronic offset for a given row [*DN*]
$P_{r,c}$ 32-bit summed data value for pixel (r,c) [*DN*]

The FSS is small but significant for normal operation of the CASI-2 (see Section **3.4.1**). It is a proportional to the ratio of the transfer time to the total integration time and varies only dependent on a column (spatial) position of the CCD array. The magnitude of the FSS is determined by a mean of 288 rows of the dark-corrected pixels for an individual column and multiplying it by the ratio of the frame transfer time to the total IT (equation [A.20]).

$$FSS_c = \frac{FTT}{(IT + FTT) \cdot 288} \cdot \sum_{r=1}^{288} \left(P_{r,c} - DS_{r,c} \right) \qquad [A.20]$$

where FTT Frame transfer time (1.8 *ms* for NERC CASI-2) [*ms*]
IT Integration time [*ms*]

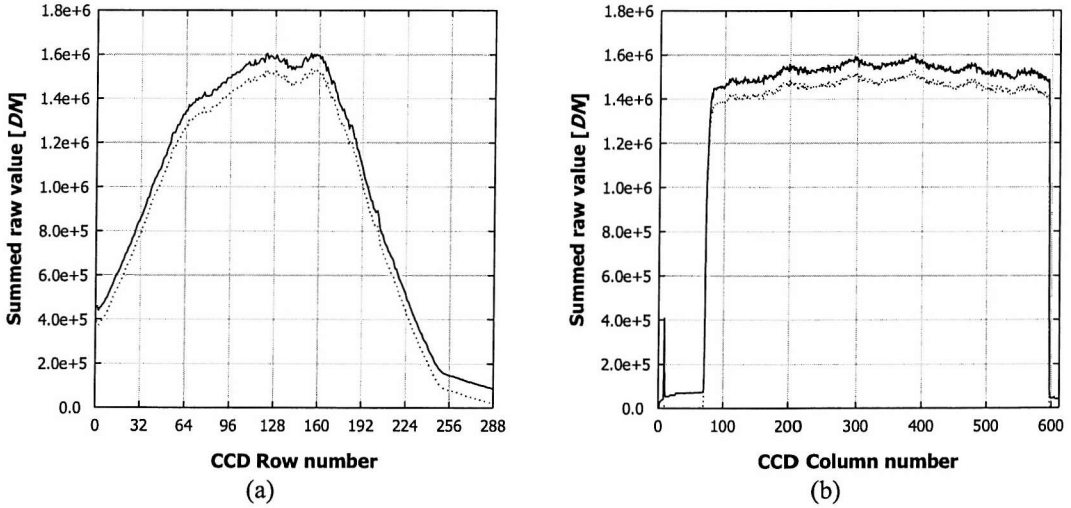

Figure A-12. The raw (solid) and the radiometric-correction-applied (dotted) uniformity data in a spectral (a) and spatial profile (b). The plots are selected at 335 column for (a) and 144 rows for (b) in Aperture 3. The data are collected during NERC CASI-2 calibration in February 2003.

The SL is determined from a range of masked CCD area within the first 80 columns where prevented from the direct exposure of light passing through the optical system of the CASI-2. Its spectral variation is considered for the radiometric calibration processing of the CASI-2, while not significantly across the slit image. The SL for each row is estimated by a mean of selected range of columns (for example, 11 column wide centred on column 50 for the NERC CASI-2) after dark signal and FSS abstraction (equation [A.21]).

$$SL_r = \frac{1}{n} \cdot \sum_{c=cl}^{cl+n-1} \left(P_{r,c} - DS_{r,c} - FSS_c \right) \qquad [A.21]$$

A typical difference between the raw and that after radiometric correction processing is shown in Figure A-12. It may be noticed that the main differences are due to the dark signal data with comparison to Figure A-10, and that the greatest fraction of the measured values are found at short wavelength region (up to 80 % at rows ~230-~288 in Figure A-11(a)).

As the radiometric correction processing shown above is applied to both uniformity and absolute data, they are supposedly holding a radiometric response other than all instrument-induced noise from the CCD array. It does not however give 'certified' spectral radiance information for the corrected uniformity data. To transform the corrected uniformity data into absolute radiometric response, an absolute correction ratio (ACR) is computed by the ratio of the corrected absolute data to the corrected uniformity data, both of which corresponding pixels are taken. Its variation along the wavelengths (row) is assumed not to change spatially (column).

$$ACR_j^k = \frac{\sum_{i=cs}^{ce} A_{i,j}^k}{\sum_{i=cs}^{ce} U_{i,j}^k} \qquad [A.22]$$

where

$A_{i,j}$	Corrected absolute value for pixel 'i,j' [DN]
$U_{i,j}$	Corrected uniformity value for pixel 'i,j' [DN]
i	CCD column index (i = 0...511)
j	CCD row index (j = 0...287)
k	Aperture setting (k = 1...5)
Cs	Start number of column of the ACR region
Ce	End number of column of the ACR region

Figure A-13 shows a typical spectral variation of the ACR from the NERC CASI-2. the ACR remains greater than 0.9, up to row 240 where it has a sudden drop (< ~480 *nm*). This indicates that reflectance of the objective lens is greater at short wavelength, as described in Section **3.2.2.**

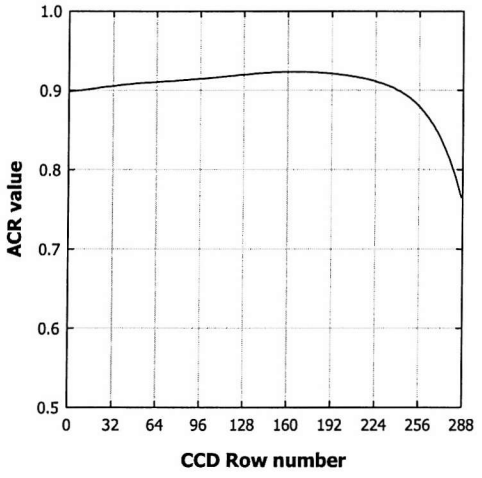

Figure A-13. A typical Absolute Correction Ratio (ACR) plot of NERC CASI-2 (acquired in February 2003).

With the ACR, corrected calibration data shown above are then applied to the generation of a radiant sensitivity coefficient (RSC) for entire imaging part of the CCD elements and for each aperture setting. As a result, the matrix of RSC will have information for correcting non-uniformities and for the conversion of DN values to units of spectral radiance ([$\mu W\ cm^{-2}\ sr^{-1}\ nm^{-1}$]) with the appropriate IT.

$$RSC_{r,c}^{k} = \frac{U_{r,c}^{k} \cdot ACR_{r}}{L(\lambda_{r}) \cdot IT^{k}} \qquad [A.23]$$

where
- IT^k Integration time used to collect the calibration-mode data for a given aperture setting [ms]
- λ_r Centre wavelength of CCD row r [nm]
- $L(\lambda)$ Spectral radiance of the integrating sphere for the centre wavelength of the CCD row j as defined as in Equation **[A.3]** [$\mu W\ cm^{-2}\ sr^{-1}\ nm^{-1}$]
- $RSC_{r,cj}^{\ k}$ Radiant sensitivity coefficient for CCD pixel 'r,c' [$DN\ (\mu W\ cm^{-2}\ sr^{-1}\ nm^{-1})^{-1}\ ms^{-1}$]

Figure A-14 shows spectral and spatial variations of the RSC derived by the above processing. The spectral profile shows that the RSC values significantly decrease toward both ends of the spectral pixels from its centre. With respect to the fact that the smaller RSC means more instrument-induced noise generated, the most sensitive spectral range of the CCD array is between row of 120 and 200 (~570 to ~720 *nm*). On the contrary, the spatial variation of the RSC value is relatively more stable, especially in the scene imaging region of the CCD array (columns from 82 to 594 for the NERC CASI-2 system). The main source of variation may be due to the slit irregularities, misalignment of the optical system, and/or pattern noises.

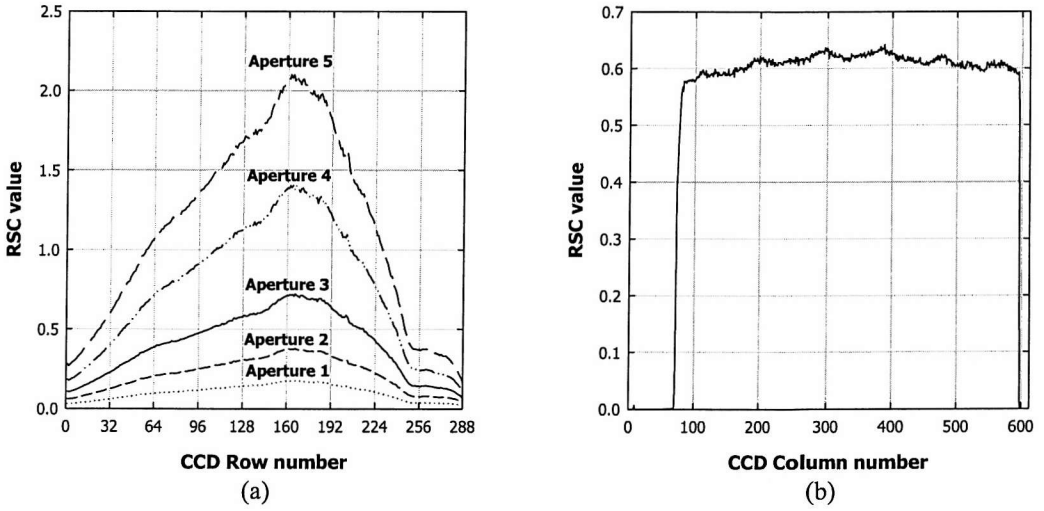

Figure A-14. A spectral (a) and spatial (b) profile of RSC. In (a), all aperture plots used for NERC CASI-2's calibration (February 2003) are shown (column 335). A spatial profile in (b) is aperture 3 and row 144.

The RSC matrices are used to convert electrical signal or voltage into radiance value. Since the spectral and full-frame modes use all pixels of the CCD array, the RSC matrix with an appropriate aperture setting is directly applied to the data values from the CCD array for the conversion. The spatial and enhanced spectral modes, on the other hand, use selective pixels of the CCD array, and the RSCs corresponding to the CCD position have to be summed to determine the integrated response as shown in equation [A.24].

$$RSC_{b,i}^{k} = \sum_{j=rs}^{re} RSC_{i,j}^{k} \qquad [A.24]$$

where
- b Band index
- rs Start row of band b
- re End row of band b
- $RSC_{b,i}$ RSCs for band b and column i $[DN\,[\mu W\,cm^{-2}\,sr^{-1}\,nm^{-1}]^{-1}\,ms^{-1}]$

The conversion process is based on inverse of equation [A.23] using the RSCs from equation [A.24] if spatial or enhanced spectral mode is selected. In addition, integration time while data recording and ACR values from the CASI-2 calibration are also needed. When rewrite equation [A.23],

$$L_{b,c}^{k} = \frac{P_{b,c}^{k}}{RSC_{b,c}^{k} \cdot IT^{k}} \qquad [A.25]$$

where
- $P^{k}_{b,c}$ Corrected pixel value for band b, column c, and aperture k $[DN]$

A.6. The ILS Calibration

The ILS is an optional CASI-2 system, used as a cosine receptor designed to measure downwelling irradiance on top of the aircraft. A fibre optic cable transfers light received by the diffuse sensor head to the optical system (between the slit and spectral grating), resulting that its spectrally dispersed light is projected onto a part of CCD array (see section **3.2.3**).

Since light from the ILS is not collected via an objective lens and grating, the magnitude of the ILS signal is independent of the aperture setting. Consequently, only a single set of data are needed as follows,

1) The spectral response measurement of the ILS probe
2) The measurement of the irradiance source
3) The ILS dark current

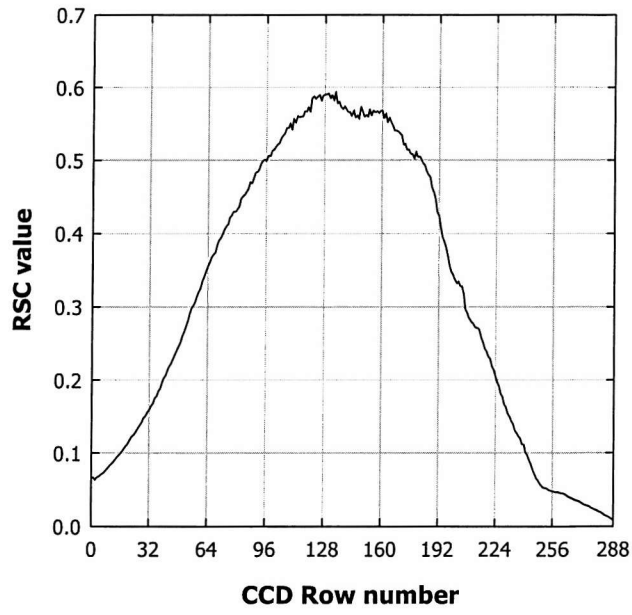

Figure A-15. A spectral profile of the ILS RSC values for column 36. The data were collected during the NERC CASI-2 calibration in February 2003).

The ILS calibration method is rather different from the radiometric calibration of the scene imaging part of the CASI-2. The irradiance source for the ILS calibration uses the 1000 *kW* Kaiser videolamp. The reason for using the videolamp is that it is bright enough to activate the CCD region for the ILS and to simulate solar irradiance despite its relative instability with comparison to the integrating sphere. The lamp is not however calibrated, so that its spectral intensity should be checked each CASI-2's ILS calibration session in 2).

To measure its intensity, the imaging part of the CCD of the CASI-2 is used as a reference calibrator for the ILS calibration procedure. The radiance measurement from the CASI-2 should be possible to estimate irradiance value, by multiplying π steradians[§§] with an assumption of uniform

[§§] The relationship between radiance (L) and irradiance (E) measurements under Lambertian irradiance source is derived as follows, (continue to the next page)

intensity distribution, i.e. Lambertian. A Spectralon® reflectance panel (see section A.2.3) is used as a reflectance standard to transform the intensity from the lamp into uniformly distributed irradiance source.

The lamp is placed on a tripod around 60 *cm* directly above the reflectance panel that faces upward on the floor, providing strong illumination over the reflectance panel. Surroundings are covered with the black cordelan fabric in order to avoid unwanted reflected signals. The CASI-2 SHU is placed with a clamp on another tripod beside the target. The CASI-2 is looking down at the target at around 60° of viewing angle at the reflectance panel.

The alignment is adjusted by looking at the CASI-2 display with spectral mode setting. The optical axis (centre) of the CASI-2's scene image should be covered by the signals from the reflectance panel, so that the radiance reflected by the panel is measured at the CCD region where absolute radiometric calibration data were recorded. The data of the ILS calibration is acquired with the same configuration of the CASI-2 as in radiometric calibration data (at least 512 frames in full frame mode).

The reflectance panel is then replaced by the ILS probe with the same setting. At this time, while CASI-2's SHU is still viewing the ILS probe, the signal recorded in non-imaging part of the CCD (columns of 30 to 40 for the NERC CASI-2) is used for the ILS calibration. At the end of the data acquisition, dark data is collected as in the radiometric calibration.

The ILS calibration processing is basically to compare data sets from both measurements, i.e. spectral response of the ILS region in the CCD array and the radiance values of the illumination source collected from the optical centre of the imaging part of the CASI-2.

Like the RSC in the scene imaging part of the CCD array, the signal from the ILS also has to be converted into the radiometric unit. The aim is to generate ILS calibration coefficients for each CCD pixel illuminated by the ILS. The relationship between them is defined as used in the radiometric calibration of the CASI-2 (equation [A.23]). The difference is that the π steradian term has to be taken into account for the ILS with an assumption that the ILS probe is a true cosine receptor and that the reflectance panel provides an ideal irradiance illumination with a given spectral reflectance. When rewritten,

$$RSC_{i,j}^{k} = \frac{U_{i,j}^{k} \cdot ACR_{j}^{k}}{\pi \cdot \rho \cdot L_{j}^{k} \cdot IT^{k}} \qquad [A.26]$$

Figure A-15 is an example of the ILS RSC. Its spectral variation shows a similar trend to the spectral response of the scene imaging part of the CASI-2 (see Figure A-12 and Figure A-14). The ILS RSCs are computed over a range of CCD columns allocated for the ILS, although only a single column is used for the at-sensor downwelling irradiance data acquisition (see section A.3.3). These are overwritten into the RSC matrix for all aperture settings.

The CASI-2's manufacturer is currently developing an improved calibration routine for the ILS (Personal communication from Itres Research Ltd., 2003).

$E = \int_{\Omega} L(\theta,\phi) \cdot d\omega$, where radiance $L(\theta,\phi) = L \cdot \cos\theta$

$2\pi \cdot \int_{0}^{\pi/2} L \cdot \cos\theta \cdot \sin\theta \cdot d\theta$

$2\pi \cdot L \cdot \left| \frac{1}{2} \cdot \sin^2\theta \right|_{0}^{\pi/2}$

$\pi \cdot L$.

A.7. Summary

For reliable and traceable calibration, it is important to employ highly stable, uniform, and non-directional source of radiance standard. The standard used for the CASI-2 calibration at NERC EPFS is an integrating sphere manufactured by Hoffman Engineering (Model number of LS-64-8D). Acquisition of the CASI-2 calibration consists of two main procedures, pre-calibration and radiometric calibration. The aim of the pre-calibration is to find out the mechanical and internal stability and uniformity of the instrument, i.e. the chamber temperature and humidity for stable operation of the CCD array, the alignment and contamination checks of the optical system (including spectral alignment test for the wavelength calibration), and other system variable checks. The instrument-induced systematic noise from the pre-calibration, i.e. dark current, electronic offset, frame shift smear, and scattered light, is important piece of information prior to retrieving accurate radiometric calibration results.

There are two main steps of data collection for radiometric calibration: uniformity and absolute measurements. The uniformity calibration aims to obtain relative pixel-to-pixel response variations due to irregularity of the CCD elements or non-uniformity of optical sub-systems for the CCD array. Absolute calibration aims to relate the CASI data to physically meaningful units of spectral radiance.

As the ILS is a part of the sensor system options of the CASI-2, the physical characteristics of the ILS are dependent upon those of the CASI-2 system.

References

Achal, S.A., Brown, J., Jensen, N., 1999, CASI's excellent hyperspectral adventure, *Proceedings of the Fourth International Airborne Remote Sensing Conference and Exhibition/ 21th Canadian Symposium on Remote Sensing*, Ottawa, Canada, 534.

Adams, J.B., Smith, M.O., Gillespie, A., 1989, Simple models for complex natural surfaces: a strategy for the hyperspectral era. Quantitative remote sensing: An economic tool for the Nineties; *Proceedings of IGARSS'89 and the 12th Canadian symposium on remote sensing*, Institute of Electrical and Electronic Engineers, New York, 1, 16-21.

Adler-Golden, S.M., Matthew, M.W., Anderson, G.P., Felde, G.W., Gardner, J.A., 2002, An algorithm for de-shadowing spectral imagery, *AVIRIS Earth Science and Applications Workshop*, NASA JPL.

Ahern, F.J., Goodenough, D.G., Jain, S.C., Rao, V.R., Rochon, G., 1977, Use of clear lakes as standard reflectors for atmospheric measurements, *Proceedings of the 11th International Symposium on Remote Sensing of the Environment*, Ann Arbor, MI, 731-755.

Ahern, F.J., Teillet, P.M., Goodenough, D.G., 1979, Transformation of atmospheric and solar illumination conditions of the CCRS image analysis system, *Proceedings of the 5th International Symposium on Machine Processing of Remotely sensed data*, Purdue Univ., Lafayette, IN, p.34

Al-Hargan, A.A.Q.K., 1997, Creation of a coastal zone information system for Qatar using remote sensing and GIS, *Southampton University, PhD thesis.*

Allen, W.A., Gausman, H.W., Richardson, A.J., 1973, Willstatter-Stoll theory of leaf reflectance evaluated by ray tracing, *Applied Optics*, **12**, 2448-2453.

Anderson, K., Milton, E.J., Rollin, E.M., 2003, The temporal dynamics of calibration target reflectance, *Proceedings of the Annual Conference Remote Sensing and Photogrammetry Society*, The University of Nottingham, UK, CD-Rom.

Anding, D. and Kauth, R., 1970, Estimation of sea surface temperatures from space, *Remote Sensing of Environment*, **1**, 217.

Anger, C.D., 1999, Airborne hyperspectral remote sensing in the future?, Proceedings on the Fourth International Airborne Remote Sensing Conference and Exhibition and 21st Canadian Symposium on Remote Sensing, Ottawa, Canada, 1-5.

Aplin, P., Atkinson, P.M., and Curran, P.J., 1999, Fine spatial resolution simulated satellite sensor imagery for land cover mapping in the UK, *Remote Sensing of Environment*, **68**, 206-216.

Asrar, G., Myneni, R.B., Kanemasu, E.T., 1989, Estimation of plant-canopy attributes from spectral reflectance measurements, In *Theory and applications of optical remote sensing*, G. Asrar Ed., John Wiley and Sons Inc., New York, 252-296.

Babey, S.K. and Soffer, R.J., 1992, Radiometric calibration of the Compact Airborne Spectrographic Imager (CASI), *Canadian Journal of Remote Sensing*, **18**, 233-242.
Badhwar, G.D, Austin, W.W., Carnes, J.G., 1982, A semi-automatic technique for multitempotal classification of a given crop within a Landsat scene, Pattern Recognition, 15, 217.

Bannari, A., Morin, D., Benie, G.B., Bonn, F.J., 1995, A theoretical review of different mathematical models of geometric corrections applied to remote sensing images, *Remote Sensing Reviews*, **13**, 27-47.

Bannehr, L., and Schwiesow, R., 1993, A technique to account for the misalignment of pyranometers installed on aircraft, *Journal of Atospheric and Oceanic Technology*, **10**, 774-777.

Baret, F. and Guyot, G., 1991, Potentials and limits of vegetation indices for LAI and APAR assessment, *Remote Sensing of Environment*, **35**, 161-173.

Baret, S. and Guyot, G., and Major, D., 1989, TSAVI: a vegetation index which minimizes soil brightness effects on LAI and APAR estimation, *In 12th Canadian Symposium on Remote Sensing and IGARSS'90*, Vancouver, Canada, 10-14 July, p. 4.

Barnsley and Curran, 1990, The role of airborne remote sensing in terrestrial ecology, *Proceedings on Annual Conference of the Remote Sensing Society on Remote Sensing and Global Change*, 19-21 September, University College Swansea, Swansea, Wales.

Barnsley, M., Strahler, A., Morris, K., Muller, J.-P., 1994, Sampling the surface bi-directional reflectance distribution function (BRDF): 1. Evaluation of current and future satellite sensors, *Remote Sensing Reviews*, **8**, 271-311.

BenDor, E. and Kruse, F.A., 1996, Detection of atmospheric gases using GER 63 channel scanner data acquired over Makhtesh Ramon, Negev, Israel, *International Journal of Remote Sensing*, **17**, 1215-1232.

Berendes, T., Sengupta, S.K., Welch, R.M., Wielicki, B.A., Navar, M., 1992, Cumulus cloud base height estimation from high spatial resolution Landsat data: A Hough

transform approach, *IEEE Transactions on Geoscience and Remote Sensing*, **30**, 3, 430-443.

Berk, A., Bernstein, L.S., Robertson, D.C., 1989, MODTRAN: A moderate resolution model for LOWTRAN-7, *AFGL-TR-89-0122, Air Force Geophysics Laboratory, Hanscom AFB*, MA 01731, U.S.A.

Berlot, P.E. and Locascio, G.A., 1991, Ultraviolet-visible photodiode array spectrophotometer wavelength calibration methos. A practical computer algorithm, *Analyst*, **116**, 313-316.

Boardman, J.W., 1993, Automating spectral unmixing of AVIRIS data using convex geometry concepts, *In: Green, R.O. (eds) Summaries of the Fourth Annual JPL Airborne Geoscience Workshop*, JPL, **1**, 11-14.

Bodmann, H.W., Eberbach, K., Reuter, P., 1988, Roof lighting and sun protection, *Energy and Buildings*, **11**, 283-287.

Boerner, A., Schaepman, M.E., Schlaepfer, D., Wiest, L., Reulke, R., 1999, Simulation of APEX data: the SENSOR approach, *In Imaging Spectrometry V, Descour, M.R. and Shen, S. S. (Eds.), Proceedings of SPIE*, **3753**, 180-191.

Bouman, B.A.M., 1992, Linking physical remote sensing models with crop growth simulation models, applied for sugar beet, *International Journal of Remote Sensing*, **13**, 2565-2581.

Bouman, B.A.M., Hoekman, D.H., 1993, Multi-temporal, multi-frequency radar measurements of agricultural crops during the Agriscatt-88 campaign in The Netherlands, *International Journal of Remote Sensing*, **14**, 1595-1614.

Brunger, A.P. and Hooper, F.C., 1991, Measured shortwave sky radiance in an urban atmosphere, *Solar Energy*, **47**, 137-142.

Brunger, A.P. and Hooper, F.C., 1993, Anisotropic sky radiance model based on narrow field of view measurements of shortwave radiance, *Solar Energy*, **51**, 53-64.

Campbell, J.B., 1996, Introduction to Remote Sensing (Second Edition), *Taylor & Francis Ltd*, London, 622p.

Carrere, V. and Conel, J.E., 1993, Recovery of atmospheric water vapor total column abundance from imaging spectrometer data around 940 nm – Sensitivity analysis and application to Airborne Visible/Infrared Imaging Spectrometer (AVIRIS) data, *Remote Sensing of Environment*, **44**, 179-204.

Cartalis, C. and Retalis, A., 1996, Exploring the need to revise atmospheric correction algorithms of satellite sensor images for the area of Greece, *International Journal of Remote Sensing*, **17**, 3083-3088.

Caselles, V. and Garcia, M.J., 1992, An alternative simple approach to estimate atmospheric correction in multispectral studies, *International Journal of Remote Sensing*, 10, 1127-1134.

Castleman, K.R., 1996, Digital image processing, *Prentice Hall International Inc.*, London, 667p.

Centre for the study of Earth from Space (CSES), 1992, SIPS User's Guide, The Spectral Image Processing System, Version 1.1, *University of Colorado, Boulder*, p. 74.

Chandrasekhar, S, 1960, Radiative Transfer, *Dover Publications, London.*

Chavez, P.S., 1975, Atmospheric, solar, and M.T.F. corrections for ERTS digital imagery, *Proceedings of American Society of Photogrammetry*, 69-69a.

Chavez, P.S., 1988, An improved dark-object subtraction technique for atmospheric scattering correction of multispectral data, *Remote Sensing of Environment*, **24**, 459-479.

Chavez, P.S., 1989, Radiometric calibration of Landsat Thematic Mapper multispectral images, *Photogrammetric Engineering and Remote Sensing*, **55**, 1285-1294.

Chavez, P.S., 1996, Image-based atmospheric corrections – revisited and improved, *Photogrammetric Engineering and Remote Sensing*, **62**, 1025-1036.

Choi, K.-Y. and Milton, E. J., 2001, A model-based approach to correcting spectral irradiance data using an upward-looking airborne sensor (CASI ILS). *RSPS2001: Geomatics, Earth Observation and the Information Society, First Annual Meeting of the Remote Sensing and Photogrammetry Society*, London, 64-75.

Choi, K.-Y. and Milton, E.J., 2002, Retrieval of at-sensor irradiance using Incident Light Sensor (ILS), *Proceedings of the Fifth Annual Remote Sensing Conference and Exhibition, ERIM*, Miami, Florida, 22-25 May 2002.

Cierniewski, J. and Karnieli, A., 2003, Virtual surfaces simulating the bidirectional reflectance of semiarid soils, *International Journal of Remote Sensing*, **24**, 1469-1486.

Clark, R.N., Swayze, G., Heidebrecht, K., Goetz, A.F.H., Green, R.O., 1993, Comparison of methods for calibrating AVIRIS data to ground reflectance, *In Green, R.O. (Eds), Summaries of the Fourth Annual JPL Airborne Geoscience Workshop*, JPL, **1**, 35-36.

Clark, R.N., Swayze, G., King, T.V.V., Livo, K.E., Kokaly, R.F., Dalton, J.B., Vance, J.S., Rockwell, B.W., McDougal, R.R., 1999, Surface reflectance calibration of terrestrial imaging spectroscopy data: a tutorial using AVIRIS, http://speclab.cr.usgs.gov/PAPERS.calibration.tutorial/calibntA.html, *US Geological Survey*, Accessed 29/09/03.

Cocks, T., Jenssen, R., Stewart, A., Wilson, I., Shields, T., 1998, The HyMap airborne hyperspectral sensor: The system, calibration and performance, Proceedings on *First EARSEL Workshop on Imaging Spectroscopy*, Zurich, 1-6.

Conel, J.E., 1990, Determination of Surface Reflectance and Estimates of Atmospheric Optical Depth and Single Scattering Albedo from Landsat Thematic Mapper Data, *International Journal of Remote Sensing*, **11**, 783-828.

Conel, J.E., Green, R.O., Vane, G., Bruegge, C.J., Alley, R.E., 1987, AIS-2 radiometry and a comparison of methods for the recovery of ground reflectance, *Proceedings of the Third Airborne Imaging Spectrometer Data Analysis Workshop, JPL Pub. 87-30,* (Pasadena, CA: Jet Propulsion Lab.), 18~47

Coombes, C.A. and Harrison, A.W., 1988, Calibration of a three-component angular distribution model of sky radiance, *Atmosphere-Ocean*, **26**, 183-192.

Coppin, P.R. and Bauer, M.E., 1994, Processing of multi-temporal Landsat TM imagery to optimise extraction of forest cover change features, *IEEE Transactions on Geoscience and Remote Sensing*, **32**, 918-927.

Cracknell, A.P. and Hayes, L.W., 1993, Atmospheric corrections to passive satellite remote sensing data, in Introduction to Remote Sensing, *Tayler & Francis, London,* 116-158.

Cramer, B. and Speciale, N., 2002, EO-1 results, in GSFC Systems Engineering Seminar, *Goddard Space Flight Center, Systems Engineering Seminar.*

Crippen, R.E., 1987, The regression intersection method of adjusting image data for band rationing, *International Journal of Remote Sensing*, **8**, 137-155.

Crippen, R.E., 1988, The dangers of underestimateing the importance of data adjustments in band rationing, *International Journal of Remote Sensing*, **9**, 767-776.

Crist, E.P. and Cicone, R.C., 1984, Application of the Tasseled Cap Concept to Simulated Thematic Mapper Data, *Photogrammetric Engineering and Remote Sensing*, **50**, 343-352.

Curcio, J.A. and Petty, C.C., 1951, The near infrared absorption spectrum of liquid water, *Journal of Optical Society America*, **41**, 302-304.

Curran, P.J., 1985, Principles of Remote Sensing, *John Wiley & Sons Inc., New York,* p.282.

Curran, P.J., Milton, E.J., Atkinson, P.M., Foody, G.M., 1998, Remote sensing: From data to understanding, *In Longley, P.L., Brooks, S.M., McDonnell, R., MacMillan, B. (Eds), Geocomputation A Primer*, John Wiley & Sons Ltd, Chichester, 33-59.

Cushinie, J., 1988, The acquisition of SPOT-1 HRV imagery over southern Britain and northern France, May 1986-May 1987, *International Journal of Remote Sensing*, **9**, 159-167.

Cutter, M.A., Lobb, D.R., Williams, T.L., Renton, R.E., 1999, Integration and testing of the compact high-resolution imaging spectrometer (CHRIS), *In Imaging Spectrometry V, Descour, M.R. and Shen, S. S. (Eds.), Proceedings of SPIE*, **3753**, 235-246.

Danson, F.M., Higgins, N.A., Trodd, N.M., 1999, Measuring land-surface directional reflectance with the along- track scanning radiometer, *Photogrammetric Engineering and Remote Sensing*, **65**, 1411-1417.

Danson, F.M., Plummer, S.E., Briggs, S.A., 1995, Remote sensing and the information extraction problem, *In Danson, F.M., and Plummer, S.E. (Eds), Advances in Environmental Remote Sensing*, John Wiley & Sons Ltd, Chichester, 171-177

Darch, J.P., Barber, J., 1983, Multitemporal remote sensing of a geobotanical anomaly, *Economic Geology*, **78**, 770-782.

Dave, J.V., 1980, Effect of atmospheric conditions on remote sensing of a surface non-homogeneity, *Photogrammetric Engineering and Remote Sensing*, **46**, 1173-1180.

Defries, R.S., Townshend, J.R.G., 1994, NDVI-derived land-cover classifications at a global-scale, *International Journal of Remote Sensing*, **15**, 3567-3586.

Dehaan, R. L. and Taylor, G. R., 2002, Field-derived spectra of salinized soils and vegetation as indicators of irrigation-induced soil salinization, *Remote Sensing of Environment*, **80**, 406-417.

Deirmendjian, 1980, A survey of light-scattering techniques used in remote sensing of atmospheric aerosols, *Review of Geophysics and space physics*, **18**, 341-360.

Derrien, M., Farki, B., Harang, L., et al., 1993, Automatic cloud detection applied to NOAA-11/AVHRR imagery, *Remote Sensing of Environment*, **46**, 246-267.

Deschamps, P.-Y., Breon, F.-M., Leroy, M., Podaire, A., Bricaud, A., Buriez, J.-C., Seze, G., 1994, The POLDER mission: instrument characteristics and scientific objectives, *IEEE Transactions on Geoscience and Remote Sensing*, **32**, 598 –615.

Dickinson, R.E., Pinty, B., Verstraete, M.M., 1990, Relating surface albedos in GCM to remotely sensed data, *Agricultural and Forest Meteorology*, **52**, 109-131.

Diner, D.J., Barge, L.M., Bruegge, C.J., Chrien, T.G., Conel, J.E., Eastwood, M.L., Garcia, J.D., Hernandez, M.A., Kurzweil, C.G., Ledeboer,W.C., Pignatano, N.D., Sarture, C.M., Smith, B.G., 1998, The Airborne Multi-angle Imaging

SpectroRadiometer (AirMISR): Instrument description and first results, *IEEE Transactions on Geoscience and Remote Sensing*, **36**, 1339 –1349.

Diner, D.J. and Martonchik, J.V., 1985, Atmospheric transmittance from spacecraft using multiple view angle imagery, *Applied Optics*, **24**, 3503-3511.

Dwivedi, R.S. and Sanker, T.R., 1992, Principal component analysis of Landsat MSS data for delineation of terrain features, *International Journal of Remote Sensing*, **13**, 2309-2318.

Dwyer, J.L., Fruse, F.A., Lefkoff, A.B., 1995, Effects of empirical versus model based reflectance calibration on automated analysis of imaging spectrometer data: A case study from the Drum Mountains, Utah, *Photogrammetric Engineering and Remote Sensing*, **61**, 1247-1254.

Dyche, D.D., 1983, Experimental determination of atmospheric scattering effects on scanner edge response, *University of Arizona, Tuscon, MSc thesis.*

Eastman, J.R., 1992, Time seriese map analysis using standarsised principal components, *ASPRS/ACSM/RT92 Technical papers, Vol.1: Global change and education*, Washington DC, 195-204.

Eastman, J.R., Fulk, M., 1993, Long sequence time series evaluation using standardised principal components, *Photogrammetric Engineering and Remote Sensing*, **59**, 1307-1312.

Egbert, D.D., 1977, A practical method for correcting bi-directional reflectance variations, *In Proceedings of Machine Processing Remotely Sensed data Symposium, Purdue University*, West Lafayette, 178-188.

Ekstrand, S., 1994, Assessment of forest damage with Landsat TM: correction for varying forest stand characteristics, *Remote Sensing of Environment*, **47**, 291-302.

Emery, D.R., Milton, E.J., Felstead, R.H., 1998, Optimising data collection for heathland remote sensing, *In Proceeding of Remote Sensing Society Conference*, Southampton, UK, 483-489.

ENVI User's Guide, 2002, version 3.5, Research Systems Limited.

European Space Agency (ESA), 1998, ENVISAT-1: Mission and System Summary, 85p.

Ferrand, W.H., Singer, R.B., Merenyi, E., 1993, Retrieval of apparent surface reflectance from AVIRIS data – A comparison of empirical line, radiative-transfer and spectral mixture methods, *Remote Sensing of Environment*, **47**, 311-321.

Ferrier, G., 1995, Evaluation of apparent surface reflectance estimation methodologies, *International Journal of Remote Sensing*, **16**, 2291-2297.

Ferrier, G. and Wadge, G., 1996, The application of imaging spectrometry data to mapping alteration zoned associated with gold mineralization if southern Spain, *International Journal of Remote Sensing*, **17**, 331-350.

Fraser, R.S. and Kaufman, Y.J., 1985, The Relative Importance of Aerosol Scattering and Absorption in Remote-Sensing, *IEEE Transactions on Geoscience and Remote Sensing*, **23**, 625-633.

Freemantle, J.R., Pu, R., Miller, J.R., 1992, Calibration of imaging spectrometer data to reflectance using pseudo-invariant features, *In Proceedings of the 15th Canadian Symposium on Remote Sensing*, Toronto, 452-455.

Foody, G.M. and Curan, P.J., 1994, Remote Sensing from Regional to Global Scales, *John Wiley & Sons Ltd*, Chichester

Foot, J.S., Kitchen, M., Readings, C.J., 1985, The measurement of diffuse solar radiation from an aircraft, *Atmospheric Environment*, **19**, 811-818.

Freemantle, J.R., Pu, R., Miller, J.R., 1992, Calibration of imaging spectrometer data to reflectance using pseudo-invariant image features, *In Proceedings of the 15th Canadian Symposium on Remote Sensing*, 452-455.

Fuller, R.M., Groom, G.B., Wallis, S.M., 1994, An availability of Landsat TM images of Great Britain, *International Journal of Remote Sensing*, **15**, 1357-1362.

Fuller, R.M., Parsell, R.J., 1990, Classification of TM imagery in the study of land use in lowland Britain: practical considerations for operational use, *International Journal of Remote Sensing*, **11**, 1901-1917.

Fung, T., LeDrew, E., 1987, Application of principal components analysis to change detection, *Photogrammetric Engineering and Remote Sensing*, **53**, 1649-1658.

Gao, B.C., Heidebrecht, K.B., Goetz, A.F.H., 1992, ATmospheric REMoval Program (ATREM) User's Guide, version 1.1, *Center for the Study of Earth From Space document*, University of Colorado, p.24.

Gao, B.C. and Li, R.-R., 2000, Quantitative improvement in the estimates of NDVI values from remotely sensed data by correcting thin cirrus scattering effects, *Remote Sensing of Environment*, **74**, 494-502.

Gastellu-Etchegorry, J.P., 1988, Cloud cover distribution in Indonesia, *International Journal of Remote Sensing*, **9**, 1267-1276.

Gates, D.M., 1980, Biophysical Ecology, *Springer-Verlag, New York*, 611p.

Gates, D.M., Keegan, H.J., Schleter, J.C., Weidner, V.R., 1965, Spectral properties of plants, *Applied Optics*, **4**, 11-20.

Gausman, H.W., Allen, W.A., Cardenas, R., 1969, Reflectance of cotton leaves and their structure, *Remote Sensing of Environment*, **1**, 19-22.

Gemmel, F. and Varjo, J., 1999, Utility of reflectance model inversion versus two spectral indices for estimating biophysical characteristics in a Boreal forest test site, *Remote Sensing of Environment*, **68**, 95-111.

Gerson, D.J. and Fehrenbach, L.K., 1983, Temporal image normalization, *Final Report, Defense Mapping Agency*.

Gilabert, M.A., Conese, C., Maselli, F., 1994, An atmospheric correction method for the automatic retrieval of surface reflectances from TM images, *International Journal of Remote Sensing*, **15**, 2065-2086.

Gilbert, M.A., Melia, J., 1993, Solar angle and sky light effects on ground reflectance measurements in a citrus canopy, *Remote Sensing of Environment*, **45**, 281-293.

Goel, N.S., 1989, Inversion of canopy reflectance models for estimation of biophysical parameters from reflectance data, *In Theory and applications of optical remote sensing, G. Asrar Ed., John Wiley and Sons Inc.*, New York, 205-251.

Goetz A.H. and Herring, M., 1989, The High Resolution Imaging Spectrometer for EOS, *IEEE Transactions on Geoscience and Remote Sensing*, **27**, 136-144.

Goetz, A.F.H., 1991, Imaging spectrometry for studying Earth, air and water, EARSeL, *Advances in Remote Sensing*, **1**, 3-15.

Goetz, A.F.H., Billingsley, F.C., Gillespie, A.R., Abrahms, M.J., Squires, R.L., Shoemaker, E.N., Luchita, I., Elston, D.P., 1975, Applications of ERIS images and image Processing to regional geologic problems and geologic mapping in Northern Arizona, Pasadena, CA: California Institute of Technology, JPL Technical Report 32-1597, p.188.

Goetz, A.F.H., Vane, G., Solomon, J.E., Rock, B.N., 1985, Imaging spectrometry for earth remote sensing, *Science*, **288**, 1147-1153.

Gong, P., Pu, R., Miller, J.R., 1995, Coniferous forest Leaf Area Index estimation along the Pregon transect using Compact Airborne Spectrographic Imager data, *Photogrammetric Engineering and Remote Sensing*, **61**, 1107-1117.

Gould, R.W. and Arnone, R.A., 1997, Remote sensing estimates of inherent optical properties in a coastal environment, *Remote Sensing of Environment*, **61**, 290-301.

Gray, L., Freemantle, J., Shepherd, P., Miller, J., Harron, J., Hersom, C., 1997, Characterization and calibration of the CASI airborne imaging spectrometer of BOREAS, *Canadian Journal of Remote Sensing*, **23**, 188-195.

Green, A.A., Berman, M., Switzer, P., Craig, M., 1988, A transformation for ordering multispectral data in terms of image quality with implications for noise removal, *IEEE Transactions on Geoscience and Remote Sensing*, **26**, 65-74.

Gueymard, C, 1986, Une paramétrisation de la luminance énergétique du ciel clair en function de la turbidité, *Atmosphere-Ocean*, **24**, 1-15.

Guindon, B., 1991, Incorporation of azimuthal control methods in the extraction of 3-dimensional topographic models from individual space-borne SAR scenes, *International Journal of Remote Sensing*, **12**, 2399-2420.

Guirguis, S.K., Hassan, H.M., El-Raey, M.E., Hyssain, M.M.A., 1996, Multi-temporal change of lake Brullus, Egypt, from 1983 to 1991, *Internaional Journal of Remote Sensing*, **17**, 2915-2921.

Gurney, C.M., 1982, The use of contextual information to detect cumulus clouds and cloud shadows in Landsat data, *International Journal of Remote Sensing*, **3**, 51-62.

Gurney, C.M., 1983, The use of contextual information in the classification of remotely sensed data, *Photogrammetric Engineering and Remote Sensing*, **49**, 55-64.

Gutman, G.G., Ignatov, A.M., Olson, S., 1994, Towards a better quality of AVHRR composite images over land: reduction of cloud contamination, *Remote Sensing of Environment*, **50**, 134-148.

Hagolle, O, Goloub, P., Deschamps, P.-Y., Cosnefroy, H., Briottet, X., Bailleul, T., Nicolas, J.-M., Parol, F., Lafrance, B., Herman, M., Results of POLDER in-flight calibration, *IEEE Transactions on Geoscience and Remote Sensing*, **37**, 1550-1566.

Harrison, A.W. and Coombes, C.A., 1988, An opaque cloud cover model of sky short wavelength radiance, *Solar Energy*, **41**, 387-392.

Hall, F.G., Strebel, D.E., Nickeson, J.E., Goets, S.J., 1991, Radiometric rectification: toward a common radiometric response among multidate, multisensor images, *Remote Sensing of Environment*, **35**, 11-27.

Hapke, B., 1984, Bidirectional reflectance spectroscopy, 3, Correction for macroscopic roughness, *Icarus*, **59**, 41-59.

Hay, J.E., 1977, An analysis of solar radiation data for selected locations in Canada, *Climatological Studies No. 32, Atmospheric Environment Service*, October, 1977,

Hay, J.E., 1978, Measurement and modelling of shortwave radiation on inclined surfaces, *In Proceedings of the Third Conference on Atmospheric Radiation, American Meteorological Society*, California, June 28-30, 150-153.

Hay, J.E., 1979, Calculation of monthly mean solar radiation for horizontal and inclined surfaces, *Solar Energy*, **23**, 301-307.

Hay, J.E., 1978, Measurement and modelling of shortwave radiation on inclined surface, *In Proceedings in Third Conference on Atmospheric radiation, American Meteorological Society*, Davis, California, June 28-30, 150-153.

Hay, J.E. and Davies, J.A., 1980, Calculation of the solar radiation incident on an inclined surface, *In J.E. Hay and T.K. Won (eds.), Proceedings on First Canadian Solar Radiation Data Workshop, April, 1978, Supply and Services Canada*, 59-72.

Hay, J.E. and McKay, D.C., 1985, Estimating solar irradiance on inclined surfaces: A review and assessment of methodologies, *International Journal of Solar Energy*, **3**, 203-386.

Hegarat-Mascle, S.Le, Vidal-Madjar, D., Peytavin, L., 1997, Data fusion between radar and optical images with partial cloud cover by introduction of spatial information in the Dempster-Shafer evidence theory: Application to forest detection, *Physical Measurements and Signatures in Remote Sensing*, Guyot and Phulpin (eds), 69-76.

Hildum, E.A., Hajek, P., Grant, P., Fitzgerald, M., 2001, Establishing and maintaining the calibration of airborne imaging linescanners, *In Proceedings of the Fifth International Airborne Remote Sensing Conference and Exhibition*, San Francisco, California, CD-Rom.

Hill, J. and Strum, B., 1991, Radiometric correction of multitemporal Thematic Mapper data for use in agricultural land-cover classification and vegetation monitoring, *International Journal of Remote Sensing*, **12**, 1471-1491.

Holm, R.G., Moran, M.S., Jackson, R.D., Slater, P.N., Yuan, B., Biggar, S.F., 1989, Surface reflectance factor retrieved from Thematic Mapper data, *Remote Sensing of Environment*, **27**, 47-57.

Hooper, F.C. and Brunger, A.P., 1980, A model for the angular distribution of sky radiance, *Journal of Solar Energy Engineering*, **102**, 196-202.

Hooper, F. C., Brunger, A. P., Chan, C. S., 1987, A clear sky model of diffuse sky radiance, *Journal of Solar Energy Engineering*, **109**, 9-14.

Hope, A.S., Pence, K.R., Stow, D.A., 1999, Response of the normalized difference vegetation index to varying cloud conditions in Artic tundra environment, *International Journal of Remote Sensing*, **20**, 207-212.

Hopkinson, G.R., Goodman, T.M., and Prince, S.R., 2000, A guide to the use and calibration of detector array equipment; For the DTI National Measurement System Policy Unit, Issue 1, *Sira Electro-Optics Ltd*, p.210.

Hopkinson, R.G., 1954, Measurements of sky luminance distribution at Stockholm, *Journal of Optical Society in America*, **44**, 455-459.

Hoyler, R.J., 1984, A two-satellite method for measurement of sea surface temperature, *International Journal of Remote Sensing*, **5**, 115-131.

Huete, A.R., 1988, A soil-adjusted vegetation index (SAVI), *Remote Sensing of Environment*, **25**, 295-309.

Huete, A.R., Hua, G., Qi, J., Chehbouni, A., van Leeuwen, W.J.D., 1992, Normalization of multispectral red and NIR reflectance with the SAVI, *Remote Sensing of Environment*, **41**, 143-154.

Hughes, N.A. and Henderson-Sellers, A., 1985, Global 3D-Nephanalysis of total cloud amount: climatology for 1979, *Journal of Climate and Applied Meteorology*, **24**, 669-686.

Huguenin, R.L., Karaska, M.A., Blaricom, D.V., Jensen, J.R., 1997, Subpixel classification of bald cypress and tupelo gum trees in Thematic Mapper imagery, *Photogrammetric Engineering and Remote Sensing*, **63**, 717-725.

Husar, R.B. and Holloway, J.M., 1984, The properties and climate of atmospheric haze, *In Hydroscopic Aerosols, Eds. Ruhnke, L.H. and Deepak, A., A. Deepak Publishers,* Hampton, VA, 129-170

Hutchison, K.D. and Choe, N.J., Application of 1.38mm imagery for thin cirrus detection in daytime imagery collected over land surfaces, *International Journal of Remote Sensing*, **17**, 3325-3342.

Isaaks, E.H., Srivastava, R.M., 1989, An introduction to applied geostatistics, Oxford, Oxford University Press, 561p.

ITRES Research Ltd., 2001, CASI User's manual

Jackson, R.D., Slater, P.N., Pinter, P.J., 1983, Discrimination of growth and water stress in wheat by various vegetation indices through clear and turbid atmospheres, *Remote Sensing of Environment*, **13**, 187-208.

Jacquemoud, S., Bacour, C., Poilve, H., Frangi, J.-P., 2000, Comparison of four radiative transfer models to simulate plant canopies reflectance: Direct and inverse mode, *Remote Sensing of Environment*, **74**, 471-481.

Jadkowski, M.A., Convery, P., Birk, R.J., Kuo, S., 1994, Aerial image databases for pipeline rights-of-way management, *Photogrammetric Engineering and Remote Sensing*, **60**, 347-355

Jakubauskas, M.E., 1996, Thematic mapper characterisation of Lodgepole pine seral stages in Yellowstone National Park, USA, *Remote Sensing of Environment*, **56**, 118-132.

Janesick, J.R., Klassen, K., Elliot, T., 1985, CCD charge collection efficiency and the photon transfer technique, *Proceedings of SPIE*, vol.**570**, 7-19.

Jensen, J.R., 1996, Introductory Digital Image Processing; A Remote Sensing Prospective, *In Clarke, K.C. (Series Editor), Prentice Hall Series in Geographic Information Science*, Prentice Hall, New Jersey, 316p.

Justice, C.O. and Townshend, J.R.G., 1994, Data Sets for Global Remote-Sensing - Lessons Learnt, *International Journal of Remote Sensing*, **15**, 3621-3639.
Kaufman, Y.J., Brakke, T.W., Eloranta, E., 1983, Field experiment to measure the radiative characteristics of a hazy atmosphere, *Presented at the Fifth Conference on Atmospheric Radiation*, 13 October 1983, Baltimore, MD.

Kaufman, Y.J., 1985, The relative importance of aerosol scattering and absorption in remote sensing, *IEEE Transactions on Geoscience and Remote Sensing*, **23**, 625-633

Kaufman, Y.J., 1988, Atmospheric effect on spectral signature-measurements and corrections, *IEEE Transactions on Geoscience and Remote Sensing*, **26**, 441-450

Kaufman, Y.J. and Fraser, R.S., 1983, Light extinction by aerosols during summer air pollution, *Journal of Applied Meteorology*, **22**, 1694-1706.

Kaufman, Y.J. and Fraser, R.S., 1984, Atmospheric effects on classification on finite fields, *Remote Sensing of Environment*, **14**, 487-507.

Kaufman, Y.J. and Sendra, C., 1988, Algorithm for automatic atmospheric corrections to visible and near-IR satellite imagery, *International Journal of Remote Sensing*, **9**, 1357-1381.

Kaufman, T.J. and Remer, L., 1994, Detection of forests using mid-IR reflectance: An application for aerosol studies, *IEEE Transactions on Geoscience and Remote Sensing*, **32**, 672-683.

Kaufman, Y.J. and Tanré, D., 1996, Strategy for direct and indirect methods for correcting the aerosol effect on remote sensing: From AVHRR to EOS-MODIS, *Remote Sensing of Environment*, **55**, 65-79

Kaufman, Y.J., Wald, A.E., Remer, L.A., Gao, B.C., Li, R.R., Flynn, L., 1997, The MODIS 2.1-mu m channel - correlation with visible reflectance for use in remote

sensing of aerosol, *IEEE Transactions on Geoscience and Remote Sensing*, **35**, 1286-1298.

Kauth, R.J. and Thomas, G.S., 1976, The Tasselled Cap- a graphic description of the spectral-temporal development of agricultural crops as seen by Landsat, *In Proceedings of the 3rd Symposium on Machine Processing of Remotely Sensed Data, LARS*, Purdue University, Lafayette, IN., pp. 41-49.

Kiedron, P.W. and Michalsky, J.J., 2003, Measurement errors in diffuse irradiance with non-Lambertian radiometers, *International Journal of Remote Sensing*, **24**, 237-247.

Kilsby, C.G., 1986, Radiative fluxes and aerosol properties measured with an aircraft during a straw burning episode, *In Proceedings of Sixth Conference on Atmospheric Radiation, American Meterological Society*, Williamsburg, Amber, 19-22.

Kim, T. and Muller, J.-P., 1998, Effects of image resolution on an automated building extraction system, *In Proceeding of Remote Sensing Society Conference*, Southampton, UK, 1259-1266.

King, M.D. and Greenstone, R., 1999, 1999 EOS Reference Handbook: A guide to NASA's Earth Science Enterprise and the Earth Observing System, *The Earth Observing System Project Science Office*, 355p.

King, M.D., Menzel, W.P., Grant, P.S., Myers, J.S., Arnold, G. T., Platnick, S.E., Gumley, L.E., Tsay, S.C., Moeller, C.C., Fitzgerald, M., Brown, K.S., Osterwisch, F.G., 1996, Airborne scanning spectrometer for remote sensing of cloud, aerosol, water vapor and surface properties, *Journal of Atmospheric and Oceanic Technology*, **13**, 777-794.

Kimbol, H.H. and Hand, I.F., 1922, Daylight illumination on horizontal vertical and sloping surfaces, *Monthly weather review*, **50**, 615-628.

Kittler, R., 1965, Standardisation of outdoor conditions for the calculation of daylight clear skies, *In Sunlight in Buildings, Proceedings of the C.I.E. Intersessional Conference*, April, 1965, University of Newcastle-Upon-Tyne, 273-285.

Kleinbaum, D.G., Kupper, L.L., Muller, K.E., and Nizam, A., 1998, Applied regression analysis and other multivariable methods, 3rd Edition, *Duxbury Press, California*, 798p.

Klucher, T.M., 1979, Evaluation of models to predict insolation on tilted surfaces, *Solar Energy*, **23**, 111-114.

Knipling, E.B., 1970, Physical and physiological basis for the reflectance of visible and near-infrared radiation from vegetation, *Remote Sensing of Environment*, **1**, 155-159.

Kollewe, M., Bienlein, J., Kollewe, T., Spitzer, H., 1996, Comparison of multispectral airborne scanner reflectance images with ground surface reflectance measurements, *In*

Proceedings of the Second International Airborne Remote Sensing Conference and Exhibition, San Francisco.

Kondratyev, K.Ya., 1969, Radiation in the atmosphere, *Academic Press, New York.*

Kruse, F.A., Kierein-Young, K.S., Boardman, J.W., 1990, Mineral mapping at Cuprite, Nevada with a 63-channel imaging spectrometer, *Photogrammetric Engineering and Remote Sensing*, **56**, 83-92.

Kumar, R. and Silva, L.F., 1973, Light ray tracing through leaf cross section, Applied Optics, **12**, 2950-2954.

Law, B.E. and Waring, R.H., 1994, Remote sensing of leaf area index and radiation intercepted by understory vegetation, *Ecological Applications*, **4**, 272-279

Leblanc,S.G., Bicheron,P., Chen,J.M., Leroy,M., Cihlar,J., 1999, Investigation of directional reflectance in boreal forests with an improved four-scale model and airborne POLDER data, *IEEE Transactions on Geoscience and Remote Sensing*, **37**, 1396 –1414.

Leblon, B., Gallant, L., Granberg, H., 1996, Effects of shadowing types on ground-measured visible and near-infrared shadow reflectance, *Remote Sensing of Environment*, **58**, 322-328.

Legg, C.A., 1991, A review of Landsat MSS image acquisition over the United Kingdom, 1976-1988, and the implication for operational remote sensing, *International Journal of Remote Sensing*, **12**, 93-106.

Lawless, K.,P.L., Milton, E.J., Anger, C.O., 1998, Investigation of changes in the reflectance of ground calibration targets (asphalt and concrete), Proceedings of 27th International Symposium on *Remote Sensing of Environment*, Tromso, Norway.

Leblanc, S.G., Bicheron, P., Chen, J.M., Leroy, M., Cihlar, J., 1999, Investigation of directional reflectance in boreal forests with an improved four-scale model and airborne POLDER data, *IEEE Transactions and Remote Sensing*, **37**, 1396-1414.

Lee, T.Y. and Kaufman, Y.J., 1986, Non-Lambertian effects on remote sensing of surface reflectance and vegetation index, *IEEE Transactions on Geoscience and Remote Sensing*, **GE-24**, 699-707.

Legg, C.A., 1991, A review of Landsat MSS image acquisition over the United Kingdom, 1976-1988, and the implications for operational remote sensing, *International Journal of Remote Sensing*, **12**, 93-106.

Lehmann, F., Oertel, D., Richter, R., Hausknecht, P., Rothfuss, H., Strobl, P., Mueller, A., Tischler, S., Mueller, R., Beran, D., Fries, J., Boehl, R., Obermeier, P., 1995, Hyperspectral applications with a new sensor, *In Proceedings on International Symposium on Spectral Sensing Research (ISSSR)*, Melbourne, Australia.

Lenney, M.P., Woodcock, C.E., Collins, J.B., Hamdi, H., 1996, The status of agricultural lands in Egypt: The use of multitemporal NDVI features derived from Landsat TM, *Remote Sensing of Environment*, **56**, 8-20.

Lewis, M., V. Jooste, and A. A. de Gasparis, 2001, Discrimination of arid vegetation with airborne multispectral scanner hyperspectral imagery, *IEEE Transactions on Geoscience and Remote Sensing*, **39**, 1471-1479.

Li, X., Yeh, A.G.O., 1998, Principal component analysis of stacked multi-temporal images for the monitoring of rapid urban expansion in the Pearl River Delta, *International Journal of Remote Sensing*, **19**, 1501-1518.

Liang, S.L., Strahler, A.H., Jin, X.F., Zhu, Q.J., 1997, Comparisons of radiative transfer models of vegetation canopies and laboratory measurements, *Remote Sensing of Environment*, **61**, 129-138.

Lillesand, T.M. and Kiefer, R.W., 1994, Remote Sensing and Image Interpretation (Third Edition), *John Wiley & Sons Ltd, New York*, p.750.

Liu, C.H., Chen, A.J., Liu, G.R., 1996, An image-based retrieval algorithm of aerosol characteristics and surface reflectance for satellite images, *International Journal of Remote Sensing*, **17**, 3477-3500.

Liu, J.G. and Moore, J.McM., 1990, Hue image RGB clour composition. A simple technique to suppress shadow and enhance spectral signature, *International Journal of Remote Sensing*, **11**, 1521-1530.

Liu, J.G. and Moore, J.McM., 1993, Cloud-shadow suppression technique for enhancement of Airborne Thematic Mapper imagery, *Photogrammetric Engineering and Remote Sensing*, **59**, 1287-1291.

Maas, S.J., 1988, Use of remotely sensed information in agricultural crops growth models, Ecology Model, **41**, 247-268.

Markham, B.L., Barker, J.L., 1987, Radiometric properties of U.S. processed Landsat MSS data, *Remote Sensing of Environment*, **22**, 39-71.

Malthus, T.J. and Madeira, A.C., 1993, High-resolution spectrometry – spectral reflectance of field bean-leaves infected by Botrytis-Fabae, *Remote Sensing of Environment*, **45**, 107-116.

Marshall, G.J., Dowdeswell, J.A., Rees, W.G., 1994, The spatial and temporal effect of cloud cover on the acquisition of high quality Landsat imagery in the European Arctic Sector, *Remote Sensing of Environment*, **50**, 149-160.

Mather, P.M., 1994, Earth observation data – or information?, *In Foody, G.M., Curran, P.J. (Eds), Environmental Remote Sensing from Regional to Global Scales*, John Wiley & Sons Ltd, Chichester, 202-213.

Mather, P.M., 1999, Computer Processing of Remotely-Sensed Images; An Introduction (Second Edition), *John Wiley & Sons Ltd*, Chichester, 292p.

McArdle, S.S., Miller, J.R., Freemantle, J.R., 1992, Airborne image acquisition under cloud: Preliminary comparisons with clear-sky scene radiance and reflectance imagery, *In Proceedings of the 15th Canadian Symposium on Remote Sensing*, Toronto, 446-449.

McClain, E.P., 1981, Multiple atmospheric-window techniques for satellite derived sea-surface temperature, *In Oceanography from Space, eds. Gower, J.F.R.*, Plenum, New York, 73.

Mekler, Y., Kaufman, Y.J., Fraser, R.S., 1984, Reflectivity of the atmosphere-inhomogeneous surface system. Laboratory simulations, *Journal of Atmospheric Sciences*, **41**, 2595–2604.

Meyer, P., Itten, K.I., Kellenberger, T., Sandmeier, S., Sandmeier, R., 1993, Radiometric corrections of topographically induced effects on Landsat TM data in Alpine environment, *Journal of Photogrammetry and Remote Sensing*, **48**, 17-28.

Michalsky, J., Perez, R., Seals, R., 1991, Evaluation of algorithms for sky luminance distribution; prospects for performance improvements, *In Arden, M.E., Burley, S.M.A., Coleman, M. (Eds), 1991 World Solar Congress*, Vol. 1, Part II, Denver, CO, 1049-1054.

Michener, W.K. and Houhoulis, P.F., 1997, Detection of vegetation changes associated with extensive flooding in a forested ecosystem, *Photogrammetric Engineering and Remote Sensing*, **63**, 1363-1374.

Milovich, J.A., Frulla, L.A., Gagliardini, D.A., 1995, Environment contribution to the atmospheric correction for Landsat-MSS images, *International Journal of Remote Sensing*, **16**, 2515-2537.

Milton, E.J., 1980, A portable multiband radiometer for ground data collection in remote sensing, *International Journal of Remote Sensing*, **1**, 153-165.

Milton, E.J., 1999, Image endmembers and the scene model, *Canadian Journal of Remote Sensing*, **25**, 112-120.

Milton, E.J., Lawless, K.P., Roberts, A., Franklin, S.E., 1997, The effect of unresolved scene elements on the spectral response of calibration targets: An example, *Canadian Journal of Remote Sensing*, **23**, 252-256.

Milton, E.J., Rollin, E.M., Brown, K.M., 2001, Practical methodologies for the reflectance calibration of CASI data, *NERC ARSF Workshop*, Nottingham.

Milton, E.J., Rollin, E.M., Emery, D.R., 1995, Advances in field spectroscopy, *In Danson, F.M., and Plummer, S.E. (Eds), Advances in Environmental Remote Sensing,* John Wiley & Sons Ltd, Chichester, 9-32

Milton, E.J. and Webb, J.P., 1987, Ground radiometry and airborne multispectral survey of bare soils, *International Journal of Remote Sensing*, **8**, 2-14.

Minnaert, M., 1941, The reciprocity principle in lunar photometry, *Astrophysical Journal*, **93**, 403-410.

Miura, T., Huete, A.R., Yoshiokab, B., Holben, B.N., 2001, An error and sensitivity analysis of atmospheric resistant vegetation indices derived from dark target-based atmospheric correction, *Remote Sensing of Environment*, **78**, 284-298.

Moran, M.S., Bryant, R., Thome, K., Ni, W., Nouvellon, Y., Gonzalez-Dugo, M.P., Qi, J., Clarke, T.R., , 2001, A refined empirical line approach for reflectance factor retrieval from Landsat-5 TM and Landsat-7 ETM+, *Remote Sensing of Environment*, **78**, 71-82.

Moran, M.S., Jackson, R.D., Clarke, T.R., Qi, J., Cabot, F., Thome, K.J., Markham, B.L., 1995, Reflectance factor retrieval from Landsat TM and SPOT HRV data for bright and dark targets, *Remote Sensing of Environment*, **52**, 218-230.

Moran, M.S., Jackson, R.D., Jackson, P.N., Teillet, P.M., 1992, Evaluation of simplified procedures for retrieval of land surface reflectance factors from satellite sensor output, *Remote Sensing of Environment*, **41**, 169-184.

Moran, M.S., Inoue, Y., Barnes, E.M., 1997, Opportunities and limitations for image-based remote sensing in precision crop management, *Remote Sensing of Environment*, **61**, 319-346.

Moran, M.S., Vidal, A., Troufleau, D., Inoue, Y., Mitchell, T., 1998, Ku- and C-band SAR for discriminating agricultural crop and soil conditions, *IEEE Transactions on Geoscience and Remote Sensing*, **36**, 265-272.

Moran, M.S., Vidal, A., Troufleau, D., 1997b, Combining multi-frequency microwave and optical data for farm management, *Remote Sensing of Environment*, **61**, 96-109.

NASA, 2000, Exploring our planet: Earth Science Enterprise, Strategic plan, National Aeronautics and Space Administration, Washington, 47p.

NASA, 2003, MODIS Airborne Simulator, http://mas.arc.nasa.gov/, Accessed in 29/01/03.

Natural Environment Research Council (NERC) Airborne Remote Sensing Facility (ARSF), 2002, http://www.nerc.ac.uk/arsf/, Accessed in 30/08/03.

Natural Environment Research Council (NERC) Airborne Remote Sensing Facility (ARSF), 2003, Airborne Thematic Mapper (ATM) and Integrated Data System (IDS), http://www.nerc.ac.uk/arsf/Contents/Instruments/PDF/atm-az16.PDF, Accessed in 30/08/03.

Nezry E., Mougin, E., Lopes, A., Gastellu-Etchegorry, J.P., Laumonier, Y., 1993, Tropical vegetation mapping with combined visible and SAR spaceborne data, *International Journal of Remote Sensing*, **14**, 2165-2184.

Nicodemus, F.E., Richmond, J.C., Hsia, J.J., Ginsberg, I.W., Limperis, T., 1977, Geometrical considerations and nomenclature for reflectance, *National Bureau of Standards, Department of Commerce, Washington D.C., Publication Report Number NBS MN-160*, p.52.

Nieke, K., Schwarzer, H., Neumann, A., Zimmermann, G., 1997, Imaging spaceborne and airborne sensor systems in the beginning of the next century, In Sensors, Systems, and Next-Generation Satellites, Hiroyuki Fujisada (Ed.), *Proceedings of SPIE*, **3221**, 581-592.

Nishidai, T., 1993, Early results from 'Fuyo-1', Japan's Earth Resources Satellite (JER-1), *International Journal of Remote Sensing*, **14**, 1825-1833.

O'Neill, N.T., Miller, J.R., Freemantle, J.R., Atmospheric correction of airborne BRF to yield surface BRF: nomenclature, theory, and methods, *Canadian Journal of Remote Sensing*, **21**, 309-327.

O'Neill, N.T., Zagolski, F., Bergeron, M., Royer, A., Miller, J.R., Freemantle, J., 1997, Atmospheric correction validation of CASI images acquired over the Boreas southern study area, *Canadian Journal of Remote Sensing*, **23**, 143-161.

Ordnance Survey, 2001, A guide to coordinate systems in Great Britain: An introduction to mapping coordinate systems and the use of GPS datasets with Ordnance Survey mapping, *v1.2, Ordnance Survey, UK*, Aug 2001, p.43.

Otterman, J., 1984, Atmospheric effects on radiometry from zenith of a plane with dark vertical protrusions, *International Journal of Remote Sensing*, **5**, 909-923.

Ouaidrari, H. and Vermote, E.F., 1999, Operational atmospheric correction of Landsat TM data, *Remote Sensing of Environment*, **70**, 4-15.

Page, J.K., 1986, Prediction of solar radiation on inclined surfaces, In Solar energy R&D in the European community, series F: Solar radiation data, Vol. 3, *D.Reidel Publishing Corporated*, Dordrecht, Holland, p.164.

Pearce, W.A., 1977, A study of the effects of the atmosphere on Thematic Mapper observations, *Final Report under NASA Contract NAS5-23639*, p.136.

Pearce, W.A., 1985, Cloud shadow effects on remote sensing, *IEEE Transactions on Geoscience and Remote Sensing*, **23**, 634-639.

Pech, R.P., Davis, A.W., Lamacraft, R.R., Graetz, R.D., 1986, Calibration of Landsat data for sparsely vegetated semiarid rangelands, *International Journal of Remote Sensing*, **7**, 1729-1750.

Peddle, D.R., White, H.P., Soffer, R.J., Miller, J.R., LeDrew, E.F., 2001, Reflectance processing of remote sensing spectroradiometer data, Computer and Geoscience, **27**, 203-213.

Pentreath, R.J., 1999, Using remote sensing to solve mesoscale environmental problems, *In Proceedings of the Annual Conference of the Remote Sensing Society on Earth Observation: From Data to Information*, Cardiff, UK, 7-8.

Perez, R., Seals, R., Michalsky, J., 1993a, All-weather model for sky luminance distribution – Preliminary configuration and validation, *Solar Energy*, **50**, 235-245.

Perez, R., Seals, R., Michalsky, J., 1993b, Erratum to All-weather model for sky luminance distribution – Preliminary configuration and validation, *Solar Energy*, **51**, 423.

Perez, R., Ineichen, P., Seals, R., Michalsky, J., Stewart, R., 1990, Modeling daylight availability and irradiance components from direct and global irradiance, *Solar Energy*, **44**, 271-289.

Perez, R., Stewart, R., Arbogast, C., Seals, R., Scott, J., 1986, An anisotropic hourly diffuse radiation model for sloping surfaces: description, performance, validation, site dependency evaluation, *Solar Energy*, **36**, 481-497.

Perry, C.R. and Lautenschlager, L.F., 1984, Functional equivalence of spectral vegetation indexes, *Remote Sensing of Environment*, **14**, 169-182.

Peterson, D.L., Spanner, M.A., Running, S.W., Teuber, K.B., 1987, Relationship of Thematic Mapper simulator data of Leaf Area Index of temperate coniferous forests, *Remote Sensing of Environment*, **22**, 323-341.

Peterson, J.T., Flowers, E.C., Berri, G.J., Reynolds, C.L., Rudisil, J.H., 1981, Atmospheric turbidity over central north California, *Journal of Applied Meteorology*, **20**, 229-241

Phinn, S.R. and Stow, D.A., 1996, Spatial, spectral, radiometric and temporal dimensions of remotely sensed data for monitoring wetland vegetation in Southern

California, *In Proceedings of Second International Airborne Remote Sensing Conference and Exhibition*, San Francisco, California, 64-73.

Piech, K.R., Schott, J.R., Stewart, K.M., 1978, The blue-to-green reflectance ratio and lake water quality, *Photogrammetric Engineering and Remote Sensing*, **44**, 1303-1319.

Piech, K.R. and Walker, J.E., 1974, Interpretation of soils, *Photogrammetric Engineering and Remote Sensing*, **40**, 87-94.

Piekutowski, T., O'Neil, N., Leckie, D., Beaubien, J., Shepherd, P., 1996, Radiometric correction of MEIS-II imagery using airborne irradiation measurements, *In Proceedings of 26th International Symposium on Remote Sensing of Environment and 18th Annual Symposium of the Canadian Remote Sensing Society*, Vancouver, British Columbia, Canada, 458-462.

Pinter, P.J., Jackson, R.D., Ezra, C.E., Gausman, H.W., 1985, Sun-angle and canopy-architecture effects on the spectral reflectance of 6 wheat cultivars, *International Journal of Remote Sensing*, **6**, 1813-1825.

Pinty, B. and Verstraete, M.M., 1991, Extracting information on surface properties from bidirectional reflectance measurements, Journal of Geophysical Research, 96, 2865-2874.

Pinty, B. and Verstraete, M.M., 1992, On the design and validation of surface bi-directional reflectance and albedo models, *Remote Sensing of Environment*, **41**, 155-167.

Pinty, B. and Verstraete, M.M., Dickinson, R.E., 1990, A physical model of the bi-directional reflectance of vegetation canopies: 2. Inversion and validation, Journal of Geophysical research-atmospheres, **95**, 11767-11775.

Plummer S.E., Danson, F.M., Wilson, A.K., 1995, Advances in remote sensing technology, *In Danson, F.M., and Plummer, S.E. (Eds), Advances in Environmental Remote Sensing*, John Wiley & Sons Ltd, Chichester, 1-7

Pollock, D.B., Murdock, T.L., Datla, R.U., Thompson, A., 2003, Data uncertainty traced to SI units. Results reported in the international system of units, *International Journal of Remote Sensing*, **24**, 225-235.

Pokrowski, G.I., 1929, Uber eien scheinbarach Mie-effect ad seine mogliche rolle in der atmospharenoptik, Zeitchrift fur Physik, **53**, 67-71.

Portigal, F., 2002, Adaptive Reflectance Calibration (ARC) method, http://www.ultraspectral.com, Accessed in 14/07/03.

Price, R.A., Anger, C.D., Mah, S., 1995, Preliminary evaluation of CASI preprocessing techniques, *In Proceedings of the 17th Canadian Symposium of Remote Sensing*, Saskatoon, 694-697.

Radeloff, V.C., Mladenoff, D.J., Boyce, M.S., 1999, Detecting jack pine budworm defoliation using spectral mixture analysis: Separating effects from determinants, *Remote Sensing of Environment*, **69**, 156-169.

Railyan, V.Ya., Korobov, R.M., 1993, Red edge structure of canopy reflectance spectra of triticale, *Remote Sensing of Environment*, **46**, 173-182.

Ranson, K.J. and Daughty, C.S., 1987, Scene shadow effects on multispectral response, *IEEE Transactions on Geoscience and Remote Sensing*, **GE-25**, 502-509.

Ray, T.W. and Murray, B.C., 1996, Nonlinear spectral mixing in desert vegetation, *Remote Sensing of Environment*, **55**, 59-64

Read, R.E., 1999, Aspects of change in air survey primary data acquisition, *Photogrammetric Record*, **16**, 417-422.

Reindl, D.T., Beckman, W.A., Duffle, J.A., 1990, Evaluation of hourly tilted surface radiation models, *Solar Energy*, **45**, 9-17.

Reinerman, P.N., Carder, K.L., Chen, F.-I.R., 1998, Satellite-sensor calibration verification with the cloud-shadow method, *Applied Optics*, **37**, 5541-5549.

Richards, J.A., 1984, Thematic mapping from multispectral image data using principal component transforms, *Remote Sensing of Environment*, **16**, 35-46.

Richardson, A.J. and Wiegand, C.L., 1977, A table look-up procedure for rapidly mapping vegetation cover and crop development, *In Symposium on Machine Processing of Remotely Sensed Data Symposium, LARS*, Purdue University, Lafayette, IN., 284-296.

Richter, R., 1990, A fast atmospheric correction algorithm applied to Landsat TM images, *International Journal of Remote Sensing*, **11**, 159-166.

Richter, R., 1996, A spatially adaptive fast atmospheric correction algorithm, *International Journal of Remote Sensing*, **17**, 1201-1214.

Riedmann, M. and Rollin, E.M., 2000. Laboratory Calibration Procedure of the Compact Airborne Spectrographic Imager (casi-2) owned by NERC. Activities of the NERC EPFS in support of the NERC ARSF. *ARSF Annual Meeting*, Keyworth, Nottingham, UK.

Roberts, D.A., Green, R.O., Adams, J.B., 1997, Temporal and spatial patterns in vegetation and atmospheric properties from AVIRIS, *Remote Sensing of Environment*, **62**, 223-240.

Roberts, D.A., Yamaguchi, Y., Lyon, R.J.P., 1986, Comparison of Various Techniques for Calibration of AIS Data, *In: Vane, G. and Goetz, A.F.H. (eds), Second Airborne*

Imaging Spectrometer Data Analysis Workshop, Jet Propulsion Laboratory, JPL Publication Number 86-35, pp. 21-30.

Robinove, C.J., Chavez, P.S., Gehring, D., Holmgren, R., 1981, Arid land monitoring using Landsat albedo difference images, *Remote Sensing of Environment*, **11**, 133-156.

Rollin, E.M., Emery, D.R., Milton, E.J., Reference panel anisotropy and the significance of diffuse radiation, *In Physical Measurements and Signatures in Remote Sensing, Guyot and Phulpin (eds)*, 143-149.

Rollin, E.M., Milton, E.J., Anderson, K., 2002, The role of field spectroscopy in airborne sensor calibration: an example of the NERC CASI, *In Proceedings of a Conference on Field Spectral Measurements in Remote Sensing, NERC EPFS*, University of Southampton, UK.

Rosen, M.A., Hooper, F.C., Brunger, A.P., 1989, The characterisation and modelling of the diffuse radiance distribution under partly cloudy skies, *Solar Energy*, **43**, 281-290.

Rosen, M.A. and Hooper, F.C., 1987, A model for instantaneous distribution of diffuse sky radiance, *In Proceedings of 11th Canadian Congress of Applied Mechanics*, Edmonton, Alberta, May 31-June4, E104-E105.

Ross, R.E., Dungan, J.L., Beck, L.R., 1994, Kriging in the shadows: Geostatistical interpolation for remote sensing, *Remote Sensing of Environment*, 49, 32-40.

Roujean, J.-L., Leory, M., Deschamps, P.-Y., 1992, A bidirectional reflectance model of the Earth's surface for the correction of remote sensing data, *Journal of Geophysical Research*, **97**, 20,455-20,468.

Rouse, J.W., Haas, R.H., Schell, J.A., Deering, D.W., Harlan, J.C., 1974, Monitoring the vernal advancement of retrogradation of natural vegetation, *NASA/GSFC, Type III, Final Report*, Greenbelt, MD, 371, 1974.

Salomonson, V.V., Barnes, W.L., Maymon, P.W., Montgomery, H.E., Ostow, H., 1989, MODIS: Advanced facility instrument for studies of the earth as a system, *IEEE Transactions on Geoscience and Remote Sensing*, **27**, 145-153.

Schott, J.R. and Henderson-Sellers, A., 1984, Satellite sensing of a Cloudy Atmosphere. *A. Henderson-Sellers (Eds), Taylor and Francis*, London, pp. 45-89.

Schott, J.R., Salvaggio, C., Volchok, W.J., 1988, Radiometric scene normalization using pseudoinvariant features, *Remote Sensing of Environment*, **26**, 1-16.

Schwartz, S.E., Wagener, R., Nemesure, S., 1995, Microphysical and compositional influences on shortwave radiative forcing of climate by sulfate aerosols, *Abstracts of papers of the American Chemical Society*, 209, 2-ENVR Part 1.

Scopatz, S., Neel, G., Romesburg, E., Zivitz, M., 1989, Calibrating a detector array based spectrometer with sub-pixel precision, Proceedings of SPIE, **1055**, 306-313.

Secker, J., Staenz, K., Gauthier, R.P., Budkewitsch, P., 2001, Vicarious calibration of airborne hyperspectral sensors in operational environment, *Remote Sensing of Environment*, **76**, 81-92.

Sharma, P.K., Chopra, R., Verma, V.K., Thomas, A., 1996, Flood management using remote sensing technology: the Punjab (India) experience, *International Journal of Remote Sensing*, **17**, 3511-3521.

Shepherd, J.D. and Dymond, J.R., 2000, BRDF correction of vegetation in AVHRR imagery, *Remote Sensing of Environment*, **74**, 397-408.

Shepherd, P.R., Freemantle, J.R., McArdle, S., Miller, J.R., 1995, A comparison of different operational reflectance generation methods applied to airborne CASI imagery, *In Proceedings of the 17th Canadian Symposium on Remote Sensing, Canadian Remote Sensing Society*, Saskatoon, Saskatchewan, June 13-15, 268-273.

Shepherd, P.R., O'Neil, N.T., Piekutowski, T., 1995, Analysis of downwelling and upwelling diffuser probe data to determine at-sensor irradiance fluxes, *In Proceedings of the 17th Canadian Symposium on Remote Sensing, Canadian Remote Sensing Society*, Saskatoon, Saskatchewan, June 13-15, 337-342.

Shepherd, P.R., Xu, Q. F., 1993, An error analysis of a reflectance conversion methodology using an irradiance sensor, *In Proceedings of 16th Canadian Symposium on Remote Sensing*, 841-845p.

Shettigara, V.K. and Sumerling, G.M., 1998, Height determination of extended objects using shadows in SPOT images, *Photogrammetric Engineering and Remote Sensing*, **64**, 1, 35-44.

Shin, D., Pollard, J.K., Muller, J.-P., 1996, Cloud detection from thermal infrared images using a segmentation technique, *International Journal of Remote Sensing*, **17**, 2845-2856.

Schmidt, E.O., Patterson, E.M., Williams, W.J., 1990, Influence of high altitude clouds on upper tropospheric radiance measurements, *Applied Optics*, **29**, 4199-4207.

Shibayama, M. and Wiegand, C.L., 1985, View azimuth and zenith, and solar angle effects on wheat canopy reflectance, *Remote Sensing of Environment*, **18**, 91-103.

Siala,, F.M.F., Rosen, M.A., Hooper, F.C., 1990, Models for the directional distribution of the diffuse sky radiance, *Journal of Solar Energy Engineering*, **112**, 102-109.

Siala, F.M.F. and Hooper, F.C., 1987, Stochastic modelling of the angular distribution of the diffuse radiance, *In Proceedings of 10th Biennial Congress of the International Solar Energy Society*, Hamburg, Germany, September 13-18, 3760-3767.

Siala, F.M.F. and Hooper, F.C., 1989, A semi-empirical model for the directional distribution of the diffuse sky radiance, *In Renewables - A Clean Energy Solution, Solar Energy Society of Canada Incorporation*, Ottawa, 322-326.

Simpson, J.J, Jin, Z., Stitt, J.R., 2000, Cloud shadow detection under arbitrary viewing and illumination conditions, *IEEE Transactions on Geoscience and Remote Sensing*, **38**, 2, 972-976.

Simpson J.J. and Stitt, J.R., 1998, A procedure for the detection and removal of cloud shadoe from AVHRR data over land, *IEEE Transactions on Geoscience and Remote Sensing*, **36**, 880-897.

Singh, A. and Harrison, A.R., 1985, Standardised principal components, *International Journal of Remote Sensing*, **6**, 883-896.

Singh, S.M., 1992, Fast atmospheric correction algorithm, *International Journal of Remote Sensing*, **13**, 933-938.

Singh, S.M., 1988, Estimation of multiple reflection and lowest order adjacency effects on remotely-sensed data, *International Journal of Remote Sensing*, **9**, 1433-1450.

Slater, P.N., 1980, Remote Sensing; Optics and optical systems, Addison-Wesley Publishing Company, Reading, Massachusetts, 575p.

Slater, P.N., 1985, Radiometric considerations in remote sensing, *Proceedings of the IEEE*, **73**, 997-1011.

Slater, P.N., 1984, The importance and attainment of accurate absolute radiometric calibration, *In Proceedings of the Society of Photo-Optical Instrumentation Engineers*, **475**, 34-40.

Smith, G.M. and Milton, E.J., 1999, The use of the empirical line method to calibrate remotely sensed data to reflectance, *International Journal of Remote Sensing*, **22**, 11-37.

Sokal, R.R. and Rohlf, F.J., 1995, Biometry: The principles and practice of statistics in biological research, 3rd Edition, *W.H. Freeman and Company*, New York, 887p.

Song, C., Woodcock, C.E., Seto, K.C., Lenney, M.P., Macomber, S.A., 2001, Classification and change detection using Landsat TM data: When and how to correct atmospheric effects?, *Remote Sensing of Environment*, **75**, 230-244.

Spanner, M.A., Pierce, L.L., Peterson, D.L., Running, S.W., 1990, Remote sensing of temperate coniferous forest leaf area index: the influence of canopy closure, understory

vegetation and background reflectance, *International Journal of Remote Sensing*, **11**, 95-111.

Spectral Imaging Ltd, 2003, http://www.specim.fi/, Accessed in 30/8/03.

Staenz, K. and Itten, K.I., 1982, Reflective properties of asphalt and concrete surfaces, Proceedings of the International Symposium of the ISPRS, WG-VII, Toulouse, France, 307-316.

Steven, M.D., 1977, Standard distribution of clear sky radiance, Quarterly Journal of the Royal Meteorological Society, **103**, 457-465.

Steven, M.D., Moncrieff, J.B., Mather, P.M., 1984, Atmospheric attenuation and scattering determined from multiheight multispectral scanner imagery, *International Journal of Remote Sensing*, **5**, 733-747.

Steven, M.D., and Rollin, E.M., 1986. Estimation of atmospheric corrections from multiple aircraft imagery. *International Journal of Remote Sensing*, **7**, 481-497.

Steven, M.D. and Unsworth, M.H., 1979, The angular distribution and Interception of diffuse solar radiation below overcast skies, Quarterly Journal of the Royal Meteorological Society, **106**, 57-61.

Stow, D.A., Burns, B.H., Hope, A.S., 1993, Spectral, spatial and temporal characteristics of Arctic Tundra reflectance, *International Journal of Remote Sensing*, **14**, 2445-2462.

Stowe, L.L., 1984, Evaluation of Nimbus-7 THIR/CLE and Air Force three-dimensional nephanalysis estimates of cloud amount, *Journal of Geophysical Research*, **89**, 5370-5380.

Strahler, A. H., 1994, Vegetation canopy reflectance modeling-recent developments and remote sensing perspectives, *In Proceedings of the Sixth International Symposium on Physical Measurements and Spectral Signatures, CNES/ISPRS*, Val d'Isere, France, 17-21 January, 593-600.

Strangeways, I., 2000, Measuring the natural environment, *Cambridge University Press*, Cambridge, 365p.

Sullivan, J.J. and Quimby, B.D., 1990, Characterisation of a computerised photodiode array spectrometer for gas chromatography – Atomic emission spectrometry, *Analytical Chemistry*, **62**, 1034-1043

Sun, Y.-Y. and Minnett, P.J., 1984, Removal of atmospheric effects in the remote sensing of ocean colour using measurements at two zenith angles, *In Proceedings of the 10th Anniversary International Conference of the Remote Sensing Society*, Reading, 1984.

Tanré, D., Deroo, C., Duhaut, P., Herman, M., Morcette, J.J., Perbos, J., Deschamps, P.Y., 1990, Description of a computer code to simulate the satellite signal in the solar spectrum: the 5S code, *International Journal of Remote Sensing*, **11**, 659-668.

Tanré, D., Deschamps, P.Y., Duhaut, P., Herman, M., 1987, Adjacency effect produced by the atmospheric scattering in Thematic Mapper data, *Journal of Geophysical Research*, **92**, 12000-12006.

Tanré, D., Herman, M., Deschamps, P.Y., 1981, Influence of the background contribution on space measurements of ground reflectance, *Applied Optics*, **20**, 3676-3684.

Tanré, D., Holben, B.N., Kaufman, Y.J., 1992, Atmospheric correction algorithm for NOAA-AVHRR products, theory and application, *IEEE Transactions on Geoscience and Remote Sensing*, **30**, 231-248

Teillet, P.M., 1986, Image correction for radiometric effects in remote sensing, *International Journal of Remote Sensing*, **7**, 1637-1651.

Teillet P.M. and Fedosejevs, G., 1995, On the dark target approach to atmospheric correction of remotely sensed data, *Canadian Journal of Remote Sensing*, **21**, 373-387.

Teillet, P.M., Staenz, K., Williams, D.J., 1997, Effects of spectral, spatial, and radiometrix characteristics on remote sensing vegetation indices of forested regions, *Remote Sensing of Environment*, **61**, 1, 139-149.

Tompkins, S., Mustard, J.F., Pieters, C.M., Forsyth, D.W., 1997, Optimization of Endmembers for Spectral Mixture Analysis, *Remote Sensing of Environment*, **59**, 472-489.

Townshend, J.R.G., Justice, C.O., Kalb, B., 1987, Characterisation and classification of South American land cover types using satellite data, *International Journal of Remote Sensing*, **8**, 1189~1207.

Townshend, J.R.G., Justice, C.O., Skole, D., Malingreau, J.P., Cihlar, J., Tiellet, P.M., Sadowski, F., Ruttenberg, S., 1994, The 1km resolution global data set: needs of the International Geosphere Biosphere Programme, *International Journal of Remote Sensing*, **15**, 3417-3442.

Tucker, C.J., 1977, Asymptotic nature of grass canopy spectral reflectance, *Applied Optics*, **16**, 1151-1156.

Tucker, C.J., Newcomb, W.W., Los, S.O., 1991, Mean and inter-year variation of growing-season Normalized Difference Vegetation Index for the Sahel 1981-1989, *International Journal of Remote Sensing*, **12**, 1133-1135.

Tucker, C., Townshend, J., Goff, T., 1985, African land-cover classification using satellite data, Science, Vol.227, **4685**, 369-375.

USGS, 2002, Landsat Program Website, http://landsat7.usgs.gov/index.php, Assessed in 02/04/03.

Valley, S.L., 1965, Handbook of geophysics and space environments, *Air Force Cambridge Research Laboratory*, Bedford, Massachusetts.

Vandermeer, F., 1994, Extraction of mineral absorption fetures from high-spectral resolution data using non-parametric geostatistical techniques, *International Journal of Remote Sensing*, **15**, 2193-2214.

Van der Meer, F., De Jong, S., Bakker, W., 2001, Imaging spectrometry: Basic analytical techniques, *In Imaging Spectrometry: Basic Principles and Prospective Applications, van der Meer, F. and De Jong, S. (Ed), Kluwer Academic Publications, Remote Sensing and Digital Image Processing*, Vol 4, the Netherlands

Van Stokkom, H.T.C. and Guzzi, R., 1984, Atmospheric spectral attenuation of airborne remotely-sensed data, Comparison between experimental and theoretical approach, *International Journal of Remote Sensing*, **5**, 925-938.

Vane, G., and Goetz, A.F.H., 1993, Terrestrial imaging spectrometry: Current status, future trends, *Remote Sensing of Environment*, **44**, 117-126.

Vane, G., Green R.O., Chrien, T.G., Enmark, H.T., Hansen, E.G., Porter, W.M., 1993, The Airborne Visible/Infrared Imaging Spectrometer (AVIRIS), *Remote Sensing of Environment*, **44**, 127-143.

Vartiainen, E., 2000, A new approach to estimating the diffuse irradiance on inclined surface, Renewable Energy, **20**, 45-64.

Veefkind, J.P., de Leeuw, G.D., Durkee, P.A., 1998, Retrieval of aerosol optical depth over land using two-angle view satellite radiometry during TARFOX, *Geophysics Research Letter*, **25**, 3135-3138.

Veefkind, J.P., de Leeuw, G.D., Stammes, P., Koelemeijer, R.B.A., 2000, Regional distribution of aerosol over land, derived from ATSR-2 and GOME, *Remote Sensing of Environment*, **74**, 377-386.

Vermote, E., Tanré, D., Deuze, J.L., Herman, M., Morcrette, J.J., 1997, Second Simulation of the Satellite Signal in the Solar Spectrum (6S), *6S User Guide Version 2*, 218p.

Verstraete, M.M., Pinty, B., Curran, P.J., 1996, MERIS potential for land applications, *International Journal of Remote Sensing*, **20**, 1747-1756.

Verstraete, M.M., Pinty, B., Dickinson, R.E., 1990, A physical model of the bidirectional reflectance of vegetation canopies: 1. Theory, *Journal of Geophysical Research*, **95**, 11755-65.

Vincent, R.K., Pleitner, P.K., Wilson, M.L., 1984, Integration of airborne Thematic Mapper and thermal infrared multispectral scanner data for lithologic and hydrothermal alteration mapping, *In Proceedings of International Symposium on Remote Sensing, Third Thematic Conference, Remote Sensing for Exploration Geology*, Ann Arber, Environmental Research Institute of Michigan, 219-226.

Viovy, N, Arino, O., Belward, A.S., 1992, The best index slope extraction (BISE): A method for reducing noise in NDVI-time series, *International Journal of Remote Sensing*, **8**, 1585-1590.

Walthall, C.L., Norman, J.M., Welles, J.M., Campbell, G., Blad, B.L., 1985, Simple equation to approximate the bidirectional reflectance from vegetative canopies and bare soil surfaces, *Applied Optics*, **24**, 383-387.

Walsh, J.W., 1961, The science of daylight, *MacDonald, London.*

Wanner, W., Li, X., Strahler, A., 1995, On the derivation of kernels for kernel-driven models of bidirectional reflectance, *Journal of Geophysical Research*, **100**, 21,077-21,089.

Wardley, N.W. and Curran, P.J., 1984, The estimation of green-leaf-area index from remotely sensed airborne multispectral scanner data, *International Journal of Remote Sensing*, **5**, 671-679.

Wang B., Ono, A., Muramatsu, K., Fujiwara, N., 1999, Automated detection and removal of clouds and their shadows from Landsat TM images, *IEICE Transactions on Information and System*, **E82-D**, 453-460.

Weiser, R.L., Asrar, G., Miller, G.P., Kanemasu, E.T., 1986, Assessing grassland biophysical characteristics from spectral measurements, *Remote Sensing of Environment*, **20**, 141-152.

Weiss, T.A. and Löf, G.O.G., 1980, The estimation of daily, clear sky, collar radiation intercepted by tilted surface, *Solar Energy*, **24**, 287-294.

Wilson, A.K., 1988, The critical dependence of remote sensing on sensor calibration and atmosphere transparency, *In Proceedings of the NERC 1987 Airborne Campaign Workshop*, NERC, Swindon, UK, 29-58.

Wilson, A.K., 1995, NERC Scientific Services Airborne Remote Sensing Facility User Guide, *Natural Environment Research Council*, p.72.

Winter, E.M., 2001, Hyperspectral array sensors: Moving beyond the pretty picture, *In Proceedings of the Fifth International Airborne Remote Sensing Conference and Exhibition*, San Francisco, California, CD-Rom.

Woolley, J.T., 1971, Reflectance and transmittance of light by leaves, *Plant Physiology*, **47**, 656-662.

Wu, D., Yin, Y., Wang, Z., Gu, X., Verbrugghe, M., Guyot, G., 1997, Radiometric characterisation of Dunhuang satellite calibration test site, *Physical Measurements and Signatures in Remote Sensing, Guyot and Pulpin (eds)*, 151-159.

Zagolski, F. and Gastellu-Etchegorry, J.P., 1995, Atmospheric corrections of AVIRIS images with a procedure based on the inversion of the 5S model, *International Journal of Remote Sensing*, **16**, 3115-3146.

Zagolski, F., O'Neill, N.T., Royer, A., 2000, CESL Project: L2 evaluation of MERIS atmospheric correction algorithms for land: Validation of a DDV-based aerosol retrieval algorithm for atmospheric corrections, http://www.callisto.si.usherb.ca/~noneill/CESL_exec.htm, Assessed in 29/09/03.